Problèmes inverses et résonances locales dans les guides d'ondes mécaniques irréguliers

Angèle Niclas

To cite this version:

Angèle Niclas. Problèmes inverses et résonances locales dans les guides d'ondes mécaniques irréguliers. Autre. Université de Lyon, 2022. Français. NNT : 2022LYSEC026 . tel-03813494

HAL Id: tel-03813494
https://theses.hal.science/tel-03813494v1

Math ICJ
Institut
Camille
Jordan
Laboratoire de recherche en mathématiques Lyon/Saint-Étienne

Inverse problems and local resonances in irregular mechanical waveguides

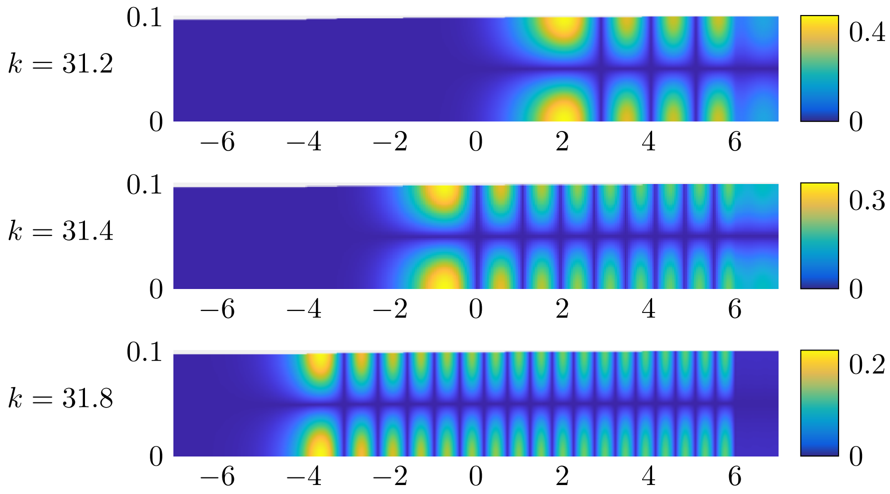

Angèle Niclas

Thèse de doctorat

ÉCOLE
CENTRALE LYON

Numéro d'ordre NNT : 2022LYSEC026

THÈSE de DOCTORAT DE L'UNIVERSITÉ DE LYON
opérée au sein de l'École centrale de Lyon

École Doctorale 512
École Doctorale InfoMaths

Spécialité de doctorat : Mathématiques et applications
Discipline : Mathématiques

Soutenue publiquement le 8 juillet 2022 par

Angèle NICLAS

Problèmes inverses et résonances locales dans les guides d'ondes mécaniques irréguliers

---

Devant le jury composé de :

Sonia Fliss	Professeur, ENSTA Paris	Présidente du jury
Fioralba Cakoni	Distinguished Professor, Rutgers University	Rapporteure
Yves Capdeboscq	Professeur des universités, Université Paris Cité	Rapporteur
Camille Carvalho	Maître de conférences, INSA de Lyon	Examinatrice
Claire Prada	Directrice de recherche au CNRS, ESPCI Paris	Examinatrice
Éric Soccorsi	Maître de conférences, Aix-Marseille Université	Examinateur
Laurent Seppecher	Maître de conférences, École Centrale de Lyon	Encadrant de thèse
Grégory Vial	Professeur des universités, École Centrale de Lyon	Directeur de thèse
Éric Bonnetier	Professeur des universités, Université Grenoble Alpes	Invité, Co-directeur

Abstract

Localization and reconstruction of defects in waveguides are crucial in the non-destructive industrial health monitoring of structures like pipelines, optics fibers, nuclear power plant conduits, or even ship hulls. This thesis aims at understanding wave propagation in irregular waveguides from a mathematical point of view to design new efficient methods to detect and reconstruct possible imperfections or defects in waveguides. Our approach is based on already existing experimental setups. One usually generates many waves propagating at different frequencies in the waveguide and measures their wavefields to get information about the defects. The use of multi-frequency measurements helps not only to localize but also to reconstruct the shape of the defect.

This manuscript develops two different multi-frequency inversion methods applicable to acoustic and elastic waveguides. The first method analyzes the scattered field generated by a known incident field. Choosing frequencies away from the set of cut-off frequencies associated with the waveguide, a Born approximation is performed to reduce the inverse problem to a Fourier inversion with partial frequency data. The second method uses a different approach: instead of avoiding cut-off frequencies, we chose to take advantage of them to obtain the reconstruction. Adapting former studies of the Schrödinger equation, we can approach the wavefield propagation at locally resonant frequencies. This approximation enables us to find a nonlinear yet exploitable link between the defect profile and the wavefield measurements.

The first part of this manuscript is focused on defects reconstruction in two or three dimensional acoustic or elastic waveguides using multi-frequency scattered data. Before studying the inverse problem, one must first understand the forward problem fully. In the time-harmonic regime, an acoustic wavefield u satisfies the Helmholtz equation

$$\Delta u + k^2 u = s, \tag{1}$$

where k stands for the frequency, and s is a source of waves. Similarly, an elastic wavefield $\boldsymbol{u}$ satisfies the elastic equation

$$\nabla \cdot \boldsymbol{\sigma}(\boldsymbol{u}) + \omega^2 \boldsymbol{u} = s, \tag{2}$$

where ω stands for the frequency and $\boldsymbol{\sigma}(\boldsymbol{u})$ is the stress tensor depending on the Lamé coefficients of the material. In those two waveguides, wavefields can be decomposed as a sum of modes in each waveguide's slice, leading to a similar treatment of both problems.

We focus on the inversion of three main types of defects: a local inhomogeneity in the waveguide, a bend of the waveguide, and a localized defect in the geometry of the waveguide. A controlled source generates wavefields for some frequencies $k \in K \subset \mathbb{R}_+$, and we assume the knowledge of the corresponding measurements $u(\boldsymbol{x})$ for every $\boldsymbol{x} \in \Sigma$ where Σ is either a section or a surface of the waveguide.

The strategy to study the impact of small geometrical defects is to provide a well-suited mapping from the perturbed waveguide to a perfect waveguide that generates some changes in the equation itself. Assuming that the defects are small in amplitude and support, we can simplify these equations using a Born approximation. Theoretical justifications of the Born approximation require controlling the norm of any wavefield by the norm of the known source that generated it. If this control is easily obtained in the acoustic case, it proves more tricky in the elastic case and requires an extensive study of the inhomogeneous Lamb modes. Then, through the reconstruction of their source term, we can recover the Fourier transform of the defects. An essential difficulty is that low spatial frequency information carried by vanishing modes is systematically missing. Assuming some regularity and compacity, we proved a key result to control the recovery error of a function from an incomplete knowledge of its Fourier transform.

This work provides a theoretical stability argument to run a mode-by-mode well-conditioned inversion using a penalized least-square technique. This method was tested on data generated by finite element methods and proved numerically efficient in getting great reconstructions of the different considered defects.

This manuscript's second part is dedicated to defects reconstruction using locally resonant frequencies. The previous method used a Born approximation to simplify the equation satisfied by the wavefield. This approximation is only valid if the frequency is far from the cut-off frequencies, where both elastic and acoustic problems are known to be ill-conditioned. However, different physical experiments prove that waves propagating at these peculiar frequencies are very sensitive to the presence of defects, making it a great potential inversion tool. We aim to explain this phenomenon and develop a new reconstruction method based on locally resonant frequencies.

Assuming that the waveguide is slowly varying, we study the propagation of wavefields using a Wentzel-Kramers-Brillouin approximation combined with former results on the Schrödinger equation near turning points. We prove that near locally resonant frequencies, wavefields can be expressed using modified Airy functions and that defects act like obstacles that stop the wave propagation and reflect it to the source.

Our strategy to reconstruct the defects is then based on this observation. The coordinate of this virtual obstacle is called the locally resonant point, and we know the local waveguides width at this point. Using wavefield measurements, we can track the displacement of the locally resonant point with respect to the frequency, which provides a high-sensibility inverse method to reconstruct defects. This method is numerically efficient and can be applied to recover different shapes of slowly varying defects. This method is tested numerically for locally resonant frequencies in acoustic waveguides and for longitudinal, transverse, and zero-group velocity critical frequencies in elastic waveguides. In each case, it produces extremely precise reconstructions of width variations.

Keywords: waveguides, inverse problems, non-destructive testing, wave propagation, mutli-frequency data, Helmholtz equation, elastic displacement equation, locally resonances.

Résumé

La détection et la reconstruction de défauts dans les guides d'ondes sont un enjeu contemporain important pour contrôler l'état de structures diverses allant des oléoducs aux fibres optiques, en passant par les conduits de centrales nucléaires ou les coques de navires. Cette thèse a pour but de mieux comprendre d'un point de vue mathématique la propagation des ondes en guide d'onde irrégulier, pour pouvoir ensuite proposer des méthodes efficaces pour détecter et reconstruire avec précision déventuels défauts. Notre approche se base sur des dispositifs physiques déjà existants où, pour détecter ces défauts, plusieurs ondes se propageant à différentes fréquences sont envoyées dans le guide d'onde puis mesurées pour obtenir de l'information sur le défaut. L'usage de données multi-frequencielles est ici particulièrement important et permet non seulement de localiser les défauts, mais aussi de reconstruire leur forme.

Ce manuscrit développe deux méthodes de reconstruction multi-frequencielles s'appliquant à la fois aux guides acoustiques et élastiques. La première méthode se base sur l'analyse du champ réfléchi par une onde incidente connue. En choisissant des fréquences éloignées des fréquences de résonance du guide d'onde, il est possible d'effectuer une approximation de Born pour réduire le problème à une inversion de Fourier avec données partielles. La deuxième méthode, au lieu d'éviter les fréquences de résonance, les utilise pour obtenir la reconstruction. En s'inspirant de résultats sur l'équation de Schrödinger, nous avons proposé une approximation des ondes se propageant aux fréquences résonnantes. Cette approximation permet d'exhiber non linéaire mais exploitable entre le défaut et les mesures de l'onde.

La première partie du manuscrit présente en détail la méthode utilisée pour reconstruire des défauts dans des guides acoustiques ou élastiques de dimension deux ou trois grâce aux mesures multi-frequencielles du champ réfléchi. Avant d'étudier le problème inverse, il est indispensable de s'intéresser au problème direct pour comprendre comment les ondes se propagent dans un guide d'onde. En régime harmonique, une onde acoustique u vérifie l'équation de Helmholtz

$$\Delta u + k^2 u = s, \tag{3}$$

où k est la fréquence de propagation et s la source générant les ondes. De même, un champ de déplacement élastique $\boldsymbol{u}$ vérifie l'équation du déplacement élastique

$$\nabla \cdot \boldsymbol{\sigma}(\boldsymbol{u}) + \omega^2 \boldsymbol{u} = s, \tag{4}$$

où ω est la fréquence de propagation et $\boldsymbol{\sigma}(\boldsymbol{u})$ est le tenseur de contrainte dépendant des coefficients de Lamé du matériau. Dans ces deux situations, les ondes peuvent se décomposer comme des sommes de modes sur chaque tranche du guide ce qui permet d'étudier les deux problèmes de manière très similaire.

Nous nous concentrons dans cette partie sur la reconstruction de trois types de défauts : une perturbation locale de l'indice du milieu de propagation, un coude dans le guide d'onde, et un défaut dans la géométrie du guide. Dans chacun des cas, une source génère une onde se propageant à une fréquence $k \in K \subset \mathbb{R}_+$ et des mesures du champ $u(\boldsymbol{x})$ sont effectuées pour $\boldsymbol{x} \in \Sigma$ où Σ désigne une section ou une surface du guide d'onde.

Pour étudier l'impact des petits défauts, nous choisissons de transformer le guide endommagé en un guide parfait grâce à un changement de variable, ce qui génère des modifications dans l'équation de propagation. Si les défauts sont petits en taille et en amplitude, ces équations peuvent être simplifiées avec une approximation de Born. Pour justifier cette approximation, il est nécessaire de contrôler la norme de toute onde par la norme de la source qui l'a généré. Si ce contrôle peut être facilement obtenu dans le cas acoustique, il est plus délicat à obtenir dans le cas élastique et nécessite une étude poussée des modes de Lamb inhomogènes. Après simplification des équations, nous avons prouvé qu'il était possible d'obtenir une approximation de la transformée de Fourier du défaut en mesurant les ondes réfléchies. Cependant, certaines basses fréquences transportées par les modes évanescents ne sont pas mesurables, ce qui rend l'inversion de Fourier difficile. En ajoutant des hypothèses de régularité et de compacité, nous avons démontré qu'il était possible de contrôler l'erreur de reconstruction d'une fonction à partir d'une connaissance incomplète de sa transformée de Fourier.

Ce travail permet de prouver la stabilité de la méthode d'inversion que nous proposons qui reconstruit mode par mode la transformée de Fourier en minimisant des moindres carrés pénalisés. Cette méthode a été testée sur des données générées par éléments finis et s'avère particulièrement efficace pour reconstruire les différents défauts évoqués plus tôt.

La seconde partie de la thèse est dédiée à la reconstruction des défauts grâce aux fréquences de résonance. Si la méthode précédente utilisait une approximation de Born pour simplifier les équations, cette technique n'est pas applicable près des fréquences de résonances où les problèmes élastiques et acoustiques sont réputés mal conditionnés. Malgré tout, de nombreuses expériences physiques montrent que les ondes se propageant aux fréquences de résonances sont particulièrement sensibles aux défauts présents dans le guide d'onde, ce qui en fait un outil intéressant pour reconstruire les défauts. Ainsi, nous avons cherché à expliquer ce phénomène et à developper une nouvelle méthode de reconstruction utilisant ces fréquences particulières.

En supposant que le guide d'onde présente des défauts de formes variant lentement, nous avons étudié la propagation des ondes grâce à une approximation de Brillouin-Kramers-Wentzel combinée avec d'anciens résultats sur le comportement des solutions de l'équation de Schrödinger près des points de retournement. Nous avons ainsi prouvé que près des fréquences localement résonantes, les ondes peuvent s'exprimer à l'aide de fonctions d'Airy modifiées et que les défauts agissent comme des obstacles stoppant la propagation de l'onde et la réfléchissant en direction de la source.

La stratégie que nous avons développée pour reconstruire le défaut se base sur cette observation. La coordonnée de l'obstacle virtuel est appelée le point de résonance locale, et la hauteur locale du guide d'onde en ce point est connue. En utilisant les mesures de l'onde, on peut suivre le déplacement de ce point de résonance locale quand la fréquence change, ce qui fournit une méthode très précise de reconstruction des variations lentes de hauteur des guides d'onde. Cette méthode a été testée numériquement aux fréquences localement résonantes en guides acoustiques et aux fréquences critiques longitudinale, transverses et à vitesse de groupe nulle des guides élastiques. Dans chacun des cas, les reconstructions des variations de hauteur sont extrêmement précises.

Mots-Clefs : guides d'ondes, problèmes inverses, contrôle non destructif, propagation des ondes, données multi-fréquencielles, équation de Helmholtz, équation du déplacement élastique, résonances locales.

Contents

Essential notations

Variables

Ω	Considered waveguide
Ω_r	Waveguide truncated for $\lvert x\rvert < r$.
$\partial\Omega$	Boundary of the waveguide
$\partial\Omega_{\mathrm{top}}$	Top boundary of the waveguide
$\partial\Omega_{\mathrm{bot}}$	Bottom boundary of the waveguide
h	Width of the waveguide
ν	Unit outer normal vector to the boundary
u	Wavefield in acoustic waveguides
u^{inc}	Incident wavefield
u^s	Scattered wavefield
$\boldsymbol{u}$	Wavefield in elastic waveguides
$\boldsymbol{\sigma}(\boldsymbol{u})$	Stress tensor
k, ω	Frequency
k_n	n-th wavenumber
δ	Distance between a frequency and the set of all the wavenumbers
η	Small parameter which control the variation of the waveguide width
N	Index of a locally resonant mode
$x^\star$	Locally resonant coordinate
d	Measured data
$a : b : m$	Discretization of the interval $[a, b]$ with m points
$\mathrm{mod}(\pi)$	Modulus π
$B_n(0, r)$	Ball of radius r centered at 0 in n-dimensions

Functional spaces

L^∞, L^1, L^2	Usual Lebesgue spaces on piecewise smooth domains
$\mathrm{W}^{1,1}$	Usual Sobolev space on piecewise smooth domains
H^1, H^2, H^3	Usual Hilbert Sobolev spaces on piecewise smooth domains
$\mathrm{H}^{1/2}$, $\mathrm{H}^{3/2}$	Usual fractional Hilbert Sobolev spaces on piecewise smooth domains
$\widetilde{\mathrm{H}}^{1/2}(-r, r)$	Closure of the distributions supported in $(-r, r)$ for the $\mathrm{H}^{1/2}$ norm (see [66])
$V_{\mathrm{loc}}(E)$	Functions f such that for all compact set $C \subset E, f \in V(C)$
$\lVert\mathcal{S}\rVert_{E_1,E_2}$	Operator norm defined by $\sup\{\lVert\mathcal{S}(x)\rVert_{E_2} \,\vert\, x \in E_1,\ \lVert x\rVert_{E_1} = 1\}$

Functions

$\mathrm{supp}(f)$	Support of the function f
ϕ	Mapping of a deform waveguide to a regular waveguide

φ_n	n-th acoustic mode
$(\boldsymbol{X}_n, \mathbf{Y}_n)$	n-th right-going Lamb mode
$\langle\cdot,\cdot\rangle$	Canonical $\mathbb{R}$-scalar product in L^2
J_n	Scalar product $\langle \boldsymbol{X}_n, \mathbf{Y}_n\rangle$
δ_s	Dirac distribution at the coordinate s
$\delta_{n=m}$	Function equal to 1 if $n = m$ and 0 otherwise
$\mathbf{1}_E$	Indicator function of the set E
f^{app}	Approximation of a function f
f^{top}	Function f defined on $\partial\Omega_{\mathrm{top}}$
f^{bot}	Function f defined on $\partial\Omega_{\mathrm{bot}}$
$\mathcal{F}(f)(\xi)$	Fourier transform of f at frequency ξ
G_n	Green function of the n-th mode
$\mathcal{A}$	Airy function of the first kind (see Figure 1)
$\mathcal{B}$	Airy function of the second kind (see Figure 1)
$H_0^{(1)}$	Hankel function of the first kind (see Figure 2)

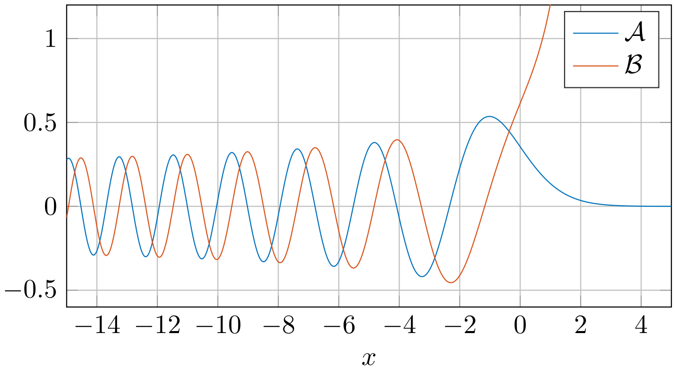

Figure 1 – Representation of the Airy functions $\mathcal{A}$ and $\mathcal{B}$ solutions of the equation $y'' + xy = 0$. More details can be found in [4, 78].

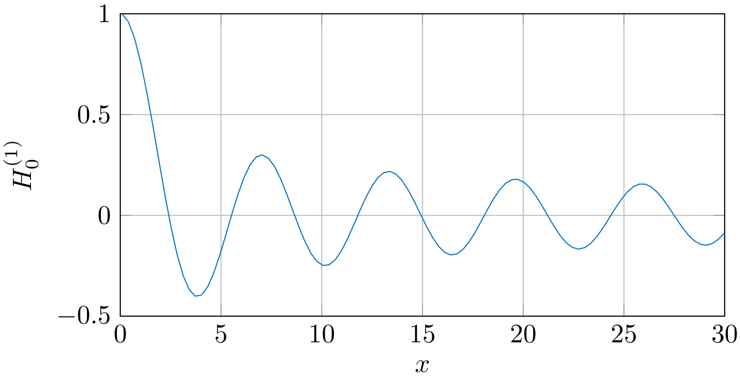

Figure 2 – Representation of the Hankel function of the first kind $H_0^{(1)}$ solution of the equation $x^2y'' + xy + x^2y = 0$. More details can be found in [4].

1

Introduction

This thesis focuses on developing new mathematical tools to monitor waveguides, which are vastly used in industry. Acoustic waveguides are good representations of structures like air ducts [71], pipes [101], ear canals [98], or even shallow water [39]. Optical waveguides may be the most famous and depict optical fibers [96, 45], dielectric materials [35], or conductive metal pipes [57].

We also consider elastic waveguides that model metal plates [48], boat hulls [83], bridges [109] or train tracks [74] for instance.

In this manuscript, we are interested in two major industrial issues. The first one is to understand how waves generated by known sources propagate in perfect or damaged waveguides at a given frequency. This issue is fundamental for evaluating the stress endured by any material during its lifetime or predicting and improving buildings' robustness [63]. The second issue relates to non-destructive control of structures: using known sources generating waves in the waveguide, one wants to detect, localize, and reconstruct possible defects [105].

In order to numerically compute the propagation of waves in waveguides, industrial usually use discretization methods and computation software [74, 62, 41, 87]. However, these kinds of numerical approach have a substantial computational cost, and one simulation on a three-dimensional waveguide can take more than one day to run [68, 69]. There is a high demand for simpler and faster codes modeling the propagation of waves and taking into account the very particular structures of waveguides. Some propagation phenomena, such as propagation near corners or at resonant frequencies, are also not yet completely understood and need to be studied in detail [87, 10].

Similarly to non-destructive control of structures, pipes and plates usually need to be inspected in production lines to detect potential defects or characterize the robustness and dimensions of the material without deteriorating it [105]. We represent in Figure 1.1 such non-destructive health monitoring. In the nuclear, chemical, or aeronautic industry, pipes and plates must be regularly checked to detect defects and avoid severe consequences [1]. Especially, there is a great need to develop precise non-destructive methods to study and fix pipes corrosion defects in French nuclear power plants in order to keep operational power stations [86].

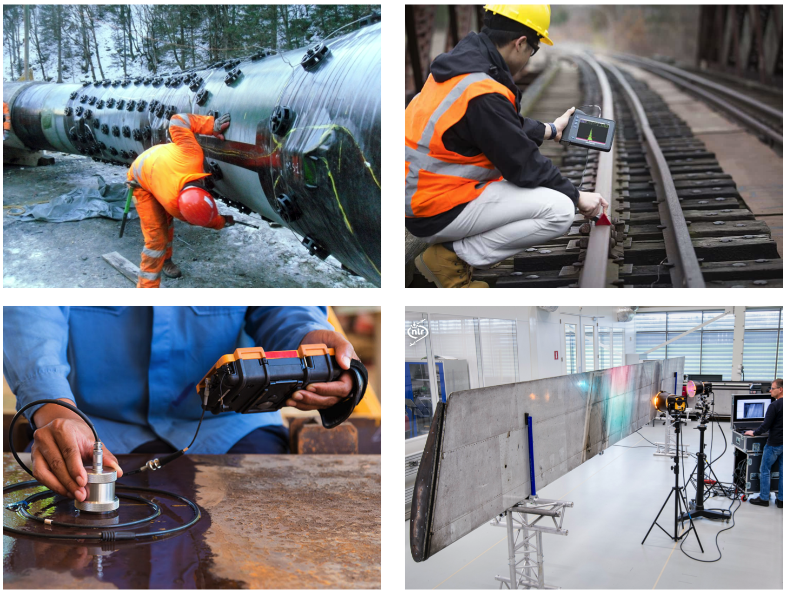

Figure 1.1 – From [89, 106, 108]: Practitioners non-destructive health monitoring of waveguides. Top left: monitoring of a pipeline. Top right: monitoring of train tracks. Bottom left: monitoring of a metal plate. Bottom right: monitoring of a large aircraft part.

This manuscript will provide partial answers to these issues. In the following, we briefly present the general mathematical framework used in the thesis and recall some of the available tools and methods already developed in this context. It will then enable us to put into perspective the main contributions of this thesis, which will be summarized and simplified here before being fully developed in the body of the manuscript.

1.1 Wave propagation in waveguides

To detect and reconstruct defects in waveguides, one usually generates multiple waves that propagate in the waveguide and carry useful information about the possible imperfections. Here, we work with two types of waves: acoustic and elastic waves. Usually, the study of acoustic waves is more straightforward than that of elastic waves. Besides being of interest in itself, the acoustic case is often used to intuit the results before reproducing them in the elastic case. We describe the acoustic and elastic mathematical frameworks below and point out the links that connect them.

1.1.1 Acoustic wave equation

1.1.1.a Acoustic waveguides

Acoustic and electromagnetic wavefields U propagating in a domain $\Omega \subset \mathbb{R}^3$ satisfy the normalized scalar wave equation

$$\partial_{tt} U(t, \boldsymbol{x}) = \Delta U(t, \boldsymbol{x}) + S(t, \boldsymbol{x}) \quad \text{in } \Omega, \tag{1.1}$$

where S is a source of waves. In most physical situations, variables of S can be separated and S is written $S(t, \boldsymbol{x}) = s(\boldsymbol{x}) f(t)$ where s stands for the physical position of the source (antennas, loud speaker, transducers...) and f represents the emitted time signal. We look for solutions in the frequency domain and consider the time signal under a Fourier decomposition of the form

$$f(t) = \int_{\mathbb{R}} F(k) e^{-ikt} \mathrm{d}k. \tag{1.2}$$

We then look for solutions of (1.1) under the form

$$U(\boldsymbol{x}, t) = \int_{\mathbb{R}} u(\boldsymbol{x}, k) e^{-ikt} \mathrm{d}k. \tag{1.3}$$

At a fixed frequency $k \in \mathbb{R}_+$, we can prove that the wavefield u is solution of the so-called Helmholtz equation

$$\Delta u + k^2 u = -F(k) s \quad \text{in } \Omega. \tag{1.4}$$

We refer to the book [40] for more details about the wave equation and the transformation to the Helmholtz equation. Given the equivalency between the temporal regime and the harmonic one, we only consider the Helmholtz equation and from now on, every acoustic wavefield satisfies (1.4) for a frequency $k > 0$.

Since we aim to reconstruct defects in waveguides, we choose to work in acoustic waveguides such as pipes, and the domain Ω is defined as the three dimensional set

$$\Omega = \mathbb{R} \times B_2(0, h) \subset \mathbb{R}^3. \tag{1.5}$$

The parameter h stands for the width of the waveguide. If the waveguide does not have any defect, h is a constant in $\mathbb{R}_+^*$ and the waveguide is called regular or perfect. Due to the different symmetries seen in the definition of Ω, people often consider the propagation of waves in sections of Ω, which simplify all the conducted studies [59, 104, 6]. It boils down to the analysis of the two-dimensional waveguide

$$\Omega = \mathbb{R} \times (-h, h). \tag{1.6}$$

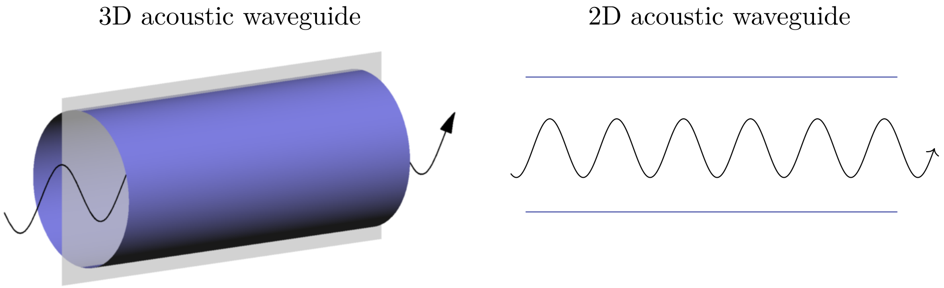

Figure 1.2 – Representation of regular acoustic waveguides in three and two dimensions. Acoustic waves propagate in the pipe according to the Helmholtz equation (1.4). Here, the three-dimensional waveguide is cut along the grey plan to get the two-dimensional waveguide.

We represent in Figure 1.2 acoustic waveguides in three and two-dimensional cases, as well as examples of waves propagation in these structures.

To get a well-posed Helmholtz equation, we need to add boundary conditions. Three types of boundary conditions are usually considered:

- The Dirichlet boundary condition, written $u = b$ on $\partial\Omega$, imposes a given wavefield b on the waveguide boundaries.
- The Neumann boundary condition, written $\partial_\nu u = b$ on $\partial\Omega$, imposes a strength b on the waveguide boundaries.
- The Robin boundary condition, written $au + \partial_\nu u = b$ on $\partial\Omega$ with $a \in \mathbb{R}^*$, is a mix between a Dirichlet condition and a Neumann condition. It can be seen as a strength b imposed on boundaries combined with frictions contained in the term au.

In this manuscript, we choose to use Neumann boundary conditions exclusively. When the boundary source term b vanishes, it models a waveguide free from constraints in a surrounding environment like air. However, the use of Dirichlet or Robin conditions would only change minor calculation steps, and the results exposed in this manuscript are valid for any of these three types of boundary conditions.

1.1.1.b Acoustic modal decomposition

The Helmholtz equation is easier to study in waveguides than in free space thanks to the existence of a modal decomposition. In acoustic pipes, any coordinate $\boldsymbol{x} \in \Omega$ can be rewritten as $\boldsymbol{x} = (x, \boldsymbol{y})$ where $x \in \mathbb{R}$ and $\boldsymbol{y} \in \Sigma := (-h, h)$ in two dimensions or $\boldsymbol{y} \in \Sigma := B_2(0, h)$ in three dimensions. We can prove that the wavefield u can be decomposed as a sum of modes

$$u(x, \boldsymbol{y}) = \sum_{n\in\mathbb{N}} u_n(x)\varphi_n(\boldsymbol{y}) \qquad \forall (x, \boldsymbol{y}) \in \mathbb{R} \times \Sigma, \tag{1.7}$$

where u_n is called the n-th modal component of u and φ_n the n-th mode. Each mode is the n-th Neumann eigenvector of the negative Laplacian [27], and satisfies

$$\left\{ \begin{array}{ll} -\Delta\varphi_n = \lambda_n\varphi_n & \text{in } \Sigma, \\ \partial_\nu\varphi_n = 0 & \text{on } \partial\Sigma, \end{array} \right. \tag{1.8}$$

where $(\lambda_n)_{n\geq 0}$ are Neumann eigenvalues of the negative Laplacian. For instance, in two dimensions, we have the simple expression

$$\varphi_n(y) = \begin{cases} \dfrac{1}{\sqrt{2h}} & \text{if } n = 0, \\ \dfrac{1}{\sqrt{h}} \cos\left(\dfrac{n\pi(y+h)}{2h}\right) & \text{if } n \geq 1. \end{cases} \tag{1.9}$$

Note that this modal decomposition still works for more general shapes Σ, although we will not use it in the following.

The family $(\varphi_n)_{n\in\mathbb{N}}$ is orthonormal in $\mathrm{L}^2(\Sigma)$ for the usual scalar product, and each modal component u_n is given by

$$u_n(x) = \int_\Sigma u(x, \boldsymbol{y})\varphi_n(\boldsymbol{y})\mathrm{d}\boldsymbol{y}. \tag{1.10}$$

Using this modal decomposition, the Helmholtz equation is equivalent to a sequence of equations on each mode:

$$u_n'' + k_n^2 u_n = s_n \qquad \text{with} \qquad k_n = \sqrt{k^2 - \frac{n^2\pi^2}{4h^2}} \qquad \forall n \in \mathbb{N}, \tag{1.11}$$

where k_n is called the n-th wavenumber [27, 34] and s_n is a modal source term. To ensure the uniqueness of u_n, we adapt the Sommerfeld condition used in free space [95] into a boundary condition at infinity called an outgoing condition. Then, this equation has a unique solution except for a countable number of frequencies. These frequencies are called resonant frequencies, cut-off frequencies, or critical frequencies depending on the communities. The one-dimensional Helmholtz equation is not well-posed at these frequencies, and its solutions explode when k is chosen near a cut-off [27]. On the contrary, each modal equation (1.11) has a unique solution u_n when k is away from cut-offs, and the whole wavefield u can be computed everywhere in the waveguide given any source term.

1.1.2 Elastic wave equation

1.1.2.a Elastic waveguides

We now move to the elastic case and compare it with the acoustic one. When elastic waves are propagating in a domain $\Omega \subset \mathbb{R}^3$, the domain is momentarily deformed along a displacement field $\boldsymbol{U}$ following the linear elasticity model

$$\partial_{tt}\boldsymbol{U}(t, \boldsymbol{x}) = \nabla \cdot \boldsymbol{\sigma}(\boldsymbol{U})(t, \boldsymbol{x}) + S(t, \boldsymbol{x}), \quad \boldsymbol{\sigma}(\boldsymbol{U}) = \boldsymbol{C} : \nabla^s(\boldsymbol{U}) \quad \text{in } \Omega, \tag{1.12}$$

where $\boldsymbol{\sigma}(\boldsymbol{U})$ is called the stress tensor, $\nabla^s = (\nabla + \nabla^T)/2$ is the symmetric part of the gradient, : is the tensor product and $\boldsymbol{C}$ is a the fourth order stiffness tensor depending on two coefficients (λ, μ) called the Lamé coefficients of the plate. We notice that this equation resembles the Helmholtz equation where the Laplacian is replaced by the operator $\nabla \cdot \boldsymbol{\sigma}$. In addition to its more complex expression, the elastic equation is different from the acoustic one since it is a vector equation: $\boldsymbol{U}$ has now two or three components instead of being a scalar. Like in the acoustic case, we choose to work in the harmonic regime and look for solutions of (1.12) of the form

$$\boldsymbol{U}(t, \boldsymbol{x}) = \int_\mathbb{R} \boldsymbol{u}(\boldsymbol{x}, \omega)e^{i\omega t}\mathrm{d}\omega. \tag{1.13}$$

Here, the frequency is denoted by ω instead of k to correspond as closely as possible to notations already used in the elasticity community. At a fixed frequency $\omega \in \mathbb{R}^+$, the wavefield $\boldsymbol{u}$ is solution of the so-called displacement elastic equation

$$\nabla \cdot \boldsymbol{\sigma}(\boldsymbol{u}) + \omega^2 \boldsymbol{u} = \boldsymbol{s} \quad \text{in } \Omega, \tag{1.14}$$

where $\boldsymbol{s}$ is a source term. We refer to books [94, 91, 5] for further details, and from now on, we only consider the elastic equation in the harmonic regime.

We choose to work in elastic waveguides such as plates, and the domain Ω is defined as the three dimensional set

$$\Omega = \mathbb{R}^2 \times (-h, h). \tag{1.15}$$

Like in the acoustic case, the parameter h stands for the width of the waveguide and is constant in $\mathbb{R}_+^*$ if the waveguide does not have any defect. Due to the symmetries seen in the definition of Ω, we also consider the propagation of elastic waves in sections of Ω which comes back to the analysis of the two-dimensional waveguide

$$\Omega = \mathbb{R} \times (-h, h). \tag{1.16}$$

We represent in Figure 1.3 regular plates in three and two-dimensional cases, as well as examples of waves propagation in these structures.

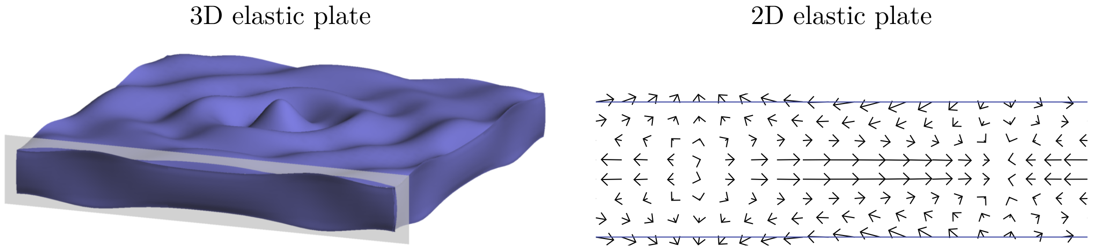

Figure 1.3 – Representation of a regular plate in two and three dimensions. Elastic displacement waves propagate in the plate according to the elastic equation (1.14). Here, the three-dimensional waveguide is cut along the grey plan to get the two-dimensional waveguide. Only the normal component is kept in the two-dimensional representation.

Similar to the acoustic case, a boundary condition needs to be added to ensure well-posedness of the elastic equation. We choose to work in this manuscript with the Neumann boundary condition $\boldsymbol{\sigma}(\boldsymbol{u}) \cdot \nu = \boldsymbol{b}$ on $\partial\Omega$ but similar studies could be conducted using Dirichlet condition $\boldsymbol{u} = \boldsymbol{b}$ or Robin condition $a\boldsymbol{u} + \boldsymbol{\sigma}(\boldsymbol{u}) = \boldsymbol{b}$ without altering the obtained results.

1.1.2.b Lamb and Shear horizontal modal decompositions

To simplify the elastic equation and find its solutions, we look for an extension of the modal decomposition presented in the acoustic case. It is usual in elasticity theory to decompose elastic wavefields $\boldsymbol{u}$ using the classic longitudinal/transverse decomposition $\boldsymbol{u} = \boldsymbol{u}_t + \boldsymbol{u}_\ell$. In this decomposition, $\boldsymbol{u}_\ell$ is a longitudinal wave (ℓ) whose displacement is parallel to the propagation direction, and $\boldsymbol{u}_t$ is a transverse wave (t) whose displacement is orthogonal to the propagation direction (see Figure 1.4). This decomposition is often used in the free space as these two components are independent and solve simpler wave equations, but it loses its interest in waveguides [91, 5]. Indeed, when a longitudinal or transverse wave meets an interface, it is reflected as a combination of (ℓ) and (t) waves (see Figure 1.4), and the resulting wave is neither a pure longitudinal nor a pure transverse wave.

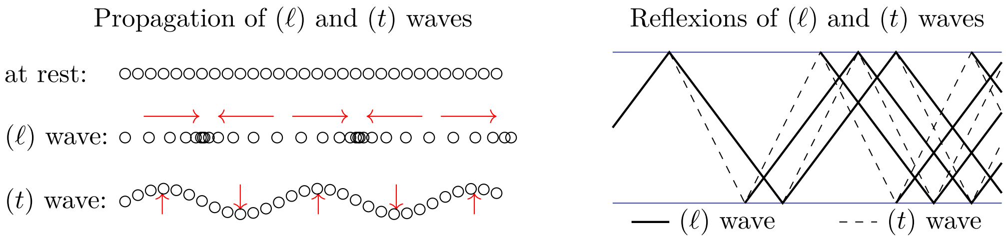

Figure 1.4 – Schematic representations of longitudinal (ℓ) and transverse (t) waves. On the left, we illustrate the propagation of (ℓ) and (t) waves. Waves propagate on a line of particles from left to right. The longitudinal displacement is parallel to the direction of propagation, while the transverse displacement is orthogonal. On the right, we represent the reflections of an incident longitudinal wave in a two-dimensional plate. At each interface, the wave is reflected into a longitudinal and a transverse part, generating a so-called Lamb wave at the end.

Nevertheless, transverse waves are useful to get a first decomposition of any wavefield $\boldsymbol{u}$ propagating in a three-dimensional plate. Physical experiments and explicitly resolutions of the elastic equation adding symmetries assumptions show that $\boldsymbol{u}$ can be decomposed as

$$\boldsymbol{u} = \boldsymbol{u}^{SH} + \boldsymbol{u}^{L}. \tag{1.17}$$

In this decomposition, $\boldsymbol{u}^{SH}$ is called the shear horizontal part of $\boldsymbol{u}$, and $\boldsymbol{u}^{L}$ is called the Lamb part of $\boldsymbol{u}$. The wavefield $\boldsymbol{u}^{SH}$ is a transverse wave represented in Figure 1.5. Given a direction of propagation p, the displacement $\boldsymbol{u}^{SH}$ is orthogonal to p and parallel to the plate surface. On the other hand, the wavefield $\boldsymbol{u}^{L}$ is in the plane orthogonal to the plate surface and containing p.

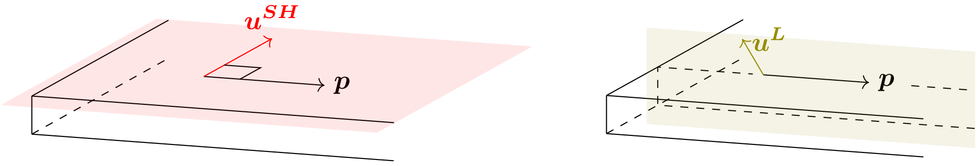

Figure 1.5 – Decomposition of an elastic wavefield $\boldsymbol{u} = \boldsymbol{u}^{SH} + \boldsymbol{u}^{L}$ propagating in the direction p in a three-dimensional plate. The shear horizontal displacement $\boldsymbol{u}^{SH}$ is a transverse wave orthogonal to p and contained in the plane parallel to the plate surface. The Lamb displacement $\boldsymbol{u}^{L}$ is contained in the plane orthogonal to the plate surface and containing p.

The main advantage of this splitting of $\boldsymbol{u}$ is that both $\boldsymbol{u}^{SH}$ and $\boldsymbol{u}^{L}$ and be decomposed using modes. The shear horizontal part can be decomposed in shear horizontal modes (SH) with expressions and wavenumbers similar to acoustic ones (1.8)-(1.11) and are already well-studied [91, 5]. The decomposition of the Lamb part $\boldsymbol{u}^{L}$ proves more difficult.

By definition, $\boldsymbol{u}^{L}$ is contained in a domain assimilated to a two-dimensional plate where coordinates are now denoted (x, z). As explained before, the decomposition in transverse and longitudinal modes fails due to the waveguide interfaces (see Figure 1.4). Instead, we consider the so-called Lamb modes to get a decomposition $\boldsymbol{u}^{L}$. From a physical point a view, Lamb modes are defined as functions $\boldsymbol{u}_n(z) = (u_n(z), v_n(z))$ associated with a wavenumber $k_n \in \mathbb{C}$ such that the Lamb wave $\boldsymbol{u}(x, z) := \boldsymbol{u}_n(z) \exp(ik_n x)$ satisfies the elasticity equation (1.14) with Neumann boundary conditions [91, 5]. Mathematicians prefer to define Lamb modes and wavenumbers k_n as eigenelements of an operator $\mathcal{L}$ defined using the elasticity equation [65, 80]. No matter which approach is chosen, it is possible to find analytical expressions of k_n and explicit expressions of Lamb modes

$(u_n(z), v_n(z))$. We represent Lamb waves in Figure 1.6 for two different values of n. Note here that the notation u_n does not hold the same meaning in elastic and acoustic waveguides: while u_n stands for the modal component in the acoustic case, it represents the modal basis in the elastic case. This choice of notation was retained despite this to remain as consistent as possible with the existing literature.

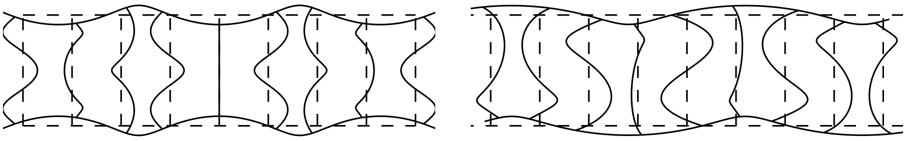

Figure 1.6 – Representation of two Lamb waves $\boldsymbol{u}(x, z) = \boldsymbol{u}_n(z)\exp(ik_nx)$. The initial shape of the two-dimensional plate is represented in dotted line while the displacement induced by the Lamb wave is represented in plain lines. On the left is the third symmetric Lamb mode and on the right is the third antisymmetric Lamb mode. Here, $\omega = 3$, $h = 1$ and the Lamé coefficients are $\lambda = 0.31$ and $\mu = 0.25$

It can be proved that the family of Lamb modes forms a complete set of functions [56, 19, 8], and any wavefield $\boldsymbol{u}^L := (u, v)$ can be decomposed as

$$u(x, z) = \sum_{n>0} a_n(x)u_n(z), \qquad v(x, z) = \sum_{n>0} b_n(x)v_n(z) \qquad \forall (x, z) \in \mathbb{R} \times (-h, h). \tag{1.18}$$

However, contrarily to the acoustic modal decomposition, Lamb modes do not form an orthonormal basis. To obtain the dependency of a_n and b_n with respect to $\boldsymbol{u}^L$, one needs to use the Fraser bi-orthogonality relation [44]:

$$a_n(x) = \frac{\int_{-h}^{h} (v_n(y)\boldsymbol{\sigma}(\boldsymbol{u}^L)_{1,2}(x, y) - \boldsymbol{\sigma}(\boldsymbol{u}_n)_{1,1}(y)u(x, y))\mathrm{d}y}{\int_{-h}^{h} (v_n(y)\boldsymbol{\sigma}(\boldsymbol{u}_n)_{1,2}(y) - \boldsymbol{\sigma}(\boldsymbol{u}_n)_{1,1}(y)u_n(y))\mathrm{d}y}, \tag{1.19}$$

$$b_n(x) = \frac{\int_{-h}^{h} (v(x, y)\boldsymbol{\sigma}(\boldsymbol{u}_n)_{1,2}(y) - \boldsymbol{\sigma}(\boldsymbol{u}^L)_{1,1}(x, y)u_n(y))\mathrm{d}y}{\int_{-h}^{h} (v_n(y)\boldsymbol{\sigma}(\boldsymbol{u}_n)_{1,2}(y) - \boldsymbol{\sigma}(\boldsymbol{u}_n)_{1,1}(y)u_n(y))\mathrm{d}y}, \tag{1.20}$$

where $\boldsymbol{\sigma}$ is the stress tensor evoked in (1.14). In Chapter 2, we will see that the formalism $\boldsymbol{X}/\boldsymbol{Y}$ developed by Pagneux and Maurel [80, 81] can simplify these bi-orthogonality relations. Then, the elastic equation is equivalent to a collection of equations on each mode, similar to the one presented for acoustic modes:

$$a_n'' + k_n^2 a_n = s_n^1, \qquad b_n'' + k_n^2 b_n = s_n^2, \tag{1.21}$$

where s_n^1 and s_n^2 are modal source terms. Each mode is uniquely defined after adding an outgoing condition and can be computed away from the cut-off frequencies. The wavefield $\boldsymbol{u}^L$ and therefore the whole wavefield $\boldsymbol{u}$ is then explicitly determined for any chosen source at each frequency $\omega \in \mathbb{R}^+$,

To synthesize, elastic and acoustic waves can be decomposed in regular waveguides using a modal decomposition. Each modal component satisfies the one-dimensional Helmholtz equation $y'' + k_n^2 y = 0$, which is well-posed and easily solved after adding an outgoing condition at infinity. Thereby, the propagation in two and three-dimensional regular waveguides, whether acoustic or elastic, is overall well understood.

1.1.3 Propagation in perturbed waveguides

To identify and reconstruct defects in waveguides, one must first understand how these defects impact wave propagation and modify the previous framework developed for regular waveguides. In this thesis, we deal with three types of defects: a local perturbation of the medium index, a bend of the waveguide, and a defect in the geometry of Ω (see Figure 1.7).

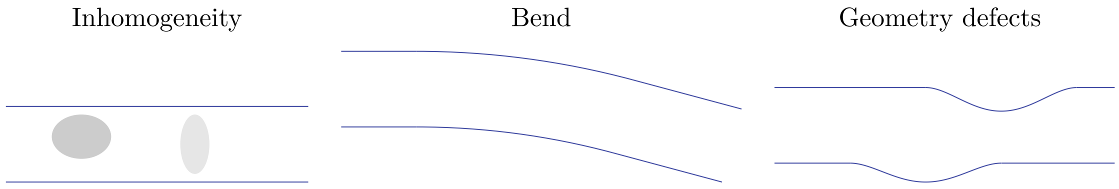

Figure 1.7 – Representation of three types of defects in a two-dimensional waveguide. From the left to the right, we see inhomogeneities in the medium index, a bend on the waveguide, and a defect in the geometry of the waveguide.

A bend or a geometry defect changes the definition of Ω and leaves equation (1.14) of (1.4) unchanged, while an inhomogeneity leaves Ω intact but introduces a perturbation $q(\boldsymbol{x})$ in the Helmholtz and elastic equations:

$$\Delta u + k^2(1+q)u = 0, \qquad \text{or} \qquad \nabla \cdot \boldsymbol{\sigma}(\boldsymbol{u}) + \omega^2(1+q)\boldsymbol{u} = 0. \tag{1.22}$$

In general, these equations cannot be solved explicitly, and we aim at finding precise and quick way to compute approximations of the solutions. Many different techniques have been developed over the years to answer this issue, and we present here a brief overview of the general ideas.

After studying wave propagation in regular waveguides, the most naive idea that could come to mind is to generalize the previous modal decomposition to perturbed waveguides. In the case of inhomogeneities, the shape of Ω has not changed, and all the previous results on modal decompositions still apply. However, if we try to project the acoustic equation (1.22) on each mode n, we obtain the system

$$\forall n \in \mathbb{N} \qquad u_n'' + k_n^2 u_n + \sum_{m\in\mathbb{N}} u_m \int_{-h}^{h} q\varphi_n\varphi_m = 0. \tag{1.23}$$

Each mode is now coupled with all the others, and we cannot find a simple equation for each mode u_n [34]. A similar result would also occur for the elastic case. As for bends and shape defects, the width of each slice varies, and every mode depends on x through the function $h(x)$:

$$u(x,y) = \sum_{n\in\mathbb{N}} u_n(x)\varphi_n(x,y), \qquad \text{or} \qquad \boldsymbol{u}(x,y) = \sum_{n>0} (a_n(x)u_n(x,y), b_n(x)v_n(x,y)). \tag{1.24}$$

After replacing these expressions in the Helmholtz equation (1.4) and projecting on each mode [81], we obtain the system

$$\forall n \in \mathbb{N} \qquad u_n'' + k_n^2 u_n + 2\sum_{m\in\mathbb{N}} u_m' \int_{-h}^{h} \partial_x\varphi_m\varphi_n + \sum_{m\in\mathbb{N}} u_m \int_{-h}^{h} \partial_{xx}u_m\varphi_m''\varphi_n = 0. \tag{1.25}$$

Again, we observe that modes are coupled like in the inhomogeneous case. We cannot get an explicit expression of every mode u_n, but we might use these modal systems to get a wavefield approximation. Norms of modal components $(u_n)_{n\in\mathbb{N}}$ are decreasing since the family is summable and we can cut the decomposition at a chosen rank $N \in \mathbb{N}$. By doing so, infinite systems (1.23) and (1.25) are reduced to a $N \times N$ matrix differential equations, which can be solved and provide an approximation of the wavefield [81, 46]. Assuming that k is away from every cut-off frequency, this method provides satisfactory numerical wavefield approximations. However, we do not control the approximation error nor have easily usable expressions of the approximated wavefield.

Instead of using the modal decomposition on each slide, other works suggest to map the perturbed waveguide to a regular one [3, 2, 61]. Different mappings can be chosen. While the easiest mapping seems to be the transformation $(x, y) \mapsto (x, y/h(x))$, this transformation does not preserve the outward normal and changes the boundary conditions. To solve this issue, one could also use a conformal mapping, which preserves all the angles [3]. If such transformations are convenient, they are rarely explicit and hardly usable in practice. Both these transformations are represented in Figure 1.8. Regardless of the chosen mapping ϕ, we notice that $v := u \circ \phi$ satisfies in the regular acoustic waveguide the equation

$$\Delta v + k^2 v = \mathcal{T}(v), \tag{1.26}$$

where $\mathcal{T}(v)$ is an application depending on ϕ, $\nabla\phi$ and $\nabla^2\phi$. Again, this equation can not be projected simply on each mode, and we are back to the problem of inhomogeneous defects. To summarize, the use of mappings from perturbed waveguides to regular ones can simplify the problem a little but mainly exchanges a shape defect problem for an inhomogeneity one.

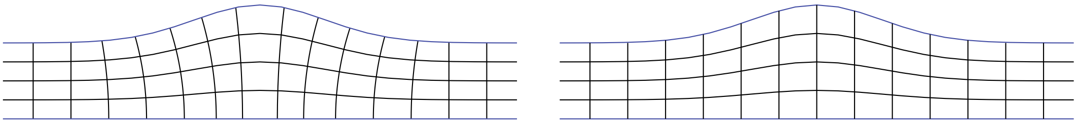

Figure 1.8 – Representation of two mappings of a perturbed waveguide with a geometry defect at the top. On the left, the mapping is conformal, meaning that it preserves the angles and especially the outward normal, but it does not have a simple expression. On the right, the mapping flattens the waveguide with the simple expression $(x, y) \mapsto (x, y/h(x))$ but does not preserve the outward normal.

Instead of cutting the modal decomposition to a finite number of modes, another method is commonly used when the wavefield is measured far from the defect area. Instead of working with the classical expression of Helmholtz and elastic equation, we can rewrite them as integral equations

$$u(\boldsymbol{x}) = \int_\Omega G(\boldsymbol{x}, \boldsymbol{x}') q(\boldsymbol{x}') u(\boldsymbol{x}') \mathrm{d}\boldsymbol{x}', \tag{1.27}$$

where G is the Green function found with the previous wave propagation studies in regular waveguides. This integral equation is also known as the Lippman-Schwinger equation. If the coordinate $\boldsymbol{x}$ is located far from the perturbation q, one can compute an asymptotic approximation of $u(\boldsymbol{x})$ using an asymptotic form of the Green function G [34, 24, 9, 13]. If this method is very efficient for computing theoretically and numerically a far-field approximation of the wavefield, it fails near the defect area. Furthermore, if this method is largely used in acoustic theory, fewer people use it in the elastic theory due to the complexity of the Green elastic function asymptotics.

Finally, let us mention one last approximation method widely used in the rest of this manuscript. If we assume that defects are small in support and size (which is often the case in physical applications), back-scattering techniques can also simplify the problem. Giving a source of wave s, we denote u_{inc} the generated wavefield in a regular waveguide, u the perturbed wavefield in the inhomogeneous waveguide, and $u^s = u - u_{\text{inc}}$ the scattered wavefield. Since the inhomogeneities are small, one could feel that u and u_{inc} should be very similar and u_s small compared to u. Such an approximation is called a Born approximation and is often used to simplify wave equations with small defects [32, 92]. Away from cut-off frequencies, we can prove that the scattered field u^s is close to the wavefield v satisfying the equation

$$\Delta v + k^2 v = -k^2 q u_{\mathrm{inc}}, \qquad \text{or} \qquad \nabla \cdot \boldsymbol{\sigma}(\boldsymbol{v}) + \omega^2 \boldsymbol{v} = -\omega^2 q \boldsymbol{u}_{\mathrm{inc}}, \tag{1.28}$$

and we can control the error between u_s and v [32]. The equation on v can now be solved easily using the Green function in the regular waveguide.

In all these approximation methods, the frequency k needs to be chosen far from cut-off frequencies to get accurate approximations. However, different physical experiments were made near these cut-off frequencies and produced encouraging results on defects reconstruction [11, 58, 29]. Thus, we also need to find suitable approximation methods around cut-off frequencies. Very few works are concerned with this issue, and to our knowledge, every one of them is done in slowly varying waveguides. Under this assumption, each mode does not interact a lot with the others, and people usually neglect terms depending on h' or h'' in modal systems (1.23) [81, 46, 82], and

$$u_n'' + k_n(x)^2 u_n = 0. \tag{1.29}$$

Since k_n depends on x through the function h, this equation is no longer so easy to solve, especially since $k_n(x)$ vanishes at cut-off frequencies. We notice that this equation can be seen as a Schrödinger equation, which is usually written under the form

$$\frac{\hbar^2}{2m}\partial_{xx}\psi + (E - V(x))\psi = 0, \tag{1.30}$$

where $\hbar$ is the reduced Planck constant, m the particle mass, ψ the probability density, E the energy, and V a potential [90]. Coordinates x such that $E = V(x)$ are called turning points, and approximations of ψ around these points have been mathematically studied by Olver [76, 77]. We represent in Figure 1.9 an example of a potential V and the associated approximation of ψ. This approximation involves the Airy function, defined as the solution of the ordinary equation $y''(x) + xy(x) = 0$ [4]. Using this link with the Schrödinger equation, general approximations of the wavefield in slowly variable waveguides have been proposed.

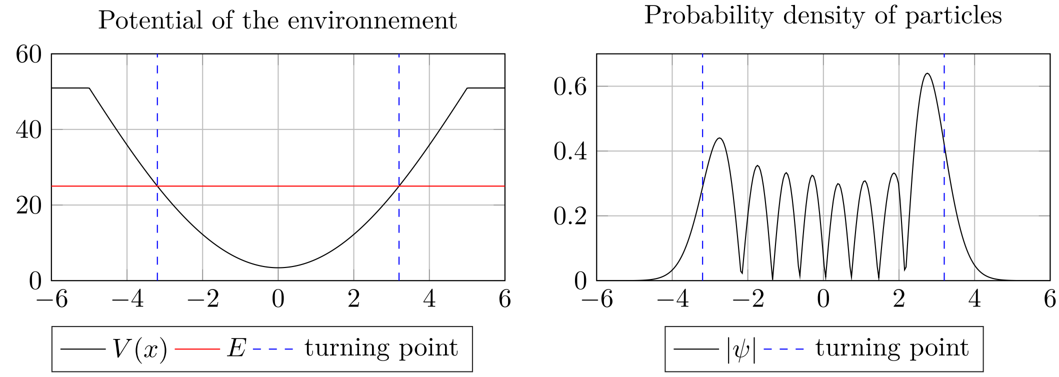

Figure 1.9 – Probability density of particles given a potential V and an energy E. On the left, we represent the potential $V(x)$, the energy E and the turning points satisfying $V(x) = E$. On the right, we plot the associated probability density ψ and we materialize the position of the turning points. The function ψ expressed using an Airy function propagates between the turning points and fast decays outside.

Other approximation methods exist in more specific cases where stronger assumptions are made on defects. Still, they globally lean on the idea presented here: cutting the number of modes in the modal decomposition, using integral representation and approximations of the Green function, or neglecting terms on the propagation equation using Born approximations.

1.2 Reconstruction of defects

1.2.1 Existing reconstruction methods

As mentioned initially, we aim to detect and reconstruct the possible waveguides defects. Using the studies of the forward problem, we want to measure the wavefield and see if it exists a usable link with the defect. Given physical constraints of the problem, we cannot take measurements everywhere in the waveguide, and Figure 1.10 illustrates the different areas where one could place receivers. On the one hand, the wavefield is often accessible on one or many sections of an acoustic pipe [55, 27]. On the other hand, measurements are only available at the top and the bottom of an elastic plate [11, 58]. In the rest of this thesis, we will alternatively use surface or sections measurements of the wavefield depending on the considered waveguide.

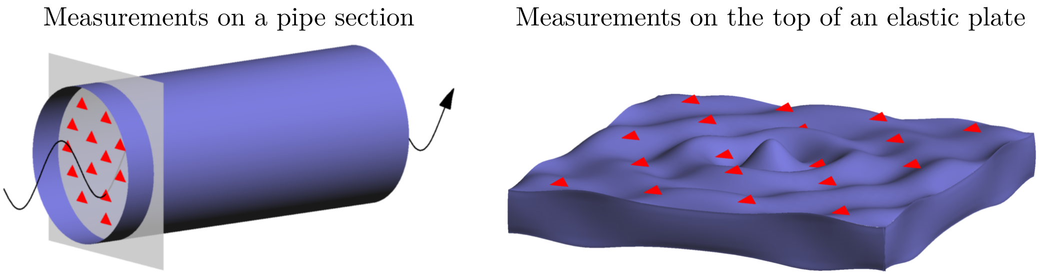

Figure 1.10 – Illustration of the available wavefields measurements in acoustic pipes and elastic plates. Receivers are represented with red triangles. They are placed along a section of the pipe, and on the top surface of the plate.

Different reconstruction methods are already developed in the literature, and many use wavefield measurements taken at a fixed frequency $k > 0$ away from cut-off frequencies.

1.2.1.a Inversion with one frequency and multiple incident waves

Many authors chose to work with a single frequency $k > 0$ and to send multiple incident waves in the waveguide to develop reconstruction methods. One of the most famous is an adaptation of the Linear Sampling Method, developed by D. Colton and A. Kirsch [31] to recover obstacles in free space, to acoustic and elastic waveguides [27, 15, 23]. The Green function of the regular waveguide is still denoted by G. After sending different incident waves of the form $G(\cdot, \boldsymbol{x}')$ where $\boldsymbol{x}'$ is located on a section Σ, we measure the scattered field on the same section and define the operator

$$Fh(\boldsymbol{x}) := \int_\Sigma u_s(\boldsymbol{x}, \boldsymbol{x}')h(\boldsymbol{x}')\mathrm{d}\boldsymbol{x}' \qquad \forall \boldsymbol{x} \in \Sigma. \tag{1.31}$$

It is possible to prove that the norm of $h_{\boldsymbol{z}}$ solution of $Fh_{\boldsymbol{z}} = G(\cdot, \boldsymbol{z})$ diverges towards infinity when $\boldsymbol{z}$ tends to the boundary of the obstacle. Solving a discretized version of this equation provides a good approximation of the support of the defect. Moreover, this method can also be generalized to elastic waveguide and surface measurements. However, it only applies to reflecting obstacles in the waveguide.

To reconstruct inhomogeneities q defined in (1.22), the same operator F can be used. At far-field, the spectral decomposition of this operator depends linearly on the inhomogeneity q [34], and one has to inverse a well-chosen matrix to reconstruct a good approximation of q. Different adaptations of these methods are also available for open and periodic waveguides [25, 26].

Even if these methods provide satisfactory results in detecting inhomogeneities and obstacles, they require sending different well-chosen incident waves on each mode, and uses only measurement at one frequency. However, in physical experiments, data are often given in the temporal regime, which provides wavefield measurements for a range of frequencies [11, 54]. One could argue that the previous reconstruction methods can still be applied frequency by frequency before taking the average of all reconstructions. However, this method does not use all the benefits of multi-frequency measurements. It is proved in the free space that multi-frequency data can help to improve the reconstruction and get mathematical insights on the uniqueness and stability of the reconstruction [7, 14, 93, 52]. For all these reasons, we will focus on this thesis on developing multi-frequency reconstruction methods.

1.2.1.b Existing multi-frequency methods

Few methods have been developed to reconstruct defects in waveguides given multi-frequency measurements. Their main idea is to use the integral equation (1.27) and to provide an asymptotic development of the quantity

$$\int_{\Omega} G(\boldsymbol{x},\boldsymbol{x}')q(\boldsymbol{x}')u(\boldsymbol{x}')\mathrm{d}\boldsymbol{x}' \qquad \forall x \in \Omega, \tag{1.32}$$

when the observation point $\boldsymbol{x}$ is far from the inhomogeneity q [24, 9, 13, 23]. The first term of this development depends linearly on the inhomogeneity's localization and volume, and the far-field measurements allow reconstruction of these parameters. If it is proven that the far-field uniquely determines the waveguide's defects, there is not, up to our knowledge, any stable and efficiently numerical multi-frequency reconstruction method.

More importantly, as mentioned before, wavefields near cut-off frequencies of the waveguide contain a lot of information on the defect. Due to the lack of well-posedness near these frequencies, every previous multi-frequency methods choose to avoid cut-off frequencies, and none uses it to obtain information on the defects.

1.2.2 Contributions of the thesis

This manuscript is decomposed in two parts, each bringing a different answer to the problems raised below. In the first part, we develop a new multi-frequency method to reconstruct inhomogeneities, geometry defects, and bends of waveguides using frequencies away from cut-off frequencies. This method leans on a Born approximation of the wavefield and a partial data Fourier inversion, and can be applied for any small defects. In addition to localize the defect, this method fully reconstructs the shape of the defect in a stable way, and we prove that it is numerically efficient by testing it on simulated data. Chapter 2 focuses on developing this method in the acoustic case, while Chapter 3 extends it to the elastic case.

The main result of Chapter 2 is Theorem 2.2 which justifies the stability of the reconstruction method and controls the reconstruction error. This theorem leans on the important Lemma 2.1 which provides a control of any function given partial measurements of its Fourier transform and enough regularity. As for Chapter 3, three important results stand out. Theorem 3.1 provides a complete characterization of critical frequencies of an elastic waveguide and help understand the mathematical analysis of Lamb modes. Avoiding these critical frequencies, we provide in Theorem 3.2 an explicit decomposition of any wavefield generated by a known internal or boundary source in Lamb modes, and we control the wavefield by the norm of the sources. This control is extremely important to apply the Born approximation and reconstruct small defects in elastic waveguides. Finally, we extend this theorem to the three-dimensional case in Theorem 3.3 where we formalize the decomposition in SH and Lamb modes in an elastic plate. All these results are then used to justify the stability and the accuracy of our multi-frequency reconstruction method in the elastic case.

The second part of the manuscript focuses on using cut-off frequencies, called here locally resonant frequencies, to get reconstructions of geometry defects in Ω. An important work is being done to understand and model the propagation of waves in slowly varying waveguides. Then, we propose new reconstruction methods using only locally resonant frequencies to recover width defects. These methods are especially of interest in elastic waveguides. It enables us to justify and better understand the zero-velocity group reconstruction method experimentally used in the non-destructive control of plates [11]. In Chapter 4, we study the forward problem near resonances in the acoustic case. We use this study to develop our reconstruction method using locally resonant frequencies in Chapter 5 given surface measurements, and in Chapter 6 given section measurements. Chapter 7 extends these results to the elastic case.

Different results are found in this second part. Theorem 4.1 provides an explicit approximation of any wavefield propagating in slowly varying waveguides at locally resonant frequencies using Airy functions, as well as a control of the approximation error. This approximation is used to reconstruct width defects. Theorem 5.3 and Theorem 6.2 prove that this reconstruction method is stable and control the reconstruction error given surface or section measurements. Finally, this method is generalized to the elastic case. Depending on the nature of the resonant point, Theorem 7.1, 7.2 and 7.3 generalize Theorem 4.1, which enables to adapt the reconstruction method from the acoustic case to the elastic one easily.

In the rest of this introduction, we summarize the main ideas and results presented in these two parts. These results are simplified to keep only their main ideas, and only a sketch of proofs will be provided. Readers may refer to the corresponding chapter of the manuscript to find more details.

1.3 Reconstruction of small defects from multi-frequency data

This part focuses on developing a new multi-frequency reconstruction method to detect any inhomogeneities, shape defects, or bends in the waveguide as long as they are small in support and amplitude. The modeling of the problem is based on experiments conducted at the “Laboratoire de Tribologie et Dynamique des Systèmes” on acoustic pipes and thin elastic cylinders [55, 54]. In these experiments, an incident pulse is sent from one waveguide section and generates a scattered field when it meets the waveguide's defect. This scattered field comes back and is measured on another section of the waveguide (see the experimental setup in Figure 1.11). By looking at the time between the emission and the reception of the signal, it is possible to predict roughly the defect localization. The following method proves that is is possible to do better and to use these data to reconstruct the defect entirely.

1.3.1 Acoustic waveguides

Chapter 2 starts by studying the simplest case of a two-dimensional acoustic waveguide. We chose to send in the waveguide an incident wave u_{inc} carried on the first mode $n = 0$, and we measure the scattered field u_s generated by defects in the waveguide. If we denote $u_{s,k}$ the scattered field at frequency k, the aim is to solve the inverse problem

$$\text{Reconstruct the defect from } u_{s,k|\Sigma} \text{ for different } k \in \mathbb{R}_+ \text{ where } \Sigma \text{ is a section of } \Omega. \tag{1.33}$$

Since all the defects are small in size, the framework of the Born approximation applies, and we know that in presence of an inhomogeneity q, the scattered wavefield is close to the solution of the

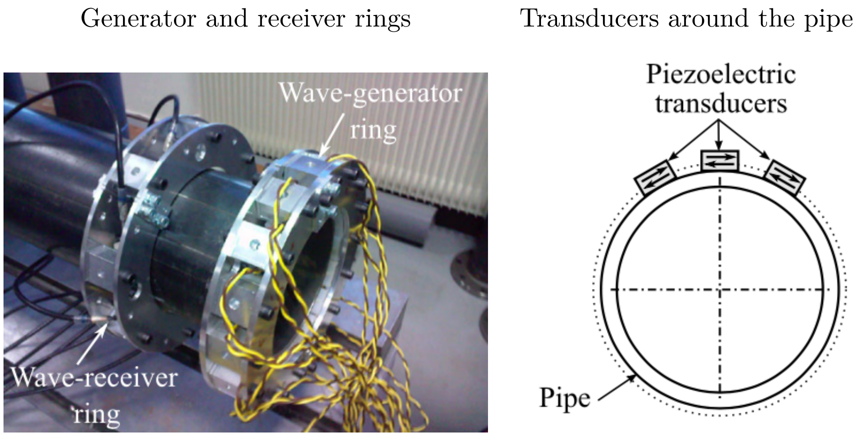

Figure 1.11 – From [55, 54]: Generation and measurement system used to localize defects in thin elastic cylinders. The first ring generates an incident wave propagating in the waveguide, and the second one measures the scattered field generated by the defect. On each ring, piezoelectric transducers are used as transmitters and receivers.

equation

$$\Delta u_s + k^2 u_s = -k^2 q u_{\text{inc}}. \tag{1.34}$$

Then, if $\mathcal{F}$ stands for the Fourier transform, we proved that measuring the wavefield u_s on a section of the waveguide is equivalent to measuring

$$\mathcal{F}(q_n)(k+k_n) = \mathcal{F}(q_n)\left(k + \sqrt{k^2 - \frac{n^2\pi^2}{4h^2}}\right) \quad \forall k \in (k_{\min}, k_{\max}), \quad k > \frac{n\pi}{2h}, \quad \forall n \in \mathbb{N}, \tag{1.35}$$

where q_n is the n-th modal component of the function q, and $(k_{\min}, k_{\max})$ is the range of measurement frequencies. To recover the function q, we need to inverse a Fourier transform with limited frequency data. The lack of high frequency, caused by the limitation $k < k_{\max}$, is easily controllable, providing some regularity on the function q. However, the lack of low frequency is a lesser studied problem and cannot be neglected here. Indeed, even if $k_{\min} = 0$, we can only measure propagative modes which imposes $k > n\pi/(2h)$. Adding minimal smoothness and compact support hypothesis on q, we prove that the function $\mathcal{F}(q_n)$ is analytic [38] and we provide a stable reconstruction of q_n even with these frequency gaps as explained in Lemma 2.1. By discretizing the interval $(k_{\min} + k_n, k_{\max} + k_n)$ into a set K and the function q_n on a set of coordinate X, we define the approximation q_n^{app} of q_n as

$$q_n^{\text{app}} = \operatorname{argmin}(J), \quad \text{where} \quad J(f) = \frac{1}{2}\|\mathcal{F}(f)(K) - \mathcal{F}(q_n)(K)\|_2^2 + \frac{\lambda}{2}\|G(f)\|_2^2. \tag{1.36}$$

Here, G stand for a discrete gradient operator and λ is a penalization parameter. We prove that q_n^{app} is well-defined for every $n \in \mathbb{N}$, and the stability result on the reconstruction of q can be summarized as follows:

Theorem 1.1. *For a chosen number of modes $N > 0$, we denote by $q^{app} := \sum_{n=0}^N q_n^{app}\varphi_n$ the reconstruction of q. If q is compactly supported in H^1 with a priori bounds, then*

$$\|q^{app} - q\|_{L^2}^2 \leq \underbrace{\frac{C_1}{k_{\max}^2}}_{\substack{\textit{lack of high}\\ \textit{frequencies}}} + \underbrace{C_2 \sum_{n=0}^{N} \|\mathcal{F}(q_n^{app}) - \mathcal{F}(q_n)\|_{L^2}^2}_{\textit{noise on measurements of } \mathcal{F}(q_n)} + \underbrace{C_3 \sum_{n=0}^{N} \|\mathcal{F}(q_n^{app}) - \mathcal{F}(q_n)\|_{L^2}^{2-2\varepsilon}}_{\textit{lack of low frequencies}}, \tag{1.37}$$

where $\varepsilon \in (0,1)$ *and* C_1, C_2, C_3 *are constants.*

This stability result is less than linear and is very similar to the one established for the Calderon problem in impedance theory [102]. Using this theorem, we can reconstruct several q_n for $n < N$, which approximate q. This reconstruction method was tested on finite element simulated data, and Figure 1.12 presents an example of reconstruction.

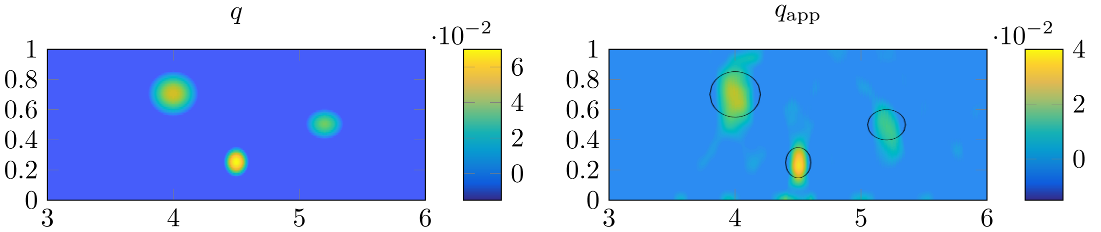

Figure 1.12 – Reconstruction of an inhomogeneity q. On the left is the initial representation of q, and on the right is the reconstruction q^{app} where the support of q is reminded in black line. In this reconstruction, $N = 20$ modes are used to reconstruct q with a range of frequencies $k_{\min} = 0.01$ and $k_{\max} = 150$.

A similar study is conducted for geometry defects and bends. We use a mapping from the perturbed waveguide to a regular waveguide (see Figure 1.8) which introduces new terms in the Helmholtz equation (see equation (1.25)). Under the Born approximation framework, we can neglect most of these terms. In the case of a bend, the scattered wavefield is close to the solution of

$$\left\{ \begin{array}{ll} \Delta u_s + k^2 u_s = f(x) u_{\text{inc}} & \text{in } \Omega, \\ \partial_\nu u = 0 & \text{on } \partial\Omega, \end{array} \right. \tag{1.38}$$

where f is a function depending explicitly on the parameters of the bend. Again, measurements on a slice of the waveguide give partial information on the Fourier transform of f. However, this case is simpler than the inhomogeneities since the first mode $n = 0$ alone carries all the needed information

$$\mathcal{F}(f)(k) \quad \forall k \in (k_{\min}, k_{\max}). \tag{1.39}$$

Using Theorem 1.1, we reconstruct f and the parameters of a bend in a stable way. An illustration of such a reconstruction is presented in Figure 1.13. Similarly, in the case of width defects, the scattered wavefield is close to the solution of

$$\left\{ \begin{array}{ll} \Delta u_s + k^2 u_s = 0 & \text{in } \Omega, \\ \partial_\nu u_s = ikh' u_{\text{inc}} & \text{on } \partial\Omega. \end{array} \right. \tag{1.40}$$

We see that we have a boundary source term instead of the internal source term. However, similar studies are conducted, and the measurements of u_s give information on the Fourier transform of h'. Here, we only need to use the modes $n = 0$ and $n = 1$ to reconstruct all the information on h'. Then, using Theorem 1.1, we reconstruct stably h', and then h. Reconstructions are shown in Figure 1.13.

1.3.2 Elastic waveguides

In Chapter 3, we are interested in generalizing the results of the previous chapter to two- and three-dimensional elastic plates satisfying the elasticity equation (1.14). The aim is to solve the inverse problem

$$\text{Reconstruct the defect from } {u_{s,k}}_{|S} \text{ for different } k \in \mathbb{R}_+ \text{ where } S \text{ is the top surface of } \Omega. \tag{1.41}$$

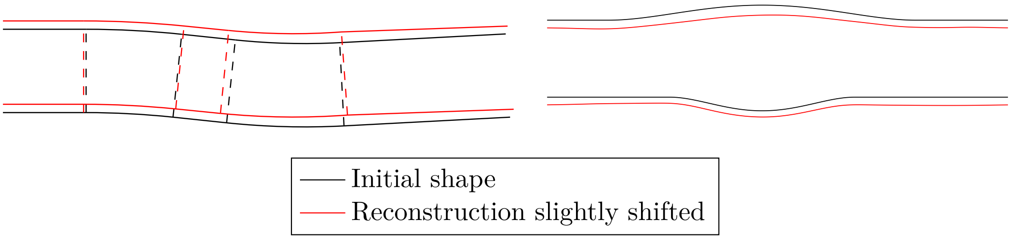

Figure 1.13 – Reconstruction of geometry defects and bends in waveguides. On the left is the reconstruction of a waveguide with two successive bends, and on the right is the reconstruction of a geometry defect. The relative L^2-errors are 8.3% and 5.3%. The black lines represent the initial shape of Ω, and the red reconstructions of Ω, slightly shifted for comparison purposes. Here, $k_{\min} = 0.01$ and $k_{\max} = 40$.

Even if the initial goal is to provide a reconstruction method in perturbed waveguides, a significant part of this chapter is dedicated to studying the forward problem in regular elastic waveguides. Indeed, to use Born approximation, we need control of any wavefield propagating in a regular waveguide by the norm of the source that generated it. This control was easily obtained in the acoustic case thanks to the orthogonality of the modes and the Parseval equality. Still, things get more complicated in the elastic case as Lamb modes do not form an orthogonal family.

We propose a study of the inhomogeneous Lamb modes when their index n tends toward infinity to resolve this issue. Relying on an old asymptotic of k_n provided by Merkulov et al. [67], we can control the decreasing of inhomogeneous Lamb modes (u_n, v_n) and the convergence to the modal decomposition $\sum a_n u_n$ and $\sum b_n v_n$. It leads to the following control Theorem:

Theorem 1.2. *Every wavefield* $\boldsymbol{u}$ *in a two-dimensional elastic waveguide generated by an internal source* $\boldsymbol{f} \in H^1(\Omega, \mathbb{R}^2)$ *and a boundary source* $\boldsymbol{b} \in \widetilde{H}^{3/2}(\mathbb{R}, \mathbb{R}^2)$*, both compactly supported, satisfies*

$$\|\boldsymbol{u}\|_{H^3(\Omega_r)} \leq C \left(\|\boldsymbol{f}\|_{H^1(\Omega)} + \|\boldsymbol{b}\|_{H^{3/2}(\mathbb{R})} \right), \tag{1.42}$$

where C *is a constant.*

While proving this result, we had to study the critical frequencies of the waveguide, where the elastic problem is not well-posed, to avoid them. By doing so, we provide a characterization of such frequencies, unproved until now:

Proposition 1.1. *Critical frequencies can be seen as frequencies satisfying one of these three equivalent definitions:*

- *The denominator of the Fraser bi-orthonormality relation* (1.19) *and* (1.20) *vanishes and prevents from recovering the coefficients* a_n *and* b_n*,*
- *The Lamb basis* (u_n, v_n) *loses its completeness and a new mode, called a generalized Lamb mode, needs to be added for the family to remain complete,*
- *The derivative* $\partial_\omega Real(k_n)$ *is infinite or equivalently, seeing* ω *as a function of* k_n*, we have* $\partial_{Real(k_n)}\omega = 0$.

Before studying the inverse problem, we also clarify the propagation of waves in three-dimensional plates. We are especially interested in finding a general definition of Lamb waves in three-dimensional spaces and understanding their interactions with the SH waves in three dimensions.

Using a Helmholtz-Hodge decomposition [88, 103] of the wavefield on the surface of the plate, we prove that any wavefield propagating in a three-dimensional plate can be explicitly decomposed as a Lamb part, which is curl-free, and an SH part, which is divergence-free:

Theorem 1.3. *Every wavefield* $\boldsymbol{u}$ *in a three dimensional waveguide can be decomposed as* $\boldsymbol{u} = \boldsymbol{u}^L + \boldsymbol{u}^{SH}$ *where*

$$\boldsymbol{u}^L(\boldsymbol{x}, z) = \left(\sum_{n>0} \boldsymbol{A_n}(\boldsymbol{x})u_n(z), \sum_{n>0} b_n(\boldsymbol{x})v_n(z)\right), \quad \boldsymbol{u}^{SH}(\boldsymbol{x}, z) = \left(\sum_{n\geq 0} \boldsymbol{C_n}(\boldsymbol{x})\varphi_n(z), 0\right), \qquad (1.43)$$

and $\boldsymbol{A_n} : \mathbb{R}^2 \to \mathbb{R}^2$*,* $b_n : \mathbb{R}^2 \to \mathbb{R}$ *and* $\boldsymbol{C_n} : \mathbb{R}^2 \times \mathbb{R}^2$ *satisfy Helmholtz equations on the surface of the waveguide. Moreover, the control* (1.42) *still holds.*

Note that this theorem enables high-speed computations of wavefields in three-dimensional waveguides since we have reduced the three-dimensional problem to a collection of two-dimensional ones.

Finally, we have all the needed tools to apply the Born approximation in elastic waveguides and reconstruct small defects. Due to the complexity of the Lamb basis, the recovery of inhomogeneity proves much more complex than in the acoustic case, and we choose to leave it aside and focus on the reconstruction of geometry defects with varying width h. We prove that by providing a post-treatment of measurements, we can extract the Fourier transform of h' (or the Hankel transform of ∇u in three dimensions), and Theorem 1.1 still applies. Reconstructions very similar to the one presented in Figure 1.13 can be obtained.

1.4 Reconstruction in slowly varying waveguides using locally resonant frequencies

The second part of the manuscript studies a different approach to reconstruct defects: instead of avoiding cut-off frequencies, we take advantage of them to do the reconstruction and we accept to deal with the non linearity of the inverse problem. Like in Chapter 3, we now focus on reconstructing only geometry defects. The modeling of our problem is inspired by the experiments conducted at the "Institut Langevin" on elastic plates with varying widths [11, 58, 29]. In these experiments, a laser source generates a wavefield propagating in the plate. When the frequency gets close to a cut-off frequency in a regular plate, the amplitude response explodes. Since cut-off frequencies are closely linked to the width of the plate (remember the exact expression (1.11) in the acoustic case), it provides a straightforward method to recover the width h of a regular waveguide.

Experiments suggest that this phenomenon can be generalized to plates with varying widths. If the frequency corresponds to a local cut-off of width $h(x^\star)$, the amplitude response should explode at the point $x^\star$ and only there. We present in Figure 1.14 experimental results that support this idea.

This part aims at investigating this phenomenon from a mathematical point of view and understand if defects can be reconstructed using these specific frequencies.

1.4.1 Forward problem in the acoustic case

In Chapter 4, we study the simplest case of a two-dimensional acoustic waveguide with varying width $h(x)$. The goal is to understand what appends exactly when the frequency is chosen as a cut-off frequency of one section $h(x^\star)$. As mentioned above, all the existing works on this topic are done

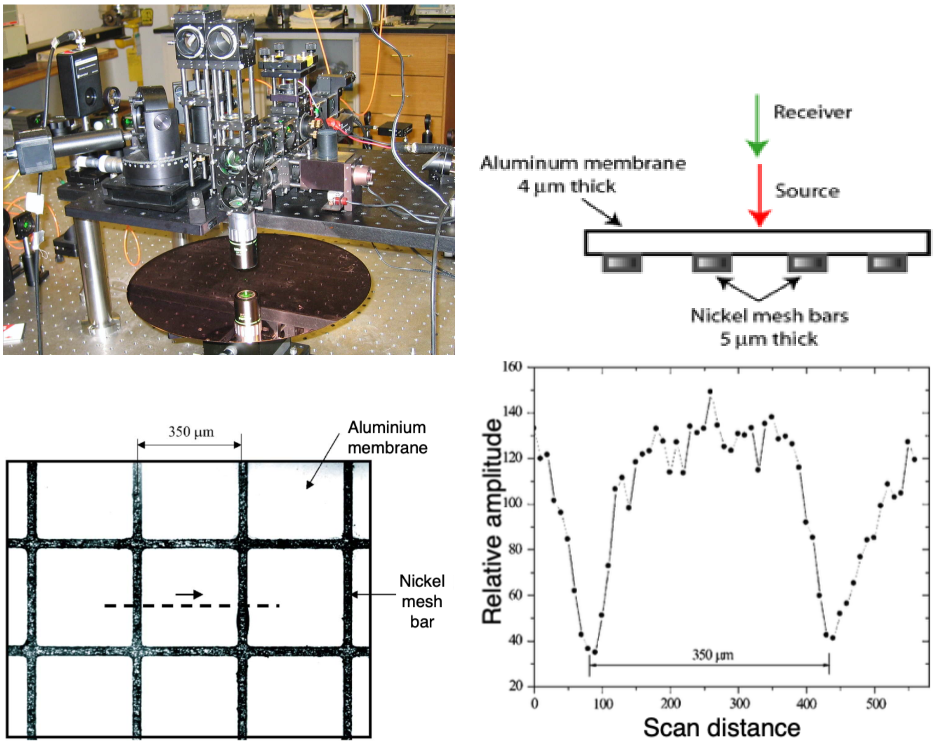

Figure 1.14 – From [11, 70]: Experimental setup to measure the amplitude response in a plate with index variations. On the top are a picture and a scheme of the experimental setup: a laser source generates elastic displacements is a sample and this displacement is measured using an heterodyne interferometer. On the bottom left is a plate representation, where black and white areas do not have the same index. Measurements are made along the dotted line. The amplitude response along the dotted line at the cut-off frequency associated with the white area is represented on the right. We notice a significant response in the white area, while the response in the black area is weak. These measurements can be used to identify the black and the white areas.

in slowly varying waveguides, and we use the same framework. We want to find an approximation of the wavefield and control the approximation error.

From now on, each frequency such that $k = N\pi/(2h(x^\star))$ for a mode $N \in \mathbb{N}$ and a coordinate $x^\star \in \mathbb{R}$ is called a locally resonant frequency, and we have $k_N(x^\star) = 0$. As mentioned in (1.29) we expect each modal component to satisfy the modal equation

$$u_n'' + k_n^2 u_n = 0, \tag{1.44}$$

and Olver extensively studied this equation in [76, 77]. Adapting his works, we can approximate the Green function of (1.44) and control the decrease of these approximations with respect to the mode n. Then, we follow the same process used to neglect terms in Born approximations. However, we adapt it to ensure that it still works around locally resonant frequencies. It enables us to provide a controlled approximation of the solution u of the Helmholtz equation, summarized in the following theorem:

Theorem 1.4. *A wavefield u in slowly variable waveguides can be approximated by*

$$u^{app}(x, y) := \sum_{n\geq 0} u_n^{app}(x)\varphi_n(y), \tag{1.45}$$

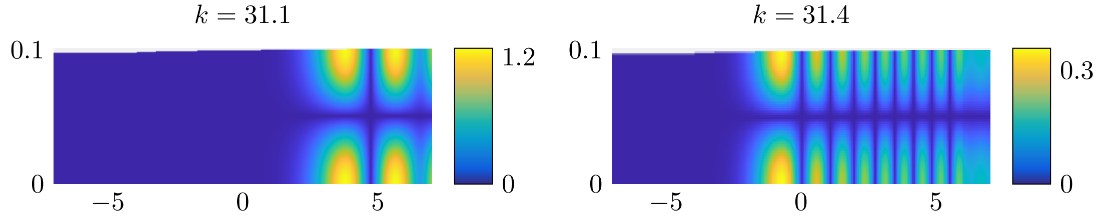

Figure 1.15 – Wavefields $|u|$ propagating in a slowly variable waveguide for two different locally resonant frequencies $k = 31.1$ and $k = 31.4$.

where u_n^{app} *is the convolution of source terms with the Green function* G_n^{app} *defined by*

$$G_n^{app}(x,s) = \begin{cases} c_1 \exp\left(i\left|\int_s^x k_n\right|\right) & \textit{if } n < N, \\ c_2 \exp\left(-\left|\int_s^x k_n\right|\right) & \textit{if } n > N, \\ c_3\, \mathcal{A}\left(-\left(\frac{3}{2}\int_{x^\star}^x k_n\right)^{2/3}\right) & \textit{if } n = N, \quad s > x > x^\star, \end{cases} \tag{1.46}$$

where $\mathcal{A}$ *stands for the Airy function [4] and* c_1, c_2, c_3 *are constants. Moreover, there exists a constant* $C > 0$ *such that*

$$\|u - u^{app}\|_{H^1} \leq C\|h'\|_\infty. \tag{1.47}$$

Using this result, we better understand the propagation of waves at a locally resonant frequencies. As illustrated in Figure 1.15, the wavefield seems very sensitive to small changes in locally resonant frequencies. More precisely, the coordinate $x^\star$ acts like an immaterial barrier that reflect the wavefield back to the source.

1.4.2 Inverse problem in the acoustic case from surface measurements

Chapter 5 uses the previous study of the forward problem near locally resonant frequencies to develop a new reconstruction method and solve the inverse problem

$$\text{Find } h \text{ from } u_{k|S} \text{ for frequencies } k \in \mathbb{R}_+ \text{ where } S \text{ is the top surface of } \Omega. \tag{1.48}$$

Since the wavefield at locally resonant frequencies is very sensitive to width defects, we plan on using measurements of u to reconstruct the coordinate $x^\star$ mentioned above. Since $x^\star$ is associated with the locally resonant frequency k, we know using (1.11) that $h(x^\star) = N\pi/(2k)$. It means that if we can find the location of $x^\star$, we immediately know the local width at this point. Then, turning the frequency to browse all the locally resonant frequencies, we should get a good approximation of h.

Since we want to use this reconstruction method for elastic plates later, we assume that we have access to measurements of the wavefield at the surface of the waveguide, even if it may not be a good physical model for acoustic pipes. Using Theorem 1.4, we already have an approximation of the wavefield. However, this approximation is hardly usable due to the complexity of the expressions at $n = N$. To simplify it, we use a Taylor approximation of the wavefield around the point $x^\star$, and we prove that measurements are close to a three parameters function

$$d^{\text{app}}_{z,\alpha,x^\star} := z\mathcal{A}(\alpha(x - x^\star)). \tag{1.49}$$

Denoting by d the measurements of $u(X,0)$ where X is a set of coordinates, we fit this three-parameter function on the data with

$$(z,\alpha,x^\star) = \operatorname{argmin}(J), \qquad \text{where} \qquad J(z,\alpha,x^\star) = \frac{1}{2}\|z\mathcal{A}(\alpha(X-x^\star)) - d\|_2. \tag{1.50}$$

We prove that this problem is well-posed and we find good approximations of z, α but most importantly of $x^\star$. Setting $h^{\mathrm{app}}(x^\star) = N\pi/(2k)$, it provides a good approximation of h at one point. We then repeat the same method when changing the frequency to get a reconstruction of h, controlled by the following theorem:

Theorem 1.5. *We denote by d the measurements of $u(x,0)$. There exists a constant $C>0$ such that*

$$\|h^{app} - h\|_\infty \leq \underbrace{C\|h'\|_\infty{}^{4/3}}_{\substack{\textit{successive approximations}\\ \textit{of measurement}}} + \underbrace{C\|h'\|_\infty\|d-u(x,0)\|_{L^2}}_{\textit{error on measurements}}. \tag{1.51}$$

This method enables to reconstruct h with a very high sensibility, as long as the waveguide slowly varies. We present two different reconstructions in Figure 1.16.

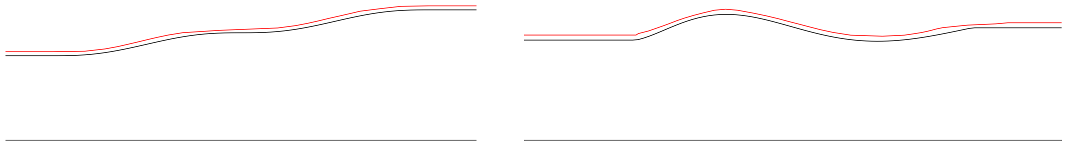

Figure 1.16 – Reconstruction of width defects in slowly varying waveguides given surface measurements. Black lines represent the initial shape of Ω, and red ones the reconstruction of Ω, slightly shifted for comparison purposes.

1.4.3 Inverse problem in the acoustic case from section measurements

In the previous Chapter, we used surface measurements to reconstruct the width of the waveguide. Even if this reconstruction method was initially thought to be applied to elastic plates, we noticed that it could also be used in acoustic pipes, providing that data are taken on one section of the waveguide instead of the surface. In Chapter 6, we explain how to adapt the reconstruction method to section data and solve the inverse problem

$$\text{Find } h \text{ from } u_{k|\Sigma} \text{ for frequencies } k \in \mathbb{R}_+ \text{ where } \Sigma \text{ is a section of } \Omega. \tag{1.52}$$

Since data are taken on one surface, we can hardly use the previous method to fit the three parameters Airy function to the data. We assume that the measurement section is located at $x = x_s$. Using the study of the forward problem presented in Theorem 1.4, we prove that we have access to

$$\Phi\left(\int_{x^\star}^{x_s} k_N(z)\mathrm{d}z\right), \qquad \text{where} \qquad \Phi(x) = \sin\left(x+\frac{\pi}{4}\right)\exp\left(ix + i\frac{\pi}{4}\right). \tag{1.53}$$

If the discretization of the frequency interval is sufficiently small, we can find a local inverse to the function Φ. Since we still want to recover the location of $x^\star$, we approximate the integral of k_N using a quadrature method of order 1. Wet get a linear system $MV = m$, where M is a known matrix, m is a vector made with measurements data and V contains the locations of each $x^\star$. Solving this system and using the previous approximation $h(x^\star) = N\pi/(2k)$ provides again a approximation h^{app} of the width of the waveguide, and we can prove the following stability result:

Theorem 1.6. *Let ρ be the discretization step of the frequency interval measurements. There exists constants $C_1, C_2 > 0$ such that*

$$\|h^{app} - h\|_\infty \leq \underbrace{C_1\|h'\|_\infty \rho^{-5/2}}_{\text{inversion of } M} + \underbrace{C_2\rho\|h'\|_\infty^2}_{\substack{\text{approximation of}\\ \text{measurements}}} . \tag{1.54}$$

This reconstruction method only works with monotonous widths since we can only put the source of waves near the measurement section. It does not provide an accurate reconstruction for general non-monotonous width variations, as illustrated in Figure 1.17.

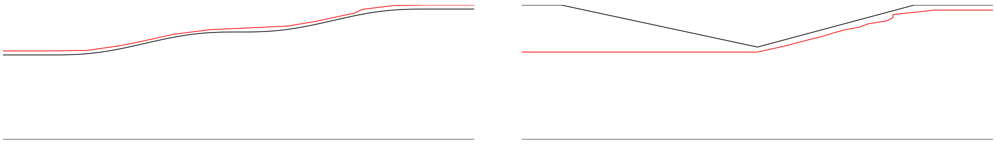

Figure 1.17 – Reconstruction of width defects in slowly varying waveguides given section measurements. Black lines represent the initial shape of Ω, and red ones the reconstruction of Ω, slightly shifted for comparison purposes.

1.4.4 Generalization to the elastic case

The last chapter of this thesis extends the results of Chapter 5 and Chapter 6 to the elastic case and solve the inverse problem

$$\text{Find } h \text{ from } u_{k|S} \text{ for frequencies } k \in \mathbb{R}_+ \text{ where } S \text{ is the top surface of } \Omega. \tag{1.55}$$

In the acoustic case, the relation between h and the vanishing of k_n was explicit and used to approach the width at the locally resonant point. The elastic case proves more difficult since the Rayleigh Lamb dispersion relation, which rules the dependency of h and k_n, does not have explicitly solutions. Moreover, contrary to the acoustic case, there are three types of critical points instead of one:

- The longitudinal points (L) where $k_n = 0$ and the Lamb mode u_n vanishes,
- The transverse points (T) where $k_n = 0$ and the Lamb mode v_n vanishes,
- The zero-group velocity points (ZGV) where $\partial_{\text{Real}(k_n)} = 0$ and $k \neq 0$.

We represent in Figure 1.18 an example of the dispersion curves of k_n and the positions of critical points.

The situation near longitudinal and transverse points is very similar to the one presented in Chapter 3 for the acoustic case, and using Theorem 1.2, we can prove a theorem similar to Theorem 1.4 in the elastic case. The situation near ZGV points is more complex and needs further studies. Using a modified Lamb basis which is continuously defined all along the varying waveguide, we provide an analysis of the forward problem. We especially prove that around the locally resonant point $x^\star$ such that $k_n(x^\star)$ is a ZGV point, the wavefield can be approached with an explicit but hardly usable expression (see Theorem 7.3 in Chapter 7). More importantly, we notice that a specific linear combination of $\boldsymbol{u}$ and $\boldsymbol{v}$ can be approached by the three parameters function

$$d^{\text{app}}_{\alpha,z,x^\star} := z\mathcal{A}(\alpha(x - x^\star)), \tag{1.56}$$

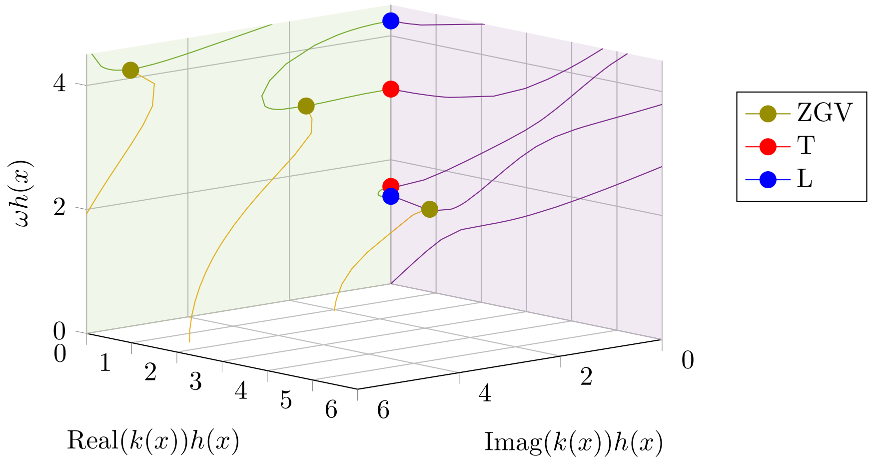

Figure 1.18 – Some dispersion curves of the relation between h and k, with the position of the three types of critical points. Purple curves are in the real plan, green one are in the purely imaginary one, and yellow one are in neither of them.

previously used in Chapter 4. Then, we can apply the reconstruction method developed in Chapter 5 to reconstruct width defects in elastic plates. Propagation and reconstructions at longitudinal and transverse points are very similar to the one presented in Figure 1.15 and 1.16. In Figure 1.19, we present one example of propagation near ZGV points and one reconstruction obtained using this locally resonant point.

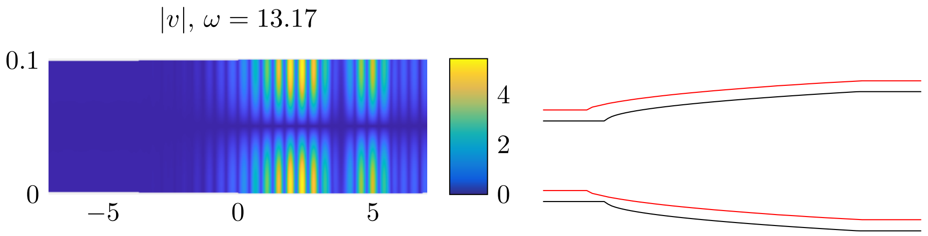

Figure 1.19 – Reconstruction method at ZGV locally resonant points. On the left, we represent the wavefield $|v|$ propagating in a slowly variable waveguide at frequency $\omega = 13.17$. On the right, we use these propagation measurements for different frequencies to reconstruct the width variations. The initial is represented in black, and the reconstruction is in red and lightly shifted for comparison purposes

Chapters of this manuscript come from published, submitted or in preparation articles. This leads to some redundancies, especially at the beginning of chapters. Still, it enables each chapter to be readable independently and aside from the others. At the end of this manuscript, we will discuss all the limitations and extensions of these results and raise possible future works related to our research.

I

Back-scattering multi-frequency reconstruction

2

Small defects reconstruction in waveguides from multifrequency one-side scattering data

The aim of this first chapter is to present a new multi-frequency inversion method to reconstruct small defects in a 2D acoustic waveguide. This case is the simplest one to study and gives insights on possible generalization to 3D acoustic waveguides or 2D elastic waveguide. Given one-side multi-frequency wavefield measurements of propagating modes, we use a Born approximation to provide a L^2-stable reconstruction of three types of defects: a local perturbation inside the waveguide, a bending of the waveguide, and a localized defect in the geometry of the waveguide. This method is based on a mode-by-mode spatial Fourier inversion from the available partial data in the Fourier domain. Indeed, in the available data, some high and low spatial frequency information on the defect are missing. We overcome this issue using both a compact support hypothesis and a minimal smoothness hypothesis on the defects. We also provide a suitable numerical method for efficient reconstruction of such defects and we discuss its applications and limits.

2.1 Introduction

In all this chapter, we present a method to detect and reconstruct small defects in a waveguide of dimension 2 from multi-frequency wavefield measurements. The measurements are taken on one section of the waveguide, and we assume that only the propagative modes can be detected. Indeed, in most of practical cases, measurements are made far from the defects where the evanescent modes vanish. In a waveguide $\Omega \subset \mathbb{R}^2$, in the time harmonic regime the wavefield u_k satisfies the Helmholtz equation

$$\Delta u_k + k^2(1+q)u_k = -s, \tag{2.1}$$

where k is the frequency, q is a compactly supported bounded perturbation inside the waveguide and the function s is a source of waves.

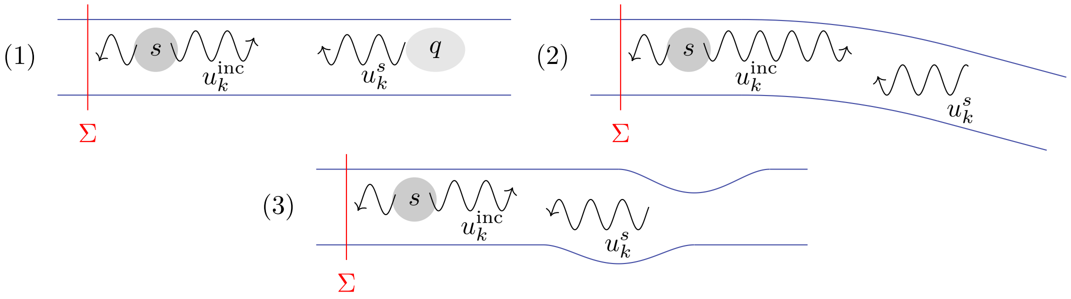

Figure 2.1 – Representation of the three types of defects: in (1) a local perturbation q, in (2) a bending of the waveguide, in (3) a localized defect in the geometry of Ω. A controlled source s generates a wavefield u_k^{inc}. When it crosses the defect, it generates a scattered wavefield u_k^s. Both u_k^{inc} and u_k^s are measured on the section Σ.

We focus on the inversion of three main types of defects represented in Figure 2.1: a local perturbation of the index q, a bend of the waveguide, and a localized defect in the geometry of Ω. The detection of such defects can be used as a non destructive means to monitor pipes, optical fibers, or train rails for instance (see [55, 54]). A controlled source s generates wavefields in Ω for some frequencies $k \in K \subset \mathbb{R}_+^*$ and we assume the knowledge of the corresponding measurements $u_k(x,y)$ for every $(x,y) \in \Sigma$ where Σ is a fixed section of Ω.

The detection of bends or shape defects in a waveguide is mentioned in the articles [61, 3, 2]. To solve the forward problem, the authors use a conformal mapping or a local orthogonal transformation to map the geometry to that of a regular waveguide. This method is very helpful to understand the propagation of waves in irregular waveguides but is not easily adaptable for the inverse problem and for the reconstruction of defects, since the transformation to a regular waveguide is not explicit and proves numerically expensive.

The recovery of inhomogeneities in a waveguide using scattered field data has been extensively studied. In [34], the authors use a spectral decomposition and assume knowledge of the far-field scattered wavefield to reconstruct the inhomogeneities in a 2D waveguide. The authors in [27] adapt the Linear Sampling Method [31] to waveguides detection of inhomogeneities in 2D or 3D. In [9], an asymptotic formula of the scattered field is used to localize small inclusions. Periodic waveguides are considered in [25]. In all these articles, the frequency in the Helmholtz equation is fixed and it is assumed that incident waves can be sent on every propagative mode in the waveguide. However, as defects may be invisible at some frequencies (as shown in [36]) the frequency has to be chosen wisely.

Our work concerns a different approach, also used in [13, 12], where we assume that data is available for a whole interval of frequencies. This provides additional information that should help not only localize but reconstruct the shape of the defect. The use of multi-frequency data provides uniqueness of the reconstruction (see [7]) and better stability (see [14, 52, 93]). In this work we assume that one only send the first propagative mode at different frequencies in the waveguide as an excitation source. This situation seems to correspond to the practice of monitoring pipes in mechanical experiments [55]. In this study, we assume that the defects are small in amplitude and/or in support in order to approximate the wavefield using its Born approximation. This seems to be a reasonable assumption considering the applications that this work intends to address. This approximation is described in [32], and is also used in [34, 9]. Our strategy to study the impact of small geometrical defects is to provide a well suited mapping from the perturbed waveguide to a perfect waveguide that generates some change in the Helmholtz equation itself. Through the reconstruction of these modifications in the equation while assuming a perfect waveguide, it is possible to recover the defects in the geometry.

An important difficulty in detecting inhomogeneities using one sided multi-frequencies measurements in a waveguide is that low spatial frequency information carried by vanishing modes about the inhomogeneities may be missing. Indeed, these modes are not measurable in practice due to their exponential decay.

One of the key results of this chapter is given by Theorem 2.2 that provides conditions to control the error of approximation in the recovery of a function from an incomplete knowledge of its Fourier transform. In this result, we assume that both high frequencies and a reasonable amount of low frequencies are missing. Nevertheless, a stable inversion in L^2 remains possible assuming a reasonable *a priori* knowledge of the smoothness and the support of the unknown perturbation. This result provides a theoretical stability argument that allows us to run a mode-by-mode well-conditioned inversion using a penalized least-square technique. This method is numerically efficient, and can be applied to recover defects of the three different types.

The chapter is organized a follows. In section 2.2, we recall some properties of the forward source problem in a waveguide using the modal decompositions of both the wavefield and the source. We then study the inverse source problem with full frequency data and then with partial frequency data. In section 2.3, we apply the results to recover all three types of defects that we are interested in: internal inhomogeneities, bending or shape defects. In section 2.4, we present the numerical method used to detect defects and some numerical simulations. To avoid the so called “inverse crime” in the numerical tests, we use two different codes. We use a finite element based solver with PML’s [18] to generate the data from a waveguide with defects. Another solver, based on a modal decomposition, allows us to recover the inhomogeneities from the simulated data. Only the second code is used in the inversion procedure.

2.2 Forward and inverse source problem in a waveguide

In this section, we present the tools required to study the forward and inverse source problems in a waveguide. First, we recall some classical results about the forward source problem and modal decomposition. These results can also be found in [27, 34]. Next, assuming that the perturbation is small enough, we show existence, uniqueness and stability of a solution to the perturbed forward source problem. Finally, we present an inversion strategy using the measurements of the wavefield on a section of the waveguide for full and partial frequency data.

2.2.1 Forward source problem in a perfect waveguide

We consider a 2D infinite perfect waveguide $\Omega = \mathbb{R} \times (0, 1)$ in which waves can propagate at frequency $k > 0$ according to the homogeneous Helmholtz equation

$$\Delta u_k + k^2 u_k = 0. \tag{2.2}$$

We choose a Neumann condition on the boundary $\partial\Omega$, but this condition can be changed to a Dirichlet or a Robin condition without altering of our results. It is known that the homogeneous Neumann spectral problem for the negative Laplacian on $(0, 1)$ has an infinite sequence of eigenvalues λ_n for $n \in \mathbb{N}$, and that it is possible to find eigenvectors φ_n that form an orthonormal basis of $\mathrm{L}^2(0, 1)$. Precisely,

$$\lambda_n = n^2\pi^2, \qquad \varphi_n = \begin{cases} 1 & \text{if } n = 0, \\ y \mapsto \sqrt{2}\cos(n\pi y) & \text{otherwise.} \end{cases} \tag{2.3}$$

This basis proves quite helpful in the study of waveguides since every function $f \in \mathrm{L}^2_{\mathrm{loc}}(\Omega)$ can be decomposed as a sum of modes:

$$f(x, y) = \sum_{n\in\mathbb{N}} f_n(x)\varphi_n(y) \quad \text{f. a. e. } (x, y) \in \Omega, \qquad f_n \in \mathrm{L}^2_{\mathrm{loc}}(\mathbb{R}). \tag{2.4}$$

Let ν be the outward unit normal on $\partial\Omega$. Using this orthonormal basis, the solutions to the homogeneous problem

$$\begin{cases} \Delta u_k + k^2 u_k = 0 & \text{in } \Omega, \\ \partial_\nu u_k = 0 & \text{on } \partial\Omega, \end{cases} \tag{2.5}$$

are linear combinations of $(x, y) \mapsto \varphi_n(y)e^{\pm ik_n x}$ where $k_n^2 = k^2 - n^2\pi^2$ and $\mathrm{Re}(k_n)$, $\mathrm{Im}(k_n) \geq 0$. This solution is called the n-th mode. In the following, we assume that $k_n \neq 0$, meaning that we do not choose a wavelength $k = n\pi$ for $n \in \mathbb{N}$. Two types of modes appear in the decomposition of u_k. Propagative modes correspond to $n < k/\pi$ and then $k_n \in \mathbb{R}$, while evanescent modes feature $n > k/\pi$ and $k_n \in i\mathbb{R}$. The amplitude of evanescent modes decays exponentially fast at one end of the waveguide. An extra condition is then needed to ensure the uniqueness of a solution to the Helmholtz problem (2.5).

Definition 2.1. *A solution $u_k \in H^2_{loc}(\Omega)$ of* (2.2) *is outgoing if it satisfies the radiation conditions:*

$$\left| \langle u_k(x, \cdot), \varphi_n\rangle' \frac{x}{|x|} - ik_n\langle u_k(x, \cdot), \varphi_n\rangle \right| \xrightarrow[|x|\to+\infty]{} 0 \quad \forall n \in \mathbb{N}, \tag{2.6}$$

where $\langle\cdot, \cdot\rangle$ is the inner scalar product in $L^2(0, 1)$.

Remark 2.1. *This condition is an adaptation to our problem of the Sommerfeld condition used in free space. The articles [34, 27] adopt another radiation condition called Dirichlet to Neumann condition, which is equivalent to our radiation condition when s is compactly supported.*

Using the previous conditions, the following proposition holds, the proof of which is given in the Appendix 2.A at the end of the chapter.

Proposition 2.1. *For every* $s \in L^1(\Omega) \cap L^2_{loc}(\Omega)$*, the problem*

$$\left\{ \begin{array}{rl} \Delta u_k + k^2 u_k = -s & \textit{in } \Omega, \\ \partial_\nu u_k = 0 & \textit{on } \partial\Omega, \\ u_k \textit{ is outgoing}, & \end{array} \right. \tag{2.7}$$

has a unique solution $u_k \in H^2_{loc}(\Omega)$*, which decomposes as*

$$u_k(x,y) = \sum_{n\in\mathbb{N}} u_{k,n}(x)\varphi_n(y) \quad \textit{where} \quad u_{k,n}(x) = \frac{i}{2k_n}\int_{\mathbb{R}} s_n(z) e^{ik_n|x-z|}\mathrm{d}z, \tag{2.8}$$

if the decomposition of s *is* $s(x,y) = \sum_{n\in\mathbb{N}} s_n(x)\varphi_n(y)$*.*

Remark 2.2. *It is interesting to note that* s *does not need to have a compact support in this context, as is the case in the free space Helmholtz problem.*

Let $\Omega_r := (-r,r)\times(0,1)$ where $r>0$ denote a restriction of length $2r$ of the waveguide. We assume that every source defined on Ω_r is extended by 0 in Ω and we define the forward Helmholtz source operator $\mathcal{H}_k$ by

$$\mathcal{H}_k : \begin{array}{rcl} \mathrm{L}^2(\Omega_r) & \to & \mathrm{H}^2(\Omega_r) \\ s & \mapsto & u_{k\,|\Omega_r} \end{array} \qquad \text{where } u_k \text{ is the solution to (2.7).} \tag{2.9}$$

The following proposition quantifies the dependence between u and the source s. Its proof is given in Appendix 2.B at the end of the chapter.

Proposition 2.2. *The forward Helmholtz source operator* $\mathcal{H}_k$ *is well defined, continuous and there exists* $C>0$ *depending only on* k *and* r *such that for every* $s \in L^2(\Omega_r)$*,*

$$\|u_k\|_{H^2(\Omega_r)} \leq C\|s\|_{L^2(\Omega_r)}. \tag{2.10}$$

Remark 2.3. *We notice from the proof that* C *increases when the distance between* k *and* $\pi\mathbb{N}$ *decreases.*

In the following, we also need to consider the problem where the source is located on the boundary of the waveguide. Let $\partial\Omega_{\text{top}} = \mathbb{R}\times\{1\}$ and $\partial\Omega_{\text{bot}} = \mathbb{R}\times\{0\}$. Similarly to Proposition 2.1, we have

Proposition 2.3. *Let* $b_1, b_2 \in L^1(\mathbb{R}) \cap H^{1/2}_{loc}(\mathbb{R})$*. The Helmholtz equation*

$$\left\{ \begin{array}{rl} \Delta u_k + k^2 u_k = 0 & \textit{in } \Omega, \\ \partial_\nu u_k = b_1 & \textit{on } \partial\Omega_{top}, \\ \partial_\nu u_k = b_2 & \textit{on } \partial\Omega_{bot}, \\ u_k \textit{ is outgoing}, & \end{array} \right. \tag{2.11}$$

has a unique solution $u_k \in H^2_{loc}(\Omega)$*, which decomposes as*

$$u_k(x,y) = \sum_{n\in\mathbb{N}} u_{k,n}(x)\varphi_n(y) \tag{2.12}$$

where

$$u_{k,n}(x) = \frac{i}{2k_n}\int_{\mathbb{R}} (b_1(z)\varphi_n(1) + b_2(z)\varphi_n(0)) e^{ik_n|x-z|}\mathrm{d}z. \tag{2.13}$$

In the restricted guide Ω_r, we assume again that every source defined on $(-r,r)$ is extended by 0 on $\mathbb{R}$ and we define the forward Helmholtz boundary source operator $\mathcal{G}_k$ by

$$\mathcal{G}_k : \begin{array}{ccc} \left(\widetilde{\mathrm{H}}^{1/2}(-r,r)\right)^2 & \to & \mathrm{H}^2(\Omega_r) \\ (b_1,b_2) & \mapsto & u_k \end{array} \qquad \text{where } u_k \text{ is the solution to (2.11)}, \tag{2.14}$$

and $\widetilde{\mathrm{H}}^{1/2}(-r,r)$ is the closure of $\mathcal{D}(-r,r)$, the space of distributions with support in $(-r,r)$, for the $\mathrm{H}^{1/2}(\mathbb{R})$ norm (see [66] for more details). A result similar to Proposition 2.2 holds:

Proposition 2.4. *The forward Helmholtz boundary source operator $\mathcal{G}_k$ is well defined, continuous and there exists a constant D depending only on k and r such that for every $b_1, b_2 \in \widetilde{H}^{1/2}(-r,r)$,*

$$\|\mathcal{G}(b_1,b_2)\|_{H^2(\Omega_r)} \leq D\left(\|b_1\|_{\widetilde{H}^{1/2}(-r,r)} + \|b_2\|_{\widetilde{H}^{1/2}(-r,r)}\right). \tag{2.15}$$

Remark 2.4. *Combining Propositions 2.1 and 2.3, we see by linearity that the problem*

$$\begin{cases} \Delta u_k + k^2 u_k = -s & \text{in } \Omega, \\ \partial_\nu u_k = b_1 & \text{on } \partial\Omega_{top}, \\ \partial_\nu u_k = b_2 & \text{on } \partial\Omega_{bot}, \\ u_k \text{ is outgoing}, & \end{cases} \tag{2.16}$$

has a unique solution $u_k \in H^2_{loc}(\Omega)$.

We represent in Figure 2.2 illustrations of wavefields u_k generated by internal and boundary sources.

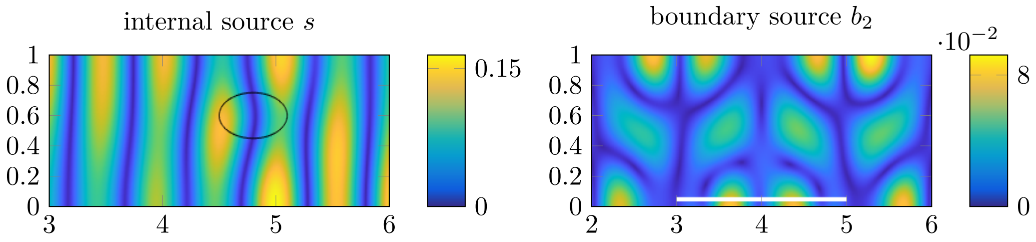

Figure 2.2 – Representation of wavefields $|u_k|$ propagating in a regular waveguide. On the left, the wavefield is generated by an internal source s whose support is delimited with a black line. On the right, the wavefield is generated by a boundary source b_2 whose support is represented with a write line. In both situations, $k=6$.

2.2.2 Forward source problem with perturbations

In the following we introduce a theoretical framework for a perturbed Helmholtz problem in a perfect waveguide. Under the Born hypothesis, we prove existence and uniqueness of a solution for the perturbed problem. Then, we provide estimates on the error between the exact solution of the perturbed problem and its Born approximation.

The perturbed Helmholtz equation takes the form

$$\begin{cases} \Delta w_k + k^2 w_k = -s - \mathcal{S}(w_k) & \text{in } \Omega, \\ \partial_\nu w_k = b_1 + \mathcal{T}_1(w_k) & \text{on } \partial\Omega_{\mathrm{top}}, \\ \partial_\nu w_k = b_2 + \mathcal{T}_2(w_k) & \text{on } \partial\Omega_{\mathrm{bot}}, \\ w_k \text{ is outgoing}, & \end{cases} \tag{2.17}$$

where $\mathcal{S}, \mathcal{T}_1, \mathcal{T}_2$ are linear operators depending on w_k. Moreover, we assume that there exists $r > 0$ such that $\operatorname{supp}(\mathcal{S}(w_k)) \subset \Omega_r$ and $\operatorname{supp}(\mathcal{T}_1(w_k)), \operatorname{supp}(\mathcal{T}_2(w_k)) \subset (-r, r)$ for every $w_k \in \mathrm{H}^2_{\mathrm{loc}}(\Omega)$.

Using the forward Helmholtz source operator $\mathcal{H}_k$ and the forward Helmholtz boundary source operator $\mathcal{G}_k$ defined in (2.9) and (2.14), we can rewrite this equation on Ω_r:

$$w_k = \mathcal{H}_k(s) + \mathcal{G}_k(b_1, b_2) + \mathcal{H}_k(\mathcal{S}(w_k)) + \mathcal{G}_k(\mathcal{T}_1(w_k), \mathcal{T}_2(w_k)). \tag{2.18}$$

Proposition 2.5. *Let* $r > 0$ *such that* $\mathcal{S} : H^2(\Omega_r) \to L^2(\Omega_r)$ *and* $\mathcal{T}_1, \mathcal{T}_2 : H^2(\Omega_r) \to \widetilde{H}^{1/2}(-r, r)$. *Let* C *and* D *be the constants defined in Propositions 2.2 and 2.4. Let* $s \in L^2(\Omega_r)$, $b_1, b_2 \in \widetilde{H}^{1/2}(-r, r)$ *and assume that*

$$\mu := C\|\mathcal{S}\|_{H^2(\Omega_r)\to L^2(\Omega_r)} + D\left(\|\mathcal{T}_1\|_{H^2(\Omega_r)\to\widetilde{H}^{1/2}(-r,r)} + \|\mathcal{T}_2\|_{H^2(\Omega_r)\to\widetilde{H}^{1/2}(-r,r)}\right) < 1. \tag{2.19}$$

Then (2.18) *has a unique solution* $w_k \in H^2(\Omega_r)$ *and*

$$w_k = \sum_{m\in\mathbb{N}} \left[\mathcal{H}_k \circ \mathcal{S} + \mathcal{G}_k \circ (\mathcal{T}_1, \mathcal{T}_2)\right]^m \left(\mathcal{H}_k(s) + \mathcal{G}_k(b_1, b_2)\right). \tag{2.20}$$

Proof. If (2.19) is satisfied then $\mathcal{H}_k \circ \mathcal{S} + \mathcal{G}_k \circ (\mathcal{T}_1, \mathcal{T}_2)$ is a contraction, and the expression (2.20) is the expansion of w_k into a Born series (see for instance [32]). ☐

Remark 2.5. *In this work, we only consider perturbations which affect the partial differential equation via a linear operator. However, the above Proposition also extends to non linear operators, assuming they are Lipschitz.*

To compute numerically w_k, we approximate the Born series by its first term.

Definition 2.2. *Let* w_k *be defined by* (2.20). *We define* v_k, *the Born approximation of* w_k *by*

$$v_k = \mathcal{H}_k(s) + \mathcal{G}_k(b_1, b_2). \tag{2.21}$$

Proposition 2.6. *Assume that* μ *satisfies* (2.19) *as in Proposition 2.5. Let* w_k *be the solution of* (2.18) *and* v_k *its Born approximation. Then*

$$\|w_k - v_k\|_{H^2(\Omega_r)} \le \left(C\|s\|_{L^2(\Omega_r)} + D\left(\|b_1\|_{\widetilde{H}^{1/2}(-r,r)} + \|b_2\|_{\widetilde{H}^{1/2}(-r,r)}\right)\right)\frac{\mu}{1-\mu}. \tag{2.22}$$

Proof. We use the definitions of w_k and v_k and the sum of geometrical series. ☐

Remark 2.6. *If* $\mathcal{S}, \mathcal{T}_1$ *and* $\mathcal{T}_2$ *are small, we have proved that the solution of* (2.17) *is very close to the solution of*

$$\begin{cases} \Delta v_k + k^2 v_k = -s & \text{in } \Omega, \\ \partial_\nu v_k = b_1 & \text{on } \partial\Omega_{top}, \\ \partial_\nu v_k = b_2 & \text{on } \partial\Omega_{bot}, \\ v_k \text{ is outgoing}, & \end{cases} \tag{2.23}$$

and we have quantified the error made by approximating w_k *by* v_k.

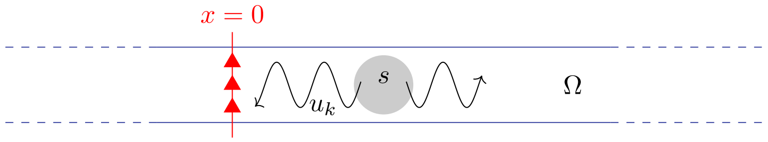

Figure 2.3 – Representation of the inverse source problem in a perfect waveguide. A source s generates a wavefield u_k propagation in Ω. This wavefield is measured on the section $x = 0$, symbolized with red triangles.

2.2.3 Inverse source problem in a perfect waveguide

In this section, we consider the inverse problem of reconstructing a real-valued source s. The goal is to determine the location of s form measurements made on the section $\{0\} \times (0, 1)$ at every frequency $k > 0$, as illustrated in Figure 2.3.

For every $k > 0$ and $0 < y < 1$, $u_k(0, y)$ is measured. Using Proposition 2.1, we know that

$$u_k(0, y) = \sum_{n \in \mathbb{N}} u_{k,n}(0)\varphi_n(y) \quad \text{where} \quad u_{k,n}(0) = \frac{i}{2k_n} \int_{\mathbb{R}} s_n(z) e^{ik_n|z|} \mathrm{d}z, \tag{2.24}$$

if the decomposition of s is $s(x, y) = \sum_{n \in \mathbb{N}} s_n(x)\varphi_n(y)$. Since

$$u_{k,n}(0) = \int_{\mathbb{R}} u_k(0, y)\varphi_n(y)\mathrm{d}y, \tag{2.25}$$

we can theoretically have access to $u_{k,n}(0)$ for every $n \in \mathbb{N}$. However, in real-life experiments, noise is likely to pollute the response of evanescent mode, so we assume that we only have access to $u_{k,n}(0)$ for every $n \in \mathbb{N}$ such that $n < k/\pi$:

$$u_{k,n}(0) = \frac{i}{2k_n} \int_{\mathbb{R}} s_n(z) e^{ik_n|z|} \mathrm{d}z \quad \forall k > 0, \forall n \in \mathbb{N}, n < k/\pi. \tag{2.26}$$

We notice that this expression depends on $k_n = \sqrt{k^2 - n^2\pi^2}$. Since

$$(k, n) \mapsto (\omega, n) := (\sqrt{k^2 - n^2\pi^2}, n), \tag{2.27}$$

is one-to-one from $\{(k, n) \in \mathbb{R}_+^* \times \mathbb{N},\, n < k/\pi\}$ to $\mathbb{R}_+^* \times \mathbb{N}$, the available data is then

$$d_{\omega,n} := \frac{i}{2\omega} \int_{\mathbb{R}} s_n(z) e^{i\omega|z|} \mathrm{d}z \quad \forall n \in \mathbb{N}, \forall \omega \in \mathbb{R}_+^*. \tag{2.28}$$

This change of variable means that given a mode n and a value $\omega > 0$, there exists a frequency $k > 0$ such that n is a propagative mode and $k_n = \omega$. In order to remove the absolute value in the expression of the available data, we assume that $\operatorname{supp}(s) \subset (0, +\infty) \times (0, 1)$, *i.e.* that the source is located to the right of the section where the measurements are made.

Definition 2.3. *Let H be the Hilbert space defined by*

$$H := \left\{ \hat{u} : \mathbb{R}_+^* \to \mathbb{C} \,\middle|\, \int_0^{+\infty} \omega^2 |\hat{u}(\omega)|^2 \mathrm{d}\omega < +\infty \right\}, \ \|\hat{u}\|_H^2 = \int_0^{+\infty} \omega^2 |\hat{u}(\omega)|^2 \mathrm{d}k. \tag{2.29}$$

We denote by Γ *the forward modal operator and by* F_{source} *the forward source operator for problem* (2.7). *Then* Γ *and* F_{source} *are defined by*

$$\Gamma : \begin{array}{ccc} L^2(\mathbb{R}_+) & \to & H \\ f & \mapsto & \left(\omega \mapsto \dfrac{i}{2\omega}\displaystyle\int_0^{+\infty} f(z)e^{i\omega z}\mathrm{d}z\right) \end{array}, \tag{2.30}$$

$$F_{source} : \begin{array}{ccc} L^2(\Omega) & \to & \ell^2(H) \\ s & \mapsto & (\Gamma(s_n))_{n\in\mathbb{N}} \end{array}, \tag{2.31}$$

if the decomposition of s *is* $s(x,y) = \sum_{n\in\mathbb{N}} s_n(x)\varphi_n(y)$.

We choose the following definition for the Fourier transform:

$$\mathcal{F}(f)(\omega) = \int_{\mathbb{R}} f(z)e^{-i\omega z}\mathrm{d}z.$$

Since s is real-valued, Γ is related to the Fourier transform:

$$\mathcal{F}(f)(\omega) = \begin{cases} \overline{\dfrac{2\omega}{i}\Gamma(f)(\omega)} & \text{if } \omega > 0 \\ \dfrac{-2\omega}{i}\Gamma(f)(-\omega) & \text{if } \omega < 0 \end{cases}.$$

Using the properties of the Fourier transform, we can prove the following Proposition:

Proposition 2.7. *The forward modal operator* Γ *and the forward source operator* F_{source} *satisfy the relations*

$$\|\Gamma(f)\|_H^2 = \frac{\pi}{4}\|f\|^2_{L^2(\mathbb{R}_+)} \quad \forall f \in L^2(\mathbb{R}_+), \tag{2.32}$$

$$\|F_{source}(s)\|^2_{\ell^2(H)} = \frac{\pi}{4}\|s\|^2_{L^2(\Omega)} \quad \forall s \in L^2(\Omega), \tag{2.33}$$

and their inverse operators are given by

$$\Gamma^{-1} : \begin{array}{ccc} H & \to & L^2(\mathbb{R}) \\ v & \mapsto & \left(x \mapsto \dfrac{i}{\pi}\displaystyle\int_0^{+\infty} \omega\overline{v(\omega)}e^{i\omega x}\mathrm{d}\omega + \dfrac{i}{\pi}\displaystyle\int_{-\infty}^{0} \omega v(-\omega)e^{i\omega x}\mathrm{d}\omega\right) \end{array}, \tag{2.34}$$

$$F_{source}^{-1} : \begin{array}{ccc} \ell^2(H) & \to & L^2(\Omega) \\ (v_n)_{n\in\mathbb{N}} & \mapsto & \left((x,y) \mapsto \displaystyle\sum_{n\in\mathbb{N}} \Gamma^{-1}(v_n)(x)\varphi_n(y)\right) \end{array}. \tag{2.35}$$

We can use the same framework for problem (2.11) when the source term is a boundary term. In this case, the measured data is

$$u_{k,n}(0) = \frac{i}{2k_n}\int_{\mathbb{R}} (-b_1(z)\varphi_n(1) + b_2(z)\varphi_n(0))e^{ik_n|z|}\mathrm{d}z \quad \forall n \in \mathbb{N}, \tag{2.36}$$

As $(k,n) \mapsto (\sqrt{k^2 - n^2\pi^2}, n)$ is one-to-one from $\{(k,n) \in \mathbb{R}_+^* \times \mathbb{N},\ n < k/\pi\}$ to $\mathbb{R}_+^* \times \mathbb{N}$, we assume that the available data is

$$d_{\omega,1} = \frac{i}{2\omega}\int_{\mathbb{R}} (b_1(z) + b_2(z))e^{i\omega|z|}\mathrm{d}z \qquad \forall \omega \in \mathbb{R}_+^*, \tag{2.37}$$

$$d_{\omega,2} = \frac{i}{2\omega}\int_{\mathbb{R}}(-\sqrt{2}b_1(z)+\sqrt{2}b_2(z))e^{i\omega|z|}\mathrm{d}z \qquad \forall \omega \in \mathbb{R}_+^*. \tag{2.38}$$

Again, we assume that $\operatorname{supp}(b_1), \operatorname{supp}(b_2) \subset (0,+\infty)$ and with the help of Proposition 2.3, we define the forward operator.

Definition 2.4. *The forward Helmholtz boundary source operator F_{bound} for the problem* (2.11) *is defined by*

$$F_{bound}: \begin{array}{ccc} \left(H^{1/2}(\mathbb{R}_+)\right)^2 & \to & H\times H \\ (b_1,b_2) & \mapsto & \begin{pmatrix} \omega \mapsto \dfrac{i}{2\omega}\displaystyle\int_0^{+\infty}(b_1(z)+b_2(z))e^{i\omega z}\mathrm{d}z \\ \omega \mapsto \dfrac{i}{\sqrt{2}\omega}\displaystyle\int_0^{+\infty}(b_2(z)-b_1(z))e^{i\omega z}\mathrm{d}z \end{pmatrix} \end{array}. \tag{2.39}$$

This operator is invertible:

Proposition 2.8. *The forward Helmholtz boundary source operator F_{bound} is invertible:*

$$F_{bound}^{-1}: \begin{array}{ccc} H\times H & \to & \left(H^{1/2}(\mathbb{R}_+)\right)^2 \\ (v_1,v_2) & \mapsto & \left(\Gamma^{-1}\left(\dfrac{\sqrt{2}v_1 - v_2}{2\sqrt{2}}\right), \Gamma^{-1}\left(\dfrac{\sqrt{2}v_1 + v_2}{2\sqrt{2}}\right)\right) \end{array}. \tag{2.40}$$

Propositions 2.7 and 2.8 show that the measurements of the wave on a section of the waveguide for every frequency $k>0$ are sufficient to reconstruct the source. Thus, the inverse operators can be computed explicitly and in a stable way. However, it is unrealistic to measure u_k for every frequency $k>0$ in practice. We address this issue of limited data in the next subsection.

2.2.4 Inverse source problem from limited frequency data

In this section, we assume that the frequency data are only known in a given interval. To reconstruct every s_n in (2.7), we need to find a way to reconstruct a function f knowing only the values of its Fourier transform on a given interval. This problem is called Fourier synthesis, and has been studied in [51] for instance. If the given interval has the form $(0,\omega_1)$, some regularity on the function is sufficient to provide a good reconstruction of f and to control the approximation error (see [38]). On the other hand, we have to deal in the next section with intervals of the form $(\omega_0,+\infty)$. This case is harder, and it seems difficult to get a good reconstruction of the function f. However, if the function f is compactly supported, its Fourier transform is analytic. Thus, the values of $\Gamma(f)(\omega)$ for ω in an interval (ω_0,ω_1) completely determine $\Gamma(f)(\omega)$ for ω in $(0,+\infty)$. In the following, we address the issue of the stability of this reconstruction.

We start with a lemma to control the L^2 norm on $(0,\omega_0)$ of an analytic function in terms of its values on $(\omega_0,\omega_0+\sigma)$ where ω_0 and σ are positive real numbers.

Lemma 2.1. *Let f be a function in $\mathcal{C}^\infty(\mathbb{R}_+)\cap L^2(\mathbb{R}_+)$ and assume that for every $j\in\mathbb{N}$ and $\omega\in\mathbb{R}_+$, $|f^{(j)}(\omega)| \leq c\dfrac{r^j}{j^\alpha}\|f\|_{L^2(\mathbb{R}_+)}$ where $r,\alpha,c\in\mathbb{R}_+^*$. Let $\omega_0,\sigma\in\mathbb{R}_+^*$ and $\varepsilon\in(0,1)$. There exists a constant ξ, depending only on $\omega_0,\sigma,r,\alpha,c,\varepsilon$, such that*

$$\frac{\|f\|_{L^2(0,\omega_0)}}{\|f\|_{L^2(\mathbb{R}_+)}} \leq \xi\left(\frac{\|f\|_{L^2(\omega_0,\omega_0+\sigma)}}{\|f\|_{L^2(\mathbb{R}_+)}}\right)^{1-\varepsilon}. \tag{2.41}$$

Proof. Let $n \in \mathbb{N}$, we define $\delta_j = c\dfrac{r^j}{j^\alpha}$ and write the Taylor expansion of f at ω_0 up to order n:

$$f(\omega) = \sum_{j=0}^{n} \frac{(\omega-\omega_0)^j}{j!} f^{(j)}(\omega_0) + R_n(\omega),$$

with

$$|R_n(\omega)| \leq \frac{\delta_{n+1}\|f\|_{L^2(\mathbb{R}_+)}|\omega-\omega_0|^{n+1}}{(n+1)!}.$$

We denote by $P_n \in \mathbb{R}_n[X]$ the Taylor polynomial associated with this expansion:

$$P_n = \sum_{j=0}^{n} a_j (X-\omega_0)^j := \sum_{j=0}^{n} \frac{f^{(j)}(\omega_0)}{j!}(X-\omega_0)^j,$$

and the operator

$$I_n : \begin{array}{ccc} \mathbb{R}_n[X] \cap \mathrm{L}^2(\omega_0, \omega_0+\sigma) & \to & \mathbb{R}_n[X] \cap \mathrm{L}^2(0,\omega_0) \\ P & \mapsto & P \end{array},$$

endowed with the norm

$$\|I_n\| := \sup_{P\in\mathbb{R}_n[X]} \frac{\|P\|_{\mathrm{L}^2(0,\omega_0)}}{\|P\|_{\mathrm{L}^2(\omega_0,\omega_0+\sigma)}}.$$

We immediately see that

$$\begin{aligned} \|f\|_{\mathrm{L}^2(0,\omega_0)} &\leq \|f-P_n\|_{\mathrm{L}^2(0,\omega_0)} + \|P_n\|_{\mathrm{L}^2(0,\omega_0)} \\ &\leq \|R_n\|_{\mathrm{L}^2(0,\omega_0)} + \|I_n\|\|P_n\|_{\mathrm{L}^2(\omega_0,\omega_0+\sigma)} \\ &\leq \|R_n\|_{\mathrm{L}^2(0,\omega_0)} + \|I_n\|\|R_n\|_{\mathrm{L}^2(\omega_0,\omega_0+\sigma)} + \|I_n\|\|f\|_{\mathrm{L}^2(\omega_0,\omega_0+\sigma)}. \end{aligned} \tag{2.42}$$

Let us compute $\|I_n\|$. Let $P = \sum_{j=0}^{n} a_k (X-\omega_0)^j$ be a polynomial in $\mathbb{R}_n[X]$, then

$$\|P\|^2_{\mathrm{L}^2(0,\omega_0)} = \int_0^{\omega_0} \sum_{k,p=0}^{n} a_k a_p (\omega-\omega_0)^{k+p} \mathrm{d}\omega = \sum_{k,p=0}^{n} a_k a_p \frac{-(-\omega_0)^{k+p+1}}{k+p+1} = \omega_0 W^T H_n W,$$

where $W := \left(a_k(-\omega_0)^k\right)_{k=0,\cdots,n}$ and $H_n = \left(\dfrac{1}{k+p+1}\right)_{p,k=0,\cdots,n}$ is the Hilbert matrix. In the same way,

$$\|P\|^2_{\mathrm{L}^2(\omega_0,\omega_0+\sigma)} = \int_{\omega_0}^{\omega_0+\sigma} \sum_{k,p=0}^{n} a_k a_p (\omega-\omega_0)^{k+p} \mathrm{d}\omega = \sum_{k,p=0}^{n} a_k a_p \frac{\sigma^{k+p+1}}{k+p+1} = \sigma V^T H_n V.$$

where $V := \left(a_k \sigma^k\right)_{k=0,\cdots,n}$. Let $\lambda_{\min}$ and $\lambda_{\max}$ be the lowest and greatest eigenvalues of H_n. It follows that

$$\omega_0 W^T H_n W \leq \omega_0 \|W\|_2^2 \lambda_{\max}, \qquad \sigma V^T H_n V \geq \sigma \|V\|_2^2 \lambda_{\min}. \tag{2.43}$$

Notice that

$$\|W\|_2^2 \leq \max(1,\omega_0)^{2n} \sum_{k=0}^{n} |a_k|^2 \leq \frac{\max(1,\omega_0)^{2n}}{\min(1,\sigma)^{2n}} \sum_{k=0}^{n} |a_k|^2 \sigma^{2k} \leq \frac{\max(1,\omega_0)^{2n}}{\min(1,\sigma)^{2n}} \|V\|_2^2.$$

Thus, if $\omega_0 \leq \sigma$, then $\|W\|_2^2 \leq \|V\|_2^2$. We follow [99] to estimate the condition number of the Hilbert matrix: There exists $c_H > 0$ such that $\mathrm{cond}_2(H_n)$ for the euclidean norm satisfies

$$\frac{\lambda_{\max}}{\lambda_{\min}} = \mathrm{cond}_2(H_n) \leq c_H \frac{(1+\sqrt{2})^{4n}}{\sqrt{n}}.$$

We conclude that

$$\|P\|^2_{\mathrm{L}^2(0,\omega_0)} \leq \frac{\omega_0}{\sigma} \left(1_{\omega_0 \leq \sigma} + 1_{\omega_0 > \sigma} \frac{\max(1,\omega_0)^{2n}}{\min(1,\sigma)^{2n}} \right) c_H \frac{(1+\sqrt{2})^{4n}}{\sqrt{n}} \|P\|^2_{\mathrm{L}^2(\omega_0,\omega_0+\sigma)}.$$

We define $C_1 := \sqrt{\dfrac{c_H \omega_0}{\sigma}}$ and $C_2 := \left(1+\sqrt{2}\right)^2 \left(1_{\omega_0 \leq \sigma} + 1_{\omega_0 > \sigma} \dfrac{\max(1,\omega_0)}{\min(1,\sigma)} \right)$, then

$$\|I_n\| \leq C_1 \frac{C_2^n}{n^{1/4}}. \tag{2.44}$$

We next bound R_n in $\mathrm{L}^2(0,\omega_0)$ by

$$\|R_n\|_{\mathrm{L}^2(0,\omega_0)} \leq \frac{\delta_{n+1} \|f\|_{\mathrm{L}^2(\mathbb{R}_+)}}{(n+1)!} \left(\int_0^{\omega_0} (\omega_0 - \omega)^{2n+2} \mathrm{d}\omega \right)^{1/2} \leq \frac{\delta_{n+1} \|f\|_{\mathrm{L}^2(\mathbb{R}_+)}}{(n+1)!} \left(\frac{\omega_0^{2n+3}}{2n+3} \right)^{1/2},$$

and in $\mathrm{L}^2(\omega_0,\omega_0+\sigma)$ by

$$\|R_n\|_{\mathrm{L}^2(\omega_0,\omega_0+\sigma)} \leq \frac{\delta_{n+1} \|f\|_{\mathrm{L}^2(\mathbb{R}_+)}}{(n+1)!} \left(\int_{\omega_0}^{\omega_0+\sigma} (\omega - \omega_0)^{2n+2} \mathrm{d}\omega \right)^{1/2} \leq \frac{\delta_{n+1} \|f\|_{\mathrm{L}^2(\mathbb{R}_+)}}{(n+1)!} \left(\frac{\sigma^{2n+3}}{2n+3} \right)^{1/2}.$$

Substituting in (2.42) we find

$$\begin{aligned} \|f\|_{\mathrm{L}^2(0,\omega_0)} \leq{}& \frac{\delta_{n+1} \|f\|_{\mathrm{L}^2(\mathbb{R}_+)}}{(n+1)!} \frac{\omega_0^{n+3/2}}{\sqrt{2n+3}} \\ &+ \frac{\delta_{n+1} \|f\|_{\mathrm{L}^2(\mathbb{R}_+)}}{(n+1)!} \frac{\sigma^{n+3/2}}{\sqrt{2n+3}} \frac{C_1 C_2^n}{n^{1/4}} + \frac{C_1 C_2^n}{n^{1/4}} \|f\|_{\mathrm{L}^2(\omega_0,\omega_0+\sigma)}. \end{aligned} \tag{2.45}$$

To simplify the notations, we define

$$C_3 := \frac{2}{\sqrt{2}} \max\left(\omega_0^{1/2}, C_1 \sigma^{1/2} \right) = \max\left(1, \sqrt{c_H}\right) \sqrt{2\omega_0}, \quad C_4 := \max(\omega_0, \sigma C_2).$$

We notice that

$$C_4 = \max\left[\omega_0, \left(1+\sqrt{2}\right)^2 \left(1_{\omega_0 \leq \sigma} \sigma + 1_{\omega_0 > \sigma} \frac{\sigma \max(1,\omega_0)}{\min(1,\sigma)} \right) \right] = \sigma c_2.$$

The expression (2.45) can be simplified and

$$\frac{\|f\|_{\mathrm{L}^2(0,\omega_0)}}{\|f\|_{\mathrm{L}^2(0,+\infty)}} \leq C_3 \frac{\delta_{n+1} C_4^{n+1}}{(n+1)! \sqrt{n+1}} + C_1 C_2^n \frac{\|f\|_{\mathrm{L}^2(\omega_0,\omega_0+\sigma)}}{\|f\|_{\mathrm{L}^2(0,+\infty)}} \qquad \forall n \in \mathbb{N}.$$

The first term does not depend on f, and this expression shows that it is impossible to obtain a Lipschitz estimate. To optimize this estimate, we play on the degree n of the polynomials. Indeed, the first term on the right hand side may be large for small values of n, while the second term blows up when n is large. We set $Q := \|f\|_{\mathrm{L}^2(\omega_0,\omega_0+\sigma)}/\|f\|_{\mathrm{L}^2(\mathbb{R}^+)}$ and for $\varepsilon \in (0,1)$ we choose the integer

$$n = \left\lfloor -\frac{\varepsilon}{\ln(C_2)}\ln(Q) + \frac{\ln(C_5)}{\ln(C_2)} \right\rfloor,$$

where $C_5 > 0$ is a constant to be determined later, and $\lfloor\,\rfloor$ is the floor function. Invoking the Stirling formula $n! \geq \sqrt{2\pi n}\dfrac{n^n}{e^n}$ and the fact that $\delta_{n+1} = c\dfrac{r^{n+1}}{(n+1)^\alpha}$, we obtain

$$C_3\frac{\delta_{n+1}C_4^{n+1}}{(n+1)!\sqrt{n+1}} \leq \frac{C_3c(erC_4)^{n+1}}{(n+1)^{\alpha+1}\sqrt{2\pi}(n+1)^{n+1}} = \frac{C_3c}{\sqrt{2\pi}}\frac{(erC_4)^{n+1}}{(n+1)^{n+\alpha+2}}.$$

To simplify the notations, we define

$$\gamma := erC_4, \quad A := \frac{\ln(C_5)}{\ln(C_2)}, \quad B := \frac{\varepsilon}{\ln(C_2)}.$$

Using the fact that $A - B\ln(Q) \leq n+1 \leq A - B\ln(Q) + 1$, we see that

$$\begin{aligned}\frac{(ert)^{n+1}}{(n+1)^{n+\alpha+2}} &\leq \exp[(A - B\ln(Q)+1)\ln(\gamma) \\ &\qquad - (A - B\ln(Q)+\alpha+1)\ln(A-B\ln(Q))] \\ &= \gamma^{A+1}Q^{-B\ln(\gamma)+B\ln(A-B\ln(Q))}(A-B\ln(Q))^{-(A+\alpha+1)}.\end{aligned}$$

The exponent of Q is greater that $1-\varepsilon$ provided

$$Q \leq \exp\left(-\frac{1}{B}\left[\exp\left(\frac{1-\varepsilon}{B} + \ln(\gamma)\right) - A\right]\right).$$

Since $Q \leq 1$, this condition is satisfied if

$$A = \exp\left(\frac{1-\varepsilon}{B} + \ln(\gamma)\right) + B\ln(\eta) = erC_4C_2^{\frac{1-\varepsilon}{\varepsilon}},$$

which fixes the value of

$$C_5 = C_2^{erC_4C_2^{\frac{1-\varepsilon}{\varepsilon}}}.$$

Using the fact that $A - B\ln(Q) \geq erC_4C_2^{\frac{1-\varepsilon}{\varepsilon}}$, it follows that

$$\frac{\|f\|_{\mathrm{L}^2(0,\omega_0)}}{\|f\|_{\mathrm{L}^2(\mathbb{R}^+)}} \leq \xi\left(\frac{\|f\|_{\mathrm{L}^2(\omega_0,\omega_0+\sigma)}}{\|f\|_{\mathrm{L}^2(\mathbb{R}^+)}}\right)^{1-\varepsilon},$$

where

$$\xi := \frac{C_3c}{\sqrt{2\pi}}C_2^{-\frac{1-\varepsilon}{\varepsilon}\left(1+\alpha+erC_4C_2^{\frac{1-\varepsilon}{\varepsilon}}\right)}(erC_4)^{-\alpha} + C_1C_2^{erC_4C_2^{\frac{1-\varepsilon}{\varepsilon}}}. \tag{2.46}$$

□

Remark 2.7. *The expression* (2.46) *certainly over-estimates the optimal constant in* (2.41)*, in particular in view of* (2.43)*.*

We now consider two functions f and f_{app} of one variable. We assume again that every function defined on (r, r) is extended by 0 on $\mathbb{R}$. The following theorem provides a control over the distance between f and f_{app} using only the values of their Fourier transforms on the interval $[\omega_0, +\infty)$.

Theorem 2.1 (Reconstruction with low frequency gap in the Fourier transform)**.** *Let $f, f_{app} \in L^2(-r, r)$ where $r \in \mathbb{R}_+^*$. Let $\omega_0, \sigma \in \mathbb{R}_+^*$. We assume that there exists $M \in \mathbb{R}_+^*$ such that*

$$\|f\|_{L^2(-r,r)} \leq M, \quad \|f_{app}\|_{L^2(-r,r)} \leq M. \tag{2.47}$$

For every $0 < \varepsilon < 1$, there exists ξ, depending on $r, \omega_0, \sigma, \varepsilon$, such that

$$\begin{aligned} \|f - f_{app}\|^2_{L^2(-r,r)} \leq \frac{\left(8\pi M^2\right)^{\varepsilon}}{\pi} \xi^2 \|\mathcal{F}(f) - \mathcal{F}(f_{app})\|^{2-2\varepsilon}_{L^2(\omega_0,\omega_0+\sigma)} \\ + \frac{1}{\pi} \|\mathcal{F}(f) - \mathcal{F}(f_{app})\|^2_{L^2(\omega_0,+\infty)}. \end{aligned} \tag{2.48}$$

Proof. We know that

$$\|f - f_{\text{app}}\|^2_{\mathrm{L}^2(-r,r)} = \frac{1}{\pi} \|\mathcal{F}(f) - \mathcal{F}(f_{\text{app}})\|^2_{\mathrm{L}^2(0,\omega_0)} + \frac{1}{\pi} \|\mathcal{F}(f) - \mathcal{F}(f_{\text{app}})\|^2_{\mathrm{L}^2(\omega_0,+\infty)}.$$

Since f is compactly supported as a function of $\mathrm{L}^2(\mathbb{R})$, we know that for every $j \in \mathbb{N}$, $\omega \in \mathbb{R}_+$,

$$\begin{aligned} \left| \frac{\mathrm{d}^j}{\mathrm{d}\omega^j} (\mathcal{F}(f) - \mathcal{F}(f_{\text{app}}))(\omega) \right| &\leq \left(2 \int_0^r x^{2j} \mathrm{d}x \right)^{1/2} \|f - f_{\text{app}}\|_{L^2(-r,r)} \\ &\leq \frac{r^j \sqrt{r} \|\mathcal{F}(f) - \mathcal{F}(f_{\text{app}})\|_{L^2(\mathbb{R}_+)}}{\sqrt{\pi}\sqrt{2j+1}}. \end{aligned}$$

It follows from Lemma 2.1 that

$$\begin{aligned} \|f - f_{\text{app}}\|^2_{\mathrm{L}^2(-r,r)} \leq \frac{1}{\pi} \xi^2 \|\mathcal{F}(f) - \mathcal{F}(f_{\text{app}})\|^{2\varepsilon}_{\mathrm{L}^2(\mathbb{R}^+)} \|\mathcal{F}(f) - \mathcal{F}(f_{\text{app}})\|^{2-2\varepsilon}_{\mathrm{L}^2(\omega_0,\omega_0+\sigma)} \\ + \frac{1}{\pi} \|\mathcal{F}(f) - \mathcal{F}(f_{\text{app}})\|^2_{\mathrm{L}^2(\omega_0,+\infty)}. \end{aligned}$$

Since $\|\mathcal{F}(f) - \mathcal{F}(f_{\text{app}})\|^{2\varepsilon}_{\mathrm{L}^2(\mathbb{R}^+)} \leq \left(2\pi \|f - f_{\text{app}}\|^2_{\mathrm{L}^2(-r,r)}\right)^{\varepsilon} \leq \left(8\pi M^2\right)^{\varepsilon}$, the result follows. ☐

Next, we generalize Theorem 2.1 to the case when we control the Fourier transform of f on a finite interval $[\omega_0, \omega_1]$.

Theorem 2.2 (Reconstruction from a finite interval of the Fourier transform)**.** *Let $f, f_{app} \in H^1(-r, r)$ where $r > 0$. Let $\omega_0, \omega_1 \in \mathbb{R}_+^*, \omega_0 < \omega_1$. We assume that there exists $M \in \mathbb{R}_+^*$ such that*

$$\|f\|_{H^1(-r,r)} \leq M, \quad \|f_{app}\|_{H^1(-r,r)} \leq M. \tag{2.49}$$

For every $0 < \varepsilon < 1$, there exists ξ, depending on $r, \omega_0, \omega_1, \varepsilon, M$, such that

$$\begin{aligned} \|f - f_{app}\|^2_{L^2(-r,r)} \leq \frac{\left(8\pi M^2\right)^{\varepsilon}}{\pi} \xi^2 \|\mathcal{F}(f) - \mathcal{F}(f_{app})\|^{2-2\varepsilon}_{L^2(\omega_0,\omega_1)} \\ + \frac{1}{\pi} \|\mathcal{F}(f) - \mathcal{F}(f_{app})\|^2_{L^2(\omega_0,\omega_1)} + \frac{8}{\omega_1^2} M^2. \end{aligned} \tag{2.50}$$

Proof. We choose $\sigma = \max(1, \omega_1)$ in the Theorem 2.1. Since $f - f_{\text{app}} \in \mathrm{H}^1(-r, r)$,

$$\|\mathcal{F}(f) - \mathcal{F}(f_{\text{app}})\|^2_{\mathrm{L}^2(\omega_1,+\infty)} = \left\| \omega \mapsto \frac{\mathcal{F}(f')(\omega) - \mathcal{F}(f'_{\text{app}})(\omega)}{\omega} \right\|^2_{\mathrm{L}^2(\omega_1,+\infty)} \leq \frac{2\pi}{\omega_1^2} \|f' - f'_{\text{app}}\|^2_{\mathrm{L}^2(-r,r)}.$$

□

Remark 2.8. *Using* (2.46)*, we notice that* $\xi \underset{\omega_0 \to 0}{\longrightarrow} 0$ *and that* $\frac{8\pi M^2}{\omega_1^2} \underset{\omega_1 \to +\infty}{\longrightarrow} 0$*. Moreover, if we define* $d = \Gamma(f)$ *and* $d_{app} = \Gamma(f_{app})$ *then* $2|\omega(d - d_{app})(\omega)| = |\mathcal{F}(f - f_{app})(\omega)|$ *so*

$$\frac{1}{\pi} \|\mathcal{F}(f) - \mathcal{F}(f_{app})\|^2_{L^2(\omega_0,\omega_1)} \underset{[\omega_0,\omega_1] \to (0,+\infty)}{\longrightarrow} \frac{4}{\pi} \|d - \tilde{d}\|^2_H, \tag{2.51}$$

which is consistent with Proposition 2.7.

Theorem 2.2 provides a theoretical control of the error of the reconstruction between f and f_{app}. However, since ξ can be very large, such control might not be sufficient to ensure a numerical convergence of f_{app} to f. To illustrate this point, we consider a source s supported on $[1-r, 1+r]$. Let X be the discretization of $[1-r, 1+r]$ with N_X points. We define $h = 2r/(N_X - 1)$. Using the fast Fourier transform, we compute the discretization of the Fourier transform $\mathcal{F}(s)$ on a set K of frequencies. We notice that $\mathcal{F}(s)(K) = Ms(X)$ where $M := h(e^{ixk})_{x \in X, k \in K}$, and that $s(X) = M^{-1}\mathcal{F}(s)(K)$. To simulate the low frequency gap, we truncate K and define $K_t = \{k \in K, k > \omega_0\}$ and $M_t = h(e^{ixk})_{x \in X, k \in K_t}$. Then, $s(X) = (M_t^T M_t)^{-1} M_t^T \mathcal{F}(s)(K_t)$. Even if $M_t^T M_t$ is invertible, its condition number strongly depends on r and ω_0 just like the constant ξ in Lemma 2.1. Figure 2.4 illustrates this fact for different values of ω_0 and r.

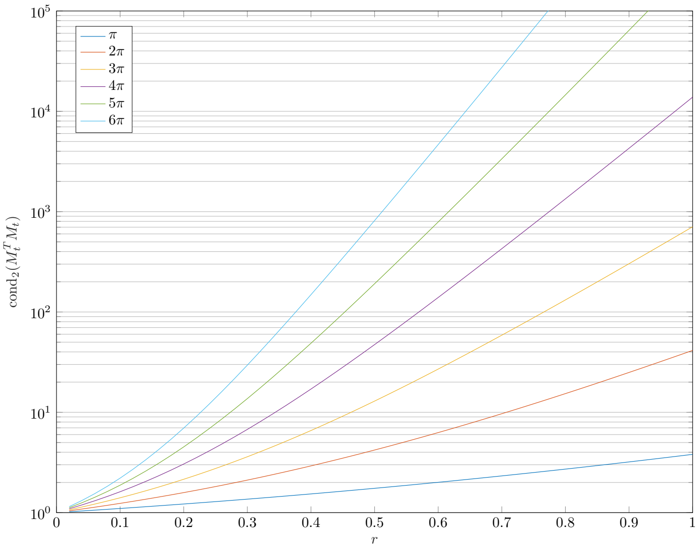

Figure 2.4 – Condition number of $M_t^T M_t$ for different sizes of support and values of ω_0. Here, X is the discretization of $[1-r, 1+r]$ with $500r + 1$ points. The x-axis represents the evolution of r, and the y-axis $\text{cond}_2(M_t^T M_t)$. Each curve corresponds to value of ω_0 as indicated in the left rectangle.

To conclude, if we only have access to perturbed Fourier transform data on a given interval of frequencies, we can build an approximation of f provided f is compactly supported and an *a priori* bound on the norm of f is known. However, depending of ω_0 and r, the error between f and its approximation can be large. We can reduce it by increasing ω_1 and by diminishing ω_0 and r.

2.3 Application to the identification of shape defects, bending or inhomogeneities

We propose a method to identify shape defects or bends in a waveguide, which is almost identical to our method of source detection. We first map the deformed waveguide to a regular waveguide, and then use the source inverse method discussed in the first section to reconstruct the parameters that characterize the defect.

2.3.1 Transformation of the deformed waveguide

Let ϕ_0 and ϕ_1 in $\mathcal{C}^1(\mathbb{R})$. We consider a deformed waveguide

$$\widetilde{\Omega} = \bigcup_{x\in\mathbb{R}} (\phi_0(x), \phi_1(x)) = \{\phi_0(x) < y < \phi_1(x), x \in \mathbb{R}\}. \tag{2.52}$$

A wave $\tilde{u}$ in $\widetilde{\Omega}$ satisfies the equation

$$\left\{\begin{array}{ll} \Delta\tilde{u} + k^2\tilde{u} = -\tilde{s} & \text{in } \widetilde{\Omega}, \\ \partial_\nu\tilde{u} = \tilde{b}_1 & \text{on } \partial\widetilde{\Omega}_{\text{top}}, \\ \partial_\nu\tilde{u} = \tilde{b}_2 & \text{on } \partial\widetilde{\Omega}_{\text{bot}}, \\ \tilde{u} \text{ is outgoing}, & \end{array}\right. \tag{2.53}$$

where $\tilde{s} \in \mathrm{L}^2_{\text{loc}}(\widetilde{\Omega})$, $\tilde{b_1} \in \mathrm{H}^{1/2}_{\text{loc}}(\partial\widetilde{\Omega}_{\text{top}})$, and $\tilde{b_2} \in \mathrm{H}^{1/2}_{\text{loc}}(\partial\widetilde{\Omega}_{\text{bot}})$. To use the tools developed in the previous section, we map $\widetilde{\Omega}$ to the regular waveguide $\Omega = (0,1)\times\mathbb{R}$. Let ϕ be a one-to-one function that maps Ω into $\widetilde{\Omega}$. Such a function exists and can even be assumed to be conformal (see for instance [3]). We define $u = \tilde{u}\circ\phi$ the wave in the regular guide, $J\phi$ the Jacobien matrix of ϕ, $\tau = |\det(J\phi)|$, $t_1 = |\nabla\phi_0|$, and $t_2 = |\nabla\phi_1|$. The variational formulation of (2.53) shows that for every $\tilde{v} \in \mathrm{H}^1(\widetilde{\Omega})$,

$$\int_{\widetilde{\Omega}} \nabla\tilde{u}\cdot\nabla\tilde{v} - k^2\int_{\widetilde{\Omega}} \tilde{u}\tilde{v} = \int_{\widetilde{\Omega}} \tilde{s}\tilde{v} + \int_{\partial\widetilde{\Omega}_{\text{top}}} \tilde{b}_1\tilde{v} + \int_{\partial\widetilde{\Omega}_{\text{bot}}} \tilde{b}_2\tilde{v},$$

or equivalently,

$$\begin{aligned} \int_\Omega (\nabla\tilde{u}\circ\phi)\cdot(\nabla\tilde{v}\circ\phi)\tau - k^2\int_\Omega(\tilde{u}\circ\phi)(\tilde{v}\circ\phi)\tau &= \int_\Omega(\tilde{s}\circ\phi)(\tilde{v}\circ\phi)\tau \\ &+ \int_{\partial\Omega_{\text{top}}} \tilde{b}_1\circ\phi_1\, t_1\,\tilde{v}\circ\phi + \int_{\partial\Omega_{\text{bot}}} \tilde{b}_2\circ\phi_0\, t_2\,\tilde{v}\circ\phi. \end{aligned} \tag{2.54}$$

Using the fact that $\nabla u = J\phi^T\nabla\tilde{u}\circ\phi$, we set $s = \tilde{s}\circ\phi$, $b_1 = \tilde{b}_1\circ\phi_1$, $b_2 = \tilde{b}_2\circ\phi_0$, and obtain that for every $v \in \mathrm{H}^1(\Omega)$,

$$\int_\Omega S\nabla u\cdot\nabla v - k^2\int_\Omega u\,v\,\tau = \int_\Omega s\,v\,\tau + \int_{\partial\Omega_{\text{top}}} b_1\,v\,t_1 + \int_{\partial\Omega_{\text{bot}}} b_2\,v\,t_2. \tag{2.55}$$

where $S = J\phi^{-1}\left(J\phi^{-1}\right)^T\tau$, which yields the equation satisfied by u:

$$\left\{\begin{array}{ll} \nabla\cdot(S\nabla u) + k^2\tau u = -\tau s & \text{in } \Omega, \\ S\nabla u\cdot\nu = b_1t_1 & \text{on } \partial\Omega_{\text{top}}, \\ S\nabla u\cdot\nu = b_2t_2 & \text{on } \partial\Omega_{\text{bot}}. \end{array}\right. \tag{2.56}$$

We write $S = I_2 + M$ and $\tau = 1 + \varepsilon$, where M and ε are expected to be small if the deformation is small. The above partial differential equation becomes

$$\begin{cases} \Delta u + k^2 u = -\tau s - \nabla \cdot (M \nabla u) - k^2 \varepsilon u & \text{in } \Omega, \\ \nabla u \cdot \nu = b_1 t_1 - M \nabla u \cdot \nu & \text{on } \partial\Omega_{\text{top}}, \\ \nabla u \cdot \nu = b_2 t_2 - M \nabla u \cdot \nu & \text{on } \partial\Omega_{\text{bot}}. \end{cases} \tag{2.57}$$

For $r > 0$, we set

$$\Sigma : \begin{array}{rcl} \mathrm{H}^2(\Omega_r) & \to & \mathrm{L}^2(\Omega_r) \\ u & \mapsto & \nabla \cdot (M \nabla u) + k^2 \varepsilon u \end{array}, \qquad \Pi : \begin{array}{rcl} \mathrm{H}^2(\Omega_r) & \to & \widetilde{\mathrm{H}}^{1/2}(-r, r) \\ u & \mapsto & M \nabla u \cdot \nu \end{array}. \tag{2.58}$$

The next Proposition follows from the definitions of Σ and Π and the dependence between $\|M\|_{\mathcal{C}^1(\Omega_r)}$, ε and ϕ.

Proposition 2.9. *The operator Σ and Π are continuous if $M \in \mathcal{C}^1(\Omega_r)$. In addition, there exists constants $A(\phi), B(\phi)$ depending only on k, r, M and ε such that*

$$\|\Sigma(u)\|_{L^2(\Omega_r)} \leq A(\phi) \|u\|_{H^2(\Omega_r)}, \qquad \|\Pi(u)\|_{H^{1/2}(\Omega_r)} \leq B(\phi) \|u\|_{H^2(\Omega_r)}. \tag{2.59}$$

Recalling section 2.2.2 and Definition 2.2, we define the Born approximation v of u by

$$\begin{cases} \Delta v + k^2 v = -\tau s & \text{in } \Omega, \\ \nabla v \cdot \nu = b_1 t_1 & \text{on } \partial\Omega_{\text{top}}, \\ \nabla v \cdot \nu = b_2 t_2 & \text{on } \partial\Omega_{\text{bot}}, \\ v \text{ is outgoing.} \end{cases} \tag{2.60}$$

Proposition 2.5 and 2.6 yield the following:

Proposition 2.10. *Let C and D be the constants defined in Propositions 2.2 and 2.4, and $A(\phi)$, $B(\phi)$ defined in Proposition 2.9. If $CA(\phi) + 2DB(\phi) < 1$ then (2.57) has a unique solution u and*

$$\begin{aligned} \|u - v\|_{H^2(\Omega_r)} \leq \frac{CA(\phi) + 2DB(\phi)}{1 - CA(\phi) + 2DB(\phi)} \Big[& C \|\tau s\|_{L^2(\Omega_r)} \\ & + D \left(\|b_2 t_2\|_{\widetilde{H}^{1/2}(-r,r)} + \|b_1 t_1\|_{\widetilde{H}^{1/2}(-r,r)} \right) \Big]. \end{aligned} \tag{2.61}$$

The Born approximation leads to a problem of source inversion similar to that of section 2.2. Using the results proved in this section, we recover τs, $b_1 t_1$ and $b_2 t_2$. In the following, we study how to characterize a defect by recovering one of those functions. In the case of a bend, one can fix $b_1 = b_2 = 0$ and reduce the inversion to the sole recovery of τs. In the case of a bump, $s = 0$ and the problem reduces to the reconstruction of $b_1 t_1$ and $b_2 t_2$.

2.3.2 Detection of bends

We first consider bends which are parallel portions of circular arcs, whose geometry is determined by the center and the arc-length of these arcs, or equivalently by the distance x_c where the guide starts bending, the angle θ and the radius of curvature r (see Figure 2.5).

More precisely, we define the mapping ϕ from Ω to $\widetilde{\Omega}$ as follow:

- If $x \leq x_c$, $\phi(x, y) = (x, y)$.

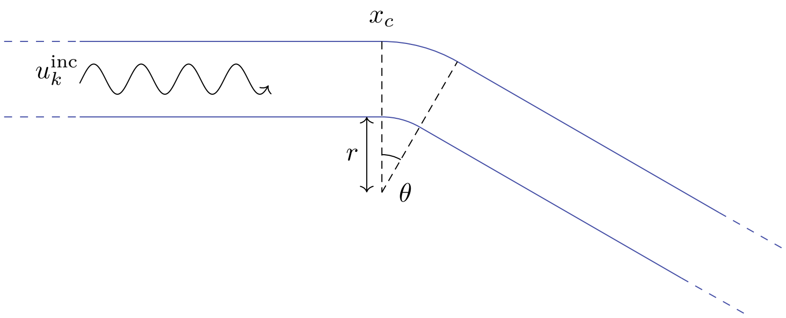

Figure 2.5 – Representation of a bend in a waveguide, with three parameters of interest: the radius of curvature r, the angle θ and the start of the bending x_c. An known incident wave u_k^{inc} is sent in the waveguide.

- If $x \in (x_c, x_c + \theta(r+1))$, then

$$\phi(x,y) = \left(x_c + (r+y)\sin\left(\frac{x-x_c}{r+1}\right), -r + (r+y)\cos\left(\frac{x-x_c}{r+1}\right)\right).$$

- If $x \geq x_c + \theta(r+1)$ then

$$\begin{aligned}\phi(x,y) = (x_c + (r+y)\sin\theta + (x - x_c - \theta(r+1))\cos\theta, -r + (r+y)\cos\theta \\ -(x - x_c - \theta(r+1))\sin\theta).\end{aligned}$$

The matrix $J\phi$ is orthogonal if $x \notin (x_c, x_c + \theta(r+1))$ and so $\tau = 1$ in this range. If $x \in (x_c, x_c + \theta(r+1))$, then

$$J\phi(x,y) = \begin{pmatrix} \frac{r+y}{r+1}\cos\left(\frac{x-x_c}{r+1}\right) & \sin\left(\frac{x-x_c}{r+1}\right) \\ -\frac{r+y}{r+1}\sin\left(\frac{x-x_c}{r+1}\right) & \cos\left(\frac{x-x_c}{r+1}\right) \end{pmatrix}, \quad \tau = \frac{r+y}{r+1},$$

$$S = J\phi^{-1}\left(J\phi^{-1}\right)^T \tau = \begin{pmatrix} \frac{r+1}{r+y} & 0 \\ 0 & \frac{r+y}{r+1} \end{pmatrix}. \tag{2.62}$$

Moreover, $t_1 = 1$ for every $x \in \mathbb{R}$, $t_2 = 1$ if $x \notin (x_c, x_c + \theta(r+1))$ and $t_2 = \frac{r}{r+1}$ otherwise.

We assume along this section that the bend is located to the right of the section $\{0\} \times (0,1)$. We introduce a source $\tilde{s}_k = -2ik\delta_0(x)$, and we notice that $s_k = \tilde{s}_k \circ \phi = \tilde{s}_k$. In the absence of defect, the wavefield generated by this source would be $u_k^{\text{inc}} := e^{ik|x|}$. Let u_k^s be the scattered wavefield defined by $u_k^s := u_k - u_k^{\text{inc}}$. Using (2.57), we notice that u_k^s satisfies the equation

$$\left\{ \begin{array}{ll} \nabla(S\nabla u_k^s) + k^2\tau u_k^s = -\tau s_k - \nabla(S\nabla u_k^{\text{inc}}) - k^2 d u_k^{\text{inc}} & \text{in } \Omega, \\ S\nabla u_k^s \cdot \nu = -S\nabla u_k^{\text{inc}} \cdot \nu & \text{on } \partial\Omega, \\ u_k^s \text{ is outgoing.} & \end{array} \right. \tag{2.63}$$

The fact that $S\nabla u_k^{\text{inc}} \cdot \nu = 0$, and

$$-\tau s_k - \nabla(S\nabla u_k^{\text{inc}}) - k^2 d u_k^{\text{inc}} = -\mathbf{1}_{x\in[x_c, x_c+\theta(r+1)]} k^2 e^{ikx} h_r(y), \tag{2.64}$$

with $h_r(y) = (y-1)\left(\frac{1}{r+y} + \frac{1}{r+1}\right)$ leads to the equation

$$\left\{\begin{array}{rl} \nabla(S\nabla u_k^s) + k^2\tau u_k^s = -\mathbf{1}_{x\in[x_c,x_c+\theta(r+1)]}k^2 e^{ikx}h_r(y) & \text{in } \Omega, \\ S\nabla u_k^s\cdot\nu = 0 & \text{on } \partial\Omega, \\ u_k^s \text{ is outgoing.} & \end{array}\right. \tag{2.65}$$

Under the assumptions of Proposition 2.10, u_k^s is close to the solution v_k of

$$\left\{\begin{array}{rl} \Delta v_k + k^2 v_k = -\mathbf{1}_{x\in[x_c,x_c+\theta(r+1)]}k^2 e^{ikx}h_r(y) & \text{in } \Omega, \\ \nabla v_k\cdot\nu = 0 & \text{on } \partial\Omega, \\ v_k \text{ is outgoing.} & \end{array}\right. \tag{2.66}$$

The measurements consist in the first mode $v_{k,0}$ of v_k for every frequency $k\in(0,k_{\max})$ where $k_{\max}\in\mathbb{R}_+^*$ is given. To simplify the source in (2.65), we define

$$f = \mathbf{1}_{x\in[x_c,x_c+\theta(r+1)]}\int_0^1 h_r(t)\mathrm{d}t. \tag{2.67}$$

Proposition 2.1 yields

$$v_{k,0}(0) = \frac{i}{2k}\int_0^{+\infty} k^2 f(y)e^{2iky}\mathrm{d}y = 2k^2\Gamma(f)(2k) \qquad \forall k\in(0,k_{\max}), \tag{2.68}$$

which shows that we have access to $\Gamma(f)(k)$ for all $k\in(0,2k_{\max})$. We denote by $d=\Gamma(f)(k)$ the data and by d_{app} the perturbed data. We use the method described in section 2.2 to reconstruct an approximation f_{app} of f. The error is controlled by the following:

Proposition 2.11. *Let f and f_{app} be two indicator functions supported in $(-a,a)$ where $a>0$. We assume that the size of the supports of f and f_{app} is greater than δ. Let $k_{max}\in R_+^*$, $d(k)=\Gamma(f)(k)$ and $d_{app}(k)=\Gamma(f_{app})(k)$ defined for $k\in(0,2k_{max})$. Let $c(k)=(\int_k^{+\infty}\mathrm{sinc}^2(x)\mathrm{d}x)^{1/2}$. Then there exists a constant $M\in\mathbb{R}_+^*$ such that*

$$\|f-f_{app}\|^2_{L^2(-a,a)} \le \frac{4}{\pi}\|d-d_{app}\|^2_H + Mc(\delta\, k_{max}). \tag{2.69}$$

Proof. We notice that $|\mathcal{F}(f)(k)| = 2|k\Gamma(f)(k)|$ and we use the fact that the Fourier transform of a indicator function is a sinc function. ☐

Remark 2.9. *This bound of the error of approximation highlights two different sources of error: the error due to the perturbed data, and the error due to the lack of measurements for frequencies above $2k_{max}$. The uncertainty on the measurements can lead to small perturbations of the data, but the most important source of perturbation comes from the Born approximation and the error given in Proposition 2.10.*

To recover the parameters of the bend from f, we see that

$$\int_0^1 h_r(t)\mathrm{d}t = 1 - \frac{1}{2(r+1)} - (r+1)\ln\left(\frac{r+1}{r}\right) = -\frac{1}{r} + o_{r\to+\infty}\left(\frac{1}{r}\right).$$

If r is large enough, we can use the approximation $1/r$ or invert the exact expression. The values of x_c and θ are then deduced from the size of $\mathrm{supp}(f)$.

To conclude, with the measurements on a section of the waveguide of the scattered field due to a source $\tilde{s}_k = -2ik\delta_0(x)$ for every frequency in $(0,k_{\max})$, we are able to reconstruct an approximation of f from which we can derive the parameters of the bend. Moreover, we can quantify the error of this approximation, and this error decreases as $k_{\max}$ increases and as θ decreases or r increases.

Remark 2.10. *This inversion can also be applied for a succession of bends, each parametrized as in Figure 2.5. In this case, the function f is a sum of disjoint indicator functions. Our framework could also certainly be used to reconstruct more general geometries of bends. However, the expression of S is then more complicated and the source function in* (2.65) *may no longer reduces to indicator function.*

2.3.3 Detection of bumps

We now consider shape defects as those depicted in Figure 2.6: the goal is to reconstruct the functions g and h that define the bump geometries, from the measurements.

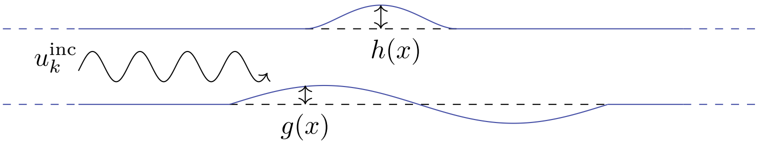

Figure 2.6 – Representation of a shape defect in a waveguide. Functions h and g represents the width variations on the top and bottom of the waveguide. An incident wave u_k^{inc} is sent in the waveguide.

We assume that $\operatorname{supp}(h), \operatorname{supp}(g)$ are compact, that $1+h>g$, and that $h, g \in \mathcal{C}^2(\mathbb{R})$ so Proposition 2.10 applies. Note that $h-1$ and g do not need to be of constant sign. We define $\phi(x,y) = (x, (1+h(x)-g(x))y + g(x))$ and compute

$$J\phi(x,y) = \begin{pmatrix} 1 & 0 \\ (h'(x)-g'(x))y + g'(x) & 1+h(x)-g(x) \end{pmatrix}, \tag{2.70}$$

$$J\phi^{-1}(x,y) = \begin{pmatrix} 1 & 0 \\ -\dfrac{(h'(x)-g'(x))y+g'(x)}{1+h(x)-g(x)} & \dfrac{1}{1+h(x)-g(x)} \end{pmatrix}.$$

Moreover, $\tau = |\det(J\phi)| = 1+h(x)-g(x)$, $t_1 = \sqrt{1+h'(x)^2}$, $t_2 = \sqrt{1+g'(x)^2}$ and

$$S = \begin{pmatrix} 1+h(x)-g(x) & -(h'(x)-g'(x))y - g'(x) \\ -(h'(x)-g'(x))y - g'(x) & \dfrac{((h'(x)-g'(x))y+g'(x))^2}{1+h(x)-g(x)} + \dfrac{1}{1+h(x)-g(x)} \end{pmatrix}.$$

Assuming that the bumps are located to the right of the section $\{0\} \times (0,1)$, we introduce a source $\tilde{s}_k = -2ik\delta_0(x)$, and notice that $s_k = \tilde{s}_k \circ \phi = \tilde{s}_k$. In the absence of defect, the wavefield generated by this source would be $u_k^{\text{inc}} := e^{ik|x|}$. Let $\tilde{u}_k^s := \tilde{u}_k - u_k^{\text{inc}}$ be the scattered wavefield which solves

$$\begin{cases} \Delta\tilde{u_k} + k^2\tilde{u_k} = \tilde{s}_k & \text{in } \widetilde{\Omega}, \\ \partial_\nu \tilde{u_k} = 0 & \text{on } \partial\widetilde{\Omega}, \\ \tilde{u_k} \text{ is outgoing.} \end{cases} \tag{2.71}$$

Using the expression of u_k^{inc} and the fact that if $x>0$ then $e^{ik|x|} = e^{ikx}$, $\tilde{u_k}^s$ satisfies the equation

$$\begin{cases} \Delta\tilde{u_k}^s + k^2\tilde{u_k}^s = 0 & \text{in } \widetilde{\Omega}, \\ \partial_\nu \tilde{u_k}^s = \dfrac{h'(x)}{\sqrt{1+h'(x)^2}} ike^{ikx} & \text{on } \partial\widetilde{\Omega}_{\text{top}}, \\ \partial_\nu \tilde{u_k}^s = \dfrac{-g'(x)}{\sqrt{1+g'(x)^2}} ike^{ikx} & \text{on } \partial\widetilde{\Omega}_{\text{bot}}, \\ \tilde{u_k}^s \text{ is outgoing.} \end{cases} \tag{2.72}$$

Transforming the deformed guide to a regular guide leads to

$$\begin{cases} \Delta u_k^s + k^2 u_s = -\nabla \cdot (M \nabla u_k^s) - k^2 \varepsilon u_k^s & \text{in } \Omega, \\ \partial_\nu u_k^s = -M \nabla u_k^s \cdot \nu + h'(x) ike^{ikx} & \text{on } \Omega_{\text{top}}, \\ \partial_\nu u_k^s = -M \nabla u_k^s \cdot \nu - g'(x) ike^{ikx} & \text{on } \Omega_{\text{bot}}, \\ u_k^s \text{ is outgoing.} \end{cases} \tag{2.73}$$

If the assumptions of Proposition 2.10 are satisfied, u_k^s is close to the solution v_k of

$$\begin{cases} \Delta v_k + k^2 v_k = 0 & \text{in } \Omega, \\ \partial_\nu v_k = h'(x) ike^{ikx} & \text{on } \Omega_{\text{top}}, \\ \partial_\nu v_k = -g'(x) ike^{ikx} & \text{on } \Omega_{\text{bot}}, \\ v_k \text{ is outgoing.} \end{cases} \tag{2.74}$$

Given $k_{\max} > 0$, we measure the first mode $v_{k,0}$ of v_k for all frequencies $k \in (0, k_{\max})$. However, since we assumed that we can measure only propagative modes, we have access to $v_{k,1}$ the second mode of v_k for all frequencies $k > \pi$, so for $k \in (\pi, k_{\max})$. Using Proposition 2.3 and the inversion of source, we have access to

$$v_{k,0}(0) = \frac{i}{2k} \int_0^{+\infty} (h'(z) - g'(z)) ike^{ikz} e^{ikz} \mathrm{d}z \qquad \forall k \in (0, k_{\max}), \tag{2.75}$$

$$v_{k,1}(0) = \frac{-i}{\sqrt{2} k_1} \int_0^{+\infty} (h'(z) + g'(z)) ike^{ikz} e^{ik_1 z} \mathrm{d}z \qquad \forall k \in (\pi, k_{\max}). \tag{2.76}$$

We notice that

$$v_{k,0}(0) = 2ik \Gamma(h' - g')(2k) \qquad \forall k \in (0, k_{\max}), \tag{2.77}$$

$$v_{k,1}(0) = -\frac{\sqrt{2} ik (k_1 + k)}{k_1} \Gamma(h' + g')(k + k_1) \qquad \forall k \in (\pi, k_{\max}). \tag{2.78}$$

We define $s_0 = h' - g'$ and $s_1 = h' + g'$. We have access to $\Gamma(s_0)(k)$ for all $k \in (0, 2k_{\max})$, and since $k \mapsto k + \sqrt{k^2 - \pi^2}$ is one-to-one from $(\pi, k_{\max})$ to $(\pi, k_{\max} + \sqrt{k_{\max}^2 - \pi^2})$, we have access to $\Gamma(s_1)(k)$ for all $k \in (\pi, k_{\max} + \sqrt{k_{\max}^2 - \pi^2})$. We denote by $d_0(k) = \Gamma(s_0)(k)$, $d_1(k) = \Gamma(s_1)(k)$ the data and consider the perturbed data $d_{0_{\text{app}}}$, $d_{1_{\text{app}}}$. The method described in section 2.2 provides approximations $s_{0_{\text{app}}}$, $s_{1_{\text{app}}}$ which we can control by the following:

Proposition 2.12. *Let $s_0, s_1, s_{0_{app}}, s_{1_{app}} \in H^1(-r, r)$ where $r \in \mathbb{R}_+^*$. Let $k_{max} \in R_+^*$, $d_0 = \Gamma(s_0)$, $d_{0_{app}} = \Gamma(s_{0_{app}})$ defined on $(0, 2k_{max})$, $d_1 = \Gamma(s_1)$, $d_{1_{app}} = \Gamma(s_{1_{app}})$ defined on $(\pi, k_{max} + \sqrt{k_{max}^2 - \pi^2})$. Assume that there exists $M \in \mathbb{R}_+^*$ such that $\|s_i\|_{H^1(-r,r)} \leq M$ and $\|s_{i_{app}}\|_{H^1(-r,r)} \leq M$ for $i = 0, 1$. Then for every $0 < \varepsilon < 1$, there exists a constant $\xi_{k_{max}}$, depending on r, M, ε, such that*

$$\|s_0 - s_{0_{app}}\|_{L^2(-r,r)}^2 \leq \frac{4}{\pi} \|d_0 - d_{0_{app}}\|_H^2 + \frac{2\pi}{k_{max}^2} M^2, \tag{2.79}$$

$$\begin{aligned} \|s_1 - s_{1_{app}}\|_{L^2(-r,r)}^2 \leq \xi_{k_{max}} \|d_1 - d_{1_{app}}\|_H^{2-2\varepsilon} + \frac{4}{\pi} \|d_1 - d_{1_{app}}\|_H^2 \\ + \frac{8\pi}{\left(k_{max} + \sqrt{k_{max}^2 - \pi^2}\right)^2} M^2. \end{aligned} \tag{2.80}$$

Proof. Noticing that $|\mathcal{F}(h')(k)| = 2|k\Gamma(h')(k)|$, we apply Theorem 2.2 and Remark 2.8 with $\omega_0 = 0$ and $\omega_1 = 2k_{\max}$, and then $\omega_0 = \pi$ and $\omega_1 = k_{\max} + \sqrt{k_{\max}^2 - \pi^2}$. ☐

Remark 2.11. *This estimate highlights the different sources of error: the error due to the perturbed data, the error due to the lack of measurements at high frequencies, and due to the lack of measurements for the low frequencies of* s_1*. Note that the error diminishes if* K *increases and if the bump gets smaller. Numerical illustrations can be found in section 2.4.4.*

2.3.4 Detection of inhomogeneities

This case is different from the two previous cases, as the presence of an inhomogeneity affects the index of the medium and leads to changes in the homogeneous Helmholtz equation:

$$\Delta u + k^2(1 + h(x,y))u = 0. \tag{2.81}$$

We assume that $\operatorname{supp}(h)$ is compact and that the inhomogeneity is located to the right of the section $\{0\} \times (0,1)$. To detect the defect, we introduce a source $s_k = -2ik\delta_0(x)$. In the absence of defect, the wavefield generated by this source would be $u_k^{\text{inc}} := e^{ik|x|}$. Let u_k^s be the scattered wavefield defined by $u_k^s := u_k - u_k^{\text{inc}}$. We know that u_k satisfies the equation (2.7), and so

$$\begin{cases} \Delta u_k^s + k^2 u_k^s = -k^2 h u_k^{\text{inc}} - k^2 h u_k^{\text{inc}} & \text{in } \Omega, \\ \partial_\nu u_k^s = 0 & \text{on } \partial\Omega, \\ u_k^s \text{ is outgoing.} \end{cases} \tag{2.82}$$

Let $\mathcal{S}(u) := k^2 h u$ which satisfies the hypothesis of Proposition 2.5, and for every $r > 0$,

$$\|\mathcal{S}\|_{\mathrm{H}^2(\Omega_r)\to\mathrm{L}^2(\Omega_r)} \leq k^2 \|h\|_{\mathrm{L}^\infty(-r,r)}. \tag{2.83}$$

Proposition 2.5 shows that if $k^2\|h\|_{\mathrm{L}^\infty(-r,r)}$ is small enough, u_k^s is close to v_k the solution of

$$\begin{cases} \Delta v_k + k^2 v_k = -k^2 h u_k^{\text{inc}} & \text{in } \Omega, \\ \partial_\nu v_k = 0 & \text{on } \partial\Omega, \\ v_k \text{ is outgoing.} \end{cases} \tag{2.84}$$

and that, with C the constant defined in Proposition 2.4,

$$\|u - v\|_{\mathrm{H}^2(-r,r)} \leq \frac{C^2 k^4 \|h\|^2_{\mathrm{L}^\infty(-r,r)} \|u_k^{\text{inc}}\|_{\mathrm{L}^2(-r,r)}}{1 - Ck^2\|h\|_{\mathrm{L}^\infty(-r,r)}}. \tag{2.85}$$

We assume that the measurements consist in the n-th propagative mode $v_{k,n}$ for all non resonant frequencies $k \in (0, k_{\max})$ where $k_{\max} > 0$ is given. Proposition 2.1 shows that for every $k \in (0, k_{\max})$,

$$v_{n,k}(0) = \frac{i}{2k_n}\int_0^{+\infty} k^2 h_n(z) e^{ikz} e^{ik_n z} \mathrm{d}z = \frac{(k + k_n)k^2}{k_n}\Gamma(h_n)(k + k_n). \tag{2.86}$$

Since we assume that only the propagative modes are measured, the frequency k must satisfy $k > n\pi$, and $k_n \in \mathbb{R}$. The function $k \mapsto k + \sqrt{k^2 - n^2\pi^2}$ is one-to-one from $(n\pi, k_{\max})$ to $(n\pi, k_{\max} + \sqrt{k_{\max}^2 - n^2\pi^2})$. This means that we have access to $\Gamma(h_n)(k)$ for every $k \in (n\pi, k_{\max} + \sqrt{k_{\max}^2 - n^2\pi^2})$. We denote by $d_n = \Gamma(h_n)$ the data and by $d_{n_{\text{app}}}$ the perturbed data. We use the method described in section 2.2 to reconstruct $h_{n_{\text{app}}}$, an approximation of h_n, and control the error using Theorem 2.2.

Proposition 2.13. *Let $n \in \mathbb{N}$, $h_{n_{app}}, h_n \in H^1(-r,r)$ where $r > 0$. Let $k_{max} > n\pi$, $d_n(k) = \Gamma(h_n)(k)$ and $d_{n_{app}}(k) = \Gamma(h_{n_{app}})(k)$ for $k \in (n\pi, k_{max}+\sqrt{k_{max}^2 - n^2\pi^2})$. We assume that there exists $M \in \mathbb{R}_+^*$ such that $\|h_n\|_{H^1(-r,r)} \leq M$, $\|h_{n_{app}}\|_{H^1(-r,r)} \leq M$. Then for every $0 < \varepsilon < 1$ there exists a constant $\xi_{n,k_{max}}$ depending on r, M, ε such that*

$$\begin{aligned}\|h_n - h_{n_{app}}\|^2_{L^2(-r,r)} \leq \xi_{n,k_{max}} \|d_n - d_{n_{app}}\|_H^{2-2\varepsilon} + \frac{4}{\pi}\|d_n - d_{n_{app}}\|_H^2 \\ + \frac{8\pi}{\left(k_{max} + \sqrt{k_{max}^2 - n^2\pi^2}\right)^2} M^2.\end{aligned} \tag{2.87}$$

Corollary 2.1. *Let $k_{max} \in \mathbb{R}_+^*$ and $N \in \mathbb{N}$ such that $N < k_{max}/\pi$. Let $h_{app}, h \in H^1(\Omega_r)$ where $r > 0$ and $d = F(h)$, $d_{app} = F_s(h_{app})$ such that d_n and $d_{n_{app}}$ are defined on $(n\pi, k_{max}+\sqrt{k_{max}^2 - n^2\pi^2})$. We assume that there exists $M \in \mathbb{R}_+^*$ such that $\|h\|_{H^1(\Omega_r)} \leq M$ and $\|h_{app}\|_{H^1(\Omega_r)} \leq M$. Then for every $0 < \varepsilon < 1$ there exists a constant $\xi_{N,k_{max}}$ depending on r, M, ε such that*

$$\begin{aligned}\|h - h_{app}\|^2_{L^2(\Omega_r)} \leq \xi_{N,k_{max}} (N+1)^{\varepsilon} \|d - d_{app}\|^{2-2\varepsilon}_{\ell^2(H)} + \frac{4}{\pi}\|d - d_{app}\|^2_{l^2(H)} \\ + \frac{8\pi(N+1)}{K^2} M^2 + \frac{4}{N^2\pi^2} M^2.\end{aligned} \tag{2.88}$$

Proof. Using the previous proposition,

$$\begin{aligned}\|h - h_{\mathrm{app}}\|^2_{\mathrm{L}^2(\Omega_r)} \leq \sum_{n=0}^{N} \xi_{n,k_{\max}} \|d_n - d_{n_{\mathrm{app}}}\|_{\mathrm{H}}^{2-2\varepsilon} + \frac{4}{\pi}\|d_n - d_{n_{\mathrm{app}}}\|^2_{\mathrm{H}} \\ + \frac{8\pi M^2}{\left(k_{\max} + \sqrt{k_{\max}^2 - n^2\pi^2}\right)^2} + \sum_{n>N} \|h_n - h_{n_{\mathrm{app}}}\|^2_{\mathrm{L}^2(-r,r)}.\end{aligned}$$

We define $\xi_{N,k_{\max}} = \max\limits_{n=0,..,N} \xi_{n,k_{\max}}$ and using the concavity of $x \mapsto x^{1-\varepsilon}$, we deduce that

$$\begin{aligned}\|h - h_{\mathrm{app}}\|^2_{\mathrm{L}^2(\Omega_r)} \leq \xi_{N,k_{\max}} (N+1)^{\varepsilon} \|d - d_{\mathrm{app}}\|^{2-2\varepsilon}_{\ell^2(H)} + \frac{4}{\pi}\|d - d_{\mathrm{app}}\|^2_{\ell^2(H)} \\ + \frac{8\pi M^2(N+1)}{k_{\max}^2} + \frac{\|\partial_y(h - h_{\mathrm{app}})\|^2_{\mathrm{L}^2(\Omega_r)}}{N^2\pi^2}.\end{aligned}$$

We conclude using the upper bound on $\|h\|_{\mathrm{H}^1(\Omega_r)}$ and $\|h_{\mathrm{app}}\|_{\mathrm{H}^1(\Omega_r)}$. □

Remark 2.12. *Again, this estimate highlights the different sources of error: the lack of measurements if the mode if greater than 1 in the low frequencies, the perturbed data, the lack of measurements in the high frequencies and finally the truncation to the N-th mode. The predominant term here seems to be the first one, and we need to find a balance between increasing N to decrease the error of truncation and diminishing N to lower the value of $\xi_{N,k_{max}}$.*

Unlike the two previous cases, the detection of inhomogeneities requires more modes than just the first two modes. However, using measurements on one section of the scattered field associated with a source $s_k = -2ik\delta_0(x)$ allows reconstruction of an approximation of h with quantified error.

2.4 Numerical Results

2.4.1 Numerical source inversion from limited frequency data

In Proposition 2.7, we have seen that the forward modal operator Γ is invertible. Knowing the measurements of the wavefield generated by a source for every frequency, we are theoretically abble to reconstruct the source. Moreover, Theorem 2.2 shows that if the source is compactly supported, measurements are only needed for a finite interval of frequencies to approximate the source. In this section, we discuss the numerical aspects of the inversion.

We assume that the wavefield in the waveguide is generated by a source f compactly supported, located between the sections $x = x_m$ and $x = x_M$. The interval $[x_m, x_M]$ is regularly discretized by a set of N_X values X, and seek an approximation of $f(X)$. The measurements of the wavefield are made for a discrete set of N_K frequencies denoted K. Let $h = \dfrac{x_M}{N_X - 1}$ denote the stepsize of the discretization X. Using Definition 2.3 and Equation (2.30), the operator $f \mapsto (k \mapsto k\Gamma(f)(k))$ maps $\mathrm{L}^2(\mathbb{R})$ onto $\mathrm{L}^2(\mathbb{R}_+^*)$ and can be discretized by the operator

$$\gamma : \begin{array}{ccc} \mathbb{C}^{N_X} & \to & \mathbb{C}^{N_K} \\ y & \mapsto & \left(\dfrac{ih}{2} \displaystyle\sum_{x \in X} y_x e^{ikx} \right)_{k \in K} \end{array} . \tag{2.89}$$

To invert this operator, we use a least square method. Given the data $d = \gamma(f(X))$, we seek an approximation of $f(X)$ by minimizing the quantity

$$\frac{1}{2} \|\gamma(y) - d\|^2_{\ell^2\left(\mathbb{C}^{N_X}\right)}.$$

To avoid small oscillations in the reconstruction we also define the discrete gradient

$$G : \begin{array}{ccc} \mathbb{C}^{N_X} & \to & \mathbb{C}^{N_X} \\ y & \mapsto & (y_i - y_{i-1})_{1 \leq i \leq N_X} \end{array} , \tag{2.90}$$

with the convention that $x_0 = x_{N_X}$ and $x_{N_X+1} = x_1$. Note that the adjoints of γ and G, denoted by γ^* and G^*, can be easily computed. For $\lambda > 0$, we minimize the quantity

$$J(y) = \frac{1}{2} \|\gamma(y) - d\|^2_{\ell^2\left(\mathbb{C}^{N_K}\right)} + \frac{\lambda}{2} \|G(y)\|^{,}_{\ell^2\left(\mathbb{C}^{N_X}\right)}. \tag{2.91}$$

with a steepest descent method, with the initialization $y_0 = \ (0)_{x \in X}$:

$$y_{m+1} = y_m - \frac{\|\nabla J(y_m)\|^2_{\ell^2\left(\mathbb{C}^{N_X}\right)}}{\|S(\nabla J(y_m))\|^2_{\ell^2\left(\mathbb{C}^{N_K}\right)} + \|G(\nabla J(y_m))\|^2_{\ell^2\left(\mathbb{C}^{N_X}\right)}} \nabla J(y_m), \tag{2.92}$$

where

$$\nabla J(y_m) = \gamma^*(\gamma(y_m) - d) + \lambda G^*(G(y_m)). \tag{2.93}$$

We use this algorithm to illustrate the results given in Theorem 2.2. Firstly, we reconstruct a source f with a gap in the high frequencies, *i.e.* for which measurements of the wavefield generated by f are available for a discrete set of frequencies between 0 and ω_1. Figure 2.7 presents the comparison between a function f and its reconstruction for different values of ω_1. As expected, we observe convergence when ω_1 increases, and the reconstruction becomes almost perfect visually. The

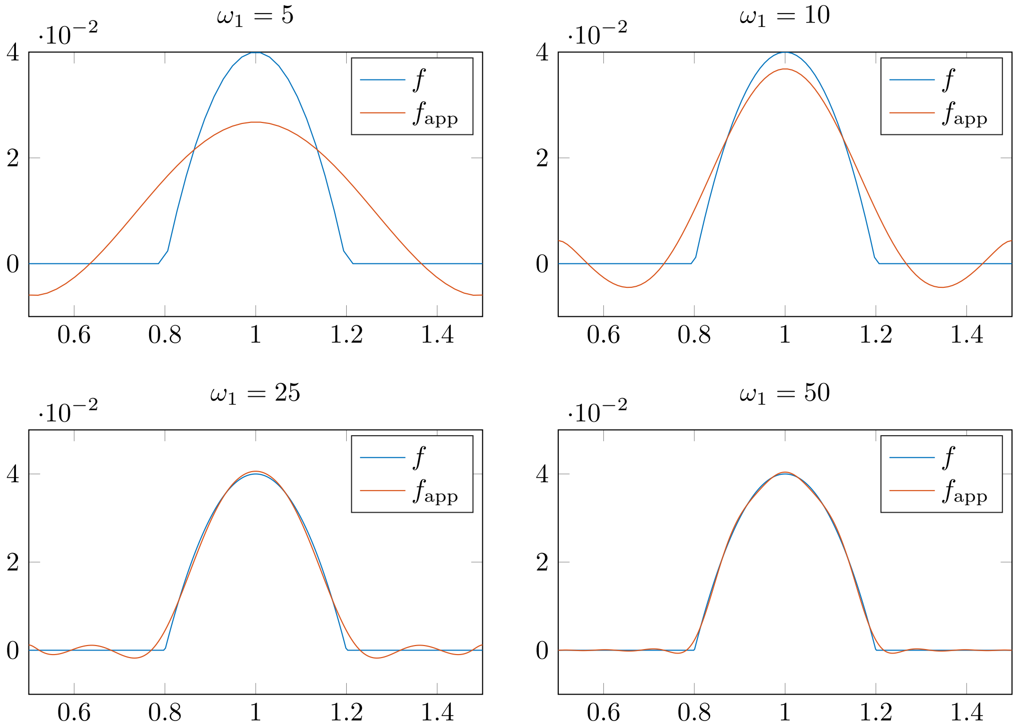

Figure 2.7 – Reconstruction of $f(x) = (x - 0.8)(1.2 - x)\mathbf{1}_{0.8 \le x \le 1.2}$ for different values of ω_1 using the discrete operator γ and the algorithm (2.92) with $\lambda = 0.001$. Here, X is the discretization of $[0.5, 1.5]$ with $10\omega_1$ points, and K is the discretization of $[0.01, \omega_1]$ with 1000 points.

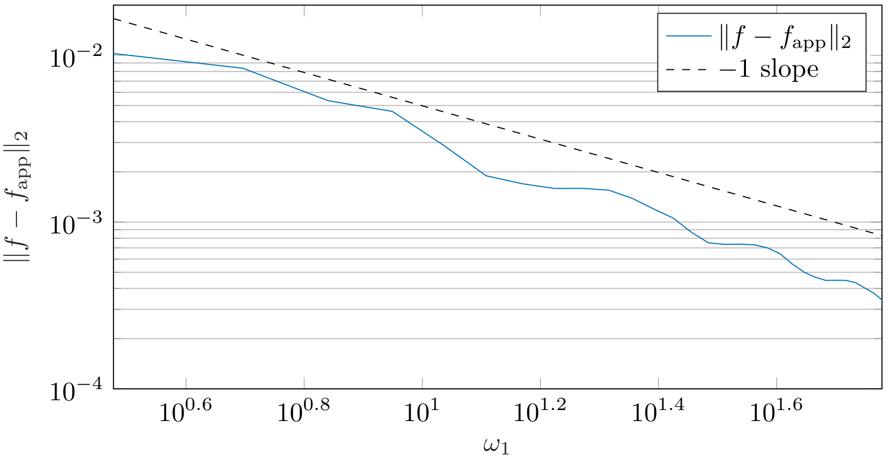

Figure 2.8 – L^2-error between $f(x) = (x - 0.8)(1.2 - x)\mathbf{1}_{0.8 \le x \le 1.2}$ and its reconstruction f_{app} for different values of ω_1 using the discrete operator γ and the algorithm (2.92) with $\lambda = 0.001$. Here, X is the discretization of $[0.5, 1.5]$ with $10\omega_1$ points, and K is the discretization of $[0.01, \omega_1]$ with 1000 points.

speed of convergence is illustrated in Figure 2.8, and as expected from Theorem 2.2, the L^2-error between the function and its approximation decreases like $1/\omega_1$.

Secondly, we investigate the influence of r and ω_0 in Theorem 2.2. Consistently with Propositions 2.12 and 2.13, we choose ω_0 to be a multiple of π. In Figure 2.9, we present the comparison between a 1D function f and its reconstruction is represented for different values of ω_0, when the support of f is fixed. Figure 2.10 depicts the comparison between a 1D function f and its reconstruction for different sizes r of support when ω_0 is fixed. As expected from the definition of the constant C in Theorem 2.2, the quality of the reconstruction deteriorates when r and ω_0 increase.

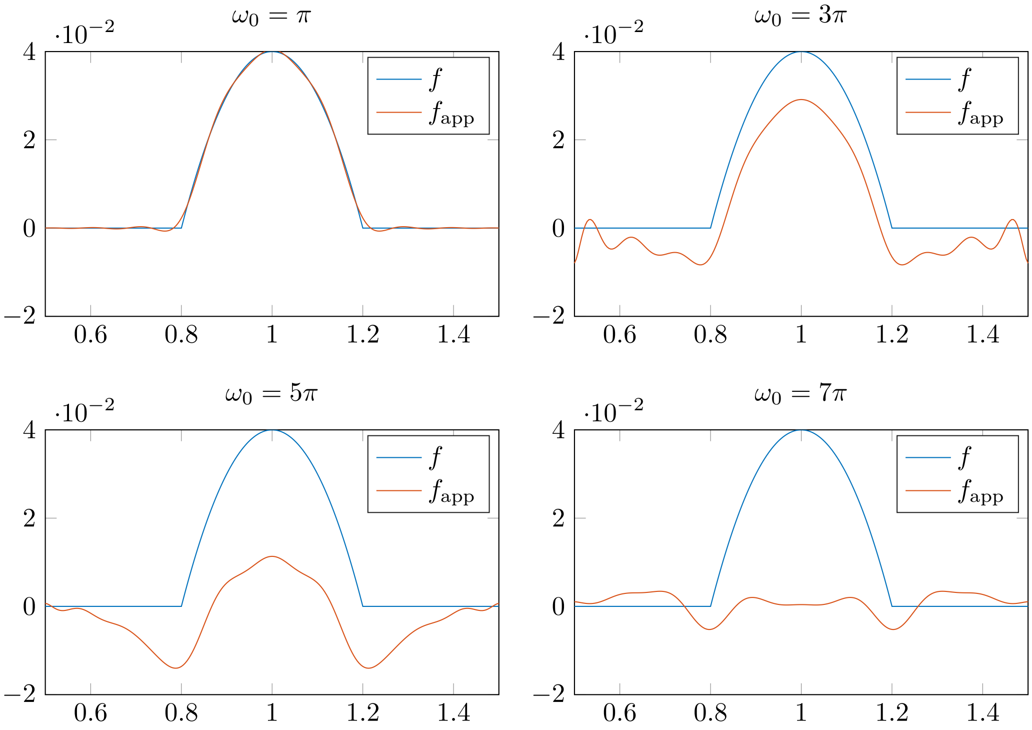

Figure 2.9 – Reconstruction of $f(x) = (x - 0.8)(1.2 - x)\mathbf{1}_{0.8 \le x \le 1.2}$ for different values of ω_0 and $r = 0.5$ using the discrete operator γ and the algorithm (2.92) with $\lambda = 0.001$. Here, X is the discretization of $[0.5, 1.5]$ with 251 points, and K is the discretization of $[\omega_0, 50]$ with 1000 points.

The reconstruction of a source is almost perfect for $\omega_0 = 0$ if we increase sufficiently ω_1. However, if $\omega_0 > 0$, the problem is ill-conditioned and if the size of the support of the source or ω_0 increase, the quality of the reconstruction is poor.

2.4.2 Generation of data for the detection of defects

Applying the results of section 2.3 requires measurements generated by a defect on a section of the wavefield. This data is generated by solving numerically the PDE with Matlab, and evaluating its solution on a section of the waveguide. The equations of propagation in a regular waveguide Ω for a bend, a bump and a inhomogeneity are given by (2.65), (2.73) and (2.82) respectively. In the following, we assume that the interesting part of the waveguide is located between $x = 0$ and $x = 8$, and that the measurements are made on the section $\{1\} \times (0, 1)$. To generate the solution of these equations of propagation on $[0, 8] \times [0, 1]$, we use the finite element method and a perfectly matched layer between $x = -19$ and $x = 0$ on the left side of the waveguide and between $x = 8$ and $x = 27$ on the right side. The coefficient of absorption for the perfectly matched layer is defined by

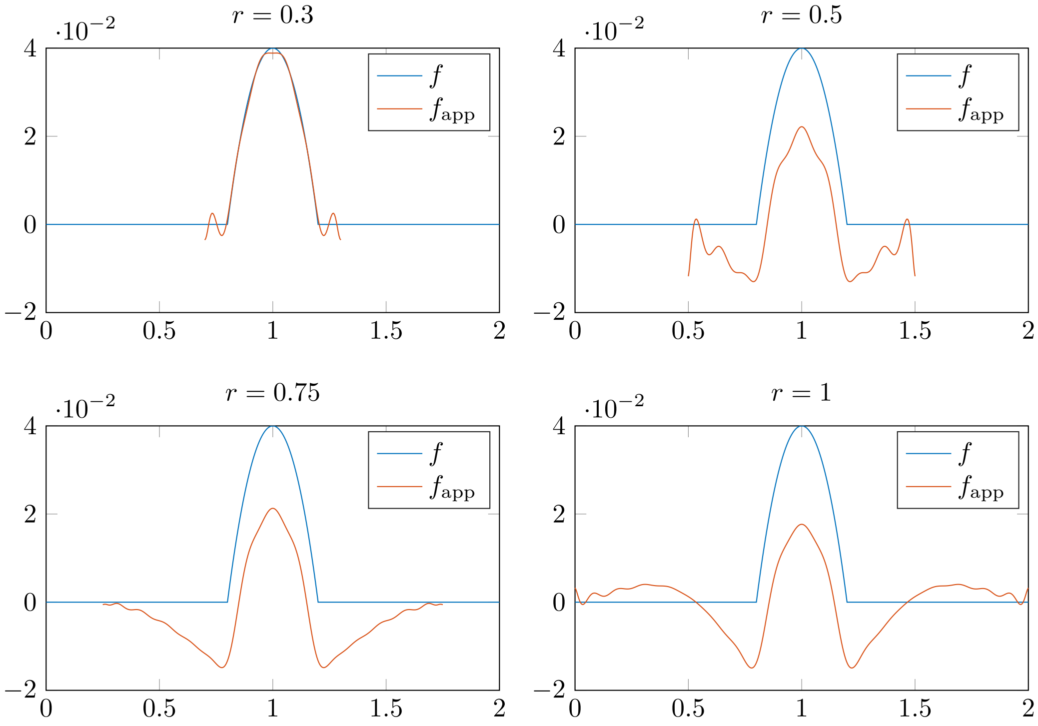

Figure 2.10 – Reconstruction of $f(x) = (x-0.8)(1.2-x)\mathbf{1}_{0.8 \le x \le 1.2}$ for different sizes of support r and $\omega_0 = 3\pi$ using the discrete operator γ and the algorithm (2.92) with $\lambda = 0.001$. Here, X is the discretization of $[1-r, 1+r]$ with $500r+1$ points, and K is the discretization of $[3\pi, 50]$ with 1000 points.

$-k((x-8)\mathbf{1}_{x\ge 8} - x\mathbf{1}_{x \le 0})$. The structured mesh is built with a stepsize 0.01.

2.4.3 Detection of bends

Using the method described in the previous subsection, we generate the solution of (2.65) for a set of frequencies K and we evaluate the solutions on the section $\{1\} \times (0,1)$. As explained in section 2.3.2 and equation (2.68), the corresponding data amounts to knowing $\Gamma(s)(2k)$ for every $k \in K$, where

$$s = \mathbf{1}_{x \in [x_c, x_c + \theta(r+1)]} \left(1 - \frac{1}{2(r+1)} - (r+1)\ln\left(\frac{r+1}{r}\right)\right). \tag{2.94}$$

Note that algorithm (2.92) could be used to construct an approximation s_{app} of s. However, since we are looking for a rectangular function, we can directly define $s_{\text{app}} = -p_1 \mathbf{1}_{x \in [p_2, p_2 + p_3]}$ and see that

$$\Gamma(s_{\text{app}})(k) = -\frac{ip_1}{k} e^{ik\frac{2p_2+p_3}{2}} \sin\left(\frac{p_3}{2} k\right). \tag{2.95}$$

We determine (p_1, p_2, p_3) by minimizing $\|\Gamma(s_{\text{app}})(2k) - \Gamma(s)(2k)\|_{\ell^2\left(\mathbb{C}^{N_K}\right)}$, and the approximations of x_c, r and θ follow. We present in Figure 2.11 the reconstructions of two different bends, and in Table 2.1 the relative error on the estimation of (x_c, r, θ) for different bends. We note that if the bend is really small, the reconstruction is very good. On the other hand, when r increases or when θ decreases, the reconstruction deteriorates due to the fact that the Born approximation is no longer a good approximation of the wavefield in the waveguide. As mentioned in Remark 2.10, our algorithm can also be used to recover a succession of bends, as shown in Figure 2.12.

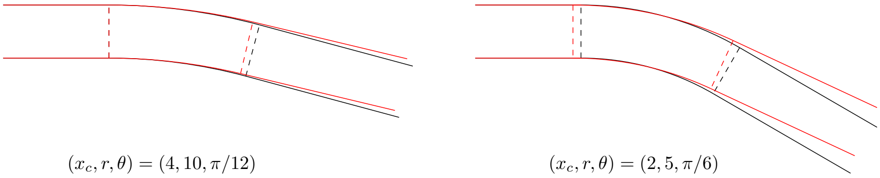

$(x_c, r, \theta) = (4, 10, \pi/12)$ $(x_c, r, \theta) = (2, 5, \pi/6)$

Figure 2.11 – Reconstruction of two different bends. The black lines represent the initial shape of Ω, and the red the reconstruction of Ω. In both cases, K is the discretization of $[0.01, 40]$ with 100 points, and the reconstruction is obtain by (2.95). On the left, the initial parameters of the bend are $(x_c, r, \theta) = (4, 10, \pi/12)$ and on the right, $(x_c, r, \theta) = (2, 5, \pi/6)$.

(x_c, r, θ)	$(2.5, 40, \pi/80)$	$(4, 10, \pi/12)$	$(2, 5, \pi/6)$
relative error on x_c	1.8%	0%	7.6%
relative error on r	3.0%	7.5%	23.8%
relative error on θ	1.6%	10.7%	16.9%

Table 2.1 – Relative errors on the reconstruction of (x_c, r, θ) for different bends. In each case, K is the discretization of $[0.01, 40]$ with 100 points, and the reconstruction is obtain by (2.95).

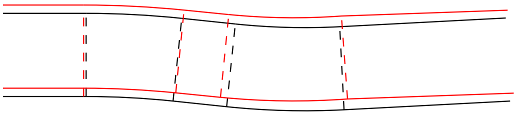

Figure 2.12 – Reconstruction of a waveguide with two successive bends. The black lines represent the initial shape of Ω, and the red the reconstruction of Ω, slightly shifted for comparison purposes. In both cases, K is the discretization of $[0.01, 40]$ with 100 points. The parameters of the two bends are $(x_c^{(1)}, r^{(1)}, \theta^{(1)}) = (2, 10, \pi/30))$ and $(x_c^{(2)}, r^{(2)}, \theta^{(2)}) = (3.8, 8, -\pi/20))$

2.4.4 Detection of bumps

Using the method described in section 2.4.2, we generate the solutions of (2.73) for a set of frequencies K and we evaluate the solutions on the section $\{1\}\times(0,1)$. In view of Remark 2.3, and to ensure that the Born hypothesis (2.19) is satisfied, we do not choose frequencies in $[n\pi - 0.2, n\pi + 0.2]$, for every $n \in \mathbb{N}$. As explained in section 2.3.3 and equations (2.77), (2.78), the data only determines $\Gamma(s_0)(2k)$ for every $k \in K$ and $\Gamma(s_1)(k + \sqrt{k^2 - \pi^2})$ for every $k \in K$, $k > \pi$, where h and g parametrize the bump (recall that $s_0 = h' + g'$, $s_1 = -\sqrt{2}h' + g'$). Using the algorithm (2.92), we find an approximation of h' and g', and the approximation of h and g follows by integration. In figure 2.13, we represent two different reconstructions of a shape defect. As predicted in Proposition 2.10, the reconstruction improves when $\|h\|_{\mathcal{C}^1(\mathbb{R})}$ and $\|g\|_{\mathcal{C}^1(\mathbb{R})}$ decrease. Table 2.2 illustrates this point as it depicts the relative error on a reconstruction of h when its amplitude increases.

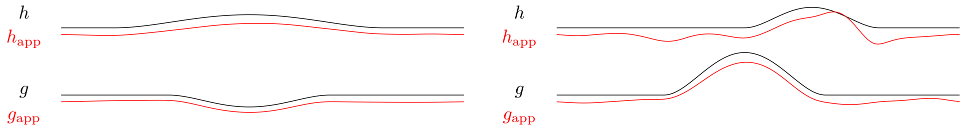

Figure 2.13 – Reconstruction of two shape defects. In black, the initial shape of Ω, and in red the reconstruction, slightly shifted for comparison purposes. In both cases, K is the discretization of $[0.01, 70] \setminus \{[n\pi - 0.2, n\pi + 0.2], n \in \mathbb{N}\}$ with 300 points, X is the discretization of $[3, 4.5]$ with 151 points and we use the algorithm (2.92) with $\lambda = 0.08$ to reconstruct s_0 and s_1. On the left, $h(x) = 5/16\mathbf{1}_{3.2\leq x\leq 4.2}(x-3.2)^2(4.2-x)^2$ and $g(x) = -35/16\mathbf{1}_{3.4\leq x\leq 4}(x-3.4)^2(4-x)^2$. On the right, $h(x) = 125/16\mathbf{1}_{3.7\leq x\leq 4.2}(x-3.7)^2(4.2-x)^2$ and $g(x) = 125/16\mathbf{1}_{3.4\leq x\leq 4}(x-3.4)^2(4-x)^2$.

A	0.1	0.2	0.3	0.5
$\|h - h_{\text{app}}\|_{\mathrm{L}^2(\mathbb{R})}/\|h\|_{\mathrm{L}^2(\mathbb{R})}$	8.82%	10.41%	15.12%	54.99%

Table 2.2 – Relative errors on the reconstruction of h for different amplitudes A. We choose $h(x) = A\mathbf{1}_{3\leq x\leq 5}(x-3)^2(5-x)^2$ and $g(x) = 0$. In every reconstruction, K is the discretization of $[0.01, 40] \setminus \{[n\pi - 0.2, n\pi + 0.2], n \in \mathbb{N}\}$ with 100 points, X is the discretization of $[1, 7]$ with 601 points and we use the algorithm (2.92) with $\lambda = 0.08$ to reconstruct h'.

2.4.5 Detection of inhomogeneities

Using the method described in section 2.4.2, we generate the solutions of (2.82) for a set of frequencies K and we evaluate the solutions on the section $\{1\} \times (0, 1)$. As explained in section 2.3.4 and equation (2.86), the data only determines $\Gamma(h_n)(k + k_n)$ for every $k \in K$, $k > n\pi$ where h_n is the n-th mode of h, and h is the inhomogeneity. We define a number of modes N used for the reconstruction of h, and with the algorithm (2.92), we find an approximation of h_n for every $n \leq N$. In Figure 2.14, we show the reconstruction of h_n for $0 \leq n \leq N = 9$. We obtain an approximation of h by using the expression $h(x, y) = \sum h_n(x)\varphi_n(y)$. Figures 2.15 and 2.16 show two reconstructions of h. In the first one, h has a small support and is very well reconstructed. In the latter, the support of h is larger. And albeit it does not yield a good approximation of h, it allows localization of the inhomogeneity in the waveguide. Moreover, if we assume that h is a positive function, we can improve the algorithm (2.92) by reconstructing h on each step and projecting on the space of positive functions (see the third part of Figure 2.16).

2.5 Conclusion

In this chapter, we have presented a new approach to recover defects in a waveguide. By sending the first propagative mode for frequencies in a given interval, the scattered wavefields generated by the defects are measured on a slice of the waveguide. Based on the Fourier transform and the Born approximation, we propose a method to reconstruct the parameters of the defect. We provide a control of the error in the approximation of the parameters of the defects if they are small enough so that the Born approximation makes sense.

Our numerical results show that the method works well for the three types of defects considered : bends, bumps, localized inhomogeneities. From measurements generated by a finite element method, we were able to numerically recover the different types of defects using the modal decomposition and a penalized least square algorithm. Our reconstruction of inhomogeneities is similar to the one presented in [34]. Even though the number of propagative modes sent in the waveguide can

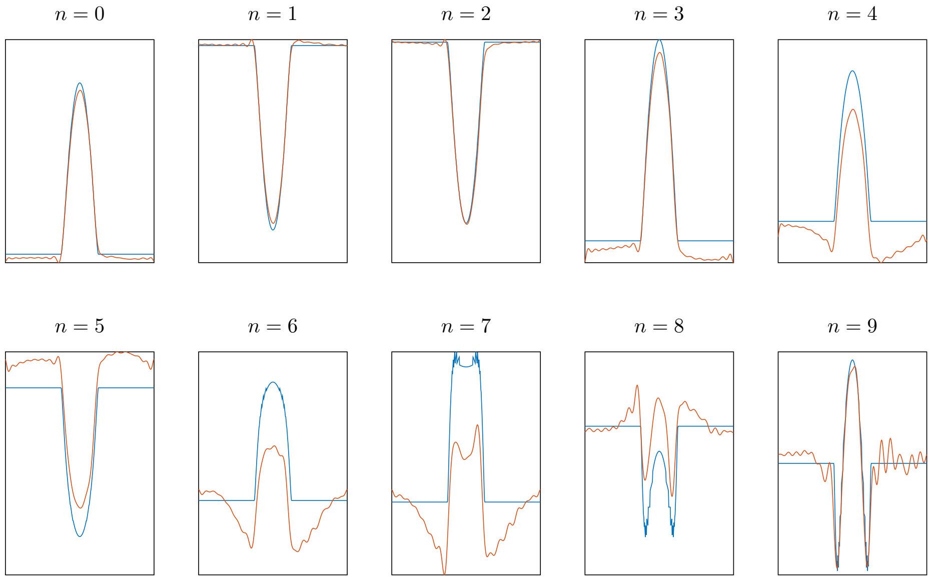

Figure 2.14 – Reconstruction of h_n for $0 \leq n \leq 9$, where $h(x) = 0.05\mathbf{1}_{\left|\left(\frac{x-4}{0.05},\frac{y-0.6}{0.15}\right)\right|\leq 1}\left|\left(\frac{x-4}{0.05},\frac{y-0.6}{0.15}\right)\right|^2$. In blue, we represent h_n and in red the reconstruction of $h_{n_{\text{app}}}$. In every reconstruction, K is the discretization of $[0.01, 150]$ with 200 points, X is the discretization of $[3.8, 4.2]$ with 101 points and we use the algorithm (2.92) with $\lambda = 0.002$ to reconstruct every h_n.

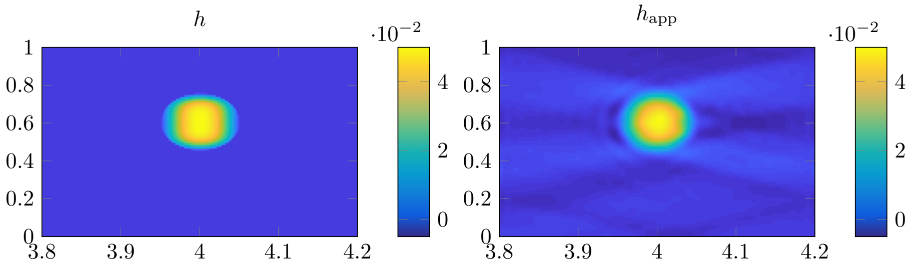

Figure 2.15 – Reconstruction of an inhomogeneity h, where $h(x) = 0.05\mathbf{1}_{\left|\left(\frac{x-4}{0.05},\frac{y-0.6}{0.15}\right)\right|\leq 1}\left|\left(\frac{x-4}{0.05},\frac{y-0.6}{0.15}\right)\right|^2$. On the left, we represent the initial shape of h, and on the right the reconstruction h_{app}. Here, K is the discretization of $[0.01, 150]$ with 200 points, X is the discretization of $[3.8, 4.2]$ with 101 points and we use the algorithm (2.92) with $\lambda = 0.002$ to reconstruct every h_n. We used $N = 20$ modes to reconstruct h.

be increased to improve the reconstruction presented in this article, so can we increase the number of frequencies.

Our work could be extended to other types of defects such as impenetrable obstacles or cracks in the waveguide. One could also try to apply this multi-frequency point of view to elastic waveguides, where a modal decomposition in terms of Lamb waves is also available.

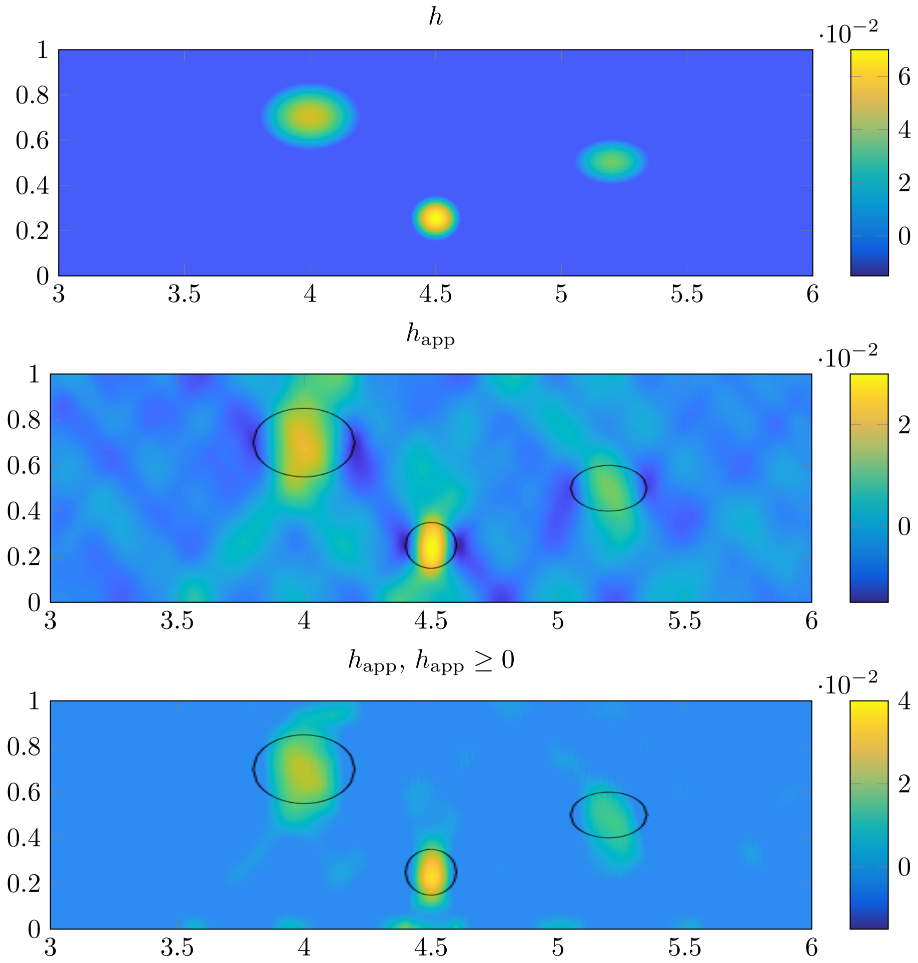

Figure 2.16 – Reconstruction of an inhomogeneity h. From top to bottom, the initial representation of h, the reconstruction h_{app} and the reconstruction h_{app} with the knowledge of the positivity of h. Here, K is the discretization of $[0.01, 150]$ with 200 points, X is the discretization of $[3, 6]$ with 3001 points and we use the algorithm (2.92) with $\lambda = 0.01$ to reconstruct every h_n. We choose used $N = 20$ modes to reconstruct h.

Appendix 2.A: Proof of Proposition 2.1 and 2.3

We begin with the proof of Proposition 2.1. Let $r > 0$, $\Omega_r = (-r, r) \times (0, 1)$ and T the application defined by

$$T : \begin{array}{rcl} \mathrm{L}^2(\Omega_r) & \to & \mathrm{L}^2(-r,r)^{\mathbb{N}} \\ u & \mapsto & \left(\displaystyle\int_0^1 u(x,y)\varphi_n(y)\mathrm{d}y\right)_{n\in\mathbb{N}} \end{array}.$$

Let H_1 denote the Hilbert space

$$\mathrm{H}_1 := \left\{(u_n) \in \ell^2(\mathrm{H}^1(-r,r)), \sum_{n\in\mathbb{N}} n^2 \|u_n\|^2_{\mathrm{L}^2(-r,r)} < +\infty\right\},$$

equipped with the inner product

$$\langle (u_n),(v_n)\rangle_{\mathrm{H}_1} = \sum_{n\in\mathbb{N}} (1+n^2\pi^2)\langle u_n, v_n\rangle_{\mathrm{L}^2(-r,r)} + \sum_{n\in\mathbb{N}} \langle u_n', v_n'\rangle_{\mathrm{L}^2(-r,r)}.$$

The mapping T is a Hilbert isomorphism between $\mathrm{H}^1(\Omega_r)$ and H_1.

The variation formulation of (2.7) takes the form, for every $v \in \mathrm{H}^1(\Omega_r)$,

$$\int_{\Omega_r} \nabla u_k \nabla v - k^2 \int_{\Omega_r} u_k v = \int_{\Omega_r} s v. \tag{2.96}$$

Set $T(u_k) = (u_{k,n})_{n\in\mathbb{N}}$, $T(v) = (v_n)_{n\in\mathbb{N}}$, and notice that the above variational formulation is equivalent to the sequence of problems

$$\forall v_n \in \mathrm{H}^1(-r,r), \qquad \int_{-r}^{r} u_{k,n}' v_n' + (n^2\pi^2 - k^2)\int_{-r}^{r} u_{k,n} v_n = \int_{-r}^{r} s_n v_n. \tag{2.97}$$

Setting $k_n^2 = k^2 - n^2\pi^2$ with $\mathrm{Re}(k_n) > 0$, $\mathrm{Im}(k_n) > 0$, the formulation (2.97) is associated to the equation $u_{k,n}'' + k_n^2 u_{k,n} = s_n$. We notice that $G_{k_n}(x) = i/(2k_n)e^{ik_n|x|}$ satisfies the equation $G_{k_n}'' + k_n^2 G_{k_n} = -\delta_0$ and so we define $u_k := T^{-1}\left((G_{k_n} * s_n)_{n\in\mathbb{N}}\right)$ and note that $u_k \in \mathrm{H}^1(\Omega_r)$ and satisfies (2.96). Moreover, u_k is outgoing. Finally, using results from elliptic regularity theory (see [47]) we deduce that $u_k \in \mathrm{H}^2(\Omega_r)$. As this result holds for every $r > 0$, we conclude that $u_k \in \mathrm{H}^2_{\mathrm{loc}}(\Omega)$.

The solution of (2.11) is constructed by the same method. The variational formulation gives for every $v \in \mathrm{H}^1(\Omega_r)$,

$$\int_{\Omega_r} \nabla u_k \nabla v - k^2 \int_{\Omega_r} u_k v - \int_{\Omega_{\mathrm{top}}} b_1 v - \int_{\Omega_{\mathrm{bot}}} b_2 v = 0. \tag{2.98}$$

This formulation is equivalent to

$$\int_{-r}^{r} u_{k,n}' v_n' + (n^2\pi^2 - k^2)\int_{-r}^{r} u_{k,n} v_n = \int_{-r}^{r} (b_1\varphi_n(1) + b_2\varphi_n(0)) v_n \quad \forall n \in \mathbb{N}.$$

The function $u_k := T^{-1}\left((G_{k_n} * (b_1\varphi_n(1) + b_2\varphi_n(0)))_{n\in\mathbb{N}}\right)$ is in $\mathrm{H}^1(\Omega_r)$, is outgoing and satisfies (2.98). From the elliptic regularity theory, we deduce that $u_k \in \mathrm{H}^2(\Omega_r)$.

To prove uniqueness for both problems, we notice that u_k satisfies $\Delta u_k + k^2 u_k = 0$ in Ω. Thus, u_k is a classical solution and $u_k \in \mathcal{C}^\infty(\Omega)$ and can be written as a linear combination of $(x,y) \mapsto \varphi_n(y)e^{\pm ik_n x}$. The outgoing character of u_k shows that $u_k = 0$ if $s = 0$ or $b_1 = b_2 = 0$.

Appendix 2.B: Proof of Proposition 2.2 and 2.4

We begin with the proof of proposition 2.2. Using the same notation as in Appendix 2.A, the function G_{k_n} satisfies

$$\|G_{k_n}\|_{\mathrm{L}^1(-2r,2r)} \leq \begin{cases} \dfrac{2r}{k_n} & \text{if } n < k/\pi, \\ \dfrac{1}{|k_n|}\min\left(\dfrac{1}{|k_n|}, 2r\right) & \text{if } n > k/\pi, \end{cases}$$

$$\|G_{k_n}'\|_{\mathrm{L}^1(-2r,2r)} \leq \begin{cases} 2r & \text{if } n < k/\pi, \\ \min\left(\dfrac{1}{|k_n|}, 2r\right) & \text{if } n > k/\pi. \end{cases}$$

We define $\delta = \min_{n\in\mathbb{N}} \left(\sqrt{|k^2 - n^2\pi^2|}\right)$, and apply the Young inequality to $u_{k,n}$:

$$\|u_{k,n}\|_{\mathrm{L}^2(-r,r)} \le \|G_{k_n}\|_{\mathrm{L}^1(-2r,2r)}\|s_n\|_{\mathrm{L}^2(-r,r)}.$$

This leads to

$$\|u_k\|^2_{\mathrm{L}^2(\Omega_r)} \le \frac{4r^2}{\delta^2}\sum_{n\in\mathbb{N}}\|s_n\|^2_{\mathrm{L}^2(-r,r)} = \frac{4r^2}{\delta^2}\|s\|^2_{\mathrm{L}^2(\Omega_r)}.$$

Applying the Young inequality to $u'_{k,n}$, we get

$$\begin{aligned}\|\nabla u_k\|^2_{\mathrm{L}^2(\Omega_r)} \le 4r^2 &\sum_{n<k/\pi}\left(1+\frac{n^2\pi^2}{k_n^2}\right)\|s_n\|^2_{\mathrm{L}^2(-r,r)}\\ &+4r^2\sum_{n>k/\pi}\left(1+\frac{n^2\pi^2}{|k_n|^2}\right)\|s_n\|^2_{\mathrm{L}^2(-r,r)}.\end{aligned}$$

If N is the largest propagative mode and if $n > k/\pi > N$,

$$1+\frac{n^2\pi^2}{|k_n|^2} \le 1+\frac{(N+1)^2\pi^2}{|k_{N+1}|^2} \le 1+\frac{(N+1)^2\pi^2}{\delta^2},$$

so that

$$\|\nabla u_k\|^2_{\mathrm{L}^2(\Omega_r)} \le 4r^2\left(1+\frac{(k+\pi)^2}{\delta^2}\right)\|s\|^2_{\mathrm{L}^2(\Omega_r)}.$$

Finally, we notice that

$$\begin{aligned}\|\nabla^2 u_k\|^2_{\mathrm{L}^2(\Omega_r)} = \sum_{n\in\mathbb{N}} n^4\pi^4\|u_{k,n}\|^2_{\mathrm{L}^2(-r,r)} &+ \sum_{n\in\mathbb{N}} 2n^2\pi^2\|u'_{k,n}\|^2_{\mathrm{L}^2(-r,r)}\\ &+\sum_{n\in\mathbb{N}}\|u''_{k,n}\|^2_{\mathrm{L}^2(-r,r)},\end{aligned}$$

and that

$$\|u''_{k,n}\|^2_{\mathrm{L}^2(-r,r)} = \|-s_n - k_n^2 u_{k,n}\|^2_{\mathrm{L}^2(-r,r)} \le \left(\|s_n\|_{\mathrm{L}^2(-r,r)} + k_n^2\|u_{k,n}\|_{\mathrm{L}^2(-r,r)}\right)^2.$$

Combining both relations yields

$$\begin{aligned}\|\nabla^2 u\|^2_{\mathrm{L}^2(\Omega_r)} \le &\sum_{n<k/\pi}\left(\frac{4r^2n^4\pi^4}{k_n^2} + 8n^2\pi^2r^2 + (1+2k_nr)^2\right)\|s_n\|^2_{\mathrm{L}^2(-r,r)}\\ &+\sum_{n>k/\pi}\left[\frac{n^4\pi^4}{|k_n|^4}+\frac{2n^2\pi^2}{|k_n|^2}+\left(1+\frac{|k_n|^2}{|k_n|}\min\left(\frac{1}{|k_n|},2r\right)\right)^2\right]\|s_n\|^2_{\mathrm{L}^2(-r,r)}.\end{aligned}$$

If N is the largest propagative mode, and if $n > k/\pi$,

$$\frac{n^4\pi^4\min\left(\frac{1}{|k_n|^2},4r^2\right)}{|k_n|^2} + 2n^2\pi^2\min\left(\frac{1}{|k_n|^2},4r^2\right) \le \frac{(k+\pi)^4}{\delta^4} + 2\frac{(k+\pi)^2}{\delta^2},$$

and the following estimate holds

$$\begin{aligned}\|\nabla^2 u\|^2_{\mathrm{L}^2(\Omega_r)} \le [\max&\left(4r^2,\frac{1}{\delta^2}\right)\left(\frac{(k+\pi)^4}{\delta^2}+2(k+\pi)^2\right)\\ &+\max((1+2kr)^2,4)]\,\|s\|^2_{\mathrm{L}^2(\Omega_r)}.\end{aligned}$$

To prove Proposition 2.4, we deduce from the results in [47] that there exists constants $d(r)$ and $\mu > 0$, such that

$$\|u_k\|_{\mathrm{H}^2(\Omega_r)} \leq d(r) \left(\| -\Delta u_k + \mu u_k \|_{\mathrm{L}^2(\Omega_r)} + \|b_1\|_{\mathrm{H}^{1/2}(-r,r)} + \|b_2\|_{\mathrm{H}^{1/2}(-r,r)} \right),$$

and if follows that

$$\|u\|_{\mathrm{H}^2(\Omega_r)} \leq d(r) \left((k^2 + \mu) \|u\|_{\mathrm{L}^2(\Omega_r)} + \|b_1\|_{\mathrm{H}^{1/2}(-r,r)} + \|b_2\|_{\mathrm{H}^{1/2}(-r,r)} \right).$$

Using the same method as for the estimation of $\|u_{k,n}\|_{\mathrm{L}^2(-r,r)}$ with the Young inequality, we get

$$\|u\|^2_{\mathrm{L}^2(\Omega_r)} \leq \left(\|b_1\|^2_{\mathrm{H}^{1/2}(-r,r)} + \|b_2\|^2_{\mathrm{H}^{1/2}(-r,r)} \right) \left(\sum_{n<k/\pi} \frac{4r^2}{k_n^2} + \sum_{n>k/\pi} \frac{1}{k_n^4} \right).$$

Finally, we obtain

$$D = d(r) \left((k^2 + \mu) \max\left(2r, \frac{1}{\delta}\right) \sqrt{\sum_{n\in\mathbb{N}} \frac{1}{k_n^2}} + 1 \right).$$

3

Lamb modes and Born approximation for small defects inversion in elastic plates

The aim of this work is to present a multi-frequency scattering method to reconstruct small defects in a 2D and 3D elastic plate. Given surface multi-frequency wavefield measurements, we use a Born approximation to reconstruct localized defect in the geometry of the plate. To justify this approximation, we introduce a rigorous framework to study the propagation of elastic wavefield generated by arbitrary sources. By studying the decreasing of inhomogeneous Lamb mode, we prove well-posedness of the PDE that model elastic wave propagation in 2D and 3D planar waveguides. This result is not valid for some critical frequencies that we study and characterize. Using these results, we generalize the shape reconstruction method already developed for acoustic waveguide and provide a stable reconstruction method based on a mode-by-mode spacial Fourier inversion given by the scattered field.

3.1 Introduction

This work is devoted to the reconstruction of small defects in a waveguide using multi-frequency scattering data. It is an extension of the method exposed in Chapter 2 in the acoustic case, to the more complex case of elastic plates. If the scalar Helmholtz case is relevant to the non destructive testing of pipes or optical fibers (see [55]), applications in the elastic case concern the monitoring of airplane or ship structural parts, offshore wind energy plants or bridges (see [105]).

The main common point between acoustic and elastic waveguides is the existence of a modal decomposition of the wavefield in explicitly guided modes. The acoustic modes form an orthonormal basis, a property not satisfied by their elastic counter-parts, called Lamb modes. Several authors have looked into this feature. The books [91, 5] provide analytic expressions of Lamb modes as well as dispersion relations for their wavenumbers. In [65, 80, 81] a new formulation is introduced, the $\boldsymbol{X}/\boldsymbol{Y}$ formulation, under which the family of Lamb mode turns out to be complete [8, 56, 19]. The associated bi-orthonormality relations [44] thus allow the use of the Lamb basis to decompose any wavefield that propagates in an elastic waveguide as a sum of Lamb modes.

However, a rigorous mathematical framework is still missing to study the propagation of an elastic wavefield generated by an arbitrary source term (see however [15, 16] in 2D). One main goal of the present chapter is to prove well-posedness of the system of PDE's, that models 2D or 3D planar elastic waveguides with internal and boundary source terms. To this end, we adapt the strategy developed for acoustic waveguides in Chapter 2, which differs from [15]. Under stronger assumptions on the regularity of the source terms than those in [15], we present a constructive proof of existence and regularity of a wavefield propagating in a two dimensional elastic waveguide in Theorem 3.2.

As it turns out, this result is not valid at some particular frequencies, which we call critical frequencies, and that are characterized in the proof of Theorem 3.2. In particular, we establish in Corollary 3.1 that the critical frequencies, for which the Lamb family is no longer complete, coincide with the vanishing of the bi-orthogonality relation established by [44]. This result, up to our knowledge, has not been proven before and may help understanding the mathematical analysis of elastic waveguides.

Concerning the study of wave propagation in three-dimensional plates, most of the work that we are aware of consists in adapting the 2D framework to situations with radial or axial symmetry (see for instance [59, 91, 6, 104]). In [100], arbitrary source terms are considered, without mathematical justification however. Introducing the Helmholtz-Hodge decomposition [20] of the wavefield, we split the three dimensional system of elasticity into a system of two independent equations. One of them fits into the scalar wave framework developed in Chapter 2, while the other can be rewritten using the $\boldsymbol{X}/\boldsymbol{Y}$ formulation. This provides a full expression for the decomposition of the wavefield generated by arbitrary source terms, see Theorem 3.3.

Equipped with these results, we can generalize the shape reconstruction method presented in Chapter 2 to the case of elastic plates, so as to determine possible defects (bumps or dips) in the geometry of a plate, from multi-frequency measurements. We use the very same procedure as in the acoustic case : after mapping the perturbed plate to a straight configuration, we simplify the resulting system of equations using a Born approximation. The scattered wavefield generated by a known incident wavefield in the original geometry, gives rise in the straightened plate to a boundary source term, that depends on the shape defect. Using measurements of the scattered field on the surface of the plate at different frequencies, we can reconstruct in a stable way the shape defect (provided the latter is small enough). Numerical reconstructions are presented in the last part of the chapter, which show the efficiency of the method.

The chapter is organized as follows. In section 3.2, we study the forward source problem in a two dimensional waveguide and introduce all the tools needed to use Lamb waves as a modal basis. In section 3.3, we generalize the results of section 3.2 to the forward source problem in three dimensional plates. Section 3.4 is devoted to the reconstruction of shape defects in two dimensional plates, generalizing the method presented in Chapter 2. Finally, in section 3.5 we show numerical illustrations of the propagation of waves in two and three dimensional plates as well as reconstructions of different shape defects.

3.2 Forward source problem in a regular 2D waveguide

In this section, we present a complete study of the forward elastic source problem in a two-dimensional regular waveguide. We use the $\boldsymbol{X}/\boldsymbol{Y}$ formulation developed in [80, 81] which allows a modal decomposition of any elastic wavefield using Lamb modes. Most of the results presented here are already known, and can be found in [81, 91, 5]. Our main contribution is to provide a rigorous proof of well-posedness for the direct problem and of the fact that its solutions can be represented in terms of Lamb modes (Theorem 3.2). We also follow the suggestions in [56] to properly define the set of critical frequencies and critical wavenumbers in Definition 3.3, and we prove in Corollary 3.1 that it coincides with the set of frequencies for which the components $\boldsymbol{X}_n$ and $\boldsymbol{Y}_n$ of the eigenmodes are orthogonal for some n.

3.2.1 Lamb modes and critical frequencies

We consider a 2D infinite, straight, elastic waveguide $\Omega = \{(x,z) \in \mathbb{R} \times (-h,h)\}$ of width $2h > 0$. The displacement field is denoted by $\boldsymbol{u} = (u,v)$. Given a frequency $\omega \in \mathbb{R}$, and given (λ,μ) the Lamé coefficients of the elastic waveguide, the wavefield $\boldsymbol{u}$ satisfies

$$\nabla \cdot \boldsymbol{\sigma}(\boldsymbol{u}) + \omega^2 \boldsymbol{u} = -\boldsymbol{f} \qquad \text{in } \Omega, \tag{3.1}$$

where $\boldsymbol{f} = (f_1, f_2)$ is a given source term, and where the stress tensor $\boldsymbol{\sigma}(\boldsymbol{u})$ is defined by

$$\boldsymbol{\sigma}(\boldsymbol{u}) = \begin{pmatrix} (\lambda+2\mu)\partial_x u + \lambda \partial_z v & \mu\partial_z u + \mu \partial_x v \\ \mu\partial_z u + \mu\partial_x v & \lambda\partial_x u + (\lambda+2\mu)\partial_z v \end{pmatrix} := \begin{pmatrix} s & t \\ t & r \end{pmatrix}. \tag{3.2}$$

In this work, we assume that a Neumann boundary condition is imposed on both sides of the plate

$$\boldsymbol{\sigma}(\boldsymbol{u}) \cdot \nu = \boldsymbol{b}^{\text{top}} \quad \text{on } \partial\Omega_{\text{top}}, \qquad \boldsymbol{\sigma}(\boldsymbol{u}) \cdot \nu = \boldsymbol{b}^{\text{bot}} \quad \text{on } \partial\Omega_{\text{bot}}, \tag{3.3}$$

where $\boldsymbol{b}^{\text{top}} = (b_1^{\text{top}}, b_2^{\text{bot}})$ and $\boldsymbol{b}^{\text{bot}} = (b_1^{\text{bot}}, b_2^{\text{bot}})$ are given boundary source terms. This condition could easily be replaced by a Dirichlet or a Robin condition, without altering our results. The setting is represented in Figure 3.1.

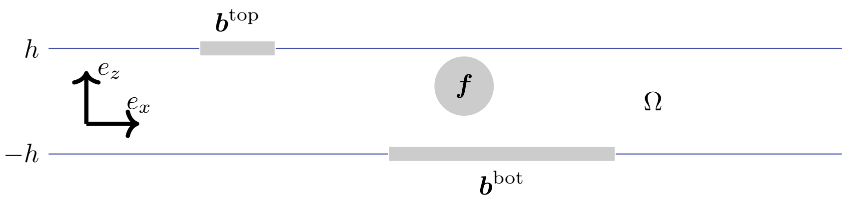

Figure 3.1 – Parametrization of a two dimensional plate Ω. Elastic wavefields are generated using an internal source term $\boldsymbol{f}$, and boundary source terms $\boldsymbol{b}^{\text{top}}$ and $\boldsymbol{b}^{\text{bot}}$.

In [65] this equation is analyzed in an operator form $\boldsymbol{Z} = \mathcal{L}(\boldsymbol{Z})$ where $\boldsymbol{Z} = (u, t, s, v)$. This idea was then adapted in [80] to formalize the so-called $\boldsymbol{X}/\boldsymbol{Y}$ formulation. We introduce the variables

$$\boldsymbol{X} := (u, t), \qquad \boldsymbol{Y} := (-s, v), \tag{3.4}$$

with which the elasticity equation can be rewritten as follows:

Proposition 3.1. *The system* (3.1)*, with the Neumann boundary conditions* (3.3)*, is equivalent to*

$$\left\{ \begin{array}{ll} \partial_x \begin{pmatrix} \boldsymbol{X} \\ \boldsymbol{Y} \end{pmatrix} = \mathcal{L}(\boldsymbol{X}, \boldsymbol{Y}) + \begin{pmatrix} 0 \\ -f_2 - b_2^{top}\delta_{z=h} - b_2^{bot}\delta_{z=-h} \\ f_1 + b_1^{top}\delta_{z=h} + b_2^{top}\delta_{z=-h} \\ 0 \end{pmatrix} & \text{in } \Omega, \\ B_1(\boldsymbol{X}) = B_2(\boldsymbol{Y}) = 0 & \text{on } \partial\Omega, \end{array} \right. \tag{3.5}$$

where $\mathcal{L}(\boldsymbol{X}, \boldsymbol{Y}) = \begin{pmatrix} F(\boldsymbol{Y}) \\ G(\boldsymbol{X}) \end{pmatrix}$ *and where* F*,* G*,* B_1 *and* B_2 *are matrix operators defined by*

$$F = \begin{pmatrix} -\dfrac{1}{\lambda + 2\mu} & -\dfrac{\lambda}{\lambda + 2\mu}\partial_z \\ \dfrac{\lambda}{\lambda + 2\mu}\partial_z & -\omega^2 - \dfrac{4\mu(\lambda + \mu)}{\lambda + 2\mu}\partial^2_{zz} \end{pmatrix}, \qquad G = \begin{pmatrix} \omega^2 & \partial_z \\ -\partial_z & \dfrac{1}{\mu} \end{pmatrix}, \tag{3.6}$$

$$B_1(\boldsymbol{X}) = \boldsymbol{X} \cdot e_z, \qquad B_2(\boldsymbol{Y}) = -\frac{\lambda}{\lambda + 2\mu}\boldsymbol{Y} \cdot e_x + \frac{4\mu(\lambda + \mu)}{\lambda + 2\mu}\partial_z \boldsymbol{Y} \cdot e_z. \tag{3.7}$$

The proof of this proposition follows the same steps as that presented in Appendix A of [81]. In this formulation, the operators F and G only depend on z, and are defined on one section of the waveguide, while derivatives with respect to x only appear in the left-hand side of (3.5). We consider the space

$$H_0 := \left\{ (\boldsymbol{X}, \boldsymbol{Y}) \in (\mathrm{H}^2(-h, h))^4 \,|\, B_1(\boldsymbol{X})(\pm h) = B_2(\boldsymbol{Y})(\pm h) = 0 \right\}, \tag{3.8}$$

and the operator

$$\mathcal{L} : \begin{array}{ccc} H_0 & \rightarrow & (\mathrm{L}^2(-h, h))^4 \\ (\boldsymbol{X}, \boldsymbol{Y}) & \mapsto & (F(\boldsymbol{Y}), G(\boldsymbol{X})) \end{array}. \tag{3.9}$$

Our goal is to diagonalize this operator and, to this end, we introduce the Lamb modes:

Definition 3.1. *A Lamb mode* $(\boldsymbol{X}, \boldsymbol{Y}) \in H_0$*, associated to the wavenumber* $k \in \mathbb{C}$*, is a non-trivial solution of*

$$\mathcal{L}(\boldsymbol{X}, \boldsymbol{Y}) \quad = \quad ik(\boldsymbol{X}, \boldsymbol{Y}).$$

The next Proposition provides the analytical expressions of these modes. The proof can be found in [5, 91].

Proposition 3.2. *The set of wavenumbers* $k \in \mathbb{C}$ *associated to Lamb modes is countable, and every such wavenumber* k *satisfies the symmetric Rayleigh-Lamb equation*

$$p^2 = \frac{\omega^2}{\lambda + 2\mu} - k^2, \qquad q^2 = \frac{\omega^2}{\mu} - k^2, \qquad \left(q^2 - k^2\right)^2 = -4k^2 pq \frac{\tan(ph)}{\tan(qh)}, \tag{3.10}$$

or the antisymmetric Rayleigh-Lamb equation

$$p^2 = \frac{\omega^2}{\lambda + 2\mu} - k^2, \qquad q^2 = \frac{\omega^2}{\mu} - k^2, \qquad \left(q^2 - k^2\right)^2 = -4k^2pq\frac{\tan(qh)}{\tan(ph)}. \tag{3.11}$$

If k satisfies (3.10)*, the associated Lamb mode is called symmetric and is proportional to*

$$\begin{pmatrix} u \\ t \\ -s \\ v \end{pmatrix} := \begin{pmatrix} ik(q^2-k^2)\sin(qh)\cos(pz) - 2ikpq\sin(ph)\cos(qz) \\ 2ik\mu(q^2-k^2)p(-\sin(qh)\sin(pz) + \sin(ph)\sin(qz)) \\ (q^2-k^2)((\lambda+2\mu)k^2 + \lambda p^2)\sin(qh)\cos(pz) - 4\mu pqk^2\sin(ph)\cos(qz) \\ -p(q^2-k^2)\sin(qh)\sin(pz) - 2k^2p\sin(ph)\sin(qz) \end{pmatrix}. \tag{3.12}$$

If k satisfies (3.11)*, the associated Lamb mode is called anti-symmetric and is proportional to*

$$\begin{pmatrix} u \\ t \\ -s \\ v \end{pmatrix} := \begin{pmatrix} ik(q^2-k^2)\cos(qh)\sin(pz) - 2ikpq\cos(ph)\sin(qz) \\ 2ik\mu(q^2-k^2)p(\cos(qh)\cos(pz) - \cos(ph)\cos(qz)) \\ (q^2-k^2)((\lambda+2\mu)k^2 + \lambda p^2)\cos(qh)\sin(pz) - 4\mu pqk^2\cos(ph)\sin(qz) \\ p(q^2-k^2)\cos(qh)\cos(pz) + 2k^2p\cos(ph)\cos(qz) \end{pmatrix}. \tag{3.13}$$

Remark 3.1. *We see on the above expressions that p and q are defined up to a multiplication by -1. However, since Lamb modes are defined up to a multiplicative constant, the choice of the sign of p or q does not change the associated value of k or the associated Lamb mode.*

We notice that if k is a solution of the Rayleigh-Lamb equation then $-k$ and $\bar{k}$ are also solutions. Figure 3.2 depicts different wavenumbers k where $\mathrm{Real}(k) \geq 0$ and $\mathrm{Imag}(k) \geq 0$, in terms of the frequency ω.

We can distinguish three different types of modes (represented in different colors in the above Figure) as in [59]:

Definition 3.2. *There are three types of Lamb modes:*

- *If $k \in \mathbb{R}$, the mode oscillates in the waveguide without energy decay and is called propagative.*
- *If $k \in i\mathbb{R}$, the mode decays exponentially to zero as $|x| \to \infty$, and is called evanescent.*
- *If $Re(k) \neq 0$ and $Im(k) \neq 0$, the mode oscillates very fast to zero and is called inhomogeneous.*

The completeness of Lamb modes depends on whether the frequency ω is critical as defined below:

Definition 3.3. *A frequency ω and a wavenumber k are said to be critical if they satisfy $k = 0$ or condition* (3.10) *and $\Gamma_S = 0$ (resp. condition* (3.11) *and $\Gamma_A = 0$) where*

$$\begin{aligned} \Gamma_S &= h(q^2-k^2)^2\sin(qh)^2 + 4k^2p^2\sin(ph)^2 && (3.14) \\ &\quad +(q^2-k^2)\sin(ph)\cos(ph)\sin(qh)^2\left(\frac{q^2-k^2}{p} - 8p - \frac{2p}{k^2} - \frac{p}{q^2}\right), \\ \Gamma_A &= h(q^2-k^2)^2\cos(qh)^2 + 4k^2p^2\cos(ph)^2 && (3.15) \\ &\quad -(q^2-k^2)\cos(ph)\sin(ph)\cos(qh)^2\left(\frac{q^2-k^2}{p} - 8p - \frac{2p}{k^2} - \frac{p}{q^2}\right). \end{aligned}$$

We denote by ω_{crit} the set of critical frequencies, and by k_{crit} the set of associated critical wavenumbers.

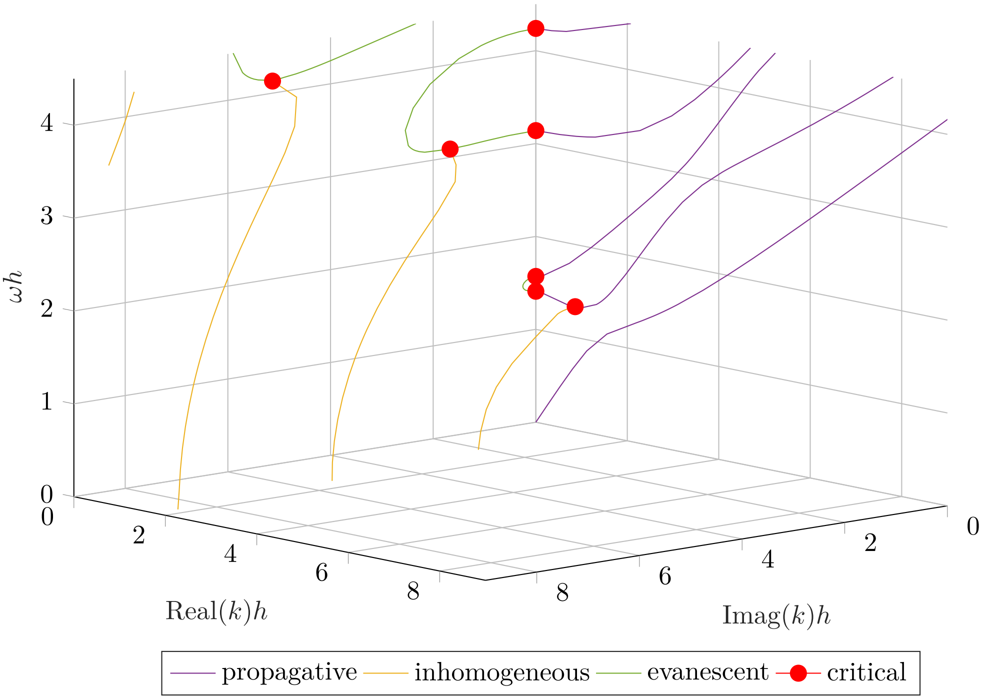

Figure 3.2 – Solutions of the symmetric Rayleigh-Lamb equation (3.12) in the space $\mathrm{Im}(k) \geq 0$, $\mathrm{Re}(k) \geq 0$ with $\mu = 0.25$ and $\lambda = 0.31$. Solutions on the full space can be obtained by axial symmetries. Propagative, evanescent and inhomogeneous modes are represented by different colors. Critical points are represented by red dots.

Critical points solution to $k = 0$ or to $\Gamma_S = 0$, where Γ_S is defined in (3.14), are represented in Figure 3.2. We notice that critical points seem to be located at the junction of branches of modes of different types (see [56, 91] for more details). Next, we introduce the functional space

$$H := \mathrm{H}^1(-h, h) \times \mathrm{L}^2(-h, h) \times \mathrm{L}^2(-h, h) \times \mathrm{H}^1(-h, h). \tag{3.16}$$

and state the following completeness result:

Theorem 3.1. *Lamb modes form a complete set of functions in H if and only if $\omega \notin \omega_{crit}$.*

Proof. Step 1 : It is shown in [8] (see also [56, 19]) that the operator $\mathcal{L}$ satisfies the following properties:

- There exists a set of five rays in the complex plane such that the angles between adjacent rays are less than $\pi/2$,
- Sufficiently far from the origin, all the points on these rays lie in the resolvent set of $\mathcal{L}$,
- There exits $N \in \mathbb{N}$ such that the resolvent of $\mathcal{L}$ satisfies

$$\|(\mathcal{L} - \ell I)^{-1})\| = \mathcal{O}(|\ell|^N) \text{ as } |\ell| \to +\infty \text{ along each ray.} \tag{3.17}$$

Invoking Theorem 6.2 in [60], one may then infer that the family of Lamb modes forms a complete set of functions if and only if for every associated wavenumber k,

$$\mathrm{Ker}(\mathcal{L} - ikI) = \mathrm{Ker}(\mathcal{L} - ikI)^2. \tag{3.18}$$

Step 2 : The above condition is however implicit and does not allow an effective determination of the frequencies for which the Lamb modes form a complete set. In [56], a simpler condition than (3.18) is derived (although not proved) with a reference to [97]. Our goal is to derive an equivalent condition, that only depends on the parameters of the problem. To this end, we generalize the approach in [91] and in view of (3.18), we seek to characterize under which conditions generalized eigenvalues exist. We present the argument in the case of a symmetric Lamb mode, the antisymmetric situation can be handled in the same manner.

Assume that $(u_0, t_0, -s_0, v_0)$ is a symmetric Lamb mode (given by (3.12)) associated with a wavenumber $k \in \mathbb{C}$. We look for $(u, t, -s, v) \in H_0$ that satisfies

$$\mathcal{L}(u, t, -s, v) = ik\mathcal{L}(u, t, -s, v) + (u_0, t_0, -s_0, v_0), \tag{3.19}$$

so that (3.18) is not satisfied. Defining

$$f_1 = -(\lambda+\mu)\partial_z u_0 - 2ik\mu v_0, \qquad f_2 = -2(\lambda+2\mu)iku_0 - (\lambda+\mu)\partial_z v_0, \tag{3.20}$$

we notice that (u, v) satisfies the equation

$$\begin{cases} (\lambda+2\mu)\partial_{zz}v + (\lambda+\mu)ik\partial_z u - \mu q^2 v = f_1 & \text{in } (-h,h), \\ \mu\partial_{zz}u + (\lambda+\mu)ik\partial_z v - p^2(\lambda+2\mu)u = f_2 & \text{in } (-h,h), \\ \partial_z u(\pm h) + ikv(\pm h) = -v_0(\pm h), & \\ \lambda iku(\pm h) + (\lambda+2\mu)\partial_z v(\pm h) = -\lambda u_0(\pm h). & \end{cases} \tag{3.21}$$

We introduce the auxiliary functions

$$\phi = -\frac{\lambda+2\mu}{\omega^2}(iku + \partial_z v), \qquad \psi = \frac{\mu}{\omega^2}(\partial_z u - ikv), \tag{3.22}$$

which turn out to solve the following second order linear ODE's with constant coefficients

$$\partial_{zz}\phi(z) + p^2\phi(z) = -2ik(q^2-k^2)\sin(qh)\cos(pz) + 2ikpq\frac{\lambda+\mu}{\mu}\sin(ph)\cos(qz), \tag{3.23}$$

$$\partial_{zz}\psi(z) + q^2\psi(z) = -(q^2-k^2)p\sin(qh)\frac{\lambda+\mu}{\lambda+2\mu}\sin(pz) + 4k^2p\sin(ph)\sin(qz). \tag{3.24}$$

The solutions of the above ODE's can be written

$$\phi(z) = A_1\cos(pz) + \left(A_2 - \frac{ik(q^2-k^2)}{p}\sin(qh)z\right)\sin(pz) + \frac{2ikpq(\lambda+\mu)}{(p^2-q^2)\mu}\sin(ph)\cos(qz), \tag{3.25}$$

$$\psi(z) = \left(A_1' - \frac{2k^2p}{q}\sin(ph)z\right)\cos(qz) + A_2'\sin(qz) - \frac{(q^2-k^2)p(\lambda+\mu)}{(\lambda+2\mu)(q^2-p^2)}\sin(qh)\sin(pz), \tag{3.26}$$

for some $A_1, A_2, A_1', A_2' \in \mathbb{C}$. Using the fact that $u = ik\phi - \partial_z\psi + f_2/\omega^2$ and $v = \partial_z\phi + ik\psi + f_1/\omega^2$, we find that

$$
\begin{aligned}
u(z) \quad = \quad & A_1 ik\cos(pz) + A_2 ik\sin(pz) + A_1' q\sin(qz) - A_2' q\cos(qz) && (3.27)\\
& + \frac{k^2(q^2-k^2)}{p}\sin(qh)z\sin(pz) - 2k^2 p\sin(ph)z\sin(qz) + \frac{2k^4\mu p}{q\omega^2}\sin(ph)\cos(qz)\\
& + \left(q^2 - k^2 + \frac{k^2(q^2-k^2)(\lambda+2\mu)}{\omega^2}\right)\sin(qh)\cos(pz),\\
v(z) \quad = \quad & -A_1 p\sin(pz) + A_2 p\cos(pz) + A_1' ik\cos(qz) + A_2' ik\sin(qz) && (3.28)\\
& - ik(q^2-k^2)\sin(qh)z\cos(pz) - \frac{2k^2 p}{q}\sin(ph)z\cos(qz) + \left(2ikp + \frac{2ik^3\mu p}{\omega^2}\right)\sin(ph)\sin(qz)\\
& - \frac{ik^3(q^2-k^2)(\lambda+2\mu)}{\omega^2 p}\sin(qh)\sin(pz).
\end{aligned}
$$

Expressing the boundary conditions, we obtain

$$
M\begin{pmatrix} A_1 \\ A_2' \end{pmatrix} = -\begin{pmatrix} b_1 \\ b_2 \end{pmatrix}, \tag{3.29}
$$

where $M = \begin{pmatrix} -2ikp\sin(ph) & (q^2-k^2)\sin(qh) \\ -\mu(q^2-k^2)\cos(ph) & 2ik\mu q\cos(qh) \end{pmatrix}$, and where

$$
\begin{aligned}
b_1 = {} & 2k^2(q^2-k^2)h\cos(ph)\sin(qh) - \frac{2(q^2-k^2)k^2 p}{q}h\cos(qh)\sin(ph)\\
& + \sin(ph)\sin(qh)\left(-9pk^2 - pq^2 + \frac{4k^2pq^2}{\omega^2} + \frac{(q^2-k^2)(k^2-p^2)(\omega^2+(\lambda+2\mu)k^2)}{p\omega^2}\right),
\end{aligned}
$$

$$
\begin{aligned}
b_2 = {} & \left(4\mu ik^3 p + \frac{ik\mu(q^2-k^2)^2}{p}\right)h\sin(ph)\sin(qh) + \cos(qh)\sin(ph)\left(4ik\mu qp - \frac{4ik^5p\mu^2}{q\omega^2}\right)\\
& + \cos(ph)\sin(qh)\left(-\frac{2ik\mu(q^2-k^2)}{\omega^2}(\omega^2 + k^2(\lambda+2\mu)) + \lambda ik(q^2-k^2)\right).
\end{aligned}
$$

Since k satisfies the symmetric Rayleigh-Lamb equation (3.10), the determinant of the matrix M vanishes.

If the first column of the matrix M is non zero, then (3.29) has a solution if and only if

$$
\begin{vmatrix} 2ikp\sin(ph) & b_1 \\ \mu(q^2-k^2)\cos(ph) & b_2 \end{vmatrix} = 0. \tag{3.30}
$$

Computing this determinant and using the relation (3.10) leads to

$$
\begin{aligned}
-2k^2\mu\Bigg[& h(q^2-k^2)^2\sin(qh)^2 + 4k^2p^2\sin(ph)^2\\
& + (q^2-k^2)\sin(ph)\cos(ph)\sin(qh)^2\left(\frac{q^2-k^2}{p} - 8p - \frac{2p}{k^2} - \frac{p}{q^2}\right)\Bigg] = 0,
\end{aligned} \tag{3.31}
$$

in other words, $\Gamma_S = 0$ and $\omega \in \omega_{\text{crit}}$.

Assume now that $M_{11} = M_{21} = 0$. Then either $k = 0$ and $q^2 \cos(ph) = 0$ (the condition $q = 0$ is excluded as it yields to a trivial eigenfunction $(u_0, t_0, -s_0, v_0)$) and the system takes the form

$$\begin{pmatrix} 0 & q^2 \sin(qh) \\ 0 & 0 \end{pmatrix} \begin{pmatrix} A_1 \\ B_2 \end{pmatrix} = \begin{pmatrix} 2pq^2 \sin(qh) \\ 0 \end{pmatrix}, \tag{3.32}$$

and has non trivial solutions (for instance $B_2 = 2p$ and $A_1 = 0$). Or $k \neq 0$, $p \in \pi\mathbb{Z}$ and $q^2 - k^2 = 0$, in which case $(b_1, b_2) = (0, 0)$ and the system also has nontrivial solutions. In this latter case, one can check that $\Gamma_S = 0$ as well.

Conversely, if (3.31) holds, then using (3.27)-(3.28) one can construct a solution $(u, t, -s, v)$ to (3.19). This shows that $\omega \in \omega_{\text{crit}}$ if an only if (3.18) is not satisfied, and concludes the proof of the Theorem. $\square$

Remark 3.2. *When $\omega \in \omega_{crit}$, one needs to add generalized eigenmodes to the Lamb modes to obtain a complete family [56, 8]. Our proof can be useful if ones want to find the expression of such generalized modes: finding (A_1, B_2) solution to* (3.29) *and replacing it in* (3.27) *and* (3.28) *gives the expression of the generalized modes.*

Remark 3.3. *If we derive equation* (3.10) *(resp.* (3.11)*) with respect to k, we notice that $\partial_k \omega = 0$ if and only if* (3.14) *(resp.* (3.15)*) is satisfied. This shows that critical points are exactly located where $\partial_k \omega = 0$. When $k \neq 0$, these points are called zero velocity group points (ZGV points) and have been extensively studied (see for instance [11]).*

3.2.2 Solution of the 2D elasticity problem

In the rest of this section, we assume that $\omega \notin \omega_{\text{crit}}$, so that Lamb modes form a complete family, however they do not necessarily yield an orthonormal basis. In order to identify the decomposition of a given function of H on the Lamb basis, we split the set of wavenumbers k in two parts:

Definition 3.4. *Let $\omega \notin \omega_{crit}$.*

- *We say that a Lamb mode with wavenumber k is right-going if Im$(k) > 0$ or Im$(k) = 0$ and $\partial_k \omega > 0$,*
- *We say that a Lamb mode is left-going if Im$(k) < 0$ or Im$(k) = 0$ and $\partial_k \omega < 0$.*

We index the right-going modes by $n \in \mathbb{N}^*$, and sort them by ascending order of imaginary part and descending order of real part.

We illustrate this classification in Figure 3.3, where right and left-going wavenumbers are represented at the frequency $\omega = 1.37$.

As mentioned previously, if k_n is a right-going mode, $-k_n$ is also solution of the Rayleigh-Lamb equation and is then a left-going mode. We also notice, using (3.12), that if $(\boldsymbol{X}_n, \boldsymbol{Y}_n)$ is (up to a multiplicative constant) the right-going Lamb mode associated to k_n and $(\widetilde{\boldsymbol{X}}_n, \widetilde{\boldsymbol{Y}}_n)$ is the left-going Lamb mode associated to $-k_n$, then

$$u_n = -\widetilde{u}_n, \quad v_n = \widetilde{v}_n, \quad s_n = \widetilde{s}_n, \quad t_n = -\widetilde{t}_n. \tag{3.33}$$

It follows that for any $(\boldsymbol{X}, \boldsymbol{Y}) \in H$, there exist $(A_n)_{n \in \mathbb{N}^*}, (B_n)_{n \in \mathbb{N}^*}$ such that

$$(\boldsymbol{X}, \boldsymbol{Y}) = \sum_{n>0} A_n (\boldsymbol{X}_n, \boldsymbol{Y}_n) + \sum_{n>0} B_n (\widetilde{\boldsymbol{X}}_n, \widetilde{\boldsymbol{Y}}_n) = \sum_{n>0} A_n (\boldsymbol{X}_n, \boldsymbol{Y}_n) + \sum_{n>0} B_n (-\boldsymbol{X}_n, \boldsymbol{Y}_n). \tag{3.34}$$

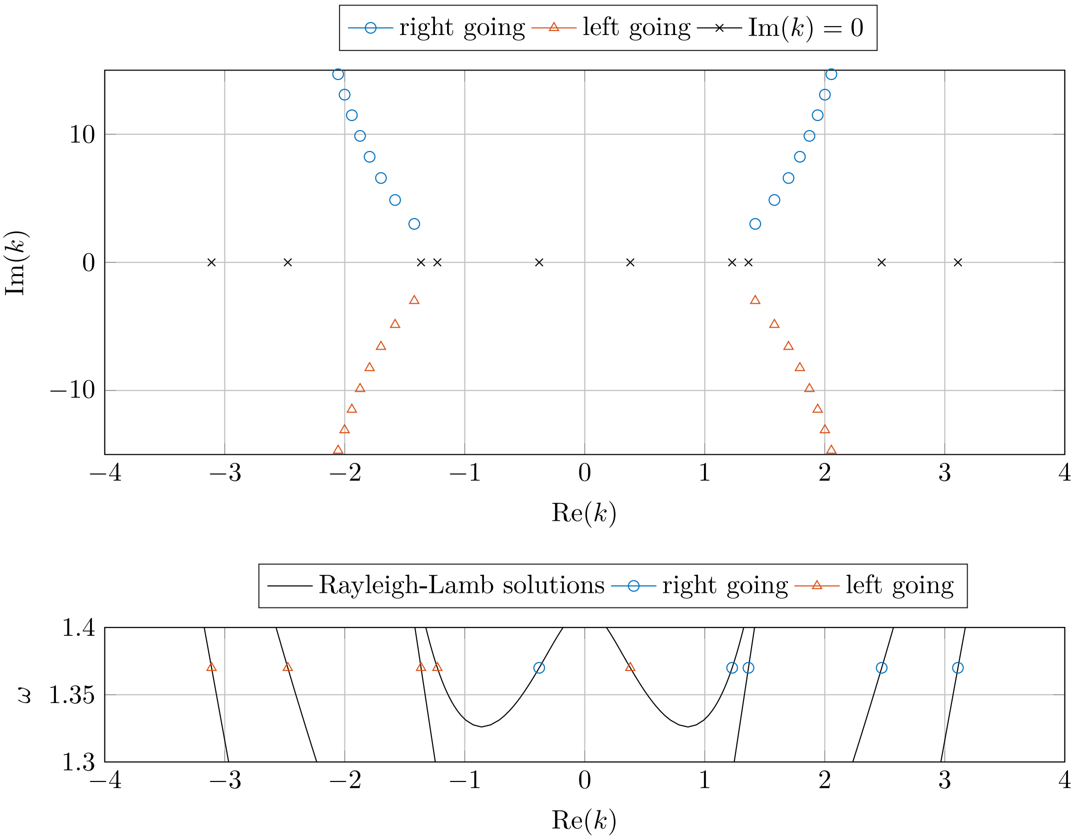

Figure 3.3 – Representation of right and left-going wavenumbers at the frequency $\omega = 1.37$ with $\mu = 0.25$ and $\lambda = 0.31$. Right-going modes are represented by circles and left-going modes by triangles. Top: classification of the wavenumbers with $\mathrm{Im}(k) \neq 0$. Bottom : classification of the wavenumbers with $\mathrm{Im}(k) = 0$ by looking at $\partial_k \omega$.

Defining $a_n = A_n - B_n$ and $b_n = A_n + B_n$,

$$\boldsymbol{X} = \sum_{n>0} a_n \boldsymbol{X}_n, \qquad \boldsymbol{Y} = \sum_{n>0} b_n \boldsymbol{Y}_n. \tag{3.35}$$

This decomposition with right-going modes is easier to handle than the full decomposition: We prove below that we can find an explicit expression of a_n and b_n given $(\boldsymbol{X}, \boldsymbol{Y})$. We denote $\langle \cdot, \cdot \rangle$ the product defined by

$$\langle (z_1, z_2), (z_3, z_4) \rangle = \int_{-h}^{h} z_1 z_3 + z_2 z_4. \tag{3.36}$$

Note that this product is not a scalar product since the z_i's are complex-valued. The following proposition states that families $(\boldsymbol{X}_n)_{n \in \mathbb{N}^\star}$ and $(\boldsymbol{Y}_n)_{n \in \mathbb{N}^\star}$ are bi-orthogonal:

Proposition 3.3. *For every* $n, m > 0$, $\langle \boldsymbol{X}_m, \boldsymbol{Y}_n \rangle = \delta_{n=m} J_n$ *where* $J_n = i\omega^2 k \Gamma_S$ *if* n *is a symmetric mode and* $J_n = i\omega^2 k \Gamma_A$ *if* n *is an anti symmetric mode, with* Γ_S *and* Γ_A *defined in* (3.14) *and* (3.15). *Especially,* $J_n \neq 0$ *if and only if* $\omega \notin \omega_{crit}$.

Proof. The proof that $\langle \boldsymbol{X}_m, \boldsymbol{Y}_n \rangle = 0$ if $m \neq n$ can be found in [44, 81]. Then, using expressions (3.12) and (3.13), we can compute $\langle \boldsymbol{X}_n, \boldsymbol{Y}_n \rangle$ as in [81]. ☐

This provides a new characterization of critical points:

Corollary 3.1. *The three following definitions of the set of critical frequencies are equivalent:*

$$\begin{aligned}\omega_{crit} &= \{\omega \in \mathbb{R}_+ \,|\, \exists n \in \mathbb{N}^\star \quad \langle \boldsymbol{X}_n, \boldsymbol{Y}_n \rangle = 0\} \\ &= \{\omega \in \mathbb{R}_+ \,|\, (\boldsymbol{X}_n, \boldsymbol{Y}_n)_{n>0} \text{ does not form a complete set of functions in } H\} \\ &= \{\omega \in \mathbb{R}_+ \,|\, \exists n \in \mathbb{N}^\star \quad \partial_{k_n} \omega = 0\}.\end{aligned} \tag{3.37}$$

Proposition 3.3 allows us to compute the coefficients in a decomposition (3.35), as

$$a_n = \frac{\langle \boldsymbol{X}, \boldsymbol{Y}_n \rangle}{J_n}, \qquad b_n = \frac{\langle \boldsymbol{Y}, \boldsymbol{X}_n \rangle}{J_n}. \tag{3.38}$$

We use the modal decomposition to provide an outgoing condition for elastic waveguides. For acoustic waves, one may ask that each modal component should satisfy a one dimensional Sommerfeld radiation condition (see Chapter 2 for instance). In the same spirit, we consider the following

Definition 3.5. *A wavefield $\boldsymbol{u} \in H^2_{loc}(\Omega)$ is said to be outgoing if $\boldsymbol{X}$ and $\boldsymbol{Y}$ defined in* (3.4) *satisfy*

$$\left| \langle \boldsymbol{Y}, \boldsymbol{X}_n \rangle'(x) \frac{x}{|x|} - ik_n \langle \boldsymbol{Y}, \boldsymbol{X}_n \rangle(x) \right| \underset{|x| \to +\infty}{\longrightarrow} 0 \quad \forall n \in \mathbb{N}^*, \tag{3.39}$$

$$\left| \langle \boldsymbol{X}, \boldsymbol{Y}_n \rangle'(x) \frac{x}{|x|} - ik_n \langle \boldsymbol{X}, \boldsymbol{Y}_n \rangle(x) \right| \underset{|x| \to +\infty}{\longrightarrow} 0 \quad \forall n \in \mathbb{N}^*. \tag{3.40}$$

This condition guarantees existence and uniqueness for the source problem (3.1) as we prove below. For every $r > 0$, we set $\Omega_r := (-r, r) \times (-h, h)$. We consider that any source defined on Ω_r (resp. $(-r, r)$) is extended by 0 on Ω (resp. $\mathbb{R}$).

Theorem 3.2. *Let $r > 0$. For every $\omega \notin \omega_{crit}$, $\boldsymbol{f} = (f_1, f_2) \in H^1(\Omega_r)$ and $\boldsymbol{b}^{top} = (b_1^{top}, b_2^{top})$, $\boldsymbol{b}^{bot} = (b_1^{bot}, b_2^{bot}) \in \widetilde{H}^{3/2}(-r, r)$, the PDE*

$$\left\{ \begin{array}{ll} \nabla \cdot \boldsymbol{\sigma}(\boldsymbol{u}) + \omega^2 \boldsymbol{u} = -\boldsymbol{f} & \text{in } \Omega, \\ \boldsymbol{\sigma}(\boldsymbol{u}) \cdot \nu = \boldsymbol{b}^{top/bot} & \text{on } \Omega_{top/bot}, \\ \boldsymbol{u} \text{ is outgoing,} & \end{array} \right. \tag{3.41}$$

has a unique solution $\boldsymbol{u} \in H^3_{loc}(\Omega)$, with a Lamb-mode decomposition

$$u(x,z) = \sum_{n>0} a_n(x) u_n(z), \qquad v(x,z) = \sum_{n>0} b_n(x) v_n(z), \tag{3.42}$$

where a_n, b_n are solutions to

$$\left\{ \begin{array}{l} a_n'' + k_n^2 a_n = ik_n F_1^n - F_2^{n\prime}, \\ b_n'' + k_n^2 b_n = F_1^{n\prime} - ik_n F_2, \end{array} \right. \tag{3.43}$$

with

$$F_1^n(x) = \frac{1}{J_n} \left(\int_{-h}^{h} f_1(x,z) u_n(z) \mathrm{d}z + b_1^{top}(x) u_n(h) + b_1^{bot}(x) u_n(-h) \right), \tag{3.44}$$

$$F_2^n(x) = \frac{1}{J_n} \left(\int_{-h}^{h} f_2(x,z) v_n(z) \mathrm{d}z + b_2^{top}(x) v_n(h) + b_2^{bot}(x) v_n(-h) \right). \tag{3.45}$$

Equivalently, $a_n = G_1^n * F_1^n - G_2^n * F_2^n$ *and* $b_n = G_2^n * F_1^n - G_1^n * F_2^n$ *with*

$$G_1^n(x) = \frac{1}{2} e^{ik_n|x|}, \qquad G_2^n(x) = \frac{x}{2|x|} e^{ik_n|x|}. \tag{3.46}$$

Moreover, there exists a constant $C > 0$*, which only depends on* h*,* ω *and* r*, such that*

$$\|\boldsymbol{u}\|_{H^3(\Omega_r)} \leq C \left(\|\boldsymbol{f}\|_{H^1(\Omega)} + \|\boldsymbol{b}^{top}\|_{H^{3/2}(\mathbb{R})} + \|\boldsymbol{b}^{bot}\|_{H^{3/2}(\mathbb{R})} \right). \tag{3.47}$$

Proof. This proof is an adaptation of the proof presented in Appendix 2.A of Chapter 2.

Step 1. We first show uniqueness of the solution. Assume that u solves (3.41) with $\boldsymbol{f} = 0$, $\boldsymbol{b}^{\text{top}} = \boldsymbol{b}^{\text{bot}} = 0$. The associated fields $\boldsymbol{X}, \boldsymbol{Y}$ defined in (3.4) can be decomposed as

$$\boldsymbol{X}(x,z) = \sum_{n>0} a_n(x) \boldsymbol{X}_n(z), \qquad \boldsymbol{Y}(x,z) = \sum_{n>0} b_n(x) \boldsymbol{Y}_n(z). \tag{3.48}$$

As proved in [81], the operators F and G defined in (3.5) are self adjoint on H_0. By projecting (3.4) with the product $\langle \cdot, \cdot \rangle$ on $\boldsymbol{X}_n$ and $\boldsymbol{Y}_n$, we see that

$$a_n' = ik_n b_n, \qquad b_n' = ik_n a_n. \tag{3.49}$$

Solving this system of ODE's and using the outgoing condition shows that $a_n = b_n = 0$, leading to $\boldsymbol{u} = 0$.

Step 2. Assume that the functions (u, v) defined in (3.42) is well defined. A quick computation shows that the associated fields $(\boldsymbol{X}, \boldsymbol{Y})$ satisfy (3.5) for every mode since

$$G_1^{n\prime} = ik_n G_2^n, \qquad G_2^{n\prime} = ik_n G_1^n + \delta_0. \tag{3.50}$$

Assuming that $|x| > r$, we also see that

$$\begin{aligned} &\left| \langle \boldsymbol{X}, \boldsymbol{Y}_n \rangle'(x) \frac{x}{|x|} - ik_n \langle \boldsymbol{X}, \boldsymbol{Y}_n \rangle(x) \right| \\ &\qquad = \left| \left(\frac{x}{|x|} G_1^{n\prime} - ik_n G_1^n \right) * F_1^n(x) - \left(\frac{x}{|x|} G_2^{n\prime} - ik_n G_2^n \right) * F_2^n(x) \right| = 0. \end{aligned} \tag{3.51}$$

Repeating this computation for $\langle \boldsymbol{Y}, \boldsymbol{X}_n \rangle$, shows that (u, v) satisfies the outgoing condition.

Step 3. We prove that the functions given by (3.42) are well-defined, in other words that the series in (3.42) converge. We know from [91] that the number of evanescent and propagative modes is finite, so we only need to study the convergence of the inhomogeneous modes. We begin by noticing that if k_n is an inhomogeneous mode, then $k_m = -\overline{k_n}$ also satisfies the dispersion relation, and $X_m = \overline{X_n}$ and $Y_m = \overline{Y_n}$. We index the subset of inhomogeneous wavenumbers with positive real part by $j \in \mathbb{N}^*$, and all the asymptotic comparison are now meant when $j \to +\infty$. Let $N = 2j - 1/2$ (resp. $N = 2j + 1/2$) if k_j is associated to a symmetric (resp. antisymmetric) mode. Using [67], we know that

$$hk_j = \frac{1}{2} \ln(2\pi N) + i\frac{\pi N}{2} - i\frac{\ln(2\pi N)}{2\pi N} + O\left(\frac{1}{N}\right). \tag{3.52}$$

Let p_j and q_j be the quantities defined in (3.10). We notice that $p_j, q_j \sim -ik_j$. Since $(p_j - ik_j)(p_j + ik_j) = \omega^2/(\lambda + 2\mu)$ and $(q_j - ik_j)(q_j - ik_j) = \omega^2/\mu$ it follows that

$$p_j = -ik_j + \underbrace{\frac{\omega^2}{(\lambda + 2\mu)\pi}}_{c_p} \frac{1}{N} + o\left(\frac{1}{N}\right), \quad q_j = -ik_j + \underbrace{\frac{\omega^2}{\mu\pi}}_{c_q} \frac{1}{N} + o\left(\frac{1}{N}\right). \tag{3.53}$$

We notice that

$$\sin(ik_j z) = \frac{iz}{2|z|} \exp\left(\frac{|z|}{h}\left(\frac{1}{2}\ln(2\pi N) + i\frac{\pi N}{2} - i\frac{\ln(2\pi N)}{2\pi N}\right)\right) + O\left(\frac{1}{N^{1-|z|/2h}}\right), \tag{3.54}$$

$$\cos(ik_j z) = \frac{1}{2} \exp\left(\frac{|z|}{h}\left(\frac{1}{2}\ln(2\pi N) + i\frac{\pi N}{2} - i\frac{\ln(2\pi N)}{2\pi N}\right)\right) + O\left(\frac{1}{N^{1-|z|/2h}}\right), \tag{3.55}$$

and if α stands for p or q,

$$\cos(\alpha_j z) \sim \cos(ik_j z) + \frac{c_\alpha}{N} z \sin(ik_j z), \quad \sin(\alpha_j z) \sim -\sin(ik_j z) + \frac{c_\alpha}{N} z \cos(ik_j z). \tag{3.56}$$

Using the definition of the symmetric modes (3.12), we find that

$$\begin{aligned}
u_j(z) &\sim \frac{\pi^3 N^2 (c_p - c_q)}{16}(h - |z|) \exp\left(\left(\frac{|z|}{h} + 1\right)\left(\frac{\ln(2\pi N)}{2} + \frac{i\pi N}{2} - \frac{i\ln(2\pi N)}{2\pi N}\right)\right), \\
v_j(z) &\sim \frac{i\pi^3 N^2 (c_p - c_q)}{16}\left(z - h\frac{z}{|y|}\right) \exp\left(\left(\frac{|z|}{h} + 1\right)\left(\frac{\ln(2\pi N)}{2} + \frac{i\pi N}{2} - \frac{i\ln(2\pi N)}{2\pi N}\right)\right), \\
t_j(z) &\sim \frac{-i\mu\pi^4 N^3 (c_p - c_q)}{16}\left(z - h\frac{z}{|z|}\right) \exp\left(\left(\frac{|z|}{h} + 1\right)\left(\frac{\ln(2\pi N)}{2} + \frac{i\pi N}{2} - \frac{i\ln(2\pi N)}{2\pi N}\right)\right), \\
s_j(z) &\sim \frac{-\mu\pi^4 N^3 (c_p - c_q)}{16}(h - |z|) \exp\left(\left(\frac{|z|}{h} + 1\right)\left(\frac{\ln(2\pi N)}{2} + \frac{i\pi N}{2} - \frac{i\ln(2\pi N)}{2\pi N}\right)\right),
\end{aligned}$$

and it follows that

$$\|u_j\|_{\mathrm{L}^2(-h,h)}, \|v_j\|_{\mathrm{L}^2(-h,h)} \sim \frac{\pi^4 h^{3/2} N^3 |c_p - c_q|}{4\ln(2\pi N)^{3/2}}, \tag{3.57}$$

$$\|t_j\|_{\mathrm{L}^2(-h,h)}, \|s_j\|_{\mathrm{L}^2(-1,1)} \sim \frac{\pi^5 h^{3/2} \mu N^4 |c_p - c_q|}{4\ln(2\pi N)^{3/2}}, \tag{3.58}$$

$$\|u_j\|_{\mathrm{L}^\infty(-h,h)}, \|v_j\|_{\mathrm{L}^\infty(-h,h)} \sim \frac{\pi^5 h N^2 |c_p - c_q|}{8}, \tag{3.59}$$

$$|J_j| \sim \frac{h^2 \pi^6 N^5 \omega^2 |c_p - c_q|}{8}. \tag{3.60}$$

Similar estimates can be derived for the antisymmetric modes, which yield the same asymptotic behaviors as (3.57), (3.58), (3.59) and (3.60). Defining

$$a_j = G_1^j * F_1^j - G_2^j * F_2^j, \qquad b_j = G_2^j * F_1^j - G_1^j * F_2^j, \tag{3.61}$$

we see using Young's inequality that

$$\|a_j\|_{\mathrm{L}^2(-r,r)} \leq \|G_1^j\|_{\mathrm{L}^1(-r,r)} \|F_1^j\|_{\mathrm{L}^2(-r,r)} + \|G_2^j\|_{\mathrm{L}^1(-r,r)} \|F_2^j\|_{\mathrm{L}^2(-r,r)}. \tag{3.62}$$

From the asymptotics of k_j it follows that $\|G_1^j\|_{\mathrm{L}^1(\mathbb{R})}, \|G_2^j\|_{\mathrm{L}^1(\mathbb{R})} \leq 1/N$. Thus if u_j^p denotes a primitive of u_j, we see that

$$\int_{-h}^{h} f_1(x,z) u_j(z) \mathrm{d}y = \left[f_1(x,z) u_j^p(z)\right]_{z=-h}^{z=h} - \int_{-h}^{h} \partial_z f_1(x,z) u_j^{p1}(z) \mathrm{d}z. \tag{3.63}$$

Using the previous estimates, we find that

$$u_j^p(z) \sim \frac{2}{i\pi N} u_j(z), \tag{3.64}$$

and so there exists a constant $c_1 > 0$, that depends on ω and h, such that

$$\|F_1^j\|_{\mathrm{L}^2(-r,r)} \leq \frac{c_1}{N^3}\left(\|f_1\|_{\mathrm{H}^1(\Omega)} + \|b_1^{\mathrm{top}}\|_{\mathrm{L}^2(\mathbb{R})} + \|b_1^{\mathrm{bot}}\|_{\mathrm{L}^2(\mathbb{R})}\right). \tag{3.65}$$

We obtain a similar estimate for F_2

$$\|F_2^j\|_{\mathrm{L}^2(-r,r)} \leq \frac{c_1}{N^3}\left(\|f_2\|_{\mathrm{H}^1(\Omega)} + \|b_2^{\mathrm{top}}\|_{\mathrm{L}^2(\mathbb{R})} + \|b_2^{\mathrm{bot}}\|_{\mathrm{L}^2(\mathbb{R})}\right). \tag{3.66}$$

Finally, using the triangular inequality,

$$\|u\|_{\mathrm{L}^2(\Omega_r)} \leq \sum_{n|k_n\in\mathbb{R},i\mathbb{R}} \|a_n\|_{\mathrm{L}^2(-r,r)}\|u_n\|_{\mathrm{L}^2(-h,h)} + 2\sum_{j\in\mathbb{N}^*}\|a_j\|_{\mathrm{L}^2(-r,r)}\|u_j\|_{\mathrm{L}^2(-h,h)}, \tag{3.67}$$

which leads to

$$\begin{aligned}\|u\|_{\mathrm{L}^2(\Omega)} \leq \Bigg[&\sum_{n|k_n\in\mathbb{R},i\mathbb{R}} \frac{2r}{|J_n|}\left(\|u_n\|_{\mathrm{L}^2(-h,h)} + \|v_n\|_{\mathrm{L}^2(-h,h)}\right)\|u_n\|_{\mathrm{L}^2(-h,h)} \\ &+ 2c_1\sum_{j\in\mathbb{N}^*}\frac{1}{(2j\pm 1/2)\ln(2j\pm 1/2)^{3/2}}\Bigg]\left(\|\boldsymbol{f}\|_{\mathrm{H}^1(\mathbb{R})} + \|\boldsymbol{b}^{\mathrm{top}}\|_{\mathrm{L}^2(\mathbb{R})} + \|\boldsymbol{b}^{\mathrm{bot}}\|_{\mathrm{L}^2(\mathbb{R})}\right),\end{aligned} \tag{3.68}$$

and similarly,

$$\begin{aligned}\|v\|_{\mathrm{L}^2(\Omega)} \leq \Bigg[&\sum_{n|k_n\in\mathbb{R},i\mathbb{R}} \frac{2r}{|J_n|}\left(\|u_n\|_{\mathrm{L}^2(-h,h)} + \|v_n\|_{\mathrm{L}^2(-h,h)}\right)\|v_n\|_{\mathrm{L}^2(-h,h)} \\ &+ 2c_1\sum_{j\in\mathbb{N}^*}\frac{1}{(2j\pm 1/2)\ln(2j\pm 1/2)^{3/2}}\Bigg]\left(\|\boldsymbol{f}\|_{\mathrm{H}^1(\mathbb{R})} + \|\boldsymbol{b}^{\mathrm{top}}\|_{\mathrm{L}^2(\mathbb{R})} + \|\boldsymbol{b}^{\mathrm{bot}}\|_{\mathrm{L}^2(\mathbb{R})}\right).\end{aligned} \tag{3.69}$$

Elliptic regularity results (see e.g. [47]) show that there exists a constant c_3 depending on r such that

$$\|\boldsymbol{u}\|_{\mathrm{H}^3(\Omega_r)} \leq c_3\left(\|\boldsymbol{u}\|_{\mathrm{L}^2(\Omega_r)} + \|\boldsymbol{f}\|_{\mathrm{H}^1(\mathbb{R})} + \|\boldsymbol{b}^{\mathrm{top}}\|_{\mathrm{H}^{3/2}(\mathbb{R})} + \|\boldsymbol{b}^{\mathrm{bot}}\|_{\mathrm{H}^{3/2}(\mathbb{R})}\right), \tag{3.70}$$

which together with (3.68)-(3.69) conclude the proof. ☐

Remark 3.4. *This result is probably not optimal: indeed, in the scalar case one can merely assume that the source term lies in* $L^2(\Omega_r)$ *and obtain a solution in* $H^2_{loc}(\Omega)$ *(see Chapter 2). However, in the present case, the Lamb modes are not orthogonal and Parseval equality does not hold, so that in the above proof, we controlled terms using the triangular inequality, which may lead to a loss of accuracy. We can see in the proof that the extra regularity of the source terms is needed to derive* (3.65) *and* (3.66)*, which in turn yields the convergence of the series* (3.67)*. Providing adaptation to elastic waveguides, the theory developed in [72] may be better adapted to treat source terms with lower regularity.*

To conclude, in this section we have constructed an explicit solution of the elasticity problem in a regular waveguide, and have shown that its norm is controlled by that of the source terms. Such estimates will be useful in the following, for the reconstruction of small defects of the waveguide.

3.3 Forward source problem in a regular 3D plate

In this section, we are interested in the forward source problem in a three-dimension regular waveguide with two infinite dimensions. Our motivation comes from the experiments reported in [11], where one tries to reconstruct width defects in thin elastic plates. The propagation of waves in three-dimension waveguides with one infinite dimension such as pipes or air ducts is a direct generalization of the two dimensional case presented in the previous section, see for instance [16]. However, to our knowledge, the case of three-dimension waveguides with two infinite dimensions has not been treated yet. Two main issues are at stake. First, as mentioned in [59], in addition to longitudinal and transverse modes, one needs to take into account horizontal shear modes in order to form a complete modal basis. Second, one would like to generalize the $(\boldsymbol{X}, \boldsymbol{Y})$ formulation of Definition 3.1 to 3D.

Given an elastic wavefield $\mathbf{u} = (u, v, w)$ that propagates in a three dimension plate, our main contribution consists in introducing two auxiliary variables α and β, that only depend on u and v (see (3.75)), which allow the decoupling of the equations of elasticity. We show that (α, w) can be decomposed using Lamb modes, while β represents the horizontal shear modes. This allows us to obtain a generalization of Theorem 3.2 to three dimensional plates.

3.3.1 Decoupling of the linear elastic equation

Let us consider a 3D infinite elastic plate $\Omega = \mathbb{R}^2 \times (-h, h)$, where $h > 0$ is half of the waveguide thickness. For every $r > 0$, we define $\Omega_r = B_2(0, r) \times (-h, h)$ where $B_2(0, r)$ is the ball in $\mathbb{R}^2$ centered at $(0, 0)$ with radius r. A point $(x, y, z) \in \Omega$ will be denoted by $(\boldsymbol{x}, z)$, and the elastic displacement by $\boldsymbol{u} = (u, v, w)$. Given a frequency $\omega \in \mathbb{R}$ and given (λ, μ) the Lamé coefficients of the elastic waveguide, the wavefield $\boldsymbol{u}$ satisfies

$$\nabla \cdot \boldsymbol{\sigma}(\boldsymbol{u}) + \omega^2 \boldsymbol{u} = -\boldsymbol{f} \qquad \text{in } \Omega, \tag{3.71}$$

where $\boldsymbol{f} = (f_1, f_2, f_3)$ is a source term and $\boldsymbol{\sigma}(\boldsymbol{u})$ is the stress tensor defined by

$$\boldsymbol{\sigma}(\boldsymbol{u}) = \begin{pmatrix} \begin{array}{l}(\lambda + 2\mu)\partial_x u \\ \quad +\lambda \partial_y v + \lambda \partial_z w\end{array} & \mu \partial_y u + \mu \partial_x v & \mu \partial_z u + \mu \partial_x w \\ \mu \partial_y u + \mu \partial_x v & \begin{array}{l}(\lambda + 2\mu)\partial_y v \\ \quad +\lambda \partial_x u + \lambda \partial_z w\end{array} & \mu \partial_z v + \mu \partial_y w \\ \mu \partial_z u + \mu \partial_x w & \mu \partial_z v + \mu \partial_y w & \begin{array}{l}(\lambda + 2\mu)\partial_z w \\ \quad +\lambda \partial_x u + \lambda \partial_y v\end{array} \end{pmatrix}. \tag{3.72}$$

In the following, we study the case of Neumann boundary conditions

$$\boldsymbol{\sigma}(\boldsymbol{u}) \cdot \nu = \boldsymbol{b}^{\text{top}} \quad \text{on } \partial\Omega_{\text{top}}, \qquad \boldsymbol{\sigma}(\boldsymbol{u}) \cdot \nu = \boldsymbol{b}^{\text{bot}} \quad \text{on } \partial\Omega_{\text{bot}}, \tag{3.73}$$

where $\boldsymbol{b}^{\text{top}} = (b_1^{\text{top}}, b_2^{\text{bot}}, b_3^{\text{bot}})$ and $\boldsymbol{b}^{\text{bot}} = (b_1^{\text{bot}}, b_2^{\text{bot}}, b_3^{\text{bot}})$ are boundary source terms. However, our analysis applies also to the case of Dirichlet or Robin boundary conditions. We represent the set-up in Figure 3.4.

To adapt the $\boldsymbol{X}/\boldsymbol{Y}$ formulation to 3D, we introduce the following notations : for a vector field $\boldsymbol{g} = (g_1, g_2, g_3)$ and a scalar field g we set

$$\text{div}_2(\boldsymbol{g}) = \partial_x g_1 + \partial_y g_2, \quad \text{curl}_2(\boldsymbol{g}) = \partial_x g_2 - \partial_y g_1, \quad \Delta_2(g) = \partial_{xx} g + \partial_{yy} g. \tag{3.74}$$

Given $\mathbf{u} = (u, v, w) \in H^1_{\text{loc}}(\Omega)$ we define

$$\alpha = \text{div}_2(\boldsymbol{u}), \qquad \beta = \text{curl}_2(\boldsymbol{u}). \tag{3.75}$$

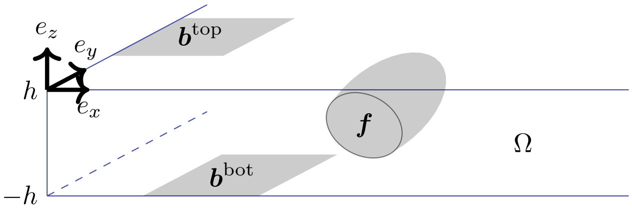

Figure 3.4 – The three dimensional plate Ω. Elastic wavefields are generated by an internal source term $\boldsymbol{f}$ and by boundary source terms $\boldsymbol{b}^{\text{top}}$ and $\boldsymbol{b}^{\text{bot}}$.

Note that α and β only involve the in-plane components of $\boldsymbol{u}$. The following proposition shows how these new variables decouple the elasticity system:

Proposition 3.4. *If* $\boldsymbol{u}$ *is solution of* (3.71) *with boundary conditions* (3.73)*, then* (α, w) *satisfies*

$$\left\{\begin{array}{cl} (\lambda+2\mu)\Delta_2\alpha + \mu\partial_{zz}\alpha + \omega^2\alpha + (\lambda+\mu)\Delta_2\partial_z w = -div_2(\boldsymbol{f}) & \text{in } \Omega, \\ (\lambda+\mu)\partial_z\alpha + (\lambda+2\mu)\partial_{zz}w + \mu\Delta_2 w + \omega^2 w = -f_3 & \text{in } \Omega, \\ \partial_z\alpha + \mu\Delta_2 w = div_2(\boldsymbol{b}^{top/bot}) & \text{on } \partial\Omega_{top/bot}, \\ (\lambda+2\mu)\partial_z w + \lambda\alpha = b_3^{top/bot} & \text{on } \partial\Omega_{top/bot}, \end{array}\right. \tag{3.76}$$

while β *satisfies*

$$\left\{\begin{array}{cl} \mu\Delta_2\beta + \mu\partial_{zz}\beta + \omega^2\beta = -curl_2(\boldsymbol{f}) & \text{in } \Omega, \\ \mu\partial_z\beta = curl_2(\boldsymbol{b}^{top/bot}) & \text{on } \partial\Omega_{top/bot}. \end{array}\right. \tag{3.77}$$

Proof. If we denote L_i the lines of (3.71) and B_i the lines of (3.73), we compute $\partial_x L_1 + \partial_y L_2$, $\partial_x B_1 + \partial_y B_2$ and with L_3 and B_3, we find (3.76). Then, $\partial_x L_2 - \partial_y L_1$ and $\partial_x B_2 - \partial_y B_1$ give (3.77). ☐

We start with the study of equation (3.77), which is a Helmholtz equation, similar to that of acoustic waveguides, for the function β. Inspired by Chapter 2, we introduce a decomposition of β as a sum of horizontal shear modes.

Definition 3.6. *For every* $n \in \mathbb{N}$*, we define* $\kappa_n^2 = \omega^2/\mu - n^2\pi^2/4h^2$ *with* $Real(\kappa_n) \geq 0$ *and* $Imag(\kappa_n) \geq 0$*. We define the* n*-th shear horizontal mode (SH mode)* φ_n *by*

$$\varphi_n(z) := \left\{\begin{array}{cl} 1/\sqrt{2h} & \text{if } n = 0, \\ \dfrac{1}{\sqrt{h}}\cos\left(\dfrac{n\pi(z+h)}{2h}\right) & \text{else.} \end{array}\right. \tag{3.78}$$

The sequence $(\varphi_n)_{n\geq 0}$ *defines an orthonormal basis of* $L^2(-h,h)$ *for the scalar product*

$$(g_1 \,|\, g_2) := \int_{-h}^{h} g_1(x)g_2(x)\mathrm{d}x. \tag{3.79}$$

Classical results on waveguides (see e.g. [27]) show that if one imposes a Sommerfeld radiation condition [95], the problem (3.77) is well-posed except for the frequencies

$$\omega_n^{sh} = \frac{\sqrt{\mu}\pi}{2h}n, \quad n \geq 0. \tag{3.80}$$

More precisely, when $\omega \notin \omega_{\text{crit}}^{sh} := \{\omega_n^{sh}, n \geq 0\}$, the following result holds:

Proposition 3.5. *For every $\omega \notin \omega_{crit}^{sh}$, $\boldsymbol{f} \in H^1(\Omega_r)$ and $\boldsymbol{b}^{top}, \boldsymbol{b}^{bot} \in \widetilde{H}^{3/2}(-r,r)$, the problem*

$$\left\{\begin{array}{lr} \mu\Delta_2\beta + \mu\partial_{zz}\beta + \omega^2\beta = -curl_2(\boldsymbol{f}) & \text{in } \Omega, \\ \mu\partial_z\beta = curl_2(\boldsymbol{b}^{bot/top}) & \text{on } \partial\Omega_{bot/top}, \\ \sqrt{R}\,[\partial_r - i\kappa_n]\,(\beta\,|\,\varphi_n)\,(Re^{i\theta}) \underset{R\to+\infty}{\longrightarrow} 0 \quad \forall n \geq 0 \quad \forall\theta \in (0,2\pi), & \end{array}\right. \tag{3.81}$$

has a unique solution $\beta \in H^2_{loc}(\Omega)$ which decomposes as

$$\beta(\boldsymbol{x},z) \;=\; \sum_{n\geq 0} -(\Gamma^n * F^n_{sh})(\boldsymbol{x})\varphi_n(z), \tag{3.82}$$

where Γ^n denotes the Hankel function of the first kind

$$\Gamma^n(\boldsymbol{x}) \;=\; -\frac{i}{4}H_0^{(1)}(\kappa_n|\boldsymbol{x}|),$$

and where

$$F^n_{sh} \;=\; \frac{1}{\mu}\left(\int_{-h}^{h} curl_2(\boldsymbol{f})\varphi_n + curl_2(\boldsymbol{b}^{top})\varphi_n(1) + curl_2(\boldsymbol{b}^{bot})\varphi_n(0)\right).$$

Proof. We follow the exact same steps as Appendix 2.A in Chapter 2. Since the φ_n form an orthonormal basis, any function β can be decomposed as $\beta = \sum \beta_n\varphi_n$. Projecting on the SH modes, the problem (3.81) is equivalent to the collection of problems indexed by $n \in \mathbb{N}$

$$\left\{\begin{array}{lr} \Delta_2\beta_n + \kappa_n^2 b_n = g^n_{sh} & \text{in } \mathbb{R}^2 \\ \sqrt{r}\,[\partial_r - i\kappa_n]\,\beta_n(Re^{i\theta}) \underset{r\to+\infty}{\longrightarrow} 0 \quad \forall\theta \in (0,2\pi). & \end{array}\right. \tag{3.83}$$

As $\Delta\Gamma^n + \kappa_n^2\Gamma^n = \delta_0$ [107], each function β_n can be expressed as the convolution $\Gamma^n * F^n_{sh}$. The series (3.82) can be shown to converge in $\mathrm{L}^2_{\mathrm{loc}}(\Omega)$ and provides a solution in the sense of distributions to (3.81). Elliptic regularity allows then to show that β is actually in $\mathrm{H}^2_{\mathrm{loc}}(\Omega)$. ☐

Next, we study equation (3.76), which resembles the two dimensional elasticity system studied in section 3.2. We propose to adapt the $\boldsymbol{X}/\boldsymbol{Y}$ formulation to this new equation. We define the variables

$$t = \mu\partial_z\alpha + \mu\Delta_2 w, \quad s = (\lambda+2\mu)\alpha + \lambda\partial_z w, \quad \boldsymbol{X} = (\alpha, t), \quad \boldsymbol{Y} = (-s, w). \tag{3.84}$$

Then, we adapt Proposition 3.1:

Proposition 3.6. *The system* (3.76) *is equivalent to*

$$\left\{\begin{array}{lr} \begin{pmatrix} \boldsymbol{X} \\ \Delta_2\boldsymbol{Y} \end{pmatrix} = \mathcal{L}(\boldsymbol{X},\boldsymbol{Y}) + \begin{pmatrix} 0 \\ -f_3 - \delta_{z=h}b_3^{top} - \delta_{z=-h}b_3^{bot} \\ div_2(\boldsymbol{f}) + \delta_{z=h}div_2(\boldsymbol{b}^{top}) + \delta_{z=-h}div_2(\boldsymbol{b}^{bot}) \\ 0 \end{pmatrix} & \text{in } \Omega, \\ B1(\boldsymbol{X}) = B2(\boldsymbol{Y}) = 0 & \text{on } \partial\Omega, \end{array}\right. \tag{3.85}$$

where $\mathcal{L}(\boldsymbol{X},\boldsymbol{Y}) = \begin{pmatrix} F(\boldsymbol{Y}) \\ G(\boldsymbol{X}) \end{pmatrix}$, and F, G, B_1 and B_2 are the same matrix operators as those defined in Proposition 3.1 in (3.6) *and* (3.7).

We thus may use Lamb modes to diagonalize the operator $\mathcal{L}$ as in the 2D situation, and obtain in this way a result similar to Theorem 3.2. Let u_n, v_n, k_n be defined as in section 3.2 and assume that $\omega \notin \omega_{\text{crit}}$.

Proposition 3.7. *For every $\omega \notin \omega_{crit}$, $\boldsymbol{f} \in H^1(\Omega_r)$ and $\boldsymbol{b}^{top}, \boldsymbol{b}^{bot} \in \widetilde{H}^{3/2}(-r,r)$, the problem*

$$\left\{\begin{array}{ll} (\lambda+2\mu)\Delta_2\alpha + \mu\partial_{zz}\alpha + \omega^2\alpha + (\lambda+\mu)\Delta_2\partial_z w = -div_2(\boldsymbol{f}) & in\ \Omega, \\ (\lambda+\mu)\partial_z\alpha + (\lambda+2\mu)\partial_{zz}w + \mu\Delta_2 w + \omega^2 w = -f_3 & in\ \Omega, \\ \partial_z\alpha + \mu\Delta_2 w = div_2(\boldsymbol{b}^{top/bot}) & on\ \partial\Omega_{top/bot}, \\ (\lambda+2\mu)\partial_z w + \lambda\alpha = b_3^{top/bot} & on\ \partial\Omega_{top/bot}, \\ \sqrt{R}\,[\partial_r - ik_n]\,\langle \boldsymbol{Y}, \boldsymbol{X}_n\rangle(Re^{i\theta}) \underset{R\to+\infty}{\longrightarrow} 0 \quad \forall n>0 \quad \forall\theta\in(0,2\pi), & \\ \sqrt{R}\,[\partial_r - ik_n]\,\langle \boldsymbol{X}, \boldsymbol{Y}_n\rangle(Re^{i\theta}) \underset{R\to+\infty}{\longrightarrow} 0 \quad \forall n>0 \quad \forall\theta\in(0,2\pi), & \end{array}\right. \tag{3.86}$$

has a unique solution $(\alpha, w) \in H^2_{loc}(\Omega) \times H^3_{loc}(\Omega)$ which decomposes as

$$\alpha(\boldsymbol{x},z) = \sum_{n>0}((k_n^2F_3^n + ik_nF_1^n) * G^n)u_n(z), \quad w(\boldsymbol{x},z) = \sum_{n>0}((-ik_nF_3^n + F_1^n) * G^n)v_n(z), \tag{3.87}$$

where

$$G^n(\boldsymbol{x}) = -\frac{i}{4}H_0^{(1)}(k_n|\boldsymbol{x}|), \tag{3.88}$$

$$F_1^n = \frac{1}{J_n}\left(\int_{-h}^{h} div_2(\boldsymbol{f})u_n + div_2(\boldsymbol{b}^{top})u_n(h) + div_2(\boldsymbol{b}^{bot})u_n(-h)\right), \tag{3.89}$$

$$F_3^n = \frac{1}{J_n}\left(\int_{-h}^{h} f_3v_n + b_3^{top}v_n(h) + b_3^{bot}v_n(-h)\right). \tag{3.90}$$

Proof. The proof is very similar to that of Theorem 3.2. We start by decomposing $(\boldsymbol{X}(x,y,z), \boldsymbol{Y}(x,y,z))$ in the form

$$\boldsymbol{X}(x,y,z) \ = \ \sum_{n>0} a_n(x,y)\boldsymbol{X}_n(z), \qquad \boldsymbol{Y}(x,y,z) \ = \ \sum_{n>0} b_n(x,y)\boldsymbol{Y}_n(z). \tag{3.91}$$

Injecting in (3.85), one obtains, instead of (3.49) in the 2D case,

$$a_n = ik_nb_n, \quad \Delta_2 b_n = ik_na_n. \tag{3.92}$$

If (3.87) is well defined, it satisfies (3.86) since $\Delta_2 G^n = -k_n^2G^n + \delta_0$. The study of the asymptotic behavior of a_n and b_n can be performed as in section 3.2, using the fact that

$$\|k_n^2G^n\|_{\mathrm{L}^1(B(0,r))} = \mathcal{O}(1), \quad \|ik_nG^n\|_{\mathrm{L}^1(B(0,r))} = \mathcal{O}(1/N), \quad \|G^n\|_{\mathrm{L}^1(B(0,r))} = \mathcal{O}(1/N^2). \tag{3.93}$$

It follows that the series (3.91) are in $\mathrm{L}^2_{\text{loc}}(\Omega)$ and provide a solution of (3.86) in the sense of distribution. Rewriting this system as an elliptic system

$$\left\{\begin{array}{ll} (\lambda+2\mu)\Delta_2\alpha + \mu\partial_{zz}(\alpha) = R(w,\mathbf{f}) & \text{in } \Omega, \\ (\lambda+2\mu)\partial_{zz}w + (\lambda+2\mu)\Delta_2 w = S(\alpha, f_3) & \text{in } \Omega, \\ \partial_z\alpha = r(\Delta_2 w, \mathbf{b}^{\text{top/bot}}) & \text{on } \partial\Omega_{\text{top/bot}}, \\ \partial_z w = s(\alpha, b_3^{\text{top/bot}}) & \text{on } \partial\Omega_{\text{top/bot}}, \end{array}\right.$$

using elliptic regularity [47] and a bootstrap argument, one further infers that $\alpha, w \in \mathrm{H}^2_{loc}(\Omega)$, which concludes the proof of the Proposition. □

3.3.2 Helmholtz-Hodge decomposition

Now that equations (3.76) and (3.77) are solved, we return to equations (3.71) and (3.73). We need to ensure that given the expressions of α and β, we can recover a unique expression for u and v. To this end, we use the Helmholtz-Hodge decomposition, which states that under certain conditions, a vector field can be decomposed in a unique way as the sum of a curl-free and divergence free fields. This decomposition is mostly used in fluid mechanics to analyze three dimensional vector fields (see for instance [20, 30]). In our case, we apply it to two dimensional vector fields, since we are only interested in finding a link between (u, v) and (α, β). We give the corresponding statement below, the proof of which and be found in [88] concerning existence, while uniqueness is addressed in [103].

Proposition 3.8. *Every vector field $\boldsymbol{\xi} \in H^1_{loc}(\mathbb{R}^3, \mathbb{C}^2)$, vanishing at infinity, can be uniquely decomposed as $\boldsymbol{\xi} = \boldsymbol{d} + \boldsymbol{c}$ where $curl_2(\boldsymbol{d}) = 0$ and $div_2(\boldsymbol{c}) = 0$. The couple $(\boldsymbol{d}, \boldsymbol{c})$ is called the Helmholtz-Hodge decomposition (HHD) of $\boldsymbol{\xi}$. Moreover, $\boldsymbol{\xi}$ is uniquely determined by $div_2(\boldsymbol{\xi})$ and $curl_2(\boldsymbol{\xi})$.*

Providing enough regularity on α and β, one can compute (u, v) using the formula [88]

$$(u, v) = -\nabla(\mathcal{G}(\alpha)) + \nabla \times (\mathcal{G}(\beta)), \tag{3.94}$$

where $\mathcal{G}$ represents the Newtonian potential operator which convolves each function with $x \mapsto \log(|\boldsymbol{x}|)/(2\pi)$. However, in the following, we will not need to use this formula. Indeed, we exhibit expressions of u and v that satisfy $\mathrm{div}_2(\boldsymbol{u}) = \alpha$ and $\mathrm{curl}_2(\boldsymbol{u}) = \beta$ and thus are the ones we look for thanks to the previous uniqueness result.

We introduce an outgoing radiation condition for 3D wavefields:

Definition 3.7. *A wavefield $\boldsymbol{u} \in H^2_{loc}(\Omega)$ is said to be outgoing if it vanishes at infinity, and if $\boldsymbol{X}, \boldsymbol{Y}$ defined in* (3.84) *and β defined in* (3.75) *satisfy*

$$\sqrt{R}\,[\partial_r - ik_n]\,\langle \boldsymbol{X}, \boldsymbol{Y}_n\rangle(Re^{i\theta}) \underset{R\to+\infty}{\longrightarrow} 0 \quad \forall n > 0 \quad \forall\theta \in (0, 2\pi), \tag{3.95}$$

$$\sqrt{R}\,[\partial_r - ik_n]\,\langle \boldsymbol{Y}, \boldsymbol{X}_n\rangle(Re^{i\theta}) \underset{R\to+\infty}{\longrightarrow} 0 \quad \forall n > 0 \quad \forall\theta \in (0, 2\pi), \tag{3.96}$$

$$\sqrt{R}\,[\partial_r - i\kappa_n]\,(\beta \,|\, \varphi_n)\,(Re^{i\theta}) \underset{R\to+\infty}{\longrightarrow} 0 \quad \forall n \geq 0 \quad \forall\theta \in (0, 2\pi). \tag{3.97}$$

Under this condition, uniqueness of solutions to the source problem in 3D will be guaranteed, as stated in the next Theorem. We first introduce some notations. We define the scalar convolution by

$$\boldsymbol{g_1} * \cdot \boldsymbol{g_2}(x) = \int \boldsymbol{g_1}(x - y) \cdot \boldsymbol{g_2}(y)\mathrm{d}y, \tag{3.98}$$

and introduce the Green functions

$$G_1^n(\boldsymbol{x}) = -\frac{i}{4}\mathrm{H}_0^{(1)}(k_n|\boldsymbol{x}|), \quad \boldsymbol{G_2^n}(\boldsymbol{x}) = \nabla G_1^n(\boldsymbol{x}), \quad G_3^n(\boldsymbol{x}) = -\frac{i}{4}\mathrm{H}_0^{(1)}(\kappa_n|\boldsymbol{x}|). \tag{3.99}$$

Let $(\boldsymbol{f^L}, \boldsymbol{f^{sh}})$, $(\boldsymbol{b^L_{\text{top}}}, \boldsymbol{b^{sh}_{\text{top}}})$, $(\boldsymbol{b^L_{\text{bot}}}, \boldsymbol{b^{sh}_{\text{bot}}})$ denote the HHD of (f_1, f_2), $(b_1^{\text{top}}, b_2^{\text{top}})$, $(b_1^{\text{bot}}, b_2^{\text{bot}})$ respectively and set

$$g_n^z(\boldsymbol{x}) = \frac{1}{J_n}\left(\int_{-h}^{h} f_3(\boldsymbol{x}, z)v_n(z)\mathrm{d}z + b_3^{\text{top}}(\boldsymbol{x})v_n(h) + b_3^{\text{bot}}(\boldsymbol{x})v_n(-h)\right), \tag{3.100}$$

$$\boldsymbol{g}_{\boldsymbol{n}}^{\boldsymbol{L}} = \frac{1}{J_n}\left(\int_{-h}^{h} \boldsymbol{f}^{\boldsymbol{L}}(\boldsymbol{x},z)u_n(z)\mathrm{d}z + \boldsymbol{b}_{\mathrm{top}}^{\boldsymbol{L}} u_n(h) + \boldsymbol{b}_{\mathrm{bot}}^{\boldsymbol{L}} u_n(-h)\right), \tag{3.101}$$

$$\boldsymbol{g}_{\boldsymbol{n}}^{\boldsymbol{sh}} = \frac{1}{\mu}\left(\int_{-h}^{h} \boldsymbol{f}^{\boldsymbol{sh}}(\boldsymbol{x},z)\varphi_n(z)\mathrm{d}z + \boldsymbol{b}_{\mathrm{top}}^{\boldsymbol{sh}} \varphi_n(h) + \boldsymbol{b}_{\mathrm{bot}}^{\boldsymbol{sh}} \varphi_n(-h)\right). \tag{3.102}$$

Theorem 3.3. *Let $r > 0$. For every $\omega \notin \omega_{crit} \cup \omega_{crit}^{sh}$, $\boldsymbol{f} \in H^3(\Omega_r)$ and $\boldsymbol{b}^{top}, \boldsymbol{b}^{bot} \in \widetilde{H}^{3/2}(-r,r)$, the problem*

$$\begin{cases} \nabla \cdot \boldsymbol{\sigma}(\boldsymbol{u}) + \omega^2 \boldsymbol{u} = -\boldsymbol{f} & \text{in } \Omega, \\ \boldsymbol{\sigma}(\boldsymbol{u}) \cdot \nu = \boldsymbol{b}^{top/bot} & \text{on } \Omega_{top/bot}, \\ \boldsymbol{u} \text{ is outgoing}, & \end{cases} \tag{3.103}$$

has a unique solution $\boldsymbol{u} \in H^3_{loc}(\Omega)$ which decomposes as $\boldsymbol{u} = \boldsymbol{u}^L + \boldsymbol{u}^{sh}$ with

$$\boldsymbol{u}^L(\boldsymbol{x},z) = \begin{pmatrix} \sum\limits_{n>0} \boldsymbol{A}_{\boldsymbol{n}}(\boldsymbol{x}) u_n(z) \\ \sum\limits_{n>0} b_n(\boldsymbol{x}) v_n(z) \end{pmatrix}, \quad \boldsymbol{u}^{Sh}(\boldsymbol{x},z) = \begin{pmatrix} \sum\limits_{n\geq 0} \boldsymbol{C}_{\boldsymbol{n}}(\boldsymbol{x})\varphi_n(z) \\ 0 \end{pmatrix}, \tag{3.104}$$

where $\boldsymbol{A}_{\boldsymbol{n}}, b_n, \boldsymbol{C}_{\boldsymbol{n}}$ satisfy the equations

$$\begin{cases} \Delta_2 \boldsymbol{A}_{\boldsymbol{n}} + k_n^2 \boldsymbol{A}_{\boldsymbol{n}} = -\nabla g_n^z + ik_n \boldsymbol{g}_{\boldsymbol{n}}^{\boldsymbol{L}}, \\ \Delta_2 \boldsymbol{C}_{\boldsymbol{n}} + \kappa_n^2 \boldsymbol{C}_{\boldsymbol{n}} = -\boldsymbol{g}_{\boldsymbol{n}}^{\boldsymbol{sh}}, \\ \Delta_2 b_n + k_n^2 b_n = -ik_n g_n^z + div_2(\boldsymbol{g}_{\boldsymbol{n}}^{\boldsymbol{L}}). \end{cases} \tag{3.105}$$

Equivalently, $\boldsymbol{A}_{\boldsymbol{n}} = -g_n^z * \boldsymbol{G}_{\boldsymbol{2}}^{\boldsymbol{n}} + ik_n \boldsymbol{g}_{\boldsymbol{n}}^{\boldsymbol{L}} * G_1^n$, $\boldsymbol{C}_{\boldsymbol{n}} = -\boldsymbol{g}_{\boldsymbol{n}}^{\boldsymbol{sh}}/\mu * G_3^n$ and $b_n = -ik_n g_n^z * G_1^n + \boldsymbol{g}_{\boldsymbol{n}}^{\boldsymbol{L}} *\cdot \boldsymbol{G}_{\boldsymbol{2}}^{\boldsymbol{n}}$. Moreover, there exists a constant $C > 0$ depending only on h, ω and r such that

$$\|\boldsymbol{u}\|_{H^3(\Omega_r)} \leq C\left(\|\boldsymbol{f}\|_{H^1(\Omega)} + \|\boldsymbol{b}^{top}\|_{H^{3/2}(\mathbb{R})} + \|\boldsymbol{b}^{bot}\|_{H^{3/2}(\mathbb{R})}\right). \tag{3.106}$$

Proof. If $\boldsymbol{f}$, $\boldsymbol{b}^{\mathrm{top}}$ and $\boldsymbol{b}^{\mathrm{bot}}$ vanish, uniqueness in Propositions 3.7 and 3.5 show that $\alpha = \beta = w = 0$. Since u and v are uniquely determined by $\mathrm{div}_2(u,v)$ and $\mathrm{curl}_2(u,v)$, it follows that $u = v = 0$ and the uniqueness of a solution is established. Moreover, Propositions 3.7 and 3.5 provide expressions of α, β and w. Using the HHD, there exists a unique wavefield $\boldsymbol{u}$ determined by (α, β) and we can check that expressions provided in (3.104) indeed provide a solution. Finally, the control of the wavefield with respect to source terms is obtained in the same manner as in the proof of Theorem 3.2, using the following estimates on the Green functions:

$$\|G_1^N\|_{\mathrm{L}^1(B(0,r))} = \mathcal{O}(1/N^2), \quad \|G_2^N\|_{\mathrm{L}^1(B(0,r))} = \mathcal{O}(1/N). \tag{3.107}$$

□

3.4 Reconstruction of small shape defects from multi-frequency measurements

In this section, we consider the inverse problem of reconstructing of small shape defects in an elastic plate from multi-frequency measurements. We first detail the method used in the two dimensional case. Its 3D generalization is discussed at the end of the section. We follow the method developed in Chapter 2 for acoustic waveguides. In the present case, given current experimental setups [59], we assume that the measurements consist in surface measurements of the displacement fields, rather than measurements in a section of the waveguide, which were considered in the acoustic case.

3.4.1 Born approximation

We consider a plate $\widetilde{\Omega}$ that contains localized bumps, defined by

$$\widetilde{\Omega} \quad = \quad \{(x,z) \in \mathbb{R}^2 \,|\, h(-1+2g_2(x)) < z < h(1+2g_1(x))\},$$

where g_1, g_2 are $\mathcal{C}^2$ functions with compact support, such that $-1+2g_2(x) < 1+2g_1(x)$, see Figure 3.5. Note that g_1 and g_2 are not required to have a constant sign. Hereafter $\widetilde{\Omega}$ is called the perturbed plate.

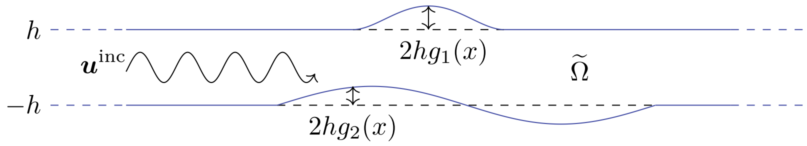

Figure 3.5 – Representation of shape defects in a plate of width h.

Our goal is to reconstruct the functions g_1 and g_2, from the wavefields scattered by the bumps. As incident wave, we use the function corresponding to the first symmetric Lamb mode of a straight guide, which we denote by $\boldsymbol{u}^{\text{inc}}(x,z) := \boldsymbol{u}_1(z)e^{ik_1x}$. The total wavefield $\widetilde{\boldsymbol{u}}$ solves the equations of elasticity in the waveguide:

$$\left\{\begin{array}{ll} \nabla\cdot\boldsymbol{\sigma}(\widetilde{\boldsymbol{u}}) + \omega^2\widetilde{\boldsymbol{u}} = 0 & \text{in } \widetilde{\Omega}, \\ \boldsymbol{\sigma}(\widetilde{\boldsymbol{u}})\cdot\nu = 0 & \text{on } \partial\widetilde{\Omega}_{\text{top/bot}}. \end{array}\right. \tag{3.108}$$

We denote by $\widetilde{\boldsymbol{u}}^s := \widetilde{\boldsymbol{u}} - \boldsymbol{u}^{\text{inc}}$ the scattered wavefield, which solves

$$\left\{\begin{array}{ll} \nabla\cdot\boldsymbol{\sigma}(\widetilde{\boldsymbol{u}}^s) + \omega^2\widetilde{\boldsymbol{u}}^s = 0 & \text{in } \widetilde{\Omega}, \\ \boldsymbol{\sigma}(\widetilde{\boldsymbol{u}}^s)\cdot\nu = -\boldsymbol{\sigma}(\boldsymbol{u}^{\text{inc}})\cdot\nu & \text{on } \partial\widetilde{\Omega}_{\text{top/bot}}, \\ \boldsymbol{u}^s \text{ is outgoing.} & \end{array}\right. \tag{3.109}$$

For every $(x,z) \in \partial\widetilde{\Omega}$, we know using the definition of Lamb modes that

$$\boldsymbol{\sigma}(\boldsymbol{u}^{\text{inc}}) = \begin{pmatrix} s_1(z) & t_1(z) \\ t_1(z) & r_1(z) \end{pmatrix} e^{ik_1x}, \tag{3.110}$$

so if $(x,z) \in \partial\widetilde{\Omega}_{\text{top}}$ then $\boldsymbol{\sigma}(\widetilde{\boldsymbol{u}}^s)\cdot\nu$ is equal to

$$-\boldsymbol{\sigma}(\widetilde{\boldsymbol{u}}^{\text{inc}})\cdot\frac{1}{\sqrt{1+4h^2g_1'(x)^2}}\begin{pmatrix} -2hg_1'(x) \\ 1 \end{pmatrix} = -\frac{e^{ik_1x}}{\sqrt{1+4h^2g_1'(x)^2}}\begin{pmatrix} -2hg_1'(x)s_1(z) + t_1(z) \\ -2hg_1'(x)t_1(z) + r_1(z) \end{pmatrix}. \tag{3.111}$$

We can also do the same thing on $\partial\widetilde{\Omega}_{\text{bot}}$ to explicit the equation of the scattered wavefield. Then, following the steps of Chapter 2, we map the perturbed waveguide $\widetilde{\Omega}$ to a regular waveguide $\Omega := \mathbb{R}\times(-h,h)$ using the mapping

$$\phi(x,z) = (x, (1+g_1(x)-g_2(x))\,z + hg_1(x) + hg_2(x))\,. \tag{3.112}$$

We define $\boldsymbol{u}^s = \widetilde{\boldsymbol{u}}^s \circ \phi$. Equation (3.109) in the perturbed waveguide $\widetilde{\Omega}$ is equivalent to the following equation in the regular waveguide Ω:

$$\left\{\begin{array}{ll} \nabla \cdot \boldsymbol{\sigma}(\boldsymbol{u}^s) + \omega^2 \boldsymbol{u}^s = -a(\boldsymbol{u}^s) & \text{in } \Omega, \\ \boldsymbol{\sigma}(\boldsymbol{u}^s)\cdot\nu = \begin{pmatrix} 2hg_1'(x)s_1(\phi(x,z)) - t_1(\phi(x,z)) \\ 2hg_1'(x)t_1(\phi(x,z)) - r_1(\phi(x,z)) \end{pmatrix} e^{ik_1x} - b(\boldsymbol{u}^s)_1 & \text{on } \partial\Omega_{\text{top}}, \\ \boldsymbol{\sigma}(\boldsymbol{u}^s)\cdot\nu = \begin{pmatrix} -2hg_2'(x)s_1(\phi(x,z)) - t_1(\phi(x,z)) \\ -2hg_2'(x)t_1(\phi(x,z)) - r_1(\phi(x,z)) \end{pmatrix} e^{ik_1x} - b(\boldsymbol{u}^s)_2 & \text{on } \partial\Omega_{\text{bot}}, \\ \boldsymbol{u}^s \text{ is outgoing,} & \end{array}\right. \tag{3.113}$$

where we denote $f_1(x) = hg_1(x) + hg_2(x)$, $f_2(x) = 1 + g_1(x) - g_2(x)$,

$$\begin{aligned} a(\boldsymbol{u}) = &-\frac{f_1'f_2 + f_2'(z-f_1)}{{f_2}^2}\begin{pmatrix} 2(\lambda+2\mu)\partial_{xz}u + (\lambda+\mu)\partial_{zz}v \\ 2\mu\partial_{xz}v + (\lambda+\mu)\partial_{zz}u \end{pmatrix} - \frac{f_2'}{{f_2}^2}\begin{pmatrix} (\lambda+2\mu)\partial_z v \\ \mu\partial_z u \end{pmatrix} \\ &+ \frac{(f_1'f_2 + f_2'(z-f_1))^2}{{f_2}^4}\begin{pmatrix} (\lambda+2\mu)\partial_{zz}u \\ \mu\partial_{zz}v \end{pmatrix} + \left(\frac{1}{f_2} - 1\right)\begin{pmatrix} (\lambda+\mu)\partial_{xz}v \\ (\lambda+\mu)\partial_{xz}u \end{pmatrix} \\ &- \frac{f_1''{f_2}^2 + (f_2'' - 2{f_2'}^2 f_2)(z-f_1) - 2f_2'f_1'f_2}{{f_2}^3}\begin{pmatrix} (\lambda+2\mu)\partial_y u \\ \mu\partial_z v \end{pmatrix} + \left(\frac{1}{{f_2}^2} - 1\right)\begin{pmatrix} \mu\partial_{zz}u \\ (\lambda+2\mu)\partial_{zz}v \end{pmatrix}, \end{aligned} \tag{3.114}$$

and

$$b(\boldsymbol{u})_1 = -g_1'(\lambda+2\mu)\partial_x u - \lambda\frac{g_1'}{f_2}\partial_z v + \mu\left(\frac{1}{f_2} - 1\right)\partial_z u + \frac{f_1'f_2 + f_2'(z-f_1)}{{f_2}^2}(g_1'(\lambda+2\mu)\partial_z u - \mu\partial_z v), \tag{3.115}$$

$$b(\boldsymbol{u})_2 = g_2'\mu\partial_x v + \mu\frac{g_2'}{f_2}\partial_z u - (\lambda+2\mu)\left(\frac{1}{f_2} - 1\right)\partial_z v - \frac{f_1'f_2 + f_2'(z-f_1)}{{f_2}^2}(g_2'\mu\partial_z v - \lambda\partial_z u). \tag{3.116}$$

From now on, we only consider small shape defects, i.e. we assume that the quantity

$$\varepsilon = \max\left(\|g_1\|_{\mathrm{W}^{2,\infty}(\mathbb{R})}, \|g_2\|_{\mathrm{W}^{2,\infty}(\mathbb{R})}\right), \tag{3.117}$$

is small compared to the size of the supports of g_1 and g_2, and compared to the width of the waveguide. We can show the following estimate on the norm of the operators a and b:

Proposition 3.9. *For every $r > 0$, there exist constants $A, B > 0$ depending on ω and r such that*

$$\|a(\boldsymbol{u})\|_{H^1(\Omega_r)} \leq A\varepsilon\|\boldsymbol{u}\|_{H^3(\Omega_r)}, \qquad \|b(\boldsymbol{u})\|_{H^{3/2}(\Omega_r)} \leq B\varepsilon\|\boldsymbol{u}\|_{H^3(\Omega_r)}. \tag{3.118}$$

Following the steps of Chapter 2, we define the Born approximation $\boldsymbol{v}$ of $\boldsymbol{u}^s$ by

$$\left\{\begin{array}{ll} \nabla \cdot \boldsymbol{\sigma}(\boldsymbol{v}) + \omega^2 \boldsymbol{v} = 0 & \text{in } \Omega, \\ \boldsymbol{\sigma}(\boldsymbol{v})\cdot\nu = \begin{pmatrix} 2hg_1'(x)s_1(\phi(x,z)) - t_1(\phi(x,z)) \\ 2hg_1'(x)t_1(\phi(x,z)) - r_1(\phi(x,z)) \end{pmatrix} e^{ik_1x} & \text{on } \partial\Omega_{\text{top}}, \\ \boldsymbol{\sigma}(\boldsymbol{v})\cdot\nu = \begin{pmatrix} -2hg_2'(x)s_1(\phi(x,z)) - t_1(\phi(x,z)) \\ -2hg_2'(x)t_1(\phi(x,z)) - r_1(\phi(x,z)) \end{pmatrix} e^{ik_1x} & \text{on } \partial\Omega_{\text{bot}}, \\ \boldsymbol{v} \text{ is outgoing.} & \end{array}\right. \tag{3.119}$$

The following proposition, the proof of which is similar to Propositions 2.5 and 2.6 of Chapter 2, shows that $\boldsymbol{v}$ is a good approximation of $\boldsymbol{u}$ if the defect is small:

Proposition 3.10. *Let $C > 0$ be the constant defined in Theorem 3.42. If $\varepsilon C(A+B) < 1$ then* (3.113) *has a unique solution $\boldsymbol{u}$ and*

$$\|\boldsymbol{u}-\boldsymbol{v}\|_{H^3(\Omega_r)} \leq \frac{\varepsilon C(A+B)}{1-\varepsilon C(A+B)} 4rCh\varepsilon(\|s_1\|_{H^2}+\|t_1\|_{H^2}+\|r_1\|_{H^2}). \tag{3.120}$$

Finally, to simplify the boundary source term and get rid of the dependency on ϕ, we notice that

$$g_1'(x)s_1(\phi(x,z)) = g_1'(x)s_1(h) + \mathcal{O}(\varepsilon^2), \quad t_1(\phi(x,z)) = (g_1'(x)-g_2'(x))\partial_z t_1(h) + \mathcal{O}(\varepsilon^2), \tag{3.121}$$

$$g_1'(x)t_1(\phi(x,z)) = \mathcal{O}(\varepsilon^2), \quad r_1(\phi(x,z)) = (g_1'(x)-g_2'(x))\partial_z r_1(h) + \mathcal{O}(\varepsilon^2). \tag{3.122}$$

We define a simpler approximation $\boldsymbol{w}$ of $\boldsymbol{v}$ by

$$\left\{\begin{array}{lr} \nabla\cdot\boldsymbol{\sigma}(\boldsymbol{w}) + \omega^2\boldsymbol{w} = 0 & \text{in } \Omega, \\ \boldsymbol{\sigma}(\boldsymbol{w})\cdot\nu = \begin{pmatrix} 2hg_1'(x)s_1(h) - (g_1'(x)-g_2'(x))\partial_z t_1(h) \\ -(g_1'(x)-g_2'(x))\partial_z r_1(h) \end{pmatrix} e^{ik_1x} & \text{on } \partial\Omega_{\text{top}}, \\ \boldsymbol{\sigma}(\boldsymbol{w})\cdot\nu = \begin{pmatrix} -2hg_2'(x)s_1(h) - (g_1'(x)-g_2'(x))\partial_z t_1(h) \\ (g_1'(x)-g_2'(x))\partial_z r_1(h) \end{pmatrix} e^{ik_1x} & \text{on } \partial\Omega_{\text{bot}}, \\ \boldsymbol{w} \text{ is outgoing.} & \end{array}\right. \tag{3.123}$$

Using the control provided by Theorem 3.1, $\boldsymbol{w}$ is a good approximation of $\boldsymbol{v}$ if ε is small enough and there exists a constant $D > 0$ such that

$$\|\boldsymbol{v}-\boldsymbol{w}\|_{\mathrm{H}^3(\Omega_r)} \leq \varepsilon^2 Dhr\left(\|s_1\|_{\mathrm{H}^2} + \|\partial_z t_1\|_{\mathrm{H}^2} + \|\partial_z r_1\|_{\mathrm{H}^2}\right). \tag{3.124}$$

3.4.2 Boundary source inversion

From now on, we denote by $\boldsymbol{u}$ the solution to (3.123) generated with boundary source terms denoted by $\boldsymbol{b}^{\text{top}}$ and $\boldsymbol{b}^{\text{bot}}$. Given a maximal frequency $\omega_{\max}$, we measure the wavefield at the surface of the perturbed plate for every $\omega \in (0,\omega_{\max})$. Using the previous Born approximation, we can assume that the wavefield $\boldsymbol{u}$ is measured on the surface $y = h$ and that the measurements may contain noise. For every frequency ω and $x \in \mathbb{R}$, the measured value of $\boldsymbol{u}(x,h)$ is denoted by $\boldsymbol{u}_\omega(x,h)$. Similarly, the associated wavenumbers and Lamb modes are denoted by $k_n(\omega)$ and $(u_{n,\omega}, v_{n,\omega})$ respectively. Using Theorem 3.2, we know that

$$u_\omega(x,h) = \sum_{n>0} a_n(x)u_{n,\omega}(h), \qquad v_\omega(x,h) = \sum_{n>0} b_n(x)v_{n,\omega}(h), \tag{3.125}$$

where $a_n = G_1^n * F_1^n - G_2^n * F_2^n$, $b_n = G_2^n * F_1^n - G_1^n * F_2^n$ and G_1^n, G_2^n are defined in (3.46) and

$$F_1^n(x) = \frac{e^{ik_1x}}{J_n}\left((2hg_1's_1(h) - (g_1'-g_2')\partial_z t_1(h))u_{n,\omega}(h) - (2hg_2's_1(h) + (g_1'-g_2')\partial_z t_1(h))u_{n,\omega}(-h)\right), \tag{3.126}$$

$$F_2^n = \frac{e^{ik_1x}}{J_n}(g_1'-g_2')\partial_z r_1(g)\left(-u_{n,\omega}(h) + u_{n,\omega}(-h)\right). \tag{3.127}$$

Assuming that x is located on the left of the support of the sources,

$$u_\omega(x,h) = \frac{1}{2}\sum_{n>0} u_{n,\omega}(h)e^{-ik_n(\omega)x}\int_{\mathbb{R}} e^{ik_n(\omega)z}(F_1^n(z) - F_2^n(z))\mathrm{d}z, \tag{3.128}$$

$$v_\omega(x,h) = \frac{1}{2}\sum_{n>0} v_{n,\omega}(h)e^{-ik_n(\omega)x}\int_{\mathbb{R}} -e^{ik_n(\omega)z}(F_1^n(z)-F_2^n(z))\mathrm{d}z. \tag{3.129}$$

As explained in [64] and illustrated in [59], we can use a spatial Fourier transform along x to separate each term of the sum. We notice that up to a multiplicative coefficient, the fields u_ω and v_ω contain the same information about the source, so that only measurements of one component of the displacement are needed.

Further, since noise is likely to pollute the response of evanescent and inhomogeneous modes in real-life experiments, we only consider the propagative modes and for these modes n we have access to

$$\int_{\mathbb{R}} e^{i(k_n(\omega)+k_1(\omega))z}(g_1'(z)c_n^1 + g_2'(z)c_n^2)\mathrm{d}z \qquad \forall \omega \in \mathbb{R}_+, \tag{3.130}$$

where c_n^1 and c_n^2 are known coefficients depending on the mode n. We use the following definition for the Fourier transform

$$\mathcal{F}(g)(\xi) = \int_{\mathbb{R}} g(z)e^{-i\xi z}\mathrm{d}z. \tag{3.131}$$

From now on, we consider that $n=1$ is the first propagative symmetric Lamb mode and $n=2$ is the first propagative antisymmetric Lamb mode. Both modes exist at any frequency ω, and $\omega \mapsto k_1(\omega)$ or $\omega \mapsto k_2(\omega)$ are increasing functions that map $\mathbb{R}_+$ to $\mathbb{R}_+$ (see an illustration in Figure 3.2 for the symmetric case, and for more details we refer to [91]). In particular, if we set $\xi = 2k_1$, the available information amounts to knowing $\mathcal{F}(c_1^1 g_1' + c_1^2 g_2')(\xi)$ for every $\xi \in (0, 2k_1(\omega_{\max}))$. Similarly, if $\xi = k_1 + k_2$, we have knowledge of $\mathcal{F}(c_2^1 g_1' + c_2^2 g_2')$ for every $\xi \in (0, k_1(\omega_{\max}) + k_2(\omega_{\max}))$. We define

$$\xi_{\max} = \min\left(k_1(\omega_{\max}) + k_2(\omega_{\max}), 2k_1(\omega_{\max})\right). \tag{3.132}$$

Looking at expressions (3.126)-(3.127), we notice that the linear combinations $c_1^1 g_1' + c_1^2 g_2'$ and $c_2^1 g_1' + c_2^2 g_2'$ are independent so the functions g_1' and g_2' can be reconstructed using the inverse Fourier transform, in a stable way as the next Proposition shows (its proof is the same as Proposition 2.12 in Chapter 2).

Proposition 3.11. *Let $g, g^{app} \in \mathcal{C}^2(-r,r)$. Let $d = \mathcal{F}(g)$ and $d^{app} = \mathcal{F}(g^{app})$ defined on $(0, \xi_{\max})$. Assume that there exists $M > 0$ such that $\|g\|_{H^1(-r,r)}, \|g^{app}\|_{H^1(-r,r)} \le M$, then*

$$\|g - g^{app}\|^2_{L^2(-r,r)} \le \frac{4}{\pi}\|d - d^{app}\|_{L^2(-r,r)} + \frac{2\pi}{\xi_{\max}^2}M^2. \tag{3.133}$$

Remark 3.5. *We notice that the above estimate is actually better than the one presented in the acoustic case in Proposition 2.12 of Chapter 2. Indeed, in the acoustic case, there is only one propagative mode at every frequency, and the function $k_1 + k_2$ is not one-to-one from $\mathbb{R}_+$ to $\mathbb{R}_+$. In the elastic case however, we take advantage of the existence of two different Lamb modes propagating at every frequency.*

Given the reconstructions of g_1' and g_2', we can integrate these functions, using the fact that g_1 and g_2 have compact support, and obtain an approximation of the shapes of the defects. In the previous estimate, the error $\|d - d^{\mathrm{app}}\|_{\mathrm{L}^2(-r,r)}$ contains both the measurement error, as well as the error caused by the Born approximation (3.120). It follows that the reconstruction error decreases when the size of the defects gets smaller and when $\omega_{\max}$ increases. We present examples of numerical reconstructions in the next section.

We conclude this section by discussing possible extensions of this work. First, the method presented here could be implemented in a similar fashion in 3D. Indeed, using a Born approximation, one can show that the measurements are close to those emanating from a wavefield generated by two boundary source terms that depend on ∇g_1 and ∇g_2 in a regular waveguide. In 3D, a Hankel transform plays the role of the Fourier transform, and one obtains thus a reconstruction. Second, by the same method, one can also reconstruct bends in an elastic waveguide, in a similar manner as in the acoustic case described in section 2.3.2 of Chapter 2. However, the detection of homogeneities seems more difficult. Following section 2.3.4 of Chapter 2, one could use a Born approximation to approximate the measurements by a wavefield generated by an internal source term $\boldsymbol{f}$, that depends on a transformed inhomogeneity in a regular waveguide. However, it does not seem easy to extract, from the measurements, something like the Fourier transform of a function, that would characterize the inhomogeneity, as in (3.130).

3.5 Numerical results

In this last section, we illustrate the results of Theorems 3.2 and 3.3, and present numerical reconstructions of small shape defects.

Concerning Theorems 3.2 and 3.3, we compare the modal expressions of $\boldsymbol{u}$ given in (3.42) and (3.104) to the wavefields generated using Matlab in 2D, and Freefem++ [49] in 3D, respectively used to solve (3.41) and (3.103). In the following, we assume that sources are supported in Ω_r where $r = 3$ in 2D and $r = 1$ in 3D. To solve the elastic equation, we use the finite element method with a perfectly matched layer (PML) [18] placed in $\Omega_8 \setminus \Omega_4$ in 2D, and $\Omega_{2.5} \setminus \Omega_{1.3}$. Since PML's do not handle the presence of right-going propagating modes correctly when the wavenumber is negative (see an example of such wavenumbers in Figure 3.3), we use the strategy presented in [21] which modify the PML to provide a correct approximation of the wavefield, for every non critical frequency. The coefficient of absorption in the PML is defined by $\alpha = -k((|x|-4)\mathbf{1}_{|x|\geq 4}$ in 2D or $\alpha = -k((|\boldsymbol{x}|-1.3)\mathbf{1}_{|\boldsymbol{x}|\geq 1.3}$ in 3D, and ω^2 is replaced in the elastic equation by $\omega^2 + i\alpha$. The structured mesh is built with a stepsize of 10^{-3} in 2D and 10^{-2} in 3D.

We first illustrate the two dimensional case, and the modal decomposition (3.42) solution to (3.41). The wavefield is generated using internal and boundary source terms defined by

$$\boldsymbol{f}(x,y) = 100\,\mathbf{1}_{(x-0.5)^2+\frac{(y-0.06)^2}{0.015^2}<1}(x,y)\left((x-0.5)^2+\frac{(y-0.06)^2}{0.015^2}\right)(x+2y;1), \tag{3.134}$$

$$\boldsymbol{b}^{\text{top}}(x) = \frac{10}{\sqrt{2\pi}}e^{-\frac{(x+0.5)^2}{200}}(1;x), \quad \boldsymbol{b}^{\text{bot}}(x) = 20\,\mathbf{1}_{[2,2.5]}(x)(x-2)(x-2.5)(1;\sin(x)). \tag{3.135}$$

Numerical representations of the wavefield $\boldsymbol{u}$, obtained using the modal decomposition (3.42) are presented in Figure 3.6 as well as the wavefields generated by the finite element method, showing good visual agreement. Their computed relative error in $\mathrm{L}^\infty(\Omega_r)$ and $\mathrm{L}^2(\Omega_r)$ is smaller than 2%.

A similar comparison is carried out in 3D for the modal decomposition (3.104) solution to (3.103). To visualize the decomposition $\boldsymbol{u} = \boldsymbol{u}^L + \boldsymbol{u}^{sh}$, we first choose a curl-free internal source

$$\boldsymbol{f}(x,y,z) = z\frac{50}{\pi}e^{-\frac{(x^2+y^2)}{200}}(-x;-y;1)\,. \tag{3.136}$$

The modal simulation is compared with the fields obtained from a finite element approximation in Figure 3.7. Again, both approximations of the true wavefield are visually similar, even if that produced by the finite element discretization seems to propagate at a higher velocity. This could be caused by the fact that the step size of the discretization may not be sufficiently small. We point out that the calculation times of these simulations are not the same: while the finite element method takes around eight hours to run, the modal decomposition produces a result in less than

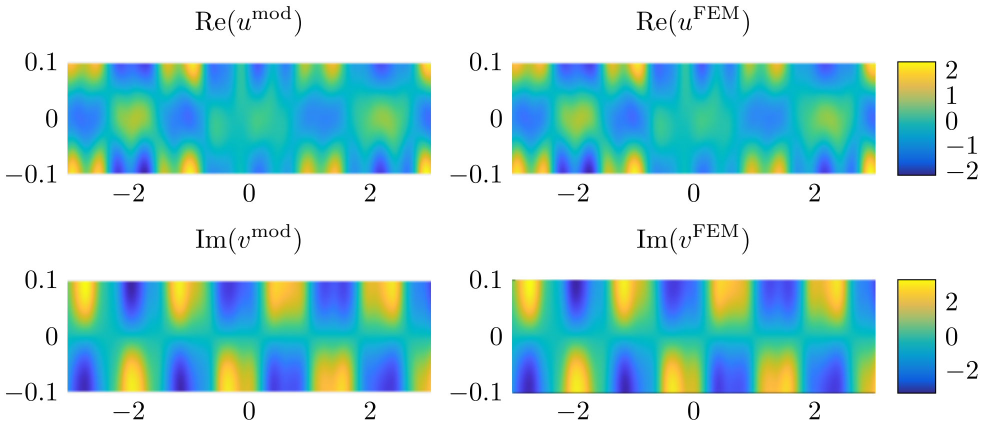

Figure 3.6 – Comparison between a wavefield $\boldsymbol{u}$ computed using the modal solution (3.42) or using a finite element method. Top: comparison between real parts of u. Bottom: comparison between imaginary parts of v. Similar results could also be obtained for $\mathrm{Im}(u)$ and $\mathrm{Re}(v)$. The parameters of the problem are $\lambda = 0.31$, $\mu = 0.25$, $h = 0.1$, $\omega = 13.7$. The sum in the modal decomposition of $\boldsymbol{u}^{\mathrm{mod}}$ is cut at $N = 20$ modes. Wavefields are generated using an internal source term $\boldsymbol{f}$ defined in (3.134) and boundary source terms $\boldsymbol{b}^{\mathrm{top}}$ and $\boldsymbol{b}^{\mathrm{bot}}$ defined in (3.135). Here, the relative $\mathrm{L}^\infty(\Omega_r)$-error is 1.7% and the $\mathrm{L}^2(\Omega_r)$-error is 1.4%.

two minutes. This underlines the interest of using the modal solution to do computations in three-dimensional perfect plates. Next, we choose a divergence-free boundary source term of the form

$$\boldsymbol{b}^{\mathrm{top}}(x,y) = \frac{25}{\pi} e^{-\frac{(x^2+y^2)}{200}}(-y;x;0), \qquad \boldsymbol{b}^{\mathrm{bot}}(x,y) = 0. \tag{3.137}$$

Comparisons are presented in Figure 3.8, and similar conclusions can be drawn.

Finally, we illustrate in Figure 3.9 two numerical reconstructions of small defects. Synthetic surface measurements are generated using the finite element method described above for different frequencies. Then, we reconstruct the derivative of defects profiles g_1 and g_2 using the penalized least square algorithm described in Chapter 2. We get reconstructions as good or even better than the one presented in the acoustic case, and we notice that the reconstruction seems more robust than the acoustic one then ε increases.

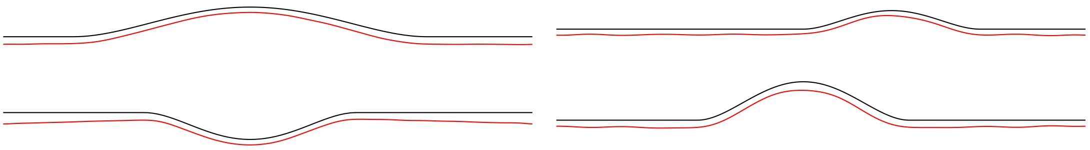

Figure 3.9 – Reconstruction of two shape defects. In black, the initial shape of Ω, and in red the reconstruction, slightly shifted for comparison purposes. In both cases, $h = 0.1$, $\omega_{\max} = 17$ and the interval $(0, \omega_{\max})$ is discretize with 170 points. On the left, $g_1(x) = \frac{5}{16}\mathbf{1}_{3.2\leq x\leq 4.2}(x-3.2)^2(4.2-x)^2$ and $g_2(x) = -\frac{35}{16}\mathbf{1}_{3.4\leq x\leq 4}(x-3.4)^2(4-x)^2$. On the right, $g_1(x) = \frac{125}{16}\mathbf{1}_{3.7\leq x\leq 4.2}(x-3.7)^2(4.2-x)^2$ and $g_2(x) = \frac{125}{16}\mathbf{1}_{3.4\leq x\leq 4}(x-3.4)^2(4-x)^2$.

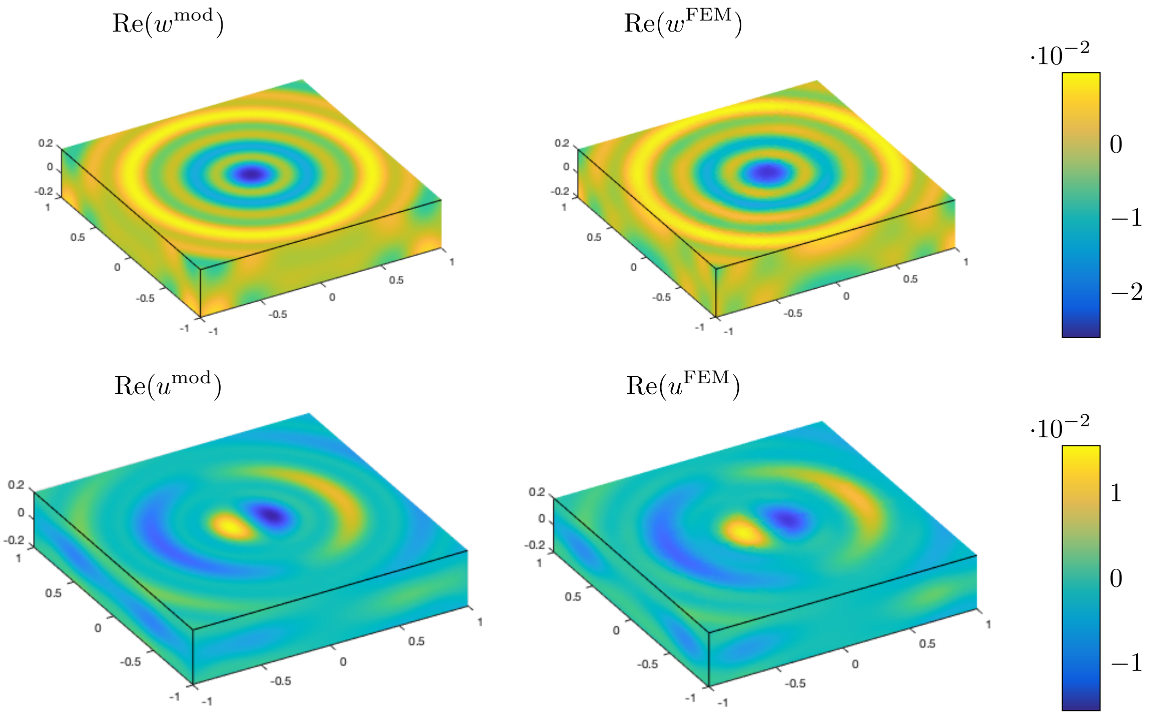

Figure 3.7 – Comparison between $\boldsymbol{u}$ computed using the modal solution (3.104) and using the finite element method with a curl-free internal source (3.136). Top: comparison of Re(w). Bottom: comparison of Re(u) (plots of Im(u), Re(v), Im(v), Im(w) look similar). The parameters are $\lambda = 0.31$, $\mu = 0.25$, $h = 0.2$, $\omega = 10$. $N = 20$ modes are used in the decomposition of $\boldsymbol{u}^{\mathrm{mod}}$. The relative $\mathrm{L}^\infty(\Omega_r)$-error is 7.2% and the $\mathrm{L}^2(\Omega_r)$-error is 9.4%.

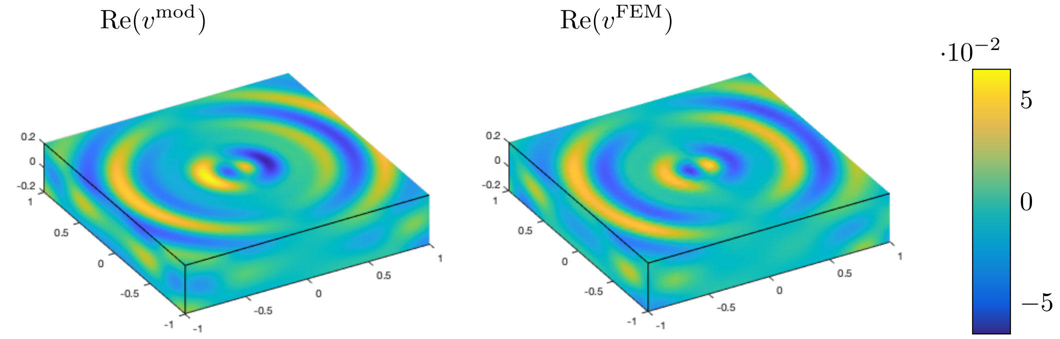

Figure 3.8 – Comparison between a wavefield $\boldsymbol{u}$ computed using the modal solution (3.104) or using a finite element method with a divergence free boundary source (3.137). The real parts of v is shown (plots of Im(v), Re(u), Im(u), Re(w), Im(w) would have similar aspect). The parameters are $\lambda = 0.31$, $\mu = 0.25$, $h = 0.2$, $\omega = 10$. $N = 10$ modes are used in the decomposition of $\boldsymbol{u}^{\mathrm{mod}}$. The relative $\mathrm{L}^\infty(\Omega_r)$-error is 5.3% and the $\mathrm{L}^2(\Omega_r)$-error is 4.1%.

II

Inversions from locally resonant frequencies

4

The Helmholtz problem in slowly varying waveguides at locally resonant frequencies

This chapter aims to present a general study of the Helmholtz problem in slowly varying waveguides. This work is of particular interest at locally resonant frequencies, where a phenomenon close to the tunnel effect for Schrödinger equation in quantum mechanics can be observed. In this situation, locally resonant modes propagate in the waveguide under the form of Airy functions. Using previous mathematical results on the Schrödinger equation, we prove the existence of a unique solution to the Helmholtz source problem with outgoing conditions in such waveguides. We provide an explicit modal approximation of this solution, as well as a control of the approximation error in $\mathrm{H}^1_{\mathrm{loc}}$. The main theorem is proved in the case of a waveguide with a monotonously varying profile and then generalized using a matching strategy. We finally validate the modal approximation by comparing it to numerical solutions based on the finite element method. The study of the forward source problem done in this chapter will then be of great use to develop a new multi-frequency method using locally resonant frequencies and presented in Chapters 5, 6 and 7.

4.1 Introduction

In this chapter, we study the propagation in the time-harmonic regime of waves generated by sources in a slowly varying waveguide of dimension 2. The waveguide is described by

$$\widetilde{\Omega} := \left\{(x, y) \in \mathbb{R}^2 \mid 0 < y < h(x)\right\}, \tag{4.1}$$

where $h \in \mathcal{C}^2(\mathbb{R}) \cap W^{2,\infty}(\mathbb{R})$ is a positive profile function defining the top boundary. Here, the bottom boundary is assumed to be flat but a similar analysis can be conducted with both slowly varying top and bottom boundaries. In the time-harmonic regime, the wavefield $\widetilde{u}$ satisfies the Helmholtz equation with Neumann boundary conditions

$$\begin{cases} \Delta\widetilde{u} + k^2\widetilde{u} = -\widetilde{f} & \text{in } \widetilde{\Omega}, \\ \partial_\nu\widetilde{u} = \widetilde{b} & \text{on } \partial\widetilde{\Omega}, \end{cases} \tag{4.2}$$

where $k > 0$ is the frequency, $\widetilde{f}$ is an interior source term and $\widetilde{b}$ is a possible boundary source term. In this work, a waveguide is said to be slowly varying when there exists a small parameter $\eta > 0$ such that $\|h'\|_{\mathrm{L}^\infty(\mathbb{R})} \leq \eta$ and $\|h''\|_{\mathrm{L}^\infty(\mathbb{R})} \leq \eta^2$. Such waveguides are good models of ducts or corroded pipes, and studying the sound transmission through this type of structure can be used to reduce noise emission (see [73]) or to perform non destructive monitoring of pipes or blood vessels (see [50]).

4.1.1 Scientific context

Wave propagation in varying waveguides, whether acoustic or elastic, has already been studied by several authors. From a numerical point of view, the articles [62, 41, 68] give different methods to adapt the finite element method to numerically compute the wavefield in varying waveguides. In [81], the authors study from the theoretical point of view the propagation of waves in a general varying elastic waveguide using a modal decomposition. The same kind of method is used in [43], in the case of a slowly varying waveguide. However, in these articles, the authors choose to avoid all the locally resonant frequencies of the waveguide, which are the frequencies $k > 0$ such that $k = \pi n/h(x^\star)$ for a mode $n \in \mathbb{N}$ and a longitudinal position $x^\star \in \mathbb{R}$.

In another approach, the authors of [82, 73, 46] choose to work near locally resonant frequencies of the waveguide. They mainly show that this problem is very close to the tunneling effect seen in quantum mechanics for the Schrödinger equation (see for instance [90]). Indeed, the wavefield can be decomposed as a sum of modes $\widetilde{u}(x, y) = \sum_{n\in\mathbb{N}} u_n(x)\varphi_n(y)$ (see section 4.2 for more details) and when $k = n\pi/h(x^\star)$, for some $x^\star \in \mathbb{R}$, the equation satisfied by the mode u_n is close to the Schrödinger equation

$$\partial_{xx}u_n(x) + (V(x) - E)u_n(x) = 0, \tag{4.3}$$

where V and E depend on h, $\widetilde{f}$ and $\widetilde{b}$ and satisfy $V(x^\star) - E = 0$. This equation for a simple mode was studied from a mathematical point of view by F. W. J. Olver in [76] and [77], and it was proved that the solution u_n could be expressed using Airy functions of the first and second kind [4]. In all the articles [82, 73, 46], the same methodology is used: first, the authors assume that mode coupling is negligible in a slowly varying waveguide. Under this so-called adiabatic approximation, every mode is independent from the others. Second, they seek solutions expressed as Wentzel Kramers Brillouin (WKB) asymptotic series (see [78]), and they use the study of the Schrödinger equation to find an approximation of the wavefield in the waveguide.

Our work is inspired by this methodology and provides a similar approximation of the wavefield in a slowly varying waveguide. However, contrary to the work mentioned above, we are not making any *a priori* assumptions on the wavefield such as WKB asymptotic development or the adiabatic decoupling of modes. Like them, we use the work of [76, 77] to get an approximation of the Schrödinger equation, but we improve it by providing precise control of the approximation error. More importantly, we provide a way to justify the adiabatic decoupling of the modes using a Born approximation of the wavefield. To this end, we again rely on [76, 77] to control the wavefield by the general source term that generated it. The main result of this chapter is given by Theorem 4.1 that proves the existence of a unique solution of the problem (4.2) when h is an increasing function in $\mathcal{C}^2(\mathbb{R}) \cap W^{2,\infty}(\mathbb{R})$ and when η is small enough (compared to $\text{supp}(h')$, $\min(h)$ and the distance between k and the left and right resonances of the waveguide). This theorem also provides an approximation of the solution of (4.2) and a control of the approximation error.

Finally, we provide a numerical validation of the approximation of the wavefield in a slowly varying waveguide. By comparing our approximation to solutions generated by a finite element method, we show that this approximation is an excellent tool to numerically compute the wavefield in a slowly varying waveguide in a very fast way.

4.1.2 Outline of the chapter

The chapter is organized as follows. In section 4.2, we briefly explain the modal decomposition in general waveguides, and we recall classical results used in the rest of the chapter. In section 4.3, we study the particular case of a slowly varying waveguide where the width h is an increasing function of x, and we prove Theorem 1. In section 4.4, we adapt the method developed in section 4.3 to the general case of a varying waveguide provided the variations of the profile are sufficiently slow, and we describe more precisely the cases of compressed or dilated waveguides. In section 4.5, we numerically validate our results by comparing the approximations derived in sections 4.3 and 4.4 with the solutions generated using a finite element solver with PML (perfectly matched layers, see [18]) in a truncated waveguide.

4.2 Modal decomposition and local wavenumbers in a varying waveguide

In this section, we recall some classical results about modal decompositions, the proofs of which can be found in Chapter 2 and[27].

Definition 4.1. *We define the sequence of functions* $(\widetilde{\varphi}_n)_{n\in\mathbb{N}}$

$$\forall (x,y) \in \widetilde{\Omega}, \quad \widetilde{\varphi}_n(x,y) := \begin{cases} 1/\sqrt{h(x)} & \text{if } n = 0, \\ \dfrac{\sqrt{2}}{\sqrt{h(x)}} \cos\left(\dfrac{n\pi y}{h(x)}\right) & \text{if } n \geq 1, \end{cases} \tag{4.4}$$

which for any $x \in \mathbb{R}$ *defines an orthonormal basis of* $L^2(0, h(x))$*. In the special case of a regular* *waveguide where* $h = 1$ *everywhere, this sequence of functions is independent of* x*, takes the form*

$$\forall y \in (0,1), \quad \varphi_n(y) := \left\{ \begin{array}{cl} 1 & \text{if } n = 0, \\ \sqrt{2}\cos(n\pi y) & \text{if } n \geq 1. \end{array} \right. \tag{4.5}$$

and defines an orthonormal basis of $L^2(0,1)$*.*

Hence, any solution $\widetilde{u} \in \mathrm{H}^2_{\mathrm{loc}}(\widetilde{\Omega})$ of (4.2) admits a unique modal decomposition

$$\widetilde{u}(x,y) = \sum_{n\in\mathbb{N}} \widetilde{u}_n(x)\widetilde{\varphi}_n(x,y) \quad \text{where} \quad \widetilde{u}_n(x) := \int_0^{h(x)} \widetilde{u}(x,y)\widetilde{\varphi}_n(x,y)\mathrm{d}y. \tag{4.6}$$

Note that when h is constant (outside of $\operatorname{supp} h'$), each mode $\widetilde{u}_n$ satisfies the simple equation $\widetilde{u}_n'' + k_n^2\widetilde{u}_n = -\widetilde{g}_n$ where k_n is the wavenumber. When h is variable, the decomposition (4.6) motivates the following definition:

Definition 4.2. *The local wavenumber function of the mode* $n \in \mathbb{N}$ *is the complex function* $k_n : \mathbb{R} \to \mathbb{C}$ *defined by*

$$k_n^2(x) := k^2 - \frac{n^2\pi^2}{h(x)^2}, \tag{4.7}$$

with $Re(k_n), Im(k_n) \geq 0$*.*

One of the main difficulties of this work is that as $h(x)$ is non constant, $k_n(x)$ can vanish for some $x \in \mathbb{R}$ and change from a positive real number to a purely imaginary number. We distinguish three different situations.

Definition 4.3. *A mode* $n \in \mathbb{N}$ *falls in one of the three following situations:*

1. *If* $n < kh(x)/\pi$ *for all* $x \in \mathbb{R}$ *then* $k_n(x) \in (0, +\infty)$ *for all* $x \in \mathbb{R}$ *and the mode* n *is called propagative.*
2. *If* $n > kh(x)/\pi$ *for all* $x \in \mathbb{R}$ *then* $k_n(x) \in i(0, +\infty)$ *for all* $x \in \mathbb{R}$ *and the mode* n *is called evanescent.*
3. *If there exists* $x^\star \in \mathbb{R}$ *such that* $n = kh(x^\star)/\pi$ *the mode* n *is called locally resonant. The associated points* $x^\star$ *are called resonant points. They are simple if* $h'(x^\star) \neq 0$*, and multiple otherwise.*

A frequency $k > 0$ *for which there exists at least a locally resonant mode is called a locally resonant frequency.*

Using the wavenumber function, one can adapt the classic Sommerfeld (or outgoing) condition, defined in Chapter 2 for regular waveguides, to general varying waveguides $\widetilde{\Omega}$. This condition will be used later to guarantee uniqueness for the source problem (4.2).

Definition 4.4. *A wavefield* $\widetilde{u} \in H^2_{loc}(\widetilde{\Omega})$ *is said to be outgoing if it satisfies*

$$\left| \widetilde{u}_n'(x)\frac{x}{|x|} - ik_n(x)\widetilde{u}_n(x) \right| \underset{|x|\to+\infty}{\longrightarrow} 0 \qquad \forall n \in \mathbb{N}, \tag{4.8}$$

where $\widetilde{u}_n$ *is given in* (4.6)*.*

4.3 The Helmholtz equation in a waveguide with increasing width

In all this work, we make the following assumptions:

Assumption 4.1. *We assume that* $h \in \mathcal{C}^2(\mathbb{R}) \cap W^{2,\infty}(\mathbb{R})$ *and satisfies*

$$\forall x \in \mathbb{R} \quad 0 < h_{\min} \leq h(x) \leq h_{\max} < \infty,$$

$$\|h'\|_{L^\infty(\mathbb{R})} < \eta, \quad \|h''\|_{L^\infty(\mathbb{R})} < \eta^2, \quad \mathit{supp}\, h' \subset \left(-\frac{R}{\eta}, \frac{R}{\eta}\right),$$

for some $\eta > 0$ *and* $R > 0$.

Moreover, in all this section, and we assume that h is increasing in $\operatorname{supp} h'$ (the general case will be treated in section 4.4). Such a waveguide is represented in Figure 4.1.

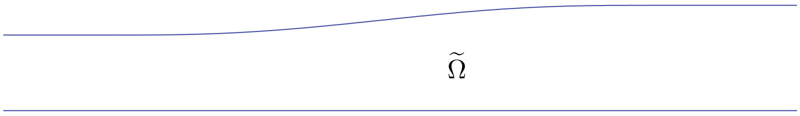

Figure 4.1 – A waveguide $\widetilde{\Omega}$ with increasing width.

The aim of this section is to state and prove the main theorem of this work, which is a triple result. It provides existence and uniqueness of the solution $\widetilde{u} \in \mathrm{H}^2_{\mathrm{loc}}(\widetilde{\Omega})$ to the source problem

$$\begin{cases} \Delta\widetilde{u} + k^2\widetilde{u} = -\widetilde{f} & \text{in } \widetilde{\Omega}, \\ \partial_\nu\widetilde{u} = \widetilde{b}_{\mathrm{top}} & \text{on } \partial\widetilde{\Omega}_{\mathrm{top}}, \\ \partial_\nu\widetilde{u} = \widetilde{b}_{\mathrm{bot}} & \text{on } \partial\widetilde{\Omega}_{\mathrm{bot}}, \\ \widetilde{u} \text{ is outgoing.} \end{cases} \tag{$\widetilde{\mathcal{H}}$}$$

It also gives an explicit modal approximation of $\widetilde{u}$, and provides a computable error bound for the local H^1-norm between the approximation and the exact solution. We first explain our strategy for proving such an existence result.

4.3.1 Sketch of proof

In order to use results on the modal decomposition in the regular waveguide, the first step is to map the perturbed waveguide to the regular one using the canonical mapping $\psi : \Omega \to \widetilde{\Omega}$ defined by $\psi : (x, y) \mapsto (x, h(x)y)$. The problem $(\widetilde{\mathcal{H}})$ is then equivalent to

$$\begin{cases} \Delta_h u + k^2 u = -f & \text{in } \Omega, \\ \partial_\nu u - D_h u = b_{\mathrm{top}} & \text{on } \partial\Omega_{\mathrm{top}}, \\ \partial_\nu u = b_{\mathrm{bot}} & \text{on } \partial\Omega_{\mathrm{bot}}, \\ u \text{ is outgoing,} \end{cases} \tag{$\mathcal{H}$}$$

where $u := \widetilde{u} \circ \psi$, $f := \widetilde{f} \circ \psi$, $b_{\mathrm{top}} := \widetilde{b}_{\mathrm{top}}\sqrt{1 + (h')^2}/h$ and $b_{\mathrm{bot}} = \widetilde{b}_{\mathrm{bot}}/h$. The operators Δ_h and D_h are differential operators of order two and one respectively (see their expressions in $(\mathcal{H})$). As there is no easy way to solve explicitly this equation we shall approach it by a simpler problem.

To this end, we neglect the small terms in the operators Δ_h and D_h, which depend on h' and h''. This leads to a much simpler problem that reads

$$\begin{cases} \partial_{xx} v + \dfrac{1}{h(x)^2}\partial_{yy} v + k^2 v = -f & \text{in } \Omega, \\ \partial_\nu v = b_{\text{top}} & \text{on } \partial\Omega_{\text{top}}, \\ \partial_\nu v = b_{\text{bot}} & \text{on } \partial\Omega_{\text{bot}}, \\ v \text{ is outgoing.} & \end{cases} \tag{$\mathcal{H}'$}$$

Next, we seek a solution to $(\mathcal{H}')$ in a modal form. To this end, we use the fact that the wavefield v and the source f can be decomposed in a sum of modes in the straight waveguide

$$\begin{aligned} v(x,y) &= \sum_{n\in\mathbb{N}} v_n(x)\varphi_n(y) \quad \text{where} \quad v_n(x) := \int_0^1 w(x,y)\varphi_n(y)\mathrm{d}y, \\ f(x,y) &= \sum_{n\in\mathbb{N}} f_n(x)\varphi_n(y) \quad \text{where} \quad f_n(x) := \int_0^1 f(x,y)\varphi_n(y)\mathrm{d}y. \end{aligned} \tag{4.9}$$

We deduce that the two dimensional problem $(\mathcal{H}')$ is equivalent to a sequence of one dimensional problems:

$$(\mathcal{H}') \;\Leftrightarrow\; \forall n \in \mathbb{N}\,(\mathcal{H}'_n) : \begin{cases} v_n''(x) + k_n(x)^2 v_n(x) = -(f_n + \varphi_n(1)b_{\text{top}} + \varphi_n(0)b_{\text{bot}})(x) & \text{in } \mathbb{R}, \\ v_n \text{ is outgoing,} & \end{cases} \tag{4.10}$$

where k_n is the local wavenumber function given in (4.7). As explained in [27], the modal problem $(\mathcal{H}'_n)$ is not well-defined when $\{x \in \mathbb{R} \,|\, k_n(x) = 0\}$ has a positive measure. Since h is increasing on $\operatorname{supp} h'$, this only occurs when $k = n\pi/h_{\text{min}}$ or $k = n\pi/h_{\text{max}}$. We assume this is not the case and that

$$\delta = \min_{n\in\mathbb{N}} \left(\sqrt{\left| k^2 - \frac{n^2\pi^2}{{h_{\text{min}}}^2} \right|}, \sqrt{\left| k^2 - \frac{n^2\pi^2}{{h_{\text{max}}}^2} \right|} \right) > 0. \tag{4.11}$$

For each type of modes $n \in \mathbb{N}$, the study of the equation $v_n'' + k_n^2 v_n = 0$ has been carried out in [76] and [77]. We summarize the main ideas bellow. The analysis depends on whether the mode n is propagative, evanescent or locally resonant.

(a) If n is propagative or evanescent, $|k_n(x)| > 0$ for all $x \in \mathbb{R}$ and we set $z(x) = \int^x |k_n|$. There is a one-to-one correspondence between x and z and if we define $w_n = \sqrt{z} v_n$, then w_n satisfies the partial differential equation

$$\partial_{zz} w_n \pm w_n = \zeta(x,z)\, w_n, \tag{4.12}$$

where $\|\zeta\|_{L^\infty(\mathbb{R})} = \mathcal{O}(\eta)$. The solutions of $y'' = \pm y$ are exponential functions, and since ζ is small, we can prove that w_n is almost equal to a sum of two exponential functions and we can control the approximation error (see (4.30) and (4.34) for more details).

(b) If n is locally resonant, since h is increasing on $\operatorname{supp} h$, there is a single resonant point $x^\star \in \mathbb{R}$ and we define

$$\xi(x) := \begin{cases} \left(-\dfrac{3}{2} i \displaystyle\int_x^{x^\star} k_n(t)\mathrm{d}t \right)^{2/3} & \text{if } x < x^\star, \\ -\left(\dfrac{3}{2} \displaystyle\int_{x^\star}^{x} k_n(t)\mathrm{d}t \right)^{2/3} & \text{if } x > x^\star. \end{cases} \tag{4.13}$$

This new variable is in one-to-one correspondence with x and if we define the function $w_n = -(\sqrt{k_n}/\xi^{1/4})v_n$, then w_n satisfies the partial differential equation

$$\partial_{\xi\xi} w_n - \xi w_n = \zeta(\xi)\, w_n, \tag{4.14}$$

where $\|\zeta\|_{L^\infty(\mathbb{R})} = \mathcal{O}(\eta)$. The solutions of $y'' = xy$ are known as the Airy functions, and since ζ is small, we can prove that w_n is approximated by a sum of Airy functions and we can control the approximation error (see (4.48) for more details).

Using these results, we prove that $(\mathcal{H}_n')$ has a unique solution and we provide an explicit approximation of this solution. By equivalence, this approach yields the unique solution to $(\mathcal{H}')$ and its approximation. With a control of the approximation error between $(\mathcal{H})$ and $(\mathcal{H}')$, we obtain an explicit approximation of $(\mathcal{H})$ and by change of variable, of $(\widetilde{\mathcal{H}})$.

4.3.2 Main result

We now state the main result of this work, which shows existence and uniqueness of the solution u of $(\mathcal{H})$ (and thus of the solution of $(\widetilde{\mathcal{H}})$) and provides an approximation of u with control of the approximation error in $\mathrm{H}^1_{\mathrm{loc}}$.

Theorem 4.1. *Let h be an increasing function which defines a varying waveguide $\tilde{\Omega}$ that satisfies assumption 4.1. Consider sources $f \in L^2(\Omega)$, $\boldsymbol{b} = (b_{bot}, b_{top}) \in (H^{1/2}(\mathbb{R}))^2$ both with compact support contained in Ω_r and Γ_r respectively, for some $r > 0$. Assume that there is a unique locally resonant mode $N \in \mathbb{N}$, associated with a simple resonant point $x^\star \in \mathbb{R}$.*

There exists $\eta_0 > 0$, depending only on $h_{\min}$, $h_{\max}$, δ, r and R, such that if $\eta < \eta_0$, then the problem $(\mathcal{H})$ admits a unique solution $u \in H^2_{loc}(\Omega)$. Moreover, this solution is approximated by u^{app} defined for almost every $(x, y) \in \Omega$ by

$$u^{app}(x,y) = \sum_{n\in\mathbb{N}} \left(\int_{\mathbb{R}} G_n^{app}(x,s)\big(f_n(s) + \varphi_n(1) b_{top}(s) + \varphi_n(0) b_{bot}(s)\big)\mathrm{d}s \right) \varphi_n(y), \tag{4.15}$$

where f_n is defined in (4.9), φ_n is defined in (4.5) and G_n^{app} is given by

$$G_n^{app}(x,s) := \begin{cases} \dfrac{i}{2\sqrt{k_n(s)k_n(x)}} \exp\left(i \left| \displaystyle\int_s^x k_n \right| \right), & \text{if } n < N, \\ \dfrac{1}{2\sqrt{|k_n|(s)|k_n|(x)}} \exp\left(- \left| \displaystyle\int_s^x |k_n| \right| \right), & \text{if } n > N, \\ \begin{cases} \dfrac{\pi(\xi(s)\xi(x))^{1/4}}{\sqrt{k_n(s)k_n(x)}} \big(i\mathcal{A} + \mathcal{B}\big) \circ \xi(s) \mathcal{A} \circ \xi(x) & \text{if } x < s, \\ \dfrac{\pi(\xi(s)\xi(x))^{1/4}}{\sqrt{k_n(s)k_n(x)}} \big(i\mathcal{A} + \mathcal{B}\big) \circ \xi(x) \mathcal{A} \circ \xi(s) & \text{if } x > s, \end{cases} & \text{if } n = N. \end{cases} \tag{4.16}$$

Th function k_n is the wavenumber function defined in definition 4.2 and the function ξ is given in equation (4.13). Moreover, there exists a constant $C > 0$ depending only on $h_{\min}$, $h_{\max}$, δ, r and R such that

$$\|u - u^{app}\|_{H^1(\Omega_r)} \le \eta C \left(\|f\|_{L^2(\Omega)} + \|\boldsymbol{b}\|_{\left(H^{1/2}(\mathbb{R})\right)^2} \right). \tag{4.17}$$

Remark 4.1. *If there are no resonant modes, the result can be adapted by deleting the line $n = N$ in (4.16). On the other hand, if there are multiple locally resonant modes, the third line of (4.16) becomes true for every resonant mode.*

Remark 4.2. *If $\widetilde{\Omega}$ is a regular waveguide, we find the same expression for the wavefield as in Chapter 2. We also see that the behavior of propagative and evanescent modes in a perturbed waveguide is similar to that in a regular waveguide. The term $\int_s^x |k_n|$ simply acts as a change of variable in the phase.*

Remark 4.3. *Looking at the proof, we can see that the constant C has a dependence on δ, r and R of the form $C = \mathcal{O}(r^2\delta^{-6} + rR\delta^{-8})$. Doing the same proof using $W^{2,\infty}$ spaces instead of H^2, we can also prove that for every $x \in \mathbb{R}$,*

$$|u_N(x) - u_N^{app}(x)| \le \eta C \left(\|f\|_{L^\infty(\mathbb{R})} + \|\boldsymbol{b}\|_{(L^\infty(\mathbb{R}))^2} \right), \tag{4.18}$$

where the constant C has a dependence on δ, r and R of the form $C = \mathcal{O}(\delta^{-6} + R\delta^{-8})$

Corollary 4.1. *Under the same assumptions as in Theorem 1, the problem $(\widetilde{\mathcal{H}})$ admits a unique solution $\widetilde{u} \in H^2_{loc}(\widetilde{\Omega})$, which can be approximated by $\widetilde{u}^{app}$ defined for almost every $(x, y) \in \widetilde{\Omega}$ by*

$$\widetilde{u}^{app}(x, y) = u^{app}\left(x, \frac{y}{h(x)}\right). \tag{4.19}$$

Moreover, there exists a constant $\widetilde{C} > 0$ depending only on $h_{\min}$, $h_{\max}$, δ, r and R such that

$$\|\widetilde{u} - \widetilde{u}^{app}\|_{H^1(\widetilde{\Omega}_r)} \le \eta \widetilde{C} \left(\|\widetilde{f}\|_{L^2(\widetilde{\Omega})} + \|\widetilde{b}\|_{(H^{1/2}(\partial\widetilde{\Omega}))} \right). \tag{4.20}$$

Proof. We use the equivalence between $(\widetilde{\mathcal{H}})$ and $(\mathcal{H})$, and we notice that

$$\|\widetilde{u} - \widetilde{u}^{\mathrm{app}}\|_{\mathrm{H}^1(\widetilde{\Omega}_r)} \le h_{\max}\|u - u^{\mathrm{app}}\|_{\mathrm{H}^1(\Omega_r)}, \qquad \|\widetilde{f}\|_{\mathrm{L}^2(\widetilde{\Omega})} \ge h_{\min}\|f\|_{\mathrm{L}^2(\Omega)},$$

$$\|\widetilde{b}\|_{(\mathrm{H}^{1/2}(\mathbb{R}))^2} \ge h_{\min}\|b\|_{\left(\mathrm{H}^{1/2}(\partial\widetilde{\Omega})\right)^2}.$$

□

4.3.3 Modal Green functions and their approximations

As mentioned in the previous section, we start by studying equations (4.10) for every $n \in \mathbb{N}$. To this end, we denote by $G_n(x, s)$ the modal Green functions associated to $(\mathcal{H}'_n)$. It satisfies for every $s \in \mathbb{R}$ the partial differential equation

$$\left\{ \begin{array}{cc} \partial_{xx}G_n(x, s) + k_n(x)^2 G_n(x, s) = -\delta_s & \text{in } \mathbb{R}, \\ G_n(\cdot, s) \text{ is outgoing.} & \end{array} \right. \tag{4.21}$$

We prove the following theorem which provides an approximation of G_n for every $n \in N$ and the control of the approximation error in $\mathrm{W}^{1,1}(\mathbb{R})$.

Theorem 4.2. *For every $s \in \mathbb{R}$, the equation*

$$\left\{ \begin{array}{ll} \partial_{xx}G_n(x, s) + k_n(x)^2 G_n(x, s) = -\delta_s & \textit{in } \mathbb{R}, \\ G_n(\cdot, s) \textit{ is outgoing.} & \end{array} \right. \tag{4.22}$$

has a unique solution $G_n(\cdot, s) \in W^{1,1}(\mathbb{R})$. This solution can be decomposed as $G_n = G_n^{app} + \mathcal{O}(\eta)$ where G_n^{app} has the explicit form given in (4.16) and $\mathcal{O}(\eta)$ is a term that tends to 0 in $W^{1,1}(\mathbb{R})$ uniformly in s as η tends to 0. Moreover, let $r > 0$. There exists $\eta_1 > 0$ depending on R, r, $h_{\min}$,

$h_{\max}$ and δ such that if $\eta < \eta_1$, there exists $\alpha, \beta > 0$ depending only on $h_{\min}$, $h_{\max}$, r, δ and R such that for every $s \in \mathbb{R}$,

$$\|G_n(\cdot, s)\|_{L^1(-r,r)} \leq \alpha_n^{(1)} := \begin{cases} \alpha & \text{if } n \leq N, \\ \dfrac{\alpha}{\min(|k_n|)^2} & \text{if } n > N, \end{cases} \tag{4.23}$$

$$\|\partial_x G_n(\cdot, s)\|_{L^1(-r,r)} \leq \alpha_n^{(2)} := \begin{cases} \alpha & \text{if } n \leq N, \\ \dfrac{\alpha}{\min(|k_n|)} & \text{if } n > N, \end{cases} \tag{4.24}$$

$$\|G_n(\cdot, s) - G_n^{app}(\cdot, s)\|_{L^1(-r,r)} \leq \beta_n^{(1)} := \eta \begin{cases} \beta & \text{if } n \leq N, \\ \dfrac{\beta}{\min(|k_n|)^2} & \text{if } n > N, \end{cases} \tag{4.25}$$

$$\|\partial_x G_n(\cdot, s) - \partial_x G_n^{app}(\cdot, s)\|_{L^1(-r,r)} \leq \beta_n^{(2)} := \eta \begin{cases} \beta & \text{if } n \leq N, \\ \dfrac{\beta}{\min(|k_n|)} & \text{if } n > N. \end{cases} \tag{4.26}$$

Remark 4.4. *The following proof shows that we can choose*

$$\eta_1 \leq \min\left(\frac{1}{9C_{N-1}}, \frac{|k_{N+1}|}{9C_{N+1}}, \frac{1}{4c_8 \pi C_N} \right), \tag{4.27}$$

where C_{N-1} and C_{N+1} are defined in (4.33), c_8 is defined in Lemma 4.3 and C_N comes from Theorem 2 in [77]. It shows that η has to be small compared to r, R, $h_{\min}$ and δ for this theorem to apply.

Remark 4.5. *By looking at the proof, we can see that α, β and C_n depend on δ, r and R as $r\delta^{-1}$, $rR\delta^{-6}$, and $R\delta^{-5}$ respectively.*

To prove this theorem, we first need a technical lemma to connect solutions of the partial differential equation (4.22) defined for $x < s$ and $x > s$.

Lemma 4.1 (Connection of the Green functions)**.** *Let $s \in \mathbb{R}$. Assume that u is a solution to $u'' + k_n^2 u = -\delta_s$ and that there exist $A, B \in \mathbb{R}$ and $w_1, w_2 \in \mathcal{C}^2(\mathbb{R})$ such that*

$$u(x) = \begin{cases} Aw_1(x) & \text{if } x < s, \\ Bw_2(x) & \text{if } x > s, \end{cases} \tag{4.28}$$

then

$$A = \frac{w_2(s)}{w_1'(s)w_2(s) - w_2'(s)w_1(s)}, \qquad B = \frac{w_1(s)}{w_1'(s)w_2(s) - w_2'(s)w_1(s)} \tag{4.29}$$

Proof. Since u is continuous in s, $Aw_1(s) = Bw_2(s)$. Then, using the jump formula for distributions, we find that

$$Bw_2'(s) - Aw_1'(s) = -1 \qquad \Rightarrow \qquad A(w_1(s)w_2'(s) - w_2(s)w_1'(s)) = -w_2(s)$$

□

Next, we study the Green function for the three types of waves, depending on the value of n.

4.3.4 Proof of Theorem 2

Proof. The propagative case $(n < N)$]

We denote $u_n = G_n(\cdot, s)$. Changing variable to $\sigma = \eta x$, we see that $w_n = u_n(\sigma/\eta)$ satisfies the equation $w_n'' + k_n^2(\sigma/\eta)w_n^2/\eta^2 = 0$ for every $\sigma \neq \eta s$ where in the case at hand, $k_n^2(\sigma/\eta) > 0$. Using Theorem 4 in [76] on w_n, shows that there exist $A, B \in \mathbb{C}$ such that

$$u_n(x) = \begin{cases} \dfrac{A}{\sqrt{k_n(x)}} \exp\left(-i\displaystyle\int_s^x k_n\right)(1+\overline{\varepsilon(x)}) & \text{if } x < s, \\ \dfrac{B}{\sqrt{k_n(x)}} \exp\left(i\displaystyle\int_s^x k_n\right)(1+\varepsilon(x)) & \text{if } x > s, \end{cases} \tag{4.30}$$

where $\varepsilon \in \mathcal{C}^1(\mathbb{R})$ is such that for all $x \in \mathbb{R}$,

$$|\varepsilon(x)| \leq e^{F/2} - 1, \quad |\varepsilon'(x)| \leq 2k_n(x)(e^{F/2} - 1), \tag{4.31}$$

$$|F| \leq \int_{\mathbb{R}} \eta \left| \frac{1}{\sqrt{k_n(\sigma/\eta)}} \partial_{\sigma\sigma}\left(\frac{1}{\sqrt{k_n(\sigma/\eta)}}\right)\right| \mathrm{d}\sigma. \tag{4.32}$$

Using the expression of k_n, we see that

$$|F| \leq \eta \int_{-R}^{R} \frac{1}{\eta^2} \left| \frac{n^2\pi^2(h''h - 3(h')^2)}{2h^4k_n^3} + \frac{5(h')^2n^4\pi^4}{4h^6k_n^5} \right| (\sigma/\eta)\mathrm{d}\sigma. \tag{4.33}$$

We deduce that there exists a constant $\gamma_1 > 0$ depending on $h_{\min}$, $h_{\max}$ and R such that

$$|F| \leq \eta\gamma_1 \left(\frac{(N-1)^2\pi^2}{\delta^3} + \frac{(N-1)^4\pi^4}{\delta^5} \right) := \eta C_{N-1}.$$

Using Lemma 4.1, we find that

$$A = \frac{i(1+\varepsilon(s))}{2\sqrt{k_n(s)}(1+R)}, \qquad B = \frac{i(1+\overline{\varepsilon(s)})}{2\sqrt{k_n(s)}(1+R)},$$

where

$$R = 2\mathrm{Re}(\varepsilon(s)) + |\varepsilon(s)|^2 + \frac{\mathrm{Im}(\varepsilon'(s)(1+\overline{\varepsilon(s)})}{k_n(s)}.$$

It follows that

$$G_n(x,s) = \begin{cases} G_n^{\mathrm{app}}(x,s)\dfrac{(1+\overline{\varepsilon(x)})(1+\varepsilon(s))}{1+R} & \text{if } x < s, \\ G_n^{\mathrm{app}}(x,s)\dfrac{(1+\varepsilon(x))(1+\overline{\varepsilon(s)})}{1+R} & \text{if } x > s, \end{cases},$$

and

$$\partial_x G_n(x,s) = \begin{cases} \partial_x G_n^{\mathrm{app}}(x,s)\dfrac{1+\varepsilon(s)}{1+R}\left(1+\overline{\varepsilon(x)} + \dfrac{2\overline{\varepsilon'(x)}k_n(x)^2h(x)^3}{2ik_n(x)^3h(x)^3 - n^2\pi^2h'(x)}\right) & \text{if } x < s, \\ \partial_x G_n^{\mathrm{app}}(x,s)\dfrac{1+\overline{\varepsilon(s)}}{1+R}\left(1+\varepsilon(x) + \dfrac{2\varepsilon'(x)k_n(x)^2h(x)^3}{2ik_n(x)^3h(x)^3 - n^2\pi^2h'(x)}\right) & \text{if } x > s. \end{cases}$$

Assuming that $\eta < \dfrac{1}{9C_{N-1}}$,then $|F| \leq 1/9$,

$$e^{F/2} - 1 \leq \frac{|F|/2}{1 - |F|/4} \leq \min\left(\frac{3}{4}\eta C_n, \frac{1}{16}\right),$$

and

$$|R| \leq 2|\varepsilon(x)| + |\varepsilon|^2 + \frac{|\varepsilon'(x)|(1 + |\varepsilon(x)|)}{k_n(x)} \leq 4(e^{F/2} - 1)e^{F/2} \leq \frac{1}{2}.$$

It follows that

$$\left|1 - \frac{(1 + \overline{\varepsilon(x)})(1 + \varepsilon(s))}{1 + R}\right| \leq \frac{|\varepsilon'(x)|(1 + \|\varepsilon\|_{L^\infty(\mathbb{R})})/k_n(x)}{1 - |R|} \leq 6\eta C_n,$$

and that

$$\|G_n(\cdot, s) - G_n^{\text{app}}(\cdot, s)\|_{\mathrm{L}^1(-r,r)} \leq \eta \frac{6C_n r}{\min(k_n)},$$

$$\|G_n(\cdot, s)\|_{\mathrm{L}^1(-r,r)} \leq \frac{2r}{\min(k_n)}.$$

In the same way,

$$\left|\frac{1 + \varepsilon(s)}{1 + R}\right| \left|\frac{2\varepsilon'(x)k_n(x)^2 h(x)^3}{2ik_n(x)^3 h(x)^3 - n^2\pi^2 h'(x)}\right| \leq 4\frac{3}{2}\frac{C_n \eta k_n(x)^3 h(x)^3}{k_n(x)^3 h(x)^3} \leq 6C_n\eta$$

and so

$$\|\partial_x G_n(\cdot, s) - \partial_x G_n^{\text{app}}(\cdot, s)\|_{\mathrm{L}^1(-r,r)} \leq \eta \frac{12C_n r}{\min(k_n)}\left(\|k_n\|_{L^\infty(\mathbb{R})} + \frac{n^2\pi^2}{18C_n \min(k_n)^2 h_{\min}^3}\right),$$

and

$$\|\partial_x G_n(\cdot, s)\|_{\mathrm{L}^1(-r,r)} \leq \frac{3r}{\min(k_n)}\left(\|k_n\|_{L^\infty(\mathbb{R})} + \frac{n^2\pi^2}{18C_n \min(k_n)^2 h_{\min}^3}\right).$$

□

The evanescent case ($n > N$). We denote $u_n = G_n(\cdot, s)$. Changing variable to $\sigma = \eta x$, we see that $w_n = u_n(\sigma/\eta)$ satisfies the equation $w_n'' + k_n^2(\sigma/\eta)w_n^2/\eta^2 = 0$ for every $\sigma \neq \eta s$. Theorem 3 in [76] on w_n yields the existence of $A, B \in \mathbb{C}$ such that

$$u_n(x) = \begin{cases} \dfrac{A}{\sqrt{|k_n|(x)}} \exp\left(\displaystyle\int_s^x |k_n|\right)(1 + \varepsilon_2(x)) & \text{if } x < s, \\ \dfrac{B}{\sqrt{|k_n|(x)}} \exp\left(-\displaystyle\int_s^x |k_n|\right)(1 + \varepsilon_1(x)) & \text{if } x > s, \end{cases} \tag{4.34}$$

where $\varepsilon_1, \varepsilon_2 \in \mathcal{C}^1(\mathbb{R})$ are such that for $i = 1, 2$ and all $x \in \mathbb{R}$,

$$|\varepsilon_i(x)| \leq e^{F/2} - 1, \quad |\varepsilon_i'(x)| \leq 2|k_n|(x)(e^{F/2} - 1), \tag{4.35}$$

where F satisfies (4.33). It follows that there exist a constant $\gamma_2 > 0$ depending on $h_{\min}$, $h_{\max}$ and R such that

$$|F| \leq \frac{\eta\gamma_2(N+1)^2\pi^2}{\min(|k_n|)\delta^2}\left(1 + \frac{(N+1)^2\pi^2}{\delta^2}\right) := \eta\frac{C_{N+1}}{\min(|k_n|)}.$$

Using Lemma 4.1, we find that

$$A = \frac{1+\varepsilon_1(s)}{2\sqrt{k_n(s)}(1+R)}, \qquad B = \frac{1+\varepsilon_2(s)}{2\sqrt{k_n(s)}(1+R)},$$

where

$$R = \left(\varepsilon_2 + \varepsilon_1 + \varepsilon_1\varepsilon_2 + \frac{\varepsilon_2'(1+\varepsilon_1)}{2|k_n|} - \frac{\varepsilon_1'(1+\varepsilon_2)}{2|k_n|}\right)(s).$$

It follows that

$$G_n(x,s) = \begin{cases} G_n^{\mathrm{app}}(x,s)\dfrac{(1+\varepsilon_2(x))(1+\varepsilon_1(s))}{1+R} & \text{if } x < s, \\ G_n^{\mathrm{app}}(x,s)\dfrac{(1+\varepsilon_1(x))(1+\varepsilon_2(s))}{1+R} & \text{if } x > s, \end{cases}$$

and

$$\partial_x G_n(x,s) = \begin{cases} \partial_x G_n^{\mathrm{app}}(x,s)\dfrac{1+\varepsilon_1(s)}{1+R}\left(1+\varepsilon_2(x) - \dfrac{2\varepsilon_2'(x)|k_n(x)|^2 h(x)^3}{h'(x)n^2\pi^2 + 2|k_n(x)|^3 h(x)^3}\right) & \text{if } x < s, \\ \partial_x G_n^{\mathrm{app}}(x,s)\dfrac{1+\varepsilon_2(s)}{1+R}\left(1+\varepsilon_1(x) - \dfrac{2\varepsilon_1'(x)|k_n(x)|^2 h(x)^3}{h'(x)n^3\pi^2 + 2|k_n(x)|^3 h(x)^3}\right) & \text{if } x > s. \end{cases}$$

We also notice that

$$\left\|\exp\left(-\int_s^x |k_n|\right)\right\|_{\mathrm{L}^1(-r,r)} \leq \|\exp\left(-\min(|k_n|)|x-s|\right)\|_{\mathrm{L}^1(-r,r)} \leq \frac{2}{\min(|k_n|)}.$$

Assuming that $\eta < \dfrac{|k_{N+1}|}{9C_{N+1}}$ then $|F| \leq 1/9$,

$$e^{F/2} - 1 \leq \frac{|F|/2}{1-|F|/4} \leq \min\left(\frac{3}{4}\frac{\eta C_{N+1}}{\min(|k_n|)}, \frac{1}{16}\right),$$

and

$$|R| \leq 2(e^{F/2}-1) + (e^{F/2}-1)^2 + 2e^{F/2}(e^{F/2}-1) \leq 4(e^{F/2}-1)e^{F/2} \leq \frac{1}{2}.$$

It follows that

$$\left|1 - \frac{(1+\varepsilon_1(x))(1+\varepsilon_2(s))}{1+R}\right| \leq \frac{|\varepsilon_1(x)|(1+\|\varepsilon_2\|_{L^\infty(\mathbb{R})}) + |\varepsilon_2(x)|(1+\|\varepsilon_1\|_{L^\infty(\mathbb{R})})}{2|k_n(x)|(1-|R|)} \leq \frac{6\eta C_{N+1}}{\min(|k_n|)}.$$

and that

$$\|G_n(\cdot,s) - G_n^{\mathrm{app}}(\cdot,s)\|_{\mathrm{L}^1(-r,r)} \leq \eta\frac{12C_{N+1}r}{\min(|k_n|)^2}, \tag{4.36}$$

$$\|G_n(\cdot,s)\|_{\mathrm{L}^1(-r,r)} \leq \frac{4r}{\min(|k_n|)^2}, \tag{4.37}$$

In the same way,

$$\left|\frac{1+\varepsilon_1(s)}{1+R}\right|\left|\frac{2\varepsilon_2'(x)|k_n(x)|^2 h(x)^3}{h'(x)n^2\pi^2 + 2|k_n(x)|^3 h(x)^3}\right| \leq 4\frac{3}{2}\frac{2C_{N+1}\eta|k_n(x)|^3 h(x)^3/\min(|k_n|)}{2|k_n(x)|^3 h(x)^3} \leq \frac{6C_{N+1}\eta}{\min(|k_n|)},$$

and so

$$\|\partial_x G_n(\cdot,s) - \partial_x G_n^{\mathrm{app}}(\cdot,s)\|_{\mathrm{L}^1(-r,r)} \leq \eta\frac{24r}{\min(|k_n|)^2}\left(\|k_n\|_{L^\infty(\mathbb{R})} + \frac{(N+1)^2\pi^2}{2\delta^2 h_{\min}^3}\right), \tag{4.38}$$

and

$$\|\partial_x G_n(\cdot,s)\|_{\mathrm{L}^1(-r,r)} \leq \frac{6r}{\min(|k_n|)^2}\left(\|k_n\|_{L^\infty(\mathbb{R})} + \frac{(N+1)^2\pi^2}{2\delta^2 h_{\min}^3}\right). \tag{4.39}$$

□

Remark 4.6. *We notice that the control of G_n, $\partial_x G_n$ and $\partial_x G_n - \partial_x G_n^{app}$ is uniform in $n > N$, with*

$$\eta < \frac{|k_{N+1}|}{9C_{N+1}}. \tag{4.40}$$

This uniform control is essential to obtain the global control $\eta < \eta_1$ in Theorem 4.2. We could also provide a uniform control in inequalities (4.36)*,* (4.37)*,* (4.38) *and* (4.39)*. However, in the following, we add these inequalities and thus we keep track of the factors $1/\min(|k_n|)$ to ensure fast decrease when n goes to infinity.*

It remains to deal with the case $n = N$. This case is more complicated, since $x \mapsto k_n(x)^2$ is not of constant sign. We first introduce two technical Lemmas used to give an approximation of the Green function for $n = N$.

Lemma 4.2. *Let us define*

$$\xi(x) = \begin{cases} \left(-\frac{3}{2}i\int_x^{x^*} k_N\right)^{2/3} & \text{if } x < x^*, \\ -\left(\frac{3}{2}\int_{x^*}^{x} k_N\right)^{2/3} & \text{if } x > x^*. \end{cases} \tag{4.41}$$

This function is a decreasing bijection from $\mathbb{R}$ to $\mathbb{R}$. Moreover, the function

$$\phi : x \mapsto (-\xi(x))^{1/4}/\sqrt{k_n(x)}, \tag{4.42}$$

is in $\mathcal{C}^2(\mathbb{R})$ and for all $x \in \mathbb{R}$, there exists a constant c_ϕ such that $|\phi'(x)| \leq c_\phi|\phi(x)|$.

Proof. This lemma can be proved by adapting section 4 of [77]. □

Lemma 4.3. *Let us define the following functions:*

$$E(x) = \exp\left(\frac{2}{3}x^{3/2}\right)1_{x>0} + 1_{x\leq 0}, \tag{4.43}$$

$$M = \sqrt{E^2\mathcal{A}^2 + E^{-2}\mathcal{B}^2}, \qquad N = \sqrt{E^2(\mathcal{A}')^2 + E^{-2}(\mathcal{B}')^2} \tag{4.44}$$

There exist a constant $c_1 \approx 0.4$ such that for all $x \in \mathbb{R}$,

$$|M(x)E(x)\mathcal{A}'(x)| \leq c_1, \qquad \left|\frac{\mathcal{B}(x)N(x)}{E(x)}\right| \leq c_1, \qquad |M(x)N(x)| \leq c_1, \tag{4.45}$$

$$\left|\frac{\mathcal{B}'(x)M(x)}{E(x)}\right| \leq c_1, \qquad |\mathcal{A}(x)E(x)N(x)| \leq c_1. \tag{4.46}$$

There also exist constants c_2, c_3 depending on $h_{\min}$, $h_{\max}$, k and R such that for every $x \in \mathbb{R}$,

$$\left|\frac{(-\xi(x))^{1/4}}{\sqrt{k_n(x)}}M(\xi(x))\right| \leq c_6, \qquad \left|\frac{\sqrt{k_n(x)}}{(-\xi(x))^{1/4}}N(\xi(x))\right| \leq c_7. \tag{4.47}$$

Proof. Using Airy's asymptotic expansions presented in section 10.4 of [4], we obtain the first constant and the control

$$M(x) = \mathcal{O}_{|x|\to\infty}\left(\frac{1}{|x|^{1/4}}\right), \qquad N(x) = \mathcal{O}_{|x|\to\infty}\left(|x|^{1/4}\right).$$

Since h' is compactly supported, we conclude the proof by noticing that

$$k_n(x) = \mathcal{O}_{|x|\to\infty}(1), \qquad \xi(x) = \mathcal{O}_{|x|\to\infty}(|x|).$$

□

The locally resonant case ($n = N$). We set $u_n = G_n(\cdot, s)$. Changing variable to $\sigma = \eta x$, we see that $w_n = u_n(\sigma/\eta)$ satisfies the equation $w_n'' + k_n^2(\sigma/\eta)w_n^2/\eta^2 = 0$ for every $\sigma \neq \eta s$. This equation is very similar to the Airy equation and from Theorem 2 in [77], we know that there exist $A, B \in \mathbb{C}$ such that

$$u_n(x) = \begin{cases} \dfrac{A(-\xi(x))^{1/4}}{\sqrt{k_n(x)}}(\mathcal{A}(\xi(x)) + \varepsilon_1(\xi(x))) & \text{if } x < s, \\ \dfrac{B(-\xi(x))^{1/4}}{\sqrt{k_n(x)}}(i\mathcal{A}(\xi(x)) + \mathcal{B}(\xi(x)) + i\varepsilon_1(\xi(x)) + \varepsilon_2(\xi(x))) & \text{if } x > s, \end{cases} \tag{4.48}$$

where $\varepsilon_1, \varepsilon_2 \in \mathcal{C}^1(\mathbb{R})$ are such that there exist C_N depending on $h_{\min}$, $h_{\max}$, δ and R such that for all $x \in \mathbb{R}$,

$$\left|\frac{E(\xi)}{M(\xi)}\right| |\varepsilon_1(\xi)| \leq \frac{1}{\lambda_1}(e^{\eta C_N \lambda_1} - 1), \qquad \left|\frac{E(\xi)}{N(\xi)}\right| |\varepsilon_1'(\xi)| \leq \frac{1}{\lambda_1}(e^{\eta C_N \lambda_1} - 1), \tag{4.49}$$

$$\left|\frac{1}{E(\xi)M(\xi)}\right| |\varepsilon_2(\xi)| \leq \frac{\lambda_2}{\lambda_1}(e^{\eta C_N \lambda_1} - 1), \qquad \left|\frac{1}{E(\xi)N(\xi)}\right| |\varepsilon_2'(\xi)| \leq \frac{\lambda_2}{\lambda_1}(e^{\eta C_N \lambda_1} - 1), \tag{4.50}$$

where $\lambda_1 > \lambda_2$ are known constants. Using Lemma 4.1 and the fact that $\mathcal{B}\mathcal{A}' - \mathcal{B}'\mathcal{A} = -1/\pi$, we find that

$$A = \frac{-\pi(-\xi(s))^{1/4}(i\mathcal{A}(\xi(s)) + \mathcal{B}(\xi(s)) + i\varepsilon_1(\xi(s)) + \varepsilon_2(\xi(s)))}{(1 - R\pi)\sqrt{k_n(s)}},$$

$$B = \frac{-\pi(-\xi(s))^{1/4}(\mathcal{A}(\xi(s)) + \varepsilon_1(\xi(s)))}{(1 - R\pi)\sqrt{k_n(s)}},$$

where

$$R = (\mathcal{A}'\varepsilon_2 + \varepsilon_1'\mathcal{B} + \varepsilon_1'\varepsilon_2 - \mathcal{B}'\varepsilon_1 - \mathcal{A}\varepsilon_2' - \varepsilon_2'\varepsilon_1)(\xi(s)).$$

It follows that

$$G_n(x,s) = \begin{cases} G_n^{\text{app}}(x,s)\left(1 + \dfrac{\varepsilon_1(\xi(x))}{\mathcal{A}(\xi(x))}\right)\dfrac{1}{1 - R\pi}\left(1 + \dfrac{i\varepsilon_1(\xi(s)) + \varepsilon_2(\xi(s))}{i\mathcal{A}(\xi(s)) + \mathcal{B}(\xi(s))}\right) & \text{if } x < s, \\ G_n^{\text{app}}(x,s)\left(1 + \dfrac{i\varepsilon_1(\xi(x)) + \varepsilon_2(\xi(x))}{i\mathcal{A}(\xi(x)) + \mathcal{B}(\xi(x))}\right)\dfrac{1}{1 - R\pi}\left(1 + \dfrac{\varepsilon_1(\xi(s))}{\mathcal{A}(\xi(s))}\right) & \text{if } x > s, \end{cases}$$

and $\partial_x G_n^{\text{app}}(x,s) =$

$$\frac{-\pi(-\xi(s))^{1/4}}{(1 - R\pi)\sqrt{k_n(s)}}\begin{cases} \left[(\mathcal{A}' + \varepsilon_1')(\xi(x))\dfrac{\sqrt{k_n(x)}}{(-\xi(x))^{1/4}} + (\mathcal{A} + \varepsilon_1)(\xi(x))\phi'(x)\right] & \\ \qquad \times(i\mathcal{A} + \mathcal{B} + i\varepsilon_1 + \varepsilon_2)(\xi(s)) & \text{if } x < s, \\ \Big[(i\mathcal{A}' + \mathcal{B} + i\varepsilon_1' + \varepsilon_2')(\xi(x))\dfrac{\sqrt{k_n(x)}}{(-\xi(x))^{1/4}} + (i\mathcal{A} & \\ \qquad + \mathcal{B} + i\varepsilon_1 + \varepsilon_2)(\xi(x))\phi'(x)\Big](\mathcal{A} + \varepsilon_1)(\xi(s)) & \text{if } x > s. \end{cases}$$

We define $c_4 = (4\lambda_2 + 2)c_1$. Assuming that $\eta \le 1/(4C_N c_4 \pi)$, we know that $\eta \le 1/(C_N\lambda_1)$ and $(e^{\eta C_N \lambda_1} - 1)/\lambda_1 \le 2\eta C_N$, so

$$|R| \le 2\eta C_N c_4, \qquad \left|\frac{R\pi}{1 - R\pi}\right| \le \frac{2\eta C_N c_4 \pi}{1 - 2\eta\pi C_N c_4} \le 4\eta\pi C_N c_4 \le 1,$$

$$\left|\frac{(-\xi(s))^{1/4}(-\xi(x))^{1/4}}{\sqrt{k_n(s)}\sqrt{k_n(x)}}\mathcal{A}(\xi(x))(i\varepsilon_1(\xi(s)) + \varepsilon_2(\xi(s)))\right| \le \\ \left|\frac{(-\xi(s))^{1/4}(-\xi(x))^{1/4}}{\sqrt{k_n(s)}\sqrt{k_n(x)}}\right| 4\lambda_2\eta C_N M(\xi(x))M(\xi(s)) \le 4\lambda_2\eta C_N c_2^2,$$

$$\left|\frac{(-\xi(s))^{1/4}(-\xi(x))^{1/4}}{\sqrt{k_n(s)}\sqrt{k_n(x)}}\varepsilon_1(\xi(x))\left(i\mathcal{A}(\xi(s)) + \mathcal{B}(\xi(s)) + i\varepsilon_1(\xi(s)) + \varepsilon_2(\xi(s))\right)\right| \le (1{+}2\lambda_2\eta C_N)4\eta C_N c_2^2.$$

It follows that

$$|G_n(x,s) - G_n^{\mathrm{app}}(x,s)| \le 4\eta\pi C_N c_4 |G_n^{\mathrm{app}}(x)| + \left(8\pi c_2^2\lambda_2\eta C_N + 24\pi\eta C_N c_2^2\right),$$

which leads to

$$|G_n(x) - G_n^{\mathrm{app}}(x)| \le 4\eta C_N\pi\left(c_4|G_n^{\mathrm{app}}(x)| + c_2^2\left(2\lambda_2 + 6\right)\right).$$

Using the same idea, we prove that

$$|G_n^{\mathrm{app}}(x,s)| \le 2c_2^2\pi,$$

and it follows that

$$\|G_n(\cdot,s) - G_n^{\mathrm{app}}(\cdot,s)\|_{\mathrm{L}^1(-r,r)} \le \eta 16 r C_N \pi c_2^2(c_4\pi + \lambda_2 + 3),$$

and

$$\|G_n(\cdot,s)\|_{\mathrm{L}^1(-r,r)} \le 4rc_2^2\pi\left(2 + \frac{\lambda_2 + 3}{c_4\pi}\right).$$

Using the same technique also prove that

$$\|\partial_x G_n(\cdot,s) - \partial_x G_n^{\mathrm{app}}(\cdot,s)\|_{\mathrm{L}^1(-r,r)} \le \eta 8 r C_N \pi c_2(c_3 + c_2 c_\phi)(2c_4 + 3\lambda_2),$$

$$\|\partial_x G_n(\cdot,s)\|_{\mathrm{L}^1(-r,r)} \le 16 r\pi c_2(c_3 + c_2 c_\phi).$$

□

4.3.5 Proof of Theorem 4.1

As mentioned at the beginning of section 4.3.1, we map the deformed waveguide $\widetilde{\Omega}$ to the regular waveguide Ω by a change of variables $\psi : (x,y) \mapsto (x, h(x)y)$. The problem $(\widetilde{\mathcal{H}})$ is equivalent in Ω to the problem

$$\left\{\begin{aligned} &\partial_{xx}u + k^2 u + \frac{1}{h^2}\partial_{yy}u - \frac{h''h - 2(h')^2}{h^3}y\partial_y u \\ &\qquad + \frac{(h')^2}{h^4}y^2\partial_{yy}u - \frac{2h'}{h^2}y\partial_{yx}u = -f && \text{in } \Omega, \\ &\partial_\nu u = b_{\mathrm{top}} + \frac{h'}{h}\partial_x u && \text{on } \partial\Omega_{\mathrm{top}}, \\ &\partial_\nu u = b_{\mathrm{bot}} && \text{on } \partial\Omega_{\mathrm{bot}}, \\ &u \text{ is outgoing.} \end{aligned}\right. \tag{$\mathcal{H}$}$$

If we try and use the modal decomposition on this equation, mode coupling appears. We can however try to approach the solutions of $(\mathcal{H})$ by the solutions of the following system

$$\begin{cases} \partial_{xx} v + \dfrac{1}{h(x)^2}\partial_{yy} v + k^2 v = -f & \text{in } \Omega, \\ \partial_\nu v = b_{\text{top}} & \text{on } \partial\Omega_{\text{top}}, \\ \partial_\nu v = b_{\text{bot}} & \text{on } \partial\Omega_{\text{bot}}, \\ v \text{ is outgoing,} \end{cases} \tag{$\mathcal{H}'$}$$

which is amenable to modal decomposition. To estimate the error of such an approximation, we need to control the dependence between the source and the solution of $(\mathcal{H}')$. In Proposition 4.1, we provide a control of the wavefield generated by a source term in the waveguide, and in Proposition 4.2, we do the same thing for a source term on its boundary. The proofs of both propositions are given in the appendix.

Remark 4.7. *$(\mathcal{H}')$ was obtained from $(\mathcal{H})$ by formally eliminating the terms likely to cause mode coupling. We cannot however neglect the term $\dfrac{1}{h(x)^2}\partial_{yy} u$ and approximate*

$$\frac{1}{h(x)^2} \approx \frac{1}{h(x_0)^2} + \eta\, \mathcal{O}_{x\to x_0}(x - x_0),$$

for a constant $x_0 \in \mathbb{R}$. Indeed, if x is large enough, $x - x_0 \gg \eta$ and

$$\frac{1}{h(x_0)^2} - \frac{1}{h_{\min}^2} = \mathcal{O}(1), \qquad \frac{1}{h(x_0)^2} - \frac{1}{h_{\max}^2} = \mathcal{O}(1).$$

Proposition 4.1. *Let $r > 0$ and $f \in L^2(\Omega_r)$. The equation*

$$\begin{cases} \partial_{xx} u + \dfrac{1}{h^2}\partial_{yy} u + k^2 u = -f & \text{in } \Omega, \\ \partial_\nu u = 0 & \text{on } \partial\Omega, \\ u \text{ is outgoing,} \end{cases} \tag{4.51}$$

has a unique solution $u \in H^2_{loc}(\Omega)$. Using notations of Theorem 4.2, if $\eta < \eta_1$ then the operator

$$\Gamma : \begin{array}{ccc} L^2(\Omega_r) & \to & H^2(\Omega_r) \\ f & \mapsto & u_{|\Omega_r} \end{array}, \qquad \text{where } u \text{ is the solution to (4.51)}, \tag{4.52}$$

is well defined, continuous and there exists a constant D_1 depending on δ, $h_{\min}$, $h_{\max}$, R and r such that

$$\|u\|_{H^2(\Omega_r)} \leq D_1 \|f\|_{L^2(\Omega_r)}. \tag{4.53}$$

Proposition 4.2. *Let $r > 0$ and $b = (b_{top}, b_{bot}) \in (\widetilde{H}^{1/2}(-r,r))^2$. The equation*

$$\begin{cases} \partial_{xx} u + \dfrac{1}{h^2}\partial_{yy} u + k^2 u = 0 & \text{in } \Omega, \\ \partial_\nu u = b_{top} & \text{on } \partial\Omega_{top}, \\ \partial_\nu u = b_{bot} & \text{on } \partial\Omega_{bot}, \\ u \text{ is outgoing.} \end{cases} \tag{4.54}$$

has a unique solution $u \in H^2_{loc}(\Omega)$. Using notations of Theorem 4.2, if $\eta < \eta_1$ then the operator

$$\Pi : \begin{array}{ccc} \left(\widetilde{H}^{1/2}(-r,r)\right)^2 & \to & H^2(\Omega_r) \\ b = (b_{top}, b_{bot}) & \mapsto & u_{|\Omega_r} \end{array}, \qquad \text{where } u \text{ is the solution to (4.54)}, \tag{4.55}$$

is well defined, continuous and there exists a constant D_2 depending on δ, $h_{\min}$, h_{max}, R and r such that

$$\|u\|_{H^2(\Omega_r)} \le D_2 \|b\|_{(\widetilde{H}^{1/2}(-r,r))^2}. \tag{4.56}$$

Using these two propositions, we are now able to justify the approximation of $(\mathcal{H})$ by $(\mathcal{H}')$ which, as in [32] and Chapter 2, is a Born approximation. However, here we show that this approximation remains valid near resonance frequencies.

Proposition 4.3 (Born approximation)**.** *Let $\mathcal{S}$ and $\mathcal{T}$ be operators where $\mathcal{S} : H^2(\Omega_r) \to L^2(\Omega_r)$ and $\mathcal{T} : H^2(\Omega_r) \to (\widetilde{H}^{1/2}(-r,r))^2$. Let D_1 and D_2 be the constants defined in Propositions 4.1 and 4.2. Let $f \in L^2(\Omega_r)$ and $b \in (\widetilde{H}^{1/2}(-r,r))^2$. If*

$$\mu := D_1 \|\mathcal{S}\|_{H^2(\Omega_r),L^2(\Omega_r)} + D_2 \|\mathcal{T}\|_{H^2(\Omega_r),(\widetilde{H}^{1/2}(-r,r))^2} < 1, \tag{4.57}$$

then the equation

$$u = \Gamma(f) + \Pi(b) + \Gamma(\mathcal{S}(u)) + \Pi(\mathcal{T}(u)), \tag{4.58}$$

has a unique solution $u \in H^2(\Omega_r)$. Moreover, if we define $v = \Gamma(f) + \Pi(b)$ then

$$\|u - v\|_{H^2(\Omega_r)} \le \left(D_1 \|f\|_{L^2(\Omega_r)} + D_2 \|b\|_{(\widetilde{H}^{1/2}(-r,r))^2} \right) \frac{\mu}{1-\mu}. \tag{4.59}$$

Proof. If (4.57) is satisfied then $\Gamma \circ \mathcal{S} + \Pi \circ \mathcal{T}$ is a contraction and u can be expressed into a Born series (see [32]). We conclude using the results on geometrical series. ☐

Coming back to equation $(\mathcal{H})$, we define the operators

$$\mathcal{S} : \begin{array}{ccl} \mathrm{H}^2(\Omega_r) & \to & \mathrm{L}^2(\Omega_r) \\ u & \mapsto & \dfrac{h''h - 2(h')^2}{h^3} y \partial_y u - \dfrac{(h')^2}{h^4} y^2 \partial_{yy} u + \dfrac{2h'}{h^2} y \partial_{yx} u \end{array},$$

and

$$\mathcal{T} : \begin{array}{ccl} \mathrm{H}^2(\Omega_r) & \to & \widetilde{\mathrm{H}}^{1/2}(-r,r) \\ u & \mapsto & \dfrac{h'}{h} \partial_x u|_{y=1} \end{array}.$$

With these definitions, $(\mathcal{H})$ can be rewritten as (4.58). We define

$$\eta_0 = \min\left(1, \eta_1, \frac{1}{2\frac{D_1}{h_{\min}{}^2}\left(3 + \frac{1}{h_{\min}{}^2} + \frac{2}{h_{\min}}\right) + 2D_2 \frac{1}{h_{\min}}}\right),$$

and we notice that if $\eta \le \eta_0$ then

$$\|\mathcal{S}\|_{\mathrm{H}^2(\Omega_r),\mathrm{L}^2(\Omega_r)} \le \frac{\eta}{h_{\min}{}^2}\left(2 + \frac{\eta}{h_{\min}{}^2} + \eta + \frac{2\eta}{h_{\min}}\right) \le \frac{\eta}{h_{\min}{}^2}\left(3 + \frac{1}{h_{\min}{}^2} + \frac{2}{h_{\min}}\right),$$

$$\|\mathcal{T}\|_{\mathrm{H}^2(\Omega_r),(\widetilde{\mathrm{H}}^{1/2}(-r,r))^2} \le \eta \frac{1}{h_{\min}}.$$

We choose μ as in (4.57) and we define $v = \Gamma(f) + \Pi(b_{\mathrm{top}}, b_{\mathrm{bot}})$. Using Proposition 4.3, the problem $(\mathcal{H})$ has a unique solution $u \in \mathrm{H}^2(\Omega_r)$ and

$$\begin{aligned} \|u - v\|_{\mathrm{H}^2(-r,r)} \le 2\eta \left(\frac{D_1}{h_{\min}{}^2}\left(3 + \frac{1}{h_{\min}{}^2} + \frac{2}{h_{\min}}\right) + D_2 \frac{1}{h_{\min}} \right) \\ \times \left(D_1 \|f\|_{\mathrm{L}^2(\Omega_r)} + D_2 \|b\|_{(\widetilde{\mathrm{H}}^{1/2}(-r,r))^2} \right). \end{aligned}$$

Using the modal decomposition, we know that

$$v(x,y) = \sum_{n\in\mathbb{N}} \left(\int_{\mathbb{R}} G_n(x,s)(f_n(s) + b_{\text{top}}(s)\varphi_n(1) + b_{\text{bot}}(s)\varphi_n(0))\mathrm{d}s \right) \varphi_n(y).$$

We now estimate the error between v and u^{app} given by (4.15), following the same idea as in the proof of Proposition 4.1. We denote $g_n = f_n + b_{\text{top}}\varphi_n(1) + b_{\text{bot}}\varphi_n(0)$ and $g = \sum_{n\in\mathbb{N}} g_n\varphi_n$. Using the Young inequality for integral operators and the results and notations of Theorem 4.2,

$$\|v_n - u_n^{\text{app}}\|_{\mathrm{L}^2(-r,r)} \leq \beta_n^{(1)}\|g_n\|_{\mathrm{L}^2(-r,r)}, \qquad \|v_n' - (u_n^{\text{app}})'\|_{\mathrm{L}^2(-r,r)} \leq \beta_n^{(2)}\|g_n\|_{\mathrm{L}^2(-r,r)}.$$

It follows that

$$\|v - u^{\text{app}}\|^2_{\mathrm{H}^1(\Omega_r)} \leq \sum_{n=0}^{N}(2+n^2\pi^2)\beta^2\eta^2\|g_n\|^2_{\mathrm{L}^2(-r,r)} + \sum_{n>N}\left(\frac{(1+n^2\pi^2)\beta^2\eta^2}{\min(|k_n|)^4} + \frac{\eta^2\beta^2}{\min(|k_n|)^2}\right)\|g_n\|^2_{\mathrm{L}^2(-r,r)},$$

and so

$$\|v - u^{\text{app}}\|^2_{\mathrm{H}^1(\Omega_r)} \leq \beta^2\eta^2 \max\left(2+N^2\pi^2, \frac{1+(N+1)^2\pi^2}{\delta^4} + \frac{1}{\delta^2}\right)\|g\|^2_{\mathrm{L}^2(\Omega_r)}.$$

We conclude by noticing that

$$\|u - u^{\text{app}}\|_{\mathrm{H}^1(\Omega_r)} \leq \|u - v\|_{\mathrm{H}^2(\Omega_r)} + \|v - u^{\text{app}}\|_{\mathrm{H}^1(\Omega_r)}.$$

4.4 Extension to general slowly varying waveguides

4.4.1 The cut and match strategy

In the previous section, we constructed an approximation for the solution to the Helmholtz equation in a slowly increasing waveguide. In this section, we generalize our result by considering a 2D infinite waveguide $\widetilde{\Omega} = \{(x,y) \in \mathbb{R}^2 \,|\, 0 < y < h(x)\}$ where $h \in \mathcal{C}^2(\mathbb{R})$ is such that h' is compactly supported and there exists a parameter η, assumed to be small compared to R and $h_{\min}$, such that $\|h'\|_{L^\infty(\mathbb{R})} \leq \eta$ and $\|h''\|_{L^\infty(\mathbb{R})} \leq \eta^2$.

When we look at the proof of Theorem 4.1, we notice that the condition that h is increasing is only required to properly define the change of variable $x \mapsto \xi(x)$ in Theorem 4.2 when $n = N$. In order to generalize Theorem 4.1, we only need to generalize Theorem 4.2 for the case $n = N$. To this end, we follow a strategy developed in the context of the Schrödinger equation, see for instance [90]. We partition $\widetilde{\Omega}$ in J regions $(S_j)_{j=1,..,J}$, on which h' has a constant sign, as shown in Figure 4.2.

If there exists $x \in \mathbb{R}$ such that $k_n(x) = 0$ in S_j, we denote this coordinate by x_j^*. Otherwise, as in section 5 of [77], x_j^* is chosen to be greater than $\max(S_j)$ if k_n^2 is positive on S_j (resp. smaller than $\min(S_j)$ if k_n^2 is negative on S_j). Then, if h is increasing in S_j, we define

$$\xi_j(x) = \begin{cases} \left(-\dfrac{3}{2}i\displaystyle\int_x^{x_j^*} k_n(t)\mathrm{d}t\right)^{2/3} & \text{if } x < x_j^* \text{ and } x \in S_j, \\ -\left(\dfrac{3}{2}\displaystyle\int_{x_j^*}^{x} k_n(t)\mathrm{d}t\right)^{2/3} & \text{if } x > x_j^* \text{ and } x \in S_j. \end{cases} \tag{4.60}$$

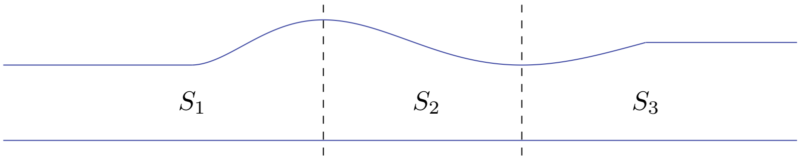

Figure 4.2 – Representation of the sections in a slowly varying waveguide.

Otherwise, if h is decreasing in S_j, we define

$$\xi_j(x) = \begin{cases} -\left(\dfrac{3}{2}\displaystyle\int_x^{x_j^*} k_n(t)\mathrm{d}t\right)^{2/3} & \text{if } x < x_j^* \text{ and } x \in S_j, \\ \left(-\dfrac{3}{2}i\displaystyle\int_{x_j^*}^{x} k_n(t)\mathrm{d}t\right)^{2/3} & \text{if } x > x_j^* \text{ and } x \in S_j. \end{cases} \tag{4.61}$$

In both cases, we denote

$$\phi_j(x) = \frac{(-\xi_j(x))^{1/4}}{\sqrt{k_n(x)}}. \tag{4.62}$$

Given $s \in \mathbb{R}$, we study the problem

$$\begin{cases} \partial_{xx} G_n(x,s) + k_n(x)^2 G_n(x,s) = -\delta_s & \text{in } \mathbb{R}, \\ G_n(\cdot, s) \text{ is outgoing.} \end{cases} \tag{4.63}$$

We denote S_{j_0} the region such that $s \in S_{j_0}$, and we assume that $j_0 \neq 1$ and $j_0 \neq J$ even if it means adding an artificial section before or after the coordinate s. Theorem 2 in [77] shows that (4.63) has a solution and that there exist $(A_j)_{j=1,\dots,J}, (B_j)_{j=1,\dots,J} \in \mathbb{C}$ such that $G_n(x,s)$ is close to

$$G_n^{\mathrm{app}}(x,s) = \begin{cases} A_1\phi_1(x)w_1(x) & \text{if } x \in S_1, \\ A_J\phi_J(x)w_J(x) & \text{if } x \in S_J, \\ \phi_j(x)(A_j\mathcal{A}(\xi_j(x)) + B_j\mathcal{B}(\xi_j(x))) & \text{if } x \in S_j,\ j \neq j_0, \\ \phi_{j_0}(x)(A_{j_0}\mathcal{A}(\xi_{j_0}(x)) + B_{j_0}\mathcal{B}(\xi_{j_0}(x))) & \text{if } x \in S_{j_0},\ x < s, \\ \phi_{j_0}(x)(b_{\mathrm{top}}\mathcal{A}(\xi_{j_0}(x)) + B_J\mathcal{B}(\xi_{j_0}(x))) & \text{if } x \in S_{j_0},\ x > s, \end{cases} \tag{4.64}$$

where

$$w_1(x) = \begin{cases} \mathcal{A}(\xi_1(x)) & \text{if } h' > 0 \text{ in } S_1, \\ i\mathcal{A}(\xi_1(x)) + \mathcal{B}(\xi_1(x)) & \text{if } h' < 0 \text{ in } S_1, \end{cases} \tag{4.65}$$

$$w_J(x) = \begin{cases} i\mathcal{A}(\xi_J(x)) + \mathcal{B}(\xi_J(x)) & \text{if } h' > 0 \text{ in } S_J, \\ \mathcal{A}(\xi_J(x)) & \text{if } h' < 0 \text{ in } S_J. \end{cases} \tag{4.66}$$

To find the value of the constants A_j and B_j, we first use the continuity of G_n^{app} and $\partial_x G_n^{\mathrm{app}}$ on the shared boundaries of each section, which gives $2J-2$ linear equations. Moreover, using the continuity of G_n^{app} at $x = s$, we find that

$$A_{j_0}\mathcal{A}(\xi_{j_0}(s)) + B_{j_0}\mathcal{B}(\xi_{j_0}(s)) = b_{\mathrm{top}}\mathcal{A}(\xi_{j_0}(s)) + B_J B_{j_0}\mathcal{B}(\xi_{j_0}(s)). \tag{4.67}$$

Using the jump formula for distributions, we also have

$$b_{\mathrm{top}}\mathcal{A}'(\xi_{j_0}(s)) + B_J\mathcal{B}'(\xi_{j_0}(s)) - A_{j_0}\mathcal{A}'(\xi_{j_0}(s)) - B_{j_0}\mathcal{B}'(\xi_{j_0}(s)) = -\phi_{j_0}(s). \tag{4.68}$$

Altogether, we obtain a linear system of $2J$ equations for the constants A_j, B_j, $1 \leq j \leq J$. We study its invertibility in the particular case $J = 2$ in the next section.

4.4.2 Example of dilations or compressions in waveguides

In this section, we apply the method described previously to the simplest case, when the sign of h' changes only once, at $x = t$. If h is increasing then decreasing, we say that the waveguide is dilated. On the other hand, if h is decreasing then increasing, we say that the waveguide is compressed. First, we study the case of dilations. Up to a change of variable $x \mapsto -x$, we can assume that $s > t$, as represented in Figure 4.3.

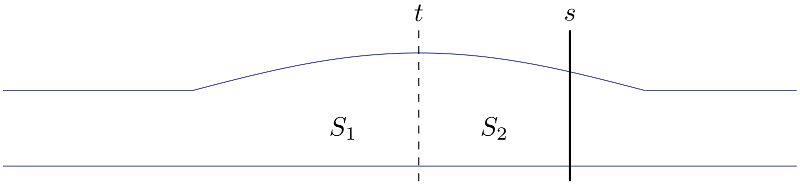

Figure 4.3 – Parametrization of a dilated waveguide: t is the unique coordinate in the interior of $\operatorname{supp} h'$ such that $h'(t) = 0$, S_1 (resp. S_2) is the section at the left (resp. right) of t, and s is a coordinate satisfying $s > t$.

We know from section 4.2 that $G_n(x, s)$ is close to

$$G_n^{\mathrm{app}}(x,s) = \begin{cases} A_1\phi_1(x)\mathcal{A}(\xi_1(x)) & \text{if } x \in S_1, \\ \phi_2(x)(B_1\mathcal{A}(\xi_2(x)) + B_2\mathcal{B}(\xi_2(x))) & \text{if } x \in S_2,\ x < s, \\ A_2\phi_2(x)\mathcal{A}(\xi_2(x)) & \text{if } x \in S_2,\ x > s, \end{cases} \tag{4.69}$$

where ϕ_1, ϕ_2 are defined in (4.62). The constants A_1, A_2, B_1, B_2 satisfy the linear system

$$M(s,t)\begin{pmatrix} A_1 \\ B_1 \\ B_2 \\ A_2 \end{pmatrix} = V(s) := \begin{pmatrix} 0 \\ 0 \\ 0 \\ -\phi_2(s) \end{pmatrix}, \tag{4.70}$$

where

$$M(s,t) = \begin{pmatrix} -(\phi_1\mathcal{A}(\xi_1))(t) & (\phi_2\mathcal{A}(\xi_2))(t) & (\phi_2\mathcal{B}(\xi_2))(t) & 0 \\ -(\phi_1\mathcal{A}(\xi_1))'(t) & (\phi_2\mathcal{A}(\xi_2))'(t) & (\phi_2\mathcal{B}(\xi_2))'(t) & 0 \\ 0 & -\mathcal{A}(\xi_2(s)) & -\mathcal{B}(\xi_2(s)) & \mathcal{A}(\xi_2(s)) \\ 0 & -\mathcal{A}'(\xi_2(s)) & -\mathcal{B}'(\xi_2(s)) & \mathcal{A}'(\xi_2(s)) \end{pmatrix}. \tag{4.71}$$

We next study when M is invertible.

Proposition 4.4. *The determinant D of $M(s,t)$ defined in* (4.71) *is*

$$D = \frac{1}{\pi}\left(-\phi_1(t)\mathcal{A}(\xi_1(t))(\phi_2\mathcal{A}(\xi_2))'(t) + (\phi_1\mathcal{A}(\xi_1))'(t)\phi_2(t)\mathcal{A}(\xi_2(t))\right). \tag{4.72}$$

Proof. We expand of the determinant along the first column and use the fact that $\mathcal{B}\mathcal{A}' - \mathcal{B}'\mathcal{A} = -1/\pi$. ☐

Remark 4.8. *Using the asymptotics of $\mathcal{A}$ provided in [82, 4], the condition $D = 0$ asymptotically reduces to*

$$\cos\left(\int_{x_1^\star}^{x_2^\star} k_n(x)\mathrm{d}x\right) = 0. \tag{4.73}$$

Under this condition, it is not possible to find the values of (A_1, B_1, B_2, A_2). This may be explained by the potential presence of trapped modes in the dilated waveguide under this condition.

Except for special values of k such that $D = 0$, we can find constants (A_1, B_1, B_2, A_2) by computing either symbolically or numerically the solution of $M(s,t)X = V(s)$.

We also study the case of compressions. Again, we assume that $s > t$, and we know that $G_n(x,s)$ is close to

$$G_n^{\text{app}}(x,s) = \begin{cases} A_1\phi_1(x)(i\mathcal{A}(\xi_1(x)) + \mathcal{B}(\xi_1(x))) & \text{if } x \in S_1, \\ \phi_2(x)(B_1\mathcal{A}(\xi_2(x)) + B_2\mathcal{B}(\xi_2(x))) & \text{if } x \in S_2,\ x < s, \\ A_2\phi_2(x)(i\mathcal{A}(\xi_2(x)) + \mathcal{B}(\xi_2(x))) & \text{if } x \in S_2,\ x > s. \end{cases} \tag{4.74}$$

The constants A_1, A_2, B_1, B_2 satisfy the linear system

$$M(s,t)\begin{pmatrix} A_1 \\ B_1 \\ B_2 \\ A_2 \end{pmatrix} = V(s) := \begin{pmatrix} 0 \\ 0 \\ 0 \\ \phi_2(s) \end{pmatrix}, \tag{4.75}$$

where

$$M(s,t) = \begin{pmatrix} -(\phi_1(i\mathcal{A}+\mathcal{B})\circ\xi_1)(t) & (\phi_2\mathcal{A}(\xi_2))(t) & (\phi_2\mathcal{B}(\xi_2))(t) & 0 \\ -(\phi_1(i\mathcal{A}+\mathcal{B})\circ\xi_1)'(t) & (\phi_2\mathcal{A}(\xi_2))'(t) & (\phi_2\mathcal{B}(\xi_2))'(t) & 0 \\ 0 & -\mathcal{A}(\xi_2(s)) & -\mathcal{B}(\xi_2(s)) & (i\mathcal{A}+\mathcal{B})(\xi_2(s)) \\ 0 & -\mathcal{A}'(\xi_2(s)) & -\mathcal{B}'(\xi_2(s)) & (i\mathcal{A}'+\mathcal{B}')(\xi_2(s)) \end{pmatrix}. \tag{4.76}$$

Proposition 4.5. *The matrice $M(s,t)$ defined in* (4.76) *is invertible.*

Proof. Its determinant D is

$$\begin{aligned} D = \frac{1}{\pi}(&-\phi_1(t)(i\mathcal{A}+\mathcal{B})(\xi_1(t))(\phi_2(i\mathcal{A}(\xi_2)+\mathcal{B}(\xi_2))'(t) \\ &+ (\phi_1(i\mathcal{A}(\xi_1)+\mathcal{B}(\xi_1))'(t)\phi_2(t)(i\mathcal{A}+\mathcal{B})(\xi_2(t)). \end{aligned}$$

The asymptotic expansions provided in [4, 82] show that there exists $\beta_1 > 0$ such that

$$\phi_1(t)(i\mathcal{A}(\xi_1(t)) + \mathcal{B}(\xi_1(t)) \approx \begin{cases} \dfrac{1}{2\sqrt{\pi}\sqrt{k_n(t)}}\exp\left(\dfrac{2}{3}\displaystyle\int_{x_1^\star}^t |k_n|(x)\mathrm{d}x\right) & \text{if } |t - x_1^\star| \gg \eta^{-1/3}, \\ \dfrac{1}{\sqrt{\beta_1}}(i\mathcal{A}+\mathcal{B})(\beta_1(t - x_1^\star)) & \text{if } |t - x_1^\star| \ll \eta^{-1/2}, \end{cases}$$

and since $h'(t) = 0$,

$$(\phi_1(i\mathcal{A}(\xi_1) + \mathcal{B}(\xi_1))'(t) \approx \begin{cases} \dfrac{|k_n(t)|}{2\sqrt{\pi}\sqrt{k_n(t)}}\exp\left(\dfrac{2}{3}\displaystyle\int_{x_1^\star}^t |k_n|(x)\mathrm{d}x\right) & \text{if } |t - x_1^\star| \gg \eta^{-1/3}, \\ \sqrt{\beta_1}(i\mathcal{A}'+\mathcal{B}')(\beta_1(t - x_1^\star)) & \text{if } |t - x_1^\star| \ll \eta^{-1/2}. \end{cases}$$

This case distinction covers every relative positions of t, $x_1^\star$ and $x_2^\star$ since $\eta^{-1/2} \gg \eta^{-1/3}$. We can do the same in S_2, and find $\beta_2 > 0$ such that

$$\phi_2(t)(i\mathcal{A}(\xi_2(t)) + \mathcal{B}(\xi_2(t)) \approx \begin{cases} \dfrac{1}{2\sqrt{\pi}\sqrt{k_n(t)}}\exp\left(\dfrac{2}{3}\displaystyle\int_t^{x_2^\star} |k_n|(x)\mathrm{d}x\right) & \text{if } |t - x_2^\star| \gg \eta^{-1/3}, \\ \dfrac{1}{\sqrt{\beta_2}}(i\mathcal{A}+\mathcal{B})(\beta_2(x_2^\star - t)) & \text{if } |t - x_2^\star| \ll \eta^{-1/2}, \end{cases}$$

$$(\phi_2(i\mathcal{A}(\xi_2)+\mathcal{B}(\xi_2))'(t) \approx \begin{cases} -\dfrac{|k_n|}{2\sqrt{\pi}\sqrt{k_n(t)}}\exp\left(\dfrac{2}{3}\displaystyle\int_t^{x_2^\star}|k_n|(x)\mathrm{d}x\right) & \text{if } |t-x_2^\star| \gg \eta^{-1/3}, \\ -\sqrt{\beta_2}(i\mathcal{A}'+\mathcal{B}')(\beta_2(x_2^\star-t)) & \text{if } |t-x_2^\star| \ll \eta^{-1/2}. \end{cases}$$

If $|t-x_2^\star| \gg \eta^{-1/3}$ and $|t-x_1^\star| \gg \eta^{-1/3}$ then

$$D \approx \exp\left(\frac{2}{3}\int_{x_1^\star}^{t}|k_n|(x)\mathrm{d}x\right)\exp\left(\frac{2}{3}\int_t^{x_2^\star}|k_n|(x)\mathrm{d}x\right) \neq 0.$$

The remaining three relative positions of t, $x_1^\star$ and $x_2^\star$ can be analyzed in the same way. It follows that $\forall(t,s)\in\mathbb{R}$, $D\neq 0$. □

Contrarily to the case of dilations, the matrix M is always invertible, and we can compute again the values of (A_1, B_1, B_2, A_2). Figure 4.9 and 4.10 show examples of such computation.

4.5 Numerical illustrations

In this section, we illustrate our results. We compare the asymptotic expression of u to data generated using the software Matlab to solve numerically the equation $(\widetilde{\mathcal{H}})$ satisfied by the wavefield in $\tilde{\Omega}$. In the following, we assume that h' is supported between $x=-7$ and $x=7$. To generate the solution $\tilde{u}$ of $(\widetilde{\mathcal{H}})$ on $\tilde{\Omega}_7$, we use the finite element method and a perfectly matched layer (see [18]) placed on the left side of the waveguide between $x=-15$ and $x=-8$, and on the right side between $x=8$ and $x=15$. The coefficient of absorption for the perfectly matched layer is defined by $\alpha=-k((x-8)\mathbf{1}_{x\geq 8}-(x+8)\mathbf{1}_{x\leq -8})$ and k^2 is replaced in the Helmholtz equation by $k^2+i\alpha$. The structured mesh is built with a stepsize of 10^{-3}.

4.5.1 Computation of the modal Green function

To test the validity of the expression (4.16) of the Green function, we consider a profile with $\alpha=0.1$, $\beta=0.04/30$ and

$$h(x)=\left(\alpha-\beta+\beta\frac{\sqrt{x+4}}{\sqrt{2}}\right)\mathbf{1}_{[-4,4]}(x)+(\alpha+\beta)\,\mathbf{1}_{(4,+\infty)}(x)+(\alpha-\beta)\,\mathbf{1}_{(-\infty,-\alpha)}(x), \tag{4.77}$$

with $k=31.5$. There is only one locally resonant mode $N=1$ associated to the resonant point $x^\star\approx -2.72$. We place an internal source $f(x,y)=d(x)\varphi_n(y/h(x))$ with $n\in\mathbb{N}$ where d is a Gaussian approximation of δ_s at $s\in\mathbb{R}$ with

$$d(x)=\frac{1}{\sqrt{2\pi}\sigma}\exp\left(-\frac{(x-s)^2}{2\sigma^2}\right), \tag{4.78}$$

and $\sigma=0.005$. We measure the wavefield $\tilde{u}$ at $y=0$, and we compare it to the expression (4.16). In Figure 4.4 (resp 4.5), we illustrate the case where $n=0<N$ (resp. $n=2>N$). In Figures 4.6, 4.7 and 4.8, we illustrate the case where $n=N$ for different values of s. The approximation seems to be accurate, and the small discrepancies observed for instance in the imaginary part of Figure 4.7 are caused by the imprecise approximation of the Dirac function δ_s by d. However, even in this particular case, the relative L^2 error is still very small.

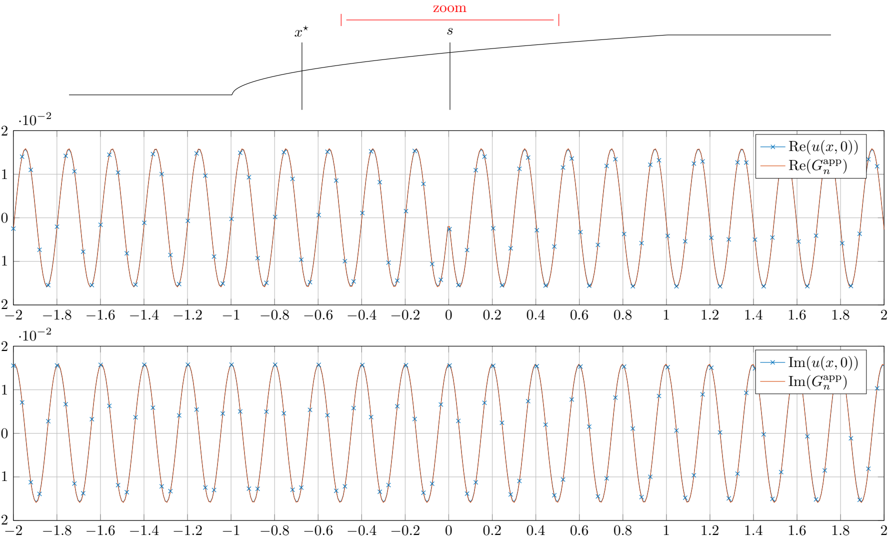

Figure 4.4 – Representation of $\widetilde{u}(x,0)$ (in blue) and $G_n^{\text{app}}(x)$ (in red) for a propagative mode $n=0$ and $s=0$ in an expanding waveguide, in the zoomed area $(-2,2)$. Top: representation of h, $x^\star$ and s. Middle: comparison between real parts of $\widetilde{u}(x,0)$ and $G_n^{\text{app}}(x)$. Bottom: comparison between imaginary parts of $\widetilde{u}(x,0)$ and $G_n^{\text{app}}(x)$. Here, the relative L^2 error between $\widetilde{u}(x,0)$ and $G_n^{\text{app}}(x)$ is 0.93%.

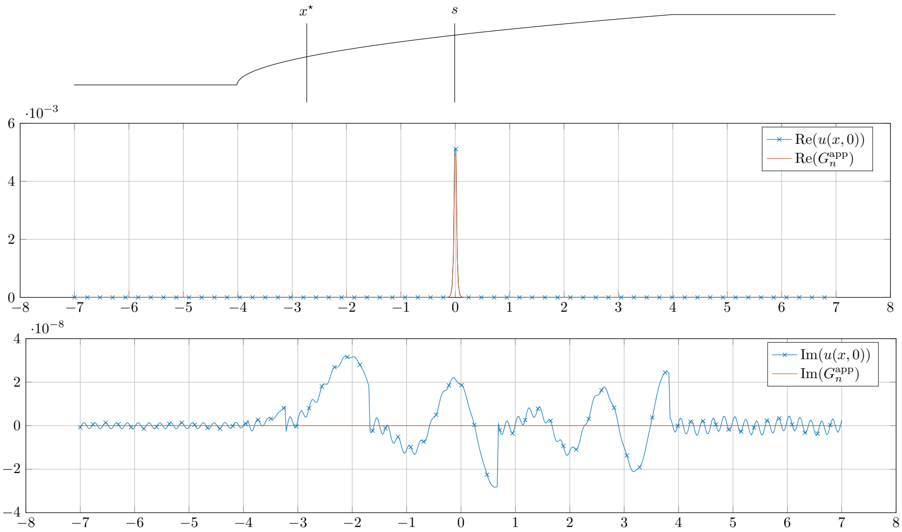

Figure 4.5 – Representation of $\widetilde{u}(x,0)$ (in blue) and $G_n^{\text{app}}(x)$ (in red) for an evanescent mode $n=2$ and $s=0$ in an expanding waveguide. Top: representation of h, $x^\star$ and s. Middle: comparison between real parts of $\widetilde{u}(x,0)$ and $G_n^{\text{app}}(x)$. Bottom: comparison between imaginary parts of $\widetilde{u}(x,0)$ and $G_n^{\text{app}}(x)$. Here, the relative L^2 error between $\widetilde{u}(x,0)$ and $G_n^{\text{app}}(x)$ is 3.68%.

We also consider a more general waveguide. As in section 4.3.2, we choose the simplest case of dilation and compression, and we compare $\widetilde{u}(x,0)$ to G_n^{app} defined in (4.69) and (4.74). First, we choose to work with a dilated waveguide, described by its width

$$h(x) = 0.1 + 0.0025\sin\left(\frac{\pi}{10}(x+5)\right)\mathbf{1}_{[-5,5]}(x), \tag{4.79}$$

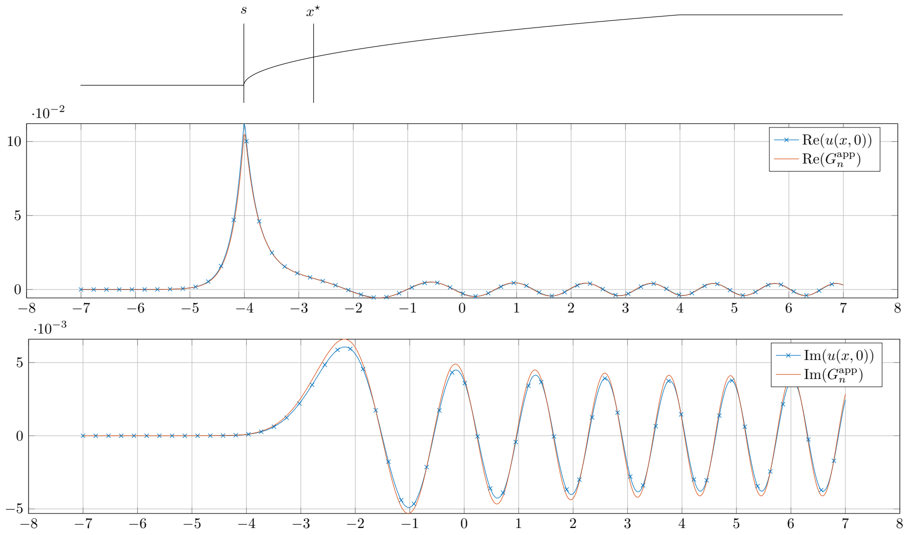

Figure 4.6 – Representation of $\widetilde{u}(x,0)$ (in blue) and $G_n^{\mathsf{app}}(x)$ (in red) for a locally resonant mode $n=1$ and $s=-4$ in an expanding waveguide. Top: representation of h, $x^\star$ and s. Middle: comparison between real parts of $\widetilde{u}(x,0)$ and $G_n^{\mathsf{app}}(x)$. Bottom: comparison between imaginary parts of $\widetilde{u}(x,0)$ and $G_n^{\mathsf{app}}(x)$. Here, the relative L^2 error between $\widetilde{u}(x,0)$ and $G_n^{\mathsf{app}}(x)$ is 5.32%.

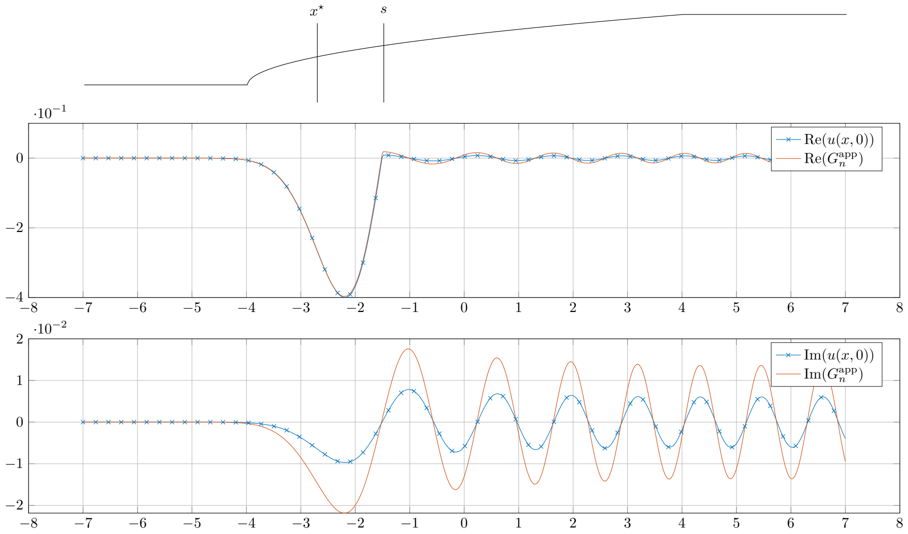

Figure 4.7 – Representation of $\widetilde{u}(x,0)$ (in blue) and $G_n^{\mathsf{app}}(x)$ (in red) for a locally resonant mode $n=1$ and $s=-1.5$ in an expanding waveguide. Top: representation of h, $x^\star$ and s. Middle: comparison between real parts of $\widetilde{u}(x,0)$ and $G_n^{\mathsf{app}}(x)$. Bottom: comparison between imaginary parts of $\widetilde{u}(x,0)$ and $G_n^{\mathsf{app}}(x)$. Here, the relative L^2 error between $\widetilde{u}(x,0)$ and $G_n^{\mathsf{app}}(x)$ is 7.24%.

at frequency $k=31$. The only locally resonant mode is still $N=1$, associated to two resonant points $x_1^\star \approx -3.19$ and $x_2^\star = -x_1^\star$. We choose the same internal source f as before, and we illustrate the case $n=N$ in Figure 4.9. Figure 4.10 illustrates the case of a compressed waveguide, with

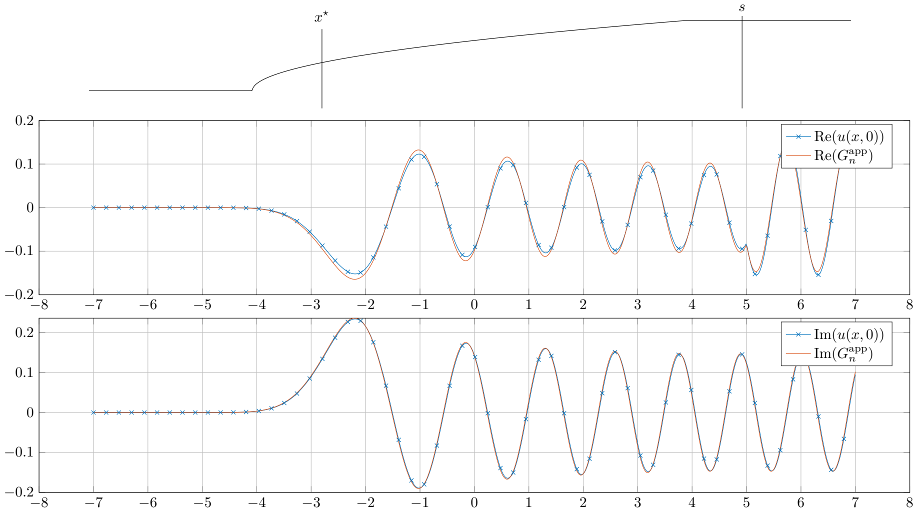

Figure 4.8 – Representation of $\widetilde{u}(x,0)$ (in blue) and $G_n^{\mathsf{app}}(x)$ (in red) for a locally resonant mode $n=1$ and $s=5$ in an expanding waveguide. Top: representation of h, $x^\star$ and s. Middle: comparison between real parts of $\widetilde{u}(x,0)$ and $G_n^{\mathsf{app}}(x)$. Bottom: comparison between imaginary parts of $\widetilde{u}(x,0)$ and $G_n^{\mathsf{app}}(x)$. Here, the relative L^2 error between $\widetilde{u}(x,0)$ and $G_n^{\mathsf{app}}(x)$ is 6.08%.

profile

$$h(x) = 0.1 - 0.0005(x+5)\mathbf{1}_{[-5,0]}(x) + \frac{0.0025}{4}(x-4)\mathbf{1}_{(0,4]}(x), \tag{4.80}$$

at frequency $k = 32.1$ with a resonant mode $N = 1$ and resonant points $x_1^\star \approx -0.74$ and $x_2^\star \approx 0.59$.

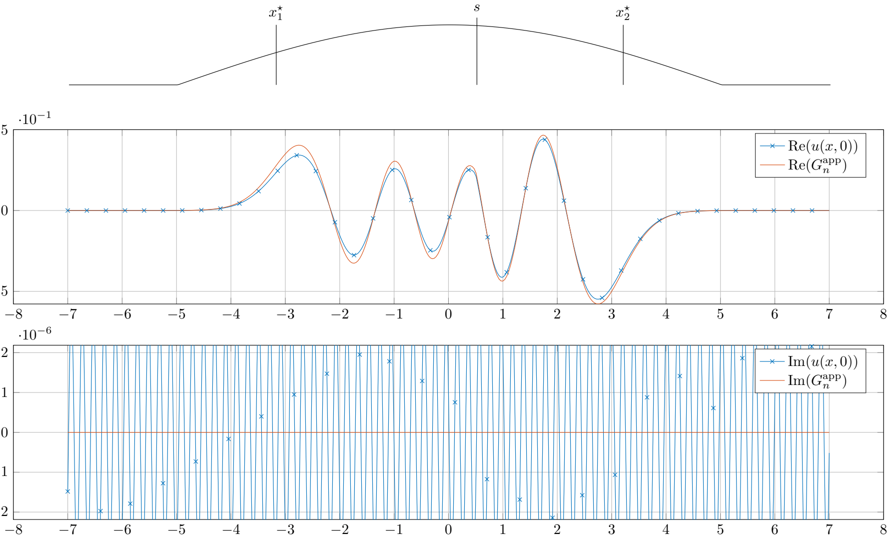

Figure 4.9 – Representation of $\widetilde{u}(x,0)$ (in blue) and $G_n^{\mathsf{app}}(x)$ (in red) for $n=1$ and $s=0.5$ in a dilated waveguide. Top: representation of h, $x_1^\star$, $x_2^\star$ and s. Middle: comparison between real parts of $\widetilde{u}(x,0)$ and $G_n^{\mathsf{app}}(x)$. Bottom: comparison between imaginary parts of $\widetilde{u}(x,0)$ and $G_n^{\mathsf{app}}(x)$ Here, the relative L^2 error between $\widetilde{u}(x,0)$ and $G_n^{\mathsf{app}}(x)$ is 10.09%.

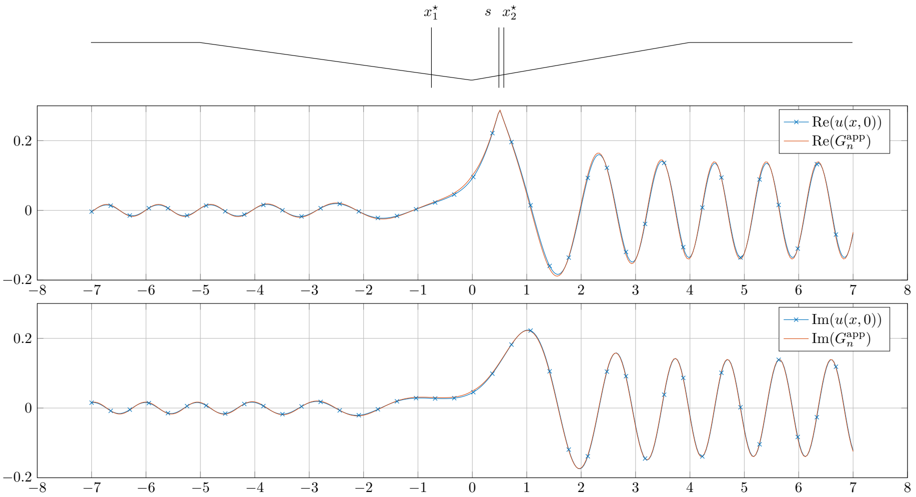

Figure 4.10 – Representation of $\widetilde{u}(x,0)$ (in blue) and $G_n^{\mathsf{app}}(x)$ (in red) for $n=1$ and $s=0.5$ in a compressed waveguide. Top: representation of h, $x_1^\star$, $x_2^\star$ and s. Middle: comparison between real parts of $\widetilde{u}(x,0)$ and $G_n^{\mathsf{app}}(x)$. Bottom: comparison between imaginary parts of $\widetilde{u}(x,0)$ and $G_n^{\mathsf{app}}(x)$. Here, the relative L^2 error between $\widetilde{u}(x,0)$ and $G_n^{\mathsf{app}}(x)$ is 4.39%.

4.5.2 General source terms

We now validate the approximation provided in (4.15) for general sources, in the same expanding waveguide defined by its width in (4.77). We choose two different types of sources : a vertical internal source (see Figure 4.11), and a boundary source (see Figure 4.12). To compute the approximation in (4.15), we choose to reduce the sum to 15 modes. Every time, we compute the relative error made between $\widetilde{u}$ and its approximation $\widetilde{u}^{\text{app}}$ defined by (4.15).

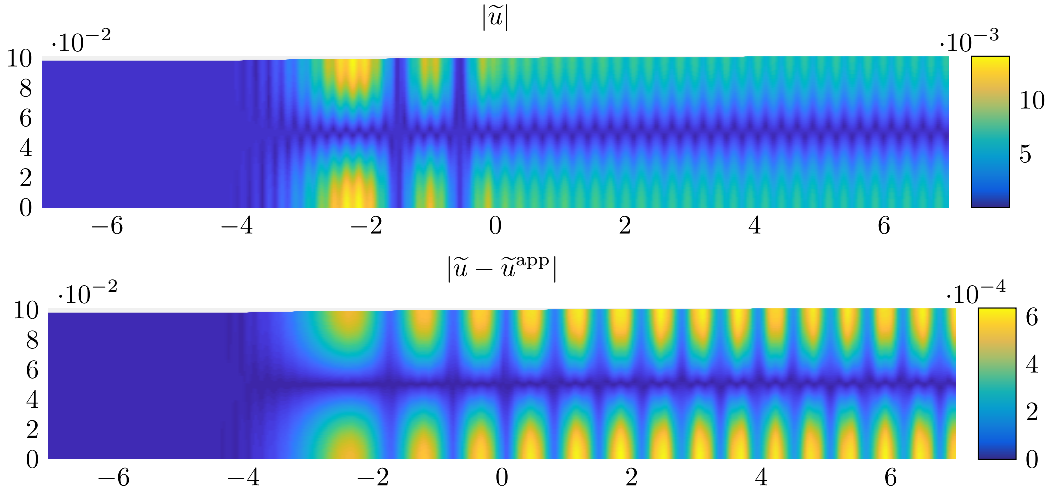

Figure 4.11 – Representation of the wavefield u generated by a source $f(x,y)=d(x)y$ where d is defined in (4.78) with $s=0$. Up, the absolute value $|\widetilde{u}|$, down, the error of approximation $|\widetilde{u}-\widetilde{u}^{\mathsf{app}}|$. Here, the relative L^2 error between $\widetilde{u}$ and $\widetilde{u}^{\mathsf{app}}$ is 6.22%.

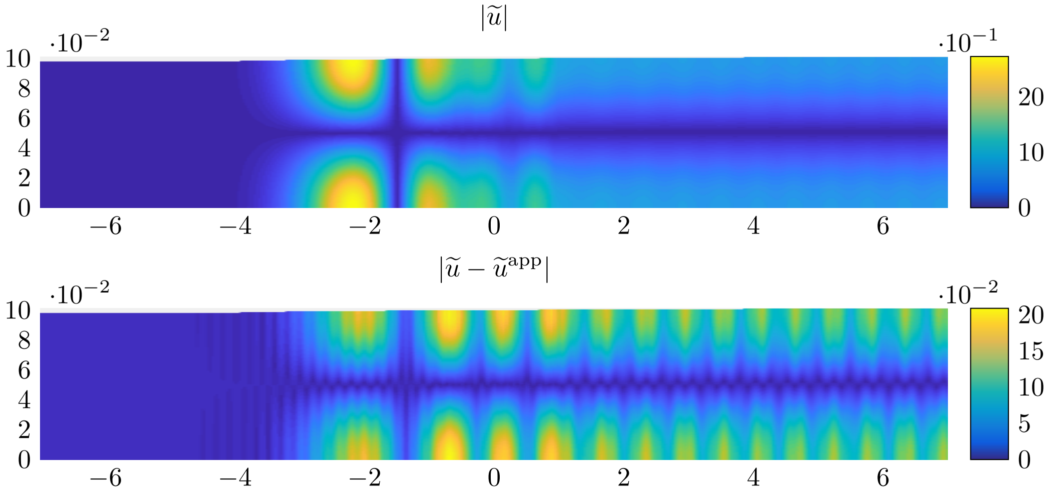

Figure 4.12 – Representation of the wavefield $\widetilde{u}$ generated by a source $b_{\text{bot}} = \mathbf{1}_{-1\leq x\leq 1}$. Up, the absolute value $|\widetilde{u}|$, down, the error of approximation $|\widetilde{u}-\widetilde{u}^{\text{app}}|$. Here, the relative L^2 error between $\widetilde{u}$ and $\widetilde{u}^{\text{app}}$ is 7.73%.

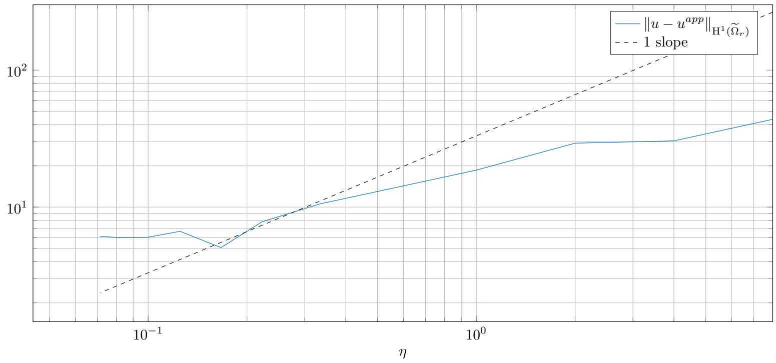

Figure 4.13 – Representation of $\|\widetilde{u}-\widetilde{u}^{\text{app}}\|_{\mathrm{H}^1(\widetilde{\Omega}_7)}$ for different values of η to illustrate the result of Theorem 4.1.

4.5.3 Dependence of the error of approximation with respect to η

Finally, we evaluate in this section the influence of the parameter η in the approximation error $\|\widetilde{u}-\widetilde{u}^{\text{app}}\|_{\mathrm{H}^1(\widetilde{\Omega}_r)}$. First, we chose large values of η to illustrate the control provided in Theorem 4.1. We work at $k = 5.23$, with an increasing waveguide parametrized by

$$h(x) = 0.5 + 0.2\eta x\mathbf{1}_{-5<x<-5+1/\eta} + 0.2\mathbf{1}_{x\geq -5+1/\eta}, \tag{4.81}$$

and a boundary source $b_{\text{bot}} = \mathbf{1}_{4<x<5}$. We present in Figure 4.13 the error of approximation with respect to η. We can see that the error grows a little bit slower than the 1 slope expected. We also notice than for small values of η, the error seems to reach a level where it is almost constant. This is the error due to the finite element method.

4.6 Conclusion

In this chapter, we have presented a complete proof of the existence of a unique solution to the Helmholtz equation in slowly variable waveguides. We also provide a suitable approximation of this solution and a control of the error of approximation in $\mathrm{H}^1_{\mathrm{loc}}(\Omega)$. We validate this approximation numerically, and show that this expression is an excellent way to compute quickly the wavefield in a slowly varying waveguide.

We believe that this work could be extended to elastic waveguides in two dimensions, using the modal decomposition in Lamb modes as in [82]. One could also try to generalize the ideas of this chapter to acoustic waveguides in three dimensions. We think it would be possible to recover some Laplacian eigenvalues of local sections, and from that to recover some information on the waveguide shape.

Finally, we plan to use this work to develop a new multi-frequency method to recover the width of a waveguide given measurements of the wavefield at the surface or on a section of the waveguide. Indeed, for a locally resonant frequency, the wavefield in a perturbed waveguide is very different from the one in a regular waveguide, even if the width h is close to a constant function. This should provide a very high sensitivity inversion method to reconstruct the width of the waveguide, and will be done in a future work.

Appendix 4.A: Proofs of Proposition 4.1 and 4.2

Source f. This proof is an adaptation of the proof presented in Appendix 2.B of Chapter 2. Using the results on the modal decomposition presented in Appendix 2.A of Chapter 2, we know that the equation (4.51) is equivalent to

$$\forall n \in \mathbb{N} \qquad \begin{cases} u_n'' + k_n(x)^2 u_n = -f_n & \text{in } \mathbb{R}, \\ u_n \text{ is outgoing}, \end{cases}$$

where

$$u(x,y) = \sum_{n\in\mathbb{N}} u_n(x)\varphi_n(y), \quad f(x,y) = \sum_{n\in\mathbb{N}} f_n(x) \quad \text{a.e. } (x,y) \in \Omega, \qquad u_n, f_n \in \mathrm{L}^2_{\mathrm{loc}}(\mathbb{R}).$$

Using Theorem 4.2, there exist a unique Green function $G_n(x,s)$ associated to this equation, and

$$\forall n \in \mathbb{N} \qquad u_n(x) = \int_{\mathbb{R}} G_n(x,s) f_n(s)\mathrm{d}s.$$

We also notice that for every $(x,s) \in \mathbb{R}^2$, $G_n(x,s) = G_n(s,x)$, and using controls from Theorem 4.2, for every $s \in \mathbb{R}$ and $x \in \mathbb{R}$,

$$\forall n \in \mathbb{N} \qquad \|G_n(\cdot,s)\|_{\mathrm{L}^1(-r,r)}, \|G_n(x,\cdot)\|_{\mathrm{L}^1(-r,r)} \leq \alpha_n^{(1)}.$$

Using Young's inequality for integral operators,

$$\forall n \in \mathbb{N} \qquad \|u_n\|_{\mathrm{L}^2(-r,r)} \leq \alpha_n^{(1)} \|f_n\|_{\mathrm{L}^2(-r,r)}.$$

Using Parseval equality and the results of Theorem 4.2,

$$\|u\|^2_{\mathrm{L}^2(\Omega_r)} \leq \alpha^2 \sum_{n=0}^{N} \|f_n\|^2_{\mathrm{L}^2(-r,r)} + \frac{\alpha^2}{\delta^4} \sum_{n>N} \|f_n\|^2_{\mathrm{L}^2(-r,r)} \leq \alpha^2 \max\left(1, \frac{1}{\delta^4}\right) \|f\|^2_{\mathrm{L}^2(\Omega_r)}.$$

Applying Young's inequality to u_n', we get

$$\|\nabla u\|^2_{\mathrm{L}^2(\Omega_r)} \leq \alpha^2 \sum_{n=0}^{N} \left(1+n^2\pi^2\right) \|f_n\|^2_{\mathrm{L}^2(-r,r)} + \alpha^2 \sum_{n>N} \left(\frac{1}{\min(|k_n|)^2} + \frac{n^2\pi^2}{\min(|k_n|)^4}\right) \|f_n\|^2_{\mathrm{L}^2(-r,r)}.$$

We deduce that

$$\|\nabla u\|^2_{\mathrm{L}^2(\Omega_r)} \leq \alpha^2 \max\left(1+N^2\pi^2, \frac{1}{\delta^2} + \frac{(N+1)^2\pi^2}{\delta^4}\right) \|f\|^2_{\mathrm{L}^2(\Omega_r)}.$$

Finally,

$$\|u_n''\|_{\mathrm{L}^2(-r,r)} \leq |k_n|^2 \|u_n\|_{\mathrm{L}^2(-r,r)} + \|f_n\|_{\mathrm{L}^2(-r,r)}$$

It follows that

$$\begin{aligned}\|\nabla^2 u\|^2_{\mathrm{L}^2(\Omega_r)} \leq & \sum_{n=0}^{N} \alpha^2 \left((k_n^2+1)^2 + 2n^2\pi^2 + n^4\pi^4\right) \|f_n\|^2_{\mathrm{L}^2(-r,r)} \\ & + \sum_{n>N} \alpha^2 \left(\left(\frac{|k_n|^2}{\min(|k_n|)^2} + 1\right)^2 + \frac{2n^2\pi^2}{\min(|k_n|)^2} + \frac{n^4\pi^4}{\min(|k_n|)^4}\right) \|f_n\|^2_{\mathrm{L}^2(-r,r)},\end{aligned}$$

and so

$$\begin{aligned}\|\nabla^2 u\|^2_{\mathrm{L}^2(\Omega_r)} \leq \alpha^2 \max \Bigg[& \left((k_N^2+1)^2 + 2N^2\pi^2 + N^4\pi^4\right) \\ & + \left(\left(\frac{|k_{N+1}|^2}{\delta^2} + 1\right)^2 + \frac{2(N+1)^2\pi^2}{\delta^2} + \frac{(N+1)^4\pi^4}{\delta^4}\right)\Bigg] \|f\|^2_{\mathrm{L}^2(\Omega_r)}.\end{aligned}$$

□

Source b. Using the same arguments as before, the equation (4.54) is equivalent to

$$\forall n \in \mathbb{N} \qquad \begin{cases} u_n'' + k_n^2 u_n = -b_{\mathrm{top}}\varphi_n(1) - b_{\mathrm{bot}}\varphi_n(0) & \text{in } \mathbb{R}, \\ u_n \text{ is outgoing}, \end{cases}$$

and we know that

$$\forall n \in \mathbb{N} \qquad u_n(x) = \int_{\mathbb{R}} G_n(x,s)(b_{\mathrm{top}}\varphi_n(1) + b_{\mathrm{bot}}\varphi_n(0))\mathrm{d}s.$$

We notice that $|\varphi_n(1)|, |\varphi_n(0)| \leq \sqrt{2}$. Using Theorem 2.3.2.9 in [47], there exist a constant $d(r)$ and $\mu > 0$ such that

$$\|u\|_{\mathrm{H}^2(\Omega_r)} \leq d(r) \left(\left\|-\partial_{xx}u - \frac{1}{h^2}\partial_{yy}u + \mu u\right\|_{\mathrm{L}^2(\Omega_r)} + \|b_{\mathrm{top}}\|_{\widetilde{\mathrm{H}}^{1/2}(-r,r)} + \|b_{\mathrm{bot}}\|_{\widetilde{\mathrm{H}}^{1/2}(-r,r)}\right),$$

and it follows that

$$\|u\|_{\mathrm{H}^2(\Omega_r)} \leq d(r) \left((k^2+\mu)\|u\|_{\mathrm{L}^2(\Omega_r)} + \|b_{\mathrm{top}}\|_{\widetilde{\mathrm{H}}^{1/2}(-r,r)} + \|b_{\mathrm{bot}}\|_{\widetilde{\mathrm{H}}^{1/2}(-r,r)}\right).$$

Finally,

$$\|u\|^2_{\mathrm{L}^2(\Omega_r)} \leq 2\alpha^2 \left(\|b_{\mathrm{top}}\|^2_{\widetilde{\mathrm{H}}^{1/2}(-r,r)} + \|b_{\mathrm{bot}}\|^2_{\widetilde{\mathrm{H}}^{1/2}(-r,r)}\right) \left(N + 1 + \sum_{n>N} \frac{1}{\min(|k_n|)^4}\right),$$

which concludes the proof. □

5

Reconstruction of smooth shape defects in waveguides using locally resonant frequencies surface measurements

This chapter uses the study of the forward problem presented in Chapter 4 to develop a new method to reconstruct slowly varying width defects in 2D acoustic waveguides using locally resonant frequencies. At these frequencies, locally resonant modes propagate in the waveguide under the form of Airy functions depending on a parameter called the locally resonant point. In this particular point, the local width of the waveguide is known and we use the shape of the wavefields to recover its location. Using the same process for different frequencies, we produce a good approximation of the width in all the waveguide. Given multi-frequency measurements taken at the surface of the waveguide, we provide a L^∞-stable explicit method to reconstruct the width of the waveguide. We finally validate our method on numerical data, and we discuss its applications and limits.

5.1 Introduction

This chapter presents a new method to reconstruct width variations of a slowly varying waveguide from multi-frequency surface measurements in dimension 2. The considered varying waveguide is described by

$$\Omega := \left\{(x, y) \in \mathbb{R}^2 \,|\, 0 < y < h(x)\right\}, \tag{5.1}$$

where $h \in \mathcal{C}^2(\mathbb{R}) \cap W^{2,\infty}(\mathbb{R})$ is a positive profile function defining the top boundary. The bottom boundary is assumed to be flat (see an illustration in Figure 5.1) but a similar analysis could be done when both boundaries are varying. In the time-harmonic regime, the wavefield u satisfies the Helmholtz equation with Neumann boundary conditions

$$\left\{\begin{array}{rl} \Delta u + k^2 u = -f & \text{in } \Omega, \\ \partial_\nu u = b & \text{on } \partial\Omega, \end{array}\right. \tag{5.2}$$

where $k \in (0, +\infty)$ is the frequency, f is an interior source term, and b is a boundary source term. In this work, a waveguide is said to be slowly varying when there exists a small parameter $\eta > 0$ such that $\|h'\|_{\mathrm{L}^\infty(\mathbb{R})} \leq \eta$ and $\|h''\|_{\mathrm{L}^\infty(\mathbb{R})} \leq \eta^2$. Such waveguides are good models of ducts, corroded pipes, or metal plates (see [50, 59]).

We focus in this work on the recovery of the function h modeling the waveguide shape from the knowledge of the wavefield $d^{\text{ex}}(x) := u(x, 0)$ on one surface of the waveguide and for multiple frequencies k. This model and inverse problem is inspired from non destructive monitoring of plates done in [11, 58, 29]. Hence we assume the knowledge of measurements of $u(x, y)$ for $x \in \mathbb{R}$ and $y = 0$ in a frequency interval $K \subset (0, +\infty)$, as shown in Figure 5.1.

If k is chosen such that $k = n\pi/h(x_k^\star)$ with $n \in \mathbb{N}$ and $x_k^\star \in \mathbb{R}$, the Helmholtz problem is not well posed in general. Nevertheless, we proved in Chapter 4 that there exists a unique solution to this problem as long as the waveguide is slowly varying. In the same work, we also give a suitable explicit approximation of the wavefield that explicitly depends on $x_k^\star$. The aim in this chapter is to recover the position of $x_k^\star$ for different frequencies also called *locally resonant frequencies*, and then the shape function h. Using these frequencies, the proposed inverse problem is highly non linear but a unique and stable recovering of h is possible up to a controllable approximation error.

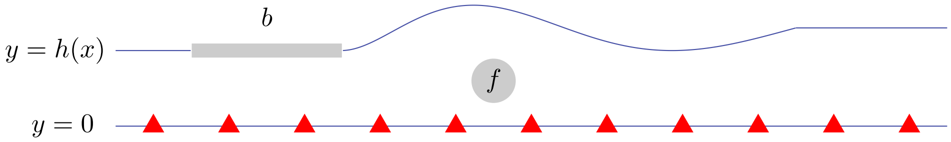

Figure 5.1 – Parametrization of a slowly variable waveguide of width h. A wavefield u is generated by an internal source f and a boundary source b. Triangles represent measurements of u taken on the surface $y = 0$.

5.1.1 Scientific context

The detection and reconstruction of shape defects in a waveguide are mentioned in different works. In articles [61, 3, 2], the authors use a conformal mapping to map the geometry of the perturbed waveguide to that of a regular waveguide. This method is beneficial to understand the propagation of waves in irregular waveguides. Still, it is not easily adaptable to the inverse problem and the reconstruction of defects since the transformation to a regular waveguide is not explicit and proves numerically expensive. Another approach based on the scattering field treatment is developed in [75]. Finally, articles [81, 43] study the forward problem and give leads on how to use surface measurements to reconstruct the width of a slowly varying waveguide.

Our work concerns a different approach, also used in [13, 12], where we assume the data to be available for a whole interval of frequencies. This provides additional information that should help localize and reconstruct the shape of the defect. Moreover, the use of multi-frequency data often provides uniqueness of the reconstruction (see [7]) and better stability (see [14, 52, 93]).

In our previous work done in Chapter 2, we already presented a method to reconstruct small width variations using back scattering data. However, we avoided all the cut-off frequencies of the waveguide, which are frequencies $k > 0$ such that $k = n\pi/h(x_k^\star)$ for a mode $n \in \mathbb{N}$ and a longitudinal position $x_k^\star$. Since experimental works presented in [11, 29] suggest that these resonant frequencies are helpful to reconstruct width variations, we choose in this chapter to work only with these frequencies. Using the study of the forward problem already done in Chapter 4, we know that if k is a locally resonant frequency, the wavefield u strongly depends on $x_k^\star$. The main idea of our reconstruction method is to use measurements of u to find back $x_k^\star$. Since $h(x_k^\star) = n\pi/k$, it then gives up the information about the waveguide's width in one point. By taking different locally resonant frequencies k, we show that we can obtain a complete approximation of the width h of the waveguide.

5.1.2 Outline of the chapter

The key result of this chapter is Theorem 5.2, which proves that u is close to a three parameters Airy function, one parameter being $x_k^\star$. As explained in Proposition 5.3, it enables us to find the value of $x_k^\star$ for every locally resonant frequency, and to prove that our reconstruction method is L^∞-stable. The chapter is organized as follows. In section 5.2, we briefly recall results on the modal decomposition and the study of the forward problem. In section 5.3, we study the inverse problem with measurements taken at the surface of the waveguide and we provide a stability result for the reconstruction of the width of the waveguide. Finally, in section 5.4, we provide numerical reconstruction of different width defects.

5.2 Brief study of the forward problem

Before studying the inverse problem associated with the reconstruction of the width in a varying waveguide, we need to study the forward problem in order to find an approximation of the available data. In this section, we briefly recall all the main results on the study of the forward problem. These results and their proofs can be found in Chapter 2 and [27].

A useful tool when working in waveguides is the modal decomposition. The following definition provides a modal decomposition in varying waveguides:

Definition 5.1. *We define the sequence of functions* $(\varphi_n)_{n\in\mathbb{N}}$ *by*

$$\forall (x,y) \in \Omega, \quad \varphi_n(x,y) := \begin{cases} 1/\sqrt{h(x)} & \text{if } n = 0, \\ \dfrac{\sqrt{2}}{\sqrt{h(x)}} \cos\left(\dfrac{n\pi y}{h(x)}\right) & \text{if } n \geq 1, \end{cases} \tag{5.3}$$

which for any fixed $x \in \mathbb{R}$ *defines an orthonormal basis of* $L^2(0, h(x))$.

Hence, a solution $u \in \mathrm{H}^2_{\mathrm{loc}}(\Omega)$ of (5.2) admits a unique modal decomposition

$$u(x,y) = \sum_{n\in\mathbb{N}} u_n(x)\varphi_n(x,y) \quad \text{where} \quad u_n(x) := \int_0^{h(x)} u(x,y)\varphi_n(x,y)\mathrm{d}y. \tag{5.4}$$

Note that u_n does not satisfy in general any nice equation. However, when h is constant (outside of $\mathrm{supp}(h')$), it satisfies an equation of the form $u_n'' + k_n^2 u_n = -g_n$ where $k_n = \sqrt{k^2 - n^2\pi^2/h^2}$ is the wavenumber. When h is variable, the decomposition (5.4) motivates the following definition:

Definition 5.2. *The local wavenumber function of the mode $n \in \mathbb{N}$ is the complex function $k_n : \mathbb{R} \to \mathbb{C}$ defined by*

$$k_n^2(x) := k^2 - \frac{n^2\pi^2}{h(x)^2}, \tag{5.5}$$

with $Re(k_n), Im(k_n) \geq 0$.

In this work, as $h(x)$ is non constant, $k_n(x)$ may vanish for some $x \in \mathbb{R}$ and change from a positive real number to a purely imaginary one. We then distinguish three different situations:

Definition 5.3. *A mode $n \in \mathbb{N}$ falls in one of these three situations:*

1. *If $n < kh(x)/\pi$ for all $x \in \mathbb{R}$ then $k_n(x) \in (0, +\infty)$ for all $x \in \mathbb{R}$ and the mode n is called propagative.*
2. *If $n > kh(x)/\pi$ for all $x \in \mathbb{R}$ then $k_n(x) \in i(0, +\infty)$ for all $x \in \mathbb{R}$ and the mode n is called evanescent.*
3. *If there exists $x_k^\star \in \mathbb{R}$ such that $n = kh(x_k^\star)/\pi$ the mode n is called locally resonant. Such points $x_k^\star$ are called resonant points, and there are simple if $h'(x_k^\star) \neq 0$, and multiple otherwise.*

A frequency $k > 0$ for which there exists at least a locally resonant mode is called a locally resonant frequency.

Using the wavenumber function, one can adapt the classic Sommerfeld (or outgoing) condition, defined in Chapter 2 for regular waveguides, to general varying waveguides Ω. This condition is used to guarantee uniqueness for the source problem given in equation (5.2).

Definition 5.4. *A wavefield $u_k \in H^2_{loc}(\Omega)$ is said to be outgoing if it satisfies*

$$\left| u_n'(x)\frac{x}{|x|} - ik_n(x)u_n(x) \right| \underset{|x|\to+\infty}{\longrightarrow} 0 \qquad \forall n \in \mathbb{N}, \tag{5.6}$$

where u_n is given in (5.4).

In all this work, we make the following assumptions:

Assumption 5.1. *We assume that $h \in \mathcal{C}^2(\mathbb{R}) \cap W^{2,\infty}(\mathbb{R})$ with h' compactly supported and that*

$$\forall x \in \mathbb{R} \quad h_{\min} \leq h(x) \leq h_{\max} \qquad \textit{for some } 0 < h_{max} < h_{\min} < \infty.$$

We also assume that $h(x) = h_{\min}$ or $h(x) = h_{\max}$ if $x \notin supp(h')$. For such a function we define a parameter $\eta > 0$ that satisfies for a constant $R > 0$

$$\|h'\|_{L^\infty(\mathbb{R})} < \eta \qquad \textit{and} \qquad \|h''\|_{L^\infty(\mathbb{R})} < \eta^2, \quad supp\, h' \subset \left(-\frac{R}{\eta}, \frac{R}{\eta}\right).$$

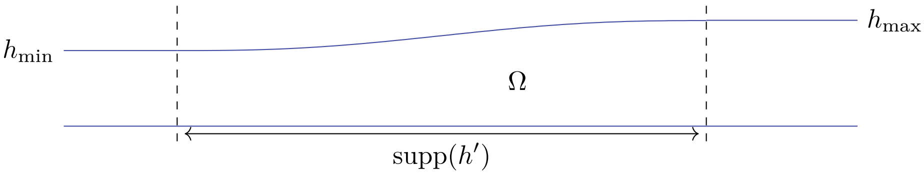

Figure 5.2 – Representation of an increasing slowly and compactly varying waveguide.

Such a waveguide is represented in Figure 5.2.

The forward source problem is defined for every frequency by

$$(\mathcal{H}_k): \quad \begin{cases} \Delta u + k^2 u = -f & \text{in } \Omega, \\ \partial_\nu u = b_{\text{top}} & \text{in } \partial\Omega_{\text{top}}, \\ \partial_\nu u = b_{\text{bot}} & \text{in } \partial\Omega_{\text{bot}}, \\ u \text{ is outgoing}, & \end{cases} \tag{5.7}$$

As explained in [27], this problem is not well-posed when $\{x \,|\, k_n(x) = 0\}$ is a non-trivial interval of $\mathbb{R}$. This especially happens when $k = n\pi/h_{\text{min}}$ or $k = n\pi/h_{\text{max}}$. We then avoid these two forbidden situations and we set

$$\delta(k) := \min_{n\in\mathbb{N}} \left(\sqrt{\left| k^2 - \frac{n^2\pi^2}{{h_{\text{min}}}^2} \right|}, \sqrt{\left| k^2 - \frac{n^2\pi^2}{{h_{\text{max}}}^2} \right|} \right). \tag{5.8}$$

From now on, we define $(f_n)_{n\in\mathbb{N}}$ the modal decomposition of f, and

$$g_n(x) = \frac{f_n(x)}{\sqrt{h(x)}} + \varphi_n(1) b_{\text{top}}(x) \frac{\sqrt{1 + (h'(x))^2}}{\sqrt{h}} + \varphi_n(0) b_{\text{bot}}(x) \frac{1}{\sqrt{h}}. \tag{5.9}$$

Using the work done in Chapter 4, we are able to provide an approximation of the solution of (5.7). If h is increasing, we can state the following result using Theorem 4.1 and Remark 4.3 in Chapter 4.

Theorem 5.1. *Let h be an increasing function defining a varying waveguide Ω that satisfies Assumption 5.1 with a variation parameter $\eta > 0$. Consider sources $f \in L^\infty_c(\Omega)$, $b := (b_{bot}, b_{top}) \in (H^{1/2}(\mathbb{R}))^2 \cap (L^\infty_c(\mathbb{R})^2)$. Assume that there is a unique locally resonant mode $N \in \mathbb{N}$, associated with a simple resonant point $x^\star_k \in \mathbb{R}$. Let $I \subset \mathbb{R}$ be an interval of length $R > 0$, and $\Omega_I := \{(x, y) \in \Omega \,|\, x \in I\}$.*

There exists $\eta_0 > 0$ depending only on h_{min}, h_{max}, $\delta(k)$ and R such that if $\eta \leq \eta_0$, then the problem $(\mathcal{H}_k)$ admits a unique solution $u \in H^2_{loc}(\Omega)$. Moreover, this solution is approached by u^{app} defined for almost every $(x, y) \in \Omega$ by

$$u^{app}(x, y) := \sum_{n\in\mathbb{N}} \left(\int_{\mathbb{R}} G^{app}_n(x, s) g_n(s) \mathrm{d}s \right) \varphi_n(y), \tag{5.10}$$

where $(f_n)_{n\in\mathbb{N}}$ *is the modal decomposition of* f*,* φ_n *is defined in* (5.3) *and* G_n^{app} *is given by*

$$G_n^{app}(x,s) := \begin{cases} \dfrac{i}{2\sqrt{k_n(s)k_n(x)}} \exp\left(i\left|\displaystyle\int_s^x k_n\right|\right), & \text{if } n < N, \\ \dfrac{1}{2\sqrt{|k_n|(s)|k_n|(x)}} \exp\left(-\left|\displaystyle\int_s^x |k_n|\right|\right), & \text{if } n > N, \\ \begin{cases} \dfrac{\pi(\xi(s)\xi(x))^{1/4}}{\sqrt{k_n(s)k_n(x)}}(i\mathcal{A}+\mathcal{B})\circ\xi(s)\mathcal{A}\circ\xi(x) & \text{if } x < s, \\ \dfrac{\pi(\xi(s)\xi(x))^{1/4}}{\sqrt{k_n(s)k_n(x)}}(i\mathcal{A}+\mathcal{B})\circ\xi(x)\mathcal{A}\circ\xi(s) & \text{if } x > s, \end{cases} & \text{if } n = N. \end{cases} \tag{5.11}$$

Function k_n *is the wavenumber function defined in Definition 5.2 and the function* ξ *is given by*

$$\xi(x) := \begin{cases} \left(-\dfrac{3}{2}i\displaystyle\int_x^{x_k^\star} k_N(t)\mathrm{d}t\right)^{2/3} & \text{if } x < x_k^\star, \\ -\left(\dfrac{3}{2}\displaystyle\int_{x_k^\star}^x k_N(t)\mathrm{d}t\right)^{2/3} & \text{if } x > x_k^\star. \end{cases} \tag{5.12}$$

Precisely, there exist a constant $C_1 > 0$ *depending only on* $h_{\min}$*,* $h_{\max}$ *and* N *such that*

$$\|u - u^{app}\|_{H^1(\Omega_I)} \leq \eta C_1 R^2 \delta(k)^{-8}\left(\|f\|_{L^2(\Omega)} + \|b\|_{\left(H^{1/2}(\mathbb{R})\right)^2}\right). \tag{5.13}$$

This result provides an approximation of the measurements of the wavefield for every frequency, and a control of the approximation error. We represent in Figure 5.3 the wavefield for different frequencies. We also point out in Figure 5.4 that the source should be located in an area where $h > h(x^\star)$ in order to generated a significant locally resonant mode.

We notice that at locally resonant frequencies, the wavefield strongly depends on the position of $x_k^\star$, which justify the idea of using it to develop an inverse method to reconstruct the width h. This method is based on surface measurements of the wavefield, meaning that we have access to

$$d^{\text{ex}} := u(x,0) \qquad \forall k > 0 \quad \forall x \in I. \tag{5.14}$$

An illustration is provided in Figure 5.5 with a representation of the wavefield u and the surface measurement $u(x,0)$ when k is a locally resonant frequency.

5.3 Shape Inversion using a monochromatic source

In this section, we describe the method to recover the width h from surface measurements of the wavefield at locally resonant frequencies. We focus here on the reconstruction of the shape of h on $\operatorname{supp}(h')$, assuming the *a priori* knowledge of the constants $h_{\min}$ and $h_{\max}$ and of an interval containing $\operatorname{supp}(h')$. We detail in Appendix 5.A how these constants can be estimated. To recover the shape function h on $\operatorname{supp}(h')$, we start by studying the simpler case of a source term f generating only a single locally resonant mode in the waveguide. Hence we assume that f takes the form

$$\forall (x,y) \in \Omega \quad f(x,y) = f_N(x)\varphi_N(y), \qquad f_N \in \mathrm{L}^2(\mathbb{R}), \tag{5.15}$$

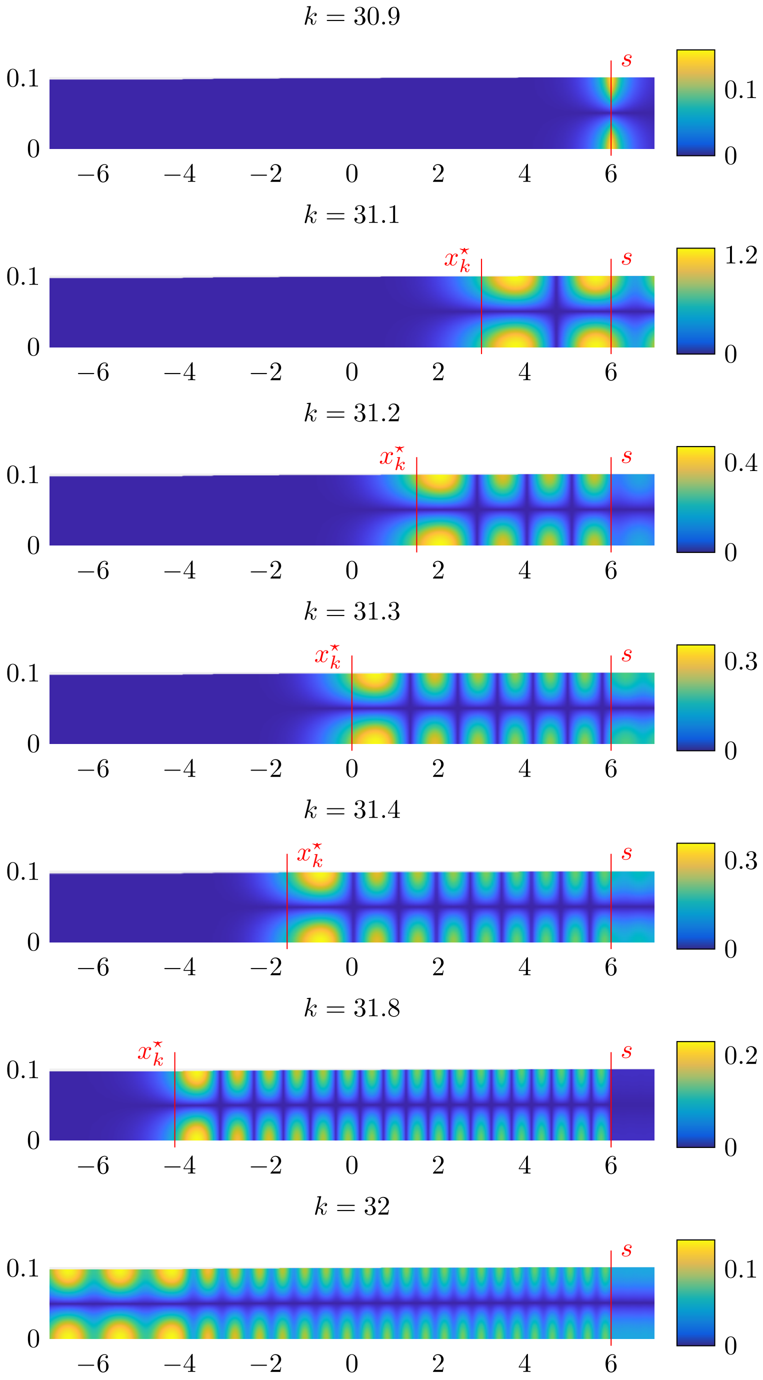

Figure 5.3 – Representation of the wavefield $|u|$ solution of (5.7) with a monochromatic source $f(x, y) = \delta_{x=6}\varphi_1(y)$ for different frequencies k. When $k = 30.9$, the mode $n = 1$ is evanescent, and the wavefield decreases very fast around the source. When $k = 31.1, 31.2, 31.3, 31.4, 31.8$, the mode $n = 1$ is locally resonant and the wavefield propagates in the waveguide as an Airy function until it reaches the point $x_k^\star$. When $k = 32$, the mode $n = 1$ is propagative and the wavefield propagates in all the waveguide. In all these representations, the width h is defined by the function (5.52).

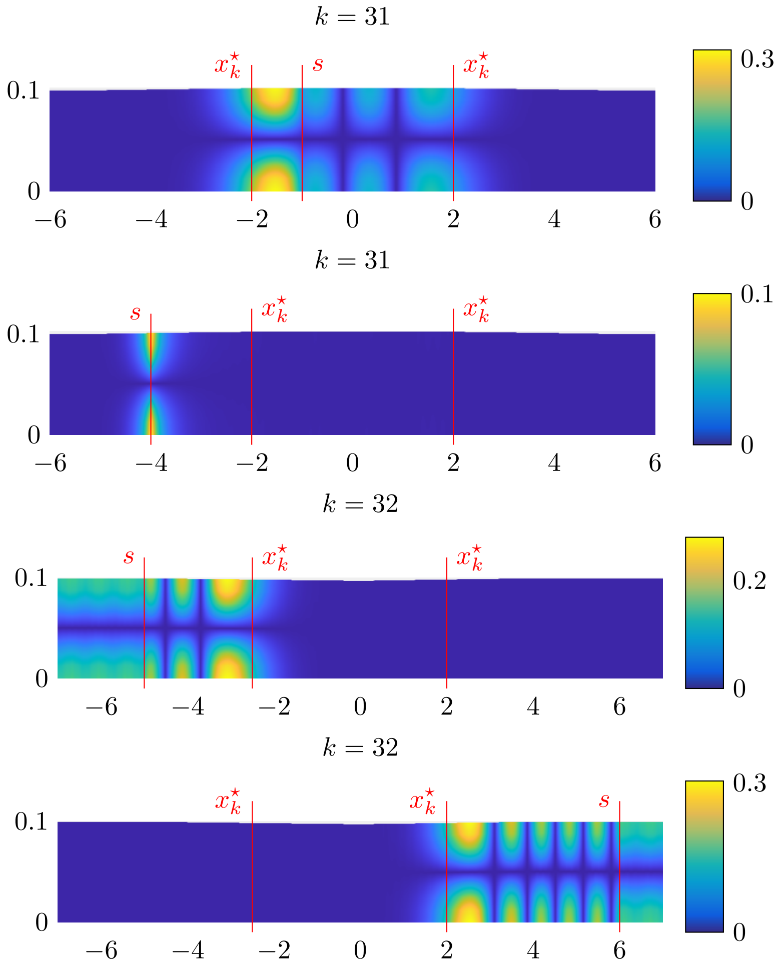

Figure 5.4 – Representation of the wavefield $|u|$ solution of (5.7) with a monochromatic source $f(x, y) = \delta_{x=s}\varphi_1(y)$ for different positions s. On the first two pictures, h is a dilation defined in (5.55) and on the last two pictures, h is a shrinkage defined in (5.56). Depending on the location of the source, we observe different behaviors. For the dilation, when s is located between the positions $x_k^\star$ the mode is locally resonant, while it is evanescent if s is outside the positions $x_k^\star$. For the shrinkage and the mode is locally resonant when s is outside the positions $x_k^\star$. In order to generate a significant locally resonant mode, the source s should be placed at a width where $h(s) > h(x_k^\star)$ and the mode only propagates until it reaches the point $x_k^\star$.

where f_N is compactly supported. We also assume the absence of boundary source term, meaning that $b = 0$. This simplified situation is useful to understand the method of reconstruction. It will be generalized to any kind of internal and boundary sources in section 5.4.

In the simplest case of a single internal source (5.15), we know from the study of the forward problem in Theorem 5.1 that the measured data without noise d^{ex} satisfies

$$d^{\text{ex}}(x) := u(x, 0) \approx u_N^{\text{app}}(x)\varphi_N(0) \quad \text{where} \quad u_N^{\text{app}}(x) = \int_{\mathbb{R}} G_N^{\text{app}}(x, s) f_N(s)\text{d}s. \tag{5.16}$$

Our reconstruction method is based on the recovery of the resonant $x_k^\star$ for every locally resonant frequencies k. It can be seen in Theorem 5.1 that the approached Green function G_N^{app} depends on

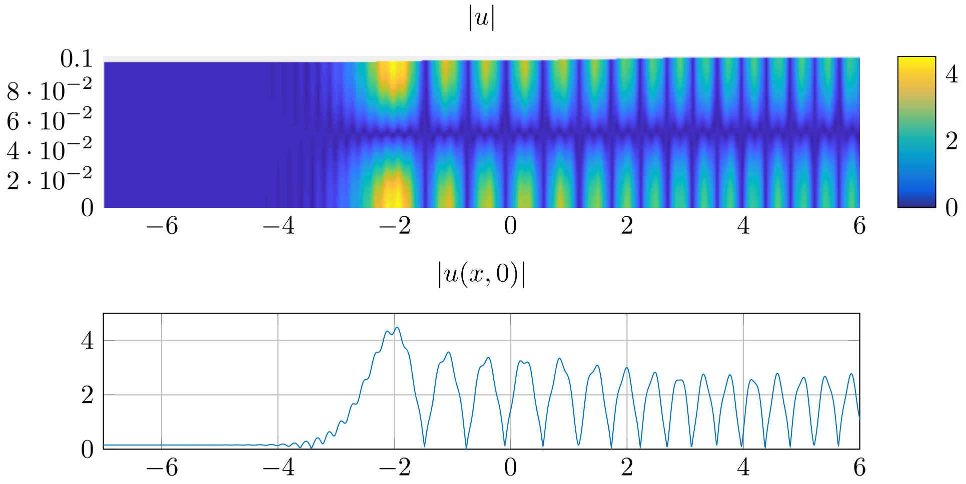

Figure 5.5 – Illustration of the wavefield measurements in a varying waveguide. The wavefield u is solution of (5.7) where the profile h is given in (5.52) and $k = 31.5$ is a locally resonant frequency. Data are generated using the finite element method described in section 5.5.1. Top: amplitude of $|u|$ in the whole waveguide Ω (non scaled). Bottom: amplitude of the measurements of $|u|$ on the surface $y = 0$.

$x_k^\star$ through the function ξ. However, this dependence is intricate and hardly usable to find a direct link between d^{ex} and $x_k^\star$. Thus we need to find a simpler approximation of the measurements. In a first part, we provide an approximation of measured data d^{ex} using a three parameters model function

$$d^{\text{app}}_{z,\alpha,x_k^\star} : x \mapsto z\mathcal{A}(\alpha(x_k^\star - x)), \tag{5.17}$$

where $z \in \mathbb{C}^*$ is a complex amplitude, $\alpha > 0$ is a scaling parameter and $x_k^\star$ is the resonant point playing the role of a longitudinal shift. In a second part, we first control the approximation error between this function and the exact measurements and then, we develop a stable way to reconstruct $x_k^\star$ from this approximated data.

5.3.1 Wavefield approximation and measurements approximation

In order to find a reconstruction of $x_k^\star$, we need to find an exploitable link between $d^{\text{ex}} := u(x,0)$ and $x_k^\star$. To do so, we make a Taylor expansion of G_N^{app} around the point $x_k^\star$. For every frequency $k > 0$ and $R > 0$, we denote

$$\Omega_R(x_k^\star) := \{(x,y) \in \Omega \mid |x - x_k^\star| < R\}, \qquad \Gamma_R(x_k^\star) := (x_k^\star - R, x_k^\star + R), \tag{5.18}$$

and we consider the Taylor expansion on the interval Γ_R. Moreover, we assume that the source is located at the right of the interval Γ_R, and we define

$$\Omega_R^+(x_k^\star) := \{(x,y) \in \Omega \,|\, x - x_k^\star > R\}, \qquad \Gamma_R^+(x_k^\star) = (x_k^\star + R, +\infty). \tag{5.19}$$

Both these sets are represented in Figure 5.6.

The following Proposition shows that u_N^{app} can be approached by a three parameters function of type $d^{\text{app}}_{z,\alpha,x_k^\star}$ if the shape function h is steep enough at $x_k^\star$.

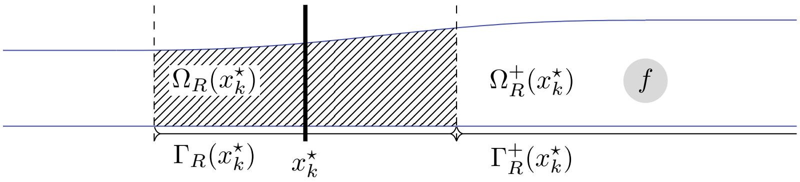

Figure 5.6 – Representation of $\Gamma_R(x_k^\star)$, $\Omega_R(x_k^\star)$, $\Gamma_R^+(x_k^\star)$ and $\Omega_R^+(x_k^\star)$. The source f is assumed to be compactly supported in $\Gamma_R^+(x_k^\star)$.

Proposition 5.1. *Assume that Ω satisfies assumptions 5.1, let $R > 0$ and $k > 0$ be a locally resonant frequency associated to the mode $N \in \mathbb{N}$ and the locally resonant point $x_k^\star$ that satisfies $h'(x_k^\star) \geq \theta\eta$ for some $\theta > 0$. There exist $z \in \mathbb{C}^*$, $\alpha > 0$ and a constant $C_2 > 0$ depending only on $h_{\min}$, $h_{\max}$, N and θ such that*

$$\|u_N^{app} - d_{z,\alpha,x_k^\star}^{app}\|_{L^2(\Gamma_R(x_k^\star))} \leq C_2 \left(R^{3/2}\eta^{5/6} + R^{5/2}\eta^{7/6}\right). \tag{5.20}$$

Proof. Using the information about the support of the source term, we know that

$$u_N^{\text{app}}(x) = \int_{x_k^\star+R}^{+\infty} G_N^{\text{app}}(x,s) f_N(s) \mathrm{d}s.$$

Using the definition of G_N^{app} given in (5.11), there exists a function q_k such that for every $x \in \Gamma_R(x_k^\star)$,

$$G_N^{\text{app}}(x,s) = q_k(s) \frac{(-\xi(x))^{1/4}}{\sqrt{k_n(x)}} \mathcal{A}(\xi(x)).$$

It follows that

$$u_N^{\text{app}}(x) = \frac{(-\xi(x))^{1/4}}{\sqrt{k_n(x)}} \mathcal{A}(\xi(x)) \int_{x_k^\star+R}^{+\infty} q_k(s) f_N(s) \mathrm{d}s.$$

In the following, we denote $\mathcal{O}(\cdot)$ bounds depending only on $h_{\max}$, $h_{\min}$ and N. We see that

$$k_N(x)^2 = \frac{2N^2\pi^2 h'(x_k^\star)}{h(x_k^\star)^3}(x - x_k^\star) + \mathcal{O}(\eta^2(x-x_k^\star)^2).$$

From now on, we assume that $x > x_k^\star$, which leads to

$$k_N(x) = \sqrt{\frac{2N^2\pi^2 h'(x_k^\star)}{h(x_k^\star)^3}}(x - x_k^\star)^{1/2} + \mathcal{O}\left(\frac{\eta^2(x-x_k^\star)^{3/2}}{\sqrt{h'(x_k^\star)}}\right), \tag{5.21}$$

and so

$$\xi(x) = \left(\frac{2N^2\pi^2 h'(x_k^\star)}{h(x_k^\star)^3}\right)^{1/3}(x_k^\star - x) + \mathcal{O}\left(\frac{\eta^2(x-x_k^\star)^2}{h'(x_k^\star)^{2/3}}\right).$$

Then,

$$\mathcal{A}(\xi(x)) = \mathcal{A}\left(\left(\frac{2N^2\pi^2 h'(x_k^\star)}{h(x_k^\star)^3}\right)^{1/3}(x_k^\star - x)\right) + \mathcal{O}\left(\frac{\eta^2(x-x_k^\star)^2}{h'(x_k^\star)^{2/3}}\right),$$

and

$$\frac{(-\xi(x))^{1/4}}{\sqrt{k_N(x)}} = \left(\frac{2N^2\pi^2 h'(x_k^\star)}{h(x_k^\star)^3}\right)^{-1/6} + \mathcal{O}\left(\frac{\eta^2(x-x_k^\star)}{h'(x_k^\star)^{7/6}}\right).$$

We set

$$z = \left(\frac{2N^2\pi^2 h'(x_k^\star)}{h(x_k^\star)^3}\right)^{-1/6} \int_{x_k^\star+R}^{+\infty} q_k(s) f_N(s)\mathrm{d}s, \qquad \alpha = \left(\frac{2N^2\pi^2 h'(x_k^\star)}{h(x_k^\star)^3}\right)^{1/3}, \tag{5.22}$$

and it follows that

$$u_N^{\mathrm{app}}(x) = z\mathcal{A}(\alpha(x_k^\star - x)) + \mathcal{O}\left(\frac{\eta^2(x-x_k^\star)}{h'(x_k^\star)^{7/6}}\right) + \mathcal{O}\left(\frac{\eta^2(x-x_k^\star)^2}{h'(x_k^\star)^{5/6}}\right).$$

The exact same study can be done in the case $x < x_k^\star$. Since $|x - x_k^\star| \leq R$, we conclude that

$$\|u_N^{\mathrm{app}} - d^{\mathrm{app}}_{z,\alpha,x_k^\star}\|_{\mathrm{L}^2(\Gamma_R(x_k^\star))} = \eta^2\mathcal{O}\left(R^{3/2}(h'(x_k^\star))^{-7/6} + R^{5/2}(h'(x_k^\star))^{-5/6}\right).$$

To conclude, we use the fact that $h'(x_k^\star) \geq \theta\eta$. □

Corollary 5.1. *Assume that Ω satisfies assumptions 5.1, let $R > 0$ and $k > 0$ be a locally resonant frequency associated to the mode $N \in \mathbb{N}$ and the locally resonant point $x_k^\star$ that satisfies $h'(x_k^\star) \geq \theta\eta$ for some $\theta > 0$. There exist $\eta > 0$ such that if $\eta \leq \eta_0$ then there exist $z \in \mathbb{C}^*$, $\alpha > 0$ and a constant $C_3 > 0$ depending only on $h_{\min}$, $h_{\max}$, N and θ such that*

$$\|d^{ex} - d^{app}_{z,\alpha,x_k^\star}\|_{L^2(\Gamma_R(x_k^\star))} \leq C_3\left(\delta(k)^{-8}R^2\eta + R^{3/2}\eta^{5/6} + R^{5/2}\eta^{7/6}\right). \tag{5.23}$$

Proof. We apply Proposition 5.1, Theorem 5.1 and trace results which prove that there exists a constant $\gamma > 0$ depending only on R, $h_{\min}$ and $h_{\max}$ such that

$$\|u(\cdot,0) - u^{\mathrm{app}}(\cdot,0)\|_{\mathrm{L}^2(\Gamma_R(x_k^\star))} \leq \|u - u^{\mathrm{app}}\|_{\mathrm{H}^{1/2}(\Gamma_R(x_k^\star))} \leq \gamma\|u - u^{\mathrm{app}}\|_{\mathrm{H}^1(\Omega_R(x_k^\star))}.$$

□

This result indicates a strategy to determine $x_k^\star$ from the exact data d^{ex}. Assuming that η is small enough to see $d^{\mathrm{app}}_{z,\alpha,x_k^\star}$ as a good approximation of d^{ex}, one may fit the three parameters $(\alpha, z, x_k^\star)$ that minimize the misfit $d^{\mathrm{ex}} - d^{\mathrm{app}}_{z,\alpha,x_k^\star}$ for some norm. We also see from this result that the error in the Taylor expansion strongly depends on the values of θ, R and $\delta(k)$. Since we plan on using different locally resonant frequencies, we need to get a uniform control over k on the Taylor expansion. Moreover, we need to control the length R of the measurement interval. If R is too large, the quality of the Taylor expansion diminishes and if R is too small, the data on the interval $\Gamma_R(x_k^\star)$ may not contain enough information to fit the three parameters $(z, \alpha, x_k^\star)$ with stability.

To prevent this, R needs to be scaled depending on the parameter α. Indeed, the change of variable $x \mapsto \alpha(x_k^\star - x)$ must cover a large enough interval to perform the desired fitting. Using the expression of α given in (5.22), we say that $\alpha(x_k^\star - x)$ covers an interval of fixed radius $\sigma > 0$ if

$$R \geq \frac{\sigma}{\alpha} \geq \frac{\sigma h_{\max}}{2\beta^{1/3}N^2\pi^2}\eta^{-1/3}.$$

This means that R needs to be scaled as $\eta^{-1/3}$ and we assume now that

$$R = R(\eta) := r\eta^{-1/3}. \tag{5.24}$$

where $r > 0$ is a constant. We can now give a uniform approximation result between d^{ex} and $d^{\mathrm{app}}_{z,\alpha,x_k^\star}$ on the interval $\Gamma_{R(\eta)(x_k^\star)}$.

Theorem 5.2. *Under the hypotheses of Theorem 5.1, and fix* $N \in \mathbb{N}^*$ *and* $\theta > 0$*. There exists* $\eta_0 > 0$ *such that if* $\eta < \eta_0$*, then for any locally resonant frequency* $k > 0$ *associated to the mode* N *and the locally resonant point* $x_k^\star$ *satisfying* $h'(x_k^\star) \geq \theta\eta$*, there exist* $\alpha > 0$ *and* $z \in \mathbb{C}$ *such that the following approximation holds on* $\Gamma_{R(\eta)}(x_k^\star)$*:*

$$d^{ex} = d^{app}_{z,\alpha,x_k^\star} + \mathcal{O}(\eta^{1/3}).$$

More precisely, there exists a constant $C_4 > 0$ *depending only on* $h_{\min}$*,* $h_{\max}$*,* θ *and* r *such that*

$$\left\| d^{ex} - d^{app}_{z,\alpha,x_k^\star} \right\|_{L^2(\Gamma_{R(\eta)}(x_k^\star))} \leq C_4 \eta^{1/3}. \tag{5.25}$$

Proof. To prove this result, we need to provide a uniform lower bound for $\delta(k)$ under the hypothesis $h'(x_k^\star) \geq \theta\eta$. From the definition of $\delta(k)$, we assume without loss of generality that $\delta(k)$ is reached by the mode number $N \in \mathbb{N}$ and that $\delta(k)^2 = \left|k^2 - N^2\pi^2/h_{\max}^2\right|$. Hence, as k is locally resonant, we know that $k = N\pi/h(x_k^\star)$ and that

$$\delta(k)^2 = N^2\pi^2 \left| \frac{1}{h(x_k^\star)^2} - \frac{1}{h_{\max}^2} \right| \leq \frac{2N^2\pi^2}{h_{\min}^2 h_{\max}} (h_{\max} - h(x_k^\star)).$$

Let us call $t \geq 0$ such that $h(x_k^\star + t) = h_{\max}$, we necessarily have $h'(x_k^\star + t) = 0$. Using the hypothesis $h'' \geq -\eta^2$, we know that $h'(x_k^\star + s) \geq \eta\theta - \eta^2 s$ for all $s \in (0,t)$. This implies that $t \geq \theta/\eta$. Then,

$$h_{\max} - h(x_k^\star) = \int_0^t h'(x_k^\star + s)\mathrm{d}s \geq \eta\theta t - \eta^2 \frac{t^2}{2} \geq \frac{\theta^2}{2}.$$

Then,

$$\delta(k) \geq \frac{N\pi}{h_{\min}\sqrt{h_{\max}}}\theta.$$

The proof of Theorem 5.2 is now straightforward, we simply replace R by $r\eta^{-1/3}$ in Corollary 5.1 and use the lower bound on $\delta(k)$. ☐

Remark 5.1. *We underline the fact that the constant in this estimation depends on the value of* θ*, and tends toward infinity if* θ *tends to zero. This result is illustrated in Figure 5.7 where we clearly notice that the error between* d^{ex} *and* $d^{app}_{z,\alpha,x_k^\star}$ *deteriorates when* θ *become too small.*

5.3.2 Stable reconstruction of $x_k^\star$

We proved so far that the surface measurements are close to the three parameters function

$$d^{\text{app}}_{z,\alpha,x_k^\star} : x \mapsto z\mathcal{A}(\alpha(x_k^\star - x)), \tag{5.26}$$

on the interval $\Gamma_{R(\eta)}(x_k^\star) = (x_k^\star - r\eta^{-1/3}, x_k^\star + r\eta^{-1/3})$. The question is now to understand if one can get a stable evaluation of $x_k^\star$ from this approached data. We define then the following forward operator

$$F : \left\{ \begin{array}{ccc} \mathbb{C}^* \times (0,+\infty) \times \mathbb{R} & \longrightarrow & \mathcal{C}^0(\Gamma_R(\beta/\alpha)) \\ (z,\alpha,\beta) & \longmapsto & (x \mapsto z\mathcal{A}(\beta - \alpha x)) \end{array} \right. . \tag{5.27}$$

If the three parameters are uniquely defined, we can deduce an approximation of the position $x_k^\star$ from the solution of $F(z,\alpha,\beta) = d^{\text{app}}_{z,\alpha,x_k^\star}$ through the formula $x_k^\star = \beta/\alpha$. The following result guarantee the uniqueness of the solution to this problem.

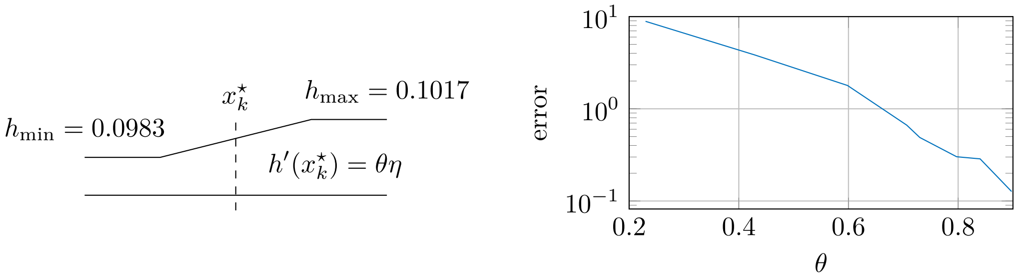

Figure 5.7 – Error of approximation $\|d^{\text{ex}} - d^{\text{app}}_{z,\alpha,x_k^\star}\|_{\mathrm{L}^2(\Gamma_R(\eta)(x_k^\star))}$ for different values of θ with a fixed value of η. The width h is represented on the left of the picture and exact data d^{ex} are generated as explained in section 5.5.1 with a locally resonant mode $N = 1$ and a source $f(x, y) = \delta_{x=6}\varphi_N(y)$. Then, d^{ex} is compared with $d^{\text{app}}_{z,\alpha,x_k^\star}$ where α and z are defined using the expression (5.22). Here, $r = 0.2$ and $\eta = 8.10^{-4}$.

Proposition 5.2. *Let $d_0 := F(z_0, \alpha_0, \beta_0)$, there exists $r_0 > 0$ such that if $r > r_0$ then the problem $F(z, \alpha, \beta) = d_0$ has a unique solution (z_0, α_0, β_0).*

Proof. If r is high enough, the interval Γ_R is large enough to contain the maximum amplitude of the function d_0 at position $x_{\max}$, and the two first zeros of the function d_0 called x_1 and x_2. Hence (z_0, α_0, β_0) are uniquely determined by

$$z_0 = \frac{d_0(x_{\max})}{\|\mathcal{A}\|_\infty}, \qquad \alpha_0 = \frac{y_1 - y_2}{x_2 - x_1}, \qquad \beta_0 = \frac{y_1 x_2 - y_2 x_1}{x_2 - x_1}, \tag{5.28}$$

where y_1 and y_2 are the two first zeros of the Airy function $\mathcal{A}$. ☐

This result of uniqueness and the corresponding inversion formulas are not directly applicable. Indeed, these formulas are not robust to noise or data uncertainties and we remind the reader that an approximation is already made between d^{ex} and $d^{\text{app}}_{z,\alpha,x_k^\star}$.

A first strategy would be to use the explicit formula (5.28) and apply some data regularization with a low-pass filter before doing the inversion (see [64] for more details). This method works perfectly with exact data, and will be called from now the “direct parameters reconstruction method”.

However, few issues can be raised with this method. Firstly, it is not sufficiently robust if data are very noisy, as illustrated in Figure 5.9 where we use this method to reconstruct parameters with a random additive noise of increasing amplitude. Secondly, as mentioned in the previous subsection, we will only make measurements of the wavefield on the interval Γ_R, and we cannot be sure that neither the first two zeros nor the maximum of $\mathcal{A}$ will occur in this interval. Finally, it is more realistic to assume that we only have access to $d^{\text{app}}_{z,\alpha,x_k^\star}$ on a finite number of receivers positions. For all this reasons, a least squares approach is introduced. On can keep the previous method to find an initial guess of the parameters $p := (z, \alpha, \beta)$.

We now assume that we have access to the data

$$d_i := F(p)(t_i), \quad i = 1, \dots, n, \tag{5.29}$$

where $p := (z, \alpha, \beta)$ and $(t_i)_{i=1,\dots,n} \in \Gamma_R$ is an increasing subdivision of Γ_R. We denote by $\boldsymbol{d} := (d_1, \dots, d_n) \in \mathbb{C}^n$ the discrete data on the subdivision $\boldsymbol{t} := (t_1, \dots, t_n)$. We aim to minimize the least squares energy functional

$$J_{\boldsymbol{d}}(p) := \frac{1}{2}\|F(p)(\boldsymbol{t}) - \boldsymbol{d}\|^2_{\ell^2}. \tag{5.30}$$

In this expression, the norm ℓ^2 is the normalized euclidean norm defined by

$$\|\boldsymbol{d}\|_{\ell^2}^2 = \frac{1}{n}\sum_{i=1}^{n} d_i^2. \tag{5.31}$$

Denoting by τ the step of the subdivision $\boldsymbol{t}$, we know using quadrature results (see [33] for more details) that for all functions $f \in \mathrm{H}^2(\Gamma_R)$,

$$\big|\|f\|_{\mathrm{L}^2(\Gamma_R)} - \|f(\boldsymbol{t})\|_{\ell^2}\big| \le 2\tau\|f\|_{\mathrm{H}^1(\Gamma_R)}. \tag{5.32}$$

It shows that the ℓ^2 norm is a good approximation of the $\mathrm{L}^2(\Gamma_R)$ norm if the step of discretization τ is small enough.

We assume the knowledge of an open set $U \subset \mathbb{C}^* \times (0, +\infty) \times \mathbb{R}$ of the form

$$U := B_{\mathbb{C}}(0, z_{\max}) \times (\alpha_{\min}, \alpha_{\max}) \times (\beta_{\min}, \beta_{\max}), \quad z_{\max}, \alpha_{\min}, \alpha_{\max} \in \mathbb{R}_+^\star, \quad \beta_{\min}, \beta_{\max} \in \mathbb{R}, \tag{5.33}$$

containing the solution p. The following proposition shows that the least squares problem is locally well-posed if the sampling size n is large enough, and it quantifies the error on the recovered parameters.

Proposition 5.3. *There exists $n_0 \in \mathbb{N}^*$ such that if $n \ge n_0$, then for every $p_0 \in U$ and $\boldsymbol{d}_0 = F(p_0)(\boldsymbol{x})$, there exist $\varepsilon > 0$ and $U' \subset U$ such that for every $\boldsymbol{d} \in \mathbb{R}^n$ satisfying $\|\boldsymbol{d} - \boldsymbol{d}_0\|_{\ell^2} < \varepsilon$ then the functional $J_{\boldsymbol{d}}$ is strictly convex on U' and admits a unique minimum point denoted $p_{LS} = (z_{LS}, \alpha_{LS}, \beta_{LS})$. Moreover, there exists a constant $C_5 > 0$ depending only on U, p_0 and n such that*

$$\|p_{LS} - p_0\|_2 \le C_5\|\boldsymbol{d} - \boldsymbol{d}_0\|_{\ell^2}. \tag{5.34}$$

Finally, if we denote

$$\Lambda : \left\{ \begin{array}{rcl} B_2(\boldsymbol{d}_0, \varepsilon) & \to & \mathbb{R} \\ \boldsymbol{d} & \mapsto & \dfrac{\beta_{LS}}{\alpha_{LS}} \end{array} \right., \tag{5.35}$$

the operator which approach the value of $x_k^\star$, there exists a constant $C_6 > 0$ depending only on U, p_0 and n such that

$$|\Lambda(\boldsymbol{d}) - \Lambda(\boldsymbol{d}_0)| \le C_6\|\boldsymbol{d} - \boldsymbol{d}_0\|_{\ell^2}. \tag{5.36}$$

The proof of this result is given in Appendix 5.B. In this proof we can see that the choice of the data discretization points $\boldsymbol{t}$ is important in order to improve the accuracy of the reconstruction. We illustrate that by choosing $p_0 = (2 + i, 1.4, -2.8)$ and comparing the direct reconstruction of the parameters (5.28) with the least squares method for three different sets $\boldsymbol{t}$:

- $\boldsymbol{t}_1$ is a discretization of $[-6, -1]$ with 100 points, where the tail of the Airy function is located.
- $\boldsymbol{t}_2$ is a discretization of $[-2, 6]$ with 100 points, where the Airy function varies.
- $\boldsymbol{t}_3$ is a discretization of $[-6, 6]$ with 200 points.

In Figure 5.8, we represent the four reconstructions where $\boldsymbol{d} = \boldsymbol{d}_0 + \mathcal{N}$ and $\mathcal{N}$ is a a uniform random additive noise of amplitude 0.3. We see that reconstructions with $\boldsymbol{t}_2$ and $\boldsymbol{t}_3$ seems more accurate than the one with $\boldsymbol{t}_1$ and the direct reconstruction. We detail this in Figure 5.9, where we compare the reconstruction errors with different noise amplitudes. We clearly see that using a least squares method improves the reconstruction if $\boldsymbol{t}$ is well-chosen.

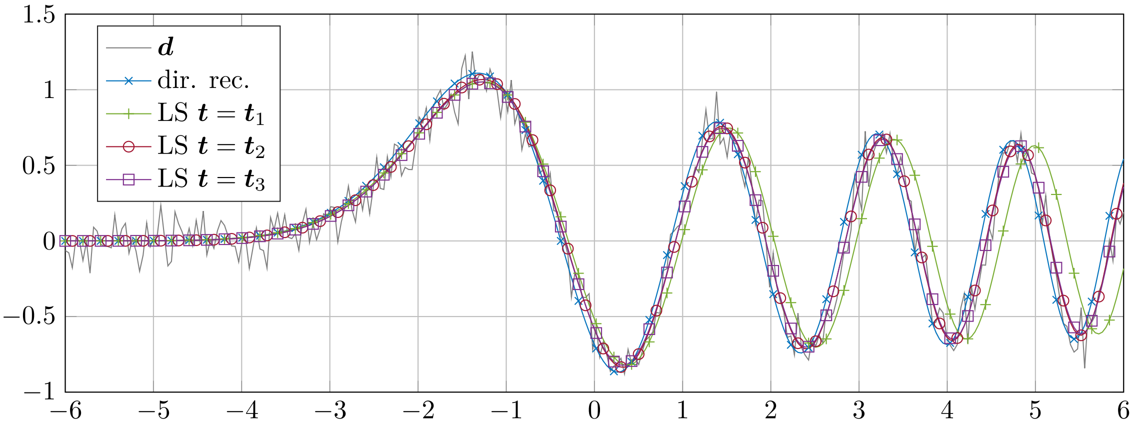

Figure 5.8 – Comparison of four different reconstructions of $F(p_0)$ where $\boldsymbol{d} - \boldsymbol{d}_0$ is a uniform random additive noise of amplitude 0.3. Blue: direct reconstruction. Green: least square reconstruction with $\boldsymbol{t} = \boldsymbol{t}_1$. Red: least square reconstruction with $\boldsymbol{t} = \boldsymbol{t}_2$. Purple: least square reconstruction with $\boldsymbol{t} = \boldsymbol{t}_3$.

We now have a stable method to reconstruct an approximation $x_k^{\star,\text{app}}$ of $x_k^\star$ from given measurements of $u(x, 0)$. Since $h(x_k^\star) = N\pi/k$, we can approximate the width at positions $x_k^{\star,\text{app}}$ with the formula

$$h^{\text{app}}(x_k^{\star,\text{app}}) = \frac{N\pi}{k}. \tag{5.37}$$

This provides an approximation of h in one point. Then, we change the frequency $k > 0$ to get approximations of h all along the support of h'. From now on, we denote u_k the wavefield propagating at frequency k. As mentioned before, we assume that we already have an approximation of $\text{supp}(h')$, $h_{\min}$ and $h_{\max}$ (see Appendix 5.A). We denote

$$k_{\max} = \frac{N\pi}{h_{\min}}, \quad k_{\min} = \frac{N\pi}{h_{\max}}. \tag{5.38}$$

and we take a finite set of frequencies $K \subset (k_{\min}, k_{\max})$. For every frequency $k \in K$, we introduce $\boldsymbol{t}_k$ a discretization of Γ_R and we set

$$\forall k \in K \qquad \boldsymbol{d}_k = u_k(\boldsymbol{t}_k, 0) + \zeta_k, \tag{5.39}$$

the measurement of u_k where ζ_k is the measurement error. For every $k \in K$, using Proposition 5.3, we have an ε_k and a constant C_6^k associated with $\boldsymbol{d}_{k,0} = d^{\text{app}}_{z,\alpha,x_k^\star}$. We define

$$\varepsilon := \min_{k\in K}(\varepsilon_k), \qquad C_6 := \max_{k\in K}(C_6^k), \tag{5.40}$$

and

$$X^{\star,\text{app}} := \{\Lambda(\boldsymbol{d}_k),\, k \in K\}. \tag{5.41}$$

Using the known approximation of $\text{supp}(h')$ provided by Appendix 5.A, we set the coordinates x_0 and x_{n+1} such that $\text{supp}(h') \subset (x_0, x_{n+1})$ and $X^{\star,\text{app}} \subset (x_0, x_{n+1})$. We then define the function h^{app} as the piecewise linear function such that

$$h^{\text{app}}(x_k^{\star,\text{app}}) = \frac{N\pi}{k} \quad \forall\, k \in K, \qquad h^{\text{app}}(x_0) = \frac{N\pi}{k_{\max}}, \qquad h^{\text{app}}(x_{n+1}) = \frac{N\pi}{k_{\min}}. \tag{5.42}$$

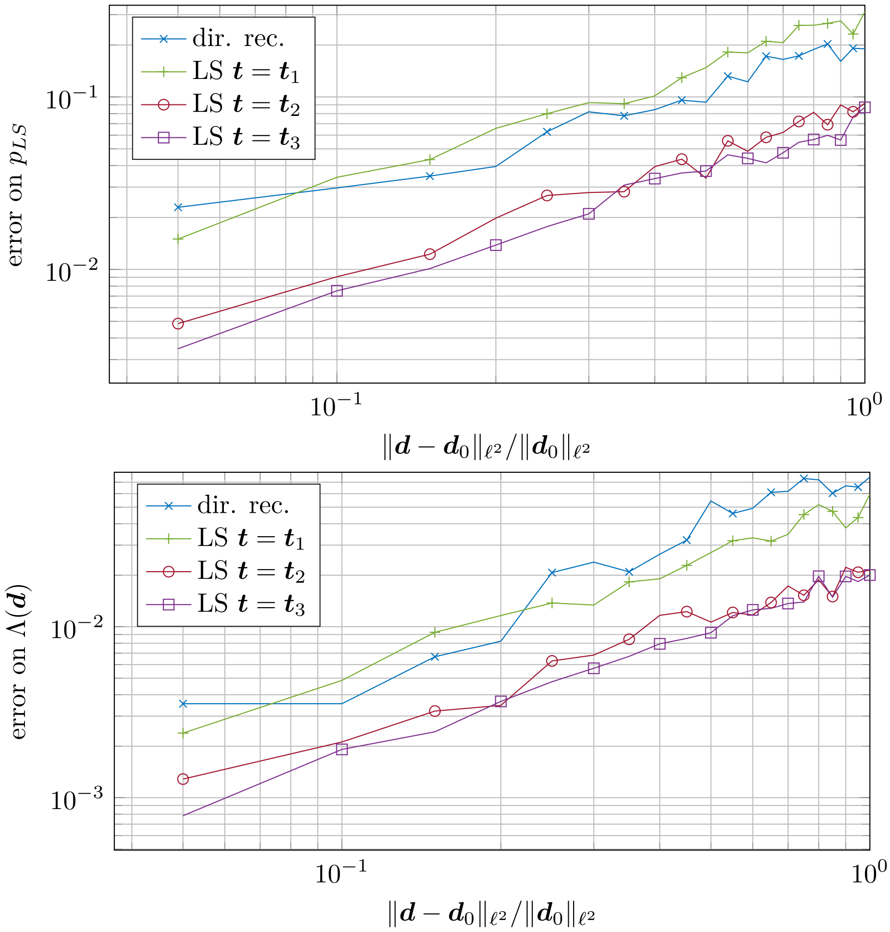

Figure 5.9 – Error of reconstruction of p_0 and $\Lambda(\boldsymbol{d}_0)$ with respect to the noise on the data for different method of reconstruction. On the left, $\|p_{\text{LS}} - p_0\|_2$ with respect to $\|\boldsymbol{d} - \boldsymbol{d}_0\|_{\ell^2} / \|\boldsymbol{d}\|_{\ell^2}$. On the right, $|\Lambda(\boldsymbol{d}_0) - \Lambda(\boldsymbol{d})|$ with respect to $\|\boldsymbol{d} - \boldsymbol{d}_0\|_{\ell^2} / \|\boldsymbol{d}\|_{\ell^2}$.

Using all the previous results, we are able to quantify the error of reconstruction between h^{app} and h:

Theorem 5.3. *Let K be a subset of $(k_{\min}, k_{\max})$. Assume the same hypotheses than in Theorem 5.1, and fix $N \in \mathbb{N}^*$ and $\theta > 0$ such that for every $k \in K$, $h'(x_k^\star) \geq \theta\eta$. There exist $\eta_1 > 0$ and $\zeta_0 > 0$ such that if $\eta < \eta_1$ and $\max_{k\in K} \|\zeta_k\|_{\ell^2} \leq \zeta_0$, then there exists a constant $C_7 > 0$ depending only on $h_{\min}$, $h_{\max}$, N, r, μ and θ such that*

$$\|h^{app}(X^\star_{app}) - h(X^\star_{app})\|_\infty \leq \eta C_7 \left(\eta^{1/3} + \max_{k\in K} \|\zeta_k\|_{\ell^2}\right). \tag{5.43}$$

Proof. For every $k \in K$, we notice that

$$|h^{\text{app}}(x_k^{\star,\text{app}}) - h(x_k^{\star,\text{app}})| = |h(x_k^\star) - h(x_k^{\star,\text{app}})| \leq \eta |x_k^\star - x_k^{\star,\text{app}}| = \eta |\Lambda(\boldsymbol{d}_0) - \Lambda(\boldsymbol{d}_{k,0})|.$$

Using Theorem 5.2 combined with the control (5.32), we know that

$$\|\boldsymbol{d}_k - \boldsymbol{d}_{0,k}\|_{\ell^2} \leq 2\eta^{1/3}\tau C_4 \left(\|d^{\text{ex}}\|_{\mathrm{H}^1(\Gamma_R)} + \|d^{\text{app}}_{z,\alpha,x_k^\star}\|_{\mathrm{H}^1(\Gamma_R)} \right).$$

Using Theorem 5.1, we can control both these norm by a constant $c_2 > 0$ which does no depend on k. Then, if η and $\max\limits_{k\in K} \|\zeta_k\|_{\ell^2}$ are small enough,

$$2\tau C_4 c_2 \eta^{1/3} + \max_{k\in K} \|\zeta_k\|_{\ell^2} \leq \varepsilon,$$

and using Proposition 5.3,

$$|h^{\text{app}}(x_k^{\star,\text{app}}) - h(x_k^{\star,\text{app}})| \leq \eta C_6 \left(2\tau C_4 c_2 \eta^{1/3} + \max_{k\in K} \|\zeta_k\|_{\ell^2} \right).$$

□

The first error term of this theorem is a consequence of the approximation of the data by an Airy function, while the second term is caused by the possible presence of measurements errors. We illustrate this reconstruction in Figure 5.10 where we choose a subset K with 20 points, and we compare $h^{\text{app}}(x_k^{\star,\text{app}})$ and $h(x_k^\star)$.

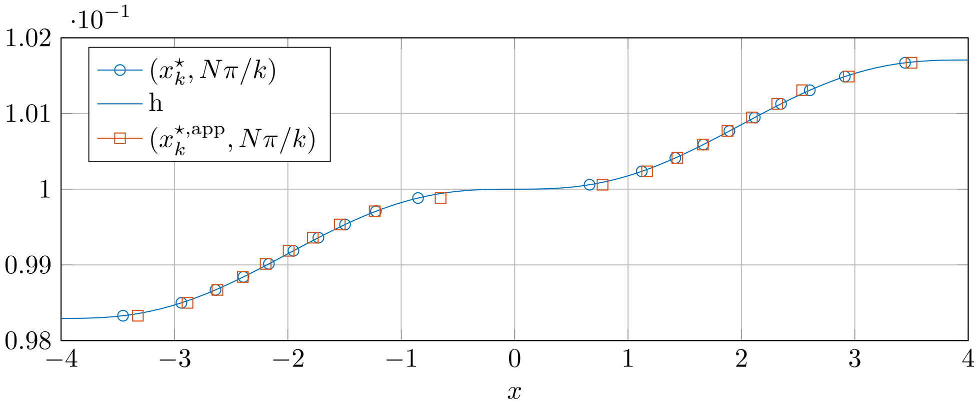

Figure 5.10 – Representation of $x_k^\star$ and $x_k^{\star,\text{app}}$ when $K = 30.9 : 31.95 : 20$. Here, h is defined in (5.50), $N = 1$, and data are generated as explained in section 5.5.1 with a source $f(x,y) = \delta_{x=6}\varphi_1(y)$.

To conclude, we have proved in this section that we are able to reconstruct in stable way a set of resonant positions $x_k^\star$, which leads to a stable reconstruction of the function h. We present in the next section the general idea needed to generalize this reconstruction to more realistic non-monochromatic source terms.

5.4 Inversion using a general source term

We now consider the general case without any a priori assumptions on the source terms f and b. We use the same idea as before to reconstruct the width using the locally resonant mode N. However, other modes may also be present in the wavefield, and the previous approximation of d^{ex} by u_N^{app} (see (5.16)) may not be valid. We provide here two methods to exploit the framework developed in the previous section.

The first idea is to treat all resonant and evanescent modes as an added noise to the locally resonant mode. Indeed, we know using Theorem 5.1 that

$$d^{\mathrm{ex}} = u(x,0) \approx \sum_{n\in\mathbb{N}} \int_{\mathbb{R}} G_n^{\mathrm{app}}(x,s) g_n(s) \mathrm{d}s \, \varphi_n(y) \,. \tag{5.44}$$

Defining the noise

$$\zeta_k(x) = \sum_{n\neq N} \int_{\mathbb{R}} G_n^{\mathrm{app}}(x,s) g_n(s) \mathrm{d}s \varphi_n(y) \,, \tag{5.45}$$

we see that

$$d^{\mathrm{ex}} \approx u_N^{\mathrm{app}}(x)\varphi_N(0) + \zeta_k(x). \tag{5.46}$$

To make a successful use of Theorem 5.3, the noise ζ_k needs to be smaller than the parameter ζ_0. Using the expression of G_n^{app} given in (5.11), we notice that

$$\forall n \in \mathbb{N}, \qquad |G_n^{\mathrm{app}}(x)| = \mathcal{O}\left(\frac{1}{\min(|k_n|)}\right). \tag{5.47}$$

Since

$$\frac{|k_N|}{|k_n|} \leq \frac{|k_N|^2 h_{\max}^2}{\sqrt{2N-1}\pi}, \tag{5.48}$$

the amplitude of ζ_k seems to be neglectable compared to the amplitude of u_N^{app} if the width $h_{\max}$ is small enough and if $\|f_n\|_{\mathrm{L}^2(\mathbb{R})} = \mathcal{O}(\|f_N\|_{\mathrm{L}^2(\mathbb{R})})$ for every $n \neq N$. We illustrate this in Figure 5.11 where we compare the amplitude of $u(x,0)$ with the amplitude of $u_N^{\mathrm{app}}(x)\varphi_N(0)$ for source terms $f(x,y) = \delta_{x=6}y^2$ and $b_{\mathrm{top}}(x) = \delta_{x=6}$. We see that it is possible to fit directly the Airy function on $u(x,0)$, since the noise is very small.

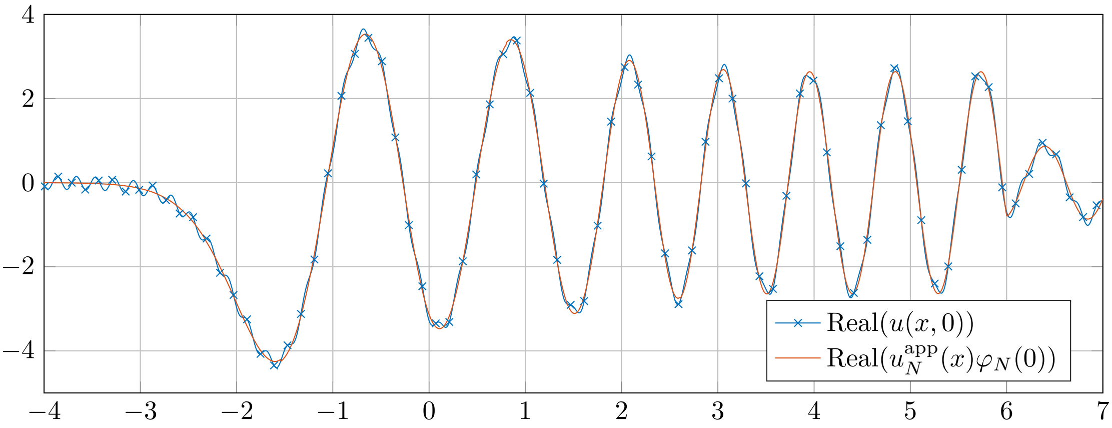

Figure 5.11 – Representation of $u(x,0)$ and $u_N^{\mathrm{app}}\varphi_N(0)$ generated by a source $f(x,y) = \delta_{x=6}y^2$ and $b_{\mathrm{top}}(x) = \delta_{x=6}$. Here $N = 1$, $k = 31.7$ and h is defined as in (5.50).

However, in the general case, the noise of the other modes cannot always be neglected. In this case, we can filter the measurements to keep only the locally resonant part. Evanescent modes vanish away from the source and so their contribution is negligible in $u(x,0)$. As for propagative modes, we notice that $k_n(x)$ is almost constant when $n < N$. Using (5.11), it means that every propagative mode is oscillating with a frequency almost equal to k_n. We illustrate it in Figure 5.12

with the Fourier transform of $u(x,0)$ and the contribution of each mode. Using a filter cutting all frequencies around $k_n(x)$ for $n < N$, we can clean the signal and get a good approximation of $u_N(x)\varphi_N(0)$ (see [64] for more details). We illustrate this in Figure 5.13 where we represent $u(x,0)$, $u_N(x)\varphi_n(0)$ and the approximation obtained using this Fourier filtering.

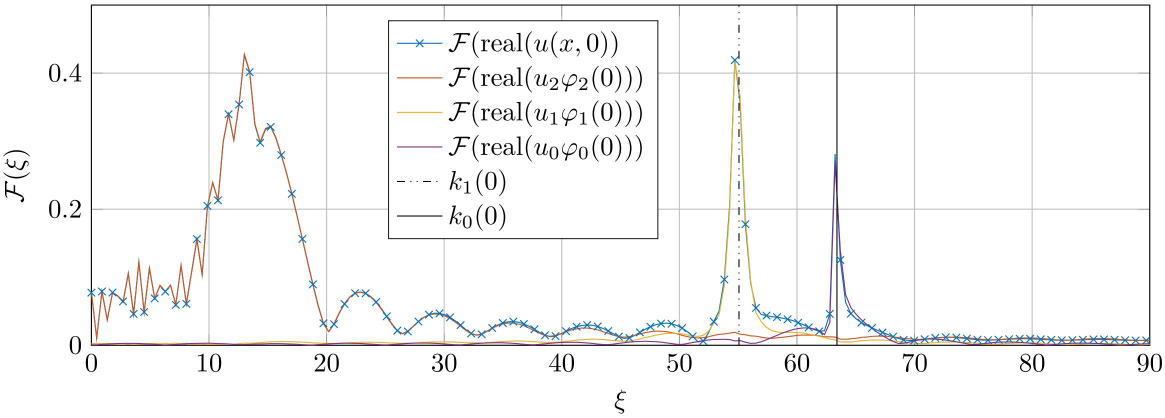

Figure 5.12 – Influence of each mode on the Fourier transform of the measurements real part. Fourier transform of Real$(u_n\varphi_n(0))$ are plotted for every non evanescent mode ($n = 0,1,2$). For comparison purpose, $k_n(0)$ is represented for every propagative modes ($n = 1,2$). Here, $k = 63.4$, $N = 2$, $f(x,y) = \delta_{x=6}(3\varphi_0(y) + 2\varphi_1(y) + \varphi_2(y))$ and $b_{\text{top}} = \delta_{x=6}$.

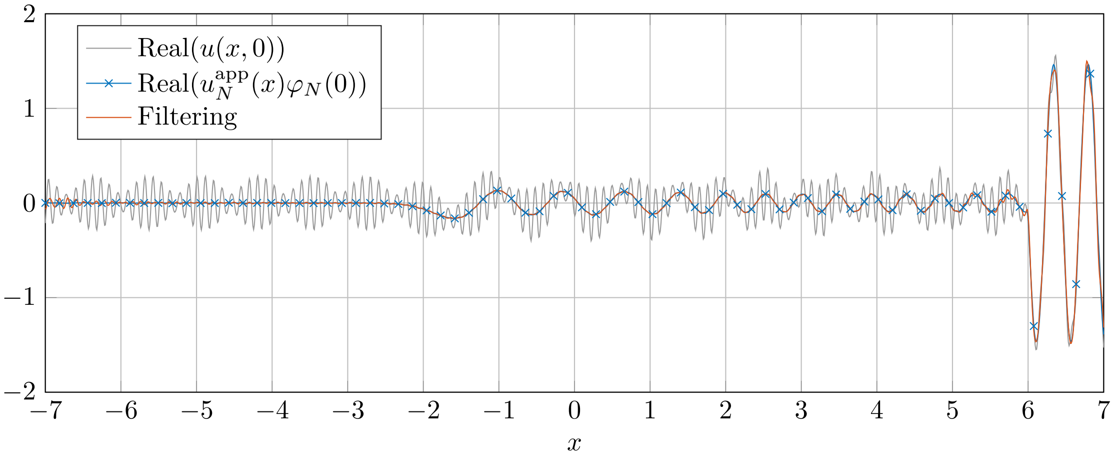

Figure 5.13 – Fourier filtering of Real$(u_k(x,0))$ and comparison with Real$(u_{k,N}^{\text{app}}(x)\varphi_N(0))$. Here, $k = 63.4$, $N = 2$, $f(x,y) = \delta_{x=6}(3\varphi_0(y) + 2\varphi_1(y) + \varphi_2(y))$ and $b_{\text{top}} = \delta_{x=6}$.

We can now fit the three parameters Airy function on the measurements, and find an approximation of $x_k^\star$ as before. It proves that our method can be used in the case of general sources, providing a filtering of propagative mode. This method can be used in a very general framework because it does not need any *a priori* information on sources, as long as their locally resonant part does not vanish. Using the extension of Theorem 5.1 to non monotone waveguides provided in section 4.4 of Chapter 4, all the results presented in this section remain true in any kind of slowly varying waveguide.

5.5 Numerical computations

In this section, we show some numerical applications of our reconstruction method on slowly varying waveguides. We simulate surface measurements using numerically generated data, and we provide reconstructions of increasing and general waveguides with different shape profiles.

5.5.1 Generation of data

In the following, numerical solutions of (5.7) are generated using the software Matlab to solve numerically the equation in the waveguide Ω. In every numerical simulation, we assume that h' is supported between $x = -7$ and $x = 7$. To generate the solution u of (5.7) on Ω_7, we use a self-coded finite element method and a perfectly matched layer [18] on the left side of the waveguide between $x = -15$ and $x = -8$ and on the right side between $x = 8$ and $x = 15$. The coefficient of absorption for the perfectly matched layer is defined as $\alpha = -k((x-8)\mathbf{1}_{x\geq 8} - (x+8)\mathbf{1}_{x\leq -8})$ and k^2 is replaced in the Helmholtz equation with $k^2 + i\alpha$. The structured mesh is built with a stepsize of 10^{-3}.

5.5.2 Method of reconstruction

Using all the previous results, we summarize here all the steps to reconstruct the approximation h^{app} of the width h.

1. Find an approximation of $\text{supp}(h')$, $k_{\min}$ and $k_{\max}$ using the method described at the beginning of Appendix 5.A.
2. Choose a set of frequencies $K \subset (k_{\min}, k_{\max})$ and sources f, b_{top}, b_{bot}. Then, for every frequency, measure the wavefield $u(x, 0)$ solution of (5.7).
3. Filter the data by eliminating in the Fourier transform responses around k_n for every a propagative mode n.
4. Find an approximation of the coordinate $x_{\max}$ where $|u(x, 0)|$ is maximal. Then, choose a length $R > 0$, and discretize the interval $[x_{\max} - R, x_{\max} + R]$ into the set $\boldsymbol{x}_k$. The available data $\boldsymbol{d}_k$ are then the measurements of $u(\boldsymbol{x}_k, 0)$.
5. For every frequency, minimize the quantity $\|\boldsymbol{d}_k - F(p)(\boldsymbol{x}_k)\|_{\ell^2(\boldsymbol{x})}$ using a gradient descent to find the approximation $x_k^{\star,\text{app}}$ of $x_k^\star$. The direct reconstruction method can be used to initialize the gradient descent method.
6. Compute h^{app} using expression (5.42).

In step 3, we should normally discretize the interval $\Gamma_R(x_k^\star)$. However, since we do not know yet the value of $x_k^\star$, we use the fact that $x_k^\star$ is located near $x_{\max}$, and that the interval $[x_{\max}-R, x_{\max}+R]$ can be included into a bigger interval $\Gamma_{R'}(x_k^\star)$ where $R' > R$.

5.5.3 Numerical results

We now apply this method to reconstruct different profiles of slowly varying waveguides. Firstly, we present in Figure 5.14 the reconstruction h^{app} obtained for different increasing functions h. We choose four different waveguide profiles

$$\Omega_1 : \quad h_1(x) = 0.1 + \gamma_1\left(\frac{x^5}{5} - 32\frac{x^3}{3} + 256x\right)\mathbf{1}_{-4\leq x\leq 4} - \gamma_2\mathbf{1}_{x<-4} + \gamma_2\mathbf{1}_{x>4}, \tag{5.49}$$

$$\Omega_2: \quad h_2(x) = 0.1 + \gamma_3\left(\frac{x^5}{5} - 2x^4 + 16\frac{x^3}{3}\right)\left(\mathbf{1}_{0\le x\le 4} - \mathbf{1}_{-4\le x<0}\right) + \gamma_4\left(\mathbf{1}_{x>4} - \mathbf{1}_{x<-4}\right), \tag{5.50}$$

$$\Omega_3: \quad h_3(x) = 0.1 + \gamma_5 x \mathbf{1}_{-4\le x\le 4} + 4\gamma_5\mathbf{1}_{x>4} - 4\gamma_4\mathbf{1}_{x<-4}, \tag{5.51}$$

$$\Omega_4: \quad h_4(x) = 0.1 - 4\gamma_5 + 4\gamma_5\frac{\sqrt{x+4}}{\sqrt{2}}\mathbf{1}_{-4\le x\le 4} + 8\gamma_5\mathbf{1}_{x>4}. \tag{5.52}$$

where $\gamma_1 = 3.10^{-6}$, $\gamma_2 = 8192/5.10^{-6}$, $\gamma_3 = 5.10^{-5}$, $\gamma_4 = 53/3.10^{-5}$, $\gamma_5 = 0.01/30$. All these profiles are represented in black in Figure 5.14. We impose that sources of (5.7) need to be located at the right of the waveguide in order to generate significant locally resonant mode (see Figure 5.4), and we define

$$f(x,y) = \delta_{x=6}y, \qquad b_{\text{top}}(x) = \delta_{x=6}, \qquad b_{\text{bot}} = 0. \tag{5.53}$$

We choose to work with the following sets of frequencies

$$K_1 = 30.92 : 31.93 : 20, \quad K_2 = 30.9 : 31.95 : 20, \quad K_3 = K_4 = 31.01 : 31.83 : 20. \tag{5.54}$$

The profile h_1 and the set K_1 satisfy all the assumptions of Theorem 5.2, while the derivative of $h_2 \in \mathcal{C}^2(\mathbb{R})$ vanishes once. The last two profiles h_3 and h_4 are not in $\mathcal{C}^2(\mathbb{R})$ and show corners where the derivative of the profile is not continuous. The function h_3' is piecewise continuous and bounded, contrary to h_4' which explodes at $x = -4$.

We plot in red in Figure 5.14 the reconstructions h^{app}, slightly shifted, obtained using our method of reconstruction. We also compute the L^∞ norm of $h - h^{\text{app}}$ in each situation. We clearly see that the reconstruction deteriorates when $h'(x_k^\star)$ is too small or when the function h is not sufficiently smooth.

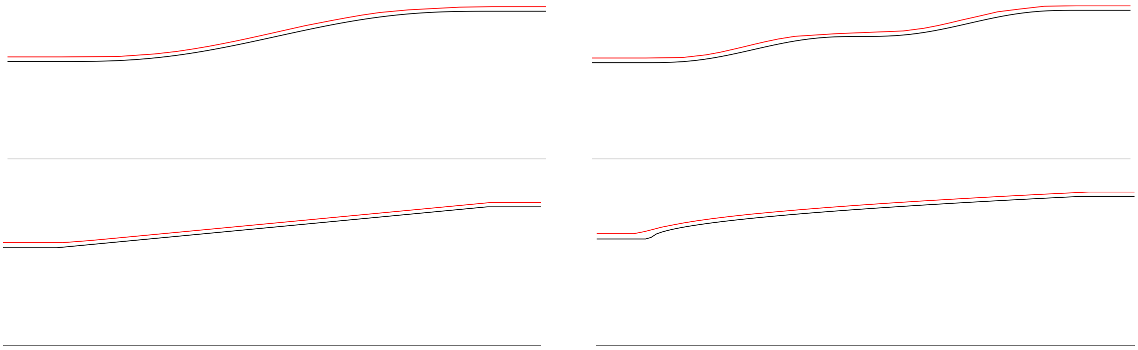

Figure 5.14 – Reconstruction of four different increasing profiles. In black, the initial shape of Ω_5 (not scaled), and in red the reconstruction, slightly for comparison purposes. In each case, $K = K_i$ is defined in (5.54), $h = h_i$ is defined in (5.49), (5.50), (5.51), (5.52), and the sources of (5.7) are defined in (5.53). Top left: $i = 1$, $\|h - h^{\text{app}}\|_\infty / h_{\max} = 0.49\%$. Top right: $i = 2$, $\|h - h^{\text{app}}\|_\infty / h_{\max} = 0.94\%$. Bottom left: $i = 3$, $\|h - h^{\text{app}}\|_\infty / h_{\max} = 0.40\%$. Bottom right: $i = 4$, $\|h - h^{\text{app}}\|_\infty / h_{\max} = 1.6\%$.

Secondly, we present in Figure 5.15 the reconstruction h^{app} obtained for different non monotoneous widths. We choose three different profiles defined by

$$\Omega_5: \quad h_5(x) = 0.1 + \gamma_6 \sin\left(\frac{\pi}{10}(x+5)\right)\mathbf{1}_{-5\le x\le 5}, \tag{5.55}$$

$$\Omega_6: \quad h_6(x) = 0.1 - \gamma_7(x+5)\mathbf{1}_{-5\le x\le 0} + \frac{\gamma_6}{4}(x-4)\mathbf{1}_{0<x\le 4}, \tag{5.56}$$

$$\Omega_7: \quad h_7(x) = 0.1 - \gamma_8\sqrt{3} + 2\gamma_8 \sin\left(\frac{4\pi\sqrt{x+5}}{3}\right)\mathbf{1}_{-3.5\le x\le 4} + 2\gamma_8 \sin\left(\frac{4\pi\sqrt{1.5}}{3}\right)\mathbf{1}_{x<-3.5}, \tag{5.57}$$

where $\gamma_6 = 25.10^{-4}$, $\gamma_7 = 5.10^{-4}$, $\gamma_8 = 4.10^{-4}$. All these profiles are represented in black in Figure 5.15. The profile h_5 represent a dilation of the waveguide, while h_6 represent a compression of the waveguide. The profile h_7 is the more general one with both compressions and dilations. Again, sources in (5.7) are located in every large area of the waveguide to generate significant locally resonant modes and are defined by

$$f^5(x,y) = \delta_{x=0}y, \quad b^5_{\mathrm{top}}(x) = \delta_{x=0}(x), \quad b^5_{\mathrm{bot}} = 0, \tag{5.58}$$

$$f^6(x,y) = (\delta_{x=6} + \delta_{x=-6})y, \quad b^6_{\mathrm{top}}(x) = (\delta_{x=6} + \delta_{x=-6}), \quad b^6_{\mathrm{bot}} = 0, \tag{5.59}$$

$$f^7(x,y) = (\delta_{x=-1.5} + \delta_{x=6})y, \quad b^7_{\mathrm{top}}(x) = (\delta_{x=-1.5} + \delta_{x=6}), \quad b^7_{\mathrm{bot}} = 0. \tag{5.60}$$

We also define the frequency sets

$$K_5 = 30.65 : 31.4 : 20, \quad K_6 = 31.42 : 32.21 : 20, \quad K_7 = 30.97 : 31.43 : 20. \tag{5.61}$$

We plot in red in Figure 5.15 the reconstructions h^{app}, slightly shifted, obtained using our method of reconstruction. We also compute the L^∞ norm of $h - h^{\mathrm{app}}$ in each situation.

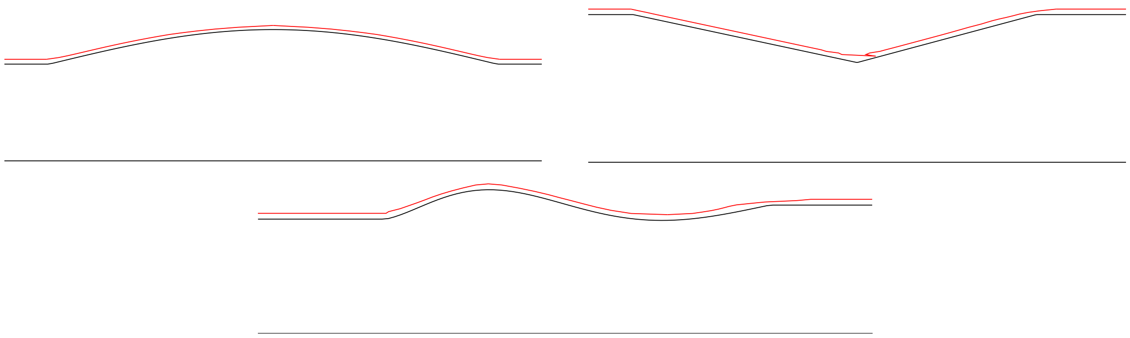

Figure 5.15 – Reconstruction of three different general profiles. In black, the initial shape of Ω_6, and in red, the reconstruction, slightly shifted for comparison purposes. In each case, $K = K_i$ is defined in (5.61), $h = h_i$ is defined in (5.55), (5.56), (5.57), and sources of (5.7) are defined in (5.58), (5.59), (5.60). Top left: $i = 5$, $\|h - h^{\mathsf{app}}\|_\infty / h_{\max} = 0.57\%$. Top right: $i = 6$, $\|h - h^{\mathsf{app}}\|_\infty / h_{\max} = 0.81\%$. Bottom: $i = 7$, $\|h - h^{\mathsf{app}}\|_\infty / h_{\max} = 0.97\%$.

To conclude, we have provided in this section a method to reconstruct slowly varying width defects given surface measurements of the wavefield at local resonant frequencies. This method works for every type of source and does not require any *a priori* information on the source except the fact that it is located away from the defect. This reconstruction method is very sensitive to small defects and works numerically to reconstruct dilations or compressions of the waveguide.

5.6 Conclusion

In this chapter, we have used the study of the forward problem in slowly varying waveguide presented in Chapter 4 and the approximation of the solutions as combination of Airy functions to develop a new inverse method to reconstruct the width of slowly varying waveguides. Given wavefield measurements at the surface of the waveguide for different locally resonant frequencies, we reconstruct the associated locally resonant points which provide a good approximation of the width of the waveguide.

One main advantage of this new method is that is does not require any *a priori* information on the sources, and we believe that it could be applied to develop new non destructive passive monitoring methods. Moreover, using locally resonant modes, this method can detect very small variations of the width with a very high sensibility. More importantly, when we compare this new method with the usual back scattering method developed for instance in Chapter 2, we notice that this new method seems a lot more precise: while the best relative reconstruction errors are of the order of 8% in Chapter 2, we reach in this chapter relative errors of the order of less than 1%. Even if measurements are not taken in the same area, this improvement of the reconstruction precision needs to be underlined.

We believe that this work could be extended to elastic waveguides in two dimensions, using the modal decomposition in Lamb modes presented in [81]. If the generalization to elastic waveguide proves successful, we plan in future works to test the method developed in this chapter on experimental data to see if the good numerical results obtained using data generated by finite element methods can be reproduced. Indeed, different physical experiments have already been conducted to recover width defects using locally resonant frequencies (see [11, 29]) and we hope that our reconstruction method could both justify and improve these width reconstructions.

Appendix 5.A: Identification of supp(h), $k_{\min}$ and $k_{\max}$

Giving a compactly perturbed waveguide Ω, we describe here how surface measurements enable to approximate very precisely the quantities supp(h), $k_{\min}$ and $k_{\max}$. The article [27] mentions that the problem (5.7) is not well-defined when $k_n(x) = 0$ in a non-trivial interval, which especially happens when $k = n\pi/h_{\min}$ or $k = n\pi/h_{\max}$. Numerically, this results in an explosion of the solution when k tends to $n\pi/h_{\min}$ (resp. $n\pi/h_{\max}$) with a source term located in the area where $h(x) = h_{\min}$ (resp. $h(x) = h_{\max}$). This behavior is illustrated in Figure 5.16.

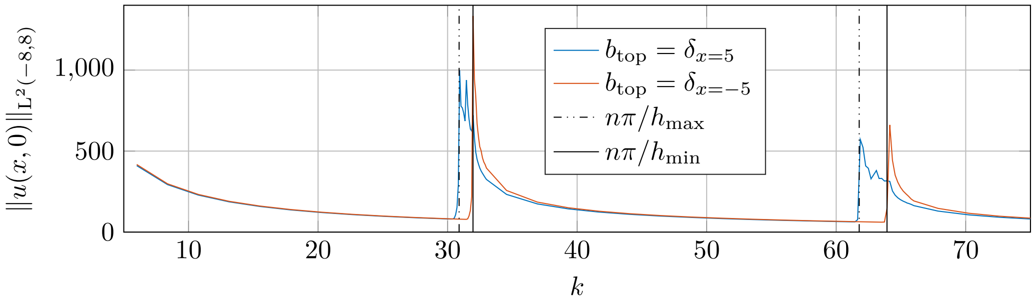

Figure 5.16 – L^2-norm of $u(x,0)$ on the interval $(-8,8)$ with respect to k for a source $b_{\text{top}} = \delta_{x=-5}$ at the left of supp(h), and a source $b_{\text{top}} = \delta_{x=5}$ at the right of supp(h). For comparison purposes, $n\pi/h_{\max}$ and $n\pi/h_{\min}$ are plotted for $n = 1$ and $n = 2$.

Measuring the surface wavefield while k varies and detecting its explosions provides a good approximation of the width at the left and the right of the waveguide. Then, we choose a frequency $k = n\pi/h_{\max}$ or $k = n\pi/h_{\min}$ and we move the sources while measuring the amplitude of the wavefield. It the source is located outside of the support of h, the wavefield is supposed to explode, which provides a good approximation of the support of h. This behavior is illustrated in Figure 5.17.

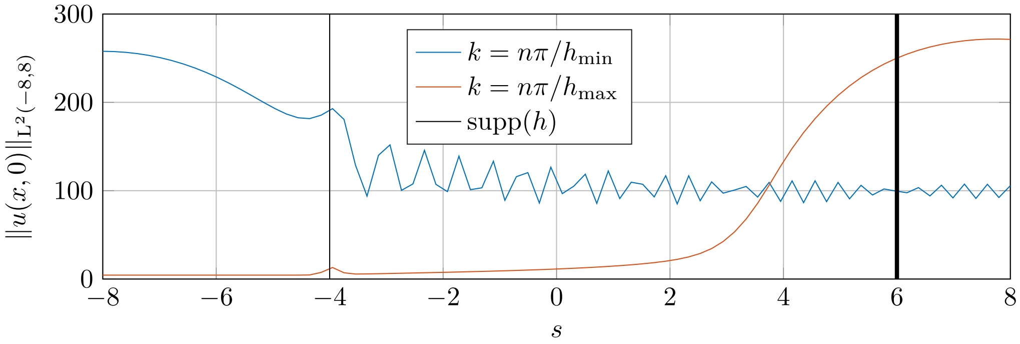

Figure 5.17 – L^2-norm of $u(x,0)$ on the interval $(-8,8)$ with respect to the position s of the source $b_{\text{top}} = \delta_{x=s}$, for a frequency $k = pi/h_{\max}$ and $k = \pi/h_{\min}$. For comparison purposes the support of h is plotted.

Appendix 5.B: Proof of Proposition 5.3

Proof. For every $p \in U$, we compute

$$\nabla J_{\boldsymbol{d}}(p) = \begin{pmatrix} \sum_{i=1}^{n} \mathcal{A}(\beta - \alpha t_i)(z\mathcal{A}(\beta - \alpha t_i) - d_i) \\ \sum_{i=1}^{n} -zt_i\mathcal{A}'(\beta - \alpha t_i)(z\mathcal{A}(\beta - \alpha t_i) - d_i) \\ \sum_{i=1}^{n} z\mathcal{A}'(\beta - \alpha t_i)(z\mathcal{A}(\beta - \alpha t_i) - d_i) \end{pmatrix}, \tag{5.62}$$

$$\nabla^2 J_{\boldsymbol{d}}(p) = \sum_{i=1}^{n} M_i(\beta - \alpha t_i), \tag{5.63}$$

with

$$M_i = \begin{pmatrix} \mathcal{A}^2 & -t_i\mathcal{A}' \times (2z\mathcal{A} - d_i) & \mathcal{A}'(2z\mathcal{A} - d_i) \\ -t_i \times \mathcal{A}' \times (2z\mathcal{A} - d_i) & \begin{array}{r} zt_i^2\mathcal{A}'' \times (z\mathcal{A} - d_i) \\ +z^2t_i^2 \times (\mathcal{A}')^2 \end{array} & \begin{array}{r} -zt_i \times \mathcal{A}''(z\mathcal{A} - d_i) \\ -t_iz^2(\mathcal{A}')^2 \end{array} \\ \mathcal{A}' \times (2z\mathcal{A} - d_i) & \begin{array}{r} -zt_i \times \mathcal{A}''(z\mathcal{A} - d_i) \\ -t_iz^2 \times (\mathcal{A}')^2 \end{array} & \begin{array}{c} z\mathcal{A}'' \times (z\mathcal{A} - d_i) \\ z^2(\mathcal{A}')^2 \end{array} \end{pmatrix}. \tag{5.64}$$

For every $h \in \mathbb{C} \times \mathbb{R}^2$, $h \neq 0$,

$$(\nabla^2 J_{\boldsymbol{d}}(p)h|h) = A(P,h) + B(P,h), \tag{5.65}$$

where

$$A(P,h) = \sum_{i=1}^{n} (\mathcal{A}(\beta - \alpha t_i) h_1 + z\mathcal{A}'(\beta - \alpha t_i)(h_3 - h_2 t_i))^2, \tag{5.66}$$

$$B(P,h) = \sum_{i=1}^{n} (z\mathcal{A}(\beta - \alpha t_i) - d_i)(2\mathcal{A}'(\beta - \alpha t_i) h_1 (h_3 - h_2 t_i) + z\mathcal{A}''(\beta - \alpha t_i)(h_3 - h_2 t_i)^2). \tag{5.67}$$

We want to prove that $A(P,h) > 0$. To do so, we use the following Lemma.

Lemma 5.1. *For every* $(h_1, h_2, h_3) \in \mathbb{C} \times \mathbb{R} \times \mathbb{R}$ *and* $(z, \alpha, \beta) \in U$*, the set of zeros of*

$$x \mapsto h_1 \mathcal{A}(\beta - \alpha x) + z\mathcal{A}'(\beta - \alpha x)\,(h_3 - h_2 x)\,, \tag{5.68}$$

is finite, and at most equal to $3\ell + 3$ *where* ℓ *is the number of zeros of* $\mathcal{A}'$ *on*

$$I := [\beta_{\min} - t, \beta_{\max} + t], \qquad \textit{where} \qquad t = \alpha_{\max} \max(|t_1|, |t_n|). \tag{5.69}$$

Proof. We do a change of variable $u = \beta - \alpha x$, and we see that for every $x \in [x_1, x_n]$, $u \in I$. We now look for $u \in I$ satisfying

$$g_1(u) := h_1 \mathcal{A}(u) + z\mathcal{A}'(u) \left(h_3 - \frac{h_2}{\alpha}(\beta - u) \right) = 0. \tag{5.70}$$

We notice that if $h_1 = 0$ then $g_1(u) = 0$ if and only if $\mathcal{A}'(u) = 0$ or $x = h_3/h_2$, which gives $\ell + 1$ zeros of g_1. Otherwise, we notice that if $\mathcal{A}'(u) = 0$ then $g_1(u) \neq 0$ since every zero of the Airy function is simple (see [4]). It means that there exist $\alpha \in \mathbb{C}$ and $\beta \in \mathbb{R}$ such that

$$g_1(u) = 0 \quad \Leftrightarrow \quad \frac{\mathcal{A}}{\mathcal{A}'}(u) = \alpha u + \beta. \tag{5.71}$$

We define

$$g_2(u) = \frac{\mathcal{A}}{\mathcal{A}'}(u) - \alpha u - \beta, \tag{5.72}$$

and then

$$g_2'(u) = \left(1 - u \left(\frac{\mathcal{A}(u)}{\mathcal{A}'(u)} \right)^2 \right), \qquad g_2''(u) = \frac{\mathcal{A}(u)}{\mathcal{A}'(u)} \underbrace{\left(2 - 2u \left(\frac{\mathcal{A}(u)}{\mathcal{A}'(u)} \right)^2 - \frac{\mathcal{A}(u)}{\mathcal{A}'(u)} \right)}_{>0}. \tag{5.73}$$

Between two zeros of $\mathcal{A}'$, $\mathcal{A}$ vanishes only once, meaning that depending of the value of α, g_2' vanishes at most twice, and so depending of the value of β, g_2 vanishes at most three times. ☐

Back to the proof of Proposition 5.3, we now set $n_0 = 3\ell + 3$, and if $n > n_0$ then it shows that $A(P,h) > 0$. We denote $\lambda_1(p) = \min_{h \in \mathbb{R}^3, h \neq 0} a(P,h)/\|h\|_2^2$. This function is continuous on a subset $U_1 \subset U$, and we denote by m the minimum of λ_1 on U_1. We also notice that

$$|b(P,h)| \leq \|z\mathcal{A}(\beta - \alpha X) - d\|_1 (\|\mathcal{A}'\|_\infty + 2z\|\mathcal{A}''\|_\infty)(1 + \|\boldsymbol{t}\|_\infty)\|h\|_2^2. \tag{5.74}$$

We see that

$$\|z\mathcal{A}(\beta - \alpha X) - d\|_1 = \|F(p) - d\|_1 \leq \|F(p) - F(p_0)\|_1 + \|\boldsymbol{d}_0 - d\|_1. \tag{5.75}$$

There exists a constant $M > 0$ depending on U such that for every $p \in U$,

$$\|F(p) - F(p_0)\|_1 \leq M\|P - p_0\|_1. \tag{5.76}$$

We define $U_2 = U_1 \cap B_1(p_0, \varepsilon_1/M)$ where

$$\varepsilon_1 := \frac{m}{4(\|\mathcal{A}'\|_\infty + 2z_{\max}\|\mathcal{A}''\|_\infty)(1 + \max(|x_1|, |x_n|)}. \tag{5.77}$$

It follows that for every $p \in U_2$ and $d \in B_1(\boldsymbol{d}_0, \varepsilon_1)$,

$$\|F(p) - F(p_0)\|_1 \leq \varepsilon_1, \quad |b(P,h)| \leq \frac{m}{2}\|h\|_2^2. \tag{5.78}$$

The operator $J_{\boldsymbol{d}}$ is then strictly convex on U_2 since

$$\|\nabla^2 J_{\boldsymbol{d}}(p)\|_2 \geq \min_{h \in \mathbb{C}\times\mathbb{R}^2, h \neq 0} \frac{|A(P,h)| - |B(P,h)|}{\|h\|_2^2} \geq \frac{m}{2} > 0 \tag{5.79}$$

We now need to prove that the minimum of $J_{\boldsymbol{d}}$ is located inside of U_2 and not on its boundary. To do so, we look for a point $p \in U_2$ such that $\nabla J_{\boldsymbol{d}}(p) = 0$. We already know that $\nabla J_{\boldsymbol{d}_0}(p_0) = 0$. Using the implicit function theorem, there exists an open set $V \subset \mathbb{R}^n$ containing $\boldsymbol{d}_0$ such that there exists a unique continuously differentiable function $G_1 : V \to \mathbb{C}\times\mathbb{R}\times\mathbb{R}$ such that $\nabla F_{\boldsymbol{d}}(G_1(\boldsymbol{d})) = 0$. We define $U' = G_1(V) \cap U_2$ and there exists $\varepsilon > 0$ such that $B_2(\boldsymbol{d}_0, \varepsilon) \subset G_1^{-1}(U') \cap B_1(\boldsymbol{d}_0, \varepsilon_1)$. It shows that the application

$$G : \left\{ \begin{array}{rcl} B_2(\boldsymbol{d}_0, \varepsilon) & \to & U' \\ \boldsymbol{d} & \mapsto & \operatorname{argmin}_{p \in U'} J_{\boldsymbol{d}}(p) \end{array} \right. , \tag{5.80}$$

is well-defined and continuously differentiable. Moreover, we also know that

$$\partial_{d_j} G(\boldsymbol{d}) = -[\nabla^2 J_{\boldsymbol{d}}(G(\boldsymbol{d}))]^{-1}[\partial_{d_j}\nabla J_{\boldsymbol{d}}(G(\boldsymbol{d}))]. \tag{5.81}$$

We denote $p_{\mathrm{LS}} = G(d)$, and

$$\|\partial_{d_j}\nabla J_{\boldsymbol{d}}(p_{\mathrm{LS}})\|_2 = \left\| \begin{pmatrix} -\mathcal{A}(\beta_{\mathrm{LS}} - \alpha_{\mathrm{LS}} t_j) \\ z_{\mathrm{LS}} t_j \mathcal{A}'(\beta_{\mathrm{LS}} - \alpha_{\mathrm{LS}} t_j) \\ -z_{\mathrm{LS}} \mathcal{A}'(\beta_{\mathrm{LS}} - \alpha_{\mathrm{LS}} t_j) \end{pmatrix} \right\|_2 \leq \sqrt{\|\mathcal{A}\|_\infty^2 + \alpha_{\max}\|\mathcal{A}'\|_\infty^2(1 + \|\boldsymbol{t}\|_\infty)} := c_1. \tag{5.82}$$

If follows that

$$\|p_{\mathrm{LS}} - p_0\|_2 = \|G(\boldsymbol{d}) - G(\boldsymbol{d}_0)\|_2 \leq \frac{2\sqrt{n}c_1}{m}\|\boldsymbol{d} - \boldsymbol{d}_0\|_2. \tag{5.83}$$

Finally,

$$|\Lambda(\boldsymbol{d}) - \Lambda(\boldsymbol{d}_0)| \leq \frac{1}{\alpha_{\min}}|\beta_{\mathrm{LS}} - \beta_0| + \frac{\beta_{\max}}{(\alpha_{\min})^2}|\alpha_{\mathrm{LS}} - \beta_{\mathrm{LS}}| \leq \left(\frac{1}{\alpha_{\min}} + \frac{\beta_{\max}}{(\alpha_{\min})^2}\right)\frac{2\sqrt{n}c_1}{m}\|\boldsymbol{d} - \boldsymbol{d}_0\|_2. \tag{5.84}$$

□

6

Reconstruction of smooth shape defects in waveguides from section measurements using locally resonant frequencies

This chapter aims to present an adaptation of the reconstruction method developed in Chapter 5 using now locally resonant frequencies one-side section measurements. At these frequencies, locally resonant modes propagate in the waveguide as periodic functions instead of Airy functions, and still depend on a locally resonant point $x^\star$. By post processing the measurements, we prove that one can get an approximation of an integral depending on $x^\star$. Then, given multi-frequency measurements taken on a section of the waveguide, we can approach this integral and provide and L^∞-stable explicit method to reconstruct the width of slowly monotonous varying waveguides. We validate this method on numerical data and discuss its limits.

6.1 Introduction

This chapter aims to extend the multi-frequency reconstruction method developed in Chapter 5 from surface measurements to section measurements. Even if this method was adapted for waveguides such as elastic plates where surface measurements are available, it is not suited to acoustic waveguides such as pipes or air ducts where data are often measured on one section of the waveguide [55, 27]. We present in the following all the adaptations required to use this method in acoustic waveguides.

6.1.1 Description of the problem

In this chapter, we work in two dimensions and we consider the varying acoustic waveguide described by

$$\Omega := \left\{(x, y) \in \mathbb{R}^2 \,|\, 0 < y < h(x)\right\}, \tag{6.1}$$

where $h \in \mathcal{C}^2(\mathbb{R}) \cap W^{2,\infty}(\mathbb{R})$ is a positive profile function defining the top boundary, and the bottom boundary is assumed to be flat (see an illustration in Figure 6.3). In the time-harmonic regime, the wavefield u satisfies the Helmholtz equation with Neumann boundary conditions

$$\begin{cases} \Delta u + k^2 u = -f & \text{in } \Omega, \\ \partial_\nu u = b & \text{on } \partial\Omega, \end{cases} \tag{6.2}$$

where k is the frequency, f is an interior source term, and b is a boundary source term. In this work, a waveguide is said to be slowly varying when there exists a small parameter $\eta > 0$ such that $\|h'\|_{\mathrm{L}^\infty(\mathbb{R})} \leq \eta$ and $\|h''\|_{\mathrm{L}^\infty(\mathbb{R})} \leq \eta^2$. We focus in this work on the recovery of the function h modeling the top boundary of the waveguide. Controlled sources f and b generate wavefields u in Ω for some frequencies $k \in K \subset \mathbb{R}_+^*$. We assume the knowledge of measurements $u(x, y)$ on the section $\Sigma := \{x_s\} \times (0, h(x_s))$ for some coordinate $x_s \in \mathbb{R}$ (see an illustration in Figure 6.3). The reconstruction of such defects given measurements on a section is good modeling of the monitoring of pipes, optical fibers, or train rails (see [50, 55, 54]).

If k is chosen such that $k = n\pi/h(x_k^\star)$ with $n \in \mathbb{N}$ and $x_k^\star \in \mathbb{R}$, the Helmholtz problem is not well posed in general [27]. Nevertheless, we proved in Chapter 4 that there exists a unique solution to this problem as long as the waveguide is slowly varying. In the same work, we also gave a suitable approximation of the wavefield that explicitly depends on $x_k^\star$. This approximation was used in Chapter 5 with surface measurements to recover the position of $x_k^\star$ for different frequencies called *locally resonant frequencies*, and then to provide a reconstruction of the shape function h. We now aim to adapt this method to section measurements and to solve the inverse problem

$$\text{Find} \quad h \quad \text{from} \quad u_k(x_s, y) \quad \forall k \in \mathbb{R}_+ \text{ where } k \text{ is a resonant frequency}, \tag{6.3}$$

and where the subscript k in u_k underlines the dependence of the wavefield u on the frequency k.

6.1.2 Scientific context

The detection and reconstruction of shape defects in a waveguide are mentioned in different works. In articles [61, 3, 2], the authors use a conformal mapping to map the geometry of the perturbed waveguide to the geometry of a regular waveguide, and suggest to inverse the mapping to recover the width defects. Different inversion methods based on the scattering field analysis are also developed in [75, 27, 34]. All these works perform the reconstruction using a single propagation frequency to perform detections and reconstructions of defects.

Our work concerns a different approach, also used in [13, 12], where we assume that data is available for a whole interval of frequencies. This usually provides additional information that should help to localize and to reconstruct the shape of the defect. Moreover, the use of multi-frequency data often provides uniqueness of the reconstruction (see [7]) and better stability (see [14, 52, 93]).

In Chapter 2, we already presented a method to recover small width variations using back scattering data. However, in this previous work, we avoided all the locally resonant frequencies of the waveguide, which are frequencies $k > 0$ such that $k = n\pi/h(x_k^\star)$ for a mode $n \in \mathbb{N}$ and a longitudinal position $x_k^\star$. In Chapter 5, we showed that these resonant frequencies could be used to recover slowly varying width defect given surface measurements. Given the high sensitivity of the reconstructions obtained using this method, we choose in this chapter to use the same approach and to work only with locally resonant frequencies.

The study of the forward problem is already done in Chapter 4, and we know that if k is a locally resonant frequency, the wavefield u strongly depends on the position $x_k^\star$. Our reconstruction method is inspired by the ideas presented in Chapter 5 and use measurements of the wavefield u to recover the position $x_k^\star$. Since $h(x_k^\star) = n\pi/k$, it gives up the information about the waveguide width at this precise location. By taking different locally resonant frequencies k and finding corresponding resonant location $x_k^\star$, we obtain a complete approximation of the width h of the waveguide.

If the global idea is the same as the one presented in Chapter 5, the realization strongly differs. Indeed, section measurements contain much less information than surface ones, and we need to recover the localization of $x_k^\star$ from the value of the resonant mode in one point instead of a whole interval. Thus, we first post process the measurements in order to find an approximation of

$$\xi(k) := \int_{x_k^\star}^{x_s} k_N, \tag{6.4}$$

where the wavenumber k_N is a known function of the width h and x_s is the source location. Then, using a quadrature formula of this integral, we show in Proposition 6.3 that all the coordinates $x_k^\star$ are close to solutions of a linear system that can be built from the data. We prove that our reconstruction method is L^∞-stable in case of an increasing width. The chapter is organized as follows. In section 6.2, we briefly recall needed results on the modal decomposition and the study of the forward problem. In section 6.3, we study the inverse problem with measurements taken at the section of the waveguide and provide a stability result for the reconstruction. Finally, in section 6.4, we illustrate our method with various reconstruction.

6.2 Brief study of the forward problem

Before studying the inverse problem associated with the reconstruction of the width in a varying waveguide, we recall some needed tools to study the forward problem. These results where already presented in Chapter 5 and their proofs can be found in Chapter 2 and [27]. However, Theorem 6.1 is slightly different from the one stated in Chapter 5 due to the change of measurements area.

A useful tool when working in waveguides is the modal decomposition. The following definition provides a modal decomposition in varying waveguides:

Definition 6.1. *We define the sequence of functions $(\varphi_n)_{n\in\mathbb{N}}$ by*

$$\forall (x,y) \in \Omega, \quad \varphi_n(x,y) := \begin{cases} 1/\sqrt{h(x)} & \text{if } n = 0, \\ \dfrac{\sqrt{2}}{\sqrt{h(x)}} \cos\left(\dfrac{n\pi y}{h(x)}\right) & \text{if } n \geq 1, \end{cases} \tag{6.5}$$

which for any fixed $x \in \mathbb{R}$ *defines an orthonormal basis of* $L^2(0, h(x))$.

Hence, a solution $u \in \mathrm{H}^2_{\mathrm{loc}}(\Omega)$ of (6.2) admits a unique modal decomposition

$$u(x,y) = \sum_{n\in\mathbb{N}} u_n(x)\varphi_n(x,y) \quad \text{where} \quad u_n(x) := \int_0^{h(x)} u(x,y)\varphi_n(x,y)\mathrm{d}y. \tag{6.6}$$

Note that u_n does not satisfy in general any nice equation. However, when h is constant (outside of $\mathrm{supp}(h')$), it satisfies an equation of the form $u_n'' + k_n^2 u_n = -g_n$ where $k_n = \sqrt{k^2 - n^2\pi^2/h^2}$ is the wavenumber. When h is variable, the decomposition (6.6) motivates the following definition:

Definition 6.2. *The local wavenumber function of the mode* $n \in \mathbb{N}$ *is the complex function* $k_n : \mathbb{R} \to \mathbb{C}$ *defined by*

$$k_n^2(x) := k^2 - \frac{n^2\pi^2}{h(x)^2}, \tag{6.7}$$

with $Re(k_n), Im(k_n) \geq 0$.

In this work, as $h(x)$ is non constant, $k_n(x)$ may vanish for some $x \in \mathbb{R}$ and change from a positive real number to a purely imaginary one. We then distinguish three different situations:

Definition 6.3. *A mode* $n \in \mathbb{N}$ *falls in one of these three situations:*

1. *If* $n < kh(x)/\pi$ *for all* $x \in \mathbb{R}$ *then* $k_n(x) \in (0, +\infty)$ *for all* $x \in \mathbb{R}$ *and the mode* n *is called propagative.*
2. *If* $n > kh(x)/\pi$ *for all* $x \in \mathbb{R}$ *then* $k_n(x) \in i(0, +\infty)$ *for all* $x \in \mathbb{R}$ *and the mode* n *is called evanescent.*
3. *If there exists* $x_k^\star \in \mathbb{R}$ *such that* $n = kh(x_k^\star)/\pi$ *the mode* n *is called locally resonant. Such points* $x_k^\star$ *are called resonant points, and there are simple if* $h'(x_k^\star) \neq 0$, *and multiple otherwise.*

A frequency $k > 0$ *for which there exists at least a locally resonant mode is called a locally resonant frequency.*

Using the wavenumber function, one can adapt the classic Sommerfeld (or outgoing) condition, defined in Chapter 2 for regular waveguides, to general varying waveguides Ω. This condition is used to guarantee uniqueness for the source problem given in equation (6.2).

Definition 6.4. *A wavefield* $u \in H^2_{loc}(\Omega)$ *is said to be outgoing if it satisfies*

$$\left| u_n'(x)\frac{x}{|x|} - ik_n(x)u_n(x) \right| \underset{|x|\to+\infty}{\longrightarrow} 0 \qquad \forall n \in \mathbb{N}, \tag{6.8}$$

where u_n *is given in* (6.6).

In all this work, we make the following assumptions:

Assumption 6.1. *We assume that* $h \in \mathcal{C}^2(\mathbb{R}) \cap W^{2,\infty}(\mathbb{R})$ *with* h' *compactly supported and that*

$$\forall x \in \mathbb{R} \quad h_{\min} \leq h(x) \leq h_{\max} \qquad \text{for some } 0 < h_{max} < h_{\min} < \infty.$$

We also assume that $h(x) = h_{\min}$ *or* $h(x) = h_{\max}$ *if* $x \notin supp(h')$. *For such a function we define a parameter* $\eta > 0$ *that satisfies for a constant* $R > 0$

$$\|h'\|_{L^\infty(\mathbb{R})} < \eta \qquad \text{and} \qquad \|h''\|_{L^\infty(\mathbb{R})} < \eta^2, \quad supp\, h' \subset \left(-\frac{R}{\eta}, \frac{R}{\eta}\right).$$

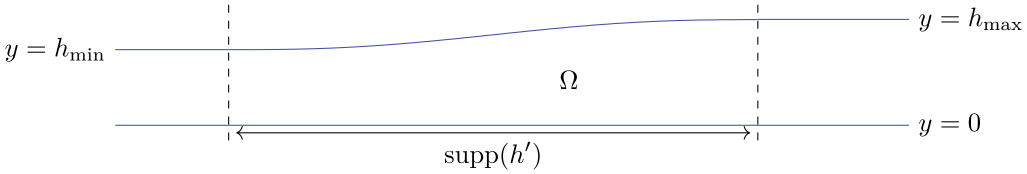

Figure 6.1 – Representation of an slowly compactly increasing varying waveguide.

Such a waveguide is represented in Figure 6.1.

The forward source problem is defined for every frequency by

$$(\mathcal{H}_k) : \begin{cases} \Delta u + k^2 u = -f & \text{in } \Omega, \\ \partial_\nu u = b_{\mathrm{top}} & \text{in } \partial\Omega_{\mathrm{top}}, \\ \partial_\nu u = b_{\mathrm{bot}} & \text{in } \partial\Omega_{\mathrm{bot}}, \\ u \text{ is outgoing}, & \end{cases} \tag{6.9}$$

As explained in [27], this problem is not well-posed when $\{x \mid k_n(x) = 0\}$ is a non-trivial interval of $\mathbb{R}$. This especially happens when $k = n\pi/h_{\min}$ or $k = n\pi/h_{\max}$. We then avoid these two forbidden situations and we set

$$\delta(k) := \min_{n\in\mathbb{N}} \left(\sqrt{\left| k^2 - \frac{n^2\pi^2}{{h_{\min}}^2} \right|}, \sqrt{\left| k^2 - \frac{n^2\pi^2}{{h_{\max}}^2} \right|} \right) > 0. \tag{6.10}$$

From now on, we define $(f_n)_{n\in\mathbb{N}}$ the modal decomposition of f, and

$$g_n(x) = \frac{f_n(x)}{\sqrt{h(x)}} + \varphi_n(1) b_{\mathrm{top}}(x) \frac{\sqrt{1 + (h'(x))^2}}{\sqrt{h}} + \varphi_n(0) b_{\mathrm{bot}}(x) \frac{1}{\sqrt{h}}. \tag{6.11}$$

Using the work done in Chapter 4, we are able to provide an approximation of the solution of (6.9). If h is increasing, we can state the following result using Theorem 4.1 and Remark 4.3 in Chapter 4:

Theorem 6.1. *Let h be an increasing function defining a varying waveguide Ω that satisfies Assumption 6.1 with a variation parameter $\eta > 0$. Consider sources $f \in L^2(\Omega) \cap L^\infty_c(\Omega)$, $b := (b_{bot}, b_{top}) \in (H^{1/2}(\mathbb{R}))^2 \cap (L^\infty_c(\mathbb{R})^2)$. Assume that there is a unique locally resonant mode $N \in \mathbb{N}$, associated with a simple resonant point $x_k^\star \in \mathbb{R}$.*

There exists $\eta_0 > 0$ depending only on $h_{\min}$, $h_{\max}$, $\delta(k)$ and R such that if $\eta \leq \eta_0$, then the problem $(\mathcal{H}_k)$ admits a unique solution $u \in H^2_{loc}(\Omega)$. Moreover, this solution is approached by u^{app} defined for almost every $(x, y) \in \Omega$ by

$$u^{app}(x, y) := \sum_{n\in\mathbb{N}} \left(\int_{\mathbb{R}} G_n^{app}(x, s) g_n(s) \mathrm{d}s \right) \varphi_n(y), \tag{6.12}$$

where $(f_n)_{n\in\mathbb{N}}$ *is the modal decomposition of* f*,* φ_n *is defined in* (6.5) *and* G_n^{app} *is given by*

$$G_n^{app}(x,s) := \begin{cases} \dfrac{i}{2\sqrt{k_n(s)k_n(x)}} \exp\left(i\left|\displaystyle\int_s^x k_n\right|\right), & \textit{if } n < N, \\ \dfrac{1}{2\sqrt{|k_n|(s)|k_n|(x)}} \exp\left(-\left|\displaystyle\int_s^x |k_n|\right|\right), & \textit{if } n > N, \\ \begin{cases} \dfrac{\pi(\xi(s)\xi(x))^{1/4}}{\sqrt{k_n(s)k_n(x)}}\big(i\mathcal{A}+\mathcal{B}\big)\circ\xi(s)\mathcal{A}\circ\xi(x) & \textit{if } x < s, \\ \dfrac{\pi(\xi(s)\xi(x))^{1/4}}{\sqrt{k_n(s)k_n(x)}}\big(i\mathcal{A}+\mathcal{B}\big)\circ\xi(x)\mathcal{A}\circ\xi(s) & \textit{if } x > s, \end{cases} & \textit{if } n = N. \end{cases} \tag{6.13}$$

Function k_n *is the wavenumber function defined in Definition 6.2 and the function* ξ *is given by*

$$\xi(x) := \begin{cases} \left(-\dfrac{3}{2}i\displaystyle\int_x^{x_k^\star} k_N(t)\mathrm{d}t\right)^{2/3} & \textit{if } x < x_k^\star, \\ -\left(\dfrac{3}{2}\displaystyle\int_{x_k^\star}^x k_N(t)\mathrm{d}t\right)^{2/3} & \textit{if } x > x_k^\star. \end{cases} \tag{6.14}$$

Precisely, given a coordinate $x_s \in \mathbb{R}$*, there exist a constant* $C_1 > 0$ *depending only on* $h_{\min}$*,* $h_{\max}$ *and* N *such that*

$$|u_N(x_s) - u_N^{app}(x_s)| \leq \eta C_1 \delta(k)^{-8}\left(\|f\|_{L^2(\Omega)} + \|b\|_{\left(H^{1/2}(\mathbb{R})\right)^2}\right). \tag{6.15}$$

This result provides an approximation of the measurements of the N-th mode for every frequency, and a control of the approximation error. We notice that at locally resonant frequencies, the wavefield strongly depends on the position of $x_k^\star$, which justifies the idea of using it to develop an inverse method to reconstruct the width h. In this work, we assume that we have access to the exact data function

$$d_k^{\text{ex}}(y) := u_k(x_s, y) \qquad \forall k > 0 \quad \forall y \in (0, h(x_s)). \tag{6.16}$$

Here, the subscript k underline the dependence on the frequency k. To lighten the notations, this subscript will be omitted in the following when it is not necessary. An illustration is provided in Figure 6.2 with a representation of the wavefield u_k and the section measurements $u(x_s, y)$ when k is a locally resonant frequency.

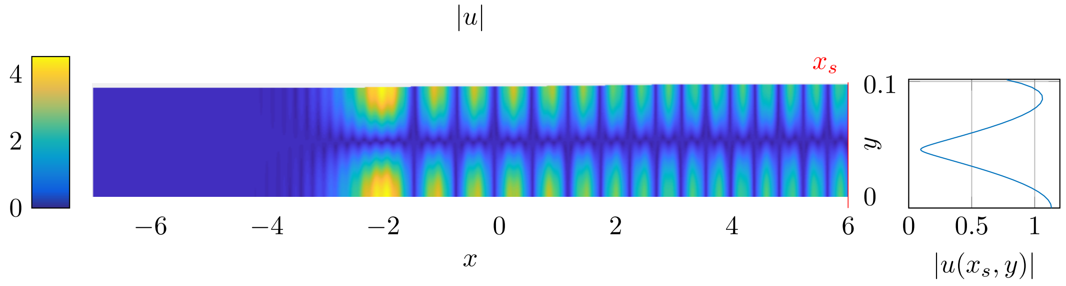

Figure 6.2 – Illustration of the wavefield measurements in a varying waveguide. The wavefield u is solution of (6.9) where h is defined in (6.51), $N = 1$ and $k = 31.5$ is a locally resonant frequency. Data are generated using the finite element method described in section 6.4.1. Left: amplitude of $|u|$ in the whole waveguide Ω. Right: measurements of $|u|$ on the section $x_s = 6$.

6.3 Inversion using section measurements

In this section, we study the inverse problem and assume that measurements on one section of the waveguide are available for every frequency. Given a chosen known source term, we assume that we have access to the wavefield on a section $x = x_s$. From now on, we assume that the waveguide is slowly increasing and that source terms f and b generating the wavefield in (6.9) are located at the right of the measurement section $x = x_s$. Such a configuration is represented in Figure 6.3.

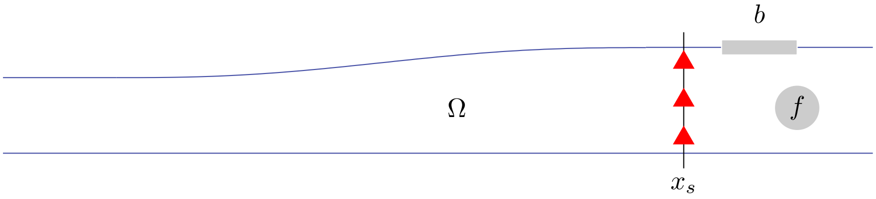

Figure 6.3 – Set up of the inversion in the slowly variable waveguide Ω. An internal source f and a boundary source b generate a wavefield propagating in the waveguide and measured on the section $x = x_2$, represented by red triangles.

Using results presented in section 6.2 on the modal decomposition, the measurements of $u(x_s, y)$ for every $y \in (0, h(x_s))$ gives us access to

$$\forall n \in \mathbb{N} \qquad u_n(x_s) = \int_0^{h(x)} u(x_s, y)\varphi_n(y)\mathrm{d}y. \tag{6.17}$$

This problem is often seen as a back scattering problem when it is studied away from locally resonant frequencies. Sending a known incident wave an measuring its scattered field, one can find useful linearised information on the width of the waveguide (see Chapter 2 and [27, 23]). However, we remind that the approach used here is different since we try to use locally resonant frequencies to develop a new method of reconstruction. Therefore, the dependence between the shape h and the scattered field becomes highly non linear.

We assume that there exists a resonant mode N, and that the modal source term g_N defined in (6.11) is not vanishing everywhere. We focus on the reconstruction of the shape of h on $\mathrm{supp}(h')$, assuming that an approximation of $h_{\max}$ and $h_{\min}$ is already given. We detail in Appendix 6.A how these constants can be estimated. Given a set of locally resonant frequencies $K = (k_i)_{1\leq i\leq m} \subset (N\pi/h_{\max}, N\pi/h_{\min})$, our method is based on the recovery of $x^\star_{k_i}$ for every locally resonant frequency $k \in K$, and we aim to solve the discretized inverse problem

$$\text{Find} \quad (x^\star_{k_1}, \dots, x^\star_{k_m}) \quad \text{from} \quad u_{k\,N}(x_s) \quad \forall k \in K = (k_1, \dots, k_m), \tag{6.18}$$

We then use the study of the forward problem at locally resonant frequencies presented in Theorem 6.1 to show that $u_N(x_s)$ is almost proportional to

$$\Phi\left(\int_{x^\star_k}^{x_s} k_N(z)\mathrm{d}z\right), \quad \text{where} \quad \Phi(x) := \sin\left(x + \frac{\pi}{4}\right)\exp\left(ix + i\frac{\pi}{4}\right), \tag{6.19}$$

Under certain conditions, we can find a reciprocal function of the π-periodic function Φ which gives access for all resonant frequencies k to

$$\zeta(k) := \int_{x^\star_k}^{x_s} k_N(z)\mathrm{d}z. \tag{6.20}$$

Using a composite rule of order 1 to approach this integral for the given set of frequencies K, we show that the vector formed with all the $x^\star_{k_i}$ is solution of a linear system, which provides a stable reconstruction of $(x^\star_{k_1}, \dots, x^\star_{k_m})$. Then, using the fact that

$$h(x^\star_{k_i}) = \frac{N\pi}{k_i}, \tag{6.21}$$

we get a good approximation of the local width h at each coordinate $x^\star_{k_i}$.

6.3.1 Approximation and processing of measurements

As mentioned before, we want to find an exploitable link between the approached data $u_N(x_s)$ and $x^\star_k$ in order to reconstruct $x^\star_k$. From now on, we denote

$$K := (k_i)_{1\le i\le m} \subset \left(\frac{N\pi}{h_{\max}}, \frac{N\pi}{k_{\min}}\right), \tag{6.22}$$

the set of locally resonant frequencies where measurements are taken. Each frequency k_i is associated to a wavenumber

$$k_{i,N}(x) := \sqrt{k_i^2 - \frac{N^2\pi^2}{h(x)^2}}, \tag{6.23}$$

and a single locally resonant point $x^\star_{k_i}$. We set $k_0 := N\pi/h_{\max}$, $k_{m+1} = N\pi/h_{\min}$ and $\mathrm{supp}(h) := (x_{m+1}, x_0)$. Finally, we define like in (6.10) the quantity

$$\delta(K) = \min_{1\le i\le m} \left(\sqrt{k_0^2 - k_i^2}, \sqrt{k_i^2 - k_{m+1}^2}\right). \tag{6.24}$$

We assume that K has a constant discretization step denoted ρ. We choose source terms f and b located at the right of the measurement section x_s, and we define g_N as in (6.11). In order to use Theorem 6.1, each locally resonant point $x^\star_{k_i}$ must be simple, meaning that $h'(x^\star_{k_i}) \neq 0$. We assume that it is the case, and that

$$\theta\eta := \inf_{x\in(x^\star_{k_m}, x^\star_{k_1})} h'(x) > 0. \tag{6.25}$$

Then, we can provide a first approximation of measured N-th mode for every frequency $k \in K$:

Proposition 6.1. *Assume that Ω satisfies assumption 6.1. Let $x_s \in \mathbb{R}$, there exist $\eta_0, A > 0$ such that if $\eta < \eta_0$ and $x_s - x_0 > A$, then there exists $C_2 > 0$ depending on δ, $h_{\min}$ and $h_{\max}$ such that for every $k \in K$,*

$$\left| u_N(x_s) - \frac{q(x_s)}{k_N(x_s)}\Phi(\zeta(k))\right| \le \eta C_2, \tag{6.26}$$

where $q(x_s) := \int_{\mathbb{R}} g_N(z)e^{ik_N(x_s)(z-x_s)}\mathrm{d}z$ depends on the source terms.

Proof. Using Theorem 6.1, we know that for every $k \in K$,

$$|u_N(x_s) - u_N^{\mathrm{app}}(x_s)| \le \eta C_1 \delta^{-8}\left(\|f\|_{\mathrm{L}^2(\mathbb{R})} + \|b\|_{\mathrm{H}^{1/2}(\mathbb{R})}\right),$$

where

$$u_N^{\mathrm{app}}(x_s) = \frac{\pi(-\xi(x_s))^{1/4}\mathcal{A}(\xi(x_s))}{k_N(x_s)} \int_{\mathbb{R}} g_N(z)(-\xi(z))^{1/4}(i\mathcal{A}+\mathcal{B})(\xi(z))\mathrm{d}z.$$

Using approximations of Airy functions provided in [78] and [37, Chap. 9.7], we see that there exists a constant $c_1 > 0$ such that for all $x > 0$,

$$\left|\sqrt{\pi}x^{1/4}\mathcal{A}(-x) + \sin\left(\frac{2}{3}x^{3/2} + \frac{\pi}{4}\right)\right| \leq \frac{c_1}{x^{5/4}},$$

$$\left|\sqrt{\pi}x^{1/4}\mathcal{B}(-x) + \cos\left(\frac{2}{3}x^{3/2} + \frac{\pi}{4}\right)\right| \leq \frac{c_1}{x^{5/4}}.$$

and so

$$\left|\sqrt{\pi}x^{1/4}(i\mathcal{A} + \mathcal{B})(-x) + \exp\left(i\frac{2}{3}x^{3/2} + i\frac{\pi}{4}\right)\right| \leq \frac{2c_1}{x^{5/4}},$$

Replacing x by $-\xi(x)$ or $-\xi(x_s)$ leads to

$$\left|u_N^{\mathrm{app}}(x_s) - \frac{q(x_s)}{k_N(x_s)}\Phi(\zeta(k))\right| \leq \delta^{-1}\|g_N\|_{\mathrm{L}^1(\mathbb{R})}\frac{3c_1 + 2c_1^2}{(-\xi(x_s))^{5/4}}.$$

We conclude the proof by noticing that

$$-\xi(x_s) = \left(\frac{3}{2}\int_{x_k^\star}^{x_s} k_N(t)\mathrm{d}t\right)^{2/3} \geq (x_s - x_0)^{2/3}k_N(x_s)^{2/3} \underset{x_s \to +\infty}{\longrightarrow} +\infty.$$

□

Since source terms are assumed to be chosen, $q(x_s)$ and $k_N(x_s)$ are explicit quantities and we consider the following modified data:

$$v_k := \frac{k_N(x_s)}{q(x_s)}u_N(x_s), \qquad v_k^{\mathrm{app}} := \Phi(\zeta(k)) = \Phi\left(\int_{x_k^\star}^{x_s} k_N(z)\mathrm{d}z\right). \tag{6.27}$$

Proposition 6.1 can be rewritten as follows:

Corollary 6.1. *Assume that Ω satisfies assumption 6.1. Let $x_s \in \mathbb{R}$, there exist $\eta_0, A > 0$ such that if $\eta < \eta_0$ and $x_s - x_0 > A$, then there exists $C_2 > 0$ depending on δ, $h_{\min}$ and $h_{\max}$ such that for every $k \in K$,*

$$|v_k - v_k^{app}| \leq \eta c_2 C_2, \tag{6.28}$$

where

$$c_2 := \max_{k \in K}\left(\frac{k_N(x_s)}{q(x_s)}\right).$$

To get access to $\zeta(k)$, we need to find the left inverse function of Φ. Since Φ is π-periodic, we can only provide a partial left inverse function Φ^{-1} modulus π satisfying $\Phi^{-1}(\Phi(\theta)) = \theta \bmod(\pi)$, with

$$\Phi^{-1}(z) := \begin{cases} \arcsin(|z|) & \text{if } |z| < 0.5 \text{ and } \mathrm{Real}(z) \geq 0, \\ \pi - \arcsin(|z|) & \text{if } |z| < 0.5 \text{ and } \mathrm{Real}(z) < 0, \\ \arccos\left(\mathrm{Real}(z)/|z|\right) & \text{if } |z| \geq 0.5. \end{cases} \tag{6.29}$$

We represent in Figure 6.4 the values of $\Phi^{-1}(v_k) \bmod(\pi)$ for different sets of frequency. We can see that the step of discretization of K needs to be sufficiently small if we expect to get rid of the modulus π. Using the fact that ζ is increasing and assuming that ρ the discretization step of K is small enough, the following proposition proves that we can get rid of the modulus π up to a constant. We set

$$\ell = \left\lfloor\frac{\zeta(k_1)}{\pi}\right\rfloor, \qquad t_i^{\mathrm{app}} = \zeta(k_i) - \ell\pi, \quad 1 \leq i \leq m. \tag{6.30}$$

Proposition 6.2. *Assume that Ω satisfies assumptions 6.1. There exist $\eta_0, A > 0$ such that if $\eta < \eta_0$, $x_s - x_0 > A$, there exist $\rho_0 > 0$ depending on x_s and η such that if $\rho < \rho_0$, then there exist a unique sequence $(t_i)_{1\leq i\leq m}$ such that*

$$\forall 1 \leq i \leq m \quad t_i = \Phi^{-1}(v_{k_i}) \ mod(\pi), \qquad |t_{i+1} - t_i| < \pi/2. \tag{6.31}$$

Moreover, there exists a constant $C_3 > 0$ depending on δ, θ, $h_{\min}$ and $h_{\max}$ such that

$$\forall 1 \leq i \leq m \quad |t_i - t_i^{app}| \leq C_3\eta. \tag{6.32}$$

Proof. Using Corollary 6.1, there exist $\eta_0, A > 0$ such that if $\eta < \eta_0$ and $x_s - x_0 > A$ then

$$|v_k - v_k^{\text{app}}| \leq \min(0.25, \eta c_2 C_2).$$

The quantity 0.25 is chosen to ensure that in each case of the definition of $\Phi^{-1}(v_k)$, we then have $|v_k|, |v_k^{\text{app}}| \leq 0.75$ or $|v_k|, |v_k^{\text{app}}| \geq 0.25$. Then, we see that for every $k \in K$,

$$|\Phi^{-1}(v_k) - \Phi^{-1}(v_k^{\text{app}})| \leq \frac{1}{\sqrt{1-0.75^2}}|v_k - v_k^{\text{app}}| < \min(1.6\,\eta c_2 C_2, \pi/8).$$

We also notice that

$$0 \leq t_{i+1}^{\text{app}} - t_i^{\text{app}} = \int_{x^\star_{k_{i+1}}}^{x^\star_{k_i}} k_{i+1,N} + \int_{x^\star_{k_i}}^{x_s} (k_{i+1,N} - k_{i,N}).$$

Using the fact that

$$|x^\star_{k_i} - x^\star_{k_{i+1}}| = \left| h^{-1}\left(\frac{N\pi}{k_i}\right) - h^{-1}\left(\frac{N\pi}{k_{i+1}}\right)\right| \leq \frac{1}{\theta\eta}\left|\frac{N\pi}{k_i} - \frac{N\pi}{k_{i+1}}\right| \leq \frac{\rho N\pi}{k_0^2\theta\eta},$$

we have

$$\int_{x^\star_{k_{i+1}}}^{x^\star_{k_i}} k_{i+1,N} \leq k_{n+1,N}(x_s)(x^\star_{k_i} - x^\star_{k_{i+1}}) = \mathcal{O}(\rho\eta^{-1}),$$

$$\int_{x^\star_{k_i}}^{x_s} (k_{i+1,N} - k_{i,N}) \leq (x_s - x_{m+1})\rho\frac{k_{m+1}}{\delta} = \mathcal{O}(\rho(x_s - x_0)),$$

we denote by $\mathcal{O}$ every majoration depending only on δ, θ, $h_{\min}$, $h_{\max}$. If ρ is small enough compared to $(x_s - x_0)^{-1}$ and η then

$$|t_{i+1}^{\text{app}} - t_i^{\text{app}}| < \pi/4.$$

Therefore,

$$|t_{i+1} - t_i| \leq |t_{i+1} - t_{i+1}^{\text{app}}| + |t_{i+1}^{\text{app}} - t_i^{\text{app}}| + |t_i^{\text{app}} - t_i| < \pi/2.$$

Since there is a one-to-one correspondence between a sequence where the distance between each term does not exceed $\pi/2$ and its representation modulus π, we conclude our proof.

□

This result is illustrated in Figure 6.4 where we see that providing a sufficiently small discretization of the frequency interval, we can recover an approximation of each t_i^{app} giving measurements of $\Phi^{-1}(v_k)$. Lastly, we have to find the constant $\ell \in \mathbb{N}$ in order to reconstruct a complete approximation of $\zeta(k)$. Since

$$t_1 \approx t_1^{\text{app}} \approx (x_s - x^\star_{k_1})k_{1,N}(x_s) - \ell\pi, \quad t_2 \approx t_2^{\text{app}} \approx (x_s - x^\star_{k_1})k_{2,N}(x_s) - \ell\pi, \tag{6.33}$$

we propose to approach ℓ by the following expression:

$$\ell^{\mathrm{app}} = \left\lfloor \frac{t_2 k_{1,N}(x_s) - t_1 k_{2,N}(x_s)}{\pi(k_{2,N}(x_s) - k_{1,N}(x_s))} \right\rfloor . \tag{6.34}$$

The following lemma proves that under certain assumptions, the closest natural number to ℓ^{app} can be a good approximation of ℓ:

Lemma 6.1. *Under the same assumptions as in Proposition 6.2, if $\delta(K)$, $x_0 - x^\star_{k_2}$ and ν are sufficiently small then $\ell = \ell^{app}$.*

Proof. We notice that

$$\ell\pi = \int_{x^\star_{k_1}}^{x_s} k_{1,N}(z)\mathrm{d}z - t_1^{\mathrm{app}} \approx (x_s - x^\star_{k_1})k_{1,N}(x_s) - t_1.$$

More precisely, we introduce ε_1 such that

$$(x_s - x^\star_{k_1})k_{1,N}(x_s) = \ell\pi + t_1 + \varepsilon_1,$$

and using Proposition 6.2, there exists a constant $c_3 > 0$ such that

$$|\varepsilon_1| \leq C_3\eta + \left| \int_{x^\star_{k_1}}^{x_0} (k_{1,N}(z) - k_{1,N}(x_0))\mathrm{d}z \right| \leq C_3\eta + c_3(x_0 - x^\star_{k_2})\delta(K).$$

Similarly, we introduce ε_2 such that $(x_s - x^\star_{k_1})k_{2,N}(x_s) = \ell\pi + t_2 + \varepsilon_2$ and

$$|\varepsilon_2| \leq C_3\eta + d_3(x_0 - x^\star_{k_2})\delta(K).$$

It follows that

$$|\ell - \ell^{\mathrm{app}}| \leq \frac{|\varepsilon_2|k_{2,N}(x_s) + |\varepsilon_1|k_{1,N}(x_s)}{k_{2,N}(x_s) - k_{1,N}(x_s)},$$

and this quantity is smaller than 1 if ε_1 and ε_2 are small enough. Since $\ell, \ell^{\mathrm{app}} \in \mathbb{N}$, it concludes the proof. ☐

Using this lemma, we can find the value of ℓ. We represent in Figure 6.4 the different steps of the post processing:

- First, we compute v_{k_i} defined in (6.27) for all $1 \leq i \leq m$ using the information on source terms and measurements of the wavefield. The quantity v_{k_i} is a good approximation of $\Phi(\zeta(k_i))$.
- Then, we recover each $\zeta(k_i)$ up to a constant ℓ by applying Φ^{-1} on v_{k_i} and getting rid of the modulus π.
- Finally, we compute the value of the constant ℓ using (6.34) and deduce a good approximation of $\zeta(k_i)$ for $1 \leq i \leq m$.

As mentioned in Proposition 6.2, we clearly see the importance of choosing a sufficiently small discretization of the frequency interval K in order to get a good approximation at the end of the postprocessing of the measurements.

To summarize, we proved in this section that if the step of discretization of K is sufficiently small, we are able to post process the measurements in order to find an approximation of $\zeta(k_i)$ for every frequency $k_i \in K$. Moreover, this approximation is improving is η diminishes. From now on, we work on data $(d_i)_{1\leq i\leq m}$ satisfying

$$\forall i = 1, \dots, m \qquad d_i := t_i + \ell\pi, \quad |d_i - \zeta(k_i)\mathrm{d}z| \leq C_3\eta. \tag{6.35}$$

The next section aims to inverse the problem and reconstruct $(x^\star_{k_i})_{1\leq i\leq m}$ using this data.

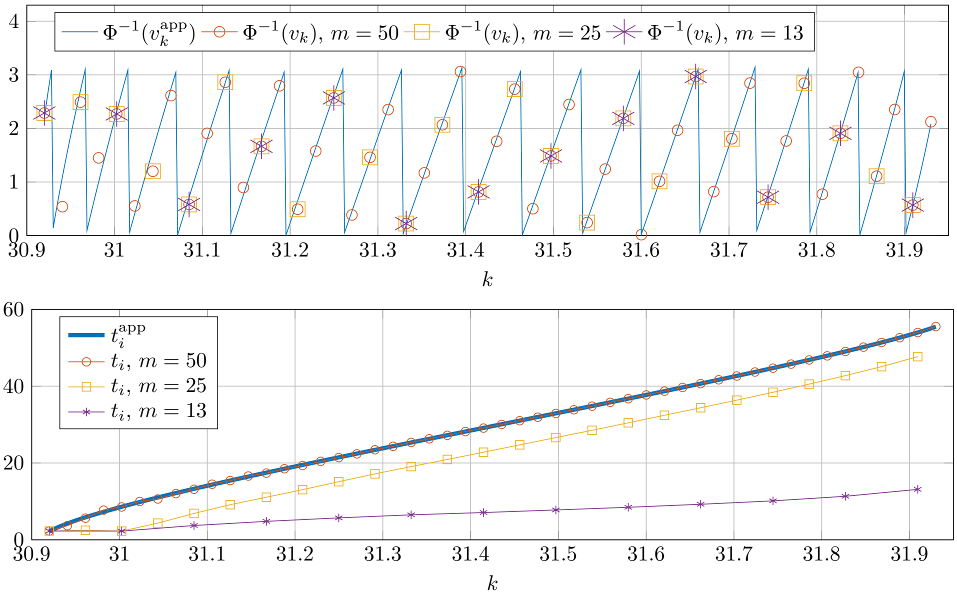

Figure 6.4 – Representation of two steps of the post processing of measurements for a set of frequencies $K = 30.92 : 31.93 : m$, $x_s = 6$, h defined in (6.48) and source defined in (6.52). On the top, representation of $\Phi^{-1}(v_k^{\text{app}})$ and $\Phi^{-1}(v_k)$ modulus π. On the bottom, representation of t_i^{app} and t_i after getting rid of the modulus π. Here, $\ell^{\text{app}} = 0$.

6.3.2 Recovery of $x_k^\star$

Using the post processing of measurements and the data provided in the previous section, we now try to reconstruct from $(\zeta(k_i))_{1\leq i\leq m}$ the set $X^\star := (x_{k_i}^\star)_{1\leq i\leq m}$. To do so, we need to find a link between $(\zeta(k_i))_{1\leq i\leq m}$ and $X^\star$. Noticing that

$$\forall 1 \leq i \leq m \quad h(x_{k_i}^\star) = \frac{N\pi}{k_i}, \qquad \forall 1 \leq j < i \leq m \quad k_{i,N}(x_{k_j}^\star) = \sqrt{k_i^2 - \frac{N^2\pi^2}{h(x_{k_j}^\star)^2}} = \sqrt{k_i^2 - k_j^2}, \tag{6.36}$$

we choose to discretize the integral $\int_{x_{k_i}^\star}^{x_s} k_{i,N}$ on the grid $(x_{k_j}^\star)_{1\leq j\leq i}$. We define

$$p_{i,j} := \sqrt{|k_i^2 - k_j^2|}. \tag{6.37}$$

Since h is increasing, $x \mapsto k_{i,N}(x)$ is concave and we know that for all $j > 2$,

$$\int_{x_{k_j}^\star}^{x_{k_{j-1}}^\star} k_{i,N} \geq (x_{k_{j-1}}^\star - x_{k_j}^\star)\frac{k_{i,N}(x_{k_j}^\star) + k_{i,N}(x_{k_{j-1}}^\star)}{2} = (x_{k_{j-1}}^\star - x_{k_j}^\star)\frac{p_{i,j} + p_{i,j-1}}{2}, \tag{6.38}$$

$$\int_{x_{k_j}^\star}^{x_{k_{j-1}}^\star} k_{i,N} \leq (x_{k_{j-1}}^\star - x_{k_j}^\star)k_{i,N}(x_{k_{j-1}}^\star) = (x_{k_{j-1}}^\star - x_{k_j}^\star)p_{i,j-1}. \tag{6.39}$$

We choose to approach the integral using the mean of these two bounds:

$$\int_{x_{k_j}^\star}^{x_{k_{j-1}}^\star} k_{i,N} \approx \frac{1}{4}(x_{k_{j-1}}^\star - x_{k_j}^\star)\left(p_{i,j} + 3p_{i,j-1}\right). \tag{6.40}$$

Remark 6.1. *We chose here to approach the integral by taking the mean of a rectangle and a trapezoidal rule. However, any barycenter between these two bounds would also work. Further investigations may prove that the mean may not be the optimal choice. However, giving the lack of regularity of* $k_{i,N}$ *around* $x^\star_{k_i}$*, any quadrature method should give the same error estimation up to a constant.*

The approximation when $j = 1$ is

$$\int_{x^\star_{k_1}}^{x_s} k_{i,N} \approx (x_s - x^\star_{k_1}) k_{i,N}(x_s) = (x_s - x^\star_{k_1}) p1, 0. \tag{6.41}$$

We define the matrix

$$M := \frac{1}{4} \begin{pmatrix} 4p_{1,0} & 0 & 0 & \dots & 0 \\ 4p_{2,0} & 3p_{2,1} & 0 & & \vdots \\ 4p_{3,0} & p_{3,2} + 3p_{3,1} & \ddots & \ddots & \vdots \\ \vdots & \vdots & \ddots & 3p_{m-1,m-2} & 0 \\ 4p_{m,0} & p_{m,2} + 3p_{m,1} & \dots & p_{m,m-1} + 3p_{m,m-2} & 3p_{m,m-1} \end{pmatrix}, \tag{6.42}$$

and we expect that

$$MV \approx d := (d_i)_{1 \le i \le n}, \qquad \text{where} \qquad V = \begin{pmatrix} x_s - x^\star_{k_1} \\ x^\star_{k_1} - x^\star_{k_2} \\ \vdots \\ x^\star_{k_{m-1}} - x^\star_{k_m} \end{pmatrix}. \tag{6.43}$$

The following proposition quantify the error of this approximation.

Proposition 6.3. *Assume that* Ω *satisfies assumption 6.1. There exist* $\eta_0, A > 0$ *such that if* $\eta < \eta_0$*,* $x_s - x_0 > A$*, there exists* $\rho_0 > 0$ *such that if* $\rho < \rho_0$*, then there exist constants* $C_4, C_5 > 0$ *depending on* δ*,* θ*,* $h_{\min}$ *and* $h_{\max}$ *such that*

$$\|d - MV\|_\infty \le 2C_3\eta + C_4 + C_5\eta\rho. \tag{6.44}$$

Proof. Using the proof of Lemma 6.1, we already know that

$$\left| \int_{x^\star_{k_1}}^{x_s} k_{i,N} - (x_s - x^\star_{k_1}) p_{i,0} \right| \le C_3\eta + c_3(x_0 - x^\star_{k_2})\delta(K).$$

Then, we denote by $z \in (x^\star_{k_j}, x^\star_{k_{j-1}})$ the coordinate such that $k_{i,N}(z) = (p_{i,j} + 3p_{i,j-1}/4$. If $j < i$, then

$$|k_{i,N}(x) - k_{i,N}(z)| \le |x - z| \frac{N^2\pi^2\eta}{h^3_{\min} k_{i,N}(x^\star_{k_j})} \le |x^\star_{k_j} - x^\star_{k_{j-1}}| \frac{N^2\pi^2\eta}{h^3_{\min}\sqrt{2}\sqrt{k_0}\sqrt{i-j}\rho^{1/2}}.$$

If $j = i$ and $x > z$, then

$$|k_{i,N}(x) - k_{i,N}(z)| \le |x^\star_{k_i} - x^\star_{k_{i-1}}| \frac{4N^2\pi^2\eta}{3h^3_{\min} p_{i,i-1}} \le |x^\star_{k_i} - x^\star_{k_{i-1}}| \frac{4N^2\pi^2\eta}{3h^3_{\min}\rho^{1/2}\sqrt{2}\sqrt{k_0}}.$$

If $j = i$ and $x < z$, we use the approximation of $k_{i,N}$ near $x^\star_{k_i}$ demonstrated in Chapter 5 and [85] to deduce that there exists a constant $c_4 > 0$ depending on θ such that

$$k_{i,N}(x) \geq c_4 (x - x^\star_{k_i})^{1/2}.$$

If follows that

$$|k_{i,N}(x) - k_{i,N}(z)| \leq |x^\star_{k_i} - x^\star_{k_{i-1}}| \frac{N^2\pi^2\eta}{h^3_{\min} c_4 (x - x^\star_{k_i})^{1/2}},$$

$$\int_{x^\star_{k_i}}^{z} |k_{i,N}(x) - k_{i,N}(z)| \mathrm{d}x \leq |x^\star_{k_i} - x^\star_{k_{i-1}}|^{3/2} \eta^{1-\nu/2} \frac{N^2\pi^2}{h^3_{\min} c_4}.$$

By noticing that $|x^\star_{k_i} - x^\star_{k_{i-1}}| = \mathcal{O}(\rho)$, we conclude that there exists a constant $c_5 > 0$ such that

$$\left| \int_{x^\star_{k_j}}^{x^\star_{k_{j-1}}} k_{i,N} - \frac{1}{4} (x^\star_{k_{j-1}} - x^\star_{k_j}) \left(p_{i,j} + 3p_{i,j-1}\right) \right| \leq c_5 \eta \rho^{3/2} \left(\delta_{i=j} + \frac{1}{\sqrt{i-j}} \delta_{i>j} \right).$$

By assembling everything, we see that

$$|m_i - (MV)_i| \leq 2C_3\eta + \delta c_3 (x_0 - x^\star_{k_2}) + c_5 \eta \rho^{3/2} \left(1 + \sum_{j=1}^{i-1} \frac{1}{\sqrt{j}} \right).$$

We conclude the proof by noticing that $\displaystyle\sum_{j=1}^{i} j^{-1/2} = \mathcal{O}\left(\sqrt{i}\right)$. ☐

Remark 6.2. *Note that D_4 is proportional to $\delta(K)$, so $\delta(K)$ needs to be small in order to diminish the error in this approximation. However, we mentioned in Chapter 5 that $\theta^{-1} \underset{\delta(K)\to 0}{\to} +\infty$. It means that if we want to diminish D_4, we might in return also increase D_5.*

The matrix M is a lower triangular matrix with non vanishing diagonal entries so it is invertible. To find an approximation of vector V and of $X^\star$ given data d, we define

$$V^{\text{app}} = M^{-1} d, \qquad (X^{\star,\text{app}})_i := x^{\star,\text{app}}_{k_i} = x_s - \sum_{j=1}^{i} V^{\text{app}}_j. \tag{6.45}$$

Since we know that $h(x^\star_{k_i}) = N\pi/k_i$, we define the approximation of the width h by

$$h^{\text{app}}(x^{\star,\text{app}}_{k_i}) = \frac{N\pi}{k_i} \quad \forall\, k_i \in K, \qquad h^{\text{app}}(x_0) = \frac{N\pi}{k_{m+1}}, \qquad h^{\text{app}}(x_{m+1}) = \frac{N\pi}{k_0}. \tag{6.46}$$

The following Theorem proves that we are able to quantify the error of reconstruction between h^{app} and h:

Theorem 6.2. *Let K be a subset of $(k_{\min}, k_{\max})$. Assume that Ω satisfies assumption 6.1. There exist $\eta_0, A > 0$ such that if $\eta < \eta_0$ and $x_s - x_0 > A$, there exists $\rho_0 > 0$ such that if $\rho < \rho_0$ then there exist constants $D_3, D_4, D_5, D_6 > 0$ depending on θ, δ, $h_{\min}$ and $h_{\max}$ such that*

$$\|h^{app}(X^{\star,app}) - h(X^{\star,app})\|_\infty \leq \eta \rho^{-5/2} D_6 \left(D_4 + \eta D_3 + \eta \rho D_5\right). \tag{6.47}$$

Proof. For every $1 \le i \le m$, we see that

$$|x^{\star,\mathrm{app}}_{k_i} - x^{\star}_{k_i}| \le \left|\sum_{j=1}^{n} V_j^{\mathrm{app}} - V_j\right| \le \left|\sum_{j=1}^{n} M^{-1}(d_j - (MV)_j)\right|.$$

We denote $a = d - MV$, and $b = M^{-1}a$. We see that

$$b_1 = \frac{a_1}{p_{1,0}}, \qquad b_i = \frac{4}{3p_{i,i-1}}\left[a_i - p_{i,0})a_1 - \sum_{j=2}^{i-1}(p_{i,j} + 3p_{i,j-1})a_j\right],$$

It follows that

$$b_1 = \mathcal{O}(\|a\|_\infty), \qquad b_i = \mathcal{O}(\rho^{-1/2} m \|a\|_\infty) = \mathcal{O}(\rho^{-3/2}\|a\|_\infty),$$

$$\left|\sum_{i=1}^{n} b_i\right| = \mathcal{O}(\|a\|_\infty \rho^{-3/2} m) = \mathcal{O}(\|a\|_\infty \rho^{-5/2}).$$

We conclude using Proposition 6.3 and the fact that

$$|h^{\mathrm{app}}(x^{\star,\mathrm{app}}_{k_i}) - h(x^{\star,\mathrm{app}}_{k_i})| \le |h(x^{\star}_{k_i}) - h(x^{\star,\mathrm{app}}_{k_i})| \le \eta |x^{\star}_{k_i} - x^{\star,\mathrm{app}}_{k_i}|.$$

□

Remark 6.3. *We notice in this inequality that if η tends to zero then the error also tends to zero. However, for a fixed η, the parameter ρ needs to be chosen wisely since it needs to be small enough in order for the post processing of the measurements to work, and high enough so that the matrix M is well conditioned. We illustrate it in Figure 6.5 where we present two different reconstructions with the same post processing data discretized for two different set of frequencies K.*

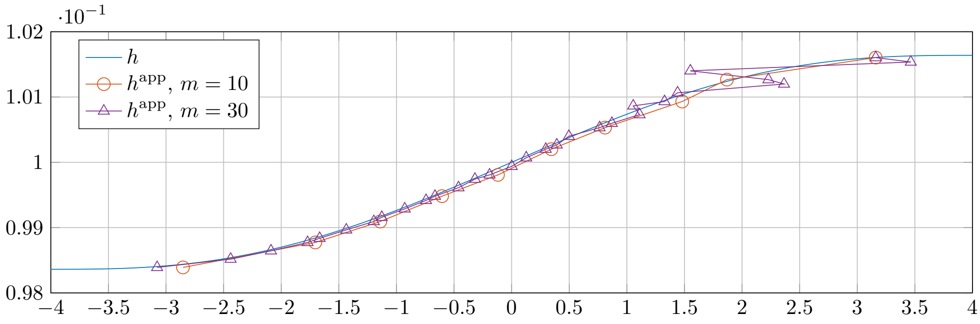

Figure 6.5 – Representation of h and h^{app} with post processing measurements discretized with $m = 10$ or $m = 30$ points. Due to the bad condition number of M, the use of too many frequency points diminishes the quality of the reconstruction. Here, $x_s = 6$, h defined in (6.48) and sources in (6.9) are defined in (6.52).

To summarize, using approximations of $\int_{x^\star_{k_i}}^{x_s} k_{i,N}$, we have discretized this integral to approach it using known parameters and values of each $x^\star_{k_i}$. It provides a linear inversible triangular system, and by solving it, we can approach each value of $x^\star_{k_i}$, and so of $h(x^\star_{k_i})$.

6.4 Numerical computations

In this section, we show some numerical applications of our reconstruction method on slowly varying waveguides. We simulate section measurements using numerically generated data, and we provide reconstructions of increasing waveguides with different shape profiles.

6.4.1 Generation of data

In the following, numerical solutions of (6.9) are generated using the software Matlab to solve numerically the equation in the waveguide Ω. In every numerical simulation, we assume that h' is supported between $x = -7$ and $x = 7$. To generate the solution u of (6.9) on Ω_7, we use a self-coded finite element method and a perfectly matched layer [18] on the left side of the waveguide between $x = -15$ and $x = -8$ and on the right side between $x = 8$ and $x = 15$. The coefficient of absorption for the perfectly matched layer is defined as $\alpha = -k((x-8)\mathbf{1}_{x\geq 8} - (x+8)\mathbf{1}_{x\leq -8})$ and k^2 is replaced in the Helmholtz equation with $k^2 + i\alpha$. The structured mesh is built with a stepsize of 10^{-3}.

6.4.2 Method of reconstruction

In the following, all the numerical measurements are generated following the process described in section 6.4.1. Using the previous results, we present all the steps to reconstruct h^{app}, an approximation of h.

1. Find an approximation of $h_{\min}$ and $h_{\max}$ using the method described in Appendix 6.A.
2. Choose a set of frequencies $K \subset (k_0, k_{m+1})$ with a very small step of discretization ρ_1, and sources f, b_{top}, b_{bot}. For every frequency $k \in K$, measure the N-th modal component $u_N(x_s)$ of the wavefield u solution of (6.9).
3. Post process the measurements by multiplying them by $k_N(x_s)/q(x_s)$ and applying Φ^{-1}. Then, get rid of the modulus π by straightening up the sequence, and compute the approximate value of ℓ using (6.34). The available data (d_i) are then the approximations of $\int_{x^\star_{k_i}}^{x_s} k_{i,N}$.
4. Reduce the number of frequencies k_i used in K and keep the associated data d_i, in order to have a bigger step size denoted $\rho_2 \geq \rho_1$. Solve $MV = d$, where M is defined in (6.42), to find an approximation of the distance between every $x^{\star,\text{app}}_{k_i}$.
5. Compute h^{app} using (6.46).

Remark 6.4. *We propose here to choose two values of ρ: the first one is very small to ensure a good post processing of the data in Proposition 6.2. The second one is bigger due to the cutting of some frequencies, which improve the precision of the reconstruction in Theorem 6.2.*

6.4.3 Numerical results

We now apply this method to reconstruct different profiles of slowly increasing waveguides. We present in Figure 6.6 the reconstruction h^{app} obtained for different profiles h:

$$h_1(x) = 0.1 + \gamma_1 \left(\frac{x^5}{5} - 32\frac{x^3}{3} + 256x \right) \mathbf{1}_{-4\leq x\leq 4} - \gamma_2 \mathbf{1}_{x<-4} + \gamma_2 \mathbf{1}_{x>4}, \tag{6.48}$$

$$h_2(x) = 0.1 + \gamma_3 \left(\frac{x^5}{5} - 2x^4 + 16\frac{x^3}{3} \right) \left(\mathbf{1}_{0\leq x\leq 4} - \mathbf{1}_{-4\leq x<0} \right) + \gamma_4 \left(\mathbf{1}_{x>4} - \mathbf{1}_{x<-4} \right), \tag{6.49}$$

$$h_3(x) = 0.1 + \gamma_5 x \mathbf{1}_{-4\le x\le 4} + 4\gamma_5 \mathbf{1}_{x>4} - 4\gamma_4 \mathbf{1}_{x<-4}, \tag{6.50}$$

$$h_4(x) = 0.1 - 4\gamma_5 + 4\gamma_5 \frac{\sqrt{x+4}}{\sqrt{2}} \mathbf{1}_{-4\le x\le 4} + 8\gamma_5 \mathbf{1}_{x>4}. \tag{6.51}$$

where $\gamma_1 = 3.10^{-6}$, $\gamma_2 = 8192/5.10^{-6}$, $\gamma_3 = 5.10^{-5}$, $\gamma_4 = 53/3.10^{-5}$, $\gamma_5 = 0.01/30$. All these profiles are represented in black in Figure 6.6. The first two profile are in $\mathcal{C}^2(\mathbb{R})$ while h_3 and h_4 show corners with an infinite derivative in h_4. Sources in (6.9) are defined by

$$f(x,y) = \delta_6(x)y, \qquad b_{\text{top}}(x) = \delta_6(x), \qquad b_{\text{bot}} = 0, \tag{6.52}$$

sets of frequencies by

$$K_1 = 30.92 : 31.93 : 50, \quad K_2 = 30.9 : 31.95 : 50, \quad K_3 = K_4 = 31.01 : 31.83 : 50, \tag{6.53}$$

and post processing data are discretized to use only 12 frequencies for the inversion. The initial profile are represented in black, while the reconstructions h^{app} are plotted in red and slightly shifted for comparison purposes. We see that the reconstruction are satisfactory and that the relative error of the reconstruction is of the same order as the one presented in Chapter 5 and even better than the one in Chapter 2.

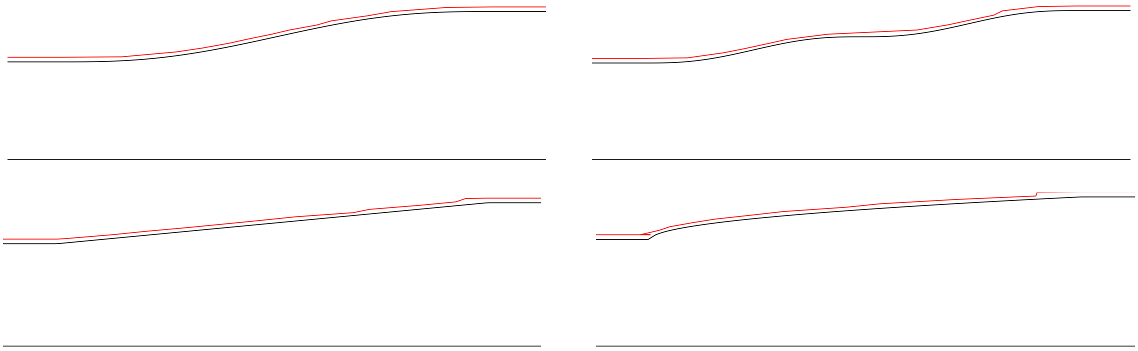

Figure 6.6 – Reconstruction of four different increasing profiles. In black, the initial shape of Ω_5, and in red, the reconstruction, slightly shifted for comparison purposes. In each case, $K = K_i$ is defined in (6.53), m is equal to 50 for the post processing of the measurements and then to 12 for the inversion of the data, $h = h_i$ is defined in (6.48), (6.49), (6.50), (6.51), and the sources of (6.9) are defined in (6.52). Top left: $i = 1$, $\|h - h^{\text{app}}\|_\infty / h_{\max} = 0.97\%$. Top right: $i = 2$, $\|h - h^{\text{app}}\|_\infty / h_{\max} = 1.0\%$. Bottom left: $i = 3$, $\|h - h^{\text{app}}\|_\infty / h_{\max} = 1.1\%$. Bottom right: $i = 4$, $\|h - h^{\text{app}}\|_\infty / h_{\max} = 1.5\%$.

In Figure 6.7, we illustrate the stability of the recovery by adding some artificial noise on measured data. We notice that the recovery is still satisfactory as long as the amplitude of the noise is small, and that the reconstruction error grows until it reaches a plateau.

Finally, we illustrate in Figure 6.8 that this method of reconstruction only works for increasing functions. We define

$$h_6(x) = 0.1 - \gamma_7(x+5)\mathbf{1}_{-5\le x\le 0} + \frac{\gamma_6}{4}(x-4)\mathbf{1}_{0<x\le 4}, \tag{6.54}$$

where $\gamma_6 = 25.10^{-4}$, $\gamma_7 = 5.10^{-4}$. The reconstruction of this function shows that if the width profile is not monotonous, we are only able to reconstruct the increasing part of the profile. To get the other part, one needs to move both the source and the receiver.

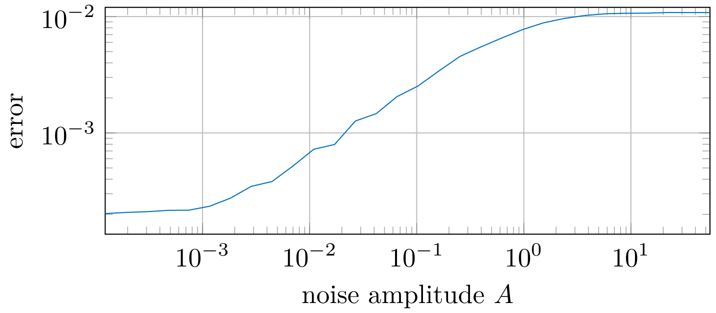

Figure 6.7 – Reconstruction error $\|h - h^{\mathsf{app}}\|_\infty$ with increasing additive noise on measured data. Given an amplitude A of the noise, we apply the inversion method with data $u_N(x_s) + A\mathcal{N}$ where $\mathcal{N}$ is a uniform random noise of amplitude 1. The width profile h is defined in (6.51), source of (6.9) are defined in (6.52), K is defined in (6.53) and $m = 50$ for the post processing an 12 or the inversion.

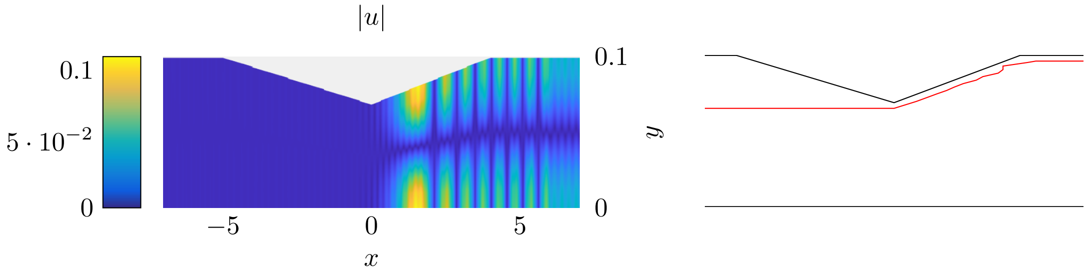

Figure 6.8 – Reconstruction of a non monotonous profile. On the left, we represent the wavefield $|u|$ at frequency $k = 32.1$. On the right, we show the reconstruction of the width profile. In black is the initial shape of Ω_5, and in red is the reconstruction slightly shifted for comparison purposes. We notice that we cannot reconstruct the left variations of the waveguide, which is explained by the fact that the wavefield u never propagates in the left area of the waveguide. In the reconstruction, $K = 31.42 : 32.1 : 50$, we only select 12 frequencies for the inversion of data, h is defined in (6.54) and the sources of (6.9) are defined in (6.52).

To conclude, using a known source located far away at the right of the defect, we are able to reconstruct slowly increasing widths. Even if this method does not work for general shape defects, it is relevant to identify and localize obstruction types of defects and gives good numerically results.

6.5 Conclusion

From the same analysis of the forward problem than in Chapter 5, we have developed a new method to recover width defect using section measurements. We have used the study of the forward problem in slowly varying waveguide presented in Chapter 4 and the approximation of the solutions using the π-periodic function Φ to develop an inverse reconstruction method in slowly varying monotonous waveguides. Given wavefield measurements on a section of the waveguide for different locally resonant frequencies, we reconstruct with stability the associated resonant points which provides a good approximation of the width in the waveguide.

Even if this method only works when sources and receivers are on the larger side of the waveguide, its reconstruction results are excellent and we believe that this method could be useful to detect and localize precisely the position of width defects in waveguides. Combined with a traditional multi-frequency back-scattering method like the one presented in Chapter 2, this method could produce great results in recovering any type of width defect as long as there are small and slowly varying.

Appendix 6.A: Identification of $k_{\min}$ and $k_{\max}$

Giving a compactly perturbed waveguide Ω, we describe here how section measurements enable to approximate very precisely the quantities $k_{\min}$ and $k_{\max}$. The article [27] mentions that the problem (5.7) is not well-defined when $k_n(x) = 0$ in a non-trivial interval, which especially happens when $k = n\pi/h_{\min}$ or $k = n\pi/h_{\max}$. Numerically, this results in an explosion of the solution when k tends to $n\pi/h_{\min}$ (resp. $n\pi/h_{\max}$) with a source term located in the area where $h(x) = h_{\min}$ (resp. $h(x) = h_{\max}$). Since our sources are located in the area $k = n\pi/h_{\max}$, measurements of the wavefield enable to find a good approximation of $h_{\max}$.

Moreover, using Theorem 6.1, we see that the Green function changes behavior when the mode N switches from an evanescent mode to a locally resonant one. This change appends exactly around the frequency $N\pi/h_{\min}$ and comparing the measurements with the known behavior of evanescent modes, we can get a good approximation of $h_{\min}$. We illustrate it in Figure 6.9.

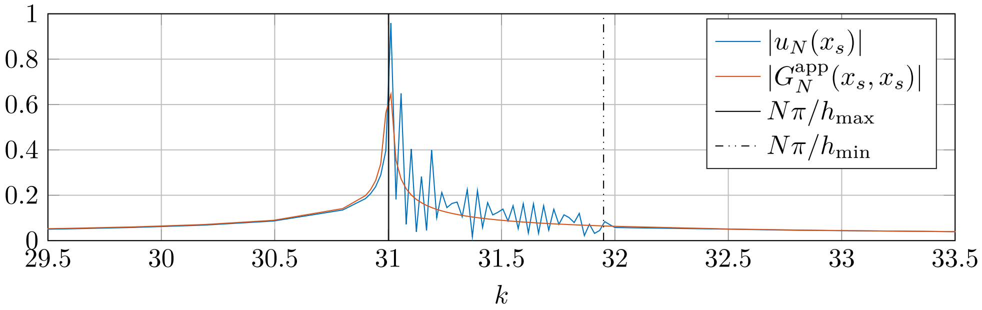

Figure 6.9 – Amplitude of $u_N(x_s)$ with respect to k for $x_s = 6$ and a source $b = \delta_{x_s}$ compared with the amplitude of the Green function $G_N^{\text{app}}(x_s, x_s)$. For comparison purposes, $N\pi/h_{\max}$ and $N\pi/h_{\min}$ are plotted.

Measuring the section wavefield while k varies and detecting its explosion and its changes of behavior provides a good approximation of the width at the left and the right of the waveguide.

7

Reconstruction of shape defects in elastic waveguides using longitudinal, transversal and ZGV resonances

This last chapter aims at extending the reconstruction method presented in Chapter 5 to elastic waveguides. Contrary to the acoustic case presented in Chapter 4, there are three types of critical points in elastic waveguides, called longitudinal, transverse and zero-group velocity points. Using modified Lamb bases, we provide a study of the elastic displacement equation near each critical point in slowly varying waveguides. We prove that modes propagate under the form of Airy functions at longitudinal and transverse points, and that this Airy function is multiplied by an oscillating exponential in the zero-group velocity case. This study of the forward problem enables us to extend the reconstruction method developed in Chapter 5 to slowly varying elastic waveguides. Given multi-frequency measurements taken at the surface of the waveguide, we provide a L^∞-stable explicit method to reconstruct variation of the width. This method is validated by numerical results and comparisons between the three types of critical points are discussed.

7.1 Introduction

In Chapter 5, we developed a shape defects reconstruction method in acoustic or electromagnetic waveguides from surface measurements at locally resonant frequencies. Here we extend it to the more complex case of elastic plates. If the acoustic case is relevant to the non destructive testing of pipes or optical fibers (see [54]), applications in the elastic case concern the monitoring of airplane or ship structural parts, offshore wind turbines or bridges (see [105]).

7.1.1 Description of the problem

In the whole chapter, we consider two-dimensional elastic waveguides described by

$$\Omega := \{(x,y) \in \mathbb{R}^2 \mid -h(x) < y < h(x)\}, \tag{7.1}$$

where $h \in \mathcal{C}^2(\mathbb{R}) \cap \mathrm{W}^{2,\infty}(\mathbb{R})$ is a positive profile function defining the local width of the waveguide (see an illustration in Figure 7.1). Such a waveguide is said to be slowly varying when there exists a small parameter $\eta > 0$ such that $\|h'\|_{\mathrm{L}^\infty(\mathbb{R})} \leq \eta$ and $\|h''\|_{\mathrm{L}^\infty(\mathbb{R})} < \eta^2$. These waveguides are good models of corroded plates and pipes (see [50, 58]). For the sake of simplicity, the waveguide is assumed to be symmetric with its top and bottom boundaries presenting the same defects. A similar analysis could also be conducted when both boundaries are varying independently.

In the time-harmonic regime, an elastic wavefield $\boldsymbol{u}$ satisfies the elastic displacement equation with Neumann boundary conditions

$$\begin{cases} \nabla \cdot \boldsymbol{\sigma}(\boldsymbol{u}) + \omega^2 \boldsymbol{u} = -\boldsymbol{f} & \text{in } \Omega, \\ \boldsymbol{\sigma}(\boldsymbol{u}) \cdot \nu = \boldsymbol{b} & \text{on } \partial\Omega, \end{cases} \tag{7.2}$$

where $\omega \in (0, +\infty)$ is the frequency, $\boldsymbol{\sigma}(\boldsymbol{u})$ is the stress tensor, f is an interior source term and b is a boundary source term. We focus here on the reconstruction of the function h which models the shape of the waveguide using surface measurements of $\boldsymbol{u}$ consistently with the experimental setups presented in [58, 29].

Several authors have already introduced inverse methods to detect and reconstruct such shape defects in general waveguides. In [61, 2], the use of conformal mapping that map the geometry of the perturbed waveguide to that of a straight one is proposed. However, this transformation is not explicit and proves numerically expensive. The article [75] develops another approach based on the treatment of the scattered field. The articles [82, 81] study the forward problem and indicate how the analysis therein may be used to reconstruct the width of the waveguide. All these methods use different sources at a fixed frequency.

Our work concerns a different approach, as in Chapter 2 and in [13, 12], where the data is assumed to be available for a whole interval of frequencies. This provides additional information that should help localize and reconstruct the shape of defects and should improve the stability of the reconstruction (see [93]). In Chapter 3, we already presented a multi-frequency method using backscattering data. There, however, we avoided the critical frequencies of the waveguide, where the elastic problem is known to be ill-posed [56].

Since experimental works [11, 29] suggest that critical frequencies may prove useful in reconstructing variations in width, and given the encouraging results already obtained in Chapter 5 for the acoustic case, we focus on these frequencies. A frequency ω is said to be locally resonant if there exists a coordinate $x^\star \in \mathbb{R}$ such that $\omega h(x^\star)$ is a critical frequency. Adapting the study of the forward problem from the acoustic case of Chapter 4, we prove in the following that the wavefield $\boldsymbol{u}$ strongly depends on $x^\star$. The main idea of our reconstruction method is to use measurements of $\boldsymbol{u}$ to determine $x^\star$. Since $\omega h(x^\star)$ is a known critical frequency, this in turn provides information about the width of the waveguide at the point $x^\star$. Choosing several resonant frequencies, we may then reconstruct the profile $h(x^\star)$ as a function of $x^\star$.

7.1.2 Outline of the chapter

The chapter is organized as follows. Section 7.2 recalls all the tools needed for the modal decomposition of wavefields in elastic waveguides. We introduce the critical points and classify them into three different categories. In section 7.3, we study the forward problem associated to each type of critical point, and we adapt the proof from in Chapter 4 to construct an approximation of the wavefield. In section 7.4, we use this approximation as in the reconstruction method presented in Chapter 5. Finally, in section 7.5, numerical illustrations of reconstructions are presented.

7.2 Modal decomposition and local wavenumbers in varying waveguides

In this section, we recall some classical results about modal decompositions in elastic waveguides, the proofs of which can be found in Chapter 3 and in [81, 91, 5].

7.2.1 Position of the problem

Let us consider a 2D infinite elastic waveguide

$$\Omega = \{(x, y) \in \mathbb{R} \mid -h(x) < y < h(x)\}, \tag{7.3}$$

where h describes half of the waveguide's varying width. In the following, we choose to work with slowly varying waveguides and we make the following assumptions on the function h:

Assumption 7.1. *We assume that* $h \in \mathcal{C}^2(\mathbb{R}) \cap W^{2,\infty}(\mathbb{R})$ *with* h' *compactly supported and that*

$$\forall x \in \mathbb{R} \quad h_{\min} \leq h(x) \leq h_{\max} \qquad \text{for some } 0 < h_{\min} < h_{\max} < \infty.$$

We also assume that $h(x) = h_{\min}$ *or* $h(x) = h_{\max}$ *if* $x \notin supp(h')$*. For such a function we define a parameter* $\eta > 0$ *that satisfies for a constant* $R > 0$

$$\|h'\|_{L^\infty(\mathbb{R})} < \eta \quad \text{and} \quad \|h''\|_{L^\infty(\mathbb{R})} < \eta^2, \quad supp\, h' \subset \left(-\frac{R}{\eta}, \frac{R}{\eta}\right).$$

Such a waveguide is represented in Figure 7.1

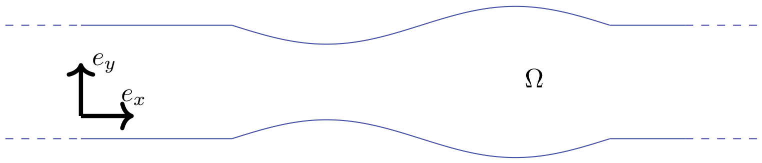

Figure 7.1 – Representation of a slowly varying waveguide Ω.

We denote by $\boldsymbol{u} = (u, v)$ the displacement field in the waveguide. Given a frequency $\omega \in \mathbb{R}$ and (λ, μ) the Lamé coefficients of the elastic waveguide, the wavefield $\boldsymbol{u}$ satisfies the elasticity equation

$$\nabla \cdot \boldsymbol{\sigma}(\boldsymbol{u}) + \omega^2 \boldsymbol{u} = -\boldsymbol{f} \qquad \text{in } \Omega, \tag{7.4}$$

where $\boldsymbol{f} = (f_1, f_2)$ is a source term and $\boldsymbol{\sigma}(\boldsymbol{u})$ is the stress tensor defined by

$$\boldsymbol{\sigma}(\boldsymbol{u}) = \begin{pmatrix} (\lambda + 2\mu)\partial_x u + \lambda \partial_y v & \mu \partial_y u + \mu \partial_x v \\ \mu \partial_y u + \mu \partial_x v & \lambda \partial_x u + (\lambda + 2\mu)\partial_y v \end{pmatrix} := \begin{pmatrix} s & t \\ t & r \end{pmatrix}. \tag{7.5}$$

In the following, we choose to impose a Neumann boundary condition

$$\boldsymbol{\sigma}(\boldsymbol{u}) \cdot \nu = \boldsymbol{b}^{\text{top}} \quad \text{on } \partial\Omega_{\text{top}}, \qquad \boldsymbol{\sigma}(\boldsymbol{u}) \cdot \nu = \boldsymbol{b}^{\text{bot}} \quad \text{on } \partial\Omega_{\text{bot}}, \tag{7.6}$$

where $\boldsymbol{b}^{\text{top}} = (b_1^{\text{top}}, b_2^{\text{bot}})$ and $\boldsymbol{b}^{\text{bot}} = (b_1^{\text{bot}}, b_2^{\text{bot}})$ are boundary source terms. This condition could be easily changed to a Dirichlet or a Robin condition without altering our results.

7.2.2 Modal decomposition

Following the formalism developed in [80], we introduce the variables

$$\boldsymbol{X} := (u, t), \qquad \boldsymbol{Y} := (-s, v). \tag{7.7}$$

The elasticity equation can then be rewritten as follows:

Proposition 7.1. *The equation* (7.4) *with Neumann boundary condition* (7.6) *is equivalent in* Ω *to*

$$\partial_x \begin{pmatrix} \boldsymbol{X} \\ \boldsymbol{Y} \end{pmatrix} = \begin{pmatrix} F(\boldsymbol{Y}) \\ G(\boldsymbol{X}) \end{pmatrix} + \begin{pmatrix} 0 \\ -f_2 - (b_2^{top} + h'\boldsymbol{X} \cdot e_y)\delta_{y=h(x)} - (b_2^{bot} - h'\boldsymbol{X} \cdot e_y)\delta_{y=-h(x)} \\ f_1 + (b_1^{top} - h'(x)\boldsymbol{Y} \cdot e_x)\delta_{y=h(x)} + (b_1^{bot} + h'(x)\boldsymbol{Y} \cdot e_x)\delta_{y=-h(x)} \\ 0 \end{pmatrix}, \tag{7.8}$$

with boundary conditions $B_1(\boldsymbol{X})(\pm h(x)) = B_2(\boldsymbol{Y})(\pm h(x)) = 0$. *Here* F, G, B_1 *and* B_2 *are matrix-valued operators defined by*

$$F = \begin{pmatrix} -\dfrac{1}{\lambda+2\mu} & -\dfrac{\lambda}{\lambda+2\mu}\partial_y \\ \dfrac{\lambda}{\lambda+2\mu}\partial_y & -\omega^2 - \dfrac{4\mu(\lambda+\mu)}{\lambda+2\mu}\partial_{yy}^2 \end{pmatrix}, \qquad G = \begin{pmatrix} \omega^2 & \partial_y \\ -\partial_y & \dfrac{1}{\mu} \end{pmatrix}, \tag{7.9}$$

$$B_1(\boldsymbol{X}) = \boldsymbol{X}\cdot e_y, \qquad B_2(\boldsymbol{Y}) = -\frac{\lambda}{\lambda+2\mu}\boldsymbol{Y}\cdot e_x + \frac{4\mu(\lambda+\mu)}{\lambda+2\mu}\partial_y \boldsymbol{Y}\cdot e_y. \tag{7.10}$$

For each value of x, we define Lamb modes:

Definition 7.1. *A Lamb mode* $(\boldsymbol{X}(x,y), \boldsymbol{Y}(x,y))$ *associated with the wavenumber* $k(x) \in \mathbb{C}$ *is a non-vanishing solution of the system*

$$\begin{cases} (F(\boldsymbol{Y}), G(\boldsymbol{X})) = ik(\boldsymbol{X}, \boldsymbol{Y}) & \text{in } (-h(x), h(x)), \\ B_1(\boldsymbol{X})(\pm h(x)) = B_2(\boldsymbol{Y})(\pm h(x)) = 0. \end{cases} \tag{7.11}$$

The set of wavenumbers $k(x) \in \mathbb{C}$ *associated to Lamb modes is countable, and every wavenumber* $k(x)$ *satisfies either the symmetric Rayleigh-Lamb equation*

$$p^2 = \frac{\omega^2}{\lambda+2\mu} - k^2, \qquad q^2 = \frac{\omega^2}{\mu} - k^2, \qquad \left(q^2-k^2\right)^2 = -4k^2pq\frac{\tan(ph)}{\tan(qh)}, \tag{7.12}$$

or the antisymmetric Rayleigh-Lamb equation

$$p^2 = \frac{\omega^2}{\lambda+2\mu} - k^2, \qquad q^2 = \frac{\omega^2}{\mu} - k^2, \qquad \left(q^2-k^2\right)^2 = -4k^2pq\frac{\tan(qh)}{\tan(ph)}. \tag{7.13}$$

If k *satisfies* (7.12), *the associated Lamb mode is called symmetric and is proportional to*

$$\begin{pmatrix} u \\ t \\ -s \\ v \end{pmatrix}(x,y) := \begin{pmatrix} ik(q^2-k^2)\sin(qh)\cos(py) - 2ikpq\sin(ph)\cos(qy) \\ 2ik\mu(q^2-k^2)p(-\sin(qh)\sin(py) + \sin(ph)\sin(qy)) \\ (q^2-k^2)((\lambda+2\mu)k^2+\lambda p^2)\sin(qh)\cos(py) - 4\mu pqk^2\sin(ph)\cos(qy) \\ -p(q^2-k^2)\sin(qh)\sin(py) - 2k^2p\sin(ph)\sin(qy) \end{pmatrix}. \tag{7.14}$$

If k *satisfies* (7.13), *the associated Lamb mode is called anti-symmetric and is proportional to*

$$\begin{pmatrix} u \\ t \\ -s \\ v \end{pmatrix}(x,y) := \begin{pmatrix} ik(q^2-k^2)\cos(qh)\sin(py) - 2ikpq\cos(ph)\sin(qy) \\ 2ik\mu(q^2-k^2)p(\cos(qh)\cos(py) - \cos(ph)\cos(qy)) \\ (q^2-k^2)((\lambda+2\mu)k^2+\lambda p^2)\cos(qh)\sin(py) - 4\mu pqk^2\cos(ph)\sin(qy) \\ p(q^2-k^2)\cos(qh)\cos(py) + 2k^2p\cos(ph)\cos(qy) \end{pmatrix}. \tag{7.15}$$

We define the set of critical frequencies:

Definition 7.2. *A frequency* ω *and a wavenumber* $k(x)$ *are said to be critical if they satisfy* (7.12) *(resp.* (7.13)*) and* $k = 0$ *or* $\Gamma_S = 0$ *(resp.* $\Gamma_A = 0$*) where*

$$\begin{aligned} \Gamma_S = h(q^2-k^2)^2\sin(qh)^2 + 4k^2p^2\sin(ph)^2 \\ + (q^2-k^2)\sin(ph)\cos(ph)\sin(qh)^2\left(\frac{q^2-k^2}{p} - 8p - \frac{2p}{k^2} - \frac{p}{q^2}\right), \end{aligned} \tag{7.16}$$

$$\Gamma_A = h(q^2-k^2)^2\cos(qh)^2 + 4k^2p^2\cos(ph)^2 \\ - (q^2-k^2)\cos(ph)\sin(ph)\cos(qh)^2\left(\frac{q^2-k^2}{p} - 8p - \frac{2p}{k^2} - \frac{p}{q^2}\right). \quad (7.17)$$

We denote by $\omega_{crit}^{h(x)}$ the set of critical frequencies at the position $x \in \mathbb{R}$, and by $k_{crit}^{h(x)}$ the set of associated critical wavenumbers. We also define as ω_{crit}^{1} the set of critical frequencies associated with the width $h = 1$.

By looking at these relations, we notice that

$$\omega \in \omega_{\text{crit}}^{h(x)} \quad \Leftrightarrow \quad \omega h(x) \in \omega_{\text{crit}}^{1}, \tag{7.18}$$

so one can easily compute the set of critical frequencies for any value of $h(x)$ from ω_{crit}^{1}.

It enables to compute very easily the set of critical frequencies of any value of $h(x)$. These frequencies are used to provide the completeness of the Lamb modes family, as proved in [8] and Chapter 3:

Proposition 7.2. *Lamb modes form a complete set of functions in $H(x) := H^1(-h(x),h(x)) \times L^2(-h(x),h(x)) \times L^2(-h(x),h(x)) \times H^1(-h(x),h(x))$ if and only if $\omega \notin \omega_{crit}^{h(x)}$.*

To identify the decomposition of a given function of H on the Lamb basis, we split the set of wavenumbers k into two parts:

Definition 7.3. *Let $\omega \notin \omega_{crit}^{h(x)}$.*

- *We say that a Lamb mode with wavenumber k is right-going if $Im(k) > 0$ or $Im(k) = 0$ and $\partial_k\omega > 0$.*
- *We say that a Lamb mode is left-going if $Im(k) < 0$ or $Im(k) = 0$ and $\partial_k\omega < 0$.*

Right-going Lamb modes are indexed by $n \in \mathbb{N}^*$ and sorted by ascending order of imaginary part and descending order of real part.

If k_n is a right-going mode associated with the Lamb mode $(\boldsymbol{X}_n, \boldsymbol{Y}_n)$, $-k_n$ is a left-going mode $(-\boldsymbol{X}_n, \boldsymbol{Y}_n)$. For any $(\boldsymbol{X}, \boldsymbol{Y}) \in H$, it follows that there exist $(a_n)_{n\in\mathbb{N}^*}, (b_n)_{n\in\mathbb{N}^*}$ such that

$$\boldsymbol{X}(x,y) = \sum_{n>0} a_n(x)\boldsymbol{X}_n(x,y), \qquad \boldsymbol{Y}(x,y) = \sum_{n>0} b_n(x)\boldsymbol{Y}_n(x,y). \tag{7.19}$$

The following proposition proves that the families $(\boldsymbol{X}_n)_{n>0}$ and $(\boldsymbol{Y}_n)_{n>0}$ are bi-orthogonal:

Proposition 7.3. *We denote by $\langle\cdot,\cdot\rangle$ the product defined by*

$$\langle(z_1,z_2),(z_3,z_4)\rangle = \int_{-h(x)}^{h(x)} z_1 z_3 + z_2 z_4.$$

For every $n, m > 0$, $\langle \boldsymbol{X}_m, \boldsymbol{Y}_n\rangle = \delta_{n=m} J_n$ where $J_n = i\omega^2 k\Gamma_S$ if n is a symmetric mode and $J_n = i\omega^2 k\Gamma_A$ if n is an anti symmetric mode, with Γ_S and Γ_A defined in (7.16) and (7.17).

Using this proposition, we obtain an expression for each modal component of the decomposition:

$$a_n = \frac{\langle \boldsymbol{X}, \boldsymbol{Y}_n\rangle}{J_n}, \qquad b_n = \frac{\langle \boldsymbol{Y}, \boldsymbol{X}_n\rangle}{J_n}. \tag{7.20}$$

Next, we adapt the classical Sommerfeld (or outgoing) condition, defined in Chapter 3 for regular waveguides, to general varying waveguides. This condition will be used later to guarantee uniqueness for the source problem (7.4).

Definition 7.4. *A wavefield $\boldsymbol{u} \in H^2_{loc}(\Omega)$ is said to be outgoing if $\boldsymbol{X}$ and $\boldsymbol{Y}$ defined in* (7.7) *satisfy*

$$\left| \langle \boldsymbol{Y}, \boldsymbol{X}_n \rangle'(x) \frac{x}{|x|} - ik_n(x) \langle \boldsymbol{Y}, \boldsymbol{X}_n \rangle(x) \right| \underset{|x| \to +\infty}{\longrightarrow} 0 \quad \forall n \in \mathbb{N}^*, \tag{7.21}$$

$$\left| \langle \boldsymbol{X}, \boldsymbol{Y}_n \rangle'(x) \frac{x}{|x|} - ik_n(x) \langle \boldsymbol{X}, \boldsymbol{Y}_n \rangle(x) \right| \underset{|x| \to +\infty}{\longrightarrow} 0 \quad \forall n \in \mathbb{N}^*. \tag{7.22}$$

7.2.3 Classification of the critical points

We investigate in more details the set of critical frequencies. As mentioned before, a symmetric critical wavenumber satisfies the symmetric Rayleigh-Lamb equation (7.16) and

$$k_n = 0 \quad \text{or} \quad \Gamma_S = 0. \tag{7.23}$$

We notice using the symmetric Rayleigh-Lamb equation (7.16) that if $k_n = 0$ then

$$\cos(p_n h) = 0 \quad \text{or} \quad \sin(q_n h) = 0. \tag{7.24}$$

Using expressions (7.14), we see that if $\cos(p_n h) = 0$ then $\boldsymbol{X}_n = 0$ and $\boldsymbol{Y}_n \neq 0$. On the other hand, if $\sin(q_n h) = 0$ then $\boldsymbol{X}_n \neq 0$ and $\boldsymbol{Y}_n = 0$ after dividing the whole expression by k_n. Because of these distinct behaviors, we split the set of critical frequencies in three parts using the terminology of [81, 11]:

Definition 7.5. *The set of critical frequencies can be split as $\omega_{crit}^{h(x)} := \omega_L^{h(x)} \cup \omega_T^{h(x)} \cup \omega_{ZGV}^{h(x)}$ where*

- *The set $\omega_L(x)$ contains all solutions of* (7.14) *(resp.* (7.15)*) where there exists $N > 0$ such that $k_N = 0$ and $\cos(p_N h) = 0$ (resp. $\sin(p_N h) = 0$). These frequencies are called longitudinal (L) critical frequencies and make $\boldsymbol{X}_N$ vanishes.*
- *The set $\omega_T(x)$ contains all solutions of* (7.14) *(resp.* (7.15)*) where there exists $N > 0$ such that $k_N = 0$ and $\sin(q_N h) = 0$ (resp. $\cos(q_N h) = 0$). These frequencies are called transverse (T) critical frequencies and make $\boldsymbol{Y}_N$ vanishes.*
- *The set $\omega_{ZGV}(x)$ contains all solutions of* (7.14) *(resp.* (7.15)*) such that $\Gamma_S = 0$ (resp. $\Gamma_A = 0$). These frequencies are called zero group velocity (ZGV) critical frequencies and at these frequencies, there exists a mode $N > 0$ such that $\partial_{k_N} \omega$ vanishes with a wavenumber $k_N \neq 0$.*

Using similar notations, we can split $k_{crit}^{h(x)} = k_L^{h(x)} \cup k_T^{h(x)} \cup k_{ZGV}^{h(x)}$.

We represent in Figure 7.2 different wavenumbers $k_n(x)$ in terms of the frequency ω and some critical points solutions to $k_n = 0$ or $\Gamma_S = 0$.

One of the main difficulties in our context is that $h(x)$ is non-constant, so the behavior of a wavenumber $k_n(x)$ changes with x. We distinguish several situations:

Definition 7.6. *A right-going mode $n \in \mathbb{N}^*$ falls in one of the four following situations:*

1. *If $k_n(x) \in \mathbb{R}$ for all $x \in \mathbb{R}$, the mode oscillates in the waveguide without energy loss and is called propagative.*
2. *If $k_n(x) \in i\mathbb{R}$ for all $x \in \mathbb{R}$, the mode decays exponentially to zero as $|x| \to \infty$ and is called evanescent.*

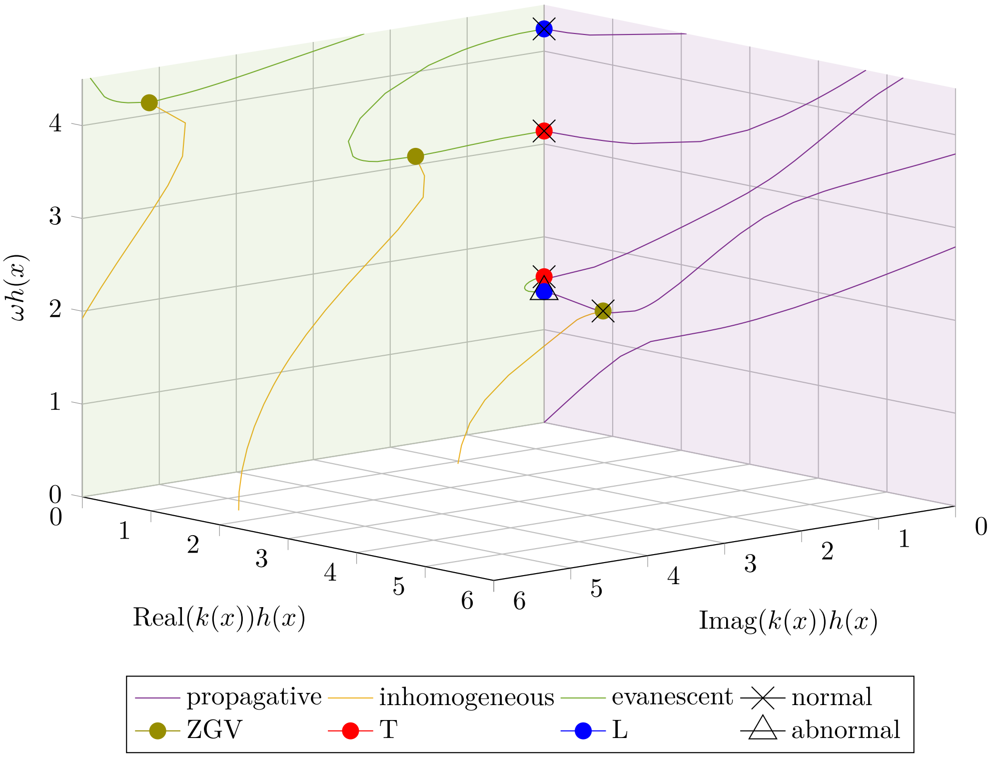

Figure 7.2 – Solutions of the symmetric Rayleigh-Lamb equation (7.14) in the space Im$(k) \geq 0$, Re$(k) \geq 0$ with $\mu = 0.25$ and $\lambda = 0.31$. Solutions on the full space can be obtained by axial symmetries. Propagative, evanescent and inhomogeneous modes are represented by different colors. Critical points are represented by dots, where green dots stand for zero group velocity points, blue dots for longitudinal points, and red dots for transverse points. Crosses indicate normal critical points, and triangles abnormal ones.

3. *If Re$(k_n(x)) \neq 0$ and Im$(k_n(x)) \neq 0$ for all $x \in \mathbb{R}$, the mode oscillates fast to zero and is called inhomogeneous.*

4. *If there exists $x^\star \in \mathbb{R}$ such that $k_n(x^\star) \in k_{crit}^{h(x^\star)}$ the mode n is called locally resonant. The associated points $x^\star$ are called resonant points. They are simple if $h'(x^\star) \neq 0$, and multiple otherwise.*

A frequency $\omega > 0$ for which there exists at least one locally resonant mode is called a locally resonant frequency.

We represent in Figure 7.2 the branches where modes are propagative, evanescent, or inhomogeneous. If $k_n(x)$ switches from one branch to another when x varies, the mode is locally resonant. If one of these branches is a propagative one, we use the terminology of [82] to distinguish two types of locally resonant points:

Definition 7.7. *A locally resonant point $x_k^\star$ is called normal if $k_n(x) \in \mathbb{R}$ when x approaches $x^\star$ from above, and abnormal if $k_n(x) \in \mathbb{R}$ when x approaches $x^\star$ from below.*

This terminology is so chosen since most of the critical points are normal (see Figure 7.2) while the abnormal one are exceptional. We represent normal and abnormal locally resonant points in Figure 7.2.

7.3 Forward problem at locally resonant frequencies

In this section, we analyse the propagation of elastic waves at locally resonant frequencies. To this end, we follow the arguments presented for acoustic waveguides in Chapter 4. Considering a slowly variable waveguide as represented in Figure 7.1 and which satisfies assumption 7.1, we intend to prove that the source problem

$$\begin{cases} \nabla \cdot \boldsymbol{\sigma}(\boldsymbol{u}) + \omega^2 \boldsymbol{u} = -\boldsymbol{f} & \text{in } \Omega, \\ \boldsymbol{\sigma}(\boldsymbol{u}) \cdot \nu = \boldsymbol{b}^{\text{top/bot}} & \text{on } \partial\Omega_{\text{top/bot}}, \\ \boldsymbol{u} \text{ is outgoing,} & \end{cases} \tag{7.25}$$

has a unique solution which can be approximated by using an explicit modal expression.

We mainly follow the proof presented in Chapter 4 for acoustic waveguides. However, a major issue arises in elastic waveguides. As mentioned before and contrary to acoustic modes, Lamb modes do not form a complete family at critical frequencies. A generalized mode needs to be added to the family in order to preserve its completeness, and consequently, the basis $(\boldsymbol{X}_n(x,y), \boldsymbol{Y}_n(x,y))$ is not continuous in x near a locally resonant point $x^\star$. We handle this problem by properly rescaling and modifying the associated critical eigenfunctions, depending on the nature of the critical point crossed by the locally resonant mode.

Firstly, we start by studying the longitudinal and transverse cases, which are very similar. Secondly, we move on to the ZGV case, which proves more complex. The study is done entirely in the longitudinal case, and then we only point out the needed changes to adapt it to the transverse and the ZGV case.

7.3.1 The Longitudinal case

To simplify the presentation of the results of this section, we assume that the profile h is strictly increasing and that given a locally resonant frequency $\omega \in \mathbb{R}_+$, there exists a unique locally resonant mode, say the N-th mode, associated with a longitudinal critical point $x^\star$. We also assume that any longitudinal critical point is not at the same time a transverse critical point. All these assumptions and their generalization are discussed at the end of the section.

Solutions of the symmetric Rayleigh-Lamb dispersion relation near a longitudinal critical point are represented in Figure 7.3. Note how the wavenumber k_N switches from a real number to a purely imaginary one around the critical point $x^\star$.

7.3.1.a Modified Lamb basis

If $\boldsymbol{u}$ is a solution of the elastic problem (7.25), it can be decomposed in the Lamb basis almost everywhere. However, as explained before, the Lamb basis loses its completeness at critical frequencies. To resolve this issue, in the spirit of the method presented in [81], we set

$$\widetilde{\boldsymbol{X}_n} := \frac{\boldsymbol{X}_n}{J_n}, \qquad \widetilde{\boldsymbol{Y}_n} := \boldsymbol{Y}_n. \tag{7.26}$$

We call this new family the modified Lamb modes, and we prove that it is a complete family even at the longitudinal critical point:

Proposition 7.4. *Modified Lamb modes* $(\widetilde{\boldsymbol{X}_n})_{n>0}$ *(resp.* $(\widetilde{\boldsymbol{Y}_n})_{n>0}$*) are well-defined and form a complete set of functions in* $H^1(-h(x), h(x)) \times L^2(-h(x), h(x))$ *for every* $x \in \mathbb{R}$ *(resp.* $L^2(-h(x), h(x)) \times H^1(-h(x), h(x))$*).*

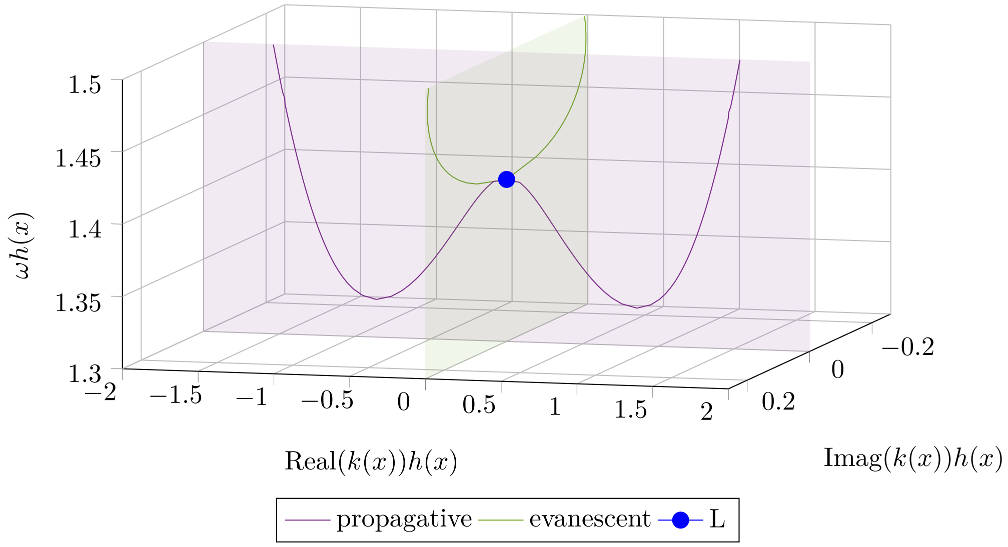

Figure 7.3 – Solutions of the symmetric Rayleigh-Lamb equation (7.14) with $\mu = 0.25$ and $\lambda = 0.31$. Propagative and evanescent branches merge at the longitudinal (L) critical point.

Proof. From Proposition 7.3, $J_n(x) \neq 0$ for all $x \in \mathbb{R}$ when $n \neq N$. Using Proposition 7.2, the modified Lamb modes are well-defined and form a complete family when x is not a locally resonant point. We assume that the mode is symmetric (the antisymmetric case could be treated similarly) and we investigate the behavior of $\widetilde{\boldsymbol{X}}_n$ around the locally resonant point. We set $h^\star = h(x^\star)$, $p^\star = \omega/\sqrt{\lambda + 2\mu}$ and $q^\star = \omega/\sqrt{\mu}$. All comparisons are written when $k_N \to 0$. Using a Taylor expansion of Γ_S and the definition of J_N, we prove that

$$J_N(h) \sim ik_N h^\star \omega^2 q^{\star 2} \sin(q^\star h^\star),$$

$$\boldsymbol{X}_N \sim ik_N q^\star \begin{pmatrix} q^\star \sin(q^\star h^\star) \cos(p^\star y) - 2p^\star \sin(p^\star h^\star) \cos(q^\star y) \\ 2\mu p^\star q^\star (\sin(p^\star h^\star) \sin(q^\star y) - \sin(q^\star h^\star) \sin(p^\star y)) \end{pmatrix}.$$

It shows that $\widetilde{\boldsymbol{X}}_n$ is well defined, and that

$$\widetilde{\boldsymbol{X}}_N(x^\star, y) = \frac{1}{h^\star \omega^2 q^\star \sin(q^\star h^\star)} \begin{pmatrix} q^\star \sin(q^\star h^\star) \cos(p^\star y) - 2p^\star \sin(p^\star h^\star) \cos(q^\star y) \\ 2\mu p^\star q^\star (\sin(p^\star h^\star) \sin(q^\star y) - \sin(q^\star h^\star) \sin(p^\star y)) \end{pmatrix}.$$

At critical frequencies, we need to add a generalized mode to ensure the completeness of the Lamb family. It follows from Theorem 3.1 of Chapter 3 that $(\widetilde{\boldsymbol{X}}_N, 0)$ is a generalized Lamb mode. Since the Lamb mode associated to k_N was written $(0, \boldsymbol{Y}_n)$ at $x = x^\star$, we conclude that $(\widetilde{\boldsymbol{X}}_n)$ and $(\widetilde{\boldsymbol{Y}}_n)$ form complete sets of functions. $\square$

The modified Lamb basis functions are continuous with respect to x, and we can now decompose continuously the wavefield $\boldsymbol{u}$ for every $x \in \mathbb{R}$ as

$$\boldsymbol{X}(x, y) = \sum_{n>0} a_n(x) \widetilde{\boldsymbol{X}}_n(x, y), \quad \boldsymbol{Y}(x, y) = \sum_{n>0} b_n(x) \widetilde{\boldsymbol{Y}}_n(x, y), \tag{7.27}$$

where the coefficients a_n and b_n can be computed as

$$a_n = \langle \boldsymbol{X}, \widetilde{\boldsymbol{Y}}_n \rangle, \quad b_n = \langle \boldsymbol{Y}, \widetilde{\boldsymbol{X}}_n \rangle. \tag{7.28}$$

7.3.1.b Sketch of the proof

Before stating the main result of this section regarding the approximation of $\boldsymbol{u}$, we first explain our strategy for proving such an existence result. We assume that

$$(\boldsymbol{X}^{(1)}, \boldsymbol{Y}^{(1)}) = \sum_{n>0} (a_n^{(1)} \widetilde{\boldsymbol{X}}_n, b_n^{(1)} \widetilde{\boldsymbol{Y}}_n), \tag{7.29}$$

is solution of the elastic problem (7.8). Using the notations of Proposition 7.1, it is proved in [81] that F and G are selfadjoint operators under the condition $B_1(\boldsymbol{X})(\pm h) = B_2(\boldsymbol{Y})(\pm h) = 0$, so that

$$\langle F(\boldsymbol{Y}^{(1)}), \widetilde{\boldsymbol{Y}}_n \rangle = \langle \boldsymbol{Y}^{(1)}, F(\widetilde{\boldsymbol{Y}}_n) \rangle = i k_n J_n \langle \boldsymbol{Y}^{(1)}, \widetilde{\boldsymbol{X}}_n \rangle = i k_n J_n b_n^{(1)},$$

$$\langle G(\boldsymbol{X}^{(1)}), \widetilde{\boldsymbol{X}}_n \rangle = \langle \boldsymbol{X}^{(1)}, G(\widetilde{\boldsymbol{X}}_n) \rangle = \frac{i k_n}{J_n} \langle \boldsymbol{X}^{(1)}, \widetilde{\boldsymbol{Y}}_n \rangle = \frac{i k_n}{J_n} a_n^{(1)}.$$

Following [81], we project equation (7.8) on each mode to see that it is equivalent to

$$\forall n > 0 \quad \begin{cases} a_n^{(1)} = \langle \boldsymbol{X}^{(1)}, \widetilde{\boldsymbol{Y}}_n \rangle, \quad b_n^{(1)} = \langle \boldsymbol{Y}^{(1)}, \widetilde{\boldsymbol{X}}_n \rangle, \\ a_n^{(1)\prime} = -\displaystyle\sum_{m>0} a_m^{(1)} \langle \partial_x \widetilde{\boldsymbol{X}}_m, \widetilde{\boldsymbol{Y}}_n \rangle + i k_n J_n b_n^{(1)} - J_n F_2^n, \\ b_n^{(1)\prime} = -\displaystyle\sum_{m>0} b_m^{(1)} \langle \partial_x \widetilde{\boldsymbol{Y}}_m, \widetilde{\boldsymbol{X}}_n \rangle + \frac{i k_n}{J_n} a_n^{(1)} + F_1^n \\ \qquad\qquad + h' \displaystyle\sum_{m>0} b_m^{(1)} \left(s_m(h) \frac{u_n(h)}{J_n} - s_m(-h) \frac{u_n(-h)}{J_n} \right), \\ a_n^{(1)}, b_n^{(1)} \text{ are outgoing,} \end{cases} \tag{E_1}$$

where

$$F_2^n(x) = \frac{1}{J_n} \left(\int_{-h(x)}^{h(x)} f_2(x,y) v_n(y) \mathrm{d}y + b_2^{\text{top}}(x) v_n(h) + b_2^{\text{bot}}(x) v_n(-h) \right), \tag{7.30}$$

$$F_1^n(x) = \frac{1}{J_n} \left(\int_{-h(x)}^{h(x)} f_1(x,y) u_n(y) \mathrm{d}y + b_1^{\text{top}}(x) u_n(h) + b_1^{\text{bot}}(x) u_n(-h) \right). \tag{7.31}$$

As there is no easy way to solve (E_1) explicitly, we shall approximate its solution by that of a simpler problem. A Born approximation, justified in Proposition 7.8, allows us to neglect all the terms that depend on h'. This leads to the equations

$$\forall n > 0 \quad \begin{cases} a_n^{(2)} = \langle \boldsymbol{X}^{(2)}, \widetilde{\boldsymbol{Y}}_n \rangle, \quad b_n^{(2)} = \langle \boldsymbol{Y}^{(2)}, \widetilde{\boldsymbol{X}}_n \rangle, \\ a_n^{(2)\prime} = i k_n J_n b_n^{(2)} - J_n F_2^n, \\ b_n^{(2)\prime} = \dfrac{i k_n}{J_n} a_n^{(2)} + F_1^n, \\ a_n^{(2)}, b_n^{(2)} \text{ are outgoing.} \end{cases} \tag{E_2}$$

Th modes are now decoupled, and we can solve independently the equations on each mode. We notice that equations on $a_n^{(2)}$ and $b_n^{(2)}$ behave differently: while k_n/J_n is bounded and tends to zero when n increases, $k_n J_n$ blows up when n increases. This difference of behavior encourages us to work with the equation on b_n. Taking a derivative, this system becomes

$$\forall n > 0 \quad \left\{ \begin{array}{c} a_n^{(2)} = \langle \boldsymbol{X}^{(2)}, \widetilde{\boldsymbol{Y}_n} \rangle, \quad b_n^{(2)} = \langle \boldsymbol{Y}^{(2)}, \widetilde{\boldsymbol{X}_n} \rangle, \\ b_n^{(2)\prime} = \dfrac{ik_n}{J_n} a_n^{(2)} + F_1^n, \\ b_n^{(2)\prime\prime} + k_n^2 b_n^{(2)} = i \left(\dfrac{k_n}{J_n} \right)' a_n^{(2)} - ik_n F_2^n + F_1^{n\prime}, \\ a_n^{(2)}, b_n^{(2)} \text{ are outgoing.} \end{array} \right. \tag{E_2'}$$

To find an approximation of the solution, we neglect the contribution of $(k_n/J_n)'$ in the equation which amounts Born approximation justified in Proposition 7.6. It leads to

$$\left\{ \begin{array}{c} b_n^{(3)\prime} = \dfrac{ik_n}{J_n} a_n^{(3)} + F_1^n, \\ b_n^{(3)\prime\prime} + k_n^2 b_n^{(3)} = -ik_n F_2^n + F_1^{n\prime}, \\ a_n^{(3)}, b_n^{(3)} \text{ are outgoing.} \end{array} \right. \tag{E_3^n}$$

The equation on $b_n^{(3)}$ is now self-governing. The study of the equation $y'' + k_n^2 y = 0$ has already been carried out for acoustic waveguides in Chapter 4 using results on the Schrödinger equation [76, 77]. This problem is well-defined when $\{x \in \mathbb{R} \,|\, k_n(x) \in k_{\text{crit}}^{h(x)}\}$ has zero measure in $\mathbb{R}$, which occurs when $\omega \notin h_{\min}\omega_{\text{crit}}^1 \cup h_{\max}\omega_{\text{crit}}^1$. We assume that this is the case, and that

$$\delta := \min_{n \in \mathbb{R}} \left\{ |\omega - \omega_n| \ \text{ where } \omega_n \in h_{\min}\omega_{\text{crit}}^1 \cup h_{\max}\omega_{\text{crit}}^1 \right\} > 0.$$

It is proved in Chapter 4 that if n is not a locally resonant mode, the solution can be approximated with exponential functions. Otherwise, we can approximate the solution using Airy functions.

Using these results, we prove that (E_3^n) has a unique solution, and we provide an explicit approximation of this solution. With a uniform control of the approximation error between (E_2') and (E_3^n), we obtain an explicit approximation of (E_2). Then, estimating the error between solutions of (E_1) and (E_2), we obtain an explicit approximation of the solution to (E_1).

7.3.1.c Main result

We now state the main result of this section which shows the existence and uniqueness of the solution $\boldsymbol{u}$ of (7.25) and provides an approximation of $\boldsymbol{u}$ with an estimate of the approximation error in $\mathrm{L}^2_{\text{loc}}$. If the critical longitudinal point is normal, we set $\chi = -1$. Otherwise, it is abnormal, and we set $\chi = 1$. We define the auxiliary function

$$\xi(x) := \left\{ \begin{array}{ll} \left(-\dfrac{3}{2} i\chi \displaystyle\int_{x^\star}^{x} k_n(t) \mathrm{d}t \right)^{2/3} & \text{if } \chi x > \chi x^\star, \\ -\left(\dfrac{3}{2} \chi \displaystyle\int_{x}^{x^\star} k_n(t) \mathrm{d}t \right)^{2/3} & \text{if } \chi x < \chi x^\star. \end{array} \right. \tag{7.32}$$

Theorem 7.1. *Let h be an increasing function which defines a non-uniform waveguide Ω that satisfies assumption 7.1. Consider sources $\boldsymbol{f} \in H^1(\Omega)$, $\boldsymbol{b}^{top}, \boldsymbol{b}^{bot} \in (H^{3/2}(\mathbb{R}))^2$ with compact support contained in Ω_r and $(-r, r)$ respectively, for some $r > 0$. Assume that there is a unique locally resonant mode $N \in \mathbb{N}$, associated with a simple longitudinal resonant point $x^\star \in \mathbb{R}$.*

There exists $\eta_0 > 0$, depending only on $h_{\min}$, $h_{\max}$, δ, r and R, such that if $\eta < \eta_0$, then the problem (7.4) admits a unique solution $\boldsymbol{u} \in H^3_{loc}(\Omega)$. Moreover, this solution is approximated by

$\boldsymbol{u}^{app}$ *defined for almost every* $(x,y)\in\Omega$ *by* $\boldsymbol{u}^{app}(x,y)=\sum(a_n^{app}(x)\boldsymbol{u}_n(x,y), b_n^{app}(x)\boldsymbol{v}_n(x,y))$ *where for all* $n>0$,

$$a_n^{app}(x)=-\frac{i}{k_n(x)}\int_{\mathbb{R}}\partial_x G_n^{app}(x,s)(ik_n(s)F_2^n(s)-F_1^{n}{}'(s))\mathrm{d}s+i\frac{F_1^n(x)}{k_n(x)}, \tag{7.33}$$

$$b_n^{app}(x)=\int_{\mathbb{R}}G_n^{app}(x,s)(ik_n(s)F_2^n(s)-F_1^{n}{}'(s))\mathrm{d}s, \tag{7.34}$$

where F_1^n *and* F_2^n *are defined in* (7.31) *and* (7.30) *and*

$$G_n^{app}(x,s)=\begin{cases}\begin{cases}\dfrac{i}{2\sqrt{k_n(s)k_n(x)}}\exp\left(i\displaystyle\int_x^s k_n\right) & \text{if } \chi x<\chi s,\\ \dfrac{i}{2\sqrt{k_n(s)k_n(x)}}\exp\left(i\displaystyle\int_s^x k_n\right) & \text{if } \chi x>\chi s,\end{cases} & \text{if } n\neq N,\\ \begin{cases}\dfrac{\pi(\xi(s)\xi(x))^{1/4}}{\sqrt{k_n(s)k_n(x)}}\big(i\mathcal{A}+\mathcal{B}\big)\circ\xi(s)\mathcal{A}\circ\xi(x) & \text{if } \chi x<\chi s,\\ \dfrac{\pi(\xi(s)\xi(x))^{1/4}}{\sqrt{k_n(s)k_n(x)}}\big(i\mathcal{A}+\mathcal{B}\big)\circ\xi(x)\mathcal{A}\circ\xi(s) & \text{if } \chi x>\chi s,\end{cases} & \text{if } n=N.\end{cases} \tag{7.35}$$

Moreover, there exists a constant $C>0$ *depending only on* $h_{\min}$, $h_{\max}$, δ, r *and* R *such that*

$$\|\boldsymbol{u}-\boldsymbol{u}^{app}\|_{L^2(\Omega_r)}\leq\eta C\left(\|\boldsymbol{f}\|_{H^1(\mathbb{R})}+\|\boldsymbol{b}^{top}\|_{H^{3/2}(\mathbb{R})}+\|\boldsymbol{b}^{bot}\|_{H^{3/2}(\mathbb{R})}\right). \tag{7.36}$$

Remark 7.1. *If there are no resonant mode, the result can be adapted by deleting the line* $n=N$ *in* (7.35)*. On the other hand, if there are multiple longitudinal locally resonant modes, the second line of* (7.35) *holds for every resonant mode. We can also generalize this result to non-monotonous slowly varying waveguides following the process described in section 4.4 of Chapter 4.*

Remark 7.2. *Comparing this result with the acoustic case in Chapter 4, we see that stronger assumptions on the regularity of the sources lead to a worse estimate of the quality of the approximation. This phenomenon, explained in Chapter 3, is due to the lack of orthogonality of the Lamb modes. The theory developed in [72] may be adapted for elastic waveguide to improve our result.*

Remark 7.3. *If* Ω *is a straight waveguide, we find the same expression for the wavefield as in Chapter 3. Moreover, the modes* $n\neq N$ *in a perturbed waveguide behave similarly to those in a straight waveguide, with the term* $\int k_n$ *acting as a variable change in the phase.*

We illustrate this result in Figure 7.4, where we compare our approximation $\boldsymbol{u}^{\mathrm{app}}$ with a wavefield $\boldsymbol{u}$ computed using a finite element method as explained in section 7.5.

7.3.1.d Proof of the Theorem

Using Theorem 4.2 of Chapter 4, we know that for every $s\in\mathbb{R}$,

$$\begin{cases}\partial_{xx}G_n(x,s)+k_n(x)^2G_n(x,s)=-\delta_s & \text{in } \mathbb{R},\\ G_n(\cdot,s) \text{ is outgoing,}\end{cases} \tag{7.37}$$

has a unique solution $G_n(\cdot,s)\in\mathrm{W}^{1,1}(\mathbb{R})$ which can be approximated by G_n^{app} defined in (7.35). Moreover, there exists $\eta_1>0$ depending on R, r, $h_{\min}$, $h_{\max}$ and δ such that if $\eta<\eta_1$, there exist $c,d>0$ depending only on $h_{\min}$, $h_{\max}$, r, δ and R such that for every $s\in\mathbb{R}$,

$$\|G_n(\cdot,s)\|_{\mathrm{L}^1(-r,r)}\leq c\left(\delta_{n=N}+\frac{\delta_{n\neq N}}{\min(|k_n|^2)}\right), \tag{7.38}$$

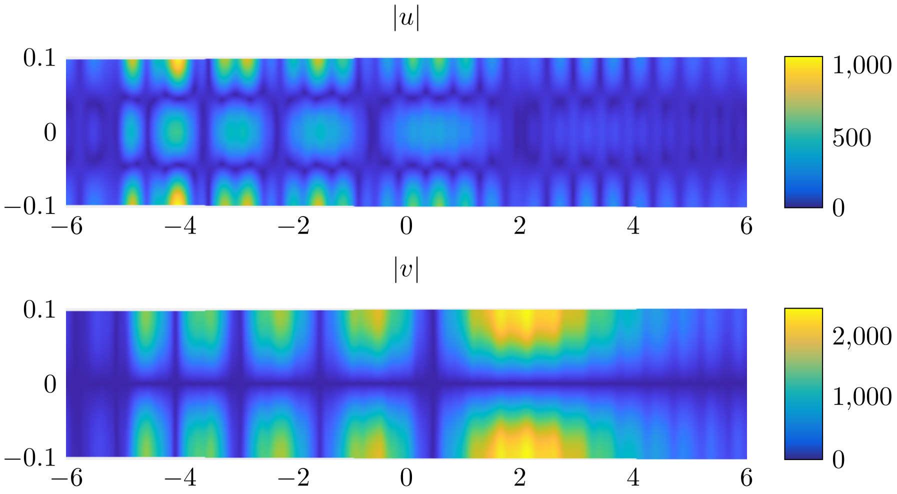

Figure 7.4 – Representation of a wavefield $\boldsymbol{u}$ computed using a finite element method as described in section 7.5. On the top, we represent $|u|$ and on the bottom $|v|$. The relative error of the approximation between $\boldsymbol{u}$ and $\boldsymbol{u}^{\mathrm{app}}$ is $\|\boldsymbol{u}-\boldsymbol{u}^{\mathrm{app}}\|_{\mathrm{L}^2}/\|\boldsymbol{u}\|_{\mathrm{L}^2} = 8.32\%$. We recognize in these pictures the Airy function and its derivative added to propagative exponentials. Here, we have $\omega = 13.98$, h is defined in (7.104), $f_1 = 0$, $\boldsymbol{b}^{\mathrm{top}} = \boldsymbol{b}^{\mathrm{bot}} = 0$ and $f_2(x,y) = \delta_{-5}(x)v_3(y)$.

$$\|\partial_x G_n(\cdot,s)\|_{\mathrm{L}^1(-r,r)} \leq c\left(\delta_{n=N} + \frac{\delta_{n\neq N}}{\min(|k_n|)}\right), \tag{7.39}$$

$$\|G_n(\cdot,s) - G_n^{\mathrm{app}}(\cdot,s)\|_{\mathrm{L}^1(-r,r)} \leq \eta d\left(\delta_{n=N} + \frac{\delta_{n\neq N}}{\min(|k_n|^2)}\right), \tag{7.40}$$

$$\|\partial_x G_n(\cdot,s) - \partial_x G_n^{\mathrm{app}}(\cdot,s)\|_{\mathrm{L}^1(-r,r)} \leq \eta d\left(\delta_{n=N} + \frac{\delta_{n\neq N}}{\min(|k_n|)}\right). \tag{7.41}$$

This Green function provides a solution to (E_3^n) for every $n > 0$. To control the approximation error between (E_2') and (E_3^n), we need to control the dependence between the source and the solution of (E_3^n).

Proposition 7.5. *Let $r > 0$, $n > 0$ and $g_1^n, g_2^n \in L^2(-r,r)$. The equation*

$$\begin{cases} \beta_n' = \dfrac{ik_n}{J_n}\alpha_n + g_1^n, \\ \beta_n'' + k_n^2\beta_n = g_2^n, \\ \alpha_n, \beta_n \text{ are outgoing,} \end{cases} \tag{7.42}$$

has a unique solution $(\alpha_n, \beta_n) \in L^2_{loc}(\mathbb{R})$. Moreover, if $\eta < \eta_1$, the operator

$$\Gamma_1 : \begin{array}{ccc} L^2(-r,r) & \to & L^2(-r,r) \\ (g_1^n, g_2^n) & \mapsto & (\alpha_n, \beta_n)_{|(-r,r)} \end{array} \quad \text{where } (\alpha_n,\beta_n) \text{ is the solution of } (7.42), \tag{7.43}$$

is well-defined, continuous and there exists a constant C_1 depending on δ, $h_{\min}$, $h_{\max}$, R and r such that

$$\|(\alpha_n,\beta_n)\|_{L^2(-r,r)} \leq C_1\left(\delta_{n=N} + \frac{\delta_{n\neq N}}{\min(|k_n|)}\right)(1+J_n)\|(g_1^n, g_2^n)\|_{L^2(-r,r)}. \tag{7.44}$$

Proof. Using the Green function G_n, we compute

$$\beta_n(x) = -\int_{\mathbb{R}} G_n(x,s) g_2^n(s)\mathrm{d}s, \quad \alpha_n(x) = i\frac{J_n}{k_n}\int_{\mathbb{R}} \partial_x G_n(x,s) g_2^n(s)\mathrm{d}s + i\frac{J_n}{k_n} g_1^n(x). \tag{7.45}$$

The upper bound (7.44) follows from Young's inequality for integral operators, inequalities (7.38), (7.39) and the fact that $\|J_n/k_n\|_{\mathrm{W}^{1,1}(\mathbb{R})} < \infty$. ☐

This proposition justifies the approximation of (E_2') by (E_3^n) which, as in [32] and Chapter 2, is a Born approximation. However, we show here that this approximation remains valid near the longitudinal critical frequencies as in the acoustic case of Chapter 4.

The proof of the following Propositions (7.6)-(7.8) and of Lemma 7.1 are given in Appendix 7.A-7.D.

Proposition 7.6 (Born approximation $(E_3^n)/(E_2')$)**.** *Let $r > 0$. There exists $\eta_2 > 0$ and $C_2 > 0$ depending on δ, $h_{\min}$, $h_{\max}$, R and r such that for every $n > 0$, $\eta < \eta_2$ and $F_1^n, F_2^n \in H^1(-r,r)$, the equation (E_2') has a unique solution $(a_n^{(2)}, b_n^{(2)}) \in L^2(-r,r)$. If $(a_n^{(3)}, b_n^{(3)})$ is the solution of (E_3^n),*

$$\|a_n^{(2)} - a_n^{(3)}\|_{L^2(-r,r)} \leq \eta C_2 J_n \left(\delta_{n=N} + \frac{\delta_{n\neq N}}{\min(|k_n|)}\right)\left(\|(F_1^n, F_2^n)\|_{L^2(-r,r)} + \frac{1}{k_n}\|F_1^{n\prime}\|_{L^2(-r,r)}\right), \tag{7.46}$$

$$\|b_n^{(2)} - b_n^{(3)}\|_{L^2(-r,r)} \leq \eta C_2 \left(\delta_{n=N} + \frac{\delta_{n\neq N}}{\min(|k_n|)}\right)\left(\|F_2^n\|_{L^2(-r,r)} + \frac{1}{k_n}\|F_1^{n\prime}\|_{L^2(-r,r)}\right). \tag{7.47}$$

Next, in order to control approximation error between (E_2) and (E_1), we seek to control the dependence between the source and the solution of (E_2). For every $\ell > 0$, we define the functional spaces

$$\mathcal{H}^\ell := \mathrm{H}^\ell_{\mathrm{loc}}(\Omega) \times \mathrm{H}^{\ell-1}_{\mathrm{loc}}(\Omega) \times \mathrm{H}^{\ell-1}_{\mathrm{loc}}(\Omega) \times \mathrm{H}^\ell_{\mathrm{loc}}(\Omega), \quad \mathcal{H}^\ell_r = \mathrm{H}^\ell(\Omega_r) \times \mathrm{H}^{\ell-1}(\Omega_r) \times \mathrm{H}^{\ell-1}(\Omega_r) \times \mathrm{H}^\ell(\Omega_r). \tag{7.48}$$

We also introduce the mappings

$$\mathcal{T}_2(\boldsymbol{X}, \boldsymbol{Y}) := \begin{pmatrix} \sum\limits_{m>0} \langle \boldsymbol{X}, \widetilde{\boldsymbol{Y}_m}\rangle \partial_x \widetilde{\boldsymbol{X}_m} \\ \sum\limits_{m>0} \langle \boldsymbol{Y}, \widetilde{\boldsymbol{X}_m}\rangle \partial_x \widetilde{\boldsymbol{Y}_m} \end{pmatrix}, \tag{7.49}$$

$$\mathcal{T}_3(\boldsymbol{X}, \boldsymbol{Y}) = h'(x) \sum_{m>0} \langle \boldsymbol{Y}, \widetilde{\boldsymbol{X}_m}\rangle \left(\begin{pmatrix} s_m(h) \\ 0 \end{pmatrix}, \begin{pmatrix} -s_m(-h) \\ 0 \end{pmatrix} \right). \tag{7.50}$$

Lemma 7.1. *The mappings $\mathcal{T}_2$ and $\mathcal{T}_3$ are well-defined and continuous from $\mathcal{H}^3_r$ into $\mathcal{H}^2_r$ and from $\mathcal{H}^3_r$ into $(\widetilde{H}^{3/2}(-r,r))^2$ respectively. There exists $C_3 > 0$ depending on δ, $h_{\min}$, $h_{\max}$, R and r such that*

$$\|\mathcal{T}_2\|_{\mathcal{H}^3_r, \mathcal{H}^2_r} \leq \eta C_3, \quad \|\mathcal{T}_3\|_{\mathcal{H}^3_r, (\widetilde{H}^{3/2}(-r,r))^2} \leq \eta C_3. \tag{7.51}$$

We can now rewrite (E_2) and estimate how its solution depends on the source terms.

Proposition 7.7. *Let $r > 0$, $\boldsymbol{g} \in \mathcal{H}^2_r$, $\boldsymbol{b}^{top}, \boldsymbol{b}^{bot} \in \widetilde{H}^{3/2}(-r,r)$. If $\eta < \min(\eta_1, \eta_2)$, the equation*

$$\partial_x \begin{pmatrix} \boldsymbol{X} \\ \boldsymbol{Y} \end{pmatrix} = \begin{pmatrix} F(\boldsymbol{Y}) \\ G(\boldsymbol{X}) \end{pmatrix} + \mathcal{T}_2(\boldsymbol{X}, \boldsymbol{Y}) + \boldsymbol{g} + \begin{pmatrix} 0 \\ -b_2^{top}\delta_{y=h(x)} - b_2^{bot}\delta_{y=-h(x)} \\ b_1^{top}\delta_{y=h(x)} + b_1^{bot}\delta_{y=-h(x)} \\ 0 \end{pmatrix}, \tag{7.52}$$

with boundary conditions $B_1(\boldsymbol{X}) = B_2(\boldsymbol{Y}) = 0$ and $\boldsymbol{X}, \boldsymbol{Y}$ outgoing has a unique solution $(\boldsymbol{X}, \boldsymbol{Y}) \in \mathcal{H}^3$. Moreover, the operator

$$\Gamma_2 : \begin{array}{ccc} \mathcal{H}^2_r \times (\widetilde{H}^{3/2}(-r,r))^2 & \to & \mathcal{H}^3_r \\ (\boldsymbol{g}, \boldsymbol{b}^{top}, \boldsymbol{b}^{bot}) & \mapsto & (\boldsymbol{X}, \boldsymbol{Y}) \end{array}, \tag{7.53}$$

where $(\boldsymbol{X}, \boldsymbol{Y})$ is the solution of (7.52) is well-defined, continuous and there exists a constant $C_4 > 0$ depending on δ, $h_{\min}$, $h_{\max}$, R and r such that

$$\|(\boldsymbol{X}, \boldsymbol{Y})\|_{\mathcal{H}^3_r} \leq C_4 \left(\|\boldsymbol{g}\|_{\mathcal{H}^2_r} + \|\boldsymbol{b}^{top}\|_{H^{3/2}(\mathbb{R})} + \|\boldsymbol{b}^{bot}\|_{H^{3/2}(\mathbb{R})} \right). \tag{7.54}$$

Finally, we can now justify the approximation of (E_1) by (E_2) which is again a Born approximation:

Proposition 7.8 (Born approximation $(E_1)/(E_2)$)**.** *Let $r > 0$, $\boldsymbol{f} \in H^1(\Omega_r)$ and $\boldsymbol{b}^{top}$, $\boldsymbol{b}^{bot} \in \widetilde{H}^{3/2}(-r,r)$. There exists $\eta_3 > 0$ such that if $\eta < \eta_3$ the equation (E_1) has a unique solution $(\boldsymbol{X}^{(1)}, \boldsymbol{Y}^{(1)}) \in H^3_{loc}(\Omega)$. In addition, if $(\boldsymbol{X}^{(2)}, \boldsymbol{Y}^{(2)})$ is the solution of (E_2), there exists $C_4 > 0$ depending on δ, $h_{\min}$, $h_{\max}$, R and r such that*

$$\|(\boldsymbol{X}^{(1)}, \boldsymbol{Y}^{(1)}) - (\boldsymbol{X}^{(2)}, \boldsymbol{Y}^{(2)})\|_{\mathcal{H}^3_r} \leq \eta C_4 \left(\|\boldsymbol{f}\|_{H^1(\mathbb{R})} + \|\boldsymbol{b}^{top}\|_{H^{3/2}(\mathbb{R})} + \|\boldsymbol{b}^{bot}\|_{H^{3/2}(\mathbb{R})} \right). \tag{7.55}$$

To conclude the proof of Theorem 7.1, we combine all the previous results. Using Young's inequality for integral operators, inequalities (7.40), (7.41) and the fact that $\|J_n/k_n\|_{\mathrm{W}^{1,1}(\mathbb{R})} < \infty$, we see that there exists $C_5 > 0$ such that for every $n > 0$,

$$\begin{aligned} \|(a_n^{(3)}, b_n^{(3)}) - (a_n^{\mathrm{app}}, b_n^{\mathrm{app}})\|_{\mathrm{L}^2(-r,r)} \leq \eta C_5 \left(\delta_{n=N} + \frac{\delta_{n\neq N}}{\min(|k_n|)} \right) (1 + J_n) \\ \times \left(\|\boldsymbol{f}\|_{\mathrm{H}^1(\mathbb{R})} + \|\boldsymbol{b}^{\mathrm{top}}\|_{\mathrm{H}^{3/2}(\mathbb{R})} + \|\boldsymbol{b}^{\mathrm{bot}}\|_{\mathrm{H}^{3/2}(\mathbb{R})} \right). \end{aligned}$$

Following the work already done in Appendix 7.C, we set $(\boldsymbol{u}^{(3)}, \boldsymbol{u}^{(3)}) = \sum (a_n^{(3)} \widetilde{\boldsymbol{u}}_n, b_n^{(3)} \widetilde{\boldsymbol{v}}_n)$ and $(\boldsymbol{u}^{(2)}, \boldsymbol{v}^{(2)}) = \sum (a_n^{(2)} \widetilde{\boldsymbol{u}}_n, b_n^{(2)} \widetilde{\boldsymbol{v}}_n)$ and there exist constants $C_6, C_7 > 0$ such that

$$\|(\boldsymbol{u}^{(3)}, \boldsymbol{v}^{(3)}) - (\boldsymbol{u}^{\mathrm{app}}, \boldsymbol{v}^{\mathrm{app}})\|_{\mathrm{L}^2(\Omega_r)} \leq C_6 \left(\|\boldsymbol{f}\|_{\mathrm{H}^1(\mathbb{R})} + \|\boldsymbol{b}^{\mathrm{top}}\|_{\mathrm{H}^{3/2}(\mathbb{R})} + \|\boldsymbol{b}^{\mathrm{bot}}\|_{\mathrm{H}^{3/2}(\mathbb{R})} \right),$$

$$\|(\boldsymbol{u}^{(2)}, \boldsymbol{v}^{(2)}) - (\boldsymbol{u}^{(3)}, \boldsymbol{v}^{(3)})\|_{\mathrm{L}^2(\Omega_r)} \leq C_7 \left(\|\boldsymbol{f}\|_{\mathrm{H}^1(\mathbb{R})} + \|\boldsymbol{b}^{\mathrm{top}}\|_{\mathrm{H}^{3/2}(\mathbb{R})} + \|\boldsymbol{b}^{\mathrm{bot}}\|_{\mathrm{H}^{3/2}(\mathbb{R})} \right),$$

We conclude by using Proposition (7.6) and Proposition (7.8).

7.3.2 The Transverse case

We now move to the study of transverse critical points. Again we assume that the profile h of the waveguide is an increasing function and that there is a unique locally resonant mode $N \in \mathbb{N}^*$ associated with a critical point $x^\star$.

In the transverse case, the dispersion relations are very similar to those presented in Figure 7.3 where the wavenumber k_N switches from a real number to a purely imaginary one. Again, the Lamb basis needs to be modified in order to remain complete at the critical point. As in the longitudinal case, we dwell on the method presented in [81]. We introduce the modified Lamb modes

$$\widetilde{\boldsymbol{X}}_n := \frac{\boldsymbol{X}_n}{k_n}, \qquad \widetilde{\boldsymbol{Y}}_n := \frac{k_n \boldsymbol{Y}_n}{J_n}, \tag{7.56}$$

which form a complete family even at the transverse critical point:

Proposition 7.9. *The modified Lamb modes $(\widetilde{\boldsymbol{X}}_n)_{n>0}$ (resp. $(\widetilde{\boldsymbol{Y}}_n)_{n>0}$) are well-defined and form a complete set of functions in $H^1(-h(x), h(x)) \times L^2(-h(x), h(x))$ for every $x \in \mathbb{R}$ (resp. $L^2(-h(x), h(x)) \times H^1(-h(x), h(x))$).*

Proof. The proof is similar to the one of Proposition 7.4, we only need to modify the study of the behavior of $\widetilde{\boldsymbol{Y}}_N$ and $\widetilde{\boldsymbol{X}}_N$ around the locally resonant point:

$$|\sin(qh)| \sim \frac{4k_N^2 p^\star \tan(p^\star h^\star)}{(q^\star)^3}, \quad J_N(h) \sim -32ik_N^3\omega^2 \frac{(p^\star)^2 \sin(p^\star h^\star)^3 \cos(p^\star h^\star)}{(q^\star)^4},$$

$$\frac{k_N \boldsymbol{Y}_N}{J_N} \sim \frac{ip^\star (q^\star)^3}{16\omega^2 \cos(p^\star h^\star)^2 \sin(p^\star h^\star)^2} \times \begin{pmatrix} 2\lambda(p^\star)^2 \cos(q^\star h^\star)\cos(p^\star y) - 2\mu(q^\star)^2 \cos(p^\star h^\star)\cos(q^\star y) \\ -2p^\star \cos(q^\star h^\star)\sin(p^\star y) - \cos(p^\star h^\star)\sin(q^\star y) \end{pmatrix},$$

$$\frac{\boldsymbol{X}_N}{k_N} \sim 2ip^\star q^\star \sin(p^\star h^\star) \begin{pmatrix} -\cos(q^\star y) \\ \mu q^\star \sin(q^\star y) \end{pmatrix}.$$

Reversing the roles of $\widetilde{\boldsymbol{X}}_n$ and $\widetilde{\boldsymbol{Y}}_n$, one concludes as in Proposition 7.4. ☐

The modified Lamb basis functions are continuous with respect to x, and we can now decompose continuously the wavefield $\boldsymbol{u}$ for every $x \in \mathbb{R}$ as

$$\boldsymbol{X}(x,y) = \sum_{n>0} a_n(x)\widetilde{\boldsymbol{X}}_n(x,y), \quad \boldsymbol{Y}(x,y) = \sum_{n>0} b_n(x)\widetilde{\boldsymbol{Y}}_n(x,y), \tag{7.57}$$

where the coefficients a_n and b_n are given by

$$a_n = \langle \boldsymbol{X}, \widetilde{\boldsymbol{Y}}_n \rangle, \quad b_n = \langle \boldsymbol{Y}, \widetilde{\boldsymbol{X}}_n \rangle. \tag{7.58}$$

Next, we follow the steps of section 7.3.1.b. We project equation (7.8) on each mode, as in [81], and after neglecting all the terms depending on h', we obtain the equations

$$\forall n > 0 \quad \begin{cases} a_n' = i\dfrac{k_n^3}{J_n} b_n - k_n F_2^n, \\ b_n' = i\dfrac{J_n}{k_n} a_n + \dfrac{J_n}{k_n} F_1^n, \\ a_n, b_n \text{ are outgoing.} \end{cases} \tag{7.59}$$

Since k_n^3/J_n is bounded and tends to zero when n increases while J_n/k_n blows up when n increases, we work with the equation on a_n. After taking its derivative, we neglect the contribution of $(k_n^3/J_n)'$ and the equation becomes

$$\begin{cases} a_n' = \dfrac{ik_n^3}{J_n} b_n - k_n F_2^n, \\ a_n'' + k_n^2 a_n = ik_n^2 F_1^n - (k_n F_2^n)', \\ a_n, b_n \text{ are outgoing.} \end{cases} \tag{7.60}$$

The second of these equations only involves a_n, and we can solve it using G_n^{app}. Following the same steps as in section 7.3.1.c, we can justify all the approximations and perform the same analysis as in the longitudinal case:

Theorem 7.2. *The statement of Theorem 7.1 remains true in the transverse case replacing the expressions of* a_n^{app} *and* b_n^{app} *by*

$$a_n^{app}(x) = \frac{1}{k_n(x)} \int_{\mathbb{R}} G_n^{app}(x,s)((k_n F_2^n)'(s) - ik_n(s)^2 F_1^n(s))\mathrm{d}s, \tag{7.61}$$

$$b_n^{app}(x) = -i\frac{1}{k_n(x)^2} \int_{\mathbb{R}} \partial_x G_n^{app}(x,s)((k_n F_2^n)'(s) - ik_n(s)^2 F_1^n(s))\mathrm{d}s - i\frac{F_2^n(x)}{k_n(x)^2}. \tag{7.62}$$

We observe that the behavior of the solution is similar to that near the longitudinal critical points, provided that we exchange a_n^{app} and b_n^{app}. We illustrate this Theorem in Figure 7.5, where we compare our approximation $\boldsymbol{u}^{\mathrm{app}}$ with a finite element method generated wavefield $\boldsymbol{u}$, as explained in section 7.5.

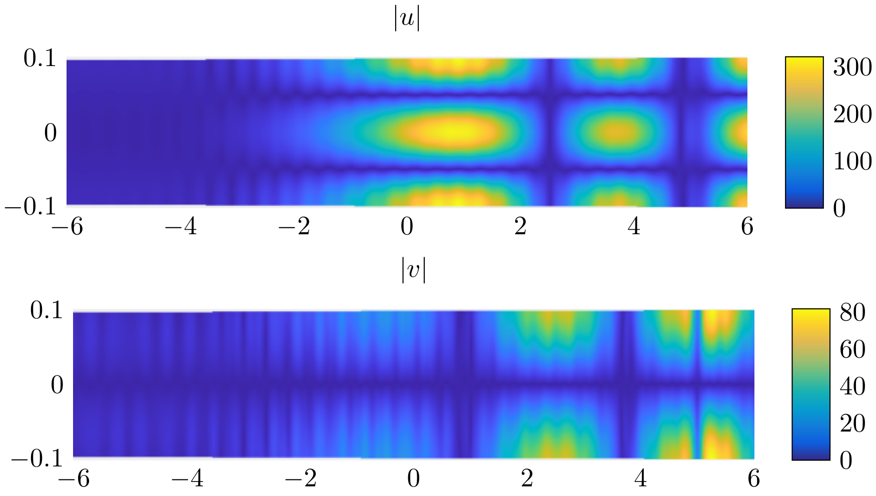

Figure 7.5 – Representation of a wavefield $\boldsymbol{u}$ generated a using finite element method described in section 7.5. On the top, we represent $|u|$ and on the bottom $|v|$. The relative error of the approximation between $\boldsymbol{u}$ and $\boldsymbol{u}^{\mathrm{app}}$ is $\|\boldsymbol{u} - \boldsymbol{u}^{\mathrm{app}}\|_{\mathrm{L}^2}/\|\boldsymbol{u}\|_{\mathrm{L}^2} = 6.58\%$. We recognize in these pictures the Airy function and its derivative added to propagative exponentials. Here, we have $\omega = 15.65$, h is defined in (7.104), $f_2 = 0$, $\boldsymbol{b}^{\mathrm{top}} = \boldsymbol{b}^{\mathrm{bot}} = 0$ and $f_1(x,y) = \delta_5(x)u_5(y)$.

7.3.3 The ZGV case

After studying longitudinal and transverse critical points, we now consider propagation near the ZGV critical points. This study is a little bit different than the one presented before. As was noted in [81], the construction of a modified complete family of modes is more complex than is the longitudinal and transverse cases. We propose a solution below.

We present solutions of the symmetric Rayleigh-Lamb dispersion relation near a ZGV critical point in Figure 7.6. Contrarily to the previous cases, we need to deal with the junction of eight different branches instead of four (or if we work only with right-going modes, with four branches instead of two). In this example, two real wavenumbers switch to two complex ones. This is the configuration that we study in detail, and which will be used in section 7.4 to reconstruct geometrical defects in the waveguide (see also [11]). However, as shown in Figure 7.2, ZGV points may also appear as transitions between evanescent and inhomogeneous waves. Our analysis would apply to this case as well.

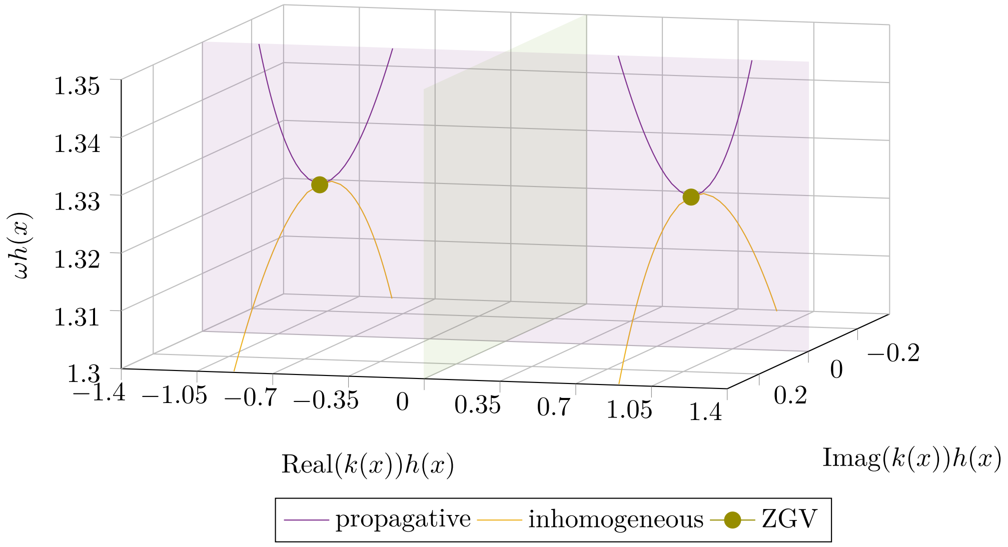

Figure 7.6 – Solutions of the symmetric Rayleigh-Lamb equation (7.14) with $\mu = 0.25$ and $\lambda = 0.31$. Propagative and inhomogeneous branches merge at the ZGV critical point.

Without loss of generality, we may assume that the modes 1 and 2 collapse at the ZGV critical point. The index 1 is used for the mode satisfying $\text{Re}(k_1) > 0$ while the index 2 designates the mode satisfying $\text{Re}(k_2) < 0$. We introduce

$$\widetilde{\boldsymbol{X}}_1 = \frac{\boldsymbol{X}_1 - \boldsymbol{X}_2}{2}, \quad \widetilde{\boldsymbol{Y}}_1 = \frac{\boldsymbol{Y}_1 + \boldsymbol{Y}_2}{2}, \quad \widetilde{\boldsymbol{X}}_2 = \frac{\boldsymbol{X}_1 + \boldsymbol{X}_2}{2J_1}, \quad \widetilde{\boldsymbol{Y}}_2 = \frac{\boldsymbol{Y}_1 - \boldsymbol{Y}_2}{2J_1}, \tag{7.63}$$

while for all $n \neq 1, 2$ we set $(\widetilde{\boldsymbol{X}}_n, \widetilde{\boldsymbol{Y}}_n) = (\boldsymbol{X}_n, \boldsymbol{Y}_n)$. These modified Lamb modes form a complete family even at the ZGV critical point:

Proposition 7.10. *The modified Lamb modes* $(\widetilde{\boldsymbol{X}}_n)_{n>0}$ *(resp.* $(\widetilde{\boldsymbol{Y}}_n)_{n>0}$*) are well-defined and form a complete set of* $H^1(-h(x), h(x)) \times L^2(-h(x), h(x))$ *(resp.* $L^2(-h(x), h(x)) \times H^1(-h(x), h(x))$*) for every* $x \in \mathbb{R}$.

Proof. The proof is similar to that of Proposition 7.4, except for the study of the behavior around $x^\star$. We assume that the mode is symmetric (the antisymmetric case could be treated similarly) and we know from [56, 91, 85] that $k_1(x^\star) = -k_2(x^\star) := k_0$. We also denote by $h_0 = h(x^\star)$, $p_0 = p(x^\star)$, $q_0 = q(x^\star)$ and $\omega_0 = \omega \times h_0$. We set $\boldsymbol{X}_0(y) = \boldsymbol{X}_1(x^\star, y) = -\boldsymbol{X}_2(x^\star, y)$ and $\boldsymbol{Y}_0(y) = \boldsymbol{Y}_1(x^\star, y) =$

$\boldsymbol{Y}_2(x^\star, y)$. Looking at the dispersion relation (7.14), also illustrated in Figure 7.2, we notice that changing the width h when the frequency ω is fixed is equivalent to changing the frequency ω when the width h is fixed. We use this idea, detailed in [85], and work at fixed width h_0 while ω varies with respect to k to simplify all the following asymptotic comparisons when $k_1 \to k_0$ and $k_2 \to -k_0$. It is shown in [85] that there exists $D > 0$ such that

$$\omega(k_1) \sim \omega^\star + D(k_1 - k_0)^2, \quad \omega(k_2) \sim \omega^\star + D(k_2 + k_0)^2. \tag{7.64}$$

It follows that

$$\boldsymbol{X}_1(y) \sim \boldsymbol{X}_0(y) + i(k_1 - k_0)\boldsymbol{X}_g(y), \quad \boldsymbol{Y}_1(y) \sim \boldsymbol{Y}_0(y) + (k_1 - k_0)\boldsymbol{Y}_g(y),$$

where expressions of $\boldsymbol{X}_g$ and $\boldsymbol{Y}_g$ are given in Appendix 7.E. Similarly,

$$\boldsymbol{X}_2(y) \sim -\boldsymbol{X}_0(y) + i(k_2 + k_0)\boldsymbol{X}_g(y), \quad \boldsymbol{Y}_1(y) \sim \boldsymbol{Y}_0(y) - (k_2 + k_0)\boldsymbol{Y}_g(y),$$

and that there exists a constant $c \neq 0$ such that $J_1 \sim (k_1 - k_0)c$ and $J_2 \sim (k_2 + k_0)c$. Using the development (7.64), we notice that when $x \to x^\star$,

$$k_1(x) \sim k_0 + \sqrt{h(x) - h_0}\frac{\sqrt{\omega}}{\sqrt{D}}, \quad k_2(x) \sim -k_0 + \sqrt{h(x) - h_0}\frac{\sqrt{\omega}}{\sqrt{D}}.$$

This implies in particular that $k_1 - k_0 \sim k_2 + k_0$, which leads to the comparisons $\widetilde{\boldsymbol{X}_1} \sim \boldsymbol{X}_0$, $\widetilde{\boldsymbol{Y}_1} \sim \boldsymbol{Y}_0$, $\widetilde{\boldsymbol{X}_2} \sim \boldsymbol{X}_g/c$ and $\widetilde{\boldsymbol{Y}_2} \sim \boldsymbol{Y}_g/c$ when $x \to x^\star$, proving that the new modes are well defined. Using the characterization of generalized Lamb modes in Theorem 3.1 of Chapter 3, it follows that $(\boldsymbol{X}_g, \boldsymbol{Y}_g)$ is a generalized mode, and we conclude that the $(\widetilde{\boldsymbol{X}_n})$'s and the $(\widetilde{\boldsymbol{Y}_n})$'s family form a complete set of functions even at the critical ZGV frequency. ☐

The new modified Lamb basis are continuous with respect to x, and we can now decompose the wavefield $\boldsymbol{u}$ for every $x \in \mathbb{R}$ as

$$\boldsymbol{X}(x, y) = \sum_{n>0} a_n(x)\widetilde{\boldsymbol{X}_n}(x, y), \quad \boldsymbol{Y}(x, y) = \sum_{n>0} b_n(x)\widetilde{\boldsymbol{Y}_n}(x, y). \tag{7.65}$$

To compute the coefficients a_n and b_n, we introduce the new variables

$$\boldsymbol{Z}_1 = \frac{\boldsymbol{Y}_1}{J_1} - \frac{\boldsymbol{Y}_2}{J_2}, \quad \boldsymbol{Z}_2 = \boldsymbol{Y}_1 + \frac{J_1}{J_2}\boldsymbol{Y}_2, \quad \boldsymbol{Z}_3 = \frac{\boldsymbol{X}_1}{J_1} + \frac{\boldsymbol{X}_2}{J_2}, \quad \boldsymbol{Z}_4 = \boldsymbol{X}_1 - \frac{J_1}{J_2}\boldsymbol{X}_2, \tag{7.66}$$

and we notice that

$$a_1 = \langle \boldsymbol{X}, \boldsymbol{Z}_1 \rangle, \quad a_2 = \langle \boldsymbol{X}, \boldsymbol{Z}_2 \rangle, \quad \forall n > 2 \quad a_n = \frac{1}{J_n}\langle \boldsymbol{X}, \widetilde{\boldsymbol{Y}_n} \rangle. \tag{7.67}$$

$$b_1 = \langle \boldsymbol{Y}, \boldsymbol{Z}_3 \rangle, \quad b_2 = \langle \boldsymbol{X}, \boldsymbol{Z}_4 \rangle, \quad \forall n > 2 \quad b_n = \frac{1}{J_n}\langle \boldsymbol{Y}, \widetilde{\boldsymbol{X}_n} \rangle. \tag{7.68}$$

We may then follow the same steps as in section 7.3.1.b. Denoting

$$k_0 = \frac{k_1 - k_2}{2}, \qquad k_g = \frac{k_1 + k_2}{2}, \tag{7.69}$$

we project equation (7.8) on each mode, as in [81], and neglecting all the terms depending on h', we find

$$\forall n > 2 \quad \begin{cases} a_n' = ik_n b_n - F_2^n, \\ b_n' = ik_n a_n + F_1^n, \\ a_n, b_n \text{ are outgoing,} \end{cases} \tag{7.70}$$

$$\begin{cases} a_1' = b_1 i k_0 + b_2 i \dfrac{k_g}{J_1} + F_2^2 - F_2^1, \\ a_2' = b_1 i J_1 k_g + b_2 i k_0 - J_1 F_2^2 - J_1 F_2^1, \\ b_1' = a_1 i k_0 + a_2 i \dfrac{k_g}{J_1} + F_1^2 + F_1^1, \\ b_2' = a_1 i J_1 k_g + a_2 i k_0 - J_1 F_1^2 + J_1 F_1^1, \end{cases} \tag{7.71}$$

where F_1^n and F_2^n are defined in (7.31) and (7.30). The set of equations for $n > 2$ is easily solved by taking derivatives and expressing the solutions to the resulting second order ODEs using the approximation Green function G_n^{app}. To solve the equations on modes 1 and 2, we introduce the auxiliary coefficients

$$c_1(x) = (a_1(x) + b_1(x)) \exp\left(-i \int_{x^\star}^{x} k_0\right), \quad c_2 = (a_2(x) + b_2(x)) \exp\left(-i \int_{x^\star}^{x} k_0\right), \tag{7.72}$$

$$d_1(x) = (a_1(x) - b_1(x)) \exp\left(i \int_{x^\star}^{x} k_0\right), \quad d_2 = (a_2(x) - b_2(x)) \exp\left(i \int_{x^\star}^{x} k_0\right), \tag{7.73}$$

which yields

$$\begin{cases} c_1' = i \dfrac{k_g}{J_1} c_2 + (-F_2^2 - F_2^1 + F_1^2 + F_1^1) e^{-i \int k_0}, \\ c_2' = i k_g J_1 c_1 + J_1(-F_2^2 + F_2^1 + F_1^2 - F_1^1) e^{-i \int k_0}, \\ d_1' = -i \dfrac{k_g}{J_1} d_2 - (F_2^2 + F_2^1 + F_1^2 + F_1^1) e^{i \int k_0}, \\ d_2' = -i k_g J_1 d_1 + J_1(-F_2^2 + F_2^1 - F_1^2 + F_1^1) e^{i \int k_0} \end{cases} \tag{7.74}$$

We notice that equations on modes 1 and 2 are different: while k_g/J_1 is bounded in $\mathrm{W}^{1,1}(\mathbb{R})$, the first derivative of $J_1 k_g$ blows up. This difference of behavior encourages us to privilege the equations on c_1 and d_1. By deriving them and neglecting the contribution of $(k_g/J_1)'$, we nearly recover to the framework developed in the previous sections. We just have to check that c_1 and d_1 are outgoing. By definition of the new Lamb basis, we already know that

$$a_1' + \frac{a_2'}{J_1} - i k_1 a_1 - i k_1 \frac{a_2}{J_1} \underset{x \to +\infty}{\longrightarrow} 0, \qquad -a_1' + \frac{a_2'}{J_1} + i k_2 a_1 - i k_2 \frac{a_2}{J_1} \underset{x \to +\infty}{\longrightarrow} 0,$$

$$b_1' + \frac{b_2'}{J_1} - i k_1 b_1 - i k_1 \frac{b_2}{J_1} \underset{x \to +\infty}{\longrightarrow} 0, \qquad b_1' - \frac{b_2'}{J_1} - i k_2 b_1 + i k_2 \frac{b_2}{J_1} \underset{x \to +\infty}{\longrightarrow} 0.$$

It follows that

$$c_2' + i k_0 c_2 - i k_g c_2 - i k_0 J_1 c_1 \underset{x \to +\infty}{\longrightarrow} 0, \qquad d_2' - i k_0 d_2 - i k_g d_2 - i k_0 J_1 d_1 \underset{x \to +\infty}{\longrightarrow} 0.$$

Using equation (7.74), we can express c_2 and d_2 using c_1 and d_1, and it proves that c_1 and d_1 are outgoing and can be approximated using the Green function G_n^{app}. Following the same steps as in section 7.3.1.c, we can justify all the approximations and perform the same analysis as in the longitudinal and transverse case. We define the sign function by

$$\chi_s(x) := \frac{|x - s|}{x - s}. \tag{7.75}$$

Theorem 7.3. *The statement of Theorem 7.1 remains true in the zero-velocity group case, replacing the expression of* $\boldsymbol{u}^{app}$ *by* $\boldsymbol{u}^{app}(x,y) = \sum(a_n^{app}(x)\widetilde{\boldsymbol{u}_n}(x,y), b_n^{app}(x)\widetilde{\boldsymbol{v}_n}(x,y))$ *where*

$$\forall n > 2 \quad a_n^{app}(x) = \int_{\mathbb{R}} G_n^{app}(x,s)(F_2^{n\prime}(s) - ik_n(s)F_1^n(s))\mathrm{d}s, \tag{7.76}$$

$$\forall n > 2 \quad b_n^{app}(x) = \int_{\mathbb{R}} G_n^{app}(x,s)(ik_n(s)F_2^n(s) - F_1^{n\prime}(s))\mathrm{d}s, \tag{7.77}$$

$$a_1^{app}(x) = \int_{\mathbb{R}} \left[(\alpha(s) + \theta(s)\chi_s(x))\, e^{i\left|\int_s^x k_0\right|} + (\beta(s) + \gamma(s)\chi_s(x))\, e^{-i\left|\int_s^x k_0\right|}\right] G_g^{app}(x,s)\mathrm{d}s, \tag{7.78}$$

$$a_2^{app}(x) = \int_{\mathbb{R}} \left[(\alpha(s)\chi_s(x) + \theta(s))\, e^{i\left|\int_s^x k_0\right|} - (\beta(s)\chi_s(x) + \gamma(s))\, e^{-i\left|\int_s^x k_0\right|}\right] \partial_x G_g^{app}(x,s)\frac{J_1(x)}{ik_g(x)}\mathrm{d}s, \tag{7.79}$$

$$b_1^{app}(x) = \int_{\mathbb{R}} \left[(\alpha(s)\chi_s(x) + \theta(s))\, e^{i\left|\int_s^x k_0\right|} - (\chi_s(x)\beta(s) + \gamma(s))\, e^{-i\left|\int_s^x k_0\right|}\right] G_g^{app}(x,s)\mathrm{d}s, \tag{7.80}$$

$$b_2^{app}(x) = \int_{\mathbb{R}} \left[(\alpha(s) + \theta(s)\chi_s(x))\, e^{i\left|\int_s^x k_0\right|} + (\beta(s) + \gamma(s)\chi_s(x))\, e^{-i\left|\int_s^x k_0\right|}\right] \partial_x G_g^{app}(x,s)\frac{J_1(x)}{ik_g(x)}\mathrm{d}s, \tag{7.81}$$

with

$$\alpha = \frac{F_1^1 + F_1^2}{2G_g^{app}} + ik_g(F_1^2 - F_1^1), \quad \beta = -\frac{F_1^2 + F_1^1}{2G_g^{app}} + ik_g(F_1^2 - F_1^1), \tag{7.82}$$

$$\theta = \frac{F_2^2 - F_2^1}{2G_g^{app}} + ik_g(F_2^2 + F_2^1), \quad \gamma = \frac{F_2^2 - F_2^1}{2G_g^{app}} - ik_g(F_2^2 + F_2^1). \tag{7.83}$$

We illustrate this Theorem in Figure 7.7, where we compare our approximation $\boldsymbol{u}^{\text{app}}$ with a wavefield $\boldsymbol{u}$ obtained by a finite element method, as explained in section 7.5.

We notice that these expressions are very similar those proposed in [82], which, along with the numerical simulations proposed in Figure 7.7, confirm our result. The main contribution of this theorem compared the result stated in [82] is to give an approximation of the wavefield for any source that generated it. Moreover, we provide a global approximation valid along the whole waveguide, while the one proposed in [82] only concerns a neighborhood of $x^\star$. Finally, we formally control the error of approximation and justify the existence of the solution in a slowly perturbed waveguide.

To conclude this section, we have provided approximations of the wavefield in slowly varying waveguides near the three types of critical points. These results were obtained using modified Lamb bases adapted to each critical point. Our results assume that the profile h of the waveguide is increasing but can be easily generalized to any waveguide using the method suggested in section 4.4 of Chapter 4. Moreover, the study of each critical point has been separated. Still, one can easily generalize it to multiple critical points by slicing the waveguide into several sections, using the appropriate theorem on each section, and then connecting solutions at the junction as in Chapter 4.

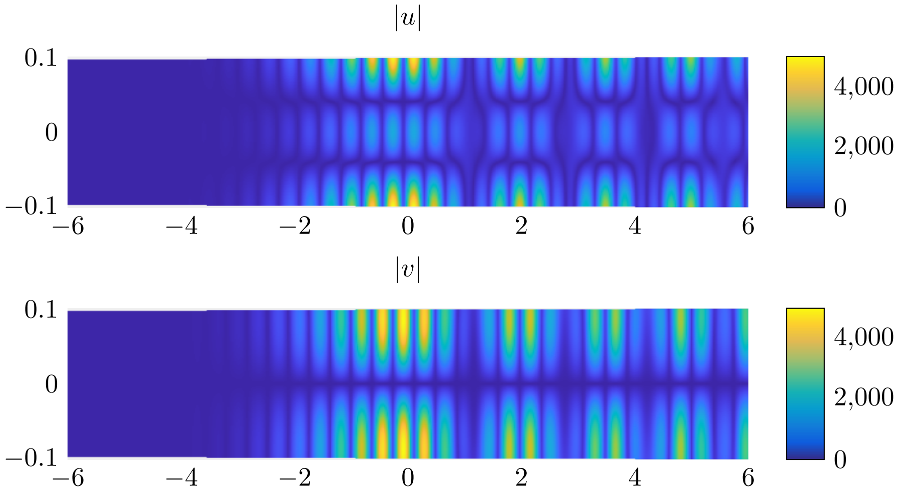

Figure 7.7 – Representation of a wavefield $\boldsymbol{u}$ generated using a finite element method described in section 7.5. On the top, we represent $|u|$ and on the bottom $|v|$. The relative approximation error between $\boldsymbol{u}$ and $\boldsymbol{u}^{\text{app}}$ is $\|\boldsymbol{u}-\boldsymbol{u}^{\text{app}}\|_{\mathrm{L}^2}/\|\boldsymbol{u}\|_{\mathrm{L}^2} = 9.3\%$. We recognize in these pictures the Airy function multiplied by an exponential function. Here, we have $\omega = 13.24$, h is defined in (7.104), $f_2 = 0$, $\boldsymbol{b}^{\text{top}} = \boldsymbol{b}^{\text{bot}} = 0$ and $f_1(x,y) = \delta_5(x)u_2(y)$.

7.4 Reconstruction of shape defects

After studying the propagation of waves in slowly varying waveguides, we present a method to recover the profile h using surface measurements of the wavefield at locally resonant frequencies. This method is the adaptation of that already developed in the acoustic case in Chapter 5. It makes use of locally resonant frequencies to recover the associated position of the locally resonant points $x^\star$, from which the values of $h(x^\star)$ is deduced. From now on, we assume that we have access to the surface measurements

$$\boldsymbol{u}(x, h(x)) \qquad \forall \omega > 0, \quad \forall x \in \mathbb{R}. \tag{7.84}$$

We focus here on the reconstruction of the shape of h on $\operatorname{supp}(h')$, assuming *a priori* knowledge of the constants $h_{\min}$ and $h_{\max}$ and of an interval containing $\operatorname{supp}(h')$. Appendix 5.A of Chapter 5 describes how such numerical approximations can be found in the acoustic case, and this method is still valid in the elastic case and can be used similarly.

Our reconstruction method is based on the use of locally resonant modes to recover $x^\star$. To underline its dependency on ω, we denote it $x^\star_\omega$. We know that $x^\star_\omega$ is a locally resonant point, meaning that $\omega \in \omega_{\text{crit}}^{h(x^\star)}$. As mentioned in section 7.2

$$\omega \in \omega_{\text{crit}}^{h(x^\star)} \quad \Leftrightarrow \quad \omega \in \omega_{\text{crit}}^{1} \times h(x^\star), \tag{7.85}$$

where ω_{crit}^1 is defined as the set of critical frequencies at width 1. Even if the elements of ω_{crit}^1 do not have any explicit expression, we can find extremely good approximations using numerical solvers to look for solutions of the Rayleigh Lamb equation satisfying $\Gamma_S = 0$ or $\Gamma_A = 0$ (see [79]). Given a locally resonant frequency ω, it gives us an extremely precise approximation of $h(x^\star)$:

$$h(x^\star) \approx \frac{(\omega_{\text{crit}}^1)_j}{\omega}, \tag{7.86}$$

where $j > 0$ stands for the index of the critical point we are working on.

The first part of this section briefly explains how the locally resonant part of the wavefield, denoted by $\boldsymbol{d}^{\text{res}}$, can be extracted from the surface measurements. This resonant part is expressed using the Green function G_n^{app}, which depends on $x_\omega^\star$ through the function ξ defined in (7.32). However, this dependency is very complicated and hardly usable to find an explicit link between the data and $x_\omega^\star$. In the second part, we approximate of the locally resonant modes using a three-parameter model function

$$d_{z,a,x_\omega^\star}^{\text{app}} : x \mapsto z\mathcal{A}(a(x_\omega^\star - x)), \tag{7.87}$$

where $z \in \mathbb{C}^*$ is a complex amplitude, $a > 0$ is a scaling factor, and $x_\omega^\star$ is the locally resonant point, playing the role of a longitudinal shift. This model function is then used to recover $x_\omega^\star$ in a stable way.

7.4.1 Filtering of data

Given measurements of the whole wavefield $\boldsymbol{u}(x, h(x))$ at a locally resonant frequency ω, we want to extract the part carried by the locally resonant modes. Looking at the results of Theorems 7.1, 7.2 and 7.3, we notice that evanescent and inhomogeneous modes vanish away from the source, meaning that their contribution in $\boldsymbol{u}(x, h(x))$ is negligible. As for propagative modes, we notice that $k_n(x)$ is almost constant since the waveguide varies slowly. Using the expression of G_n^{app} given in (7.35), we see that the propagative modes are oscillating with a frequency almost equal to k_n.

As mentioned in section 5.4 of Chapter 5, since

$$\forall n > 0 \qquad G_n^{\text{app}} = \mathcal{O}\left(\frac{1}{\min(|k_n|)}\right), \tag{7.88}$$

the amplitude of propagative modes is negligible compared to the amplitude of a locally resonant one if each F_1^n and F_2^n are of comparable amplitude. In this case, one can assume that only the locally resonant mode contributes to $\boldsymbol{u}(x, h(x))$ while the contributions of the other modes is burried in the noise. However, in the general case, the amplitudes of the F_1^n's and F_2^n's are not always comparable, and we cannot neglect the influence of propagative modes.

In this case, inspired by the experimental post-treatment of the wavefield carried out in [59, 58], we filter out all spatial frequencies around $k_n(x)$ for every propagative mode n. It cleans the signal and keeps only the locally resonant part of it. This filtering creates a negligible noise on the data as explained in [64]. More details and illustrations on this filtering method can be found in [64] and in Chapter 5.

7.4.2 Wavefield approximation

From now on, we assume that our data is the locally resonant part of $\boldsymbol{u}(x, h(x))$, denoted by $\boldsymbol{d}^{\text{res}}$. In the case of a longitudinal or transverse locally resonant mode denoted by N, Theorem 7.1 and 7.2 state that

$$\boldsymbol{d}^{\text{res}} \approx (a_N^{\text{app}}(x)\boldsymbol{u}_N(x, h(x)), b_N^{\text{app}}(x)\boldsymbol{v}_N(x, h(x)))\,. \tag{7.89}$$

In the ZGV case, using the notations of section 7.3.3,

$$\boldsymbol{d}^{\text{res}} \approx (a_1^{\text{app}}(x)\widetilde{\boldsymbol{u}}_1(x, h(x)) + a_2^{\text{app}}(x)\widetilde{\boldsymbol{u}}_2(x, h(x)), b_1^{\text{app}}(x)\widetilde{\boldsymbol{v}}_1(x, h(x)) + b_2^{\text{app}}(x)\widetilde{\boldsymbol{v}}_2(x, h(x)))\,. \tag{7.90}$$

To find an exploitable link between $\boldsymbol{d}^{\text{res}}$ and $x_\omega^\star$, we consider the Taylor expansions of these approximations following the steps of section 5.3 in Chapter 5. For $R > 0$, we define the interval

$$\Gamma_R(x_\omega^\star) := (x_\omega^\star - R, x_\omega^\star + R),$$

and we assume from now on that the sources are located to the right of this interval. Moreover, we assume in the longitudinal and transverse cases that $F_2^N, F_1^N \neq 0$, and in the ZGV case that $F_1^1, F_1^2, F_2^1, F_2^2 \neq 0$. Then, we can prove the following proposition:

Proposition 7.11. *Let $r > 0$ and h satisfying assumption 7.1. Assume that at the frequency $\omega > 0$, there exists a unique locally resonant point $x_\omega^\star$ satisfying $h'(x_k^\star) \geq \theta\eta$ for some $\theta > 0$. Then there exist $\eta_0 > 0$ and $C_1 > 0$ depending only on $h_{\min}$, $h_{\max}$, θ and r such that*

- *In the longitudinal case,*

$$\|\boldsymbol{d}_2^{res} - d^{app}_{z,a,x_k^\star}\|_{L^2(\Gamma_{r\eta^{-1/3}}(x_\omega^\star))} \leq C_1\eta^{1/3}. \tag{7.91}$$

- *In the transverse case,*

$$\|\boldsymbol{d}_1^{res} - d^{app}_{z,a,x_k^\star}\|_{L^2(\Gamma_{r\eta^{-1/3}}(x_\omega^\star))} \leq C_1\eta^{1/3}. \tag{7.92}$$

- *In the ZGV case,*

$$\left\|\left|\frac{\boldsymbol{d}_1^{res}}{u_n(x_\omega^\star, h(x_\omega^\star))} + \frac{\boldsymbol{d}_2^{ex}}{v_n(x_\omega^\star, h(x_\omega^\star))}\right| - \left|d^{app}_{z,a,x_k^\star}\right|\right\|_{L^2(\Gamma_{r\eta^{-1/3}}(x_\omega^\star))} \leq C_1\eta^{1/6}, \tag{7.93}$$

for some $z \in \mathbb{C}$ and $a > 0$ depending on the source terms.

Remark 7.4. *Here, the interval $\Gamma_R(x_\omega^\star)$ is resized with $R = r\eta^{-1/3}$ to keep the same accessible window of the Airy function for any choice of η. More details are provided in Chapter 5.*

Proof. In the longitudinal and transverse cases, the Taylor expansions of a_N and b_N are exactly the same as in the acoustic case presented in Proposition 5.2 of Chapter 5. Using the Taylor expansions of u_N and v_N presented in the proofs of Propositions 7.4 and 7.9 yields the result. As for the ZGV case, we use the Taylor expansion of $G_n^{\rm app}$ presented in Proposition 5.1 of Chapter 5. Expanding also $\partial_x G_n^{\rm app}$, we notice that

$$\|\partial_x G_n^{\rm app}\|_{\mathrm{L}^\infty(\Gamma_{r\eta^{-1/3}}(x_\omega^\star))} = \mathcal{O}(\eta^{1/3}), \quad \|\partial_x G_n^{\rm app}\|_{\mathrm{L}^2(\Gamma_{r\eta^{-1/3}}(x_\omega^\star))} = \mathcal{O}(\eta^{1/6}),$$

which shows that the components $a_2^{\rm app}$ and $b_2^{\rm app}$ can be included in the error term. Since the sources are located to the right of the zone of measurements, we know that $\chi_s(x) = -1$. Using expressions (7.78) and (7.80), there exists a function g such that

$$a_1^{\rm app}(x) + b_1^{\rm app}(x) = e^{i\int_0^x k_0} \int_{\mathbb{R}} g(s) G_g^{\rm app}(x, s)\mathrm{d}s.$$

By taking the absolute value, we eliminate the phase shift and cast this expression in the framework of Proposition 5.2 of Chapter 5. We conclude using the Taylor expansions of u_1, v_1, u_2, v_2 presented in the proof of Proposition 7.10. ☐

Note that in the ZGV case, we have full knowledge of $u_n(x_\omega^\star, h(x_\omega^\star))$ and $v_n(x_\omega^\star, h(x_\omega^\star))$ since we can determine ω and $h(x_\omega^\star)$ using (7.86).

7.4.3 A stable reconstruction of $x_\omega^\star$

Using the previous approximations of measurements, we are now back to the same framework as in the acoustic case, and we can use the stable algorithm already presented there to recover $x_\omega^\star$ from $d^{\mathrm{app}}_{z,a,x_\omega^\star}$. Given a discretization X of the interval $\Gamma_{r\eta^{-1/3}}(x_\omega^\star)$, we recover the three parameters z, a and $x_\omega^\star$ by minimizing the function

$$(z,a,x_\omega^\star) \mapsto \|d - d^{\mathrm{app}}_{z,a,x_\omega^\star}(X)\|_2, \tag{7.94}$$

with a gradient descent algorithm where d stands for $\boldsymbol{d}_1^{\mathrm{res}}$, $\boldsymbol{d}_2^{\mathrm{res}}$ or $\boldsymbol{d}_1^{\mathrm{res}}/u_n(x_\omega^\star, h(x_\omega^\star))+\boldsymbol{d}_2^{\mathrm{res}}/v_n(x_\omega^\star, h(x_\omega^\star))$ depending on the nature of the critical point. Proposition 5.3 of Chapter 5 shows that if the noise on the data is small enough, the algorithm converges and gives a good approximation of $x_\omega^\star$, which we thereafter denote by $x_\omega^{\star,\mathrm{app}}$. Then, we approximate the width at $x_\omega^{\star,\mathrm{app}}$ by

$$h^{\mathrm{app}}(x_\omega^{\star,\mathrm{app}}) = \frac{(\omega^1_{\mathrm{crit}})_j}{\omega}. \tag{7.95}$$

This provides an approximation of h in one point. Then, we sweep through a range of frequencies to get approximations of h all along the support of h'. Using the approximations of h_{min} and h_{max} provided by Appendix 5.A of Chapter 5, we set

$$\omega_{\mathrm{max}} = \frac{(\omega^1_{\mathrm{crit}})_j}{h_{\mathrm{min}}}, \quad \omega_{\mathrm{min}} = \frac{(\omega^1_{\mathrm{crit}})_j}{h_{\mathrm{max}}}, \tag{7.96}$$

and we take a set of locally resonant frequencies $W \subset (\omega_{\mathrm{min}}, \omega_{\mathrm{max}})$. For every frequency $\omega \in W$, we introduce X_ω a discretization of $\Gamma_{r\eta^{-1/3}}(x_\omega^\star)$ and we measure $\boldsymbol{d}^{\mathrm{res}}$, the resonant part of $\boldsymbol{u}(x, h(x))$, with a small noise denoted by ζ_ω. We introduce $X^{\star,\mathrm{app}}$ the set of all $x_\omega^{\star,\mathrm{app}}$, and we assume that $\mathrm{card}(X^{\star,\mathrm{app}}) = \mathrm{card}(W)$. If we set $\mathrm{supp}(h') = (x_0, x_{n+1})$ the known approximation of the support determined as in Appendix 5.A of Chapter 5, the function h^{app} is then defined as the piecewise linear function such that

$$h^{\mathrm{app}}(x_\omega^{\star,\mathrm{app}}) = \frac{(\omega^1_{\mathrm{crit}})_j}{\omega} \quad \forall\, \omega \in W, \qquad h^{\mathrm{app}}(x_0) = h_{\mathrm{min}}, \qquad h^{\mathrm{app}}(x_{n+1}) = h_{\mathrm{max}}. \tag{7.97}$$

We can quantify the error of reconstruction between h^{app} and h:

Theorem 7.4. *Let W be a subset of $(\omega_{\mathrm{min}}, \omega_{\mathrm{max}})$. If for every $\omega \in K$, $h'(x_\omega^\star) \geq \theta\eta$ for some $\theta > 0$, then there exists $\eta_1 > 0$, $Z > 0$, $C_2 > 0$ depending on h_{min}, h_{max}, θ and r such that*

$$\|h^{app}(X^{\star,app}) - h(X^{\star,app})\|_\infty \leq \eta C_2 \left(C_1 \eta^{1/3} + \max_{k\in K} \|\zeta_k\|_2 \right), \tag{7.98}$$

for all $\eta < \eta_1$ and $\max_{\omega \in W} \|\zeta_\omega\|_2 \leq Z$.

Proof. The proof is similar to that of Theorem 5.2. □

To conclude, we have provided here a stable reconstruction of the profile of slowly varying elastic waveguides using the recovery of the locally resonant points $x_\omega^\star$ of locally resonant frequencies. This method can be used in a very general framework as it does not require any *a priori* assumption on the sources except compact support, as long as their locally resonant parts do not vanish.

Note that in this section, we chose to reconstruct $x_\omega^\star$ using the component of the wavefield, which is convoluted with G_n^{app}. However, in the longitudinal and transverse case, we could have used the other component convoluted with $\partial_x G_n^{\mathrm{app}}$ to fit the derivative of an Airy function instead of an Airy function. This could be useful if only one component on the wavefield is available.

7.5 Numerical Results

In this section, we show numerical applications of our reconstruction method of the profile of slowly varying elastic waveguides. We simulate surface measurements using numerically generated data, and we provide reconstructions of increasing and non monotonous profiles of waveguides with different shapes, using the three types of locally resonant frequencies. .

7.5.1 Generation of the data

In the following, numerical solutions of (7.25) are generated using the software Matlab with which the equations of elasticity are solved in the waveguide Ω. In each numerical simulation, we assume that h' is supported between $x = -7$ and $x = 7$. To generate the solution $\boldsymbol{u}$ of (7.25) in Ω_7, we use a self-coded finite element method and a perfectly matched layer (PML) [18] on the left side of the waveguide, between $x = -15$ and $x = -8$, and on the right side between $x = 8$ and $x = 15$. Since PML's do not correctly handle the presence of right-going propagating modes with negative wavenumbers, we use the strategy presented in [21] to correct the PML's in order to obtain a true approximation of the wavefield for every non critical frequency. The coefficient of absorption for the perfectly matched layer is set to be $\alpha = -k((x-8)\mathbf{1}_{x\geq 8} - (x+8)\mathbf{1}_{x\leq -8})$ and ω^2 is replaced in the Helmholtz equation with $\omega^2 + i\alpha$. The structured mesh is built with a stepsize of 10^{-3}.

7.5.2 Method of reconstruction

We summarize the steps of the reconstruction. These steps are adapted from Chapter 5 and more details on the computations can be found there.

1. Determine an approximation of $\mathrm{supp}(h')$, $\omega_{\min}$ and $\omega_{\max}$ using the method described at the beginning of Appendix 5.A.
2. Choose a set of frequencies $W \subset (\omega_{\min}, \omega_{\max})$ and sources $\boldsymbol{f}$, $\boldsymbol{b}^{\text{top}}$, $\boldsymbol{b}^{\text{bot}}$. Then, for every frequency, measure the wavefield $\boldsymbol{u}(x, h(x))$ solution of (7.25).
3. Filter the data by eliminating the Fourier transform responses near k_n for every propagative mode n to obtain $\boldsymbol{d}^{\text{res}}$.
4. Compute the available data d depending on the nature of the chosen critical point as explained in Proposition 7.11.
5. For every frequency, minimize the quantity $\|d - d^{\text{app}}_{z,a,x^\star_\omega}\|_2$ using a gradient descent to find the approximation $x^{\star,\text{app}}_\omega$ of $x^\star_\omega$.
6. Compute h^{app} from expression (7.97).

7.5.3 Numerical results

We now apply this method to reconstruct a few specific profiles of slowly varying waveguides. In Figure 7.8, we present two reconstructions of the profiles defined by

$$h_1(x) = 0.1 + \gamma_1 x^3 \mathbf{1}_{-4\leq x\leq 4} + \gamma_2 \mathbf{1}_{x>4} - \gamma_2 \mathbf{1}_{x<-4}, \tag{7.99}$$

$$h_2(x) = 0.1 + \gamma_3 \sin\left(\frac{\pi}{10}(x+5)\right) \mathbf{1}_{-5\leq x\leq 5}, \tag{7.100}$$

where $\gamma_1 = 2.08.10^{-5}$, $\gamma_2 = 0.0013$ and $\gamma_3 = 25.10^{-4}$. The profile h_1 is increasing while h_2 represents a dilation of the waveguide. The sources in (7.25) are defined depending on the nature of the critical point by

$$\boldsymbol{f} = 0, \quad \boldsymbol{b}^{\text{bot}} = 0, \quad \boldsymbol{b}^{\text{top},(1)} = (\delta_{\zeta 5}(x), 0), \quad \boldsymbol{b}^{\text{top},(2)} = \begin{cases} (\delta_0(x), 0) & \text{if } \chi = 1, \\ (\delta_{-5}(x) + \delta_5(x), 0) & \text{if } \chi = -1. \end{cases} \tag{7.101}$$

We recall that $\chi = 1$ if the critical point is normal and $\chi = -1$ if it is abnormal (see Figure 7.2). The sets of used frequencies are

$$W_{L1} = 13.96 : 14.32 : 30, \quad W_{T1} = 15.51 : 15.9 : 30, \quad W_{ZGV1} = 13.09 : 13.43 : 30, \tag{7.102}$$

$$W_{L2} = 14.07 : 14.13 : 30, \quad W_{T2} = 15.63 : 15.69 : 30, \quad W_{ZGV2} = 13.2 : 13.26 : 30. \tag{7.103}$$

We plot in Figure 7.8 the reconstructions h^{app} obtained for every critical point. We also compute the L^∞ relative reconstruction error in each situation. We notice that each reconstruction seems to fit very well the defect, even if the ZGV one seems more precise than the others, especially around the corners of h_1 and h_2.

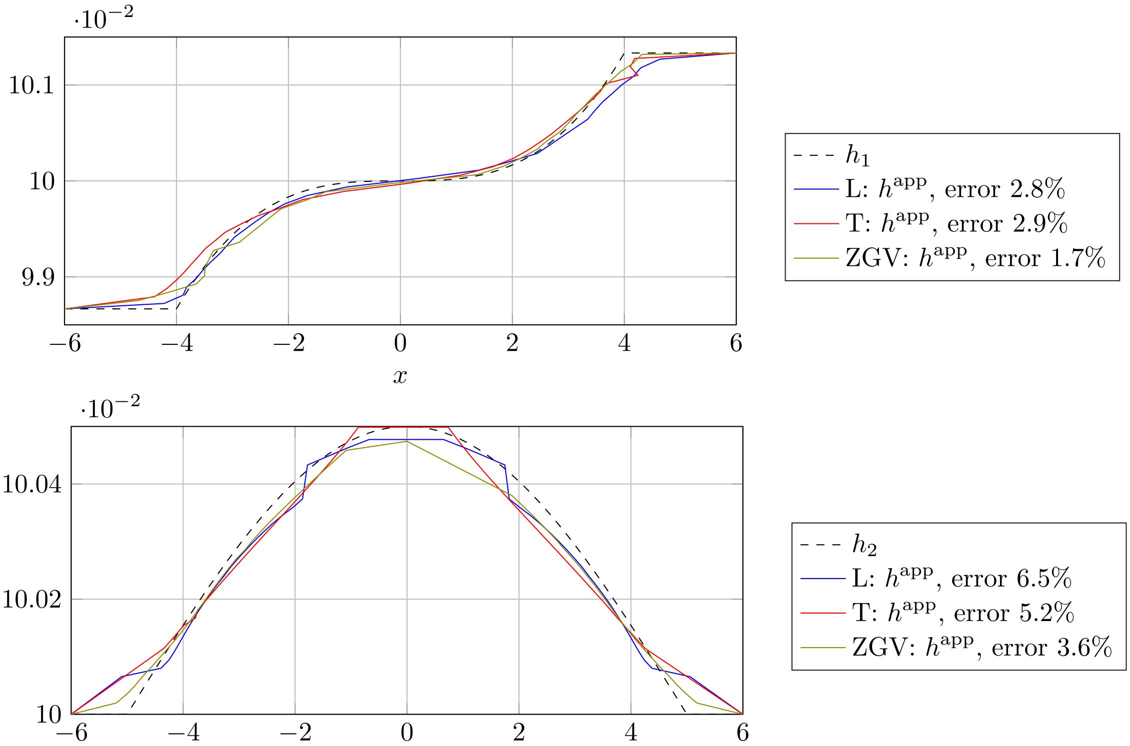

Figure 7.8 – Reconstruction of two varying profiles. In black, the initial shapes of h_1 and h_2 defined in (7.99) and (7.100). In blue, red and olive, the reconstructions h^{app} obtained with longitudinal, transverse and zero-group velocity frequencies. In each case, the set of used frequencies are defined in (7.102) and (7.103) and sources of (7.25) are defined in (7.101). We also print the relative error of the reconstruction $\|h - h^{\text{app}}\|_\infty / \|h\|_\infty$.

We investigate in Table 7.1 the quality of the reconstruction given different profiles with increasing values of η. We notice that the ZGV numerical reconstructions seems more robust than the L and T ones.

η	9.10^{-4}	3.10^{-3}	7.10^{-3}	1.10^{-2}
L, $\\|h-h^{\text{app}}\\|_\infty/\\|h\\|_\infty$	2.8%	7.6%	13.2%	23.4%
T, $\\|h-h^{\text{app}}\\|_\infty/\\|h\\|_\infty$	2.9%	5.3%	10.2%	17.4%
ZGV, $\\|h-h^{\text{app}}\\|_\infty/\\|h\\|_\infty$	1.7%	2.3%	5.7%	8.2%

Table 7.1 – Relative L^∞ errors on the reconstruction of h for increasing values of η. In each case, the width profile is defined in (7.99) and dilated to increase the value of η.

Finally, we present in Figure 7.9 two additional shape reconstructions using ZGV frequencies with

$$h_3(x) = 0.1 + \gamma_5 x \mathbf{1}_{-4\le x\le 4} + 4\gamma_4 \mathbf{1}_{x>4} - 4\gamma_4 \mathbf{1}_{x<-4}, \tag{7.104}$$

$$h_4(x) = 0.1 - \gamma_6\sqrt{3} + 2\gamma_6 \sin\left(\frac{4\pi\sqrt{x+5}}{3}\right)\mathbf{1}_{-3.5\le x\le 4} + 2\gamma_6 \sin\left(\frac{4\pi\sqrt{1.5}}{3}\right)\mathbf{1}_{x<-3.5}, \tag{7.105}$$

where $\gamma_4 = 53/3.10^{-5}$, $\gamma_5 = 0.01/30$, and $\gamma_6 = 25.10^{-4}$. In these examples, we choose

$$\boldsymbol{f} = 0, \quad \boldsymbol{b}^{\text{bot}} = 0, \quad , \boldsymbol{b}^{\text{top},(3)} = (\delta_5(x), 0), \quad \boldsymbol{b}^{\text{top},(4)} = (\delta_{-1.5}(x) + \delta_6(x), 0), \tag{7.106}$$

and

$$K_{ZGV3} = 13.09 : 13.43 : 30, \quad K_{ZGV4} = 13.07 : 13.27 : 30. \tag{7.107}$$

We notice that even for more complex defects, our reconstruction method produces great results, with relative errors or the order of a percent.

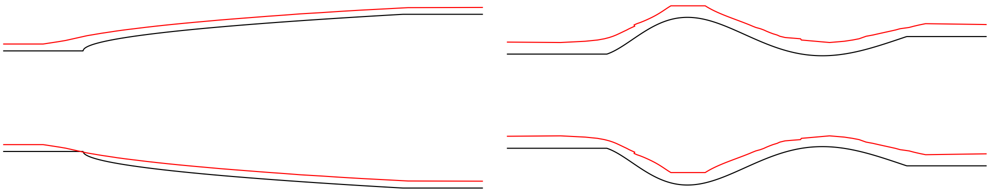

Figure 7.9 – Reconstruction of two varying width profiles with ZGV critical frequencies. In black, the initial shape of h_3 and h_4 defined in (7.104) and (7.105) and in red the reconstruction slightly shifted for comparison purposes. Sources of (7.25) are defined in (7.106) and used frequencies in (7.107). The relative reconstruction error is $\|h-h^{\text{app}}\|_\infty/\|h\|_\infty = 3.1\%$ for h_3 and $\|h-h^{\text{app}}\|_\infty/\|h\|_\infty = 1.5\%$ for h_4.

7.6 Conclusion

In this chapter, we have extended the method for reconstructing shape defects presented in Chapter 5 to the more complex case of elastic plates. After studying the propagation of elastic wavefields near locally resonant frequencies using modified Lamb basis, we prove that solutions can be approximated by Airy functions as in acoustic case (Chapter 4). We use these approximations to reconstruct the associated locally resonant points for several locally resonant frequencies, which provides a good approximation of the profile of the waveguide.

This method enables very precise numerical reconstructions of shape defects. We noticed that ZGV points are particularly adapted and robust and provide good reconstructions. This method requires little *a priori* information on the sources, and provides some theoretical justification of the experimental work reported in [11]. We plan in future work to test this method on experimental data to see if the quality of the reconstructions persists.

We believe that this work could also be generalized to three dimensional elastic plates, in view of our results in Chapter 3.

Appendix 7.A: The Born approximation $(E_2')/(E_3^n)$

Using the operator Γ_1 introduced in Proposition 7.5, equation (E_2') can be rewritten

$$(a_n^{(2)}, b_n^{(2)}) = \Gamma_1(F_1^n, -ik_nF_2^n + F_1^{n\prime}) + \Gamma_1(\mathcal{T}_1(a_n^{(2)}, b_n^{(2)})), \tag{7.108}$$

where

$$\mathcal{T}_1 : \begin{array}{ccc} \mathrm{L}^2(-r,r) & \to & \mathrm{L}^2(-r,r) \\ (a_n^{(2)}, b_n^{(2)}) & \mapsto & \left(0, i\left(\dfrac{k_n}{J_n}\right)' a_n^{(2)}\right) \end{array}.$$

We notice that

$$\left(\frac{k_n}{J_n}\right)' = h'(x)\partial_h\left(\frac{k_n}{J_n}\right),$$

and it follows that there exists a constant $c_1(n)$ depending on the parameters of the problem such that

$$\|\mathcal{T}_1\|_{\mathrm{L}^2(-r,r),\mathrm{L}^2(-r,r)} \leq \eta c_1(n).$$

The application $\Gamma_1 \circ \mathcal{T}_1$ is a contraction in $\mathrm{L}^2(-r,r)$ if

$$\eta < \eta_2(n) := \frac{C_1\left(\delta_{n=N} + \frac{\delta_{n\neq N}}{\min(|k_n|)}\right)(1+J_n)}{c_1(n)}.$$

To ensure a uniform control over n, we use asymptotic approximations of k_n and J_n presented in Chapter 3. We index the subset of inhomogeneous wavenumbers with positive real part by $j \in \mathbb{N}^\star$, and all the asymptotic comparisons are now meant when $j \to +\infty$. We define $N = 2n - 1/2$ if k_n is associated to a symmetric mode, and $N = 2j + 1/2$ if k_j is associated to an antisymmetric one. Then,

$$\partial_h\left(\frac{k_n}{J_n}\right) = \mathcal{O}(N^{-4}), \quad \frac{1+J_n}{k_n} = \mathcal{O}(N^4), \quad \eta_2(n) = \mathcal{O}(1).$$

We then define $\eta_2 = \min\{\eta_2(n),\, n > 0\}$. If $\eta < \eta_2$, the mapping $\Gamma_1 \circ \mathcal{T}_1$ is a contraction for every $n > 0$ and (7.108) has a unique solution $(a_n^{(2)}, b_n^{(2)})$ which can be expressed as a Born series (see [32] and Chapter 2). The solution $(a_n^{(3)}, b_n^{(3)})$ of (E_3^n) is the first term of this series, and

$$\|(a_n^{(2)}, b_n^{(2)}) - (a_n^{(3)}, b_n^{(3)})\|_{\mathrm{L}^2(-r,r)} \leq \|\Gamma_1(F_1^n, -ik_nF_2^n + F_1^{n\prime})\|_{\mathrm{L}^2(-r,r)} \frac{\eta}{\eta_2 - \eta}.$$

Recalling (7.45), we can compute more precisely $\|\Gamma_1(F_1^n, -ik_nF_2^n + F_1^{n\prime})\|_{\mathrm{L}^2(-r,r)}$ and conclude the proof.

Appendix 7.B: Control of the operators $\mathcal{T}_2$ and $\mathcal{T}_3$

For every function ϕ, $\partial_x \phi = h'(x)\partial_h \phi$. If we denote by $(\boldsymbol{X}_m^{(0)}, \boldsymbol{Y}_m^{(0)})$ the Lamb basis for $h = 1$, it follows from (7.14) and (7.15) that

$$\boldsymbol{X}_m(x,y) = h(x)^3 \boldsymbol{X}_m^{(0)}(y/h), \quad \mathbf{Y}_m(x,y) = h(x)^3 \mathbf{Y}_m^{(0)}(y/h),$$

from which we easily compute $\partial_h \widetilde{\boldsymbol{X}_m}$ and $\partial_h \widetilde{\boldsymbol{Y}_m}$. We use the same notations for inhomogeneous modes as in Appendix 7.A. The asymptotic comparisons provided in Chapter 3 show that there exists a constant $d_1 > 0$ such that $\partial_h \widetilde{u}_j \sim d_1 t_j$ and $\partial_h \widetilde{v}_j \sim d_1 s_j$. It follows that when $M \to +\infty$,

$$\sum_{m>M} \langle \boldsymbol{X}, \widetilde{\boldsymbol{Y}_m} \rangle \partial_h \widetilde{u}_m \sim d_1 \sum_{m>M} \langle \boldsymbol{X}, \widetilde{\boldsymbol{Y}_m} \rangle \widetilde{t}_m, \qquad \sum_{m>M} \langle \boldsymbol{Y}, \widetilde{\boldsymbol{X}_m} \rangle \partial_h \widetilde{v}_m \sim d_1 \sum_{m>M} \langle \boldsymbol{Y}, \widetilde{\boldsymbol{X}_m} \rangle \widetilde{s}_m,$$

proving that there exists a constant $d_2 > 0$ such that

$$\left\| \sum_{m>0} \langle \boldsymbol{X}, \widetilde{\boldsymbol{Y}_m} \rangle \partial_h \widetilde{u}_m \right\|_{\mathrm{H}^2(\Omega_r)} \leq d_2 \left\| \sum_{m>0} \langle \boldsymbol{X}, \widetilde{\boldsymbol{Y}_m} \rangle \widetilde{t}_m \right\|_{\mathrm{H}^2(\Omega_r)} = d_2 \|t\|_{\mathrm{H}^2(\Omega_r)} \leq d_2 \|(\boldsymbol{X}, \boldsymbol{Y})\|_{\mathcal{H}^3_r}.$$

Similarly, there exists $d_3 > 0$ such that

$$\left\| \sum_{m>0} \langle \boldsymbol{Y}, \widetilde{\boldsymbol{X}_m} \rangle \partial_h \widetilde{v}_m \right\|_{\mathrm{H}^2(\Omega_r)} \leq d_3 \left\| \sum_{m>0} \langle \boldsymbol{Y}, \widetilde{\boldsymbol{X}_m} \rangle \widetilde{s}_m \right\|_{\mathrm{H}^2(\Omega_r)} = d_3 \|s\|_{\mathrm{H}^2(\Omega_r)} \leq d_3 \|(\boldsymbol{X}, \boldsymbol{Y})\|_{\mathcal{H}^3_r}.$$

Next, we notice that $\partial_h \widetilde{s}_m$ and $\partial_h \widetilde{t}_m$ can be expressed as linear combinations of

$$\partial_h \widetilde{u}_m, \quad \partial_{hh} \widetilde{u}_m, \quad \partial_h \widetilde{v}_m, \quad \partial_{hh} \widetilde{v}_m,$$

which leads to the control of $\mathcal{T}_2$ in $\mathcal{H}^2_r$. To control $\mathcal{T}_3$, we notice that

$$\sum_{m>0} \langle \boldsymbol{Y}, \widetilde{\boldsymbol{X}_m} \rangle s_m(h) = s(x,h).$$

Since $s \in \mathrm{H}^2(\Omega_r)$ has a trace $s(\cdot, h) \in \mathrm{H}^{3/2}(-r,r)$, there exists a constant $d_4 > 0$ such that

$$\left\| \sum_{m>0} \langle \boldsymbol{Y}, \widetilde{\boldsymbol{X}_m} \rangle s_m(h) \right\|_{\mathrm{H}^{3/2}(-r,r)} \leq d_4 \|s\|_{\mathrm{H}^2(\Omega_r)} \leq d_4 \|(\boldsymbol{X}, \boldsymbol{Y})\|_{\mathcal{H}^3_r}.$$

Appendix 7.C: Control of the operator Γ_2

Following [81], we project (7.52) on the modified Lamb basis to notice that each modal component $(a_n^{(2)}, b_n^{(2)})$ satisfies (E_2') with

$$F_1^n(x) = \frac{1}{J_n} \left(\int_{-h(x)}^{h(x)} (g_3(x,y) u_n(y) + g_4(x,y) t_n(y)) \mathrm{d}y + b_1^{\mathrm{top}}(x) u_n(h) + b_1^{\mathrm{bot}}(x) u_n(-h) \right),$$

$$F_2^n(x) = \frac{1}{J_n} \left(\int_{-h(x)}^{h(x)} (g_1(x,y) s_n(y) - g_2(x,y) v_n(y)) \mathrm{d}y + b_2^{\mathrm{top}}(x) u_n(h) + b_2^{\mathrm{bot}}(x) u_n(-h) \right).$$

Invoking Proposition 7.6, there exists a unique couple $(a_n^{(2)}, b_n^{(2)})$ of solutions to (E_2') for every $n > 0$. Moreover, using the triangular inequality, there exists $c_2 > 0$ such that

$$\|a_n^{(2)}\|_{\mathrm{L}^2(-r,r)} \leq c_2 J_n \left(\delta_{n=N} + \frac{\delta_{n\neq N}}{\min(|k_n|)}\right) \left(\|(F_1^n, F_2^n)\|_{\mathrm{L}^2(-r,r)} + \frac{1}{k_n}\|{F_1^n}'\|_{\mathrm{L}^2(-r,r)}\right),$$

$$\|b_n^{(2)}\|_{\mathrm{L}^2(-r,r)} \leq c_2 \left(\delta_{n=N} + \frac{\delta_{n\neq N}}{\min(|k_n|)}\right) \left(\|F_2^n\|_{\mathrm{L}^2(-r,r)} + \frac{1}{k_n}\|{F_1^n}'\|_{\mathrm{L}^2(-r,r)}\right).$$

We need to ensure that $(\boldsymbol{X}, \boldsymbol{Y}) = \sum(a_n^{(2)}\widetilde{\boldsymbol{X}}_n, b_n^{(2)}\widetilde{\boldsymbol{Y}}_n)$ is well defined. To this end, we adapt the proof of Theorem 3.2 to control the decay of the modes. It is shown in [91] that only a finite set E of modes are evanescent, propagative or locally resonant. We use the same notations as in Appendix 7.A to denote by $j \in \mathbb{N}^*$ the inhomogeneous modes. The asymptotic comparisons provided in Chapter 3 show that there exists $c_3 > 0$ such that

$$\|F_1^j\|_{\mathrm{L}^2(-r,r)}, \|F_2^j\|_{\mathrm{L}^2(-r,r)}, \|{F_1^j}'/k_j\|_{\mathrm{L}^2(-r,r)} \leq \frac{c_3}{N^3}\left(\|\boldsymbol{g}\|_{\mathcal{H}_r^2} + \|\boldsymbol{b}^{\mathrm{top}}\|_{\mathrm{L}^2(\mathbb{R})} + \|\boldsymbol{b}^{\mathrm{bot}}\|_{\mathrm{L}^2(\mathbb{R})}\right). \tag{7.109}$$

Triangular inequality shows that,

$$\|\boldsymbol{X}_1\|_{\mathrm{L}^2(\Omega_r)} \leq \sum_{n\in E}\|A_n\|_{\mathrm{L}^2(-r,r)}\left\|\frac{u_n}{J_n}\right\|_{\mathrm{L}^\infty(\mathrm{L}^2(-h,h))} + 2\sum_{j\in\mathbb{N}^*}\|A_j\|_{\mathrm{L}^2(-r,r)}\left\|\frac{u_j}{J_j}\right\|_{\mathrm{L}^\infty(\mathrm{L}^2(-h,h))}.$$

Asymptotic comparisons of u_j and J_j provided in Chapter 3 show that there exists $c_4 > 0$ such that

$$\|\boldsymbol{X}_1\|_{\mathrm{L}^2(\Omega_r)} \leq \left[c_4 + 4c_2c_3\sum_{j\in\mathbb{N}^*}\frac{1}{(2j\pm 1/2)\ln(2j\pm 1/2)^{3/2}}\right] \times \left(\|\boldsymbol{g}\|_{\mathcal{H}_r^2} + \|\boldsymbol{b}^{\mathrm{top}}\|_{\mathrm{L}^2(\mathbb{R})} + \|\boldsymbol{b}^{\mathrm{bot}}\|_{\mathrm{L}^2(\mathbb{R})}\right).$$

Similarly,

$$\|\mathbf{Y}_2\|_{\mathrm{L}^2(\Omega_r)} \leq \sum_{n\in E}\|B_n\|_{\mathrm{L}^2(-r,r)}\,\|v_n\|_{\mathrm{L}^\infty(\mathrm{L}^2(-h,h))} + 2\sum_{j\in\mathbb{N}^*}\|B_j\|_{\mathrm{L}^2(-r,r)}\,\|v_j\|_{\mathrm{L}^\infty(\mathrm{L}^2(-h,h))},$$

and there exists $c_5 > 0$ such that

$$\|\mathbf{Y}_2\|_{\mathrm{L}^2(\Omega_r)} \leq \left[c_5 + 4c_2c_3\sum_{j\in\mathbb{N}^*}\frac{1}{(2j\pm 1/2)\ln(2j\pm 1/2)^{3/2}}\right] \times \left(\|\boldsymbol{g}\|_{\mathcal{H}_r^2} + \|\boldsymbol{b}^{\mathrm{top}}\|_{\mathrm{L}^2(\mathbb{R})} + \|\boldsymbol{b}^{\mathrm{bot}}\|_{\mathrm{L}^2(\mathbb{R})}\right).$$

To conclude the proof, we invoke results on elliptical regularity [47] to deduce that there exists a constant $c_6 > 0$ such that

$$\|(\boldsymbol{X}, \boldsymbol{Y})\|_{\mathcal{H}_r} \leq c_6\left(\|(\boldsymbol{X}_1, \mathbf{Y}_2)\|_{\mathrm{L}^2(\Omega_r)} + \|\boldsymbol{g}\|_{\mathcal{H}_r^2} + \|\boldsymbol{b}^{\mathrm{top}}\|_{\mathrm{H}^{3/2}(\mathbb{R})} + \|\boldsymbol{b}^{\mathrm{bot}}\|_{\mathrm{H}^{3/2}(\mathbb{R})}\right).$$

Appendix 7.D: The Born approximation $(E_1)/(E_2)$

Using the operator Γ_2 introduced in Proposition 7.7, equation (E_1) can be rewritten

$$(\boldsymbol{X}^{(1)}, \boldsymbol{Y}^{(1)}) = \Gamma_2((0, -f_2, f_1, 0), \boldsymbol{b}^{\mathrm{top}}, \boldsymbol{b}^{\mathrm{bot}}) + \Gamma_2(\mathcal{T}_2(\boldsymbol{X}^{(1)}, \boldsymbol{Y}^{(1)}), \mathcal{T}_3(\boldsymbol{X}^{(1)}, \boldsymbol{Y}^{(1)})). \tag{7.110}$$

As a consequence of Appendix 7.B, the mapping $\Gamma_2 \circ (\mathcal{T}_2, \mathcal{T}_3)$ is a contraction in $\mathcal{H}_r^3$ if

$$\eta < \eta_3 := \frac{1}{2C_3C_4},$$

and (7.110) has a unique solution $(\boldsymbol{X}^{(1)}, \boldsymbol{Y}^{(1)}) \in \mathcal{H}_r^3$ which can be expressed as a Born series. The solution of $(\boldsymbol{X}^{(2)}, \boldsymbol{Y}^{(2)})$ of (E_2) is the first term of this series, and

$$\|(\boldsymbol{X}^{(1)}, \boldsymbol{Y}^{(1)}) - (\boldsymbol{X}^{(2)}, \boldsymbol{Y}^{(2)})\|_{\mathcal{H}_r^3} \leq \|\Gamma_2((0, -f_2, f_1, 0), \boldsymbol{b}^{\mathrm{top}}, \boldsymbol{b}^{\mathrm{bot}})\|_{\mathcal{H}_r^2 \times (\widetilde{H}^{3/2}(-r,r))^2} \frac{\eta}{\eta_3 - \eta}.$$

Using Proposition 7.7 on $\Gamma_2((0, -f_2, f_1, 0), \boldsymbol{b}^{\mathrm{top}}, \boldsymbol{b}^{\mathrm{bot}})$, we conclude the proof.

Appendix 7.E: Generalized mode at ZGV frequency

The asymptotic expansion of the expressions $\boldsymbol{X}_1$, $\boldsymbol{X}_2$, $\boldsymbol{Y}_1$ and $\boldsymbol{Y}_2$ given in (7.14) leads to

$$\begin{aligned}(\boldsymbol{X}_g)_1(y) = {} & i\frac{k_0(q_0^2 - k_0^2)}{p_0} \sin(q_0 h_0) \sin(p_0 y) y - 2ik_0^2 p_0 \sin(p_0 h_0) \sin(q_0 y) y \\ & - i\frac{(q_0^2 - k_0^2)k_0^2}{q_0} h_0 \cos(q_0 h_0) \cos(p_0 y) + 2ik_0^2 q_0 h_0 \cos(p_0 h) \cos(q_0 h) \\ & + i(q_0^2 - k_0^2) \sin(q_0 h_0) \cos(p_0 y) - 4ik_0^2 \sin(q_0 h) \cos(p_0 y) \\ & - 2ip_0 q_0 \sin(p_0 h_0) \cos(q_0 y) + i\frac{2k_0^2 q_0}{p_0} \sin(p_0 h) \cos(q_0 y) + i\frac{2k_0^2 p_0}{q_0} \sin(p_0 h) \cos(q_0 y),\end{aligned}$$

$$\begin{aligned}(\boldsymbol{X}_g)_2(y) = {} & 2i\mu(\sin(p_0 h_0) \sin(q_0 y) - \sin(q_0 h_0) \sin(p_0 y)) \left((q_0^2 - k_0^2) p_0 - 4k_0^2 p_0 - \frac{k_0^2}{p_0}(q_0^2 - k_0^2) \right) \\ & + 2ik_0^2 \mu (q_0^2 - k_0^2) \sin(q_0 h_0) \cos(p_0 y) - 2ik_0^2 \mu (q_0^2 - k_0^2) \frac{p_0}{q_0} \sin(p_0 h_0) \cos(q_0 y) y \\ & + 2ik_0^2 (q_0^2 - k_0^2) \frac{p_0}{q_0} h_0 \sin(p_0 y) \cos(q_0 h_0) - 2ik_0^2 (q_0^2 - k_0^2) h_0 \sin(q_0 y) \cos(p_0 h_0),\end{aligned}$$

$$\begin{aligned}(\boldsymbol{Y}_g)_1(y) = {} & -\left(4k_0((\lambda + 2\mu)k_0^2 + \lambda p_0^2) + (q_0^2 - k_0^2) \left(\frac{(\lambda + 2\mu)k_0}{p_0} + 2\lambda k_0 \right) \right) \sin(q_0 h_0) \cos(p_0 y) \\ & + (q_0^2 - k_0^2)((\lambda + 2\mu)k_0^2 + \lambda p_0^2) \left(\sin(q_0 h_0) \sin(p_0 y) \frac{k_0}{p_0} y - \cos(p_0 y) \cos(q_0 h_0) \frac{k_0}{q_0} h_0 \right) \\ & + \left(\frac{4\mu k_0^3 q_0}{p_0} + \frac{4\mu k_0^3 p_0}{q_0} - 8\mu p_0 q_0 k_0 \right) \sin(p_0 h_0) \cos(q_0 y) \\ & - 4\mu p_0 q_0 k_0^2 \left(\sin(p_0 h_0) \sin(q_0 y) \frac{k_0}{q_0} y - \cos(q_0 y) \cos(p_0 h_0) \frac{k_0}{p_0} h_0 \right),\end{aligned}$$

$$
\begin{aligned}
(\boldsymbol{Y}_g)_2(y) = (q_0^2 - k_0^2)k_0 \sin(q_0 h_0)\cos(p_0 y)y + 2\frac{k_0^3 p_0}{q_0}\sin(p_0 h_0)\cos(q_0 y)y \\
- \frac{p_0(q_0^2 - k_0^2)k_0}{q_0} h_0 \cos(q_0 h_0)\sin(p_0 y) + 2k_0^3 h_0 \cos(p_0 h)\sin(q_0 h) \\
+ \frac{k_0}{p_0}(q_0^2 - k_0^2)\sin(q_0 h_0)\sin(p_0 y) + 4k_0 \sin(q_0 h)\sin(p_0 y) \\
+ \frac{2k_0^3}{p_0}\sin(p_0 h_0)\sin(q_0 y) - 4k_0 p_0 \sin(p_0 h)\sin(q_0 y),
\end{aligned}
$$

It follows from the definition given in Theorem 3.1 that $(\boldsymbol{X}_g, \boldsymbol{Y}_g)$ is a generalized Lamb mode.

8

Conclusion

In this manuscript, we have presented our main original contributions. This last Chapter summarizes them and discusses their applications and limits. We also present some generalizations and possible future works in continuation of these different researches.

8.1 Main contributions

8.1.1 Summary of the results

Our work is structured into two main parts, each describing a different multi-frequency reconstruction method. The first method presented in Part I is a multi-frequency back-scattering inverse method relying on the small size and amplitude of defects. Under such assumption, the scattering field generated by an incident wave contains linear information about the Fourier transform of the defect. The main difficulty of this inversion is to deal with the lack of low frequency Fourier data due to the evanescent modes. This is the main difference with the classical back-scattering theory used in the free space. In Chapter 2, we recover the Fourier transform using section measurements in acoustic waveguides. Making a Born approximation and using a partial data Fourier inversion, we develop a new reconstruction method and control its accuracy. Numerical simulations are run on simulated data and show excellent recoveries of inhomogeneities, geometry defects, and bends in acoustic waveguides.

Our method's scope is then extended to elastic waveguides in Chapter 3. After studying the propagation of Lamb waves in regular elastic waveguides, we prove that the Born approximation can be generalized in the elastic case. It enables us to adapt our multi-frequency method to defects in elastic waveguides and provide a stable reconstruction of geometry defects. Again, we run numerical reconstructions on simulated data with good reconstruction results. Along with this chapter, we also exhibit a new mathematical framework to generalize the $\boldsymbol{X}/\boldsymbol{Y}$ formulation to the three-dimensional elastic plates.

The second part of this manuscript develops a different multi-frequency method focused on using locally resonant frequencies to recover width defects. Chapter 4 presents a complete mathematical study of the forward problem at these peculiar frequencies. Using Airy functions, we provide an explicit approximation of any wavefield propagating in a waveguide with varying width and we control this approximation.

This study of the forward problem is then used in Chapters 5 and 6 to recover width defects in scalar waveguides. Our reconstruction method uses different locally resonant frequencies and finds the associated locally resonant point $x^\star$ to recover the local width at this coordinate. In Chapter 5, we use surface measurements and prove that they are close to Airy functions depending on three parameters, one being $x^\star$. It provides a stable reconstruction of the waveguide's width, illustrated by convincing numerical reconstructions. In Chapter 6, we switch to section measurements and demonstrate that data can be post-treated to obtain an approximation of an integral quantity depending on $x^\star$. Then, we discretize this integral to recover the value of $x^\star$. If the width defect is monotonous, we also provide satisfactory numerical reconstructions.

Finally, in Chapter 7, we generalize this method to elastic waveguides with varying widths. In the elastic case, there are three types of critical points (longitudinal, transverse, and zero-group velocity), and we provide a complete study of the forward problem like in Chapter 4 near each critical point. Then, using surface measurements, we prove that we can recover the same type of three-parameters Airy function as in Chapter 5, which leads to a stable reconstruction of the width. We then compare numerical reconstructions using these three types of critical points.

8.1.2 Commentary and discussions on the results

The results and numerical simulations of the multi-frequency back-scattering method presented in Part I are encouraging. Under the assumptions of small defects in size and amplitude, we obtain precise reconstructions of inhomogeneities, bends, and geometry defects with relative errors of the order of a percent with noised measured data generated independently from the inverse solver. It is difficult to provide complete comparisons with other existing methods since the framework, the type of defects, and the assumptions are slightly different from ours. However, we can notice that our reconstruction results seem more precise than the one presented in [27, 34, 24] where a single working frequency is used, especially if we compare it with the back-scattering reconstructions. The same ascertainment holds when we compare our results with the multi-frequency method [9], where we recover the support and the volume of the defects as well or even better depending on the defect.

We also want to point out that this reconstruction method seems simpler to implement than the one presented in [27, 34]: indeed, it only requires sending the first propagative mode in the waveguide instead of all modes. Moreover, it fully uses the potential of physical measurements collected in the temporal regime and then turned into multi-frequency measurements, as explained in [55, 16].

Yet, this multi-frequency back-scattering method has some drawbacks as well. The more important one is that it needs an *a priori* information on the defect in the waveguide. Given the measurements of the scattered wavefield, it is not straightforward to differentiate an inhomogeneity, a bend, or a geometry defect and we did not prove that measurements could be used to identify the nature of the defects. Moreover, we did not study the detection of inclusions with boundaries or cracks in the waveguide. Therefore, our method needs to be used in cases where one looks for specific defects. Fortunately, it is often the case in the industrial applications we had in mind where one looks for corrosion defects [39] or structural deformations [101].

We also want to mention that since our method uses back-scattering data, the measurements are likely to have low amplitude compared to the incident wave. It could be a problem if measurement noises are too high or if defects are almost non-existent.

The second multi-frequency reconstruction method in Part II partially answers these last concerns. Indeed, one of the great benefits of using locally resonant frequencies is that the amplitude response is very high, even if we proved in Chapter 4 that it does not explode as initially thought. The measurement noise is, therefore, less of a problem. Moreover, we demonstrated that even the smallest width defect radically changes the propagation of waves at locally resonant frequencies, enabling us to reconstruct tiny defects.

Another great benefit of this method is that it does not require many hypotheses on the source of waves. We proved that as long as the source has a non-vanishing locally resonant component, it is possible to retrieve the location of the locally resonant point $x^\star$. This general framework is adapted to the non-destructive control of structures, where sources of waves are not always known entirely, and could also be of great use in non-destructive passive monitoring.

The main weakness of this second multi-frequency reconstruction method is that it can only reconstruct slowly varying width defects at present. Contrary to the multi-frequency method of Part I, this method can not detect width variations where the top and the bottom of the waveguides vary independently with functions h and g. In this situation, our method would only provide a reconstruction of the width differential $h - g$. More importantly, if [82] suggests that this method could be used to detect inhomogeneities, we did not study this situation at all in this manuscript. The reconstruction of inhomogeneities and the generalization to non slowly varying defects are part of the possible future works presented in the next section.

8.2 Future works

In this last section, we present our ongoing works and future idea to expand the scope of our multi-frequency reconstruction methods.

8.2.1 Reconstruction using experimental data

The numerical simulations presented in this manuscript were done using simulated data generated by finite element methods and perfectly matched layers. Since these numerical tests give excellent reconstructions of different defects even with noisy data, the next step would be to test these multi-frequency methods on experimental data. As mentioned in the introduction, the reconstruction method of Part I could be tested on experimental data generated at the "Laboratoire de Tribologie et Dynamique des Systèmes" at Ecole Centrale de Lyon, in collaboration with O. Bareille. Regarding Part II, it is designed to be applied to the experimental data available at "Institut Langevin" in Paris in collaboration with C. Prada.

To use the data provided by experiments done at "Laboratoire de Tribologie et Dynamique des Systèmes" [55, 54], we first need to adapt our methods. Indeed, the studied waveguide is a thin elastic cylinder in these experiments. However, experiments suggest that torsional waves in thin elastic cylinders satisfy a Helmholtz equation like wavefields in acoustic waveguides. We need to verify that this assumption is true and understand how defects in three-dimensional thin cylinders are passed on the Helmholtz equation to apply our reconstruction method. Using the studies of thin elastic shells done in [17, 42], we did an asymptotic analysis to approximate the problem by a two-dimensional equation on the surface of the cylinder, depending on the mean of the defects in the cylinder's thickness. Decomposing the displacement wavefield as $\boldsymbol{u} = (u_x, u_r, u_\theta)$ in cylinder coordinates, we prove that the displacement field (u_θ, u_x) satisfies up to a change of basis two Helmholtz equations

$$\left\{ \begin{array}{l} \partial_{zz} u_\theta + k_1^2 u_\theta = 0, \\ \partial_{zz} u_x + k_2^2 u_x = 0, \end{array} \right. \tag{8.1}$$

where k_1 and k_2 are modified frequencies depending on the initial frequency ω and the Lamé coefficients of the waveguide (λ, μ). Given a source term, we can compute a good approximation of the wavefield in thin cylinders, as illustrated in Figure 8.1.

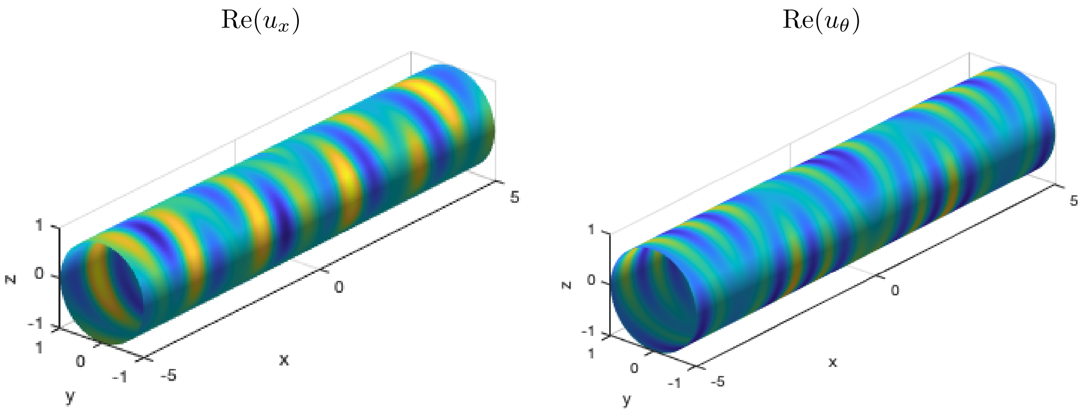
$\mathrm{Re}(u_x)$ $\mathrm{Re}(u_\theta)$

Figure 8.1 – Exemple of displacement wavefields u_z and u_θ in a thin cylinder. Here, $\omega = 25$, and an internal source located at $(x, \theta) = (0, \pi/4)$ generates the wavefield.

Even if we have already understood the forward problem in thin cylinders, we still have some work to do on this topic. Indeed, we have to provide control of the approximation error in our asymptotic analysis of the cylinder. Moreover, we need to control the wavefield by the source term in regular cylinders to prove that the Born approximation is still valid in this case. Once these theoretical points are sorted out, the results and reconstruction method presented in Chapter 1 will apply immediately, and we will be able to test our data on experimental data obtained in experiments [55, 54].

Less work is needed to apply the multi-frequency method developed in Part II to experimental data obtained at Institut Langevin. Some data are already available in [58] for three-dimensional width defects. Under certain radial symmetries, we hope that these data can be seen as measurements in two-dimensional waveguides. We are currently working on these data. Otherwise, it is possible to create slowly varying plates with width defect invariant in one direction to get real two-dimensional data and test our method in this experimental setup.

8.2.2 Generalization in three dimensions

Instead of reconstructing only two-dimensional defects, we can also think of generalizing our locally resonant multi-frequency inversion method to defects in three-dimensional plates or pipes. We have already started to study this situation in acoustic pipes. In the three-dimensional case, the main difference lies in the modal decomposition. Instead of using eigenelements of the negative laplacian in $(0, h)$, we need to consider the problem in each section of the waveguide. It still gives a basis of eigenfunctions φ_n and wavenumbers k_n, but they are no longer explicit. Like in the two-dimensional case, we have the modal decomposition $u = \sum u_n(x)\varphi_n(y,z)$. However, in the case of width defects, sections of the waveguide may vary, as represented in Figure 8.2.

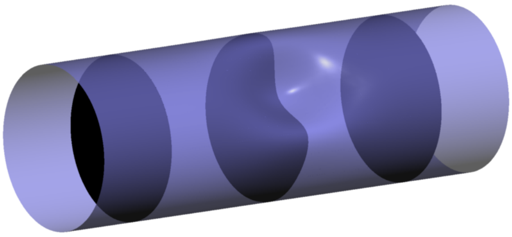

Figure 8.2 – Representation of a three dimensional pipe with a width defect. Three sections of the pipe are represented in black.

Then, k_n depends on the two parameters of the width defect, and the wavefield u can be decomposed as $u(x,y,z) = \sum u_n(x)k_n(x,y,z)$. We are confident that by adapting the strategy developed in Chapter 7 for Lamb modes, we can prove that each mode u_n is close to the solution of $u_n'' + k_n^2 u_n = 0$, which brings us back to the framework developed in Chapter 4 and 5. Using measurements of the wavefield, it might be possible to recover the vanishing of k_n. However, we no longer have a simple link between the vanishings of k_n and the parametrization of the defect. We should get access to a part of the eigenvalues of the Laplacien of each section and recovering the sections shape is now a classical and well studied problem [53]. Further research in this direction might provide some results to complete our reconstruction of three-dimension pipes.

As for the study of three-dimensional plates, we can use the study done in Chapter 3 to guess that if Born approximations are still valid, then each coefficient a_n of the modal decomposition should satisfy the equation

$$\Delta_2 a_n + k_n(x,y)^2 a_n = 0, \tag{8.2}$$

where k_n depends on the width variation $h(x,y)$. The framework is then different, and one needs to study this equation when k_n can vanish. However, given the already high complexity of the study made in Chapter 7 for two-dimensional elastic waveguide, we have chosen to leave this problem aside for now.

8.2.3 Study of the Lamb modes

Some questions are also left concerning the use of Lamb modes. Chapters 3 and 7 mentioned that every theorem proven in the elastic case needed more robust hypotheses on the source term regularity than in the acoustic case. It is due to the fact that the Lamb basis is not orthogonal and that there does not exist any substitution results to the Parceval equality. However, the theory developed in [72] might provide a different approach to control the rest in the Lamb mode sum. With some work, this theory could be used to improve the hypothesis needed on source terms in Chapters 3 and 7.

Another open question raised by our work concerns the study of inhomogeneities in elastic waveguides. As mentioned at the end of Chapter 3, we miss some results on Lamb modes to reconstruct inhomogeneities. In the acoustic case, we used the recovery of $\int f\,\varphi_n$ for some $n < N$

to get a good approximation of the source f. However, in the elastic case, our reconstruction method provides instead information on $\int f\,u_m$ where u_m are all the Lamb modes associated with a given real wavenumber k, as illustrated in Figure 8.3.

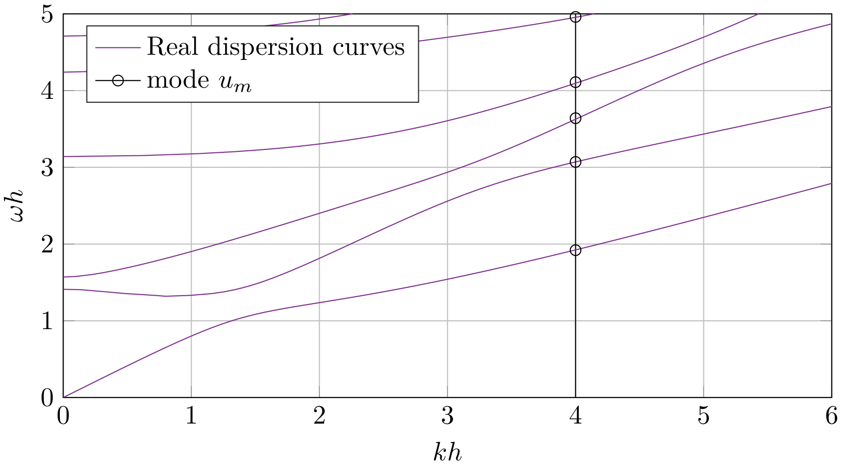

Figure 8.3 – Real symmetric Rayleigh-Lamb dispersion curves and associated modes at a fixed wavenumber $k = 4$.

Completeness of $(u_m)_{m>0}$ is established when the frequency ω is fixed [8], but completeness when the wavenumber k is fixed is an open question up to our knowledge. Numerically, functions u_m oscillate with an increasing frequency as m increases, and we guess that a result similar to the Fourier series decay may be accurate. However, we failed to prove a completeness result or a decomposition formula. It could be an interesting problem for specialists of the Lamb decomposition.

8.2.4 Study of discontinuous width variations

Finally, we have chosen to work in the second part of this manuscript with slowly varying waveguides in order to apply the existing results of Olver [76, 77]. However, we notice that most of the experiments at “Institut Langevin” are done with waveguides presenting with discontinuous steps [29, 11]. Studying this setup would be very interesting to understand the propagation of waves in varying-width waveguides. Some numerical tests ran in such waveguides suggest that similar behavior may occur near locally resonant frequencies, as illustrated in Figure 8.4. We notice that at each step, the wavefield behavior changes from an evanescent to a propagative mode like in the slowly varying waveguide.

However, the study carried on in slowly varying waveguides can not be reproduced in this situation since the Born approximation is not valid anymore, and different modes can mix. Note that the study of width steps is also interesting away from resonant frequencies since it was experimentally proved in [84, 28, 59] that such waveguides could act like negative index material when the size of the step is chosen well. Indeed, if we denote by h_1 and h_2 the two widths at discontinuity, a right-going mode can propagate at a frequency ω in the width h_1 and turn into a right-going mode at the width h_2 for the same frequency. Such a situation is illustrated in Figure 8.5.

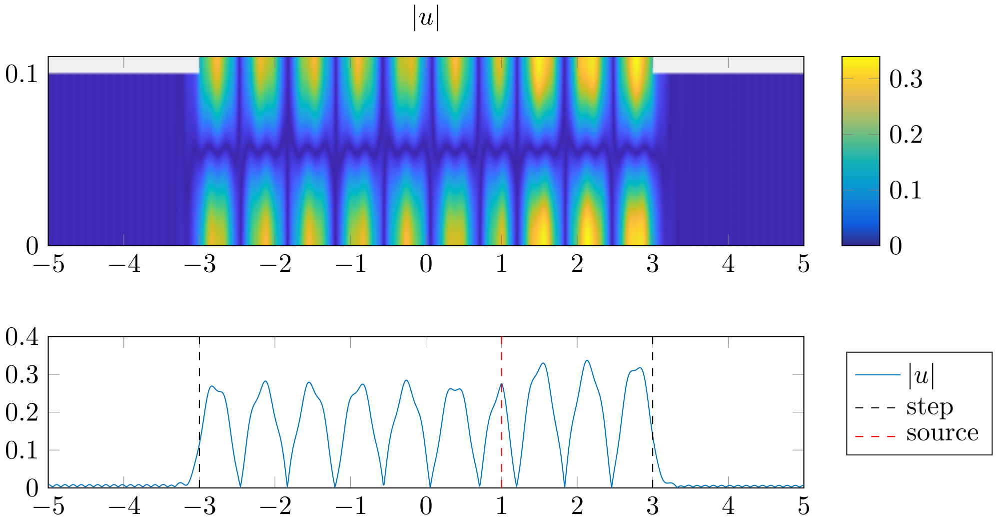

Figure 8.4 – Numerical simulation of an acoustic wavefield propagating in a waveguide with discontinuous variations of width. Here, the wavefield is generated by a source located at $x = 1$ and the frequency $k = 29$ is chosen such that k_1 is propagative inside the step and evanescent outside the step. On the top, we represent the wavefield in the whole waveguide, and on the bottom, we represent the measurements at $y = 0$.

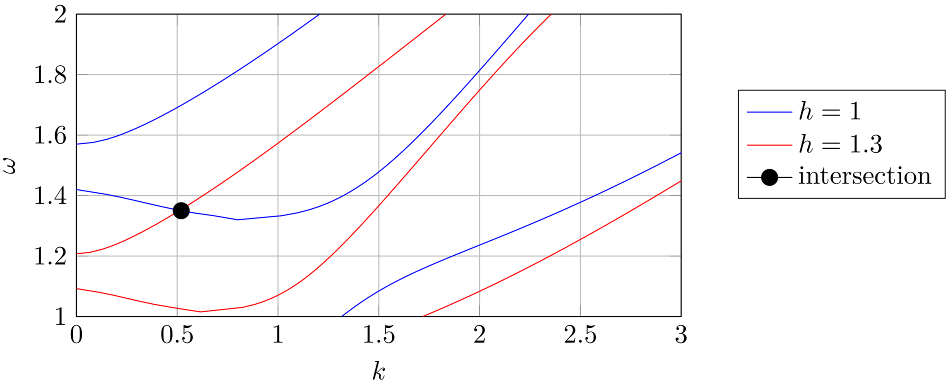

Figure 8.5 – Real Rayleigh-Lamb symmetric dispersion curves for two different widths $h = 1$ (in blue) and $h = 1.3$ (in red). At the intersection, these two curves intersect and the corresponding Lamb modes are left-going for $h = 1$ and right-going for $h = 1.3$.

The study of this problem at these particular frequencies is interesting with potential fallout in the conception of negative index materials and perfect lens, as explained in [58]. In a three-dimensional plate, we think that the surface wavefield generated by negative Lamb modes satisfies a propagation equation with a negative medium index. We started to look for asymptotic wavefield developments with respect to the length of the width step inspiring of the work [22] with the Green expansions provided in [23]. This work is still in process.

Bibliography

[1] K. Abbasi and H. Hashizume. Microwave detection of circumferential crack in piping system of nuclear power plants. In *Proc. 2nd Int. Conf. Technical Inspection NDT*, 2008.

[2] L. Abrahamsson. Orthogonal grid generation for two-dimensional ducts. *Journal of Computational and Applied Mathematics*, 34(3):305–314, 1991.

[3] L. Abrahamsson and H. O. Kreiss. Numerical solution of the coupled mode equations in duct acoustics. *Journal of Computational Physics*, 111(1):1–14, 1994.

[4] M. Abramowitz and I. A. Stegun. *Handbook of Mathematical Functions: With Formulas, Graphs, and Mathematical Tables.* Applied mathematics series. Dover Publications, 1965.

[5] J. D. Achenbach. *Wave propagation in elastic solids.* North-Holland Series in Applied Mathematics and Mechanics. Elsevier, Amsterdam, 1975.

[6] J. D. Achenbach and Y. Xu. Use of elastodynamic reciprocity to analyze point-load generated axisymmetric waves in a plate. *Wave Motion*, 30(1):57–67, 1999.

[7] S. Acosta, S. Chow, J. Taylor, and V. Villamizar. On the multi-frequency inverse source problem in heterogeneous media. *Inverse Problems*, 28(7):075013, 2012.

[8] J.-L. Akian. A proof of the completeness of lamb modes. *Mathematical Methods in the Applied Sciences*, 45(3):14021419, 2021.

[9] H. Ammari, E. Iakovleva, and H. Kang. Reconstruction of a small inclusion in a two-dimensional open waveguide. *SIAM Journal on Applied Mathematics*, 65(6):2107–2127, 2005.

[10] T. Angkaew, M. Matsuhara, and N. Kumagai. Finite-element analysis of waveguide modes: A novel approach that eliminates spurious modes. *IEEE Transactions on Microwave Theory and Techniques*, 35(2):117–123, 1987.

[11] O. Balogun, T. W. Murray, and C. Prada. Simulation and measurement of the optical excitation of the s1 zero group velocity lamb wave resonance in plates. *Journal of Applied Physics*, 102(6):064914, 2007.

[12] G. Bao and P. Li. Inverse medium scattering problems for electromagnetic waves. *SIAM Journal on Applied Mathematics*, 65(6):2049–2066, 2005.

[13] G. Bao and F. Triki. Reconstruction of a defect in an open waveguide. *Science China Mathematics*, 56(12):2539–2548, 2013.

[14] G. Bao and F. Triki. Stability for the multifrequency inverse medium problem. *Journal of Differential Equations*, 269(9):7106–7128, 2020.

[15] V. Baronian, A. Bonnet-Ben Dhia, and E. Lunéville. Transparent boundary conditions for the harmonic diffraction problem in an elastic waveguide. *Journal of Computational and Applied Mathematics*, 234(6):1945–1952, 2010.

[16] V. Baronian, L. Bourgeois, B. Chapuis, and A. Recoquillay. Linear Sampling Method applied to Non Destructive Testing of an elastic waveguide: theory, numerics and experiments . *Inverse Problems*, 34(7):075006, 2018.

[17] M. Beaudouin. *Analyse modale pour les coques minces en révolution*. PhD thesis, Université Rennes 1, 2010.

[18] J. P. Berenger. A perfectly matched layer for the absorption of electromagnetic waves. *Journal of Computational Physics*, 114(2):185–200, 1994.

[19] H. Besserer and P. G. Malischewsky. Mode series expansions at vertical boundaries in elastic waveguides. *Wave Motion*, 39(1):41–59, 2004.

[20] H. Bhatia, G. Norgard, V. Pascucci, and P. Bremer. The helmholtz-hodge decomposition - a survey. *IEEE Transactions on Visualization and Computer Graphics*, 19(8):1386–1404, 2013.

[21] A. S. Bonnet-Ben Dhia, C. Chambeyron, and G. Legendre. On the use of perfectly matched layers in the presence of long or backward propagating guided elastic waves. *Wave Motion*, 51(2):266–283, 2014.

[22] E. Bonnetier and F. Triki. Asymptotic of the Green function for the diffraction by a perfectly conducting plane perturbed by a sub-wavelength rectangular cavity. *Mathematical Methods in the Applied Sciences*, 33(6):772–798, 2010.

[23] L. Borcea and S. Meng. Factorization method versus migration imaging in a waveguide. *Inverse Problems*, 35(12):124006, 2019.

[24] L. Borcea and D. L. Nguyen. Imaging with electromagnetic waves in terminating waveguides. *Inverse Problems and Imaging*, 10(4):915–941, 2016.

[25] L. Bourgeois and S. Fliss. On the identification of defects in a periodic waveguide from far field data. *Inverse Problems*, 30(9), 2014.

[26] L. Bourgeois, J.-F. Fritsch, and A. Recoquillay. Scattering in a partially open waveguide: the inverse problem. preprint, 2022.

[27] L. Bourgeois and E. Lunéville. The linear sampling method in a waveguide: A modal formulation. *Inverse Problems*, 24(1), 2008.

[28] S. Bramhavar, C. Prada, A. A. Maznev, A. G. Every, T. B. Norris, and T. W. Murray. Negative refraction and focusing of elastic lamb waves at an interface. *Physical Review B*, 83:014106, 2011.

[29] M. Cès. *Etude théorique et expérimentale des résonances mécaniques locales de modes guidés par des structures complexes*. Theses, Université Paris-Diderot - Paris VII, 2012.

[30] A. J. Chorin, J. E. Marsden, and J. E. Marsden. *A mathematical introduction to fluid mechanics*, volume 3. Springer, 1990.

[31] D. Colton and A. Kirsch. A simple method for solving inverse scattering problems in the resonance region. *Inverse Problems*, 12(4):383–393, 1996.

[32] D. Colton and R. Kress. *Inverse Acoustic and Electromagnetic Scattering Theory.* Applied Mathematical Sciences. Springer Berlin Heidelberg, 1997.

[33] P. J. Davis and P. Rabinowitz. *Methods of Numerical Integration.* Academic Press, second edition, 1984.

[34] S. Dediu and J. R. McLaughlin. Recovering inhomogeneities in a waveguide using eigensystem decomposition. *Inverse Problems*, 22(4):1227–1246, 2006.

[35] M. D. Deshpande, C. J. Reddy, P. I. Tiemsin, and R. Cravey. A new approach to estimate complex permittivity of dielectric materials at microwave frequencies using waveguide measurements. *IEEE Transactions on Microwave Theory and Techniques*, 45(3):359–366, 1997.

[36] A. S. B.-B. Dhia, L. Chesnel, and S. A. Nazarov. Perfect transmission invisibility for waveguides with sound hard walls. *Journal de Mathématiques Pures et Appliquées*, 111:79–105, 2018.

[37] *NIST Digital Library of Mathematical Functions.* `http://dlmf.nist.gov/`, Release 1.1.5 of 2022-03-15. F. W. J. Olver, A. B. Olde Daalhuis, D. W. Lozier, B. I. Schneider, R. F. Boisvert, C. W. Clark, B. R. Miller, B. V. Saunders, H. S. Cohl, and M. A. McClain, eds.

[38] H. Dym and H. P. McKean. *Fourier series and integrals.* Academic Press New York, 1972.

[39] G. L. DSpain and W. A. Kuperman. Application of waveguide invariants to analysis of spectrograms from shallow water environments that vary in range and azimuth. *The Journal of the Acoustical Society of America*, 106(5):2454–2468, 1999.

[40] L. C. Evans. *Partial Differential Equations.* Graduate studies in mathematics. American Mathematical Society, 2010.

[41] A. T. Fabro, N. S. Ferguson, and B. R. Mace. Wave propagation in slowly varying waveguides using a finite element approach. *Journal of Sound and Vibration*, 442:308–329, 2019.

[42] E. Faou. *Développements asymptotiques dans les coques minces linéairement élastiques.* PhD thesis, Rennes 1, 2000.

[43] A. Folguera and J. G. Harris. Coupled raleigh surface waves in slowly varying elastic waveguide. *Proceedings of the Royal Society of London. Series A: Mathematical, Physical and Engineering Sciences*, 455(1983):917–931, 1999.

[44] W. B. Fraser. Orthogonality relation for the rayleighlamb modes of vibration of a plate. *The Journal of the Acoustical Society of America*, 59(1):215–216, 1976.

[45] E. J. Friebele, C. G. Askins, M. E. Gingerich, and K. J. Long. Optical fiber waveguides in radiation environments, ii. *Nuclear Instruments and Methods in Physics Research Section B: Beam Interactions with Materials and Atoms*, 1(2):355–369, 1984.

[46] V. B. Galanenko. On coupled modes theory of two-dimensional wave motion in elastic waveguides with slowly varying parameters in curvilinear orthogonal coordinates. *The Journal of the Acoustical Society of America*, 103(4):1752–1762, 1998.

[47] P. Grisvard. *Elliptic Problems in Nonsmooth Domains.* Society for Industrial and Applied Mathematics, 2011.

[48] G. W. Hanson. Quasi-transverse electromagnetic modes supported by a graphene parallel-plate waveguide. *Journal of Applied Physics*, 104(8):084314, 2008.

[49] F. Hecht. New development in freefem++. *J. Numer. Math.*, 20(3-4):251–265, 2012.

[50] F. Honarvar, F. Salehi, V. Safavi, A. Mokhtari, and A. N. Sinclair. Ultrasonic monitoring of erosion/corrosion thinning rates in industrial piping systems. *Ultrasonics*, 53(7):1251–1258, 2013.

[51] M. Isaev and R. G. Novikov. Hölder-logarithmic stability in fourier synthesis. *Inverse Problems*, 36(12):125003, 2020.

[52] V. Isakov and S. Lu. Increasing stability in the inverse source problem with attenuation and many frequencies. *SIAM J. Appl. Math.*, 78:1–18, 2018.

[53] M. Kac. Can one hear the shape of a drum? *The American Mathematical Monthly*, 73(4):1–23, 1966.

[54] M. Kharrat, O. Bareille, W. Zhou, and M. Ichchou. Nondestructive assessment of plastic elbows using torsional waves: Numerical and experimental investigations. *Journal of Nondestructive Evaluation*, 35(1):1–14, 2016.

[55] M. Kharrat, M. N. Ichchou, O. Bareille, and W. Zhou. Pipeline inspection using a torsional guided-waves inspection system. part 1: Defect identification. *International Journal of Applied Mechanics*, 6(4), 2014.

[56] P. Kirrmann. On the completeness of lamb modes. *Journal of Elasticity*, 37(1):39–69, 1994.

[57] J. G. Kretzschmar. Wave propagation in hollow conducting elliptical waveguides. *IEEE Transactions on Microwave Theory and Techniques*, 18(9):547–554, 1970.

[58] F. Legrand. *Ondes de Lamb et Réfraction Négative.* PhD thesis, Sorbonne University , UPMC, 2020.

[59] F. Legrand, B. Gérardin, J. Laurent, C. Prada, and A. Aubry. Negative refraction of lamb modes: A theoretical study. *Physical Review B*, 98(21), 2018.

[60] H. R. Locker and J. Locker. *Spectral theory of non-self-adjoint two-point differential operators.* American Mathematical Soc., 2000.

[61] Y. Y. Lu. Exact one-way methods for acoustic waveguides. *Mathematics and Computers in Simulation*, 50(5):377–391, 1999.

[62] Y. Y. Lu. A fourth-order magnus scheme for helmholtz equation. *Journal of Computational and Applied Mathematics*, 173(2):247–258, 2005.

[63] A. Mal, F. Ricci, S. Banerjee, and F. Shih. A conceptual structural health monitoring system based on vibration and wave propagation. *Structural Health Monitoring*, 4(3):283–293, 2005.

[64] S. Mallat. *A Wavelet Tour of Signal Processing, Chapter 1: Sparse Representations.* Academic Press, Boston, third edition, 2009.

[65] V. Maupin. Surface waves across 2-D structures: a method based on coupled local modes. *Geophysical Journal International*, 93(1):173 – 185, 1988.

[66] W. McLean. *Strongly Elliptic Systems and Boundary Integral Equations.* Cambridge University Press, 2000.

[67] L. G. Merkulov, S. I. Rokhlin, and O. P. Zobnin. Calculation of the spectrum of wave numbers for lamb waves in a plate. *The Soviet journal of nondestructive testing*, 6:369–373, 1970.

[68] D. A. Mitsoudis, C. Makridakis, and M. Plexousakis. Helmholtz equation with artificial boundary conditions in a two-dimensional waveguide. *SIAM Journal on Mathematical Analysis*, 44(6):4320–4344, 2012.

[69] F. Moser, L. J. Jacobs, and J. Qu. Modeling elastic wave propagation in waveguides with the finite element method. *NDT and E International*, 32(4):225–234, 1999.

[70] T. W. Murray and O. Balogun. High-sensitivity laser-based acoustic microscopy using a modulated excitation source. *Applied Physics Letters*, 85(14):2974–2976, 2004.

[71] R. Nawaz, M. Afzal, and M. Ayub. Acoustic propagation in two-dimensional waveguide for membrane bounded ducts. *Communications in Nonlinear Science and Numerical Simulation*, 20(2):421–433, 2015.

[72] S. A. Nazarov. The mandelstam energy radiation conditions and the umov–poynting vector in elastic waveguides. *Journal of Mathematical Sciences*, 195(5):676–729, 2013.

[73] R. B. Nielsen and N. Peake. Tunnelling effects for acoustic waves in slowly varying axisymmetric flow ducts. *Journal of Sound and Vibration*, 380:180–191, 2016.

[74] C. M. Nilsson, C. J. C. Jones, D. J. Thompson, and J. Ryue. A waveguide finite element and boundary element approach to calculating the sound radiated by railway and tram rails. *Journal of Sound and Vibration*, 321(3):813–836, 2009.

[75] M. Norgren, M. Dalarsson, and A. Motevasselian. Reconstruction of boundary perturbations in a waveguide. *2013 International Symposium on Electromagnetic Theory*, pages 934–937, 2013.

[76] F. W. J. Olver. Error bounds for the liouvillegreen (or wkb) approximation. *Mathematical Proceedings of the Cambridge Philosophical Society*, 57(4):790–810, 1961.

[77] F. W. J. Olver. Error bounds for first approximations in turning-point problems. *Journal of the Society for Industrial and Applied Mathematics*, 11(3):748–772, 1963.

[78] F. W. J. Olver, D. W. Lozier, R. F. Boisvert, and C. W. Clark. *NIST handbook of mathematical functions.* Cambridge university press, 2010.

[79] V. Pagneux and A. Maurel. Determination of lamb mode eigenvalues. *The Journal of the Acoustical Society of America*, 110(3):1307–1314, 2001.

[80] V. Pagneux and A. Maurel. Lamb wave propagation in inhomogeneous elastic waveguides. *Proceedings of the Royal Society of London. Series A: Mathematical, Physical and Engineering Sciences*, 458(2024):1913–1930, 2002.

[81] V. Pagneux and A. Maurel. Lamb wave propagation in elastic waveguides with variable thickness. *Proceedings of the Royal Society A: Mathematical, Physical and Engineering Sciences*, 462(2068):1315–1339, 2006.

[82] M. V. Perel, J. D. Kaplunov, and G. A. Rogerson. An asymptotic theory for internal reflection in weakly inhomogeneous elastic waveguides. *Wave Motion*, 41(2):95–108, 2005.

[83] R. A. Pethrick. *Non-Destructive Evaluation (NDE) of Polymer Matrix Composites.* Woodhead Publishing Series in Composites Science and Engineering. Woodhead Publishing, 2013.

[84] F. D. Philippe, T. W. Murray, and C. Prada. Focusing on plates: Controlling guided waves using negative refraction. *Scientific Reports*, 5(1):11112, 2015.

[85] C. Prada, D. Clorennec, and D. Royer. Power law decay of zero group velocity lamb modes. *Wave Motion*, 45(6):723–728, 2008.

[86] A. Pécout. EDF de plus en plus inquiet pour son parc nucléaire, en raison de problèmes de corrosion. *Le Monde*, `https://www.lemonde.fr/economie/article/2022/04/21/edf-de-plus-en-plus-inquiet-pour-son-parc-nucleaire-en-raison-de-problemes-de-corrosion_6123074_3234.html`, 2022. Accessed: 2022.04.25.

[87] B. M. A. Rahman, F. A. Fernandez, and J. B. Davies. Review of finite element methods for microwave and optical waveguides. *Proceedings of the IEEE*, 79(10):1442–1448, 1991.

[88] P. C. Ribeiro, H. F. de Campos Velho, and H. Lopes. Helmholtzhodge decomposition and the analysis of 2d vector field ensembles. *Computers and Graphics*, 55:80–96, 2016.

[89] Roctest. Systèmes de surveillance de la sécurité des pipelines. *Le Monde*, `https://roctest.com/fr/application/pipeline/`. Accessed: 2022.05.02.

[90] S. Roy, A. K. Ghatak, I. C. Goyal, and R. L. Gallawa. Modified airy function method for the analysis of tunneling problems in optical waveguides and quantum-well structures. *IEEE Journal of Quantum Electronics*, 29(2):340–345, 1993.

[91] D. Royer, D. P. Morgan, and E. Dieulesaint. *Elastic Waves in Solids I: Free and Guided Propagation.* Advanced Texts in Physics. Springer Berlin Heidelberg, 1999.

[92] J. Sarkar, C. Marandet, P. Roux, S. Walker, B. D. Cornuelle, and W. A. Kuperman. Sensitivity kernel for surface scattering in a waveguide. *The Journal of the Acoustical Society of America*, 131(1):111–118, 2012.

[93] M. Sini and N. T. Thanh. Inverse acoustic obstacle scattering problems using multifrequency measurements. *Inverse Problems and Imaging*, 6(4):749–773, 2012.

[94] W. S. Slaughter. *The Linearized Theory of Elasticity.* Birkhäuser Boston, 2002.

[95] A. Sommerfeld. *Partial Differential Equations in Physics.* Academic press, 1949.

[96] D. D. Stancil, O. K. Tonguz, A. Xhafa, A. Cepni, P. Nikitin, and D. Brodtkorb. High-speed internet access via hvac ducts: a new approach. 6:3604–3607, 2001.

[97] S. Stange. *Die Ausbreitung von Oberflächenwellen in Erdmodellen mit ebenen und zylindrischen vertikalen Strukturgrenzen.* PhD thesis, Inst. für Geophysik der Univ., 1992.

[98] G. Szwoch and B. Kostek. Waveguide model of the hearing aid earmold system. *Diagnostic Pathology*, 1(1):6, 2006.

[99] J. Todd. The condition number of the finite segment of the hilbert matrix. *National Bureau of Standarts, Applied Mathematics Series*, (39):109–119, 1954.

[100] F. Treyssède. Three-dimensional modeling of elastic guided waves excited by arbitrary sources in viscoelastic multilayered plates. *Wave Motion*, 52:33–53, 2015.

[101] V. S. Tynchenko, A. V. Milov, S. O. Kurashkin, V. E. Petrenko, Y. A. Tynchenko, and D. V. Rogova. Mathematical model of the waveguide pipe heating in the process of induction brazing. *IOP Conference Series: Materials Science and Engineering*, 1047(1):012112, 2021.

[102] G. Uhlmann. *Inverse Problems and Applications: Inside Out II.* Mathematical Sciences Research Institute Publications. Cambridge University Press, 2013.

[103] A. Wiebel, G. Scheuermann, and C. Garth. Feature detection in vector fields using the helmholtz-hodge decomposition. Master's thesis, University of Kaiserslautern, 2004.

[104] P. Wilcox. Modeling the excitation of lamb and sh waves by point and line sources. *AIP Conference Proceedings*, 700(1):206–213, 2004.

[105] C. Willberg, S. Duczek, J. M. Vivar-Perez, and Z. A. B. Ahmad. Simulation Methods for Guided Wave-Based Structural Health Monitoring: A Review. *Applied Mechanics Reviews*, 67(1), 2015. 010803.

[106] A. Williams. Best practice and innovation in the non-destructive testing of composites. *Aerospace testing international*, `https://www.aerospacetestinginternational.com/features/the-latest-developments-in-technology-and-standards-for-the-ndt-of-composites.html`, 2021. Accessed: 2022.05.02.

[107] E. G. Williams. *Fourier Acoustics.* Academic Press, 1999.

[108] Yateks. What is nondestructive testing? *FAQ of Borescope*, `https://yateks.com/what-is-nondestructive-testing/`, 2019. Accessed: 2022.05.02.

[109] C. Zhao and P. Wang. Controlling bridge vibrations using a viscoelastic waveguide absorber. *Proceedings of the Institution of Mechanical Engineers, Part F: Journal of Rail and Rapid Transit*, 232(4):1088–1102, 2018.

dernière page de la thèse

AUTORISATION DE SOUTENANCE

Vu les dispositions de l'arrêté du 25 mai 2016,

Vu la demande du directeur de thèse

Monsieur G. VIAL

et les rapports de

Mme F. CAKONI
Distinguished Professor - Department of Mathematics, Rutgers University, 722 Hill Center
Busch Campus,110 Frelinghuysen Road, Piscataway, NJ 08854-8019, USA

et de

M. Y. CAPDEBOSCQ
Professeur - Bureau 5018 Bâtiment Sophie Germain - Université de Paris
8 Place Aurélie Nemours - 75205 Paris Cedex 13

Madame NICLAS Angèle

est autorisée à soutenir une thèse pour l'obtention du grade de **DOCTEUR**

Ecole doctorale Informatique et Mathématiques

Fait à Ecully, le 5 juillet 2022

Le directeur de l'Ecole centrale de Lyon

Service Scolarité

Pascal RAY

Problèmes inverses et résonances locales dans les guides d'ondes mécaniques irréguliers

Résumé : La détection et la reconstruction de défauts dans les guides d'ondes sont un enjeu contemporain important pour contrôler l'état de structures diverses allant des oléoducs aux fibres optiques, en passant par les conduits de centrales nucléaires ou les coques de navires. Cette thèse a pour but de mieux comprendre d'un point de vue mathématique la propagation des ondes en guide d'onde, pour pouvoir ensuite proposer des méthodes efficaces pour détecter et reconstruire avec précision d'éventuels défauts. Pour modéliser au mieux les dispositifs expérimentaux disponibles, on choisit ici d'utiliser des ondes se propageant à des fréquences variables et parfois voisines des fréquences de résonances. Si les fréquences sont éloignées des résonances, on montre que la reconstruction de défaut s'apparente à de l'inversion de Fourier avec données partielles, ce qui permet de reconstruire de manière stable la plupart des petits défauts présents dans les guides d'ondes. Si la fréquence est proche des résonances, les équations mathématiques sont très mal posées mais les ondes sont particulièrement sensibles aux défauts présents dans le guide. Des parallèles avec des travaux de physique quantique permettent une approximation asymptotique formelle de ces ondes sous forme de fonctions d'Airy lorsque le guide varie lentement. Grâce à ces approximations, on propose une méthode précise se basant sur le profil des fonctions d'Airy pour reconstruire entièrement les défauts de hauteur du guide.

Mots clés : guides d'ondes, problèmes inverses, contrôle non destructif, propagation des ondes, données multi-fréquencielles, équation de Helmholtz, équation du déplacement élastique, résonances locales.

Inverse problems and local resonances in irregular mechanical waveguides

Abstract : Localization and reconstruction of defects in waveguides are crucial in the nondestructive evaluation of structures like pipelines, optics fibers, nuclear power plant conduits, or even ship hulls. This thesis aims to understand waves propagation in waveguides from a mathematical point of view to design new efficient methods to detect and reconstruct potential waveguides defects. To fit the existing experimental setups, we use multi-frequency data with frequencies sometimes close to resonant ones. Far from the resonant frequencies, we prove that the defects reconstruction is equivalent to a Fourier inversion from partial data, and we provide a stable reconstruction method working for small defects. On the other hand, mathematical equations are not well-posed near resonant frequencies, but waves seem very sensitive to potential defects. Drawing a parallel with quantum mechanics, we provide an asymptotic approximation of these waves as Airy functions when the width of the waveguide slowly varies. Using these approximations, we develop a precise method based on the shape of Airy functions to reconstruct width defects in waveguides.

Keywords : waveguides, inverse problems, non-destructing testing, wave propagation, mutli-frequency data, Helmholtz equation, elastic displacement equation, locally resonances.

Image en couverture : Propagation d'une onde acoustique aux fréquences localement résonantes.

ED 512
INFOMATHS
Ecole doctorale

UNIVERSITÉ
DE LYON